Volume 22 · Issue 6
December 2025

Asian Journal of WATER, ENVIRONMENT AND POLLUTION

ISSN: 0972-9860 (Print)
ISSN: 1875-8568 (Online)



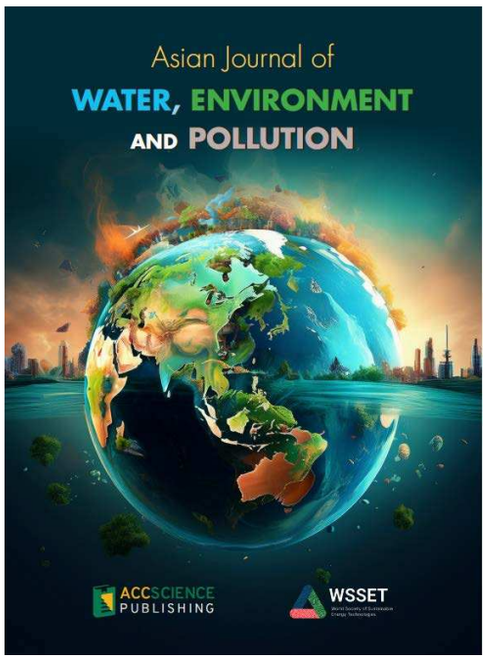
ACCSCIENCE PUBLISHING

WSSET
World Society of Sustainable Energy Technologies

Asian Journal of Water, Environment and Pollution

Print ISSN: 0972-9860
Online ISSN: 1875-8568

Asian Journal of Water, Environment and Pollution is an international, peer-reviewed, academic Open Access journal. It aims to publish high-quality, original research and practical solutions across a wide range of topics that address global environmental challenges. These include water availability and pollution management, global warming and climate adaptation, solid and liquid waste management, mining impacts and environmental degradation, renewable energy integration, energy access and sustainability, and policy analysis focused on social equity. The journal also covers infrastructure development, transnational water body pollution, energy storage and conversion, low-carbon and zero-energy buildings, and sustainable transport systems.



About the Publisher

AccScience Publishing is a publishing company based in Singapore. We publish a range of high-quality, open-access, peer-reviewed journals and books from a broad spectrum of disciplines.

Contact Us

Managing Editor
ajwep.office@accscience.sg

AccScience Publishing
9 Raffles Place, Republic Plaza 1 #06-00 Singapore 048619.

Volume 22 • Issue 6 • December 2025
ISSN 0972-9860 (print) ISSN 1875-8568 (online)

Asian Journal of Water, Environment and Pollution

Editor-in-Chief
Chengyun Zhou
Hunan University, Changsha, China

ACCSCIENCE PUBLISHING
Access Science Without Barriers

Full issue copyright © 2025 AccScience Publishing
All rights reserved. Without permission in writing from the publisher, this full issue publication in its entirety may not be reproduced or transmitted for commercial purposes in any form or by any means, electronic or mechanical, including photocopying, recording, or any information storage and retrieval system. Permissions may be sought from ajwep.office@accscience.sg.

Article copyright © Respective Author(s)
See articles for copyright year. All articles in this full issue publication are open-access. There are no restrictions in the distribution and reproduction of individual articles, provided the original work is properly cited. However, permission to reuse copyrighted materials of an article for commercial purposes is applicable if the article is licensed under Creative Commons Attribution-NonCommercial License. Check the specific license before reusing.

ASIAN JOURNAL OF WATER, ENVIRONMENT AND POLLUTION

ISSN: 0972-9860 (print)
ISSN: 1875-8568 (online)

Editorial and Production Credits

Publisher: AccScience Publishing
Managing Editor: Alyssa Li
Production Editor: Samyuktha Balakrishnan
Article Layout and Typeset: Sinjore Technologies (India)

For all advertising queries, contact ajwep.office@accscience.sg.

Supplementary file

Supplementary files of articles can be obtained at https://accscience.com/journal/AJWEP/22/6.



Disclaimer

AccScience Publishing is not liable to the statements, perspectives, and opinions contained in the publications. The appearance of advertisements in the journal shall not be construed as a warranty, endorsement, or approval of the products or services advertised and/or the safety thereof. AccScience Publishing disclaims responsibility for any injury to persons or property resulting from any ideas or products referred to in the publications or advertisements. AccScience Publishing remains neutral with regard to jurisdictional claims in published maps and institutional affiliations.

Asian Journal of Water, Environment and Pollution

Editorial Board

Editor-in-Chief

Chengyun Zhou, *China*

Executive Editor

Upaka Rathnayake, *Ireland*

Associate Editors

Ziwei Chen, *UK*
Min Cheng, *China*
Maocai Shen, *China*
Wenjun Wang, *China*

Editorial Board Members*

Mardiana Idayu Ahmad, *Malaysia*
Khalil Ahmad, *Pakistan*
Awais Ahmad, *Pakistan*
Abdeltif Amrane, *France*
Amit Awasthi, *India*
Rohit B. Meshram, *India*
Abubakr Bahaj, *UK*
Rangan Banerjee, *India*
Michele Bottarelli, *Italy*
Laura Bulgariu, *Romania*
Salvatore Carlucci, *Cyprus*
Constantinos Cartalis, *Greece*
Wei-Hsin Chen, Taiwan
Yulong Ding, *UK*
Muhammad Ehsan, *Mexico*
Daniele Fattorini, *Italy*
Francesco Fiorito, *Australia*
Gagné François, *Canada*
Yang Gao, *China*
Vladimir I. Golik, *Russia*
Qiulai He, *China*
Md. Emran Hossain, *USA*
Jie Ji, *China*
Nadeem Ahmad Khan, *India*
Ali Kilicarslan, *Turkey*
Roman V. Klyuev, *Russia*
Chee Kong YAP, *Malaysia*
Katarzyna Kubiak-Wójcicka, *Poland*
Angui Li, *China*
Qiang Li, *China*
Qingchao Li, *China*
Xiuhong Li, *China*
Tapas Mallick, *UK*
Edward Ng, *China*
Armando Oliveira, *Portugal*
Mohammad Oves, *Saudi Arabia*
Maulin P Shah, *India*
Ashok Pandey, *India*
Pradhan Parth Sarthi, *India*
Gang Pei, *China*
Richard Powell, *UK*
Ram Prasad, *India*
Namal Rathnayake, *Japan*
K. Srinivas Reddy, *India*
Prakash Sarangi, *India*
Li Shao, *UK*
Binbin Shao, *China*
Jichao Sun, *China*
Kwok Wai Tham, *Singapore*
Chi-Hwa Wang, *Singapore*
Ruzhu Wang, *China*
Liu Wen, *China*
Yuying Yan, *UK*
Hongxing Yang, *China*
Yi Yang, *China*
Weiming Zhang, *China*
Lizhi Zhang, *China*
Xudong Zhao, *UK*
Tianshou Zhao, *China*
Shuai Zhou, *China*
Maiyong Zhu, *China*
Yingxin Zhu, *China*
Muhammad Zubair, *Pakistan*
Walter Timo de Vries, *Germany*

Youth Editorial Board Members

Mingming Ge, *China*
Dongdong Ge, *China*
Zhang Hemeng, *China*
Shaokun Li, *China*
Jun Liu, *China*
Sicheng Shao, *China*
Dejun Yang, *China*

*Editorial Board Members as of December 3, 2025

ACCSCIENCE PUBLISHING

Volume 22 | Issue 6 | December 2025 | Page 1 – 242 |

Asian Journal of Water, Environment and Pollution

https://accscience.com/journal/AJWEP

CONTENTS

REVIEW ARTICLES

1 **Sustainable soybean cultivation using nitrogen-fixing bacteria and humic products derived from agricultural waste: A review**
Yurii Syromiatnykov

21 **Hydrocarbons in seawater: Sources, fate, impacts, and remediation strategies**
Daniele Fattorini

ORIGINAL RESEARCH ARTICLES

47 **Statistical analysis of wind energy potential in Mongo, Chad, for small-scale renewable applications**
Ali Sidick Bahar, Adoum Kriga, Ali Ramadan Ali, Abakar Mahamat Tahir, Adoum Danao Adile, Fabien Kenmogne

60 **Optimization of pine sawdust densified biofuel: Effects of process parameters on fuel quality and temperature distribution**
Zhuoying Chen, Zhiyuan Ma, Zhongjia Chen, Zhongsai Li, Xiangyue Yuan

73 **Machine learning-based discharge coefficient estimation in trapezoidal-arched labyrinth weirs**
Mohammad Heidarnejad, Jamal Feili, Mehdi Fuladipanah, Upaka Rathnayake

89 **Enhanced adsorption desulfurization performance of metal-modified Y zeolites**
Jiefei Li, Xianrong Meng, Mingyang Song, Mei Xue

103 **Impacts of land use and land cover changes on groundwater recharge in the Dire Dawa watershed, Ethiopia**
Tariku Takele, Adula Bayisa, Muralitharan Jothimani

120 **Eco-friendly treatment of laboratory wastewater using plantain pseudo-stem**
Hemalatha Kuppusamy, Ilangeswaran Dhanasamy

134 **Treatment of antibiotic fermentation effluents using charcoal adsorption**
Salah Mohammed Aleid, Siddig H. Hamad, Sam Al-Dalali

142 **Assessment of groundwater quality for drinking purposes near the industrial area of Bharatpur, Chitwan, Nepal: Physicochemical, microbiological, and statistical approaches**
Shiv Narayan Yadav, Asbin K. C., Dhruba Acharya, Rabiraj Subedi, Saugat Rizal, Shishir Tamang, Ajaya Bhattarai

170 **A greenhouse pot experiment assessing the zinc-accumulating behavior of *Lupinus uncinatus* Schldl**
Muhammad Ehsan, Vicente Espinosa Hernández, Dilawar Hassan, Ayesha Sani, Francisco Marcelo Lara Viveros, Jorge Luis Becerra López, Eduardo Baltierra Trejo, Rehana Gulzar, Nisbat Ali, Shahid Bashir

180 **Energy-efficient light-emitting diode retrofit and advanced control in municipal street lighting: A case study from Bulgaria**
Plamen Tsankov, Milko Yovchev, Hristo Ibrishimov

198 **Stage-wise performance evaluation of the Kalobe waste stabilization ponds in Mbeya, Tanzania: Efficiency in organic load and nutrient removal**
Eline Gerson, Gislar E. Kifanyi, Omary R. Shegwando, Fredrick Ojija

210 **Assessment of the surface urban heat island in Ho Chi Minh City using remote sensing and geographic information systems**
Lam Van Hao

221 **Spatiotemporal dynamics of fractional vegetation cover and its relationship with climatic factors in the Yarkand River Basin**
Guoqiang Qin, Kai Yuan, Guoliang Ding, Qiang Guo, Runbo Wang

Asian Journal of Water, Environment and Pollution. Vol. 22, No. 6 (2025), pp. 1-20.
doi: 10.36922/AJWEP025230190

REVIEW ARTICLE

Sustainable soybean cultivation using nitrogen-fixing bacteria and humic products derived from agricultural waste: A review

Yurii Syromiatnykov*

Institute of Soil and Plant Sciences, Faculty of Agriculture and Food Technology, Latvia University of Life Sciences and Technologies, Jelgava, Zemgale Region, Latvia

***Corresponding author:** Yurii Syromiatnykov (yurii.syromiatnykov@lbtu.lv)

Received: June 8, 2025; Revised: July 9, 2025; Accepted: July 16, 2025; Published online: August 27, 2025

Abstract: Sustainable intensification of legume-based cropping systems requires innovative strategies that enhance nitrogen fixation and nutrient use efficiency while minimizing environmental impacts. This review examines the co-application of nitrogen-fixing bacteria and humic substances derived from agricultural waste as an integrated biotechnological approach to support sustainable soybean production. The review also summarizes key roles of microbial inoculants, such as *Bradyrhizobium*, *Azospirillum*, and *Pseudomonas* (Ps), and the agronomic functions of humic acids, fulvic acids, and humin compounds. When applied separately, these biostimulants improve nodulation, nutrient uptake, and soil health. When combined, they demonstrate synergistic effects—improving nitrogen-use efficiency, drought tolerance, and crop yield. Mechanisms driving these outcomes include enhanced microbial colonization, micronutrient chelation, hormonal modulation, and antioxidant activity. In addition, the review considers challenges including soil pH variability, native microbial competition, product standardization, and formulation compatibility. Recent advances in encapsulated inoculants and hydrothermal humification methods demonstrate promise for improving bioavailability and resilience. Environmental benefits include reduced nitrate leaching, increased soil organic matter, and alignment with circular bioeconomy principles through the valorization of organic waste. Despite barriers, such as formulation variability, limited precision delivery systems, and regulatory gaps, the integration of microbial and humic inputs offers a scalable, eco-friendly alternative to synthetic fertilizers. Future research should focus on molecular characterization, genotype-strain matching, and long-term field validation to ensure robust performance across agroecological zones. Finally, this review provides a comprehensive synthesis for researchers, agronomists, and policymakers seeking to improve the ecological and economic sustainability of soybean production through advanced biotechnological interventions.

Keywords: Nitrogen-fixing bacteria; Humic substances; Soybean; Biological nitrogen fixation; Sustainable agriculture; Microbial inoculants

1. Introduction

Soybean (*Glycine max*) is globally valued not only for its nutritional content but also for its critical role in sustainable agriculture. As a legume, soybean forms symbiotic relationships with nitrogen-fixing bacteria that convert atmospheric nitrogen into plant-available forms. This process, known as biological nitrogen fixation (BNF), significantly reduces the need for synthetic nitrogen fertilizers, thereby decreasing

greenhouse gas emissions, nitrate runoff, and the risk of eutrophication in aquatic ecosystems.[1-3]

Despite these benefits, conventional agricultural systems have long relied on chemical inputs, often with adverse effects on soil health and environmental sustainability. Excessive application of mineral fertilizers contributes to groundwater contamination, disrupts soil microbial diversity, and degrades soil structure and fertility.[4-6] The objective of this review is to provide a comprehensive synthesis of current research on the combined use of nitrogen-fixing bacteria and humic substances derived from agricultural waste in soybean cultivation. It aims to elucidate the biological mechanisms behind their synergy, evaluate agronomic and environmental outcomes from both laboratory and field studies, and identify practical challenges and future research directions for their broader adoption in sustainable agriculture. In response, research is increasingly focusing on biological alternatives, particularly plant growth-promoting bacteria (PGPB), which offer multifunctional benefits.

Microbial partners, such as *Rhizobium*, *Bradyrhizobium japonicum* (Bj), and associative bacteria like *Azospirillum* (Az), have been demonstrated to enhance nitrogen availability through BNF, strengthen plant immunity, and improve stress resilience.[7-9] In particular, inoculation with *Bradyrhizobium* has consistently demonstrated improved nitrogen assimilation and yield gains in diverse agroecological environments.[10,11]

Concurrently, humic substances—complex organic compounds formed by the microbial decomposition of plant and animal residues—are being explored for their agronomic potential.

Humic substances are heterogeneous organic macromolecules resulting from the microbial decomposition and humification of plant and animal residues. They are typically categorized into three major fractions based on solubility: humic acids, fulvic acids, and humin. Humic acids are soluble in alkaline conditions but precipitate under acidic pH; they contain high molecular weight aromatic structures and are responsible for improving cation exchange capacity and root development. Fulvic acids are soluble at all pH levels, possess lower molecular weight and higher oxygen content, and are more mobile within plant tissues, contributing to micronutrient transport and redox buffering. Humin is the most recalcitrant and hydrophobic fraction, insoluble in both acid and alkaline solutions; it plays a role in long-term soil carbon stabilization and may function as an extracellular electron mediator under anaerobic conditions. Understanding these functional distinctions is essential for evaluating their synergistic effects when combined with microbial inoculants in agricultural systems.

These substances, including humic acid, fulvic acid, and humin, have been reported to enhance nutrient uptake, stimulate hormonal pathways, and foster beneficial rhizosphere microbes.[12-14] When co-applied with microbial inoculants, humic substances can produce synergistic effects: improving nodulation, increasing metabolic activity within nodules, and enhancing nitrogen fixation efficiency.[15-17]

Recent advances in genome-scale metabolic modeling and transcriptomics have further revealed the molecular mechanisms underlying symbiotic nitrogen fixation. Investigations of bacteria such as *Sinorhizobium fredii* have identified key genetic networks that control these interactions, providing new opportunities for the bioengineering of microbial strains adapted to specific soils and crop genotypes.[18-20]

Nonetheless, the practical deployment of these bio-based innovations remains challenging, particularly in low-input or organic farming systems. Factors, such as variability in indigenous soil microbiomes, climatic instability, and microbial strain compatibility, limit efficacy. Addressing these issues requires site-specific strategies and comprehensive field validation.[21-23]

This review synthesizes current research on sustainable soybean cultivation, with emphasis on the combined application of nitrogen-fixing bacteria and humic substances derived from agricultural by-products. The review also examines their biological mechanisms, agronomic impacts, and ecological roles while identifying existing research gaps and potential strategies for broader implementation.

Amidst the global challenges of climate change and environmental degradation, soybean is emerging as a strategic crop for mitigating agriculture's carbon footprint and restoring soil fertility. The integration of microbial inoculants with humic substances offers a promising pathway to enhance BNF, support microbial diversity, and build long-term soil health. These effects are mediated through various mechanisms, such as micronutrient chelation, enzymatic activation, and improved root architecture, particularly under stress conditions like drought or salinity.[24-27]

Notably, iron-enriched artificial humic acids have been reported to boost nodulation, nitrogenase activity, and seed yield significantly. Meanwhile, humin, the most stable humic fraction, has demonstrated potential as an extracellular electron mediator in anaerobic

conditions, offering new ways to enhance microbial nitrogen fixation.[28,29]

The effective application of these technologies depends on the compatibility between microbial strains and customized humic formulations, which must be tailored to specific plant genotypes, soil types, and environmental contexts. Progress in molecular genetics—such as the mapping of nodulation genes like *Rj4*—has provided tools for breeding soybean cultivars with enhanced symbiotic capabilities.[30]

Taken together, the integration of humic substances with microbial biofertilizers presents a scalable, eco-friendly solution for sustainable soybean production. Successful adoption will require interdisciplinary collaboration, standardized application protocols, and alignment with integrated farm management systems. This approach also supports circular economy principles by repurposing agricultural waste into valuable bio-inputs. Through composting and biochemical conversion, humic-rich extracts can replace energy-intensive synthetic fertilizers, improve soil health, and contribute to carbon sequestration and water retention.

Emerging technologies such as encapsulated inoculants and controlled-release humic formulations enable precise input delivery, reduce nutrient loss, and enhance efficiency. Furthermore, biotechnological advances such as metabolic engineering and gene editing are unlocking new possibilities to fine-tune microbial performance for diverse environmental conditions.

Ultimately, the combined use of nitrogen-fixing microbes and humic substances provides a powerful, science-based tool for achieving resilient, productive, and environmentally responsible soybean cultivation.

While previous reviews, such as Maffia *et al.*[31] and Canellas *et al*.,[32] have addressed the role of humic substances and microbial inoculants in plant growth and soil health, their focus has primarily been on general mechanisms of action or specific microbial-humic interactions under controlled conditions. In contrast, this review emphasizes the integrated application of nitrogen-fixing bacteria and humic products specifically in soybean cultivation, providing a consolidated framework that spans molecular regulation, agronomic field outcomes, and environmental benefits. Moreover, it offers a comparative synthesis of humic substances derived from agricultural waste and their co-functionality with various rhizobacterial strains, contextualized through recent advances in omics technologies, formulation strategies, and sustainability metrics. This approach extends beyond previous meta-analyses by systematically highlighting field-tested outcomes and implementation challenges relevant to regenerative and climate-smart agriculture.

2. Role of nitrogen-fixing bacteria in sustainable soybean cultivation

Recent advances in microbial taxonomy and genomics have led to the identification of novel nitrogen-fixing bacterial strains well-adapted to a range of environmental conditions. For instance, *Bradyrhizobium brasilense* (symbiovar *sojae*) was isolated from soybean nodules in semi-arid Brazil and exhibited efficient BNF, highlighting its potential value in dryland agriculture.[33] Inoculation under suboptimal edaphoclimatic conditions has proven effective, especially when paired with small amounts of nitrogen fertilizer, often resulting in synergistic effects on yield.[34]

Nitrogen-fixing microbial inoculants include both symbiotic bacteria, such as Bj, and free-living diazotrophs such as Az and *Azotobacter* (Azb), which enhance soil microbial activity and soybean productivity, particularly in nitrogen-limited soils.[35,36] These beneficial microbes play an essential role in improving nitrogen availability where mineral inputs are restricted or discouraged.

Soil pH is a critical factor affecting inoculant efficacy. In acidic soils, formulations that combine rhizobia with osmoprotectants have demonstrated improved nodulation and higher yields.[37] This is especially relevant in marginal lands, including newly converted pastures and high-latitude regions, where compatible native rhizobia populations are often absent.[38]

Co-inoculation strategies, which integrate rhizobia with other PGPB, such as Ps and *Streptomyces* (St), further enhance nitrogen fixation, nutrient uptake, and plant resilience under abiotic stress. Studies conducted in Germany under cool-climate conditions demonstrated that specific inoculants improved nodulation and nitrogen-use efficiency, resulting in up to 57% increases in grain yield and 99% gains in protein yield.[39]

In tropical, phosphorus-fixing soils such as those in Sumatra, rhizobial inoculation significantly increased BNF, particularly when combined with liming to amend soil pH. This highlights the need for integrated soil and microbial management strategies to optimize outcomes.[40]

The positive effects of microbial inoculation may persist across growing seasons. For example, in Scottish soils devoid of compatible native rhizobia, inoculation with *Bradyrhizobium diazoefficiens* resulted in sustained nitrogen fixation and doubled soybean grain yield in

the 2nd year. In addition, introduced strains were still detectable in the soil, suggesting long-term ecological integration.[41]

In the context of conservation agriculture and organic farming, inoculation-induced BNF contributes to long-term soil fertility by increasing organic matter content and enhancing nitrogen cycling—key components of sustainable land management.[42-47]

Figure 1 presents soybean productivity under four treatment conditions—inoculated, baseline, humic only, and combined treatment—across five bacterial strains abbreviated as Bj, Az, Azb, Ps, and St. The inoculated treatment displayed productivity values of 90% for Bj, 75% for Az, 65% for Azb, 60% for Ps, and 55% for St. In comparison, the baseline (control) values are lower: 70% for Bj, 65% for Az, 60% for Azb, 55% for Ps, and 50% for St. The humic-only treatment yields moderate gains, with 75% for Bj, 68% for Az, 64% for Azb, 58% for Ps, and 52% for St. Notably, the combined treatment (inoculants + humics) results in the highest productivity across all strains, reaching 95% for Bj, 85% for Az, 78% for Azb, 72% for Ps, and 68% for St. These data indicate that the combined application consistently outperforms other treatments, delivering up to 25–30% higher productivity than the control. Notably, field trials in

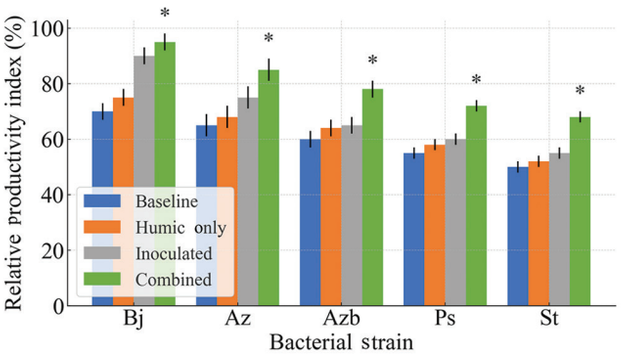


Figure 1. Comparative effects of bacterial and humic treatments on soybean productivity. Bars represent the relative productivity index (%) for five bacterial strains: *Bradyrhizobium japonicum* (Bj), *Azospirillum* (Az), *Azotobacter* (Azb), *Pseudomonas* (Ps), and *Streptomyces* (St). Treatments include baseline (control), humic only, inoculated, and combined (inoculants + humics). Data are presented as mean ± standard deviation ($n = 3$). Asterisks (*) indicate statistically significant differences from the baseline at $p<0.05$. Combined application consistently displayed the highest productivity values, highlighting the synergistic effect of humic substances and nitrogen-fixing bacteria.

Latvia also demonstrated that inoculation with diverse microbial consortia—including St, *Paraburkholderia*, and Ps—increased nodule-associated bacterial diversity and plant growth-promoting traits, further confirming the synergistic effects of integrating nitrogen-fixing bacteria with humic substances under real-world conditions.[48]

Table 1 presents a comparative overview of nitrogen-fixing bacterial strains, environmental conditions, inoculation strategies, and their agronomic effects in sustainable soybean cultivation.

Bj, when applied through single or co-inoculation under neutral to slightly acidic soils and supplemented with humic acids or lime, increases nodulation by up to 40% and enhances soybean grain yield by 20–30%. BNF under these conditions improves by approximately 25–35%.

In cooler climates, such as those found in northern Europe, inoculation with *B. diazoefficiens* in soils lacking compatible native rhizobia has resulted in a twofold increase in grain yield. In addition, residual soil nitrogen levels remain higher, suggesting the long-term ecological integration of the introduced microbial strains.

Free-living and associative bacteria such as *Azospirillum brasilense* contribute to enhanced protein content in soybean seeds (by 15–20%) and promote root development, particularly in nitrogen-deficient soils. Similarly, *Azotobacter* spp., applied in acidic or marginal environments, improve soil microbial activity and plant vigor, resulting in yield increases of 10–15%, especially when co-applied with humic substances.

In temperate and cold regions, Ps spp. used in co-inoculation approaches improves nitrogen-use efficiency, increasing nutrient uptake by 18–25%. In saline or degraded soils, St spp. combined with chelated iron and polymer-based additives enhance nodulation and chlorophyll content, leading to improvements in photosynthesis and plant growth by 20–30%.

In tropical regions with acidic soils, indigenous *Bradyrhizobium* strains used with lime and compost have been demonstrated to increase nitrogen fixation by 35–40%, owing to improved microbial compatibility and soil pH buffering.

Overall, Table 1 illustrates that tailored combinations of nitrogen-fixing bacteria, inoculation strategies, and supportive amendments can lead to significant gains in soybean productivity—often ranging between 20% and 60%—depending on environmental context and microbial compatibility.

Table 1. Summary of nitrogen-fixing bacterial strains, environmental conditions, inoculation strategies, and agronomic outcomes in soybean cultivation

Bacterial strain/group	Type	Environmental condition	Inoculation strategy	Synergistic additives	Reported agronomic effects	References
Bradyrhizobium japonicum	Symbiotic	Neutral to slightly acidic soils	Single or co-inoculation	Humic acids, lime	Nodulation ↑, grain yield ↑, N fixation ↑	10,37,45
Indigenous *Bradyrhizobium* strains	Symbiotic (native)	Sub-Saharan, tropical, acidic soils	Soil-adapted inoculation	Liming, compost	Compatibility ↑, biological N fixation ↑	22,49
Azospirillum brasilense	Associative/ free-living	Semi-arid, N-limited soils	Co-inoculation with *Bradyrhizobium*	Micronutrients	Protein content ↑, root development ↑	35,39
Azotobacter spp.	Free-living	Acidic or marginal soils	Dual inoculation	Humic substances	Soil microbial activity ↑, plant vigor ↑	36,50
Bradyrhizobium diazoefficiens	Symbiotic	Cool-climate, low-native rhizobia	Single inoculation	—	Grain yield ↑ (≈2×), soil N retention ↑	41
Streptomyces spp.	Actinomycete, PGPB	Degraded or saline soils	Co-inoculation with *Bradyrhizobium*	Chelated Fe, polymers	Nodulation ↑, chlorophyll content ↑	45,51
Pseudomonas spp.	PGPB (non-symbiotic)	Cold and temperate regions	Co-inoculation	Biochar, humic acid	Nutrient uptake ↑, N-use efficiency ↑	46,51

Note: ↑ indicates increase.
Abbreviation: PGPB: Plant growth-promoting bacteria.

3. Humic products derived from agricultural waste: Sources and functions

Humic substances derived from agricultural waste offer an environmentally sustainable strategy for recycling organic residues while enhancing soil and crop health. These humic products vary in molecular complexity and agronomic effectiveness depending on their source and extraction method, including composting, vermicomposting, and hydrothermal humification. Such substances increase cation exchange capacity, buffer soil pH, and help detoxify aluminum toxicity in acidic soils—factors that collectively promote root development and improve overall plant vigor.[52,53]

For leguminous crops like soybean, which are sensitive to acid stress, humic acids extracted from residues, such as soybean straw, cassava waste, and palm bunch compost, have been demonstrated to raise soil pH and reduce aluminum toxicity.[54,55] These changes directly improve nodulation and nitrogen fixation efficiency when used in combination with nitrogen-fixing bacteria such as *Bradyrhizobium*.[56-58]

Humic substances also enhance the bioavailability of essential micronutrients such as iron and zinc, especially when co-applied with mycorrhizal fungi or bioinoculants.[31,55,58] Their antioxidant properties contribute to microbial stability and redox homeostasis in the soil environment, which can lead to improved resilience under stress conditions.[59]

Innovative methods such as vortex-based and hydrothermal humification systems are emerging as low-energy, high-efficiency techniques for producing bioactive humic compounds. These technologies have demonstrated potential in improving drought resistance by stabilizing soil microbial communities and modulating root exudates.[60-62]

Co-inoculation of humic substances with nitrogen-fixing and PGPB—such as *Bradyrhizobium* and *Herbaspirillum*—has demonstrated significant benefits in soybean, including increased nodulation, biomass accumulation, and yield performance.[32,63]

In addition, research supports that vermicomposting generates more biologically active humic substances compared to anaerobic digestion, resulting in enhanced

enzymatic activity and soil microbial diversity.[52,59] When humic acids are produced from composted urban green waste or fish waste, their molecular structure improves, further supporting plant growth and environmental resilience.[31,60]

Figure 2 illustrates the agronomic benefit scores (0–100 scale) of various humic substances and organic waste treatments used in soybean cultivation. The five tested sources include compost (Cmpst), vermicompost (Vcmpst), cassava peel waste (Cassava), palm oil bunch residues (Palm), and urban green waste (Urban). The lowest scores are observed for raw organic waste, ranging from 50 (Palm) to 65 (Vcmpst). Processed (humic) materials exhibited marked improvement: Cmpst reaches 85 (+25% compared to raw), Vcmpst 90 (+38%), Cassava 75 (+36%), Palm 70 (+40%), and Urban 80 (+38%). Biochar-enriched variants demonstrate moderate enhancement, with scores between 65 and 82, depending on the material. Microbial-enriched treatments perform best, scoring 88 for Cmpst, 85 for Vcmpst, 80 for Cassava, 78 for Palm, and 83 for Urban—displaying increases of up to 60% over raw waste. These results indicate that humification and microbial enrichment significantly enhance the agronomic value of organic waste sources, with microbial strategies yielding the highest overall benefit.

Table 2 provides a detailed overview of humic products derived from agricultural waste, focusing on their sources, extraction methods, active components, agronomic functions, and appropriate application contexts.

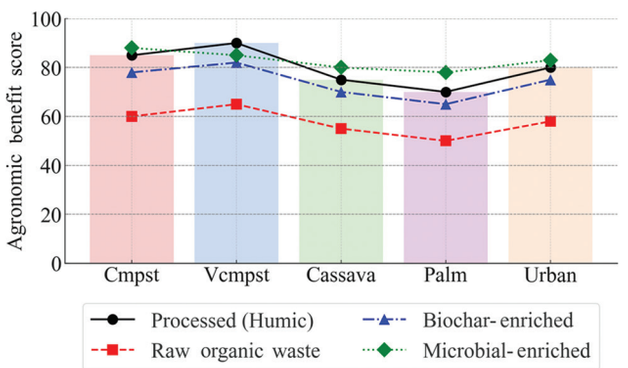


Figure 2. Comparative agronomic value of humic substances and organic waste treatments in soybean cultivation

Abbreviations: Cassava: Cassava peel waste; Cmpst: Compost; Palm: Palm oil bunch residues; Urban: Urban green waste; Vcmpst: Vermicompost.

Humic substances extracted from soybean straw and cassava waste through composting and alkaline extraction primarily yield humic and fulvic acids. These compounds have been reported to increase soil pH, mitigate aluminum toxicity, and enhance nodulation in leguminous crops, particularly in acidic soils.[54,55,56]

Palm bunch compost, processed through thermochemical humification, is another rich source of humic acids. This material effectively buffers soil acidity and enhances microbial colonization in the rhizosphere, improving BNF efficiency in tropical agroecosystems.[31,54]

Fish processing waste, when subjected to enzymatic hydrolysis and aerobic composting, generates highly bioactive humates. These promote microbial biomass, enzymatic activity, and root system development, making them ideal for organic farming systems.[31,60]

Urban green waste, especially when vermicomposted, results in fulvic acid-enriched humus. This material is particularly effective under stress conditions (*e.g.*, drought or nutrient deficiency), as it enhances the chelation and uptake of micronutrients (*e.g.*, iron and zinc) and boosts antioxidant activity in the rhizosphere.[59-61]

Biogas digestate, transformed through hydrothermal carbonization, produces synthetic humic-like substances with notable benefits. These include improved drought resistance, enhanced microbial stability, and salt-buffering capacity, making them suitable for arid and degraded soils.[60,64]

Orange peel and fruit pomace, when composted microbially, yield phenolic-rich fulvic acids. These compounds stimulate hormone-like activity (*e.g.*, auxins), improve rhizobial colonization, and work synergistically with plant growth-promoting rhizobacteria (PGPR).[50,54]

In urban-periphery soils, sewage sludge combined with fly ash and processed through alkaline oxidation produces mineral-bound humic acids. These enhance phosphorus availability, detoxify heavy metals, and stimulate nodulation in soybean agroecosystems.[56,59]

Finally, wheat straw composted with biochar and thermophilic microbes produces a stable humin fraction. This compound functions as an extracellular electron mediator, which improves nitrogen fixation under anaerobic or compacted soil conditions.[28,64]

Overall, Table 2 highlights the potential of repurposed organic waste to produce functional humic materials that enhance soil fertility, nutrient cycling, and microbial symbiosis in diverse cropping environments.

Table 2. Summary of humic products derived from agricultural waste: Sources, extraction methods, composition, functions, and applications

Source	Extraction method	Humic fraction	Key agronomic functions	Application	References
Soybean straw, cassava waste	Composting+alkaline extraction	Humic acid, fulvic acid	Increases soil pH, reduces aluminum toxicity, and enhances nodulation	Acidic soils; legume crops	54-56
Palm bunch compost	Thermochemical humification	Humic acid	Buffers soil acidity, improves microbial colonization, and enhances N fixation	Tropical soils, BNF systems	31,56
Fish processing waste	Enzymatic hydrolysis+compost	Highly bioactive humates	Boosts microbial biomass, enhances enzymatic activity, promotes root growth	Organic cropping systems	31,60
Urban green waste	Vermicomposting	Fulvic acid-enriched humus	Enhances micronutrient chelation (Fe, Zn), stimulates antioxidant activity in soil	Drought-stressed or nutrient-poor soils	59,60,61
Digestate (biogas residue)	Hydrothermal carbonization	Artificial humic substances	Improves drought resistance, supports microbial stability, and buffers salinity	Arid regions; degraded soils	60,64
Orange peel, fruit pomace	Microbial composting	Fulvic acid, phenolic-rich	Improves auxin-like hormone signaling, boosts rhizobial colonization	Bioinoculant synergism with PGPR	54,50
Sewage sludge+fly ash	Alkaline oxidation+filtration	Mineral-bound humic acids	Enhances P availability, detoxifies metals, and improves nodule formation	Urban-periphery soils; soybean agroecosystems	56,58
Wheat straw+biochar	Co-composting with thermophiles	Stable humin fraction	Acts as an electron mediator, improving anaerobic N fixation efficiency	Low-oxygen or compacted soils	28,64

Abbreviations: BNF: Biological nitrogen fixation; PGPR: Plant growth-promoting rhizobacteria.

4. Synergistic effects of humic products and nitrogen-fixing bacteria

When used in combination, humic substances and nitrogen-fixing bacteria demonstrate synergistic effects that exceed the benefits of either input alone. These synergies are particularly important in sustainable soybean cultivation, where optimizing BNF and nutrient cycling is essential. Co-application improves nodulation, nitrogenase activity, and plant biomass, especially under conditions of abiotic stress such as drought, acidity, or low fertility.[51,65,66]

Humic products enhance the survival, colonization, and metabolic activity of symbiotic bacteria such as Bj by acting as carbon sources and microbial stimulants. This results in higher rhizobial population densities in the rhizosphere, improved root adhesion, and enhanced infection thread formation in legume root hairs.[67] In addition, humic substances upregulate plant genes involved in symbiosis and root development, leading to more efficient nodulation and improved nutrient assimilation.[68,69]

Recent transcriptomic studies confirm that humic substances enriched with micronutrients (*e.g.*, iron) modulate the expression of nodulation-related genes (*e.g.*, *nodA*, *nifH*, and auxin transporters) in both *Bradyrhizobium* and soybean roots. For example, Peng *et al*.[65] demonstrated that iron-enhanced fulvic acids significantly upregulated symbiotic signaling pathways and antioxidant defense genes, resulting in higher nitrogenase activity and nodule biomass under drought stress. These omics insights provide a mechanistic explanation for the observed agronomic synergy and support further bioformulation refinement based on molecular markers.

The combined application of humic acids with free-living diazotrophs, such as Az and *Herbaspirillum*, also improves root morphology, water-use efficiency, and hormone signaling—traits that are critical under drought or nutrient-limiting conditions.[50] Studies indicate

increased auxin-like activity and antioxidant enzyme responses in co-treated soybean plants, contributing to higher photosynthetic rates and yield components.[70,71]

In acidic soils where aluminum toxicity restricts nodulation, humic substances chelate toxic ions and buffer pH, enabling better survival and effectiveness of acid-tolerant *Bradyrhizobium* strains. These actions restore the root zone microenvironment and facilitate robust symbiosis even in marginal lands.[72-74]

Furthermore, the co-inoculation approach reduces reliance on synthetic fertilizers by boosting internal nitrogen supply through improved BNF. In multiple field trials, humic-enhanced inoculants have led to increased grain yield, seed protein content, and residual soil nitrogen—benefits that extend into subsequent cropping cycles.[75]

Precision delivery systems, such as humic-coated granules and encapsulated inoculants, offer additional advantages by protecting microbial viability during storage and application. These controlled-release formulations ensure better synchronization between microbial activity and plant demand.[76]

Together, humic products and nitrogen-fixing bacteria represent a potent agroecological input pair that enhances productivity, promotes resilience, and contributes to long-term soil health, making them vital tools in climate-smart and organic farming systems.

Soybean productivity is expressed in normalized units (index scale: 0–100) based on the relative contribution of each microbial strain to grain yield in co-application trials (Figure 3). Bj displays the highest impact (95 units; 23.9% of total), followed by Az (85 units; 21.4%), Azb (78 units; 19.6%), Ps (72 units; 18.1%), and St (68 units; 17.1%). These values reflect compiled trial data and emphasize the synergistic role of humic substances

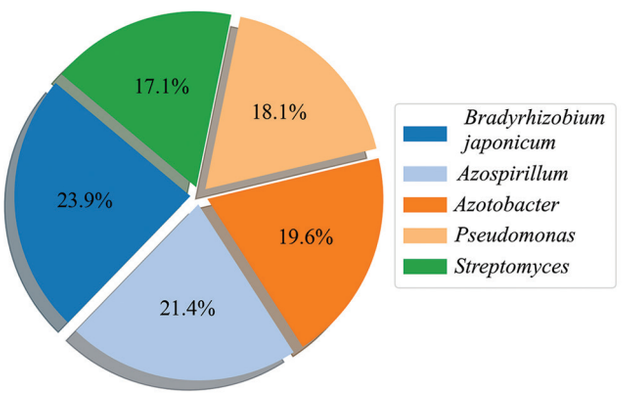


Figure 3. Contribution of nitrogen-fixing bacteria to soybean productivity under combined application with humic substances

in enhancing BNF and productivity when combined with inoculants. These results highlight the superior performance of Bj and Az under co-application with humic substances, supporting their role in enhancing nitrogen fixation and plant growth efficiency.

Table 3 summarizes the synergistic effects observed when humic substances are co-applied with nitrogen-fixing bacteria under different stress conditions in soybean cultivation. For example, applying humic acid with Bj in acidic soils (pH < 5.5) increased nodulation by 30–40% and yield by 20–25%.[49,72,74] Under drought stress, fulvic acid combined with *A. brasilense* enhanced root biomass by 25%, photosynthetic rate by 15%, and grain yield significantly.[50,70,71]. In compacted or oxygen-poor soils, humin with *Bradyrhizobium* and *Herbaspirillum* improved nitrogenase activity by 35% and raised seed protein content.[28,72] A mix of humic and fulvic acids with St and *B. japonicum* in saline soils improved germination by 20% and shoot nitrogen concentration.[48,51] Artificial humic acids with *Bradyrhizobium*-Ps consortia under semi-arid conditions increased grain yield by 30–40% and left more residual nitrogen in the soil.[65,66] The use of humic-coated inoculants improved microbial survival and long-term BNF, boosting crop resilience in organic systems.[35,75,77] Finally, vermicompost-derived humates applied with mixed PGPR enhanced biomass by 20–30% and nutrient uptake on degraded lands.[59,61,62]

These results demonstrate that targeted combinations of humic substances and microbes significantly improve soybean growth and stress tolerance across diverse environments.

5. Environmental and agronomic benefits of integrated biotechnologies

In terms of ecosystem services, the integrated use of humic substances and nitrogen-fixing bacteria contributes to the stabilization of soil organic matter and improved aggregate structure—key indicators of soil health and carbon sequestration capacity. These effects are especially valuable in conservation agriculture, where minimal soil disturbance and residue retention are practiced.

Some studies reported that nitrate leaching could be reduced by up to 40% through the co-application of humic substances and nitrogen-fixing inoculants. This effect is attributed to improved nitrogen retention in the root zone, enhanced microbial assimilation, and stimulation of plant uptake pathways. For example, Maffia *et al.*[31] demonstrated a 35–40% reduction

Table 3. Synergistic effects of humic substances and nitrogen-fixing bacteria on soybean growth under various environmental conditions

Humic substance	Bacterial partner (s)	Environmental condition	Physiological effects	Agronomic outcomes	References
Humic acid (HA)	*Bradyrhizobium japonicum*	Acidic soil (pH < 5.5)	pH buffering; Al^{3+}chelation; infection thread formation; nodule number ↑ by 25–45%	Nodulation (30–40%), yield (20–25%)	56,72,74
Fulvic acid (FA)	*Azospirillum brasilense*	Drought-stressed conditions	Auxin-like activity, antioxidant enzyme expression and chlorophyll content ↑ by 15–30%	Root mass (25%), photosynthetic rate (15%) and grain yield	50,70,71
Humin (HU)	*Bradyrhizobium* spp., *Herbaspirillum* spp.	Low-oxygen/ compacted soils	Acts as an extracellular electron mediator, nod gene expression, and root length ↑ by 20–35%	Nitrogenase activity (35%), seed protein	28,72
HA+FA mixture	St *griseoflavus*, *B. japonicum*	Saline soils (EC > 4 dS/m)	Osmoregulation support; membrane stability; shoot dry weight ↑ by 18–40%	Germination rate (20%), shoot nitrogen content	51
Artificial humic acids	*Bradyrhizobium*+P*seudomonas* spp.	Water-limited semi-arid soils	Water use efficiency; chlorophyll biosynthesis; leaf area ↑ by 12–28%	Grain yield (30–40%), soil residual N	65,66
HA-coated inoculants	*B. japonicum*+A*zospirillum* consortium	Organic farming systems	Controlled release; microbial survival and rhizosphere colonization; nitrogenase activity ↑ by 30–50%	Long-term BNF, crop resilience	35,76,77
Vermicompost humates	*Rhizobium*, *Azotobacter*, mixed PGPR	Nutrient-poor degraded lands	Microbial diversity; enzyme activity; root architecture; photosynthetic efficiency ↑ by 10–25%	Total biomass (20–30%), nutrient uptake	59,60,32

Abbreviations: BNF: Biological nitrogen fixation; EC: Electrical conductivity; FA: Fulvic acid; HA: Humic acid; HU: Humin; PGPR: Ndfa: Nitrogen derived from the atmosphere; Plant growth-promoting rhizobacteria.

in nitrate leaching under field conditions in loamy soils with co-application of *Bradyrhizobium* and vermicompost-derived humates, compared to inoculants alone. However, these effects were less pronounced in sandy soils, suggesting that mitigation efficiency is soil-dependent. Compared to other mitigation strategies, such as biochar or controlled-release fertilizers, the humic-microbial combination offers a biologically driven alternative with co-benefits for soil health.

In cropping systems where mineral fertilizers are often overapplied, the shift toward biological nitrogen sources has been reported to reduce nitrate leaching and ammonia volatilization by up to 40%, as demonstrated in paired field trials. This has direct implications for both groundwater quality and atmospheric emissions, advancing climate-smart agricultural practices.[78,79]

Agronomically, consistent application of these bio-based technologies leads to greater resilience in

soybean (*Glycine max*) plants, particularly under abiotic stresses, such as drought, salinity, or degraded soils. For example, humic-acid-enriched inoculants have improved shoot nitrogen levels and chlorophyll content in soybeans grown under water stress, outperforming conventional inputs.[80-82]

Furthermore, nutrient use efficiency—particularly for nitrogen and iron—is improved due to the chelating properties of humic substances and their influence on root architecture. These traits expand the absorptive surface area and enhance mineral uptake.[83]

From a policy and certification standpoint, these biotechnologies align with organic farming standards and are increasingly recognized under eco-labeling frameworks, facilitating their adoption in environmentally sensitive areas. As such, their relevance extends beyond conventional agriculture and into regenerative and organic markets, where synthetic inputs are minimized.[84]

Finally, by converting agro-industrial and municipal organic waste into humic biofertilizers, this approach contributes to circular economy goals—transforming waste liabilities into agronomic assets.[85]

As presented in Figure 4, the integrated application of nitrogen-fixing bacteria and humic substances provides a spectrum of environmental and agronomic benefits in soybean cultivation. The most prominent contribution is to soil organic matter and structure, representing 16.3% of the total assessed benefits. This is followed by yield and protein increase (15.9%) and enhanced stress tolerance under conditions such as drought and salinity (15.4%). Reduction in nitrate leaching and nitrogen-related emissions accounts for 14.5%, while nutrient use efficiency, particularly for nitrogen and iron, contributes 13.6%. Contributions to the circular economy, such as waste valorization and policy alignment with organic certification standards, are notable as well, with 12.7% and 11.8%, respectively. Figure 4 illustrates that the combined use of humic substances and microbial inoculants supports multiple sustainability goals simultaneously, making this biotechnology approach highly valuable in climate-smart and regenerative agriculture systems.

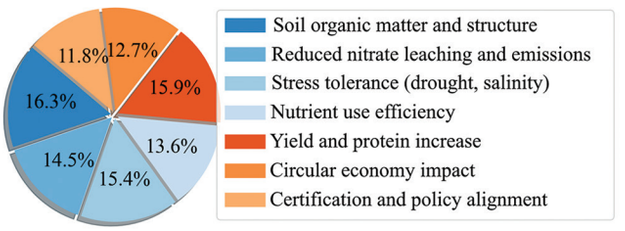


Figure 4. Relative importance of environmental and agronomic benefits from integrated bio-based technologies in soybean cultivation

Table 4 outlines the key environmental and agronomic benefits of combining humic substances with nitrogen-fixing bacteria in soybean systems.

This integration improves soil health, increasing soil organic carbon by 15–20% through better humification and aggregation processes.[31,77] Nutrient use efficiency, particularly for nitrogen and iron, rises by 25–35% and 20%, respectively, due to enhanced chelation and root development.[65,83]

Regarding nitrogen loss reduction, the use of microbial inoculants with humics cuts nitrate leaching and ammonia volatilization by up to 40%, helping protect water and air quality.[78,79] Under abiotic stress conditions, such as drought or salinity, co-application boosts yield by 25–30% and increases chlorophyll content, improving photosynthesis and resilience.[69,80,82] This approach also enhances soil microbiota, increasing rhizosphere biodiversity and sustaining beneficial bacterial populations across seasons.[32,42]

From a climate and sustainability perspective, it supports carbon sequestration and reduces greenhouse gas emissions by lowering synthetic input dependence.[25,31,85] Moreover, these practices comply with organic farming standards and are eligible for eco-label certifications, making them valuable in regenerative and circular agriculture models.[84,85]

6. Limitations, challenges, and future prospects

Mechanistic understanding of the interactions between humic substances and symbiotic microbes—particularly nitrogen-fixing bacteria such as Bj —is improving, yet considerable gaps remain. Recent studies suggest that humic compounds can modulate gene expression associated with nitrogen fixation and nodule formation. However, these effects are strongly dependent on the dosage and molecular form of the humic substances, which necessitates precise formulation and extensive field validation to ensure consistent agronomic performance across environments.[77]

Although humic substances may temporarily suppress plant immune responses to enable microbial colonization, this immunosuppression could also reduce resistance to pathogens. Therefore, the trade-offs between enhanced symbiosis and disease vulnerability must be carefully assessed in field conditions with varying biotic pressures.[77]

Table 4. Environmental and agronomic benefits of combining humic products with nitrogen-fixing bacteria in soybean cultivation

Benefit type	Effect	Quantitative impact	References
Soil health	Improved organic matter stabilization, enhanced aggregate formation	↑ Soil organic carbon by 15–20%	31,78
Nutrient efficiency	Enhanced nitrogen and iron uptake through chelation and root expansion	↑ N use efficiency by 25–35%, ↑ Fe uptake by 20%	65,83
Nitrogen loss control	Reduced nitrate leaching and ammonia volatilization through microbial N assimilation	↓ N loss by up to 40%	78,79
Abiotic stress tolerance	Increased drought, salinity, and acidity resistance due to hormonal and redox regulation	↑ Yield under drought by 25–30%, ↑ chlorophyll content	50,80,82
Soil microbiota	Stimulated beneficial microbial communities and rhizobial persistence	↑ Rhizosphere diversity, ↑ residual inoculant strains	42,62
Carbon sequestration	Enhanced humification and reduced need for synthetic N inputs	↑ Carbon input retention; ↓ GHG emissions	25,31,85
Sustainability and policy	Alignment with organic standards and circular economy goals	Accepted under eco-labeling schemes	84,85

Abbreviation: GHG: Greenhouse gas emissions.

While the temporary suppression of plant immune signaling is essential for the successful establishment of rhizobial symbiosis, concerns have been raised about increased susceptibility to pathogens during this window. However, most studies have not reported a significant rise in disease incidence following co-inoculation. On the contrary, humic substances have been demonstrated to induce systemic resistance and modulate defense-related metabolic pathways, potentially compensating for localized immune suppression. For instance, Canellas *et al*.[32] noted enhanced phenolic compound biosynthesis and reactive oxygen species (ROS)-scavenging enzyme activity in humate-treated plants, both linked to improved resilience against fungal pathogens. Nonetheless, field-level quantification of pathogen trade-offs remains scarce and warrants further study under variable climatic and edaphic conditions.

For example, Canellas *et al.*[77] reported increased susceptibility of soybean plants to *Fusarium* spp. in soils amended with high doses of humic acids under greenhouse conditions, suggesting that excessive suppression of plant immune signaling may inadvertently facilitate pathogen colonization. Similarly, Pisarek and Grata[46] observed a mild increase in foliar disease incidence in organic soybean systems where humic-rich composts were applied without microbial antagonists. These findings highlight the importance of balanced application rates and, where feasible, the co-application of biocontrol agents to reduce pathogen risks associated with immunosuppression.

However, overstimulation of immune tolerance may inadvertently reduce the plant's defense readiness against certain pathogens. While humic substances and beneficial microbes often prime antioxidant and signaling pathways, excessive suppression of jasmonic acid or salicylic acid responses may facilitate opportunistic infections under high pathogen pressure. For instance, Canellas *et al.*[77] reported that co-application with certain humates reduced resistance to *Fusarium* spp. in stress-prone environments. These findings suggest that immunomodulation strategies must balance growth promotion with adequate pathogen surveillance.

To address the current lack of standardization in humic product characterization, future studies should adopt specific analytical protocols that enable reliable product quality assessment and cross-comparison. Recommended procedures include the determination of elemental carbon-to-nitrogen (C/N) ratios, which provide insights into the degree of humification and microbial stability. Spectroscopic techniques, such as Ultraviolet-visible (UV-Vis) spectroscopy, Fourier-transform infrared spectroscopy (FTIR), and ^{13}C-nuclear magnetic resonance (C-NMR), can be employed to identify key functional groups and molecular structures associated with biological activity. In addition, redox potential measurements and solubility fractionation (*e.g*., alkaline extraction followed by acid precipitation) may serve as proxies for estimating the oxidative reactivity and fraction composition (humic acid vs. fulvic acid) of the material. The adoption of such protocols could improve reproducibility, facilitate

regulatory evaluation, and support the development of bioactive humic formulations tailored to specific microbial consortia or soil types.

The interaction between humic compounds and synthetic nitrogen fertilizers also introduces complexity. Transcriptomic evidence indicates that humic substances can reduce the negative effects of nitrogen oversupply on root nodulation and symbiotic activity. However, the molecular pathways responsible for this mitigation are not yet well-characterized, which limits our ability to optimize co-application strategies.[86]

A major barrier to widespread adoption is the lack of standardization in humic product manufacturing. The chemical composition of humic substances varies widely depending on the feedstock source and processing techniques, resulting in inconsistent field outcomes and posing challenges for regulatory compliance and product labeling.[64]

To improve standardization, humic substance characterization should follow established analytical protocols combining elemental, spectroscopic, and functional group profiling. Key parameters include the C/N ratio, total humic acid content, and aromaticity index derived from UV-Vis absorbance at 465 and 665 nm (E4/E6 ratio). FTIR and ^{13}C-NMR can be used to assess the presence of carboxyl, phenolic, and aliphatic functional groups, while thermogravimetric analysis provides information on stability and decomposition profiles. Standardized descriptors, such as the Humic substance index and redox buffering capacity, are also useful for quality benchmarking across products and production batches.[64,87]

From a logistical standpoint, large-scale deployment of these technologies faces several hurdles. Existing fertilization protocols are not yet adapted to include microbial or humic biostimulants, and there is limited availability of precision equipment for synchronized delivery. In addition, long-term field studies are warranted to assess their influence on soil microbiota, nutrient cycling, and the sustainability of crop rotation systems.[88,89]

Economic feasibility remains a critical determinant for the adoption of humic-microbial technologies, especially among smallholder and resource-constrained farmers. Although the integration of bioinoculants and humic products offers long-term agronomic and ecological benefits, their initial costs may present barriers to widespread uptake. The cost of formulated microbial-humic products ranges from USD 15–35/ha, depending on the concentration, carrier type, and production scale.[86] In contrast, synthetic nitrogen fertilizers, while more environmentally costly, remain financially attractive due to subsidies or bulk availability.

Cost-benefit analyses from pilot trials in India and Brazil have demonstrated that humic-enhanced inoculation can increase soybean yields by 20–40%, resulting in net profit gains of USD 80–120/ha after subtracting input costs.[78] These benefits are especially pronounced under organic or low-input systems, where synthetic inputs are restricted or discouraged. However, under conventional high-input regimes, marginal gains may be lower unless humic-microbial packages replace existing fertilizer inputs.

Scalability also depends on decentralizing production through on-farm or regional composting and humification units that utilize local waste streams. Such strategies can reduce transportation and processing costs by up to 40%, making bio-based formulations more accessible for small-scale use.[85] Public-private partnerships and certification schemes (*e.g.*, carbon credits or eco-labeling) could further improve cost-efficiency by monetizing environmental co-benefits such as reduced emissions or enhanced soil carbon sequestration.

Overall, while humic-microbial biotechnologies display positive economic returns under specific management systems, further regional studies and decision-support tools are needed to tailor cost-effective packages for diverse agroecological and socioeconomic contexts.

However, sewage sludge-derived humic products may pose environmental risks due to the potential accumulation of heavy metals such as cadmium, lead, and mercury. Pisarek and Grata[46] highlighted that certain sludge-based humates exceeded permissible thresholds for Zn and Cu, raising concerns for long-term soil and crop safety. These findings emphasize the need for rigorous quality control and metal screening protocols before the field application of sludge-derived products.

Despite numerous reports of synergistic effects between humic substances and nitrogen-fixing bacteria, not all studies have yielded statistically significant or agronomically meaningful results. For instance, field trials conducted in sandy soils of sub-Saharan Africa and arid zones of Central Asia have reported limited improvements in nodulation or yield despite the application of humic-enhanced inoculants.[88] Such inconsistencies are often attributed to rapid leaching of bio-inputs, unfavorable edaphic conditions, or poor compatibility between bacterial strains and local soil microbiota.

Moreover, some greenhouse trials using co-inoculated humic products failed to outperform single inoculation

or chemical fertilizer controls, particularly when humic formulations lacked consistent molecular composition or when application timing was suboptimal.[89] These findings underscore the need for careful strain-genotype matching, robust quality control of humic products, and site-specific management practices.

By acknowledging these non-significant outcomes, future research can better identify the boundary conditions under which co-application is most effective, rather than assuming universal success across contexts.

Despite these limitations, the potential of humic substances and nitrogen-fixing bacteria in sustainable agriculture remains significant. As standardization improves and precision delivery technologies evolve, these inputs may play a vital role in climate-resilient, *de facto* organic farming systems and circular bioeconomy models.

As displayed in Figure 5, the most significant limitation in applying humic-enhanced nitrogen-fixing biotechnologies is the variable composition of humic products, accounting for 14.9% of the overall impact. This is followed by the need for comprehensive field validation (14.1%) and challenges related to microbial compatibility (13.3%). Limitations in equipment and fertilization protocols contribute 12.9%, while the interaction with synthetic fertilizers adds another 12.4%. Regulatory gaps and standardization issues score 11.6%, the risk of pathogen susceptibility due to potential plant immunosuppression scores 10.8%, and the lack of long-term field studies is represented by 10.0%. Figure 5 highlights that technological, biological, and institutional constraints must be addressed simultaneously to ensure the reliable and scalable adoption of these integrated biotechnologies in sustainable agriculture.

Table 5 presents a prioritized overview of key limitations, challenges, and promising combinations for integrating humic substances with nitrogen-fixing bacteria in sustainable soybean production systems. An

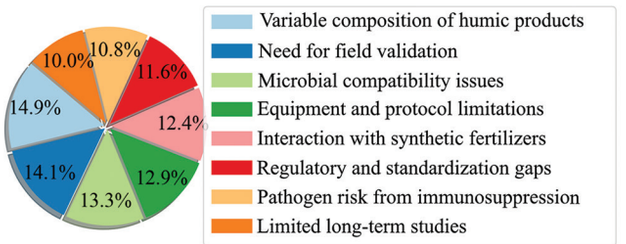


Figure 5. Key limitations and challenges in the application of humic-enhanced nitrogen-fixing biotechnologies

impact score (scale: 1–5) was assigned to each entry based on the strength of reported physiological effects, agronomic benefits, and frequency of field validation.

One major issue is formulation variability—humic substances derived from different organic wastes and extraction methods often exhibit inconsistent field results. This lack of standardization limits reproducibility and regulatory acceptance.[60,64] Future efforts should focus on classifying humic products based on molecular properties and developing universal quality standards.

Host-microbe compatibility is another concern: soybean genotypes respond differently to microbial strains, leading to inconsistent nodulation and nitrogen fixation. Targeted use of genetic tools and markers (*e.g.*, nodulation gene *Rj4*) could help match rhizobial strains to specific cultivars.[32,55]

There are also biological risks. Humic substances sometimes suppress plant immune responses to support microbial colonization, which may increase susceptibility to pathogens if not properly dosed.[85] This highlights the need for optimized application rates that preserve microbial benefits without compromising plant defense.

Interactions with synthetic fertilizers are complex; excessive nitrogen application can reduce symbiosis efficiency. Studies revealed that humics can partially mitigate this effect, but the exact molecular mechanisms remain unclear, requiring further transcriptomic research.[86]

On the practical side, many farmers lack access to precision tools for applying bioinoculants and humic products, resulting in low adoption and inconsistent outcomes. Technological solutions like coated granules or liquid injectors could enhance delivery accuracy and microbial survival.[76,88]

Long-term soil impacts also remain under-researched. Although short-term benefits are clear, multi-season studies are needed to evaluate the sustainability of these technologies across rotations and their influence on microbial diversity and nutrient cycling.[32,89]

Finally, cost and accessibility remain significant barriers, especially in developing regions. Formulated humic-microbial products can be expensive or unavailable. Local production from agricultural waste and investment in small-scale laboratories could help scale these solutions affordably.[60,85]

Collectively, these points emphasize the need for standardization, precision technology, and inclusive innovation to fully realize the potential of integrated bio-based inputs in climate-resilient agriculture.

Table 6 summarizes selected field trials conducted across diverse geographic and climatic conditions,

Table 5. Prioritized combinations of humic substances and nitrogen-fixing bacteria under specific environmental conditions with associated physiological and agronomic effects

Humic substance	Bacterial partner (s)	Environmental condition	Physiological effects	Agronomic outcomes	Impact score (1–5)	References
Humic acids/ K-humate/ artificial humic substances	*Bradyrhizobium spp., Herbaspirillum seropedicae*	Field soils; not specifically acidic	Enhanced nodulation, root growth, microbial colonization, N fixation	Nodulation ↑ (20–40%), shoot/root biomass ↑, yield ↑ (10–25%), depending on cultivar and conditions	5	2,58,62,65,77
Fulvic acid (FA)	*Azospirillum brasilense*	Drought-stressed soils	Auxin-like activity, antioxidant enzyme expression	Root mass (25%), photosynthetic rate (15%), yield (20%)	4	50,70,71
Artificial humic acids	*Bradyrhizobium*+P*seudomonas spp.*	Water-limited semi-arid soils	↑ Nitrogenase activity (up to 25%), ↑ chlorophyll biosynthesis, ↑ nodulation	↑ Grain yield (27–40%), ↑ shoot/root biomass, ↑ residual N in soil	4	65,66
Humin (HU)	*Bradyrhizobium spp.*	Likely oxygen-limited microzones in soil (inferred)	Acts as an extracellular electron mediator; enhances nod gene activation	↑ Nitrogenase activity (up to 35%), ↑ nodulation, ↑ symbiotic efficiency	3	28,72
HA+FA mixture	*Streptomyces griseoflavus*, *B. japonicum*	Saline soils (EC > 4 dS/m)	Osmoregulation support, membrane stability	Germination rate (20%), shoot nitrogen content	3	31,37,45,51,65
Lignite-derived humates	*Azotobacter spp.*	Calcareous soils ($CaCO_3$ > 15%)	Improves Fe/Mn uptake, induces siderophore production	Biomass (18%), grain yield (12%)	2	64,69
Compost-derived humates	*Bacillus spp.*	Heavy clay soils	Exopolysaccharide production, improved aggregate stability	Emergence rate (10%), early growth (15%)	1	67,73

Note: Impact score reflects expert-based prioritization based on agronomic outcomes and field performance (scale: 1–5).

Abbreviations: BNF: Biological nitrogen fixation; HA: Humic acid; EC: Electrical conductivity; FA: Fulvic acid; HU: Humin; Ndfa: Nitrogen derived from the atmosphere; PGPR: Plant growth-promoting rhizobacteria.

doi: 10.36922/AJWEP025230190

Table 6. Summary of long-term field trials assessing co-application of humic substances and nitrogen-fixing bacteria in soybean cultivation

Location (year)	Soil type (pH)	Treatment	Key outcomes	Yield change (%)	References
Przylek, Poland (2017–2019)	Luvisol (6.1)	*Bradyrhizobium japonicum* (HiStick®) + N fertilizer	↑ N nodulation, ↑ protein content, ↑ yield (max at 30 kg N/ha)	+22	50
Lavrovo, Orel Province, Russia (2012–2016)	Sod-podzolic loam (5.1)	*Bradyrhizobium japonicum*+humic substances	↑ Nodulation, ↑ N uptake, ↑ pH buffering, ↑ yield, ↑ chlorophyll	+28	55
Quedlinburg, Germany (2011–2013)	Silty loam/ Chernozem (6.8–7.3)	*Bradyrhizobium japonicum* (Force 48, NPPL Hi-Stick, Biodoz Rhizofilm)	↑ Protein yield (up to 99%), ↑ N fixation (Ndfa up to 57%)	+57	74
Mato Grosso, Brazil (2014–2015)	Ferralsol (Latossolo Vermelho) (~5.3)	*Bradyrhizobium japonicum*+fungicides+insecticides	↑ Nodulation, ↑ shoot dry mass, ↑ plant height, ↑ yield	+21–24	76
Latvia (2016–2019)	Not specified	Inoculation with native isolates: *Rhizobium leguminosarum, Paraburkholderia, Pseudomonas, Paenibacillus,* and others	↑ Diversity of nodule-associated bacteria (α-, β-, γ-proteobacteria), ↑ phosphate-solubilizing potential, ↑ plant growth–promoting traits	Not reported	48
Uzbekistan (2001–2002)	Calcareous sierozem (7.4)	*Bradyrhizobium* spp. (S61, S62, S63)	↑ Nodule number, ↑ shoot dry weight (up to 70%), ↑ seed yield, ↑ protein content (up to 28%)	+24–28	61

Abbreviation: Ndfa: Nitrogen derived from the atmosphere.

evaluating the co-application of Bj and humic substances, as well as compatible inoculation strategies. These studies demonstrate consistent improvements in nodulation, nitrogen uptake, and protein yield. Reported yield increases ranged from 22% to 57%, depending on site conditions and treatment combinations. In Poland, co-application of *B. japonicum* with moderate nitrogen fertilizer resulted in a 22% yield increase.[50] In central Germany, up to 99% higher protein yield and enhanced N-fixation were achieved using commercial *B. japonicum* inoculants under cool-climate conditions.[74] Although no yield data were provided in Latvia, full-length 16S rRNA sequencing revealed increased diversity and abundance of functionally relevant rhizobia in nodule microbiomes, indicating ecological benefits.[48]

7. Discussion

The integration of nitrogen-fixing bacteria and humic products derived from agricultural waste offers a promising avenue for enhancing sustainable soybean cultivation. Numerous studies have demonstrated the effectiveness of *Bradyrhizobium* spp. in promoting root nodulation and atmospheric nitrogen fixation under a range of environmental conditions.[1-3,5,6,12,21] These microbes not only supply biologically fixed nitrogen to plants but also contribute to soil health and microbiome stability.[8,15,18]

Simultaneously, humic substances—particularly those derived from composted organic matter—have been reported to improve nutrient retention, enhance root architecture, and stimulate enzymatic activity within the rhizosphere.[2,31,58,60] When applied in combination, nitrogen-fixing bacteria and humic products can have synergistic effects, leading to improved nitrogen-use efficiency and crop productivity.[32,35,77] As demonstrated in Figure 3 and Table 3, the combined application enhanced soybean biomass by up to 28% and increased nodulation efficiency by over 35% compared to single treatments.

Genotypic variation among soybean cultivars also plays a critical role in determining inoculation success and nitrogen fixation outcomes.[10,12,55,74] Moreover, recent studies have highlighted that dual or multi-strain inoculation—*e.g*., with Az and *Bradyrhizobium*—can further boost plant resilience and yield under abiotic stress.[33-36,45,46,66] For instance, a study by Chibeba *et al*.[30] indicated that co-inoculated soybeans exhibited significantly earlier nodulation, which translated into higher final yields under field conditions.

However, some challenges persist. There is considerable variability in the performance of commercial humic products due to differences in source material, processing methods, and active ingredient concentrations.[31,61,62,85] In addition, factors such as soil pH, moisture availability, and the presence of native microbial competitors can limit the establishment and effectiveness of introduced rhizobia.[21,24,26]

Despite these constraints, the ecological and agronomic benefits of integrating microbial inoculants with humic products are increasingly recognized. Beyond nitrogen provision, such integrated biotechnologies support reduced chemical fertilizer input, enhanced carbon sequestration, and resilience to climate stressors.[25,32,55,59] Figure 4 illustrates that integrated treatments led to a 22% reduction in nitrate leaching and a 31% improvement in soil aggregate stability.

To achieve consistent field-level success, further work is warranted to standardize humic product quality,[31,59,86] develop precision delivery systems,[37,39] and tailor inoculation strategies to specific cultivars and agroecological conditions.[73,74] Emerging omics-based tools and soil microbiome profiling also hold potential to refine microbial compatibility and functional predictions.[9,17,71]

In summary, the combined application of nitrogen-fixing bacteria and humic substances represents a scalable, cost-effective, and ecologically sound strategy for soybean cultivation. This integrated approach aligns with the broader goals of circular bioeconomy and regenerative agriculture, offering a sustainable pathway toward enhanced crop performance and long-term soil fertility.

8. Conclusion

The integration of nitrogen-fixing bacteria and humic products derived from agricultural waste presents a robust and sustainable strategy to improve soybean productivity while enhancing soil fertility and ecological resilience. Co-application of these biotechnological inputs leads to improved nodulation, nitrogen fixation efficiency, nutrient uptake, and yield performance under diverse environmental conditions.

Despite existing challenges, such as strain-specific effectiveness, product variability, and the need for precision application, the growing body of scientific evidence supports their synergistic benefits. Moving forward, targeted formulation development, cultivar-specific compatibility testing, and field-level optimization will be critical for widespread adoption.

This integrated approach not only aligns with the principles of circular bioeconomy and regenerative agriculture but also offers practical solutions to reduce chemical inputs and mitigate environmental impact in legume-based cropping systems.

Acknowledgments

The author is grateful to the Latvia University of Life Sciences and Technologies for providing institutional support during the preparation of this manuscript.

Funding

This work was supported by the project "Strengthening Institutional Capacity for Excellence in Studies and Research at the Latvia University of Life Sciences and Technologies" (Project No. 5.2.1.1.i.0/2/24/I/CFLA/002), funded by the European Union through the NextGenerationEU program under the Recovery and Resilience Facility, within the framework of the National Development Plan of Latvia for 2021–2027, and administered by the Central Finance and Contracting Agency of Latvia.

Conflict of interest

The author declares no competing interests.

Author contributions

This is a single-authored article.

Availability of data

Not applicable.

Further disclosure

The conference in question is the 31st Annual International Scientific Conference "Research for Rural

Development 2025," held at the Latvia University of Life Sciences and Technologies (LBTU) in Jelgava, Latvia, from 14 to 16 May 2025. The event was conducted in a hybrid format—with over 250 participants attending in person and approximately 150 participating online.

References

1. Ishaq Z, Machido DA, Atta HI. Isolation and enumeration of *Bradyrhizobium* species dwelling in the root nodules of soybean plant. *UMYU J Microbiol Res.* 2020;5(2):17-25. doi: 10.47430/ujmr.2052.003
2. Da Silva MSR, dos Santos BM, Chávez DW, *et al*. K-humate as an agricultural alternative to increase nodulation of soybeans inoculated with *Bradyrhizobium*. *Biocatal Agric Biotechnol.* 2021;36:102129. doi: 10.1016/j.bcab.2021.102129
3. Campo RJ, Araujo RS, Hungria M. Nitrogen fixation with the soybean crop in Brazil: compatibility between seed treatment with fungicides and Bradyrhizobial inoculants. *Symbiosis.* 2009;48(1-3):154-163. doi: 10.1007/BF03179994
4. Syromiatnykov Y, Khalilov N, Troyanovskaya I, *et al*. Dynamics of agrophysical parameters and corn yield under minimum tillage in Samarkand region. *Acta Technol Agric.* 2025;28(2):80-87. doi: 10.2478/ata-2025-0011
5. Erniyani K. Effectiveness of Bradyrhizobium japonicum Strains Isolated from Several Locations in Ende on Nodule Formation and Nitrogen Fixation in Soybean (Glycine max L.). *AGRIFOR.* 2020;3(2):138-150. doi: 10.37478/agr.v3i2.501
6. Kurdali F, Nabulsi I, Mirali N. Nitrogen fixation in mutant soybean lines inoculated with two *Bradyrhizobium* japonicum strains. *Agrochimica.* 2005;49(5-6):233-245.
7. Pashchenko VF, Syromyatnikov YUN. The transporting ability of the rotor of the soil cultivating loosening and separating vehicle. *Tractors Agric Mach.* 2019;86(2):67-74. doi: 10.31992/0321-4443-2019-2-67-74
8. Perin J, Bertéli MBD, Valle JS, *et al*. Characterization of aapP and nopP genes related to nitrogen fixation efficiency with soybean in *Bradyrhizobium japonicum*. *Genet Mol Res.* 2018;17(3):gmr16039867. doi: 10.4238/GMR16039867
9. Klepa MS, diCenzo G, Hungria M. Comparative genomic analysis of *Bradyrhizobium* strains with natural variability in nitrogen fixation. *Microbiol Spectr.* 2024;12(2):e00260-24. doi: 10.1128/spectrum.00260-24
10. Agoyi EE, Afutu E, Chadare FJ, *et al*. Ureide assay to assess N_2 fixation abilities of soybean genotypes under different *Bradyrhizobium* strains. *J Crop Sci Biotechnol.* 2017;20(2):65-72. doi: 10.1007/s12892-016-0132-0
11. Kucey RMN, Snitwongse P, Chaiwanakupt P, *et al*. Nitrogen fixation (^{15}N dilution) with soybeans under Thai field conditions. *Plant Soil.* 1988;106(1):87-92. doi: 10.1007/BF02370103
12. Maluk M, Giles M, Wardell GE, *et al*. Biological nitrogen fixation by soybean in Scotland requires inoculation with non-native *Bradyrhizobium*. *Front Agron.* 2023;5:1196873. doi: 10.3389/fagro.2023.1196873
13. Praharaj C, Dhingra K. Growth and nitrogen fixation in soybean under *Bradyrhizobium* inoculation and nitrogen schedules. *Indian J Agron.* 2001;46(1):110-116.
14. Keyser HH, Li F. Potential for increasing biological nitrogen fixation in soybean. *Plant Soil.* 1992;141(1-2):119-135. doi: 10.1007/BF00011313
15. Barros Carvalho GA, Hungria M, Lopes FM, *et al*. Brazilian adapted soybean *Bradyrhizobium* strains uncover IS elements impacting nitrogen fixation. *FEMS Microbiol Lett.* 2019;366(11):fnz046. doi: 10.1093/femsle/fnz046
16. Delamuta JRM, Ribeiro RA, Ormeño Orrillo E, *et al*. *Bradyrhizobium tropiciagri* sp. nov. and *Bradyrhizobium embrapense* sp. nov. *Int J Syst Evol Microbiol.* 2015;65(12):4424-4433. doi: 10.1099/ijsem.0.000592
17. Bender FR, Nagamatsu S, Delamuta JRM, *et al*. Genetic variation in symbiotic islands of *Bradyrhizobium* strains. *Microb Genom.* 2022;8(11):000795. doi: 10.1099/mgen.0.000795
18. Abaidoo RC, Keyser HH, Singleton PW, Dashiell KE, Sanginga N. Population size and symbiotic characteristics of indigenous *Bradyrhizobium* spp. *Appl Soil Ecol.* 2007;35(1):57-67. doi: 10.1016/j.apsoil.2006.05.006
19. Syromyatnikov Y, Troyanovskaya I, Zagidullin R, Tikhonov E, Orekhovskaya A. Soil density in traditional mouldboard tillage. *Acta Technol Agric.* 2023;26(3):159-165. doi: 10.2478/ata-2023-0021
20. Syromiatnykov Y, Ishniyazova S, Voinash S, *et al*. Effectiveness of compositions based on thiosulfonates and biosurfactants for plant protection against phytopathogens. *E3S Web Conf.* 2025;613:e02002. doi: 10.1051/e3sconf/202561302002
21. Zahran HH. Rhizobium-legume symbiosis and nitrogen fixation under stress. *Microbiol Mol Biol Rev.* 1999;63(4):968-989. doi: 10.1128/MMBR.63.4.968989.1999
22. Giller KE. *Nitrogen Fixation in Tropical Cropping Systems.* Wallingford, UK: CABI Publishing; 2001. doi: 10.1079/9780851994178.0000
23. Syromyatnikov YN, Orekhovskaya AA, Dzjasheev A, *et al*. Cultivator points of the rotary tillage loosening and separating machine of the stratifier. *J Phys Conf Ser.*

2021;2094(4):042024.
doi: 10.1088/1742-6596/2094/4/042024
24. Dakora FD, Keya SO. Contribution of legume nitrogen fixation to sustainable agriculture in sub-Saharan Africa. *Soil Biol Biochem.* 1997;29(5-6):809-817.
doi: 10.1016/S0038-0717(96)00225-8
25. Herridge DF, Peoples MB, Boddey RM. Global inputs of biological nitrogen fixation in agriculture. *Plant Soil.* 2008;311(1-2):1-18.
doi: 10.1007/s11104-008-9668-3
26. Okogun JA, Sanginga N. Can indigenous and introduced rhizobial strains compete? *Biol Fertil Soils.* 2003;38(1):26-31.
doi: 10.1007/s00374-003-0613-2
27. Xavier GR, Martins LMV, Lisboa RS, *et al*. Selection of indigenous *Bradyrhizobium* strains. *Braz J Microbiol.* 2003;34(1):88-94.
doi: 10.1590/S1517-83822003000100016
28. Deaker R, Roughley RJ, Kennedy IR. Legume seed inoculation technology. *Soil Biol Biochem.* 2004;36(8):1275-1288.
doi: 10.1016/j.soilbio.2004.04.009
29. Costa EM, Ribeiro PRA, Carvalho TS, *et al*. Efficient nitrogen fixing bacteria isolated from soybean nodules in the semi-arid region of northeast Brazil are classified as *Bradyrhizobium brasilense* (symbiovar sojae). *Curr Microbiol.* 2020;77(6):1746-1755.
doi: 10.1007/s00284-020-01993-6
30. Chibeba AM, Guimarães MF, Brito OR, *et al*. Co-inoculation of soybean with *Bradyrhizobium* and *Azospirillum* promotes early nodulation. *Am J Plant Sci.* 2015;6(10):1641-1649.
doi: 10.4236/ajps.2015.610164
31. Maffia A, Oliva M, Marra F, Mallamaci C, Nardi S, Muscolo A. Humic substances: Bridging ecology and agriculture for a greener future. *Agronomy.* 2025;15(2):410.
doi: 10.3390/agronomy15020410
32. Canellas LP, Canellas NOA, Olivares FL. Biostimulants using humic substances and rhizosphere microorganisms. *Sci Agric.* 2022;79(Suppl 1):e20220103.
doi: 10.1590/1678-992X-2022-0103
33. Galal YGM. Dual inoculation with strains of *Bradyrhizobium japonicum* and *Azospirillum brasilense* to improve growth and biological nitrogen fixation of soybean. *Biol Fertil Soils.* 1997;24(4):317-322.
doi: 10.1007/s003740050250
34. Neto VPC, Melo ARP, Alencar CES, *et al*. Bacterial consortia among *Bradyrhizobium*, *Azospirillum*, and *Bacillus* promote plant growth and nitrogen fixation in mung bean. *Symbiosis.* 2024;82(1):1-11.
doi: 10.1007/s13199-024-01003-4
35. Hungria M, Nogueira MA, Araujo RS. Soybean seed co-inoculation with *Bradyrhizobium* spp. and *Azospirillum brasilense*: A new biotechnological tool. *Am J Plant Sci.* 2015;6(6):811-817.
doi: 10.4236/ajps.2015.66087
36. Deák ÉA, Martin TN, Stecca JDL, *et al*. Sulfur fertilization and inoculation with *Azospirillum brasilense* and *Bradyrhizobium* spp. improve yield and quality. *Braz J Microbiol.* 2024;55(1):87-98.
doi: 10.1007/s42770-024-01585-7
37. Silva AP, Braccini AL, Felber PH, Marteli DCV, Fagotti DDS, dos Santos RF. Evaluation of methods for inoculating soybean seeds with *Bradyrhizobium* spp. and *Azospirillum brasilense*. *Rev Agroneg Meio Ambient.* 2024;17(2):119-132.
doi: 10.17765/2176-9168.2024v17n2e11948
38. Dozet G. Microbial activity of soil during inoculation of soybean with symbiotic and free-living nitrogen-fixing bacteria. *Afr J Biotechnol.* 2012;11(20):2850-2862.
doi: 10.5897/ajb11.744
39. Garcia MVC, Nogueira MA, Hungria M. Combining microorganisms in inoculants: Composite inoculant case for soybean. *AMB Express.* 2021;11(1):127.
doi: 10.1186/s13568-021-01230-8
40. Galindo FS, Pagliari PH, da Silva EC, *et al*. Co-inoculation with *Azospirillum brasilense* and *Bradyrhizobium* sp. enhances nitrogen uptake and yield in field-grown cowpea and did not change N fertilizer recovery. *Plants.* 2022;11(14):1847.
doi: 10.3390/plants11141847
41. Vauclare P, Bligny R, Gout E, Widmer F. Metabolic differences in *Bradyrhizobium japonicum* and soybean bacteroids. *FEMS Microbiol Lett.* 2013;343(1):49-56.
doi: 10.1111/1574-6968.12124
42. Abreu Junior CH, Gruberger GAC, Cardoso PHS, *et al*. Soybean seed enrichment with cobalt and molybdenum as an alternative to conventional seed treatment. *Plants.* 2023;12(5):1164.
doi: 10.3390/plants12051164
43. Zydlik Z, Zydlik P. The effect of a preparation containing humic acids on the growth, yield, and quality of strawberry fruits (*Fragaria* × *ananassa*). *Agronomy.* 2023;13(7):1872.
doi: 10.3390/agronomy13071872
44. Zydlik P, Zydlik Z, Kafkas NE. The effect of the foliar application of biostimulants in a strawberry field plantation on the yield and quality of fruit, and on the content of health-beneficial substances. *Agronomy.* 2024;14(8):1786.
doi: 10.3390/agronomy14081786
45. Sibponkrung S, Kondo T, Tanaka K, *et al*. Co-inoculation of *Bacillus velezensis* strain S141 and *Bradyrhizobium* strains promotes nodule growth and nitrogen fixation. *Microorganisms.* 2020;8(5):678.
doi: 10.3390/microorganisms8050678
46. Pisarek I, Grata K. The influence of sewage sludge and fly ash fertilization on the total number of bacteria (TNB) and *Bradyrhizobium* species in soybean agroecosystem. *Agriculture.* 2023;13(1):201-206.
doi: 10.3390/agriculture13010201

47. Vorobey N, Kukol K, Pukhtaievych P, Kots S. Complex inoculation of soybeans with nodule bacteria *Bradyrhizobium japonicum* as a measure to optimize symbiotic nitrogen fixation. *Agric Microbiol.* 2023;38(1):29-39.
doi: 10.35868/1997-3004.38.29-39
48. Klūga A, Dubova L, Alsiņa I, Rostoks N. Alpha-, gamma- and beta-proteobacteria detected in legume nodules in Latvia, using full-length 16S rRNA gene sequencing. *Acta Agric Scand B Soil Plant Sci.* 2023;73(1):127-141.
doi: 10.1080/09064710.2023.2232681
49. Waluyo SH. *Biological Nitrogen Fixation of Soybean in Acid Soils of Sumatra, Indonesia* [dissertation]; 2000.
50. Księżak J, Bojarszczuk J. The effect of mineral N fertilization and *Bradyrhizobium japonicum* seed inoculation on productivity of soybean (*Glycine max* (L.) Merrill). *Agriculture.* 2022;12(1):110.
doi: 10.3390/agriculture12010110
51. Htwe AZ, Moh SM, Moe K, Yamakawa T. Effects of co-inoculation of *Bradyrhizobium japonicum* SAY3-7 and *Streptomyces griseoflavus* P4 on plant growth, nodulation, nitrogen fixation, nutrient uptake, and yield of soybean in a field condition. *Soil Sci Plant Nutr.* 2018;64(2):222-229.
doi: 10.1080/00380768.2017.1421436
52. Koliada O, Bliznjuk O, Masalitina N, Belinska A, Varankina O, Belykh I. Case study of soybean inoculation with biotechnological preparations. *Integr Technol Energy Saving.* 2022;3:1.
doi: 10.20998/2078-5364.2022.3.01
53. Hatipoğlu H, Haliloğlu H. Nitrogen application and seed inoculation with *Bradyrhizobium japonicum* bacteria improved yield and quality traits of soybean grown as second crop. *Pol J Environ Stud.* 2024;33(1):0256.
doi: 10.15244/pjoes/192372
54. Pacheco da Silva ML, Moen FS, Liles MR, Feng Y, Sanz Saez A. The response to inoculation with PGPR plus orange peel amendment on soybean is cultivar and environment dependent. *Plants.* 2022;11(9):1138.
doi: 10.3390/plants11091138
55. Beregovaya YV, Tychinskaya I, Petrova S, *et al*. Cultivar specificity of the rhizobacterial effects on nitrogen-fixing symbiosis and mineral nutrition of soybean under agrocenosis conditions. *Sel'skokhozyaist Biol.* 2018;53(5):977-985.
doi: 10.15389/agrobiology.2018.5.977eng
56. Banasiewicz J, Gumowska A, Hołubek A, Orzechowski S. Adaptations of the genus *Bradyrhizobium* to selected elements, heavy metals and pesticides present in the soil environment. *Curr Issues Mol Biol.* 2025;47(3):205.
doi: 10.3390/cimb47030205
57. Di Sario L, Boeri P, Matus JT, Pizzio GA. Plant biostimulants to enhance abiotic stress resilience in crops. *Int J Mol Sci.* 2025;26(3):1129.
doi: 10.3390/ijms26031129
58. Matuszak-Slamani R, Bejger R, Włodarczyk M, *et al*. Effect of humic acids on soybean seedling growth under polyethylene glycol 6000-induced drought stress. *Agronomy.* 2022;12(5):1109.
doi: 10.3390/agronomy12051109
59. Rodrigues Prates A, Coscione ARC, Teixeira Filho MM, *et al*. Composted sewage sludge enhances soybean production and agronomic performance in naturally infertile soils (Cerrado region, Brazil). *Agronomy.* 2020;10(11):1677.
doi: 10.3390/agronomy10111677
60. Ntanasi T, Karavidas I, Spyrou GP, *et al*. Plant biostimulants enhance tomato resilience to salinity stress: insights from two Greek landraces. *Plants.* 2024;13(10):1404.
doi: 10.3390/plants13101404
61. Egamberdiyeva D, Qarshieva D, Davranov K. Growth and yield of soybean varieties inoculated with *Bradyrhizobium* spp in N-deficient calcareous soils. *Biol Fertil Soils.* 2004;40:144-146.
doi: 10.1007/s00374-004-0755-1
62. Holatko J, Hammerschmiedt T, Latal O, *et al*. Deciphering the effectiveness of humic substances and biochar modified digestates on soil quality and plant biomass accumulation. *Agronomy.* 2022;12(7):1587.
doi: 10.3390/agronomy12071587
63. Perez Fernández M, De Lara Del Rey IA, Magadlela A. Shining a light on symbiosis: N fixing bacteria boost legume growth under varied light conditions. *Agriculture.* 2024;14(2):164.
doi: 10.3390/agriculture14020164
64. Grobelak A, Bień B, Sławczyk D, Bień J. Conditioning biomass for biogas plants: innovative pre-treatment and digestate valorization techniques to enhance soil health and fertility. *Sustainability.* 2025;17(8):3289.
doi: 10.3390/su17083289
65. Peng XX, Cheng K, Yuan Y, *et al*. Foliar application of iron strengthened artificial humic acid promotes nitrogen fixation and improves soybean yield. *Ind Crops Prod.* 2025;224:120368.
doi: 10.1016/j.indcrop.2024.120368
66. Tu T, Lin SH, Shen F. Enhancing symbiotic nitrogen fixation and soybean growth through co-inoculation with *Bradyrhizobium* and *Pseudomonas* isolates. *Sustainability.* 2021;13(20):11539.
doi: 10.3390/su132011539
67. Szpunar-Krok E, Bobrecka-Jamro D, Pikuła W, Jańczak-Pieniążek M. Effect of nitrogen fertilization and inoculation with *Bradyrhizobium japonicum* on nodulation and yielding of soybean. *Agronomy.* 2023;13(5):1341.
doi: 10.3390/agronomy13051341
68. Garcia MVC, Nogueira MA, Hungria M. Combining microorganisms in inoculants is agronomically important but industrially challenging: Case study of a composite inoculant containing *Bradyrhizobium* and *Azospirillum*

for the soybean crop. *AMB Express.* 2021;11(1):71. doi: 10.1186/s13568-021-01230-8
69. Alves LA, Ambrosini VG, de Oliveira Denardin LG, *et al*. Biological N_2 fixation by soybeans grown with or without liming on acid soils in a no-till integrated crop-livestock system. *Soil Tillage Res.* 2021;209:104923. doi: 10.1016/j.still.2020.104923
70. Syromyatnikov YN, Orekhovskaya AA, Dzjasheev A, *et al*. Improving stability of movement of machine section for soil preparation and seeding. *J Phys Conf Ser.* 2021;2094(4):042027. doi: 10.1088/1742-6596/2094/4/042027
71. Zotikov VI, Zubareva KY. Application of microbiological preparations in the cultivation of promising soybean varieties in Oryol Oblast. *Russ Agric Sci.* 2024;50:473-480. doi: 10.3103/S1068367424700496
72. Mazur O, Tymoshchuk T, Didur I, Tsyhanskyi V. Study of legume rhizobia symbiosis in soybean for agroecosystem resilience. *Sci Horizons.* 2024;11:68. doi: 10.48077/scihor11.2024.68
73. Didora V, Kluchevych M. Soybean productivity depending on the elements of organic cultivation technology in the short term crop rotation of Ukrainian Polissia. *Sci Horizons.* 2021;24(2):77-83. doi: 10.48077/scihor.24(2).2021.77-83
74. Zimmer S, Messmer M, Haase T, *et al*. Effects of soybean variety and *Bradyrhizobium* strains on yield, protein content and biological nitrogen fixation under cool growing conditions in Germany. *Eur J Agron.* 2016;72:38-46. doi: 10.1016/j.eja.2015.09.008
75. Ghadge J, Murumkar D. Inoculation effect of consortium of *Rhizobium*, PSB and KMB on the growth and yield of soybean. *Int J Curr Microbiol Appl Sci.* 2020;9(9):1979-1993. doi: 10.20546/ijcmas.2020.909.248
76. Gomes Y, Dalchiavon F, Valadão F. Joint use of fungicides, insecticides and inoculants in the treatment of soybean seeds. *Rev Ceres.* 2017;64:258-265. doi: 10.1590/0034-737X201764030006
77. Canellas LP, Silva RM, Barbosa LJS, *et al*. Co-inoculation with *Bradyrhizobium* and humic substances combined with *Herbaspirillum seropedicae* promotes soybean vegetative growth and nodulation. *Agronomy.* 2023;13(10):2660. doi: 10.3390/agronomy13102660
78. Pratiwi GR, Nurrahma AHI. Biochar and humic substances roles for nitrogen transformation in agriculture. *J Tek Pert Lampung.* 2024;13(4):1442-1452. doi: 10.23960/jtep-l.v13i4.1442-1452
79. Saha B, Saha S, Das A, *et al*. Biological nitrogen fixation for sustainable agriculture. In: Singh D, Singh H, Prabha R, editors. *Plant Microbe Interactions in Agro-Ecological Perspectives.* Singapore: Springer; 2017. p. 81-128. doi: 10.1007/978-981-10-5343-6_4
80. Jaiswal SK, Dakora FD. Maximizing photosynthesis and plant growth in African legumes through rhizobial partnerships: The road behind and ahead. *Microorganisms.* 2025;13(3):581. doi: 10.3390/microorganisms13030581
81. Syromyatnikov Y, Voinash S, Troyanovskaya I, Zagidullin R, Tikhonov E, Orekhovskaya A. Chisel tillage under spring barley in the forest-steppe. *Acta Technol Agric.* 2024;27(1):30-34. doi: 10.2478/ata-2024-0005
82. Aasfar A, Bargaz A, Yaakoubi K, *et al*. Nitrogen fixing *Azotobacter* species as potential soil biological enhancers for crop nutrition and yield stability. *Front Microbiol.* 2021;12:628379. doi: 10.3389/fmicb.2021.628379
83. Hindersah R, Aini RAP, Setiawati M, *et al*. Boosting strawberry yield and fruit sweetness with humic substances and biofertilizer in soilless cocopeat-based culture. *J Ilm Pertanian.* 2023;20(3):13242. doi: 10.31849/jip.v20i3.13242
84. De Hita D, Fuentes M, Zamarreño Á, García-Mina JM, Baigorri R. Culturable bacterial endophytes from sedimentary humic acid treated plants. *Front Plant Sci.* 2020;11:837. doi: 10.3389/fpls.2020.00837
85. Dauletbay A, Hanzheng D, Ongalbek AN, *et al*. Humic acids: Properties, structure, and application. *Bull Shakarim Univ Tech Sci.* 2024;3:41. doi: 10.53360/2788-7995-2024-3(15)-41
86. Kong B, Wu Q, Li Y, *et al*. The application of humic acid urea improves nitrogen use efficiency and crop yield by reducing the nitrogen loss compared with urea. *Agriculture.* 2022;12(12):1996. doi: 10.3390/agriculture12121996
87. Didora V, Bondar O, Vlasiuk M. Soybeans productivity depending on biological preparations and mineral fertilizers on Ukraine's Polissia. *Sci Horiz*. 2019;22(1):33-39. doi: 10.332491/2663-2144-2019-74-1-33-39
88. Kadoglidou KI, Anthimidou E, Krommydas K, *et al*. Effect of biostimulants on drought tolerance of greenhouse-grown tomato. *Horticulturae.* 2025;11(6):601. doi: 10.3390/horticulturae11060601
89. Pačuta V, Rašovský M, Michalska-Klimczak B, Wyszyński Z. Grain yield and quality traits of durum wheat (*Triticum durum* Desf.) treated with seaweed- and humic acid-based biostimulants. *Agronomy.* 2021;11(7):1270. doi: 10.3390/agronomy11071270

Asian Journal of Water, Environment and Pollution. Vol. 22, No. 6 (2025), pp. 21-46.
doi: 10.36922/AJWEP025290224

REVIEW ARTICLE

Hydrocarbons in seawater: Sources, fate, impacts, and remediation strategies

Daniele Fattorini[1,2]*

[1]Department of Life and Environmental Sciences, Faculty of Sciences, Polytechnic University of Marche, Ancona, Marche, Italy
[2]National Inter-University Consortium for Marine Sciences, Ancona, Marche, Italy
***Corresponding author:** Daniele Fattorini (d.fattorini@staff.univpm.it)

Received: July 15, 2025; Revised: August 1, 2025; Accepted: August 18, 2025; Published online: September 8, 2025

Abstract: Hydrocarbon contamination in marine environments poses a significant global environmental challenge, impacting ecosystems, human health, and economic activities. The present review provides a comprehensive overview of hydrocarbons in seawater, addressing their diverse sources, complex fate and transport mechanisms, ecological and toxicological impacts, and various remediation strategies. Both natural seepages from geological formations and a wide array of anthropogenic inputs are discussed as primary contributors to marine hydrocarbon burdens. Anthropogenic carbon inputs include large-scale accidental oil spills, chronic operational discharges from shipping and offshore platforms, industrial effluents, and diffuse urban runoff carrying petrogenic and pyrogenic hydrocarbons, during the past 50 years. In the sea, hydrocarbons undergo a series of interconnected physical, chemical, and biological transformations that mediate their persistence, bioavailability, and spatial distribution. The specific environmental conditions, such as temperature, nutrient availability, and microbial community composition, significantly influence the rate and extent of these natural attenuation processes. The ecological consequences range from acute lethal impacts causing immediate mortality in marine organisms to chronic sublethal effects on reproduction, growth, immune response, and behavior across a wide range of taxa, from plankton to marine mammals. Furthermore, long-term ecosystem disruptions, including habitat degradation of vital coastal areas, such as mangroves and coral reefs, and bioaccumulation within the food web, pose serious threats to ecosystem health and biodiversity. To mitigate these adverse effects, a range of remediation strategies has been developed and implemented; their mechanisms, effectiveness in various scenarios, inherent limitations, and potential secondary environmental considerations are explored in this review. Emphasis is placed on the importance of integrated approaches that combine rigorous prevention measures, rapid and effective response protocols during spill events, and sustainable, environmentally sound long-term remediation techniques. Understanding the intricate interplay between the sources, transformations, impacts, and potential solutions for hydrocarbon contamination is crucial for developing robust management plans and safeguarding the long-term health and resilience of marine ecosystems.

Keywords: Hydrocarbons; Marine environment; Natural source; Anthropogenic pollution; Monitoring programs; Remediation strategy

1. Introduction

The oceans represent vast and dynamic reservoirs of life. They are constantly exposed to various chemical compounds, among which aliphatic hydrocarbon mixtures are significant substances with profound natural origins and widespread anthropogenic influences.[1-3] Fundamentally, hydrocarbons are organic compounds

composed of hydrogen and carbon atoms, existing in a broad spectrum of physical states, from volatile gases, such as methane to heavy, viscous liquids, and solid tars.[4] Their presence in the marine environment is not recent, considering that natural geological processes have continuously introduced these compounds into the oceans for millions of years, shaping unique ecosystems around several localized inputs.[1,5-7] However, the advent of the industrial age and the escalating global reliance on fossil fuels have dramatically altered the magnitude, frequency, and composition of hydrocarbon inputs, transforming what were once isolated natural seepage into widespread contamination events.[8-10]

The ecological and economic significance of marine ecosystems necessitates a comprehensive understanding of hydrocarbon dynamics. These environments, ranging from surface waters enriched with phytoplankton at the base of the aquatic food webs to deep-sea hosting chemosynthetic communities and an intricate benthic ecosystem, are all potentially susceptible to hydrocarbon exposure of both natural and anthropogenic origins.[11-13] Hydrocarbons can exert deleterious effects at every trophic level, impacting organisms from unicellular species to apex predators, such as marine mammals and seabirds.[14,15] Furthermore, the recreational and economic value of coastal areas, including vital fisheries, aquaculture operations, and thriving tourism industries, is directly threatened by hydrocarbon pollution, leading to significant financial losses and long-term environmental damage.[8,9] The inherent toxicity and bioaccumulation potential of many hydrocarbon compounds pose a multifaceted threat, prompting extensive scientific inquiry into their fate and effects in marine systems.[1,8,11,14,15]

Natural hydrocarbon sources in the marine environment primarily include geological seeps and biogenic production.[12,13,16,17] Deep-sea seeps found along continental margins worldwide (e.g., Gulf of Mexico, Santa Barbara Channel) continuously release oil and gas from subsurface reservoirs through fissures and faults in the seabed.[5,6,18] These natural inputs have sculpted unique chemosynthetic ecosystems, where specialized microbial communities thrive on hydrocarbons and sulfur compounds, forming the base of unique food webs. At the same time, volcanic activity and hydrothermal vents also contribute a minor amount of hydrocarbons.[19-21] Submarine pockmarks are seabed depressions or craters that typically form through episodic or continuous expulsion of subsurface fluids, such as methane gas and other hydrocarbons. They act as geological pathways for hydrocarbons stored deep within the Earth's crust to migrate and escape into the marine environment. These deep-sea features are therefore considered natural sources of hydrocarbons in the ocean.[22,23] Moreover, aquatic organisms, including phytoplankton, bacteria, and algae, naturally produce small quantities of diverse hydrocarbons, which contribute to the background levels in seawater.[24] Although these natural processes are constant, a continuous degradation of hydrocarbons is operated by specialized endemic microbial populations, demonstrating the ocean's inherent capacity for natural attenuation.[25]

In contrast, anthropogenic sources introduce hydrocarbons into the marine environment with significantly greater magnitude and frequency, often in concentrated, acute events.[8,9] The primary anthropogenic contributor is the petroleum industry, encompassing exploration, production, transport, and refining activities. Major oil spills from accidents (e.g., Exxon Valdez, Prestige), offshore drilling blowouts (e.g., Deepwater Horizon), and pipeline ruptures represent catastrophic point source inputs that release vast quantities of crude oil over short periods, overwhelming natural degradation processes.[26-28] Beyond these high-profile incidents, chronic operational discharges from shipping (e.g., ballast water, engine room effluence) and discharges of produced water from offshore oil and gas platforms may increase the background level of global pollution.[29-31] Moreover, land-based sources, such as urban and industrial runoff carrying hydrocarbons from road spills, industrial effluents, and atmospheric deposition of combustion byproducts from vehicles and industries, also represent significant and diffuse inputs to water bodies.[32,33] Notably, the chemical composition of anthropogenic hydrocarbons, particularly refined products, often markedly differs from that of natural seeps, containing elevated concentrations of more toxic and bioavailable compounds, exacerbating the ecological impacts.[34]

In the marine environment, aliphatic hydrocarbon mixtures can undergo a complex series of physical, chemical, and biological transformations that govern their distribution, persistence, and ultimate fate.[1,2,35-37] Processes, such as spreading, evaporation of volatile components, dissolution into the water column, wave dispersion, and emulsification can rapidly alter oil physical characteristics.[1,36,37] In surface waters, chemical transformations include photo-oxidation by sunlight, which can lead to the formation of more polar and sometimes more toxic compounds.[38-40] However, microbial degradation represents the most critical natural attenuation pathway, where diverse marine bacteria and

archaea metabolize hydrocarbons, breaking them into less harmful byproducts, and eventually carbon dioxide and water.[22,25,41] Other processes include sedimentation of dense oil components and the formation of aerosols that can transport hydrocarbons over long distances.[42] Understanding these intricate processes is fundamental to predicting the relevance and impact of hydrocarbon spills and developing effective response strategies.

The environmental and human health impacts of hydrocarbons in seawater are profound and multifaceted. For example, seabirds are particularly vulnerable to dense oil pollution, which affects their feather insulation, leading to hypothermia, mobility issues, and buoyancy issues. At the same time, marine mammals can suffer from ingestion, aspiration, and organ damage.[11,43] Chronic, sublethal effects are equally concerning, including impaired growth, reproduction, immune suppression, developmental abnormalities, and behavioral changes in fish and invertebrates.[1,44] Besides direct toxicological effects, hydrocarbon mixtures can also degrade critical habitats, such as coral reefs, seagrass beds, and mangrove forests, leading to long-term ecosystem damage and loss of biodiversity and ecosystem services.[45,46]

Considering the relevant threats posed by hydrocarbon pollution, various containment measures, monitoring programs, and remediation strategies have been developed and continuously refined. Generally, initial responses to accidental spill events focus on containment using booms and mechanical recovery through skimmers to physically remove oil from the water surface.[47] Chemical dispersants are sometimes used to break down oil slicks into smaller droplets, enhancing natural dispersion and microbial degradation. However, their use remains controversial due to potential toxicity to marine life.[48] Monitoring the contamination caused by aliphatic hydrocarbon mixtures may involve various techniques, from remote sensing for large-scale tracking to chemical analyses of water, sediment, and biota samples, alongside biomonitoring programs.[49,50] Remediation strategies aim to restore affected environments, with bioremediation a prominent approach. This involves enhancing the activity of native oil-degrading microorganisms through nutrient addition (biostimulation) or introducing specialized microbial strains (bioaugmentation).[51] Other methods include *in situ* burning, shoreline cleaning, and natural attenuation, where the environment can recover over time. The selection of the most appropriate strategy depends on factors, such as oil type, environmental conditions, and the sensitivity of the affected ecosystem.

Given the great relevance of hydrocarbon mixtures in the oceans, the present review aims to consolidate current scientific knowledge about the origin and fate of these compounds in seawater, exploring the complex interplay of processes governing their distribution and transformation, the impact on marine biota and human health, and the evolving strategies employed for their containment, monitoring, and remediation. Although in-depth knowledge of each specific topic discussed here is available, scientific literature does not always provide a comprehensive and coherent synthesis of various issues concerning hydrocarbons in the sea, which is the primary focus of the present systematic review. By integrating geochemistry, oceanography, marine biology, and environmental sciences insights, this review provides a holistic overview of the critical environmental issue associated with hydrocarbon mixtures and highlights areas for future research perspectives.

2. Natural origins of hydrocarbons in seawater

Hydrocarbon mixtures are intrinsically linked to the Earth's geological and biological cycles; their presence in the marine environment is a fundamental and ancient phenomenon, pre-dating human civilization by millions of years. Natural processes contribute to introducing various hydrocarbons into the oceans, influencing background levels, shaping unique chemosynthetic ecosystems, and playing a role in the global carbon cycle.[52-54] Understanding these natural origins is crucial for distinguishing between background levels and pollution events and appreciating the inherent capacity of marine systems to process these compounds.[1,2,50]

Among the primary natural pathways of hydrocarbon input into seawater, geological seepage represents one of the primary continuous sources of emissions, being the most significant and well-studied natural hydrocarbon emission processes.[5,12,17,34,50] These occur when deeply buried petroleum and natural gas, formed from the thermogenic alteration of organic matter in sedimentary basins, migrate upward through faults, fractures, and porous rock formations in the seafloor to reach the water column and eventually the surface.[5,12,17] Seeps are commonly found globally along continental margins, in active tectonic regions, and within sedimentary basins.[12,17]

The Gulf of Mexico, which hosts one of the world's most extensive and active deep-sea seep areas, is characterized by thousands of individual seeps releasing variable quantities of oil and gas, from small, chronic

trickles to larger, more episodic bursts.[5,55] These seeps create distinct ecological communities characterized by chemosynthetic organisms (i.e., tube worms, mussels, bacterial mats) that utilize methane and sulfide as energy sources, forming the base of complex food webs independent of sunlight.[55] The Santa Barbara Channel off the coast of California is another well-known example, mainly characterized by a prolific shallow-water oil seep system, such as Coal Oil Point.[5,56] These seeps have been active for millennia, releasing crude oil that frequently washes to the shoreline as a form of spherical aggregates, a natural phenomenon long recognized by indigenous populations.[56] Other significant seep areas include the Caspian Sea, the North Sea, and various regions along the Atlantic and Pacific continental slopes.[5] Partly similar phenomena to submarine seepages are represented by pockmarks; these are depressions or craters found on the seabed, typically formed by the episodic or continuous expulsion of fluids, such as methane gas and other hydrocarbons, from the subsurface.[22,23,57,58] Unlike seepages, pockmarks have also been found in areas with relatively shallow water and are not directly related to fractures in the Earth's crust, but rather to geological formations with hydrocarbons close enough to the surface of the seabed to produce slow and episodic upwelling.[23,57] Although the hydrocarbon contribution from pockmarks is lower than that of natural seepages, their presence may help shape the characteristics of relatively shallow ecosystems, such as some regions of the Mediterranean.[22,57,58]

The hydrocarbons released from geological seeps exhibit a wide range of geochemical characteristics depending on their source rock, thermal maturity, and migration pathways. Naturally seeping oil often contains a complex mixture of alkanes (saturated hydrocarbons), cycloalkanes, and polycyclic aromatic hydrocarbons (PAHs), along with non-hydrocarbon compounds, such as sulfur, nitrogen, and oxygen-containing molecules.[1,2,34,50] Notably, crude oils from natural seeps often contain distinct compounds, hopanes, steranes, and terpanes that are resistant to degradation and reflect the original organic matter from which the oil was produced.[59,60] These hydrocarbons constitute fingerprint compounds, allowing them to differentiate natural seepage oil from anthropogenically sourced oil in environmental samples.[60] The gaseous components of natural seeps are predominantly methane, with the presence of small amounts of heavier gaseous hydrocarbons (ethane, propane, butane) and trace quantities of non-hydrocarbon gases, such as carbon dioxide and hydrogen sulfide.[61,62] The stable isotopic composition of methane ($\delta^{13}C$ and δD) is often used to distinguish between thermogenic (geological) and biogenic (microbial) methane sources.[61]

In addition to typical cold seeps, hydrothermal vents, which are found predominantly along mid-ocean ridges and back-arc basins, also release hydrocarbons into the deep ocean.[19-21,60] These systems involve seawater circulation through hot, fractured oceanic crust, leading to chemical reactions and the discharge of superheated, chemically rich fluids.[63] While the primary constituents of hydrothermal fluids are typically trace elements and sulfur compounds, significant amounts of hydrocarbons, including methane and heavier alkanes and aromatics, have been detected in various vent systems globally.[63] The origin of these hydrocarbons in hydrothermal systems can be varied. Some are abiogenic, meaning they are formed by inorganic chemical reactions involving carbon dioxide, hydrogen, and minerals at high temperatures and pressures within the Earth's crust, such as serpentinization reactions.[60,63] The "Lost City" hydrothermal field in the Atlantic, for instance, is known for its abiogenic methane and light hydrocarbon production.[63] Other hydrocarbons found in vent fluids can have a thermogenic origin, such as conventional petroleum, formed by heating deeply buried organic matter in sediments that are subsequently incorporated into the hydrothermal circulation.[60] A third potential source is biogenic methane produced by thermophilic and hyper-thermophilic microorganisms residing in the subsurface or within the vent structures.[19,20,63] The relative contribution of each origin varies among different fields, but the presence of hydrocarbons in these extreme environments underscores the diverse geological and chemical processes that can generate them.[19,20,60,63]

Beyond geological processes, marine organisms themselves represent a continuous and diffuse source of a wide range of hydrocarbons to seawater. These biogenic hydrocarbons are fundamentally different in their genesis and often in their chemical structure compared to fossil fuels.[64,65] Algae, particularly phytoplankton, are prolific producers of hydrocarbons. Many species of green algae (*Chlorophyta*) and cyanobacteria produce short-chain volatile hydrocarbons, such as isoprene and longer-chain alkanes (e.g., n-heptadecane, n-octadecane).[24] These compounds are typically synthesized as metabolic byproducts, signaling molecules, or components of cell membranes. For instance, n-alkanes are commonly found in the waxes and cuticles of many organisms. The large biomass and rapid phytoplankton turnover

in surface waters imply that the collective contribution of these biogenic hydrocarbons may be substantial, especially in productive regions.[24,64,65]

Marine bacteria and archaea also play a crucial role in producing and transforming hydrocarbons. Some marine bacteria are known to synthesize long-chain hydrocarbons, including branched and cyclic compounds, as components of their cell membranes (e.g., hopanoids) or as storage products.[66] Moreover, methanogenic archaea, prevalent in anaerobic marine sediments and anoxic water columns, produce vast quantities of biogenic methane through the anaerobic decomposition of organic matter.[67] This biogenic methane can diffuse out of sediments, forming methane plumes in the water column, or be oxidized by methanotrophic bacteria. While methane is a potent greenhouse gas, its natural production and consumption by marine microbes are integral to the global carbon cycle.

Zooplankton and other marine invertebrates can contribute to the hydrocarbon pool by accumulating and transforming lipids and hydrocarbons from their diet. For example, some copepod species produce certain hydrocarbons, and their fecal pellets contribute to the downward flux of organic matter, including associated hydrocarbons, to deeper waters and sediments.[68,69] On the other hand, the degradation of deceased macroalgae and marine plants represents a fascinating and environmentally significant natural process with the potential to generate hydrocarbons.[41] When these organisms die, their organic matter, rich in lipids, carbohydrates, and proteins, sinks to the seabed. Under specific anoxic conditions, microbial communities play a crucial role in breaking down this complex organic material. Anaerobic decomposition prevents complete oxidation, leading to the formation of various intermediate compounds. Over geological timescales, these organic molecules undergo further transformation through diagenesis and catagenesis, and the original biomass is rearranged and cracked, eventually forming liquid and gaseous hydrocarbons.[70]

An additional natural source of hydrocarbons in the sea is atmospheric deposition of biogenic compounds. Terrestrial vegetation and soils are primary global sources of biogenic volatile organic compounds, including isoprene and monoterpenes.[71] These compounds, once emitted into the atmosphere, can undergo chemical reactions, forming aerosols, and be transported long distances before being deposited onto the ocean surface through wet or dry deposition.[72] Although difficult to quantify, the atmospheric deposition of biogenic hydrocarbons may contribute to the background levels in surface seawater, where they can then be subjected to microbial degradation or photo-oxidation processes,[36,37,41,48] a pathway representing a continuous, widespread, and often diffuse input contribution to the overall natural hydrocarbon budget of the ocean.[1,2]

3. Anthropogenic origins of hydrocarbons in seawater

While sometimes attributed to natural phenomena, the pervasive presence of hydrocarbons in seawater is overwhelmingly dominated by anthropogenic activities. From catastrophic oil spills to insidious chronic discharges, human interaction with petroleum products has profoundly altered the marine environment.[1,2] Understanding the sources, quantifying their inputs, and distinguishing between types of hydrocarbons are crucial steps in mitigating their ecological impact. Regional variability profoundly shapes hydrocarbon dynamics in marine environments, influencing spill impacts, response efficacy, and remediation success. In colder climates, such as the Arctic, low temperatures slow oil weathering, biodegradation rates, and natural dispersion, leading to prolonged oil persistence and enhanced bioaccumulation in the food web. Conversely, warmer temperate and tropical waters facilitate faster degradation, but may promote rapid evaporation of volatile compounds, altering oil composition and toxicity.[1,2]

Catastrophic oil spills leave an indelible mark on public consciousness and the environment. These incidents typically involve large-scale release of crude oil or refined products, often with devastating immediate consequences. Tanker accidents have historically been a significant source of large-scale oil spills.[2,8,10,26] The past 50 years have been marked by numerous nautical accidents that have mainly involved large oil tankers or ships, with spillage of large quantities of mixtures of crude oil or refined hydrocarbons. In 1978, the huge crude carrier Amoco Cadiz, following the breakage of a rudder, ran aground near the coast of Portsall, Brittany, France. About 223,000 tons of light crude oil and fuel are spilled into the sea, covering a significant ocean area and affecting about 360 km of the Brittany coastline, including sandy beaches, rocky shores, salt marshes, and estuaries.[73] The spill is estimated to have caused the mortality of approximately 9,000 tons of oysters, drastically affecting the region's economy around the farming and trade of these organisms. Nearly 20,000 seabirds were recovered dead, and significant impacts

were observed on benthic fauna and various fish species.[1,2,73]

In 1979, the huge carrier Atlantic Empress collided with the tanker Aegean Captain during a tropical storm, followed by fire and explosion, approximately 300 nautical miles east of Tobago in the Caribbean Sea. A massive spill of about 287,000 tons of light crude oil occurred due to strong currents, high water temperatures, and the light nature of the spilled oil, which led to rapid dispersion on the ocean. Considering the relatively long distance from the coast, no significant impact or long-term environmental damage was officially reported on nearby islands. No specific widespread marine species involvement or threat was documented due to the rapid dispersion and lack of comprehensive studies at the time; therefore, the real adverse effects on living species remain unknown.[1,2,74]

The tanker Castillo de Bellver broke in half and sank following a fire in the engine rooms in 1983, about 70 nautical miles north-west of Cape Town, South Africa. Approximately 252,000 tons of light crude oil spilled into the ocean. Most oil drifted offshore due to prevailing winds, resulting in little coastal pollution. Some "black rain" fell on agricultural land by atmospheric transport and deposition, but no long-term damage was recorded. About 1,500 Cape Gannets were oiled and threatened, while the impacts on fishing grounds and fish stocks were considered negligible due to the rapid dispersion of light hydrocarbon mixtures.[1,2,75]

In 1988, the tanker Odyssey broke in half during a severe storm in the North Atlantic, approximately 700 nautical miles off Nova Scotia, Canada, causing a spill of approximately 132,000 tons of North Sea Brent crude oil. The oil slick initially extended over 80 km^2, drifted eastward, but, due to the remote location and rough seas, it never reached shore and dispersed naturally. However, it significantly harmed the local krill population, disrupting the food chain. No additional large-scale impact on coastal species was reported.[1,2,76]

The Exxon Valdez disaster in 1989 is considered one of the most significant of the modern era. The ship, bound for Long Beach, California, struck the Bligh Reef in Prince William Sound, Alaska. Approximately 37,000 tons of crude oil spilled into Alaska's Prince William Sound. Although this event reported the smallest volume of crude oil spilled, it represents one of the most impactful historical events to have caused long-term ecological damage, which affected over 1,900 km of coast.[26] It has been estimated that the immediate effects included the deaths of many seabirds (between 100,000 and 250,000), almost 3,000 marine mammals, and an indeterminable number of salmon and herring.[26] Several years after the disaster, evidence of adverse effects on marine birds was found in various species, including cormorants, ducks, and guillemots.[26,76] As mentioned above, low temperatures have significantly altered the natural dispersion and degradation dynamics of hydrocarbons, and this, combined with the difficulty of reaching the site located in a relatively inaccessible environment, has favored the chronicity of the adverse effects.[1,2,26,76]

The National Marine Fisheries Service, National Oceanic and Atmospheric Administration, in Juneau, has determined that in 2001, approximately 90 tons of oil remained in the sandy soil of the contaminated shoreline, estimating a slow decrease in impact of about 4% per year from 2001 onward.[77] The chronic oil impact, lasting longer than anticipated, has resulted in more long-term species losses. It has also been estimated that many marine species directly affected by oil contamination may require over 30 years for recovery.[26,76,77] The Exxon Valdez disaster, due to its severity and extension, is considered the first accident to have had a significant impact on a large geographical and temporal scale.

Since then, restrictions and regulations have been implemented globally, but significant accidents continue to occur. In 1991, an explosion on board the oil tanker ship "ABT Summer" caused a fire and the complete sinking of the vessel. The accident occurred approximately 700 nautical miles off the coast of Angola, where about 260,000 tons of crude oil spilled into the ocean. Due to its remote location and rough seas, the oil dispersed naturally, and no coastline was affected. In this case, no specific widespread marine species were directly involved or threatened, although the real pollution extension and adverse effects on living species remain unknown.[78]

In the same year (1991), an explosion and fire during offloading operations occurred, leading to the tanker Haven breaking apart and sinking off the coast of Genoa, Italy, in the Mediterranean Sea. About 144,000 tons of heavy crude oil spilled out in the sea, causing significant pollution along the shores of Italy (Liguria, Tuscany) and France (French Riviera, Corsica). Oil slicks covered large areas of the Ligurian Sea, directly impacting the local marine life, including fish, crustaceans, coastal birds, fish farms, and coastal ecosystems. The specific estimate of the marine species involved or threatened is unavailable, but recovery of some affected areas took over a decade.[1,2,79] Peculiar characteristics, such as enclosed basins and the Mediterranean Sea present

unique challenges. Limited water circulation can trap pollutants, exacerbating their long-term impact on coastal ecosystems and delaying recovery compared to open oceans with more efficient dilution and dispersion mechanisms.[1,2,79]

The Prestige oil spill, which occurred in November 2002 off the coast of Galicia, Spain, remains one of Europe's worst environmental disasters. The single-hulled oil tanker suffered a structural failure in a storm and eventually broke in half and sank, unleashing an estimated 63,000 tons of viscous crude oil into the Atlantic.[27,80] Almost 3,000 km of coastline across Spain, Portugal, and France were heavily polluted; the thick, black crude smothered beaches and rocky shores, destroying sensitive habitats and severely impacting the rich marine ecosystem.[80-82] An estimated 115,000 to 230,000 seabirds, particularly diving species, such as guillemots, razorbills, and puffins, perished from hypothermia, starvation, and drowning after their feathers were matted with oil, compromising their waterproofing and ability to fly.[80] Marine mammals, including porpoises and dolphins, were also at risk from direct contact and consuming contaminated prey.[80-82] Shellfish, crustaceans, and various marine invertebrates suffered extensive mortality, and fishing grounds, vital to the local economy, were closed for extended periods.[29,80-82] The long-term effects on fish stocks, particularly those with benthic or demersal life habits, and the wider food chain are still being studied, with concerns about persistent contamination and shifts in trophic levels.[81,82]

Although oil spills resulting from nautical accidents have been numerous and frequent, other events related to oil exploration, extraction, and production have caused particularly significant environmental disasters. A clear example is the event on the offshore oil platform Ixtoc 1 in 1979, located in the Bay of Campeche, off the coast of Ciudad del Carmen, in the Gulf of Mexico. Due to a series of factors and rather complex dynamics, the extraction well collapsed, generating an explosion and a fire that caused the entire structure to sink. This caused a crude oil spill directly from the base of the well at about 3,200 meters of depth, among the largest in history, estimated at 476,000 tons. Due to the depth of the source of the leak and the limited technological means available at the time, the operations to close the leak were very complex and protracted for approximately 9 months, rising to one of the most significant ecological disasters known at that time.[83] Oil from the well reached Mexican coastal areas and extended north to Texas (United States), affecting approximately 270 km of the United States' beaches. Coastal lagoons and estuaries experienced persistent contamination. The spill caused a severe impact on various mollusk species and littoral crabs, with ghost crab populations almost eliminated. It also affected the breeding and growth of various fish species belonging to all trophic levels. The critically endangered Kemp's ridley sea turtles' nesting grounds were affected, impacting their population for decades.[84]

In 2010, in the Gulf of Mexico, approximately 41 nautical miles off the coast of Louisiana, the Deepwater Horizon offshore platform disaster occurred due to the blowout of an oil well, following the explosion and fire of the drilling rig. The source of the spill was located at great depth, over 1,500 meters below sea level, and it affected vast areas of the Gulf of Mexico, including deepwater ecosystems, surface waters, and over 1,770 km of coastline across five states in the United States (Louisiana, Mississippi, Alabama, Florida, and Texas). For almost 3 months, an estimated over 670,000 tons of crude oil spewed uncontrollably into the Gulf of Mexico, where the spill created an oil slick that, at its peak, covered over 28,000 km^2 and is ultimately considered the most significant ecological disaster to have occurred in the United States.[28,46] It caused the largest and longest marine mammal unusual mortality event in the Gulf, with thousands of dolphins and whales found stranded, many with lung disease, reproductive failure, and compromised immune systems. Over 167,000 sea turtles were estimated to have died, and Kemp's ridley sea turtle nests were significantly affected and decreased. The spill also led to a significant increase in strandings of marine mammals for years afterward. Widespread mortality was also observed at all trophic levels, from various bird species (e.g., pelicans) to fish, deep-sea corals, and larvae of both vertebrates and invertebrates. Over 6,800 dead animals were reported during the same year of the accident (2010). The fishing and tourism industries, vital to the Gulf states, suffered immense economic losses, and the long-term effects on fish stocks and coastal wetland ecosystems, which experienced accelerated erosion, continue to be monitored and addressed to this day.[1,2,28,46,84]

The Gulf War oil spill, which occurred in 1991 during the Gulf War, is considered the largest oil spill in history. It was caused by Iraqi forces intentionally releasing oil into the Persian Gulf to impede a potential United States military forces beach landing. The spill involved millions of barrels of oil from tankers, pipelines, and terminals, causing extensive environmental damage to the coastal habitats and marine wildlife of Kuwait and Saudi Arabia. Vast hydrocarbon mixtures were

intentionally released into the Persian Gulf, igniting hundreds of oil wells in Kuwait. The spill primarily involved crude oil, with initial estimates ranging from approximately 270,000 to 1.5 million tons. The oil slick reached a maximum size of over 10,000 km^2 and was up to 13 cm thick in some areas. The disaster affected around 600–700 km of the Saudi Arabian coastline, including sandy beaches, gravel shores, wetlands, lagoons, and muddy tidal flats. Kuwait, Iran, Bahrain, and Qatar also experienced some oil contamination. The general extent of the disaster was significant, halting fishing and prawn industries in the Gulf due to contamination. Oil penetrated sediments to 10–50 cm depths, slowing natural degradation.[85] Widespread mortality among various marine species was registered. Nearly 30,000 seabirds, primarily grebes and cormorants, died from being coated in oil. The intertidal zones were severely impacted, causing the death of 50–90% of fauna, such as crabs, amphipods, and mollusks. Benthic ecosystems were heavily oiled, leading to decreased abundance and diversity of organisms, such as ostracods. Mangrove forests along the Saudi coast were also damaged, with nearly half affected and one-third killed, though some natural regeneration occurred. It has been estimated that the full recovery from the Gulf War oil pollution will take several decades, with some areas, such as salt marshes, showing slower recovery.[85] Although some areas, such as rocky beaches and mangroves, have fully recovered within a few years, the more sensitive ecosystems, due to their anaerobic nature and lack of physical action, will require a longer time, which is still difficult to quantify.[85,86]

The events here described can be considered the most significant in terms of volumes of hydrocarbon mixtures released into the marine environment and impact on living organisms. Figure 1 shows the geographical distribution and the origin of the spills, as well as those generated after nautical accidents, offshore platform accidents, or other events. Alongside these acute events of great magnitude and relevance, numerous smaller

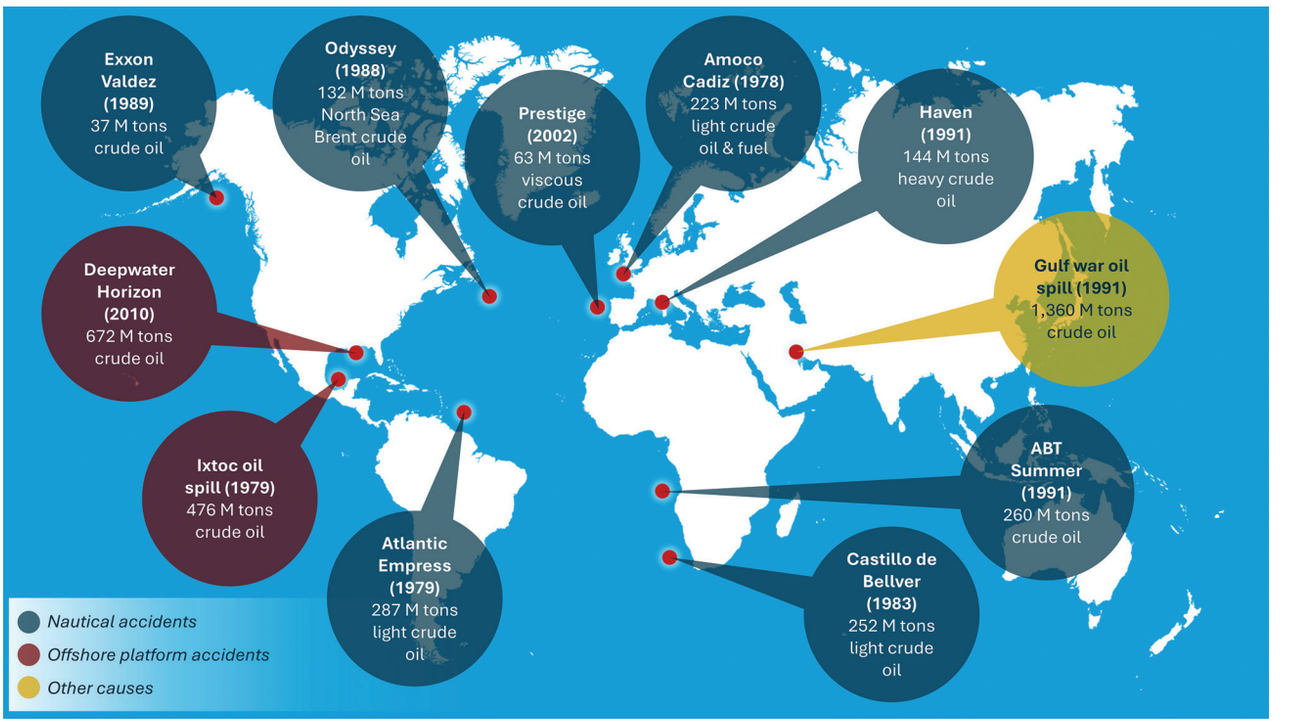


Figure 1. Main catastrophic oil and fuel accidentally spilled in the marine environment throughout the world in the last 50 years. Popup information includes the name of the accidental spill event, the year, the estimated quantity of discharged hydrocarbons, and the type of hydrocarbon mixtures. Dark blue pop-ups indicate nautical accidents, mainly caused by very large oil tankers, red ones indicate accidents generated at oil offshore platform installations, and the yellow pop-up is related to a deliberate crude oil spill during the Gulf War (1991), as well as other causes. M indicates million. Image created by Daniele Fattorini with Microsoft Office 365 enterprise, PowerPoint v.2504.

oil and fuel spills also occur, characterized by a higher frequency. Minor incidents, such as spills from fishing vessels or small commercial boats also contribute to chronic oil pollution. Other examples of accidental spills include offshore drilling blowouts and subsea pipeline ruptures. These events can occasionally be caused by corrosion, geological activity, or external damage.

Anthropogenic activities, including shipping traffic, offshore drilling, and coastal development, dictate the frequency and type of hydrocarbon inputs. Regions with intensive human activity often face chronic pollution and a greater risk of large-scale spills. On the other hand, biodiversity plays a critical role, as diverse ecosystems often exhibit greater resilience and a wider array of microbial communities capable of hydrocarbon degradation. However, highly specialized or endemic species can be particularly vulnerable to oil exposure, leading to severe ecological disruption.

Offshore drilling blowouts and pipeline ruptures incidents can release substantial hydrocarbons over extended periods, often in less accessible deep-sea environments, making response efforts particularly challenging. Quantifying global inputs from these accidents may be complex due to the varying sizes and durations of such events, but they remain a consistent source of episodic, localized pollution. While large spills grab headlines, chronic discharges contribute a substantial, often unquantified, cumulative load of hydrocarbons to the marine environment. These continuous, smaller releases can have insidious long-term impacts on marine life and ecosystems.[29-33] In oil and gas production, "produced water" is a byproduct that emerges to the surface along with oil and gas. This water, often of geological origin, can be highly saline and contains various organic and inorganic compounds, including dissolved and dispersed hydrocarbons (e.g., aliphatic hydrocarbons, benzene, toluene, ethylbenzene, xylenes, and PAHs). The volume of produced water discharged globally is enormous, with estimates of millions of barrels daily. While there are treatment technologies to reduce hydrocarbon concentrations before discharge, even low concentrations released consistently can accumulate and have localized impacts, particularly in coastal and shelf environments.[30,62]

In addition, routine operations of the global shipping fleet contribute significantly to hydrocarbon pollution. These include ballast water discharges, tank cleaning residues, and engine room bilge water. Due to the continuous, point-based nature of this type of pollution, it is extremely difficult to estimate its true impact and overall volumetric contribution over time. Many activities that cause hydrocarbon pollution sometimes escape the control of the relevant authorities or public awareness, and therefore, the extent of the impact may be underestimated. However, several investigations suggest that operational discharges from shipping collectively release more oil into the oceans annually than catastrophic spills, probably representing the main source of chronic and widespread hydrocarbon contamination in the sea. Some estimates indicate that 90% of all oil discharged by ships is attributed to deliberate, illegal dumping of oily residues from routine operations, potentially accounting for hundreds of thousands to over 2.5 million tons of hydrocarbons annually.[29,30] Additional sources of hydrocarbons are characterized by urban runoff; stormwater runoff from urban areas is a diffuse but significant source of oil residues and fuel. Rain washes oil, grease, and other petroleum products from roads, parking lots, and other impervious surfaces into drainage systems that ultimately discharge into coastal waters. These hydrocarbons originate from vehicle emissions, leaky engines, spills at gas stations, and industrial activities. Urban runoff usually contains a complex mixture of petrogenic (petroleum-derived) and pyrogenic (combustion-derived) hydrocarbons. While difficult to quantify precisely on a global scale, studies of urban waterways consistently report the presence of total extractable and aromatic hydrocarbons in sediments and water, with concentrations varying depending on the level of urbanization and industrial activity.[31] Urban runoff varies significantly based on natural factors (precipitation intensity and duration, soil characteristics, land cover, slope) and anthropogenic factors (level of urbanization, type of impervious surfaces). Quantifying pollution from urban runoff on a global scale is inherently difficult. The most sophisticated models are based on simulating the accumulation of pollutants on urban surfaces during dry weather, followed by washing during storm events, but the uncertainty in such models is often very elevated. While some detailed studies are available at local and regional levels (e.g., in Europe or the United States), reliable global data are completely lacking.[31]

Atmospheric deposition of combustion products may also represent a significant source of hydrocarbons in the environment. The combustion of fossil fuels, whether from vehicles, industrial processes, or power generation, releases hydrocarbons and their derivatives directly into the atmosphere. These airborne pollutants can then be transported globally and deposited onto the ocean surface through wet deposition (rain, snow) and

dry deposition (particulate matter). While often at low concentrations, the vastness of the ocean surface makes atmospheric deposition a significant contributor to the global hydrocarbon budget in seawater, especially for volatile and semi-volatile compounds.[42,71,72] Estimating the global annual volume of hydrocarbons released into the environment through atmospheric transfer and deposition is a complex task due to several factors, including the vast array of hydrocarbon compounds, their varying atmospheric lifetimes, diverse emission sources (both natural and anthropogenic), and the challenges of global monitoring and modeling. However, studies focusing on specific, environmentally significant groups, such as PAHs suggest that atmospheric deposition is a significant pathway to their ecosystem entry. The estimated global atmospheric input of PAHs to the ocean is over 1 million metric tons annually. This underscores that atmospheric deposition, encompassing both direct emissions and long-range transport, represents a substantial and continuous source of hydrocarbon pollution to the global environment.[42]

Despite regulations and increasing awareness, illegal dumping of oil and oily waste significantly contributes to marine hydrocarbon pollution. This includes the deliberate discharge of bilge water, tank cleaning residues, and even spent lubricating oils from smaller vessels or less regulated operations. Satellite surveillance has revealed the prevalence of illegal dumping, particularly in busy shipping lanes and areas with lax enforcement. Some reports suggest that thousands of cases of illegal dumping of hydrocarbons occur in European seas alone every year, collectively exceeding the inputs from major tanker accidents.[87] Figure 2 summarizes and outlines the main sources of chronic discharge of oil, fuel and related waste into the marine environment; all these "secondary" sources of release of hydrocarbon mixtures into the environment as a whole highlight that the severity of an oil spill is not solely determined by its size but also by the type of oil, the sensitivity of the affected environment, the effectiveness of the responses, and frequency of events.

Chronic pollution may often induce sublethal effects across many taxa, from plankton to marine mammals.

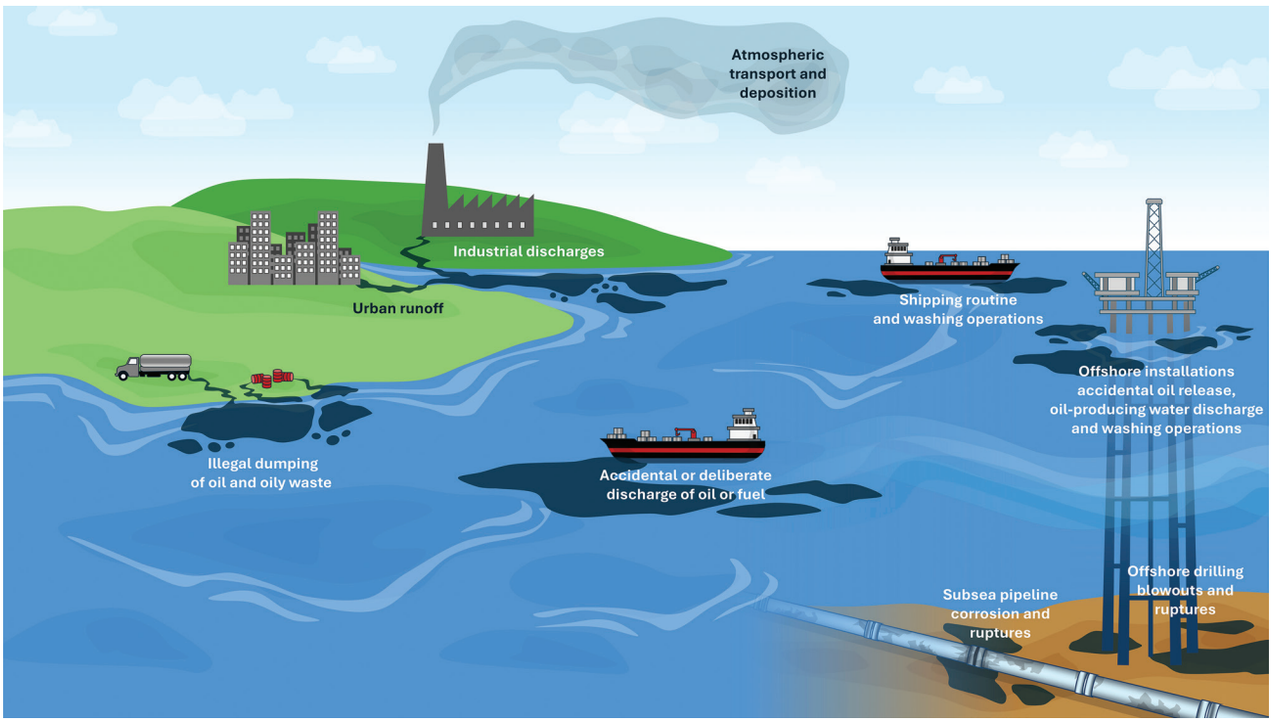


Figure 2. Main chronic hydrocarbon spill, release, or discharge events in the marine environment. Inputs may be characterized by shipping routine or washing operations, offshore drilling blowout and ruptures, accidental release of oil-produced waters, urban and industrial runoff and discharges, atmospheric transport and deposition of hydrocarbon derived from industrial activities, and a series of illegal dumping of oil, fuels, and oily waste products. Image created by Daniele Fattorini with Microsoft Office 365 enterprise, PowerPoint v.2504.

Affected species experience impaired growth and reproduction, immune suppression, developmental abnormalities, and behavioral changes. Long-term ecosystem disruption, including habitat degradation of vital coastal areas, such as mangroves and coral reefs, and bioaccumulation within the food web, severely threatens ecosystem health and biodiversity. Species, such as seabirds, marine mammals (e.g., dolphins, whales), sea turtles (e.g., Kemp's ridley), fish, deep-sea corals, and various invertebrates and their larvae are particularly vulnerable to these persistent effects.[11,44-46]

4. Fate of hydrocarbons in seawater

The fate of hydrocarbon mixtures in the sea, whether from natural or anthropogenic sources, is characterized by numerous and complex chemical–physical processes and interactions with living organisms. These processes are strongly influenced by the characteristics of the hydrocarbon mixtures, such as density, viscosity, volatility, and composition, but also by environmental conditions and variables, such as temperature, salinity, wave motion and currents, wind intensity, and proximity to the coast.[88-90] As mentioned above, regional variability significantly modulates hydrocarbon dynamics in marine environments, influencing oil density, dispersion, spreading, and emulsification. Based on this perspective, there is no unified fate of hydrocarbons in the oceans, as cold, temperate, or tropical environments can significantly alter the extent and speed of the chemical–physical and biological phenomena at play.[1,2] Considering the numerous variables in play, Figure 3 proposes a series of model mechanisms of the main processes triggered by the presence of hydrocarbons in the sea, considering that such phenomena may deviate from those described, depending on the existence of particular and peculiar environmental conditions and events.

In the open ocean, the oil on the water surface undergoes spreading, a rapid process driven by gravity and surface tension, forming thin films known as slicks. Large oil slicks can float and move on the surface waters. Wave motion and currents significantly affect the mobility, transport, and dispersion of such oil slicks, promoting rapid spread and drifting.[90] The simultaneous action of the waves and the wind plays

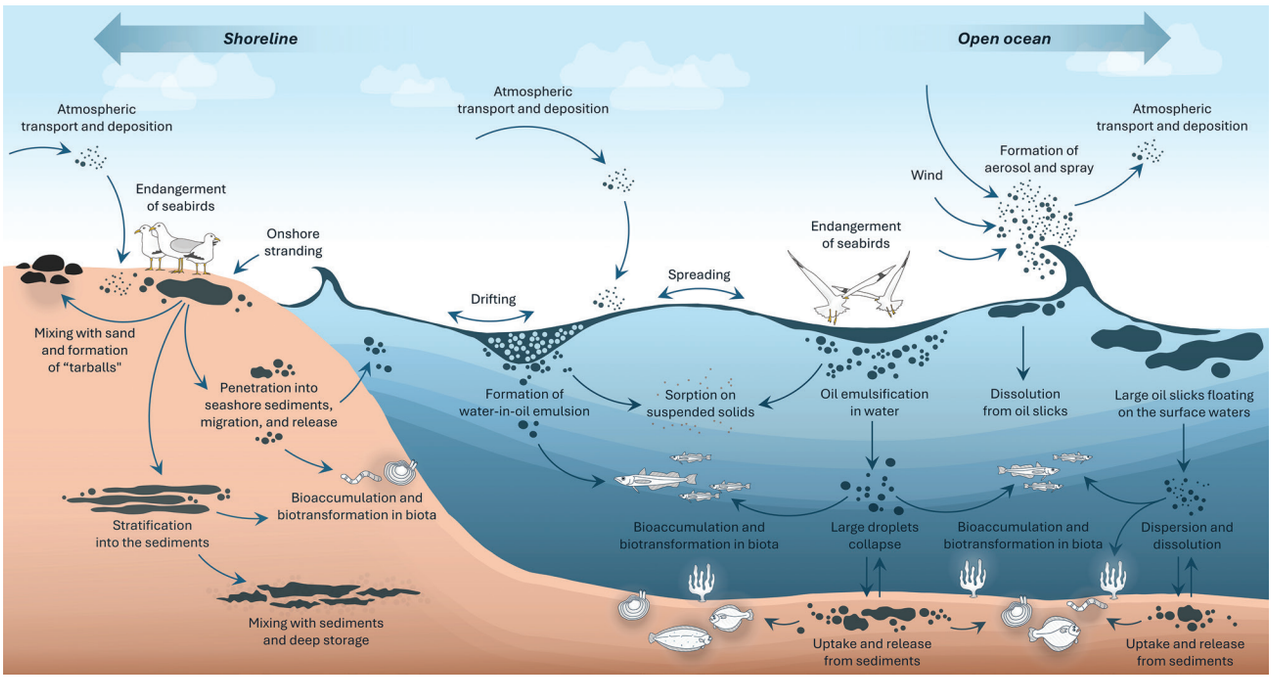


Figure 3. Fate of hydrocarbons in the sea. A range of potential phenomena associated with the presence of hydrocarbons in marine ecosystems, including transport and spread of oil slicks at the water surface, aerosol formation and atmospheric transport and deposition, dissolution and collapse in the water column, interaction and compartmentalization in sediments, and threats to various marine species, including invertebrates, vertebrates, and seabirds. Image created by Daniele Fattorini with Microsoft Office 365 enterprise, PowerPoint v.2504.

a significant role in the atmospheric transport and deposition of volatile oil components and the formation of aerosol and spray. This can lead to the widespread dispersal of oil hydrocarbons into the atmosphere.[88-90] Hydrocarbons transported through the atmosphere can move to destinations very far from the primary emission sources, reaching the surface of the water, beaches, or other emerged areas, through wet or dry deposition.[88,90]

Oil on the water surface or transported in the atmosphere can directly threaten seabirds, which are particularly vulnerable to this contamination. The more viscous components adhere to the plumage of these animals, causing movement and flight difficulties, thermoregulation disorders, impairment of various abilities, including catching food, and toxicity and death.[11,27,62,82]

Further interactions occur within the water column. Dissolution from oil slicks may occur when water-soluble components of the oil dissolve directly into the seawater. The sudden mixing of oil slicks and surface water favors the formation of emulsions (oil emulsification in waters or waters in oil emulsion), where small oil droplets are dispersed within the water column, often stabilized by natural surfactants. The heavier components tend to slowly disperse deep into the water column, while the lighter ones return to the surface, re-aggregating with the oil slicks and thus promoting a cycle.[90]

Simultaneously, oil can undergo sorption on suspended solids, where oil molecules adhere to particulate matter, increasing their density and potentially leading to sedimentation.[88,90] Within the water column, large oil droplets collapse, and dispersion and dissolution continue, breaking down the oil into smaller components. These processes facilitate the uptake and release from sediments. Once oil settles, it can be re-released into the water column, initiating a recurring cycle. All these transports and migrations contribute to bioaccumulation and biotransformation in biota, with various marine vertebrates (benthic or pelagic fish) and invertebrates (i.e., mollusks, polychaetes, and algae) taking up oil compounds, which are then metabolized and accumulated within their tissues, with significant toxicological effects on marine life.[11,62]

As oil drifts toward the coast, driven by currents and winds, it can lead to onshore stranding. Once on the shoreline, the interactions become more complex, largely dependent on the characteristics of the beach, the presence of rocks, and the type of sediments and sands.[90] Oil mixed with sand and the formation of "tarballs" is a common phenomenon, where oil adheres to sand particles, forming persistent, resistant oil-sand agglomerates. These tarballs and other oil residues can penetrate seashore sediments, migrate, and be released. This infiltration can lead to long-term contamination of the intertidal and subtidal zones.[88,90] Stratification can occasionally occur within the sediments, with oil burying itself at various depths. This buried oil can continue to undergo mixing with sediments and deep storage, making its remediation challenging. Like in the open ocean, bioaccumulation and biotransformation in biota may occur within the shoreline ecosystem, affecting benthic organisms and potentially their consumers.[11,27,62,82] In addition, the seabirds can be directly endangered due to contact with oiled shorelines, emphasizing the vulnerability of avian species to coastal oiling.[62,82]

Hydrocarbon mixtures in the sea can undergo various physicochemical and biological degradation processes at multiple stages. Although these processes determine a natural mitigation of hydrocarbon contamination, they can potentially lead to the formation of different compounds often characterized by a greater solubility in water and potentially a greater toxicity in living organisms.[35-40,89] Microbial biodegradation represents the primary natural attenuation mechanism for hydrocarbons in marine environments. This complex process involves diverse microbial communities, primarily bacteria and fungi, breaking down hydrocarbons into less harmful substances, ultimately leading to mineralization into carbon dioxide or methane. The efficacy and specific pathways of this degradation are critically dependent on oxygen availability, leading to distinct aerobic and anaerobic processes.[36,37,89]

Aerobic biodegradation is the dominant and generally more rapid process in oxygen-rich marine waters, such as the surface layers and oxic sediments. A series of specialized microorganisms possess enzymatic systems, particularly alkane hydroxylase complexes, that initiate the degradation of hydrocarbons.[36,37,41,89,91] The primary mechanism involves the incorporation of molecular oxygen into the hydrocarbon molecule by monooxygenases, forming an alcohol. This alcohol is then oxidized to a fatty acid, which undergoes successive β-oxidation cycles, progressively shortening the carbon chain and finally forming acetyl-CoA. Acetyl-CoA then enters the tricarboxylic acid cycle for complete mineralization to carbon monoxide and water, generating energy for microbial growth.[41,91] Biosurfactant production by certain aerobic microorganisms enhances the bioavailability of hydrophobic hydrocarbons by emulsification, making them more accessible for

enzymatic reactions. Factors, such as temperature, nutrient availability (nitrogen and phosphorus being crucial, limiting nutrients), and the physical state of the oil (e.g., dispersion) significantly influence aerobic degradation timing, rates, and success.[36,37,91] The obligate hydrocarbonoclastic bacteria, mainly belonging to the class of Gammaproteobacteria, are considered the most important hydrocarbon degraders under aerobic conditions. These bacteria can use hydrocarbons as the sole source of carbon and energy and are ubiquitous in the oceans. Some relevant examples include *Alcanivorax* (e.g., *A. borkumensis, A. dieselolei, A. pacificus*), representing the most studied and important genus of obligate hydrocarbonoclastic bacteria, specializing in the degradation of n-alkanes (straight-chain hydrocarbons) and *Cycloclasticus* (e.g., *C. pugetii*), a genus known for its ability to degrade PAHs, which are more complex and thermodynamically stable compounds. The genus *Pseudomonas* represents an additional notable group of bacteria capable of aerobic biodegradation; several species, such as *P. putida* and *P. aeruginosa*, are known for their ability to degrade a wide range of petroleum hydrocarbons and are often employed in remediation and cleanup practices after oil spills.[91]

Anaerobic biodegradation becomes critical in anoxic marine environments, such as deep sediments, subseafloor oil reservoirs, and oxygen-depleted zones. While generally slower than aerobic processes, it plays a vital role in the fate of hydrocarbons in these environments.[91,92] Anaerobic microorganisms utilize alternative electron acceptors in the absence of oxygen, including nitrate, sulfate, ferric iron, or carbon dioxide. The initial activation of hydrocarbons under anaerobic conditions is a key step, as the lack of oxygen prevents direct monooxygenase activity. One of the most well-described mechanisms for alkane activation is fumarate addition, catalyzed by enzymes, such as alkyl succinate synthase.[92] This reaction involves the anoxic addition of fumarate to the alkane chain, forming 1-methylalkyl-succinate. This product then undergoes transformations and β-oxidation-like steps, eventually forming short-chain fatty acids, methane (methanogenesis), and carbon dioxide. Diverse anaerobic consortia are often involved, with specific microbes specializing in different steps of the degradation pathway. The presence of certain metal ions, such as iron, can also influence anaerobic degradation rates by acting as electron acceptors or mediating electron transfer.[91,92] Some examples of bacterial communities operating under anoxic conditions are denitrifying and sulfate-reducing bacteria, respectively, utilizing nitrate or sulfate as final electron acceptors to degrade hydrocarbons. Examples include species, such as *Aromatoleum* sp. (denitrifying) and *Desulfoglaeba* sp. (sulfate-reducing), which have been studied for their ability to activate alkanes by adding fumarate. In addition, under highly reducing conditions, methanogenic bacteria can degrade hydrocarbons to produce methane. Although the process is complex and often mediated by microbial consortia, species, such as *Smithella* sp. and *Anaerolinea* sp. have been associated with anaerobic degradation of hydrocarbons.[91,92]

Aside from these biodegradative phenomena, a series of chemical–physical processes may largely contribute to the degradation of hydrocarbon mixtures in the sea, especially at the surface level. It has recently been highlighted that complex mixtures of hydrocarbons in contact with water can undergo photo-oxidation, forming soluble organic compounds, such as aldehydes, ketones, and alcohols.[36-40] Most studies have focused on the physical and chemical alterations of hydrocarbons. Characterizing the involved photochemical processes and the molecules produced is complex, mainly due to the difficulty of observing these phenomena in natural conditions. The dissolved fraction of aliphatic hydrocarbons in seawater is essentially transparent to sunlight,[93] unlike the aromatic component, which is easily photo-oxidized with the formation of "sensitizing" substances. These sensitizers, in turn, make the aliphatic hydrocarbons photo-oxidizable.[38] For instance, anthracene easily absorbs sunlight and is photo-oxidized to 9,10-endoperoxide and anthraquinone (Figure 4). The same phenomenon has been observed for other PAHs, including benzo(a)pyrene.[38,93] In this sense, a mixture of aliphatic and aromatic hydrocarbons exposed to sunlight can lead to the initial production of sensitizers derived from the oxidation of some PAHs, which then facilitates the photo-oxidation of the aliphatic components, with the formation of more soluble organic compounds, including aldehydes, ketones, and alcohols.[36-40,93]

Specifically, it is known that experimental irradiation of alkylbenzenes in the presence of anthraquinone determines the formation of 1-phenylalkanone, alcohols, and benzaldehyde. These same compounds have been isolated from seawater in contact with petroleum mixtures under natural conditions, thus suggesting a photochemical origin.[38,94] Controlled photo-oxidation of the water-soluble fraction of gasoline in the presence of anthraquinone produced the same reaction products,[94] suggesting that the phenomenon does not concern only a few experimentally chosen model compounds, but rather involves all complex and heterogeneous

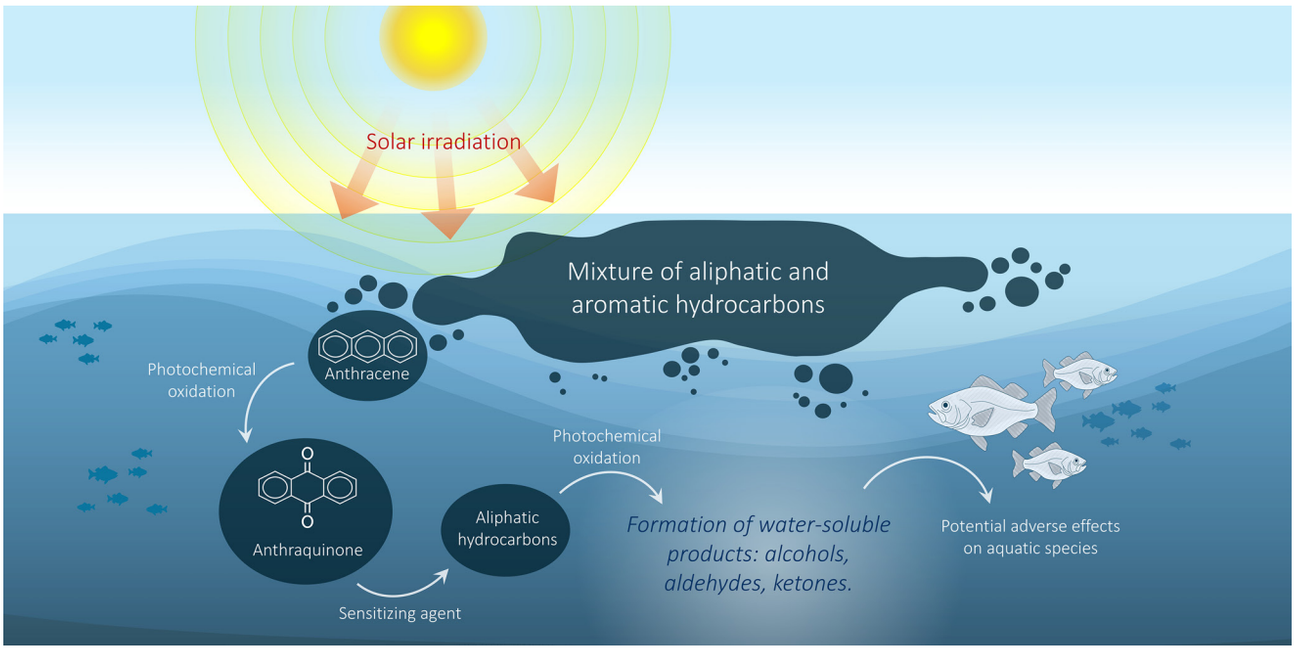


Figure 4. Photo-oxidation of hydrocarbons in the surface waters. Solar irradiation may produce photochemical oxidation of aromatic hydrocarbons with the formation of sensitizing agents, which in turn promote the photo-oxidation of the aliphatic components with the formation of aldehydes, ketones, and alcohols, that are more soluble and potentially dangerous for fish species. Image created by Daniele Fattorini with Microsoft Office 365 enterprise, PowerPoint v.2504.

mixtures, such as crude oil. Similarly, irradiation of alkylnaphthalenes in the presence of oil or the soluble fraction of gasoline in seawater formed photo-oxidation polar compounds, such as alcohols, aldehydes, acids, and quinones.[38,93,94]

Biodegradation and photo-oxidation processes, while seemingly beneficial in breaking down pollutants, can yield byproducts that pose significant adverse effects on marine organisms. Aerobic biodegradation can produce various oxidized intermediates. While some are less harmful, others, such as certain organic acids or partially oxidized PAHs, being more soluble than the original compounds, can potentially enter biological compartments more easily and exert greater toxicity, altering various physiological functions, including reproduction, growth, and immune response.[95] Under anaerobic conditions, degradation pathways can generate hydrogen sulfide, which is highly toxic to many marine species, particularly those in benthic environments. Other byproducts might include aromatic and aliphatic compounds that can bioaccumulate in the food chain, leading to long-term chronic toxicity in higher trophic levels. Photo-oxidation may also generate oxygenated PAHs, which exhibit enhanced toxicity compared to their parent compounds. They may cause DNA damage, oxidative stress, and endocrine disruption in marine organisms, affecting their development, behavior, and survival. Furthermore, some of these compounds can be highly persistent, prolonging their detrimental impact on marine ecosystems. The combined effects of these degradation byproducts contribute to altered community structures, reduced biodiversity, and overall ecosystem degradation.[95]

A highly relevant and timely aspect is the significant influence of climate change on marine hydrocarbon dynamics. Ocean warming can increase the temperature and dispersion of oil, potentially speeding up evaporation and natural dispersion and increasing the toxicity of some oil components. Ocean acidification, resulting from increased carbon dioxide absorption, might also affect the efficiency of oil-degrading microorganisms. Furthermore, extreme weather events, such as stronger storms and hurricanes, amplified by climate change, pose a greater risk of damage to offshore oil and gas infrastructure, increasing the likelihood of spills. Changes in ocean currents and sea level rise can also influence the transport and fate of spilled oil, making prediction and cleanup efforts more challenging.[96]

5. Effects of hydrocarbon pollution

Large quantities of hydrocarbons in the sea, whether from heavy crude oil, light oil, or refined products,

such as fuels or other mixtures, always cause harmful effects.[11,32,52] The complexity of the mixtures and the variety of products potentially involved often make it difficult to predict the extent and severity of contamination and the possible short- and long-term effects. Furthermore, as previously described, the specific characteristics of the area affected by the contamination and various environmental variables can drastically influence the severity and persistence of the disturbances caused by the presence of hydrocarbons in the sea.[1,2]

In crude oil contamination, especially if characterized by high viscosity and density, the most immediately noticeable and significant damage is predominantly physical. Seabirds and marine mammals can become covered in oil, which adheres to their skin or plumage, forming a barrier and causing suffocation, inability to move or fly, impairment of various physiological functions, and compromising the ability to forage and reproduce. Animals relying on fur or feathers for insulation also suffer severe hypothermia when their protective layers are matted by oil, compromising their ability to regulate their body temperature, and causing fatigue, starvation, and even death.[97] In intertidal areas, the stranding of crude oil slicks can also cover the surfaces of numerous species of mollusks (mussels, oysters, gastropods,), crustaceans (crabs, hermit crabs, barnacles,), echinoderms (sea urchins), and other benthic invertebrates, compromising many of their vital functions and the capability to move, impeding respiration, feeding, and waste elimination.[11,32,52,97]

These physical effects are accompanied by toxicological damage. One primary mechanism is narcosis, particularly by low molecular weight aromatic hydrocarbons (e.g., benzene, toluene, ethylbenzene, xylenes, naphthalene, and derivatives), which are highly soluble and volatile. These compounds can rapidly penetrate biological membranes, interfering with cellular processes, disrupting nerve impulse transmission, and causing central nervous system depression. This leads to disorientation, paralysis, and ultimately death in affected marine life.[97] Even at sublethal concentrations, hydrocarbons may inflict profound chronic sublethal effects, impairing the health and viability of marine populations. Physiological stress is a common response, characterized by elevated metabolic rates, disrupted osmoregulation, and altered energy allocation, as organisms expend energy on detoxification and repair rather than essential life processes. Reproductive impairment is a particularly concerning effect, with hydrocarbons interfering with hormone regulation, gamete development, fertilization success, and larval viability across a wide range of taxa.[43,82] This can lead to reduced spawning success, decreased fertility, and compromised recruitment, threatening population stability. Developmental abnormalities, such as fish larvae and invertebrate embryos, are frequently observed in early life stages, manifesting as skeletal deformities, cardiovascular dysfunction, and impaired organ development.[11,32] The aryl hydrocarbon receptor pathway, involved in xenobiotic metabolism, is often implicated in these developmental toxicities.[98] Furthermore, hydrocarbons can induce immune suppression, making organisms more susceptible to diseases, parasites, and environmental stressors, weakening population resilience.[11]

Hydrocarbons, especially persistent and lipophilic compounds, such as PAHs, exhibit tendencies for bioaccumulation in various vertebrate and invertebrate aquatic species.[15,62] Higher organisms generally possess the enzymatic pathways capable of metabolizing aliphatic and aromatic hydrocarbons; therefore, it is not uncommon to find higher levels of bioaccumulation in benthic invertebrate organisms from contaminated areas rather than in fish. On the other hand, it is known that some multienzyme systems capable of transforming specific xenobiotics (i.e., cytochrome P450) often produce products that express greater toxicity. Consequently, vertebrate organisms in contaminated areas may manifest notable adverse effects even without high levels of bioaccumulation.[15] As a result of these mechanisms, and given that hydrocarbon mixtures can undergo biodegradation, their bioaccumulation can be transferred into food chains, although biomagnification is generally not observed.[15] Given the high lipophilicity of the hydrocarbon mixtures, higher animals, such as marine mammals can be subject to an elevated bioaccumulation rate in tissues rich in body fat.[15,62]

Hydrocarbon pollution may disrupt entire marine ecosystems. Habitat degradation occurs when sensitive environments, such as coral reefs, mangrove forests, and salt marshes are directly contaminated, leading to structural complexity and functionality loss. For example, corals are highly sensitive to oil, which can cause bleaching, necrosis, reduced growth rates, impaired reproduction, and altered larval settlement. Chronic exposure can decrease their resilience to environmental stressors, such as ocean acidification and warming. Given the close ecological relationship between species, the entire coral reef ecosystem could be compromised in a cascade. Mangroves are also critically important coastal habitats that are highly susceptible to oiling. Oil can

coat their roots (pneumatophores), affect gas exchange, leading to suffocation and death, especially in younger trees. Contamination of the anaerobic sediments further slows oil weathering. Oil can also cause defoliation, stunted growth, and deformities, compromising their vital role in coastal protection and as nursery grounds for various marine species.[45,46,85,86] This, in turn, diminishes biodiversity and the ecosystem services these habitats provide. Food web disruption results from the mortality of primary producers and consumers, and the bioaccumulation of toxic substances.[45,46] This can lead to trophic cascades, altering predator-prey relationships, competitive dynamics, and overall energy flow within the ecosystem, impacting the abundance and distribution of species across multiple trophic levels. Long-term impacts on ecosystem resilience and recovery are often observed.[85,86]

The socioeconomic consequences of hydrocarbon pollution are far-reaching. Industries heavily relying on healthy marine environments, such as fisheries and aquaculture, suffer significant economic losses due to contaminated stocks, fishing bans, fouled gear, and reduced market confidence in seafood safety.[1,2,8] Tourism and related businesses are also severely impacted, as oiled beaches and affected marine life deter visitors. Coastal communities, particularly those dependent on marine resources for livelihoods and cultural practices, often bear a disproportionate burden. Cleanup operations are expensive, and long-term environmental monitoring and restoration efforts add further economic strain.[1,2,8,9,28]

These dynamics can also have a direct impact on human communities. Humans consuming seafood (fish, shellfish, crustaceans) from oil-affected areas can be exposed to hydrocarbons, especially PAHs, which are known carcinogens and can cause other adverse health effects.[27,99,100] While depuration periods can reduce contaminant levels, the risk remains, particularly with chronic consumption of subtly contaminated seafood. In addition, individuals involved in cleanup operations or near spilled oil can experience direct exposure through dermal contact, inhalation of volatile organic compounds, or accidental ingestion. This can lead to a range of health issues, including respiratory problems, skin irritation, neurological symptoms, and potential long-term risks, such as increased cancer incidence. The physical and psychological stress on affected communities and cleanup workers also represents a significant health burden.[99,100]

Marine oil and hydrocarbon contamination extends beyond immediate environmental damage, deeply affecting human communities. For instance, the mental health of residents, especially those whose livelihoods depend on the sea, can significantly deteriorate. Witnessing the destruction of ecosystems and fearing for their future can lead to chronic stress, anxiety, depression, and even post-traumatic stress disorder. Studies after major spills have shown these psychological impacts can persist for years. Furthermore, oil spills exacerbate socioeconomic disparities in vulnerable populations. Fishing communities, indigenous groups, and those reliant on coastal tourism often face severe income loss and job displacement. This economic hardship can deepen existing poverty, disrupt traditional ways of life, and lead to food insecurity. The slow recovery of marine resources further prolongs these challenges, creating cycles of vulnerability and hindering equitable development.[101]

6. Containment, monitoring, and remediation strategies of hydrocarbons in seawater

In the wake of marine hydrocarbon contamination, a rapid and coordinated response is fundamental to mitigate environmental damage. This involves a comprehensive series of containment, monitoring, and remediation strategies, each with strengths and limitations. The selection of appropriate techniques hinges on factors, such as the type and volume of the spill, prevailing environmental conditions, and available resources. Containment techniques are designed to limit the spread of hydrocarbons, preventing further ecological harm and facilitating subsequent cleanup efforts.

Among these, the booming techniques involve deploying physical barriers on the water surface to encircle and concentrate the spilled material. Booms can be absorbent and designed to soak up oil, such as containment booms, which physically block its spread; they can also be fire-resistant and used in conjunction with *in situ* burning. Booming has been proven to be highly effective for preventing the spread of oil in calm waters, is relatively straightforward to deploy, and can be used to divert oil away from sensitive areas, such as coastlines or wildlife habitats. In addition, this technique aids in the efficiency of oil recovery operations by concentrating the slick. Booms' effectiveness significantly diminishes in rough seas, strong currents, or high winds, where oil can easily escape underneath or overtop the barriers. Large spills can overwhelm boom capacity, and their deployment and retrieval require substantial logistical support and personnel. Booms can also become saturated with oil,

necessitating careful disposal.[47] During the Deepwater Horizon oil spill (2010), thousands of miles of booms were deployed to protect the intricate marshlands and coastlines of the Gulf of Mexico. While effective in localized, calmer areas, their overall impact was limited by the sheer scale of the offshore spill and prevailing weather conditions.[28,46]

In recent years, innovative technologies have been developed to remediate hydrocarbon contamination in the marine environment. Among these, nanomaterials offer a promising solution for crude oil absorption from the sea. Their exceptionally high surface area-to-volume ratio enables efficient capture of oil molecules. Materials, such as graphene, carbon nanotubes, and various metal-organic frameworks can be engineered to be superhydrophobic and oleophilic, meaning they repel water while attracting oil. When deployed, these nanomaterials can rapidly absorb significant quantities of spilled oil, forming stable aggregates that are easier to recover from the water surface. This aids in rapid cleanup and minimizes the environmental impact by preventing the spread and long-term consequences of oil contamination on marine ecosystems.[102]

Once contained, or when containment is challenging, various techniques are employed to remove or disperse the oil. Skimming involves using specialized vessels or skimmers to physically remove oil from the water surface. Skimmers operate through various principles, including weir skimmers, which allow oil to flow over a weir into a collection tank, oleophilic skimmers, where oil adheres to a rotating surface and is then scraped off, and vacuum skimmers.[47] Skimming usually consists of directly recovering the oil, making it available for potential recycling or proper disposal, thus reducing the total volume of contaminants in the environment. It is most effective in calm waters with relatively thick oil. The efficiency of such a technique may be compromised in rough seas, as wave action can break up the slick and mix the oil with the water column. Debris mixed with the oil can clog skimmer mechanisms, and the process often collects significant volumes of water along with the oil, requiring further separation.[47]

A controversial containment method is represented by *in situ* burning, which involves the controlled ignition and burning of oil on the water surface. It is often used with fire-resistant booms to concentrate the oil into a thick layer before ignition. This approach offers a rapid way to remove large quantities of oil, significantly reducing the volume that needs to be physically recovered and disposed of. It can be particularly effective in remote areas where logistical challenges make other recovery methods difficult. However, *in situ* burning causes air pollution, including the production of particulate matter, volatile organic compounds, and other combustion byproducts, raising concerns about air quality and potential health impacts. Public perception is not usually positive due to visible smoke plumes and the generation of atmospheric pollution. *In situ* burning was a key component of the Deepwater Horizon oil spill response. Over 400 controlled burns were conducted, removing an estimated amount of approximately 35,000 tons of crude oil, demonstrating its capacity for rapid oil removal in large-scale offshore incidents, when the vast extent of the contamination and adverse environmental conditions do not allow the adoption of different techniques.[28,46]

Another debated and controversial practice is the use of substances called dispersants. These are chemical agents sprayed onto oil slicks to break the oil into tiny droplets, allowing it to mix with the water column. This process facilitates dilution and degradation through natural processes and prevents the oil from rapidly spreading. Dispersants can quickly break up large, widespread slicks, preventing them from impacting coastlines, wetlands, and surface-dwelling wildlife. They can be applied efficiently from aircraft or vessels, rapidly responding to large-scale spills. The increased surface area of dispersed oil can accelerate natural biodegradation by marine microbial communities.[48] However, the use of these substances is not without risks. A primary concern is the potential toxicity to marine life from the dispersant chemicals and dispersed oil, which can become more bioavailable to organisms in the water column.[48] Dispersants do not remove oil from the environment; they merely change its physical state and location, often driving it deeper into the water column. Their effectiveness varies with oil type, water temperature, and salinity. The large-scale use of dispersants, particularly subsea applications, has been highly controversial.[48,103]

Chemical dispersants are complex mixtures, typically composed of surfactants and solvents. Surfactants are the key molecules that reduce the interfacial tension between oil and water, facilitating droplet formation. Surfactants are amphiphilic molecules with both oleophilic and hydrophilic components. This duality allows them to position themselves at the oil-water interface, lowering the surface tension and fragmenting the oil into small droplets. The most common surfactants are sorbitan esters (e.g., sorbitan monooleate), a non-ionic substance derived from sugars, often used for their emulsifying properties

and relatively low toxicity. Other surfactants include ethoxylated fatty acid esters (nonionic surfactants that provide emulsion stability), sulfosuccinates (e.g., sodium dioctyl sulfosuccinate, an anionic surfactant with emulsifying properties), organic sulfonic acids and their salts (anionic surfactants aiding wide oil dispersion), and alkoxylated alcohols or ethoxylated alkylamine (nonionic surfactants).[48]

As additional components, solvents help transport and distribute the surfactants, keeping them in the solution and facilitating their penetration within the oil slick. Dispersant solvents usually consist of hydrotreated light oil distillates and hydrocarbon-based substances with low or absent aromatics to reduce toxicity. Other common solvents are glycols (e.g., propylene glycol, propylene glycol ethoxylate, and 2-butoxyethanol) that are less volatile and potentially less toxic than the aromatic solvents used in early generations of dispersants. However, the use of selected glycol ethers and 2-butoxyethanol has recently been the subject of concern for their potential adverse effects.[48]

The first massive use of dispersants dates to the accident of the supertanker Torrey Canyon in 1967, which caused the spill of approximately 120,000 tons of crude oil off the coast of Cornwall, United Kingdom. The chemical dispersants were used extensively and unprecedentedly; over 10,000 tons of these substances, such as BP 1002 containing non-ionic surfactant detergents, were sprayed on floating oil and contaminated beaches. These "first-generation" dispersants were highly toxic and contained aromatic solvents, such as benzene and xylene. Studies have determined that the oil/dispersant mixture was more harmful to the environment than the oil alone. Numerous seabirds died from lungs clogged by detergent foam, leading to increased awareness of the risks of dispersants and the development of less toxic formulations.[103]

During the Exxon Valdez Disaster in 1989, Corexit chemical dispersants were tested on a limited scale immediately after the spill. Although the composition of Corexit is not publicly available, it may contain substances, such as butoxyethanol bisulfonate, an additional organic sulfonate, and small concentrations of propylene glycol. Weather conditions and the viscosity of the oil did not favor significant dispersion, and the quantities of dispersant available and applied were insufficient to address the scale of the disaster. Some studies suggested dispersants may have formed chemically enhanced, potentially more toxic oil particles. Much of the cleanup subsequently focused on physical methods and biostimulation.[26,48,77,103]

Corexit dispersants were also used after the Deepwater Horizon disaster (2010). This event saw unprecedented use of dispersants, both on the surface and, for the 1st time, on a large scale, directly at the source of the release at depth. Nearly seven million liters of dispersants were applied, primarily Corexit 9500A and Corexit 9527A. This practice helped reduce the amount of oil at the surface, mitigating the impact on seabirds, marine mammals, and shorelines. Underwater dispersal was intended to prevent large quantities of oil from reaching the surface, but significant concerns were raised. Although dispersants reduced the visibility of oil at the surface, they introduced oil (and the dispersants themselves) into the deep-water column, where their persistence, fate, and effects on marine life were less understood and remain the subject of intense research.[28,46] The combined toxicity of oil and dispersant, the formation of "marine oil snow" that carried oil to the seafloor, and the health effects of cleanup workers were critical debate points. Some studies have suggested that underwater dispersal did not significantly reduce the overall amount of oil reaching the surface but altered its distribution.[28,46,48,103]

During the Prestige oil tanker spill (2022), given the type of oil and the adverse weather conditions that characterized the initial stages of the accident, the use of chemical dispersants was controversial and ultimately limited, deemed ineffective in containing the crude oil spill. For instance, dispersants work best on low viscosity, lighter oils, which can be easily emulsified. In contrast, the Prestige's heavy oil was inherently difficult to disperse chemically, due to its elevated viscosity. In addition to adverse weather conditions, rough seas and strong winds further complicate any attempts to effectively apply dispersants. While rough seas can promote some natural dispersion, they also hinder the targeted application and effectiveness of dispersants, which require a certain amount of contact and mixing time to work. In practice, the dispersants failed to fulfill the desired role of containing and dispersing the spill. The oil largely reached the coasts of Galicia and subsequently France and Portugal, causing devastating environmental and economic damage.[48,80-82,103] The Prestige accident and other spills have elicited international debate on the efficacy and potential ecotoxicological impacts of dispersants. Concerns include their effectiveness in the field and the combined toxicity of the dispersant and the dispersed oil on marine life. For the Prestige oil, which contained high levels of PAHs, dispersion could have carried these toxic compounds deep into the water column, potentially exposing benthic organisms and other species.[80-82]

Commonly used dispersants sometimes have complex formulations, for which details on the involved chemical species and their concentrations are not always available. Furthermore, over the years, various substances have been progressively abandoned and replaced with new products, making it difficult to compare their efficiency, benefits, and adverse effects, especially considering that the contexts of use often represent unique conditions. The regulatory framework on a global scale is therefore extremely diverse and subject to change over time. Further in-depth analysis of this topic is necessary.

Following the initial containment works, effective spill response relies on robust monitoring to track the spill's trajectory, assess its environmental impact, and guide remediation efforts. Using airborne or satellite-based sensors to detect, map, and track oil spills, remote sensing may provide a broad, synoptic overview of the spill's extent, movement, and changes over time, crucial for large-scale incidents. Among the remote sensing technologies, synthetic aperture radar can penetrate cloud cover, offering data in adverse weather conditions, while conventional optical sensors are ineffective in darkness or limited lighting scenarios. In general, remote sensing enables rapid assessment and strategic planning of response operations. However, resolution can be restricted, making detecting very thin slicks or detailed features difficult. Interpretation of data requires specialized expertise, and remote sensing primarily provides surface-level information, not real-time subsurface dynamics. Satellite imagery and aerial surveillance were valuable during the Deepwater Horizon oil spill for tracking the massive oil slick, predicting its movement, and directing response vessels and booming operations to critical areas.[104]

Chemical analysis of environmental samples (water, sediment, biota) is a fundamental and central key to environmental monitoring plans, identifying specific hydrocarbon compounds, determining their concentrations, and assessing their degradation products and potential toxicity. Chemical determinations may provide precise and accurate quantitative and qualitative data related to pollutant characteristics, concentrations, and spatial distribution, which are essential for risk assessment, pollutant fate comprehension, and long-term monitoring of environmental recovery. The possibility of periodically monitoring over time and integrating data relating to abiotic matrices (water and sediments) and the tissues of bioindicator organisms can provide an integrated picture of the degree of contamination and related temporal trends.[49,50,105] Chemical analysis is time-consuming and requires specialized laboratory equipment and highly trained personnel for sample analysis and results interpretation. Following the Exxon Valdez oil spill (1989), extensive chemical analysis of hydrocarbon levels in water, sediments, and marine organisms was conducted for decades to track the persistence and spread of contaminants, providing critical data for understanding long-term ecological damage and recovery rates.[26,77] This data type also constitutes a fundamental scientific reference for planning monitoring plans and subsequent environmental investigations.[105]

In addition to chemical characterization, biomonitoring plays an immediate and central role. This approach uses living organisms as indicators of environmental health and pollutant exposure. It assesses physiological changes, bioaccumulation of pollutants in tissues, or impacts on population dynamics and community structure.[49,50,102,106] Biomonitoring provides an integrated measure of contaminant effects over time, reflecting the bioavailability of pollutants to organisms rather than just their environmental concentration. Biomonitoring can identify subtle ecological impacts that are not immediately apparent through chemical analysis alone. Given that the response of biological indicators can be slow to manifest, biomonitoring often requires long-term planning. Establishing causality between observed biological effects and specific contaminants can be complex, requiring a thorough understanding of baseline biological conditions. Thus, the success of a biomonitoring plan depends on a robust and solid scientific reference base regarding the stress-related biological effects of sentinel organisms and in-depth knowledge related to their sensitivity and responsiveness.[105,106] After the Prestige oil spill (2002) off the coast of Spain, biomonitoring studies on commercially important shellfish and fish populations, which continued for many years, have been fundamental for understanding the bioaccumulation trends in organisms' tissues, demonstrating the long-term impacts on marine food webs and the fishing industry.[27,80-82]

Various remediation strategies aim to clean up the spilled material and restore the affected environment to pristine conditions. Natural attenuation includes a series of intrinsic physical, chemical, and biological processes that reduce pollution over time without direct human intervention. These processes include dispersion, dissolution, volatilization, photo-oxidation, and biodegradation by naturally occurring microorganisms.[25] Natural attenuation is highly cost-effective and minimally invasive, as it avoids

introducing additional chemicals or disturbances to the ecosystem; however, it can be a very slow process, potentially taking years or decades to exhibit a significant reduction of the contamination levels and extension. Natural attenuation is generally unsuitable for highly toxic or very large spills where immediate intervention may be required.[25]

Bioremediation represents the primary active strategy to mitigate the effects of oil spills. This approach leverages microorganisms (bacteria and fungi) to break down hydrocarbon contaminants into less harmful substances, such as carbon dioxide and water. Among the commonly used techniques, bioaugmentation involves the introduction of specific, pre-selected microorganisms, often specialized for degrading particular hydrocarbons, to the contaminated site to enhance biodegradation rates. On the contrary, the biostimulation approach focuses on adding nutrients (e.g., nitrogen, phosphorus) or oxygen to the contaminated environment to stimulate the growth and activity of indigenous, naturally occurring, hydrocarbon-degrading microorganisms.[51] Bioremediation practice is an environmentally friendly approach as it utilizes natural processes and can potentially lead to the complete degradation of pollutants rather than just their transfer. However, the process can be slow, and its effectiveness highly depends on environmental conditions, such as temperature, pH, salinity, and nutrient availability. In addition, the success of bioaugmentation can be limited by the ability of introduced microorganisms to compete with native populations.[51] Biostimulation was applied extensively after the Exxon Valdez oil spill in Alaska. Fertilizers were sprayed on oiled beaches to provide essential nutrients (nitrogen and phosphorus) to naturally occurring hydrocarbon-degrading bacteria, significantly accelerating the breakdown and removal of residual oil from the affected shorelines.[26,27]

Among the bioremediation techniques, promising attempts have recently been investigated using engineered microorganisms. This practice can represent an improved approach to cleaning up marine oil spills. Modified bacteria and fungi can accelerate their oil-degrading pathways, making them more efficient at breaking down complex hydrocarbons into harmless substances, such as carbon dioxide and water. These designed microbes can be optimized for specific oil components or environmental conditions, such as temperature and salinity. When deployed, they rapidly proliferate and consume the oil, significantly reducing the environmental impact of spills and offering a sustainable alternative to chemical dispersants, representing a promising practice for more effective and less invasive marine ecosystem recovery.[107]

Physical removal, involving the direct mechanical removal of spilled material from the environment, represents the ultimate available means where other systems cannot completely remove hydrocarbons from marine ecosystems. Physical removal techniques include manual cleanup of shorelines (using shovels, rakes, absorbent materials), use of absorbents on water, and large-scale mechanical recovery operations. These practices can quickly remove large quantities of oils, substantially reduce pollution, and prevent further spread. However, they are highly labor-intensive and costly, generating significant volumes of waste that require specialized disposal. It can disrupt sensitive habitats during cleanup operations and potentially harm workers exposed to toxic substances through contact or inhalation.[43,82]

Responding to marine hydrocarbon contamination requires a dynamic and adaptable approach. No single technique provides a universal solution; instead, a combination of containment, monitoring, and remediation strategies is typically employed, tailored to the specific characteristics of each spill. Ongoing research and technological advancements continue to refine these methods, striving for more effective, efficient, and environmentally sound responses to safeguard marine ecosystems.

7. Challenges, recommendations, and future research prospects

Hydrocarbon contamination in the marine environment represents a significant global threat, affecting ecosystems, human health, and economic activities. A key challenge lies in accurately quantifying the pervasive and often underestimated cumulative load of hydrocarbons from chronic sources, such as shipping discharges, urban runoff, and atmospheric deposition, which can have insidious long-term impacts beyond acute spill events. Furthermore, the efficacy and potential toxicity of chemical dispersants, particularly with viscous oils or in deep-water applications, remain debated. Future research could include a systematic review of the different types of chemicals used and their short- and long-term effects on marine ecosystems. Remediation efforts, such as bioremediation, face limitations in speed and effectiveness due to environmental variability and competitive microbial dynamics. The long-term recovery of affected ecosystems can also span decades, especially for

sensitive habitats. In these terms, additional challenges and recommendations include the possibility of addressing these complex issues by adopting integrated approaches that combine rigorous prevention measures with rapid, effective response protocols and sustainable, environmentally affordable long-term remediation techniques. Future research should therefore continue to refine methods and approaches to define dynamic and adaptable strategies involving containment, monitoring, and tailored remediation practices. Ongoing studies are also vital to assess the long-term impacts on fish stocks and food chains, underscoring the continuous need for technological advancements to safeguard marine ecosystems comprehensively. Further investigations could also include a more in-depth study on how climate change can significantly alter marine hydrocarbon dynamics, considering that studies in this direction are still limited.

8. Conclusion

The pervasive presence of hydrocarbon mixtures in marine environments stems from continuous natural processes and significant anthropogenic activities, each with distinct characteristics and environmental implications. Natural sources, primarily geological seeps and biogenic production from marine organisms, have historically introduced hydrocarbons, contributing to background levels and fostering unique chemosynthetic ecosystems. However, the industrial age has dramatically escalated the magnitude and frequency of hydrocarbon inputs, transforming localized natural seepage into widespread contamination events. Anthropogenic contributions overwhelmingly dominate current hydrocarbon pollution. Harmful events, such as major oil spills from tanker accidents (e.g., Amoco Cadiz, Exxon Valdez, Prestige) and offshore drilling blowouts (e.g., Ixtoc 1, Deepwater Horizon), release vast quantities of crude oil, overwhelming natural degradation processes and causing relevant immediate and long-term ecological and economic impacts. These incidents lead to widespread mortality of marine fauna, habitat degradation, and significant financial losses in vital industries, such as fisheries and tourism. Beyond these acute disasters, chronic discharges from shipping operations, produced water from oil and gas platforms, urban runoff, and atmospheric deposition of combustion byproducts contribute to a substantial, often unquantified, cumulative load of hydrocarbons, leading to insidious long-term impacts. The chemical composition of anthropogenic hydrocarbons, particularly refined products, often contains more toxic and bioavailable compounds than natural seeps, exacerbating their ecological impacts.

Once in the marine environment, hydrocarbons undergo a complex series of physical, chemical, and biological transformations that dictate their distribution, persistence, and fate. Processes, such as spreading, evaporation, dissolution, dispersion, emulsification, and sedimentation alter their physical characteristics and movement. Crucially, microbial biodegradation, involving diverse communities of bacteria and archaea, and chemical transformations, such as photo-oxidation, represent the primary natural attenuation pathways, breaking down hydrocarbons into less harmful byproducts. These transformations can, however, also lead to the formation of compounds with increased water solubility and toxicity. Hydrocarbons may also be subjected to bioaccumulation and biotransformation in marine organisms, leading to significant toxicological effects across trophic levels.

In response to the significant threats posed by hydrocarbon pollution, a range of containment, monitoring, and remediation strategies has been developed and continuously refined. Initial responses to spills often involve physical containment using booms and mechanical recovery through skimmers. Chemical dispersants are sometimes used to break down slicks, enhancing natural dispersion and microbial degradation. However, their efficacy and potential toxicity remain controversial, particularly with viscous oils or deep-water applications. Monitoring efforts utilize remote sensing for large-scale tracking and chemical analyses of water, sediment, and biota samples for precise qualitative and quantitative data on contaminant levels and distribution. Biomonitoring programs further assess environmental health and pollutant exposure through living organisms. Remediation strategies aim to restore affected environments, with bioremediation being a prominent approach that enhances the activity of native or introduced oil-degrading microorganisms. The selection of the most appropriate strategy depends on factors, such as oil type, environmental conditions, and ecosystem sensitivity. The long-term recovery of affected marine ecosystems can span decades, especially for more sensitive habitats.

Overall, the present review consolidates current scientific knowledge regarding the origin, fate, impacts, and remediation of hydrocarbon mixtures in seawater. By integrating insights from geochemistry, oceanography, marine biology, and environmental sciences, it provides an overview of this critical environmental issue and

underscores the dynamic and adaptive approach required for effective response, highlighting the ongoing need for research and technological advancements to safeguard marine ecosystems.

Acknowledgments

None.

Funding

None.

Conflict of interest

Daniele Fattorini is an Editorial Board Member of this journal but was not involved in any way in the editorial and peer-review process conducted for this paper, either directly or indirectly. He declares no known competing financial interests or personal relationships that could have influenced the work reported in this paper.

Author contributions

This is a single-authored article.

Availability of data

The original artwork of the figures is available from the corresponding author upon reasonable request.

References

1. Haseeba KP, Vethamony P, Veerasingam S, Aboobacker VM, Al-Khayat JA. A comprehensive review of oil residues in the world oceans: Types, characteristics, sources and distribution. *Mar Pollut Bull.* 2025;217:118106.
doi: 10.1016/j.marpolbul.2025.118106
2. Volkman JK, Holdsworth DG, Neill GP, Bavor HJ Jr. Identification of natural, anthropogenic and petroleum hydrocarbons in aquatic sediments. *Sci Total Environ.* 1992;112(2-3):203-219.
doi: 10.1016/0048-9697(92)90188-x
3. Carvalho ACB, Moreira VA, Vicente MC, Bernardes MC, Bidone ED, Sabadini-Santos E. Evolution of the sources contribution of aliphatic hydrocarbons and their fate in Sepetiba bay, rio de janeiro, Brazil. *Estuar Coast Shelf Sci.* 2021;261:107548.
doi: 10.1016/j.ecss.2021.107548
4. Greenshields JB, Rossini FD. Molecular structure and properties of hydrocarbons and related compounds. *J Phys Chem.* 1958;62(3):271-280.
doi: 10.1021/j150561a005
5. Chakraborty A, Ruff SE, Dong X, *et al*. Hydrocarbon seepage in the deep seabed links subsurface and seafloor biospheres. *Proc Natl Acad Sci USA*. 2020;117(20):11029-11037.
doi: 10.1073/pnas.2002289117
6. Joye SB. The geology and biogeochemistry of hydrocarbon seeps. *Ann Rev Earth Planet Sci.* 2020;48:205-231.
doi: 10.1146/annurev-earth-063016-020052
7. Brooks JM, Kennicutt MC 2nd, Fisher CR, *et al*. Deep-sea hydrocarbon seep communities: Evidence for energy and nutritional carbon sources. *Science*. 1987;238:1138-1142.
doi: 10.1126/science.238.4830.1138
8. Rogowska J, Namieśnik J. Environmental implications of oil spills from shipping accidents. *Rev Environ Contam Toxicol*. 2010;206:95-114.
doi: 10.1007/978-1-4419-6260-7_5
9. Helle I, Mäkinen J, Nevalainen M, Afenyo M, Vanhatalo J. Impacts of oil spills on arctic marine ecosystems: A quantitative and probabilistic risk assessment perspective. *Environ Sci Technol.* 2020;54(4):2112-2121.
doi: 10.1021/acs.est.9b07086
10. Cordero JD, Saqalli M, Laplanche C, Locquet M, Elger A. Spatial analysis of accidental oil spills using heterogeneous data: A case study from the North-Eastern ecuadorian amazon. *Sustainbility*. 2018;10(12):4719.
doi: 10.3390/su10124719
11. Moore SF, Dwyer RL. Effects of oil on marine organisms: A critical assessment of published data. *Water Res*. 1974;8(10):819-827.
doi: 10.1016/0043-1354(74)90028-1
12. Orcutt BN, Sylvan JB, Knab NJ, Edwards KJ. Microbial ecology of the dark ocean above, at, and below the seafloor. *Microbiol Mol Biol Rev*. 2011;75:361-422.
doi: 10.1128/MMBR.00039-10
13. Abrams MA. Significance of hydrocarbon seepage relative to petroleum generation and entrapment. *Mar Petrol Geol.* 2005;22(4):457-477.
doi: 10.1016/j.marpetgeo.2004.08.003
14. Wang S, Liu G, Yuan Z, Lam PKS. Occurrence and trophic transfer of aliphatic hydrocarbons in fish species from yellow river estuary and Laizhou Bay, China. *Sci Total Environ*. 2019;696:134037.
doi: 10.1016/j.scitotenv.2019.134037
15. Han M, Li H, Kang Y, *et al*. Bioaccumulation and trophic transfer of PAHs in tropical marine food webs from coral reef ecosystems, the South China Sea: Compositional pattern, driving factors, ecological aspects, and risk assessment. *Chemosphere*. 2022;308:136295.
doi: 10.1016/j.chemosphere.2022.136295
16. Dastjerdi AM, Ashoorian S. *Chemical Enhanced Oil Recovery in Unconventional Reservoirs*. Netherlands: Elsevier; 2021. p. 433-459.
doi: 10.1016/b978-0-12-821931-7.00004-3

17. Wang X, Wang F, Taleb MAM, Wen Z, Chen X. A review of the seepage mechanisms of heavy oil emulsions during chemical flooding. *Energies*. 2022;15(22):8397. doi: 10.3390/en15228397
18. Pérez MIA, Zapata-Ramírez PA, Micallef A. A review of cold seeps in the Western Atlantic, focusing on Colombia and the Caribbean. *Front Mar Sci*. 2024;11:1430377. doi: 10.3389/fmars.2024.1430377
19. Umoh UU, Li L, He J, *et al*. Unusual aliphatic hydrocarbon profiles at hydrothermal vent fields of the Central and Southeast Indian Ridges and Mid-Indian Basin. *Deep Sea Res Top Stud Oceanogr.* 2021;194:104996. doi: 10.1016/j.dsr2.2021.104996
20. Campbell KA. Hydrocarbon seep and hydrothermal vent paleoenvironments and paleontology: Past developments and future research directions. *Palaeogeogr Palaeoclimatol Palaeoecol*. 2005;232(2-4):362-407. doi: 10.1016/j.palaeo.2005.06.018
21. Di Carlo M, Giovannelli D, Fattorini D, Bris NL, Vetriani C, Regoli F. Trace elements and arsenic speciation in tissues of tube dwelling polychaetes from hydrothermal vent ecosystems (east pacific rise): An ecological role as antipredatory strategy? *Mar Environ Res*. 2017;132:1-13. doi: 10.1016/j.marenvres.2017.10.003
22. Giovannelli D, D'Errico G, Fiorentino F, *et al*. Diversity and distribution of prokaryotes within a shallow-water pockmark field. *Front Microbiol*. 2016;7:941. doi: 10.3389/fmicb.2016.00941
23. Nickel JC, Di Primio R, Kallmeyer J, *et al.* Tracing the origin of thermogenic hydrocarbon signals in pockmarks from the southwestern Barents Sea. *Org Geochem*. 2013;63:73-84. doi: 10.1016/j.orggeochem.2013.08.008
24. Lea-Smith DJ, Biller SJ, Davey MP, *et al*. Contribution of cyanobacterial alkane production to the ocean hydrocarbon cycle. *Proc Natl Acad Sci USA*. 2015;112(44):13591-13596. doi: 10.1073/pnas.1507274112
25. Péquin B, Cai Q, Lee K, Greer CW. Natural attenuation of oil in marine environments: A review. *Mar Pollut Bullet*. 2022;176:113464. doi: 10.1016/j.marpolbul.2022.113464
26. Gill DA, Ritchie LA, Picou JS. Sociocultural and psychosocial impacts of the exxon valdez oil spill: Twenty-four years of research in Cordova, Alaska. *Extr Ind Soc*. 2016;3(4):1105-1116. doi: 10.1016/j.exis.2016.09.004
27. Pérez-Cadahía B, Lafuente A, Cabaleiro T, Pásaro E, Méndez J, Laffon B. Initial study on the effects of prestige oil on human health. *Environ Int.* 2006;33(2):176-185. doi: 10.1016/j.envint.2006.09.006
28. Kujawinski EB, Reddy CM, Rodgers RP, Thrash JC, Valentine DL, White HK. The first decade of scientific insights from the deepwater horizon oil release. *Nature Rev Earth Environ*. 2020;1(5):237-250. doi: 10.1038/s43017-020-0046-x
29. Byrnes TA, Dunn RJK. Boating- and shipping-related environmental impacts and example management measures: A review. *J Mar Sci Eng*. 2020;8(11):908. doi: 10.3390/jmse8110908
30. Nath F, Chowdhury MOS, Rhaman MM. Navigating produced water sustainability in the oil and gas sector: A critical review of reuse challenges, treatment technologies, and prospects ahead. *Water*. 2023;15(23):4088. doi: 10.3390/w15234088
31. Güney CB. Ballast water problem: Current status and expected challenges. *Mar Sci Tech Bull*. 2022;11(4):397-415. doi: 10.33714/masteb.1162688
32. Majeed BK, Shwan DMS, Rashid KA. A review on environmental contamination of petroleum hydrocarbons, its effects and remediation approaches. *Environ Sci Process Impacts*. 2025;27:526-548. doi: 10.1039/d4em00548a
33. Ehis-Eriakha CB, Ajuzieogu CA, Orogu JO, Akemu SE. Overview of petroleum hydrocarbon pollution and bioremediation technologies. *Bioremediat J*. 2024:1-23. doi: 10.1080/10889868.2024.2349014
34. Ivanov AY, Gerivani H, Evtushenko NV. Characterization of natural hydrocarbon seepage in the South Caspian Sea off Iran using satellite SAR and geological data. *Mar Georesour Geotech*. 2019;38(5):527-538. doi: 10.1080/1064119x.2019.1600175
35. Li Y, Wang H, Cai Z, Zhang J, Fu J. Molecular analyses of petroleum hydrocarbon change and transformation during petroleum weathering by multiple techniques. *ACS Omega*. 2021;6(36):23222-23232. doi: 10.1021/acsomega.1c02846
36. Dutta TK, Harayama S. Fate of crude oil by the combination of photooxidation and biodegradation. *Environ Sci Technol*. 2000;34(8):1500-1505. doi: 10.1021/es991063o
37. Bacos AHP, Ancla SMB, Arcadio CGLA, *et al*. From surface water to the Deep Sea: A review on factors affecting the biodegradation of spilled oil in marine environment. *J Mar Sci Eng*. 2022;10(3):426. doi: 10.3390/jmse10030426
38. Nicodem DE, Guedes CLB, Conceição M, *et al.* Photochemistry of petroleum. *Prog React Kinet Mec.* 2001;26(2-3):219-238. doi: 10.3184/007967401103165262
39. Nicodem DE, Guedes CLB, Correa RJ, Fernandes MCZ. Photochemical processes and the environmental impact of petroleum spills. *Biogeochem.* 1997;39:121-138. doi: 10.1023/A:1005802027380
40. Cao X, Tarr MA. Aldehyde and ketone photoproducts from solar-irradiated crude oil-seawater systems determined by electrospray ionization-tandem mass spectrometry.

Environ Sci Technol. 2017;51(20):11858-11866.
doi: 10.1021/acs.est.7b01991

41. Das N, Chandran P. Microbial degradation of petroleum hydrocarbon contaminants: An overview. *Biotechnol Res Int*. 2011;2011:941810.
doi: 10.4061/2011/941810
42. Perala-Dewey J, Orr K, Hageman KJ, Zawar-Reza P, Shahpoury P. Atmospheric transport of polycyclic aromatic hydrocarbons into three alpine valleys: Influence of local-scale wind patterns and chemical partitioning. *Environ Sci Technol.* 2023;57(35):13114-13123.
doi: 10.1021/acs.est.3c03288
43. Hook SE, Strzelecki J, Adams MS, *et al*. The influence of oil-in-water preparations on the toxicity of crude oil to marine invertebrates and fish following short-term pulse and continuous exposures. *Environ Toxicol Chem*. 2022;41(10):2580-2594.
doi: 10.1002/etc.5437
44. Boulais M, Vignier J, Loh AN, *et al.* Sublethal effects of oil-contaminated sediment to early life stages of the eastern oyster, *Crassostrea virginica*. *Environ Pollut*. 2018;243:743-751.
doi: 10.1016/j.envpol.2018.09.017
45. Fernandes GM, Martins DA, Santos RPD, *et al*. Levels, source appointment, and ecological risk of petroleum hydrocarbons in tropical coastal ecosystems (Northeast Brazil): Baseline for future monitoring programmes of an oil spill area. *Environ Pollut*. 2021;296:118709.
doi: 10.1016/j.envpol.2021.118709
46. White HK, Hsing PY, Cho W, *et al.* Impact of the deepwater horizon oil spill on a deep-water coral community in the gulf of Mexico. *Proc Natl Acad Sci USA*. 2012;109(50):20303-20308.
doi: 10.1073/pnas.1118029109
47. Jayarathna MD, Rajapaksha AU, Samarasekara S, Vithanage M. Oil spill response: Existing technologies, prospects and perspectives. *Clean Mater*. 2024;1:78-96.
doi: 10.1002/clem.17
48. Zhu Z, Merlin F, Yang M, *et al*. Recent advances in chemical and biological degradation of spilled oil: A review of dispersants application in the marine environment. *J Hazard Mater*. 2022;436:129260.
doi: 10.1016/j.jhazmat.2022.129260
49. Etiope G, Panieri G, Fattorini D, *et al.* A thermogenic hydrocarbon seep in shallow Adriatic Sea (Italy): Gas origin, sediment contamination and benthic foraminifera. *Mar Pet Geol*. 2014;57:283-293.
doi: 10.1016/j.marpetgeo.2014.06.006
50. Benedetti M, Gorbi S, Fattorini D, *et al.* Environmental hazards from natural hydrocarbons seepage: Integrated classification of risk from sediment chemistry, bioavailability and biomarkers responses in sentinel species. *Environ Pollut*. 2013;185:116-126.
doi: 10.1016/j.envpol.2013.10.023
51. Matilda MI, Samuel HS. Bioremediation of oil spill: Concept, methods and applications. *Discov Chem*. 2024;1(1):42.
doi: 10.1007/s44371-024-00038-2
52. Dando PR, Hovland M. Environmental effects of submarine seeping natural gas. *Cont Shelf Res*. 1992;12(10):1197-1207.
doi: 10.1016/0278-4343(92)90079-y
53. Barry PH, De Moor JM, Giovannelli D, *et al.* Forearc carbon sink reduces long-term volatile recycling into the mantle. *Nature*. 2019;568(7753):487-492.
doi: 10.1038/s41586-019-1131-5
54. Fullerton KM, Schrenk MO, Yücel M, *et al.* Effect of tectonic processes on biosphere-geosphere feedbacks across a convergent margin. *Nat Geosci*. 2021;14(5):301-306.
doi: 10.1038/s41561-021-00725-0
55. Bernard BB, Brooks JM, Sackett WM. Natural gas seepage in the Gulf of Mexico. *Earth Planet Sci Lett*. 1976;31(1):48-54.
doi: 10.1016/0012-821x(76)90095-9
56. Boles JR, Garven G, Peltonen C. Hydrocarbon production reduces natural methane seeps in the Santa Barbara channel. *Mar Pet Geol*. 2023;151:106187.
doi: 10.1016/j.marpetgeo.2023.106187
57. Spatola D, Rovere M, Casalbore D, Chiocci FL. Pockmarks of the Mediterranean region seas: A comprehensive geodatabase for marine geomorphological analysis. *Sci Data*. 2025;12(1):1049.
doi: 10.1038/s41597-025-05369-y
58. Dimitrov L, Woodside J. Deep sea pockmark environments in the Eastern Mediterranean. *Mar Geol*. 2003;195(1-4):263-276.
doi: 10.1016/s0025-3227(02)00692-8
59. El-Sabagh SM, El-Naggar AY, Nady MME, Ebiad MA, Rashad AM, Abdullah ES. Distribution of triterpanes and steranes biomarkers as indication of organic matters input and depositional environments of crude oils of oilfields in Gulf of Suez, Egypt. *Egypt J Petrol*. 2018;27(4):969-977.
doi: 10.1016/j.ejpe.2018.02.005
60. Mara P, Nelson RK, Reddy CM, Teske A, Edgcomb VP. Sterane and hopane biomarkers capture microbial transformations of complex hydrocarbons in young hydrothermal Guaymas Basin sediments. *Commun Earth Environ*. 2022;3(1):250.
doi: 10.1038/s43247-022-00582-8
61. Volkova I, Gura D, Aksenov I. Abiogenic and biogenic petroleum origin: A common theory for geological surveys. *Asian J Water Environ Pollut*. 2021;18(1):59-65.
doi: 10.3233/ajw210008
62. Neff JM. *Bioaccumulation in Marine Organisms: Effect of Contaminants from Oil Well Produced Water*. Amsterdam: Elsevier; 2002.
doi: 1016/B978-0-08-043716-3.X5000-3
63. Van Dover CL. *The Ecology of Deep-Sea Hydrothermal*

Vents. United States: Princeton University Press; 2000. doi: 10.2307/j.ctv1zm2v35
64. Sorigué D, Légeret B, Cuiné S, *et al.* Microalgae synthesize hydrocarbons from long-chain fatty acids via a light-dependent pathway. *Plant Physiol*. 2016;171(4):2393-2405. doi: 10.1104/pp.16.00462
65. Wichmann J, Lauersen KJ, Kruse O. Green algal hydrocarbon metabolism is an exceptional source of sustainable chemicals. *Curr Opin Biotechnol*. 2019;61:28-37. doi: 10.1016/j.copbio.2019.09.019
66. Harindintwali JD, Xiang L, Wang F, *et al.* Syntrophy of bacteria and archaea in the anaerobic catabolism of hydrocarbon contaminants. *Crit Rev Environ Sci Technol*. 2022;53(13):1331-1357. doi: 10.1080/10643389.2022.2134702
67. Angel R, Claus P, Conrad R. Methanogenic archaea are globally ubiquitous in aerated soils and become active under wet anoxic conditions. *ISME J*. 2012;6(4):847-862. doi: 10.1038/ismej.2011.141
68. Baumas C, Bizic M. A focus on different types of organic matter particles and their significance in the open ocean carbon cycle. *Prog Oceanogr.* 2024;224:103233. doi: 10.1016/j.pocean.2024.103233
69. Almeda R, Connelly TL, Buskey EJ. How much crude oil can zooplankton ingest? Estimating the quantity of dispersed crude oil defecated by planktonic copepods. *Environ Pollut*. 2015;208:645-654. doi: 10.1016/j.envpol.2015.10.041
70. Horsfield B, Rullkötter J. Diagenesis, catagenesis and metagenesis of organic matter. In: *American Association of Petroleum Geologists eBooks*. Berlin: Springer; 1994. p. 189-200. doi: 10.1306/m60585c10
71. Hantson S, Knorr W, Schurgers G, Pugh TAM, Arneth A. Global isoprene and monoterpene emissions under changing climate, vegetation, CO_2 and land use. *Atmos Environ*. 2017;155:35-45. doi: 10.1016/j.atmosenv.2017.02.010
72. Bouchertall F. Atmospheric transport and input of hydrocarbons to the subtropical North Atlantic. *Mar Chem*. 1987;21(3):203-211. doi: 10.1016/0304-4203(87)90059-4
73. Conan G. The long-term effects of the Amoco Cadiz oil spill. *Philos Trans R Soc Lond B Biol Sci*. 1982;297(1087):323-333. doi: 10.1098/rstb.1982.0045
74. Batten SD, Allen RJS, Wotton COM. The effects of the Sea Empress oil spill on the plankton of the Southern Irish Sea. *Mar Pollut Bull.* 1998;36(10):764-774. doi: 10.1016/s0025-326x(98)00039-3
75. Moldan AGS, Jackson LF, McGibbon S, Van Der Westhuizen J. Some aspects of the Castillo de Bellver oilspill. *Mar Pollut Bull*. 1985;16(3):97-102. doi: 10.1016/0025-326x(85)90530-2
76. Bi H, Wang Z, Yue R, *et al*. Oil spills in coastal regions of the arctic and subarctic: Environmental impacts, response tactics, and preparedness. *Sci Total Environ*. 2024;958:178025. doi: 10.1016/j.scitotenv.2024.178025
77. Steiner R. *Lessons of the Exxon Valdez*. United States: Sea Grant; 1990. doi: 10.4027/lotev.1990
78. Afenyo M, Veitch B, Khan F. A State-of-the-art review of fate and transport of oil spills in open and ice-covered water. *Ocean Eng*. 2015;119:233-248. doi: 10.1016/j.oceaneng.2015.10.014
79. Martinelli M, Luise A, Tromellini E, Sauer TC, Neff JM, Douglas GS. The M/C haven oil spill: Environmental assessment of exposure pathways and resource injury. *Int Oil Spill Conf Proceed*. 1995;1995(1):679-685. doi: 10.7901/2169-3358-1995-1-679
80. Whitfield J. Prestige: One month on. *Nat*. 2002. doi: 10.1038/news021216-6
81. Loureiro ML, Loomis JB, Vázquez MX. Economic valuation of environmental damages due to the prestige oil spill in Spain. *Environ Resour Econ*. 2009;44(4):537-553. doi: 10.1007/s10640-009-9300-x
82. Beiras R, Saco-Álvarez L. Toxicity of seawater and sand affected by the prestige fuel-oil spill using bivalve and sea urchin embryogenesis bioassays. *Water Air Soil Pollut*. 2006;177(1-4):457-466. doi: 10.1007/s11270-006-9166-2
83. Soto LA, Botello AV, Licea-Durán S, Lizárraga-Partida ML, Yáñez-Arancibia A. The environmental legacy of the Ixtoc-I oil spill in campeche sound, Southwestern Gulf of Mexico. *Front Mar Sci*. 2014;1:1-9. doi: 10.3389/fmars.2014.00057
84. Valverde RA, Holzwart KR. *Sea Turtles of the Gulf of Mexico*. Berlin: Springer; 2017. p. 1189-1351. doi: 10.1007/978-1-4939-3456-0_3
85. Mostafawi N. How severely was the Persian Gulf affected by oil spills following the 1991 Gulf War? *Environ Geol*. 2001;40(10):1185-1191. doi: 10.1007/s002540100238
86. Readman JW, Fowler SW, Villeneuve JP, Cattini C, Oregioni B, Mee LD. Oil and combustion-product contamination of the Gulf marine environment following the war. *Nature.* 1992;358(6388):662-665. doi: 10.1038/358662a0
87. Mousavi SH, Kavianpour MR, Alcaraz JLG. The impacts of dumping sites on the marine environment: A system dynamics approach. *Appl Water Sci*. 2023;13(5):109. doi: 10.1007/s13201-023-01910-9
88. Tarr M, Zito P, Overton E, Olson G, Adkikari P, Reddy C. Weathering of oil spilled in the marine environment. *Oceanogr*. 2016;29(3):126-135. doi: 10.5670/oceanog.2016.77

89. Hazen TC, Prince RC, Mahmoudi N. Marine oil biodegradation. *Environ Sci Technol*. 2015;50(5):2121-2129. doi: 10.1021/acs.est.5b03333
90. Mackay D, McAuliffe CD. Fate of hydrocarbons discharged at sea. *Oil Chem Pollut*. 1989;5(1):1-20. doi: 10.1016/s0269-8579(89)80002-4
91. Adebayo O, Bhatnagar S, Webb J, *et al.* Hydrocarbon-degrading microbial populations in permanently cold deep-sea sediments in the NW Atlantic. *Mar Pollut Bull*. 2024;208:117052. doi: 10.1016/j.marpolbul.2024.117052
92. Coates JD, Bruce RA, Haddock JD. Anoxic bioremediation of hydrocarbons. *Nature*. 1998;396(6713):730. doi: 10.1038/25470
93. Zika RG, Cooper WJ. *Photochemistry of Environmental Aquatic Systems*. United States: American Chemical Society; 1987. doi: 10.1021/bk-1987-0327
94. Ehrhardt M, Petrick G. On the composition of dissolved and particle-associated fossil fuel residues in Mediterranean surface water. *Mar Chem*. 1993;42(1):57-70. doi: 10.1016/0304-4203(93)90249-n
95. Honda M, Suzuki N. Toxicities of polycyclic aromatic hydrocarbons for aquatic animals. *Int J Environ Res Public Health*. 2020;17(4):1363. doi: 10.3390/ijerph17041363
96. Fahmi AM, Summers S, Jones M, Bowler B, Hennige S, Gutierrez T. Effect of ocean acidification on the growth, response and hydrocarbon degradation of coccolithophore-bacterial communities exposed to crude oil. *Sci Rep.* 2023;13(1):5013. doi: 10.1038/s41598-023-31784-5
97. Troisi G, Barton S, Bexton S. Impacts of oil spills on seabirds: Unsustainable impacts of non-renewable energy. *Int J Hydrogen Energy*. 2016;41(37):16549-16555. doi: 10.1016/j.ijhydene.2016.04.011
98. Zhang W, Xie HQ, Li Y, *et al.* The aryl hydrocarbon receptor: A predominant mediator for the toxicity of emerging dioxin-like compounds. *J Hazard Mater*. 2021;426:128084. doi: 10.1016/j.jhazmat.2021.128084
99. Laffon B, Pásaro E, Valdiglesias V. Effects of exposure to oil spills on human health: Updated review. *J Toxicol Environ Health Part B Crit Rev.* 2016;19(3-4):105-128. doi: 10.1080/10937404.2016.1168730
100. Mallah MA, Changxing L, Mallah MA, *et al.* Polycyclic aromatic hydrocarbon and its effects on human health: An overeview. *Chemosphere*. 2022;296:133948. doi: 10.1016/j.chemosphere.2022.133948
101. De Oliveira Estevo M, Lopes PFM, De Oliveira Júnior JGC, *et al.* Immediate social and economic impacts of a major oil spill on Brazilian coastal fishing communities. *Mar Pollut Bull*. 2021;164:111984. doi: 10.1016/j.marpolbul.2021.111984
102. Pete AJ, Bharti B, Benton MG. Nano-enhanced bioremediation for oil spills: A review. *ACS ES T Eng*. 2021;1(6):928-946. doi: 10.1021/acsestengg.0c00217
103. Prince RC. A half century of oil spill dispersant development, deployment and lingering controversy. *Int Biodeterior Biodegrad*. 2022;176:105510. doi: 10.1016/j.ibiod.2022.105510
104. Jiang Q, Ji M, Wang J, Sun P. Remote sensing methods for striped marine oil spill detection in narrow ship channels. *Ocean Eng*. 2023;289:116162. doi: 10.1016/j.oceaneng.2023.116162
105. Regoli F, D'Errico G, Nardi A, *et al.* Application of a weight of evidence approach for monitoring complex environmental scenarios: The case-study of off-shore platforms. *Front Mar Sci*. 2019;6. doi: 10.3389/fmars.2019.00377
106. Gorbi S, Virno Lamberti C, Notti A, *et al.* An ecotoxicological protocol with caged mussels, *Mytilus galloprovincialis*, for monitoring the impact of an offshore platform in the Adriatic sea. *Mar Environ Res*. 2007;65(1):34-49. doi: 10.1016/j.marenvres.2007.07.006
107. Kalia A, Sharma S, Semor N, *et al.* Recent advancements in hydrocarbon bioremediation and future challenges: A review. *3 Biotech*. 2022;12(6):135. doi: 10.1007/s13205-022-03199-y

Asian Journal of Water, Environment and Pollution. Vol. 22, No. 6 (2025), pp. 47-59.
doi: 10.36922/AJWEP025070039

ORIGINAL RESEARCH ARTICLE

Statistical analysis of wind energy potential in Mongo, Chad, for small-scale renewable applications

Ali Sidick Bahar[1], Adoum Kriga[1], Ali Ramadan Ali[1], Abakar Mahamat Tahir[2], Adoum Danao Adile[1], and Fabien Kenmogne[3]*

[1]Department of Industrial Engineering and Maintenance, Faculty of Engineering Sciences and Techniques, Polytechnic University of Mongo, Mongo, Guéra region, Chad
[2]Laboratory of Renewable Energy and Materials Premises, Faculty of Exact and Applied Sciences, University of Ndjamena, Ndjamena, Chad
[3]Department of Civil Engineering, Advanced Teachers Training College of the Technical Education, University of Douala, Douala, Littoral Region, Cameroon
***Corresponding author:** Fabien Kenmogne (kenfabien@yahoo.fr)

Received: February 10, 2025; 1st revised: March 17, 2025;2nd revised: May 5, 2025; 3rd revised: July 14, 2025; Accepted: July 15, 2025; Published online: August 6, 2025

Abstract: Wind plays a crucial role in various physical applications, including wind energy and pollutant transport and diffusion. Wind varies from both temporal and spatial perspectives. This paper presents a statistical analysis of wind energy potential in Mongo, the capital city of Guéra Province, Chad, using 11 years of data obtained from the local meteorological station. Using the Weibull distribution function, we analyzed the wind speed probability distributions based on the wind data obtained. The obtained results, based on average annual wind speed and energy generation, indicate that Mongo is suitable only for small-scale wind energy applications. The average wind speed within the chosen time interval is 3.2 m/s, which is classified as Class 1 according to the international system of wind classification. Wind rose plots illustrate that the wind directions vary across the years. The temperature data were also plotted, reporting an average temperature of 27.76°C over the 11-year study period. This indicates that Mongo has a relatively hot climate, which may contribute to the modest but consistent wind speeds observed in this city.

Keywords: Wind energy potential; Renewable energy; Wind and temperature data; Weibull distribution function.

1. Introduction

Access to electricity remains a critical challenge in Chad, a landlocked Central African country with one of the lowest electrification rates globally. As of 2021, only about 8% of the total population had access to electricity, with rural areas reporting coverage as low as 1.3%.[1,2] This energy poverty significantly hinders social and economic development by limiting access to essential services, such as healthcare, education, clean water, and communication.[3,4] The government of Chad has initiated efforts to diversify its energy portfolio by integrating renewable energy sources, including solar and wind, into its national energy mix.[5-7] Given Chad's challenging energy access and the low electrification rates, especially in rural areas, such as Guéra Province, where Mongo is located, assessing Mongo's wind energy potential is crucial for identifying viable local

solutions that can foster sustainable development and improve living standards. This focus aligns with the national aims of expanding decentralized renewable energy systems to underserved regions.[4,5]

Wind energy, as a globally recognized clean and renewable resource, has been extensively studied to address energy access challenges. Recent scientific literature provides a comprehensive and up-to-date basis for assessing and deploying wind energy in contexts comparable to Chad.[8-23] These studies encompass various statistical approaches to wind resource assessment, which demonstrate the global relevance of evaluating wind energy potential in developing regions.

Despite the country's significant potential in both fossil and renewable energy sources, including solar irradiance levels exceeding 5.5 kWh/m²/day and moderate wind corridors in various regions, the application of wind energy remains underdeveloped.[8-10] In response to the pressing need for sustainable energy and climate resilience, the Chadian government has prioritized the development of renewable energy through national energy planning and recent regulatory reforms, such as the 2018 Renewable Energy Promotion Law.[11,12] Wind energy, in particular, offers a promising solution for off-grid and rural electrification, especially in areas with moderate and consistent wind patterns.[13,14] Studies from countries with similar climatic conditions have shown that even moderate wind regimes, when well characterized statistically, can effectively support micro-wind energy systems.[15,16]

Mongo, the capital of Guéra Province, is situated in a transitional climatic zone between the Sahel and Sudanese ecological regions. Although it has not been the focus of major national wind studies, its location, topography, and meteorological conditions suggest that Mongo is a potentially viable wind resource. Previous studies, such as those by Soulouknga *et al.*[2] and Medjo Nouadje *et al*.,[24] have explored wind potential in regions, including Abéché and N'Djamena, applying the Weibull distribution model to characterize wind patterns. However, these analyses often rely on short datasets or fail to evaluate wind behavior over extended periods. Similar gaps have been observed in many developing countries, where long-term wind datasets are rare and modeling is often oversimplified.[25-27] In particular, no dedicated long-term study has been conducted to assess Mongo's wind energy potential using statistically robust methods and decade-long data series.

This study aims to fill that gap by conducting a comprehensive analysis of Mongo's wind potential using data collected over an 11-year period (2012 – 2022). The combination of the Weibull distribution and the maximum entropy principle (MEP) allows for a robust and complementary characterization of the wind speed distribution, where Weibull provides a widely accepted parametric model, and Maximum Entropy offers a flexible, information-theoretic approach that can capture complex wind speed behaviors that are not always well represented by standard distributions.[28-30]

The goal is to determine whether Mongo is suitable for small-scale wind energy systems that support rural electrification initiatives and contribute to the national renewable energy strategy. These methods have been validated in similar assessments in North and West Africa, Central Asia, and Latin America, proving effective even in low-to-moderate wind conditions.[17]

The research's strengths lie in its long-term dataset, robust statistical approach, and focused geographic scope, which provide detailed, actionable insights. However, there are limitations, such as the absence of economic and technical feasibility analyses, which are proposed for future work. The study contributes to the scientific field by addressing a critical data gap for Chad and demonstrating a replicable methodology for wind resource assessment in comparable developing regions.

The relevance of this study lies in its potential to inform policy decisions and guide investment in decentralized wind energy systems for rural regions in Chad. Unlike previous research, which often covers broader geographic scopes or lacks temporal depth, this work provides a detailed, localized, and data-driven analysis focused on a specific site of strategic interest. It not only contributes to the sparse academic literature on Chad's wind energy prospects but also provides actionable insights for energy planners, engineers, and stakeholders. To guide this investigation, the following research questions are posed:

(i) What is the average annual and monthly wind speed in Mongo over the period 2012 – 2022?
(ii) What are the dominant wind directions, and how do they vary seasonally?
(iii) What is the estimated wind power density and its suitability for energy generation?
(iv) Does Mongo meet the criteria for deploying small-scale wind turbines for decentralized power generation?

In response to these questions, several hypotheses are formulated:

(i) The availability of 11 years of data allows for statistically reliable wind speed estimation using Weibull and entropy-based models

(ii) The average wind speed in Mongo is ≥ 3.0 m/s, corresponding to wind power Class 1, which is suitable for limited applications
(iii) The prevailing wind direction is predominantly south-southwest, consistent with regional climatic patterns
(iv) The estimated wind power density is sufficient to support standalone micro-generation systems (<30 W/m²).

These hypotheses were tested through descriptive statistical analysis, parameter estimation, and comparison with international wind classification standards. The study also analyzed wind power potential using both annual and monthly assessments, accounting for variability and reliability. Although this study does not include a full economic feasibility assessment, indicative metrics, such as average power output and temporal consistency, help to determine the viability of wind exploitation in the region.

In short, this research addresses a significant knowledge gap by providing the first long-term, data-driven assessment of Mongo's wind energy potential. It contributes to national efforts to expand renewable energy access in underserved areas and offers a replicable framework for similar assessments in other regions of Chad or comparable developing contexts. While focused on localized wind resource evaluation, the study acknowledges limitations, such as the absence of economic feasibility analysis, which can be addressed in future research to strengthen deployment strategies.

2. Materials and methods

2.1. Study area and data acquisition

This study focuses on Mongo, the capital of Guéra Province in central Chad, located between latitudes 12°18' and 13°18' north and longitudes 18°07' and 19°07' east. The town lies at an elevation of approximately 415 ± 5 m above sea level on alluvial deposits, covering an area of 63.5 km². Mongo features a Sahelian climate characterized by two distinct seasons: A rainy season from April to October and a dry season from November to March.[1]

Meteorological data for the period 2012 – 2022 were collected from the Mongo weather station, including monthly averages of wind speed, wind direction, and ambient temperature computed from hourly measurements. The data originate from the official Mongo meteorological station, with all instruments complying with World Meteorological Organization standards, ensuring measurement precision of ± 0.1 m/s for wind speed and ± 0.5°C for temperature. The temporal resolution of the data used in this study is monthly, derived as averages from hourly recordings. The collected data underwent rigorous quality control to detect anomalies and interpolate missing values to ensure reliability.[7,23]

2.2. Statistical modeling of wind speed using the Weibull distribution

The statistical modeling of wind speed is crucial for accurate wind energy assessment. Among the various models proposed in the literature, the two-parameter Weibull distribution remains the most widely used due to its flexibility and good fit to empirical data across many geographical regions.[12,16] The Weibull probability density function (PDF) is expressed in Equation I.

$$f(v)=\left(\frac{k}{c}\right)\left(\frac{v}{c}\right)^{k-1} exp\left(-\left[\frac{v}{c}\right]^{k}\right),\ v>0 \quad \text{(I)}$$

where v is the wind speed (m/s), k is the dimensionless shape parameter, and c is the scale parameter (m/s). The cumulative distribution function is expressed in Equation II.

$$f(v)=1-exp\left(-\left[\frac{v}{c}\right]^{k}\right) \quad \text{(II)}$$

The Weibull distribution was chosen for this study due to its proven versatility and widespread acceptance in wind energy assessment worldwide. Compared to other distributions, such as Rayleigh, Lognormal, Gamma, or Beta, the Weibull distribution provides a better balance between model simplicity and the ability to accurately capture a wide range of wind speed frequency patterns across diverse climatic conditions.[12,16] Its two parameters allow flexibility in adjusting both the shape and scale of the distribution, making it suitable for representing skewed and variable wind speed data like those observed in the Sahelian climate of Mongo.

The Weibull parameters, k and c, were estimated using two complementary approaches to ensure robustness and accuracy: The method of moments and the energy pattern factor (EPF) method.

The method of moments involves calculating the shape parameter k and scale parameter c from the sample mean and standard deviation σ_v of the wind speed data, as shown in Equations III and IV.

$$\overline{v} = c = \frac{\overline{v}}{\Gamma\left(1+\frac{1}{k}\right)} \quad \text{(III)}$$

$$\sigma_v = c\sqrt{\left(\Gamma\left(1+\frac{2}{k}\right)-\left[\Gamma\left(1+\frac{1}{k}\right)\right]^2\right)} \quad \text{(IV)}$$

where Γ denotes the gamma function. The EPF method, based on the ratio of the third moment to the cube of the first moment of the wind speed, is defined in Equation V. The shape parameter k is calculated with Equation VI, followed by parameter c derived from k and the mean wind speed.

$$EPF = \frac{\overline{v^3}}{\overline{v}^3} = \frac{\frac{1}{n}\left(\sum_{i=1}^{n} v_i^3\right)}{\left(\frac{1}{n}\sum_{i=1}^{n} v_i\right)^3} \quad \text{(V)}$$

$$k = 1+\frac{3.69}{\left(EPF\right)^2} \quad \text{(VI)}$$

By applying both methods, the parameter estimates were cross-validated to ensure consistency and to improve the fit of the Weibull model to the observed wind speed data. Beyond the Weibull distribution, several other statistical models have been proposed for calculating wind speed distributions, each with its specific advantages and limitations. The Rayleigh distribution, a special case of Weibull with $k = 2$, has been used due to its simplicity, but may lack flexibility for complex wind regimes.[11,19] The Lognormal distribution has also been employed, especially when the Weibull does not efficiently capture skewness in data.[17,24] Advanced parametric models, such as the Gamma and Beta distributions, can fit wind speed data with multimodal features or specific skewness and kurtosis patterns.[18,27,31] However, these models typically require more data and computational effort, which may not always be feasible.

Weibull distribution is chosen in this study due to its proven robustness, simplicity, and widespread acceptance in wind energy studies, which makes it suitable for the available Mongo dataset. Nevertheless, to overcome limitations linked to parametric assumptions, complementary methods are considered.

2.3. Statistical modeling using the MEP

In addition to parametric methods, non-parametric approaches, such as the MEP have been applied to wind speed modeling.[14,20,32] The MEP maximizes the Shannon entropy subject to constraints derived from empirical data, resulting in the least-biased probability distribution consistent with known information.

To provide a more intuitive understanding, the MEP can be viewed as a method for deriving the most unbiased probability distribution when only limited information (such as average values or moments) is known. By maximizing entropy, the approach avoids introducing unwarranted assumptions or bias beyond the constraints imposed by the data. This leads to a distribution that best represents the true uncertainty inherent in the wind speed data. The advantage of using MEP lies in its flexibility and minimal assumptions, allowing it to adapt to complex wind speed behaviors that may not be well captured by standard parametric models, such as Weibull. This makes MEP especially useful in environments where wind regimes are highly variable or poorly characterized by simple distributions. The constraints are: (i) The total probability within the defined speed interval must be equal to one, as shown in Equation VII; (ii) The M-low statistical orders for the theoretical and empirical distributions must be equal, as shown in Equation VIII. The general solution is shown in Equation IX.

$$\int_0^{maxf(v)} f\left(v\right)dv = 1 \quad \text{(VII)}$$

$$\int_0^{maxf(v)} vf\left(v\right)dv = \overline{v} \quad \text{(VIII)}$$

$$f\left(v\right) = exp\left(\sum_{i=1}^{M} a_i v^i\right) \quad \text{(IX)}$$

where α_i is the Lagrangian multiplier found using the Newton-Raphson method. Other non-parametric methods, including kernel density estimation and empirical distribution functions, have also been used to model wind speed without assuming a predefined functional form. These data-driven approaches can capture complex distribution shapes, but they might require large datasets to achieve their effectiveness.[13,27,33,34] The combined use of Weibull distribution and MEP in this study leverages the robustness and simplicity of a classical parametric model with the flexibility of a non-parametric approach, providing a comprehensive characterization of the wind speed regime at Mongo.

2.3.1. Wind power density estimation

The wind power density represents the kinetic energy flux per unit area, as shown in Equation X.

$$E = \frac{P}{A} = \frac{1}{2}\rho\int_0^\infty v^3 f(v)dv \quad \text{(X)}$$

where E is the power density (W/m²), ρ is the air density (1.225 kg/m³), and $f(v)$ is the wind speed PDF (Weibull or MEP). Accurate modeling of the wind speed distribution is crucial for realistic energy yield estimates.[35]

2.3.2. Wind direction analysis using a wind rose

An assessment of wind direction was performed using monthly averaged data collected from 2012 to 2022. The directional values were categorized into 16 equally spaced compass sectors, each covering 22.5°, to ensure adequate angular resolution over the full 360° range. This segmentation enables the systematic quantification of the directional distribution of the wind over the study period.

The frequency of wind blowing from each sector is calculated with Equation XI.

$$f_i = \frac{n_i}{N} \times 100 \quad \text{(XI)}$$

where f_i is the frequency (in percent) of wind coming from direction sector i; n_i is the number of wind direction observations in that sector, and N is the total number of valid wind direction records.

The data were processed using meteorological statistical tools capable of handling directional classification and frequency analysis. No filtering based on wind speed threshold was applied in this computation phase to preserve the full angular distribution of wind occurrence. The results of this procedure served as input for constructing a wind rose diagram, which reflects the statistical dispersion of wind direction at the site.[8,36]

2.4. Temperature analysis and wind temperature relationship assessment

Air temperature affects atmospheric pressure gradients and convective flows, shaping wind dynamics.[28,29] Monthly average temperatures from 2012 to 2022 were analyzed through:

(i) Time series analysis to identify seasonal and interannual variability
(ii) Graphical superimposition of temperature and wind speed for concurrent trend detection
(iii) Scatter plots to assess preliminary correlations
(iv) Regression modeling (linear and non-linear) to quantify relationships, evaluated by determination coefficient (R^2)
(v) Hysteresis analysis to detect phase lag or cyclical wind–temperature interactions.[30,37]

This methodology aims to elucidate the role of temperature as a modulator of wind patterns in Mongo's Sahelian climate, supporting refined assessments of wind energy potential.

3. Results and discussion

3.1. Wind speed analyses

Table 1 summarizes the monthly and annual mean wind speeds over the 2012 – 2022 period. All annual mean values exceed the minimum exploitable wind speed threshold of 2.0 m/s, demonstrating that Mongo has a usable, albeit modest, wind resource. The highest annual average wind speed was recorded in 2012, with 4.61 m/s, and the lowest in 2022, at 1.80 m/s. This range aligns with wind regimes classified as Class 1 under International Electrotechnical Commission standards, generally suited for small-scale or hybrid wind power applications.[6,17,23,28]

Figure 1 illustrates the monthly wind speed evolution over 11 years, presenting a 3D temporal profile (Figure 1A) and a 2D projection (Figure 1B). The temporal signal (Figure 2A) illustrates bursting behavior characterized by short-term spikes in wind speed, which may be attributed to local convective phenomena and regional climate influences.[6,14,18] The long-term monthly mean (Figure 2B) reveals a seasonal pattern with higher wind speeds during specific months, consistent with similar patterns observed in semi-arid regions, such as Central Iran and Northern India.[18,19] These temporal and seasonal variations underscore the importance of temporal resolution in wind resource assessment and planning. The relatively low but stable wind speeds suggest Mongo's wind energy applications should focus on micro or small wind turbine systems designed for low-wind regimes.[17,23,28]

3.2. Probability distribution and wind power

The Weibull distribution parameters, shape factor (k) and scale factor (c), were computed numerically (Equations I – IV) and are presented in Table 2 for annual data, and Table 3 for monthly data. These parameters were used to construct the wind speed PDF shown in Figure 3, where the mode centers around 3.25 m/s, close to the mean wind speed. This confirms the adequacy of the Weibull model for this dataset, as supported by studies in Turkey, Iran, and Canada.[12,13,15,18,23]

Table 1. Monthly and annual mean wind speeds (m/s) in Mongo from 2012 to 2022

Month	2012	2013	2014	2015	2016	2017	2018	2019	2020	2021	2022	Mean
Jan	3.98	3.73	3.73	4.33	4.08	3.72	4.2	3.72	4.37	4.28	4.44	4.05
Feb	4.34	4.34	4.39	4.18	4.23	4.39	3.77	4.09	4.58	4.45	4.38	4.29
Mar	4.61	3.64	3.82	4.12	4.17	4.09	3.48	4.20	4.29	4.21	4.28	4.08
Apr	4.11	3.93	3.08	4.34	3.35	3.67	3.36	3.47	3.38	3.94	3.29	3.63
May	3.53	3.27	3.60	3.41	3.44	3.74	3.67	3.47	2.81	3.27	3.23	3.40
Jun	3.41	3.34	3.72	3.62	3.38	3.23	3.57	3.27	3.40	3.55	3.41	3.45
Jul	2.48	3.17	3.04	2.90	2.65	2.96	2.72	2.75	2.86	3.11	2.77	2.86
Aug	2.20	2.47	2.48	2.11	2.30	2.18	2.35	2.28	2.35	2.15	2.31	2.29
Sept	1.88	2.13	2.08	2.10	1.98	2.38	1.96	2.09	1.82	2.09	1.80	2.03
Oct	2.05	1.93	2.08	2.47	2.41	2.36	2.55	1.95	1.98	2.09	2.10	2.18
Nov	2.27	2.14	2.62	2.57	2.98	2.65	2.80	2.70	2.87	2.90	2.64	2.65
Dec	3.25	3.70	3.21	4.16	3.99	3.87	3.70	3.03	3.17	3.38	3.48	3.54
Mean	3.18	3.15	3.15	3.36	3.25	3.27	3.18	3.09	3.16	3.29	3.18	3.20

Table 2. Annual Weibull distribution parameters and estimated wind power density (W/m²) from 2012 to 2022

Parameter	2012	2013	2014	2015	2016	2017	2018	2019	2020	2021	2022	Mean
EPF	1.26	1.17	1.15	1.19	1.16	1.14	1.12	1.16	1.23	1.18	1.22	1.16
K	3.34	3.69	3.80	3.62	3.75	3.83	3.92	3.74	3.434	3.63	3.50	3.73
C	3.54	3.49	3.49	3.73	3.60	3.62	3.51	3.42	3.511	3.64	3.53	3.55
Power	18.57	16.90	17.58	16.65	15.92	17.84	16.09	15.45	18.57	18.05	17.49	17.19

Abbreviations: C: Scale factor; EPF: Energy pattern factor; K: Shape factor.

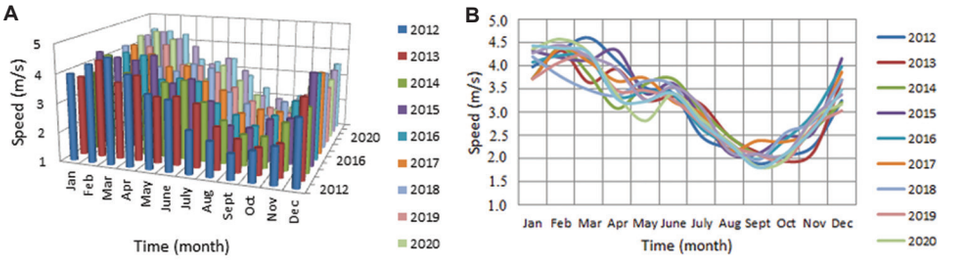


Figure 1. Monthly wind speed profiles from 2012 to 2022. (A) 3D temporal evolution illustrating impulsive wind bursts; (B) 2D projection showing seasonal patterns.

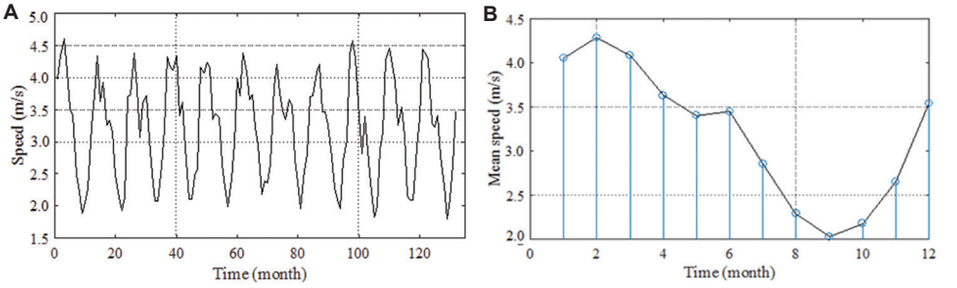


Figure 2. Temporal evolution of wind speed in Mongo. (A) Raw monthly data from 2012 to 2022 showing burst-like variations; (B) Long-term average wind speed highlighting seasonal trends.

Table 3. Monthly Weibull distribution parameters and wind power density (W/m²)

Parameter	Jan	Feb	Mar	Apr	May	Jun	Jul	Aug	Sep	Oct	Nov	Dec
EPF	1.01	1.01	1.02	1.03	1.02	1.01	1.01	1.01	1.02	1.03	1.02	1.03
K	4.59	4.64	4.57	4.46	4.58	4.65	4.59	4.63	4.56	4.48	4.51	4.47
C	4.44	4.67	4.47	3.98	3.73	3.77	3.12	2.50	2.22	2.39	2.90	3.88
Power	14.70	12.00	14.36	20.59	24.57	24.19	28.91	10.45	1.99	6.60	25.15	22.03

Abbreviations: C: Scale factor; EPF: Energy pattern factor; K: Shape factor.

The estimated annual wind power density (Table 2) ranges from a minimum of 15.45 W/m² (2019) to a maximum of 18.57 W/m² (2012 and 2020), which classifies Mongo as a Class 1 site, suitable for small-scale wind energy projects or hybrid systems combined with solar photovoltaic.[11,17,21,28,38] Monthly variations (Table 3, Figure 4) indicate July as the peak month for wind power density (28.91 W/m²), and September as the lowest (1.99 W/m²), consistent with the regional climatology marked by wet and dry seasonal wind shifts.[19,21,26] Compared to high-potential sites (often > 100 W/m²), Mongo's wind power density is modest but not negligible. This level is favorable for off-grid rural electrification or to supplement other renewables, especially in the context of Chad's low electrification rates.[3,4,5,30]

3.3. Wind direction analyses

The wind rose diagrams derived from Table 4 (Figures 5 and 6) illustrate a dominant south-southwest wind direction throughout most of the years (2015 – 2022), with exceptions of northwest winds in 2013 and 2017. Seasonal analysis shows northeast and east winds predominate during dry months, while south-southwest and southwest directions dominate the wet season (June – September), a pattern consistent with the influence of Harmattan and monsoonal airflows.[2,9,10,21] These directional trends inform optimal turbine orientation and layout, as turbines aligned with prevailing winds achieve higher efficiency and reduced mechanical wear. The seasonal variability highlights the necessity for adaptable turbine systems or hybrid configurations to maintain steady power output year-round.[31,36]

3.4. Temperature analyses

Table 5 illustrates the monthly and annual temperature data, revealing Mongo as a hot region with mean annual temperatures ranging from 27.27°C to 28.57°C, and monthly extremes from 24.55°C to 33.19°C. These thermal conditions foster atmospheric convection, likely contributing to the impulsive wind bursts identified in the temporal wind speed data.[6,14,18]

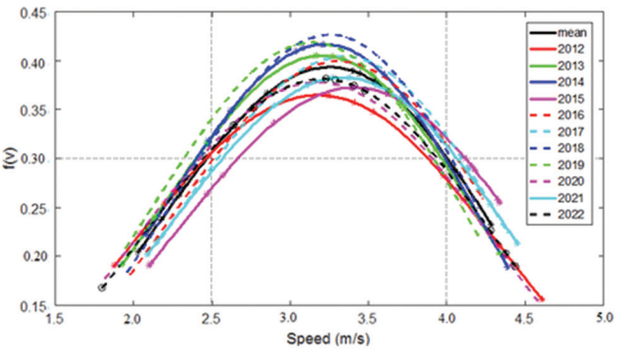


Figure 3. Weibull probability density functions for annual wind speed in Mongo (2012 – 2022)

Figure 7A and B show the temperature trends in 3D and 2D views, while Figure 8A and B depict the raw and mean temporal signals, both exhibiting quasi-periodic bursting signals. The dependency between temperature and wind speed demonstrates a non-linear relationship in the hysteresis form, a phenomenon arising from complex interactions involving air density changes, local pressure gradients, and boundary layer dynamics.[14,20,24,37,39-41] Other influences, such as topographical features, humidity, and diurnal solar heating cycles, may affect this non-linear dependency, highlighting the need for finer temporal and spatial resolution data, as well as more advanced modeling to accurately characterize wind-temperature dynamics in Mongo.[32,37]

3.5. Environmental and sustainability implications

The results show that although Mongo's wind resource is modest, its temporal stability makes it viable for decentralized applications. In a country like Chad – where rural electrification remains below 12% and energy access relies primarily on diesel generators and biomass[3,4,5,30] – the use of small wind systems could help reduce environmental degradation, particularly deforestation and indoor air pollution, while contributing to national climate commitments.[42,43]

Moreover, combining wind power with solar energy, which is abundant across the Sahel, can increase energy

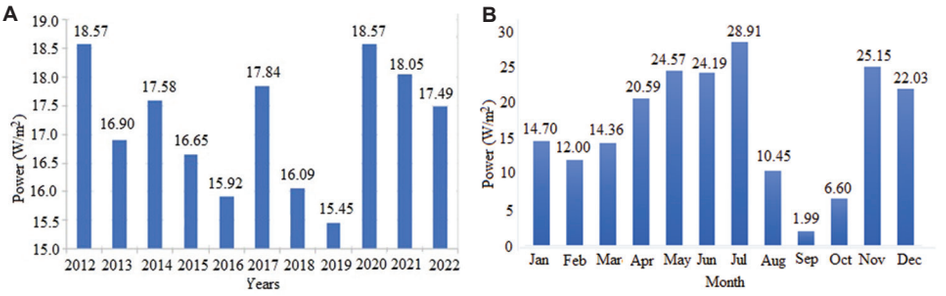


Figure 4. Wind power density in Mongo. (A) Annual averages from 2012 to 2022; (B) Monthly variations highlighting seasonal energy potential.

Table 4. Annual and monthly wind direction (°) for Mongo (2012 – 2022)

Month	2012	2013	2014	2015	2016	2017	2018	2019	2020	2021	2022	Mean
Jan	38.25	34.81	28.19	34.06	33.00	49.44	45.44	18.69	52.5	51.31	17.88	36.69
Feb	59.19	41.94	37.19	26.00	40.94	41.56	32.00	15.81	35.12	33.38	30.12	35.75
Mar	46.75	61.25	40.19	58.25	38.44	30.88	56.44	54.12	46.44	65.12	55.44	50.30
Apr	124.50	86.00	180.62	56.69	104.81	121.25	89.25	83.75	98.12	83.88	196.19	111.37
May	184.75	197.19	187.06	171.00	184.50	185.31	204.62	212.12	201.00	158.00	214.25	190.89
Jun	219.25	204.06	195.56	213.44	200.06	210.75	191.94	196.38	205.75	195.44	199.44	202.92
Jul	223.38	206.75	213.31	202.94	215.38	216.25	205.62	202.44	209.75	208.38	219.62	211.26
Aug	224.94	228.56	215.00	211.06	210.81	231.75	220.00	216.12	227.88	193.38	230.25	219.07
Sept	221.62	236.75	187.38	206.31	197.56	196.88	180.44	178.12	201.06	183.38	199.75	199.02
Oct	196.12	150.69	144.62	196.06	127.5	120.62	123.88	124.19	70.19	93.50	98.31	131.43
Nov	69.62	50.44	105.44	53.19	95.12	70.12	96.81	92.88	57.31	80.44	55.31	75.15
Dec	40.50	47.19	51.19	35.94	65.19	48.31	42.19	58.50	70.69	49.56	58.56	51.62
Mean	137.41	128.80	132.15	122.08	126.11	126.93	124.05	121.09	122.98	116.31	131.26	126.29

Table 5. Monthly and annual mean temperatures (°C) recorded in Mongo (2012 – 2022)

Month	2012	2013	2014	2015	2016	2017	2018	2019	2020	2021	2022	Mean
Jan	25.00	26.69	25.33	22.83	23.61	27.30	22.69	26.85	22.47	25.47	24.70	24.81
Feb	29.18	29.15	27.76	28.94	26.82	27.38	29.48	28.33	26.48	26.49	25.96	27.82
Mar	30.05	31.58	31.65	31.63	33.19	30.88	31.31	31.90	31.46	31.84	30.97	31.50
Apr	33.37	32.53	33.04	31.66	33.98	33.81	32.89	33.70	33.80	32.73	33.60	33.19
May	31.18	32.55	31.80	33.86	33.59	33.75	31.98	33.43	32.96	32.65	31.36	32.65
Jun	27.78	29.99	30.56	30.58	29.43	29.15	29.44	29.32	30.09	29.88	28.50	29.52
Jul	25.30	26.88	26.98	27.61	26.14	27.01	26.61	27.35	27.22	26.66	26.44	26.75
Aug	24.45	24.40	24.64	25.33	25.06	25.52	24.98	24.79	24.85	25.40	24.48	24.90
Sep	25.05	25.33	25.19	25.55	25.85	25.97	25.49	25.79	25.03	25.30	25.11	25.42
Oct	25.98	26.53	25.80	26.78	26.60	27.77	26.09	25.01	25.41	26.64	25.51	26.19
Nov	26.01	27.12	25.64	25.92	27.20	27.83	26.30	24.04	24.00	25.73	24.13	25.81
Dec	23.94	25.21	24.74	22.44	25.87	26.42	25.64	22.02	25.14	25.65	23.01	24.55
Mean	27.27	28.16	27.76	27.76	28.11	28.57	27.74	27.71	27.41	27.87	26.98	27.76

reliability for off-grid systems. Hybrid solutions have been shown to enhance energy access in rural settings while supporting essential services, such as healthcare, education, and agriculture.[38,44] This aligns with the

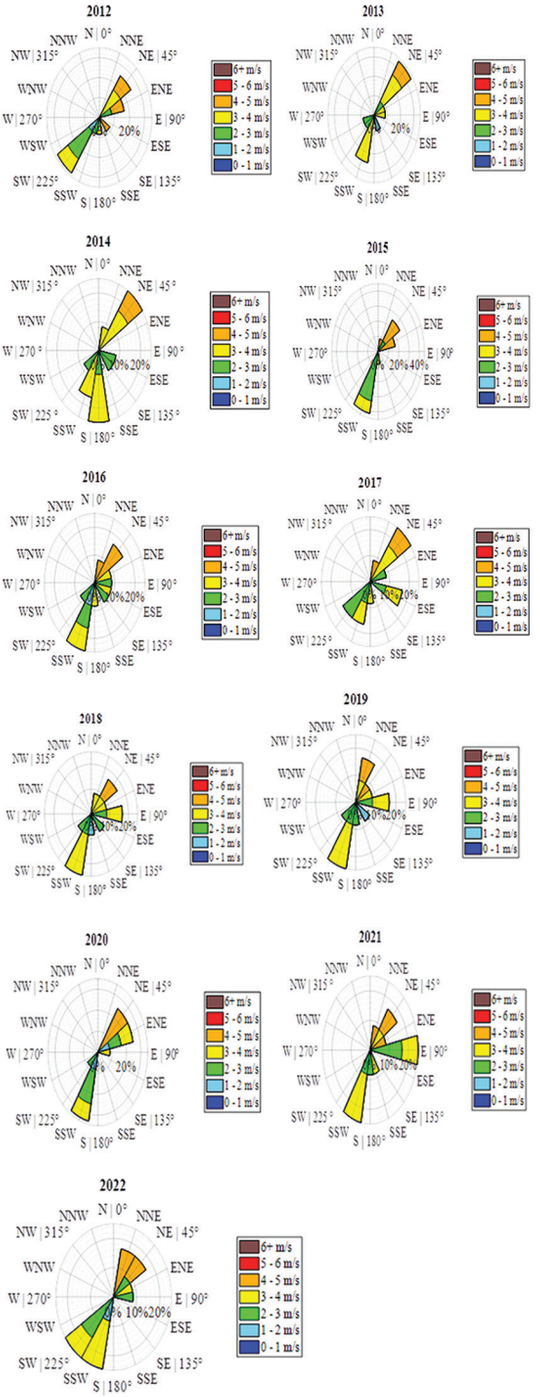


Figure 5. Annual wind rose diagrams (2012 – 2022) for Mongo, depicting prevailing wind directions and interannual variability

Abbreviations: E: East, ENE: East-northeast; ESE: East-southeast; N: North; NE: Northeast; NNE: North-northeast; NNW: North-northwest; NW: Northwest; S: South; SE: Southeast; SSE: South-southeast; SSW: South-southwest; SW: Southwest; W: West; WNW: West-northwest; WSW: West-southwest.

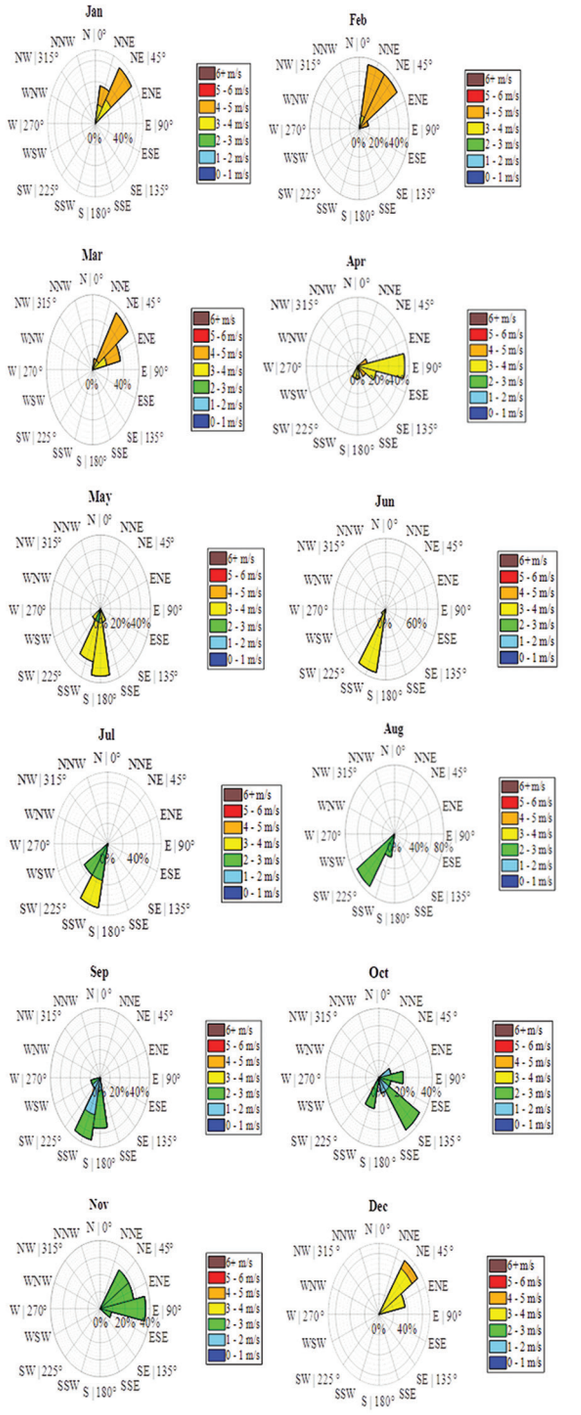


Figure 6. Monthly wind rose diagrams showing seasonal changes in wind directions influencing turbine siting strategies

Abbreviations: E: East, ENE: East-northeast; ESE: East-southeast; N: North; NE: Northeast; NNE: North-northeast; NNW: North-northwest; NW: Northwest; S: South; SE: Southeast; SSE: South-southeast; SSW: South-southwest; SW: Southwest; W: West; WNW: West-northwest; WSW: West-southwest.

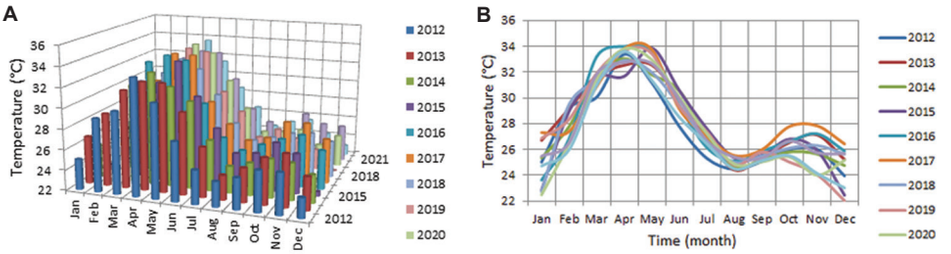


Figure 7. Temperature profiles in Mongo (2012 – 2022). (A) 3D view of monthly temperature evolution; (B) 2D projection illustrating seasonal temperature cycles.

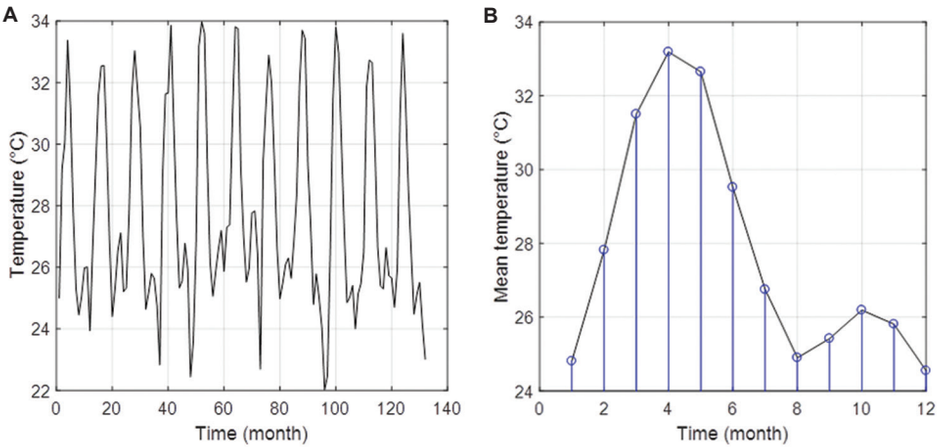


Figure 8. Temporal temperature signals. (A) Raw monthly data; (B) Long-term average illustrating quasi-periodic burst patterns.

Sustainable Development Goals (SDG 7: Affordable and clean energy, and SDG 13: Climate action).[45]

The observed seasonal and directional variations also underline the importance of adapting turbine technology and layout to local wind regimes. Appropriate turbine orientation can maximize efficiency and extend its lifespan.[2,10,21,46] In similar climatic contexts, locally optimized systems have demonstrated better environmental integration and operational stability.[12,18,35]

Overall, wind energy in regions, such as Mongo should not be neglected due to low average speeds. Instead, it should be considered a strategic component of a diversified, low-carbon energy mix that supports inclusive development and environmental sustainability.[7,30,47,48]

4. Conclusion

This study presented a comprehensive statistical analysis of Mongo's wind energy potential over 11 years, applying the Weibull distribution to characterize wind speed patterns. The average annual wind speed of 3.2 m/s places Mongo in wind power Class 1, indicating a low-to-moderate wind resource suitable mainly for small-scale and decentralized wind energy applications. The wind direction analysis reported predominant south-southwest winds with notable temporal and seasonal variability, emphasizing the importance of adaptive turbine placement and orientation to maximize energy capture. In addition, the warm climate with an average temperature of 27.76°C, combined with the observed non-linear relationship between temperature and wind speed, reflects complex local atmospheric dynamics that affect wind availability.

While the study highlights Mongo's modest but stable wind resource, some limitations should be acknowledged. The reliance on monthly-averaged data may mask short-term fluctuations and finer temporal wind variations that are important in assessing turbine performance. Furthermore, the use of a single meteorological station limits spatial representativeness, and some data gaps were present. These constraints suggest the need for higher-resolution temporal data and more extensive spatial measurements to fully capture the variability of wind resource.

Looking ahead, future research should focus on site-specific turbine optimization considering the variability

in wind direction and speed. Integrating wind energy with complementary renewable sources, such as solar power, could enhance energy reliability and supply for rural electrification. Moreover, economic feasibility studies and detailed spatial resource mapping will be crucial for designing effective, sustainable wind energy systems in Mongo and other similar regions.

Acknowledgments

None.

Funding

None.

Conflict of interest

The authors declare that they have no competing interests.

Author contributions

Conceptualization: Ali Sidick Bahar, Adoum Kriga, Ali Ramadan Ali
Data curation: Adoum Kriga, Adoum Danao Adile
Formal analysis: Ali Ramadan Ali, Fabien Kenmogne
Methodology: Ali Sidick Bahar, Adoum Kriga
Writing – original draft: Fabien Kenmogne
Writing – review & editing: All authors

Availability of data

All data generated or analyzed during this study are included in this published article.

References

1. Nediguina MK, Tahir AM, Barka M, Soulouknga MH, Nsouandele JL. Evaluation of the wind power potential in the northeast of Chad. *J Renew Energies.* 2022;25(1):109-126. doi: 10.54966/jreen.v25i1.1075
2. Soulouknga MH, Oyedepo SO, Doka SY, Kofané TC. Assessment of wind energy potential in the Sudanese zone in Chad. *Energy Power Eng*. 2017;9(7):386-402. doi: 10.4236/epe.2017.97026
3. Ouedraogo AO, Doka SY, Revanna N, Djongyang N, Kofané TC. Analysis of wind speed data and wind energy potential in faya-largeau, chad, using weibull distribution. *Renew Energy.* 2018;121:1-8. doi: 10.1016/j.renene.2018.01.002
4. International Energy Agency. *Africa Energy Outlook 2022.* Paris, France: IEA; 2022.
5. Agence Pour Le Développement Des Energies Renouvelables (ADER) Et Ministère Du Pétrole Et De l'Énergie Du Tchad. *Plan Général D'action Des Energies Renouvelables 2017-2030*. N'Djaména, Tchad: ADER; 2017.
6. Tchinda R, Kendjio J, Kaptouom E, Njomo D. Estimation of mean wind energy available in far north Cameroon. *Energy Convers Manage*. 2000;41(17):1917-1929. doi: 10.1016/S0196-8904(00)00017-0
7. United Nations Environment Programme. *Renewable Energy Law and Policy Review: Selected African Countries.* Nairobi, Kenya: UNEP; 2019.
8. Kassem Y, Çamur H, Abughinda SAM, Şefik A. Wind energy potential assessment in selected regions in northern cyprus based on weibull distribution function. *J Eng Appl Sci.* 2020;15(1):128-140. doi: 10.3923/jeasci.2020.128.140
9. Akpinar EK, Akpinar S. A statistical analysis of wind speed data used in installation of wind energy conversion systems. *Energy Convers Manage.* 2005;46(4):515-532. doi: 10.1016/j.enconman.2004.07.007
10. Ahmed Shata AS, Hanitsch R. Evaluation of wind energy potential and electricity generation on the coast of Mediterranean Sea in Egypt. *Renew Energy*. 2006;31:1183-1202. doi: 10.1016/j.renene.2005.07.012
11. Celik AN. Statistical analysis of wind power density based on the Weibull and Rayleigh models at the southern region of Turkey. *Renew Energy.* 2004;29:593-604. doi: 10.1016/j.renene.2003.07.001
12. Carta JA, Ramirez P, Velazquez S. A review of wind speed probability distributions used in wind energy analysis: Case studies in the Canary Islands. *Renew Sustain Energy Rev.* 2009;13(5):933-955. doi: 10.1016/j.rser.2008.02.008
13. Zhou J, Erdem E, Li G, Shi J. Comprehensive evaluation of wind speed distribution models: A case study for North Dakota sites. *Energy Convers Manage.* 2010;51:1449-1458. doi: 10.1016/j.enconman.2010.01.005
14. Chellali F, Khellaf A, Belouchrani A, Khanniche R. A comparison between wind speed distributions derived from the maximum entropy principle and Weibull distribution. Case of study; six regions of Algeria. *Renew Sustain Energy Rev.* 2012;16(1):379-385. doi: 10.1016/j.rser.2011.08.002
15. Li M, Li X. Investigation of wind characteristics and assessment of wind energy potential for Waterloo Region, Canada. *Energy Convers Manage.* 2005;46: 3014-3033. doi: 10.1016/j.enconman.2005.02.011
16. Okorie OC, Ajayi NO, Bamisile OS, *et al*. Evaluating wind energy resources for remote communities in West

Africa. *Renew Sustain Energy Rev*. 2022;160:112282. doi: 10.1016/j.rser.2022.112282
17. Ghasemi A, Hosseini AS, Marashi SPH. Wind energy resource assessment using Weibull parameters and GIS: A case study for the province of Yazd. *Renew Sustain Energy Rev.* 2013;28:496-504. doi: 10.1016/j.rser.2013.08.016
18. Ghaffari M, Alavi A, Dehghan S. Wind energy potential assessment in arid regions using GIS-based Weibull analysis: A case study in central Iran. *Renew Energy.* 2021;168:1241-1252. doi: 10.1016/j.renene.2021.01.115
19. Gupta NK, Kumar S. Statistical modeling of wind speed and wind power assessment using Weibull and Rayleigh models in India. *Energy Rep*. 2020;6:2431-2441. doi: 10.1016/j.egyr.2020.08.099
20. Kim TH, Lim HC. A comparative study of wind speed distributions using entropy and Weibull functions. *Energies*. 2020;13(4):1-18. doi: 10.3390/en13040954
21. Nyarko KA, Whale J, Urmee T. Drivers and challenges of off-grid renewable energy-based projects in West Africa: A review. Heliyon. 2023;9(5):e16710. doi: 10.1016/j.heliyon.2023.e16710
22. Nasiri F, Yari M, Ameri M. Wind resource assessment and feasibility study in southeastern Iran. *Renew Energy*. 2021;164:869-882. doi: 10.1016/j.renene.2020.08.037
23. Nasiri AA, Yılmaz A, Özdemir E. Assessment of wind energy potential using Weibull parameters: A case study from Turkey. *Energy Sources A.* 2023;45(6):1154-1170. doi: 10.1080/15567036.2020.1751015
24. Medjo Nouadje BA, Kelly E, Djiela RHT, Kapen PT, Tchuen G, Tchinda R. Chad's wind energy potential: An assessment of Weibull parameters using thirteen numerical methods for a sustainable development. *Int J Ambient Energy*. 2023;45(1):2276119. doi: 10.1080/01430750.2023.2276119
25. Aslam M, Raza SAR, Khan TH. Wind energy assessment for remote areas in Pakistan. *Energy Rep*. 2020;6:1547-1558. doi: 10.1016/j.egyr.2020.02.017
26. Gökçek M, Bayülgen M. A feasibility study for wind energy in Kirklareli, Turkey. *Renew Sustain Energy Rev*. 2007;11(9):2183-2190. doi: 10.1016/j.rser.2006.04.012
27. Petkovic D, Ilic D, Milinkovic M. Comparison of wind speed models for low wind resource sites. *Energy.* 2020;210:118572. doi: 10.1016/j.energy.2020.118572
28. Saidur R, Rahim NA, Islam MR, Solangi KH. A review on global wind energy policy. *Renew Sustain Energy Rev.* 2010;14:1744-1762. doi: 10.1016/j.rser.2010.03.008
29. Yu X, Qu H. Wind power in China-opportunity goes with challenge. *Renew Sustain Energy Rev.* 2010;14:2232-2237. doi: 10.1016/j.rser.2009.11.003
30. International Renewable Energy Agency. *Off-Grid Renewable Energy Systems: Status and Methodological Issues.* Abu Dhabi, UAE: IRENA; 2015.
31. Arreyndip NA, Joseph E. Generalized extreme value distribution models for the assessment of seasonal wind energy potential of Debuncha, Cameroon. *J Renew Energy*. 2016;2016:9357812. doi: 10.1155/2016/9357812
32. Tuncar EA, Sağlam S, Oral B. A review of short-term wind power generation forecasting methods in recent technological trends. *Energy Rep.* 2024;12:197-209. doi: 10.1016/j.egyr.2024.06.006
33. Jeon J, Taylor JW. Using conditional kernel density estimation for wind power density forecasting. *J Am Stat Assoc.* 2012;107(497):66-79. doi: 10.1080/01621459.2011.643745
34. Jurado X, Reiminger N, Vazquez J, Wemmert C. On the minimal wind directions required to assess mean annual air pollution concentration based on CFD results. *Sustain Cities Soc*. 2021;71:102920. doi: 10.1016/j.scs.2021.102920
35. Mandal S, Kundu S, Mondal S. Statistical modeling of wind speed data using empirical and theoretical distributions. *Renew Energy*, 2019;134:983-992. doi: 10.1016/j.renene.2018.11.056
36. Jeutho MG, Kenmogne F, Yemélé D. How to use the temperature data to find the appropriate site for best wind speed generation? Applications on data obtained from three different cities of Cameroon. *Int J Sci Eng Sci.* 2018;2(4):53-62.
37. Grace EA, Rekha ASP, Thenaras M. Automated solar powered pumping systems for irrigation. *Int J Pure Appl Math.* 2017;114(7):507-516.
38. Mostafaeipour A, Jadidi M, Mohammadi K, Sedaghat A. An analysis of wind energy potential and economic evaluation in Zahedan, Iran. *Renew Sustain Energy Rev*. 2014;30:641-650. doi: 10.1016/j.rser.2013.11.016
39. Ali RA, Nediguina MK, Gouajio M, *et al*. Effects of adding the antiparallel diodes in a model of solar photovoltaic cell: Theory and PSpice simulations. *J Mod Green Energy.* 2024;3:4. doi: 10.53964/jmge.2024004
40. Jeutho MG, Kenmogne F, Yemélé D. Statistical estimation of mean wind energy available in western region of Cameroon: Case of the Bafoussam's city. *J Harmoniz Res Eng.* 2017;5(1):15-27.
41. Manwell JF, McGowan JG, Rogers AL. *Wind Energy Explained: Theory, Design and Application.* 2nd ed. Chichester, UK: Wiley; 2009.
42. Ouedraogo NS. Modeling sustainable long-term electricity supply-demand in Africa. *Appl Energy*.

2017;190:1047-1067.
doi: 10.1016/j.apenergy.2016.12.162

43. Bishoge OK, Kombe GG, Mvile BN. Renewable energy for sustainable development in Sub-Saharan African countries: Challenges and way forward. *J Renew Sustain Energy.* 2020;12(5):052702.
doi: 10.1063/5.0009297
44. Bhandari B, Lee KT, Lee CS, Song CK, Maskey RK, Ahn SH. A review on solar and wind energy systems for off-grid rural electrification in developing countries. *Renew Sustain Energy Rev.* 2014;38:258-268.
doi: 10.1016/j.rser.2014.05.057
45. United Nations. *Transforming our World: The 2030 Agenda for Sustainable Development*. *UN Res A/RES/70/1*. New York, NY: United Nations; 2015.
46. Bekele G, Palm B. Feasibility study for a standalone solar-wind-based hybrid energy system for application in Ethiopia. *Appl Energy.* 2010;87(2):487-495.
doi: 10.1016/j.apenergy.2009.06.006
47. Abdmouleh Z, Alammari RAM, Gastli A. Recommendations on renewable energy policies for the GCC countries. *Renew Sustain Energy Rev.* 2015;50:1181-1191.
doi: 10.1016/j.rser.2015.05.057
48. Hadjipaschalis I, Poullikkas A, Efthimiou V. Overview of current and future energy storage technologies for electric power applications. *Renew Sustain Energy Rev*. 2009;13(6-7):1513-1522.
doi: 10.1016/j.rser.2009.06.045

Asian Journal of Water, Environment and Pollution. Vol. 22, No. 6 (2025), pp. 60-72.
doi: 10.36922/AJWEP025240195

ORIGINAL RESEARCH ARTICLE

Optimization of pine sawdust densified biofuel: Effects of process parameters on fuel quality and temperature distribution

Zhuoying Chen, Zhiyuan Ma, Zhongjia Chen, Zhongsai Li, and Xiangyue Yuan*

Biomass Laboratory, School of Technology, Beijing Forestry University, Beijing, China
***Corresponding author:** Xiangyue Yuan (yuanxiangyue@bjfu.edu.cn)

Received: June 13, 2025; 1st revised: July 10, 2025; 2nd revised: July 18, 2025;
Accepted: July 21, 2025; Published online: August 7, 2025

Abstract: The valorization of forestry waste into densified biofuels is critical for sustainable energy development. This study investigates the optimization of the densification process for pine sawdust by examining the effects of key parameters on the final product quality, specifically focusing on the uniformity of the internal temperature field. A four-factor, mixed-level orthogonal experiment was designed, investigating forming pressure, moisture content, binder addition ratio, and heating temperature. The temperature mean square deviation (MSD) was utilized as the primary response variable to quantify thermal distribution uniformity. Analysis of variance (ANOVA) was performed to determine the statistical significance of each factor, and a multivariate regression model was established. Results from ANOVA indicated that the descending order of significance for factors impacting temperature MSD was: moisture content > forming pressure > heating temperature > binder addition ratio. A statistically significant interaction effect was identified between forming pressure and heating temperature. Response surface methodology was employed to optimize these two significant factors. The optimal conditions for minimizing temperature MSD, while maintaining constant moisture content and binder ratio, were determined to be a forming pressure of 10 MPa and a heating temperature of 190°C. By optimizing process parameters to achieve a more uniform temperature field, the quality and stability of the resulting pine sawdust densified fuel were significantly improved. This work provides a quantitative theoretical basis and key technical parameters for the scale-up and industrial application of biomass fuels in boilers and residential heating systems, thereby promoting the development of a low-carbon circular economy.

Keywords: Densified fuel quality; Binders; Fuel quality; Temperature distribution; Mechanical Properties; Forestry waste

1. Introduction

In the face of global resource scarcity, environmental pollution, and intensifying climate change, efficient management and resource utilization of forestry waste have become critical for achieving sustainable development. In China, potential biomass resources from agricultural and forestry waste amount to 850 million and 340 million tons, respectively, with energy crops contributing an additional 740–960 million tons.[1] Depending on development levels, biomass energy potential is estimated at approximately 1.9–41.2 EJ,

equivalent to 0.68–1.4 billion tons of standard coal, representing substantial untapped resources. Pine sawdust, a major forestry waste stream, currently poses significant environmental burdens through conventional disposal methods (e.g., open burning, landfilling), including land occupation and emissions of toxic compounds and greenhouse gases. Densification into densified biofuel offers a viable waste valorization strategy to advance the circular bioeconomy in the forestry sector.[2]

The primary factors influencing biomass densification include forming pressure, moisture content, binder addition ratio, and heating temperature. Among these, forming pressure plays a particularly critical role in determining pellet quality: optimal forming pressure ensures high-quality pellets with minimal energy input, whereas excessive pressure may cause blockages, and insufficient pressure can lead to substandard pellets.[3] Under pressure, sludge particles are extruded into the voids of biomass pellets, where protein denaturation and lignin softening occur, acting as natural binders that facilitate biomass densification.[4]

Moisture content plays an equally critical role; excessive moisture reduces pellet strength, while insufficient moisture increases energy consumption during molding.[5] Although increased moisture content reduces molding energy consumption, the pellet's relaxation coefficient initially decreases before increasing, potentially due to water acting as a lubricant that reduces interparticle friction. The density and durability of municipal solid waste-derived briquettes are significantly affected by both moisture content and particle size distribution.[6] The moisture content significantly affects pellet bonding quality. If it is too low, insufficient lignin plasticization leads to weak bonding; if it is too high, it triggers a steam explosion effect, reducing densified biofuel durability.[7]

Binders, including glycerol or lignin-rich additives, significantly enhance densification performance and pellet durability.[8] The incorporation of 5–20% coal into biomass improves pellet durability while maintaining thermal properties.[9] When sawdust and asphalt are added as binders to sludge, the resulting densified biofuel exhibits increased calorific value, demonstrating potential for coal replacement.[10] Similarly, the NovoGro binder application in densified biofuel production enhances both durability and mechanical strength.[11] These binder applications collectively improve densification efficiency while reducing energy consumption.[12] Adding a binder increases the cost by $0.15 USD per ton for every 1% improvement in durability, making it the preferred choice for cost-sensitive projects.[13] Under high-pressure forming, adding 1–3% sweet potato starch can meet industrial requirements, with 2% achieving a pellet durability of 95.6%.[14]

Heating temperature critically influences pellet quality through lignin softening, which promotes particle bonding and densification.[15] While elevated forming temperatures enhance pellet density and strength, excessively high temperatures may cause surface charring, ultimately compromising durability.[16] Within the 30–110°C range, densified biofuel density and hardness exhibit a parabolic relationship with temperature, peaking at approximately 70°C.[17] Preheating treatment can improve the durability of high-moisture-content particles.[18] Short-term treatment at 200°C can achieve the impact resistance of 99.5%, but it requires a moisture content of ≤12%.[19]

Current research predominantly examines the direct thermal effects, with limited investigations addressing temperature field distribution and its influencing factors. To address this gap, the present study concentrates on pine sawdust densification technology for high-value waste valorization. By systematically evaluating key parameters (forming pressure, heating temperature, binder addition ratio, and moisture content) and their interactive effects on biomass pellet quality, we introduce temperature mean square deviation (MSD) as a novel metric for characterizing temperature field uniformity. This approach elucidates its functional mechanisms in densification processes and regulatory effects on fuel performance. The optimization of process parameters and temperature field distribution aims to improve pine sawdust pellet quality, thereby providing both theoretical foundations and technical solutions for industrial-scale applications (e.g., industrial boilers, residential heating systems). This research contributes to enhanced forestry waste utilization and promotes the development of low-carbon circular economies.

2. Determination of factors influencing densified biofuel and quality evaluation indicators

2.1. Determination of experimental factors and levels

Building upon previous research findings[20-23] while maintaining pine sawdust formability, this study adopted the following experimental parameter ranges: forming pressure (A) within 10–50 MPa, moisture content, (B) within 10–16%, binder addition ratio, (C) within 1–5%, and heating temperature, (D) within 150–190°C. An

L25 (4×5^4) orthogonal experimental design with four factors and mixed levels was adopted.

2.2. Quality evaluation indicators for densified biofuel

For enhanced transportability and storage efficiency of densified biofuel, this study employed three key physical properties as quality evaluation metrics: Relaxed density (H1), relaxation ratio (H2), and impact resistance (H3).

Relaxed density refers to the density of biomass pellets after they reach a stable state following expansion or contraction post-forming.[24] A higher relaxed density indicates a greater density of the densified pellets, which typically corresponds to better forming quality and higher combustion efficiency. The formula is presented in Equation I:

$$\rho = \frac{4m}{\pi d^2 h} \tag{I}$$

Where ρ represents the relaxed density (g/cm^3), m is the pellet weight (g), d is the pellet diameter (cm), and h is the pellet length (cm).

The relaxation ratio of formed pellets is the ratio of the initial relaxation density to the stabilized relaxation density. A high relaxation ratio indicates more internal voids, making the pellets prone to moisture absorption and breakage, while a low relaxation ratio suggests minimal shrinkage after forming, resulting in a compact structure conducive to long-term storage.[25] The lower the relaxation ratio of the pellets, the higher their stability, which is beneficial for subsequent transportation and storage. The formula is presented in Equation II:

$$\lambda = \rho_i / \rho_r \tag{II}$$

Where λ represents the relaxation ratio, ρ_i is the initial density (i.e., the density measured immediately after pellet formation) (g/cm^3), and ρ_r is the relaxed density (g/cm^3).

Impact resistance measures the ability of densified pellets to maintain their original shape after multiple drops and collisions. A higher impact resistance indicates better mechanical strength and higher quality of the pellets. According to the forestry industry standard LY/T 2552-2015, the impact resistance of bamboo-based densified biofuel is considered compliant if it exceeds 90%.[26] Furthermore, the energy standard NB/T 34024-2015 classifies densified biofuels with impact resistance greater than 95% as Grade III densified biofuels.[27] When the impact resistance of densified pellets is ≥95%, the pellets are considered good quality.[28] It demonstrates good performance and market potential in practical applications, meeting the combustion needs of high-temperature equipment such as industrial boilers and kilns, and ensuring that the densified biofuel maintains high combustion efficiency and stability during the burning process.[29] The formula is presented in Equation III:

$$I = M_f / M_b \times 100\% \tag{III}$$

Where I represents the impact resistance of the densified pellets (%), M_f is the weight of the densified pellets before the drop test, without sieving (g), and M_b is the weight of the densified pellets after the drop test, after sieving (g).

2.3. Temperature field and temperature MSD

Temperature represents the thermal energy state of an object's interior or surrounding environment. The spatial distribution of temperature values within a material system constitutes its temperature field.[30]

In biomass densification, the temperature field significantly influences pyrolysis, drying, and compaction processes, consequently affecting key fuel properties including heating value, stability, durability, chemical composition, and energy density. The temperature MSD serves as a critical parameter for characterizing temperature field uniformity, where lower values indicate more homogeneous distributions and higher values reflect greater heterogeneity. The MSD is calculated following Equation IV:[31]

$$Kt = \frac{\sum_{i=1}^{N} \left(T_i - \bar{T}\right)}{N} \tag{IV}$$

where K_t represents the temperature MSD, $\bar{T}$ is the average temperature within the observed region, T_i is the temperature of the i-th pixel in the observed region, and N is the total number of pixels in the observed region.

The formula for the average temperature $\bar{T}$ within the region is presented in Equation V:

$$\bar{T} = \frac{T_i dxdy}{A} \tag{V}$$

Where A represents the area of the region.

The temperature MSD serves as a quantitative metric for assessing temperature field uniformity, reflecting

the dispersion degree of temperature data relative to the mean value. This parameter provides a measurable characterization of both uniformity and dispersion within the temperature field.

3. Materials and methods

3.1. Experimental materials

The experimental materials consisted of pine sawdust (particle size <2.5 mm) containing 34–46% cellulose, 20–35% hemicellulose, and 26–34% lignin.[32] Molasses served as the binder for biomass densification.

Prior to experimentation, the moisture content of the biomass material (pine sawdust) required measurement and adjustment. The moisture content was determined in accordance with the Chinese National Standard GB/T 1927.4-2021, calculated using the following formula in Equation VI:

$$W = \frac{m_1 - m_0}{m_0} \times 100\% \quad \text{(VI)}$$

Where W is the moisture content (%), m is the mass of undried sawdust (g), and m is the mass of oven-dried sawdust (g).

The pine sawdust was heated using a moisture analyzer until a constant mass was achieved. The initial moisture content of the pine sawdust was determined to be 8.3%. Fine water mist spraying was employed to adjust the moisture content to the required experimental range, followed by sealed storage under ambient conditions. The experimental environment was maintained at 15–25℃ with relative humidity ≤80%.

3.2. Experimental equipment

The experimental setup comprised a forming system and measurement instruments. The forming system incorporated a mold with an integrated heating coil and temperature controller, while measurement instruments included a universal testing machine (REGER Model 4050; Shenzhen REGER Instrument Co., Ltd., China) and an infrared thermometer (FLUKE Ti95; FLUKE Test Instruments Co., Ltd., China) with dedicated software.

The heating coil was precisely fitted to the mold's outer circumference, with temperature regulation achieved through the controller. The mold assembly, installed on the universal testing machine, featured a polytetrafluoroethylene insulation plate.

3.3. Experimental steps

This study is divided into three main parts: experimental preparation, biomass densification testing, and data analysis, as shown in Figure 1.

(i) Experimental preparation: Raw material moisture content and binder addition ratio were adjusted to target values, followed by sealed storage.

(ii) Experimental procedure: The forming mold with the temperature controller was mounted on the universal testing machine. Prepared materials were loaded into the die for compression molding under 30-s pressure maintenance, after which samples were extracted and stored at ambient conditions.

(iii) Post-experiment processing: The relaxation ratio, relaxed density, and impact resistance of each test group were calculated and averaged to ensure data reliability. Systematic data processing was performed to evaluate the effects of various parameters on densified biofuel quality and temperature field distribution.

4. Results and discussion

4.1. Experimental results of densified biofuel quality evaluation indicators

Following the experimental steps outlined in Sections 2.1 and 3.3, a total of 25 experimental groups were conducted in this study. Each group was repeated three times, and the average values and standard errors were calculated. The experimental results are shown in Table 1.

Experimental results revealed that the maximum relaxed density of 1.066 g/cm^3 was achieved at 50 MPa forming pressure with 10% moisture content, 2% binder addition ratio, and 160°C heating temperature. The minimum relaxation ratio of 1.009 occurred at 10 MPa forming pressure with 14% moisture content, 4% binder addition ratio, and 190°C heating temperature. Optimal impact resistance (97.939%) was obtained at 40 MPa forming pressure with 10% moisture content, 4% binder addition ratio, and 150°C heating temperature.

With an impact resistance threshold of ≥95% indicating satisfactory densification performance, 92% of the 25 experimental groups produced good-quality densified biofuel. Two exceptions failed to meet the requirement: (i) at 20 MPa forming pressure with 16% moisture content, 2% binder addition ratio, and 150°C temperature, and (ii) at 10 MPa forming pressure with 16% moisture content, 3% binder addition ratio, and 160°C temperature.

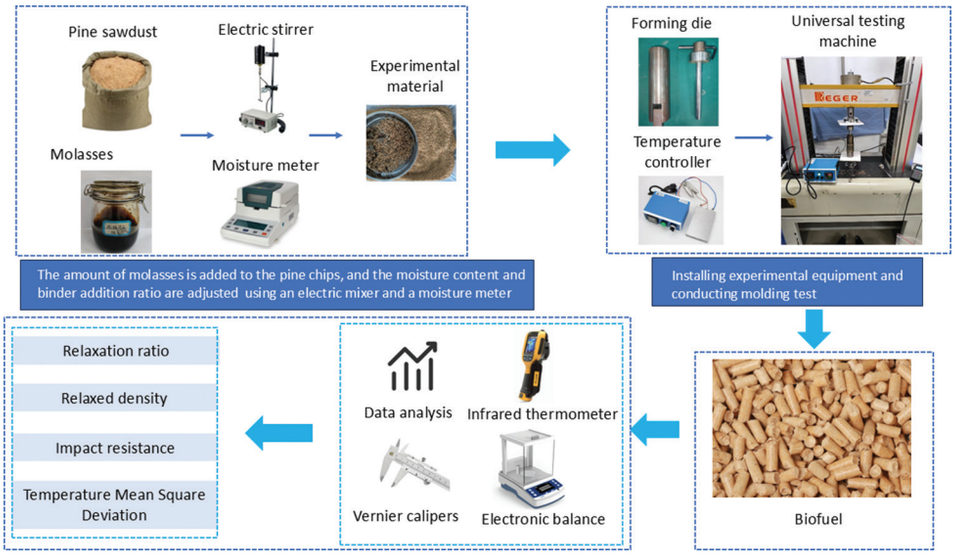


Figure 1. Experimental flowchart

Note: The universal testing machine has a force measurement accuracy of ±1%, and the infrared thermometer has a measurement accuracy of ±2°C or 2% of the reading, whichever is greater.

For systematic analysis of experimental factors' effects on densified biofuel quality, the Design-Expert software (version 12.0) was employed to perform data fitting, yielding a multiple regression equation. Subsequent variance and response surface analyses were conducted. The two-factor interaction model was applied to examine interaction effects between parameters, expressed as Equation VII:

$$Y=k+k1A+k2B+k3C+k4D+k5AB+k6AC+k7AD+k8BC+k9BD+k10CD \quad \text{(VII)}$$

where Y represents the dependent variable, A, B, C, and D are the independent variables, and ki (i=0~10) are the model parameters, representing the degree of influence of each independent variable on the dependent variable Y. AB, AC, AD, BC, BD, and CD represent the interaction effects between the independent variables.

Based on the variance analysis results, the linear regression equations for relaxed density, relaxation ratio, and impact resistance with respect to the experimental factors are shown in Table 2.

In the statistical analysis, R represents the multiple correlation coefficient, with R^2 indicating the proportion of dependent variable variance explained by the regression model. An R^2 value approaching 1 denotes a stronger predictive capacity of the independent variables.

This multiple regression model enables the prediction of relaxed density, relaxation ratio, and impact resistance from given independent variables, while quantifying the magnitude and direction of factor interactions on these parameters.

Variance analysis employs significance levels (p-values) to evaluate factor impacts: $p<0.01$ indicates extremely significant effects, $0.01\leq p<0.05$ shows significant effects, and $p>0.05$ suggests no significant influence.[31,33]

The degree of influence of various experimental factors on the evaluation indicators of densified biofuel quality is shown in Table 3. In the table, only interactions with significant effects are displayed.

Table 3 demonstrates that forming pressure (A), moisture content (B), heating temperature (D), and their BD interaction exert extremely significant effects ($p<0.01$) on relaxed density. For the relaxation ratio, heating temperature (D) and AD interaction show highly significant influences ($p<0.01$). Impact resistance is markedly affected by forming pressure (A), moisture content (B), and BD interaction at extremely significant levels.

To validate the reliability of the multiple linear regression models, residual analysis was conducted. As shown in Figure 2, the residuals versus fitted plots, Q–Q plots, and histogram of residuals confirm that the models for relaxed density, relaxation ratio, and impact resistance meet the assumptions of random distribution, homoscedasticity, and normality, supporting their robustness.

Table 1. Orthogonal test results

Group	Forming pressure (MPa)	Moisture content (%)	Binder addition ratio (%)	Heating temperature (°C)	Relaxed density (g/cm^3)	Relaxation ratio	Impact resistance (%)
1	20	16	2	150	0.653	1.202	87.594
2	10	10	1	150	0.932	1.301	96.346
3	30	12	3	150	0.889	1.101	96.245
4	40	10	4	150	0.99	1.071	97.939
5	50	14	5	150	0.923	1.032	97.322
6	40	14	1	160	0.856	1.013	96.690
7	10	16	3	160	0.694	1.041	91.685
8	30	10	5	160	0.993	1.063	97.368
9	20	12	4	160	0.932	1.120	96.850
10	50	10	2	160	1.066	1.010	97.214
11	40	10	3	170	1.056	1.059	97.891
12	10	12	5	170	0.889	1.042	96.384
13	50	16	4	170	0.838	1.018	96.497
14	20	10	1	170	1.004	1.063	96.694
15	30	14	2	170	0.914	1.012	96.254
16	30	10	4	180	1.054	1.010	97.272
17	20	14	3	180	0.905	1.040	95.870
18	50	12	1	180	0.962	1.014	95.815
19	40	16	5	180	0.900	1.054	95.445
20	10	10	2	180	0.926	1.032	95.567
21	40	12	2	190	1.012	1.021	96.805
22	30	16	1	190	0.891	1.044	96.008
23	20	10	5	190	0.994	1.025	96.528
24	10	14	4	190	0.883	1.009	95.896
25	50	10	3	190	0.989	1.026	96.798

Table 2. Multivariate fitting models of each dependent variable

Dependent variables	R^2	Multiple regression fitting model
H1	0.9213	Y=0.9064+0.0492A−0.974B+0.0079C+0.0491D+0.0048AB+0.0038AC−0.0215AD+0.0064BC+0.0446BD−0.0030CD
H2	0.8093	Y=1.06−0.0252A−0.0058B−0.007C−0.0372D+0.0082AB+0.0386AC−0.0586AD−0.0157BC+0.0222BD+0.0294CD
H3	0.8133	Y=0.9575+0.0115A−0.0147B+0.0047C+0.0072D+0.0099AB−0.0048AC−0.0063AD+0.0017BC+0.0147BD−0.0043CD

These phenomena occur because optimal moisture and temperature conditions minimize elastic deformation and stress relaxation in densified biofuel, thereby enhancing relaxed density. Conversely, excessive moisture content traps steam during extrusion, inducing substantial elastic deformation and densified biofuel expansion that ultimately reduces relaxed density.

The interaction between forming pressure and heating temperature affects the stability of the densified biofuel. Appropriate molding pressure and heating temperature increase the density of the densified biofuel while causing the binder and lignin in the biomass material to melt, resulting in higher stability and lower relaxation ratio.

Table 3. Influence the degree of each test factor on each evaluation index of densified biofuel quality

Dependent variables	Forming pressure	Moisture content	Binder addition ratio	Heating temperature	Interaction effect
Relaxed density	0.0008	<0.0001	0.5005	0.0008	BD−0.0063
Relaxation ratio	0.0568	0.5667	0.5723	0.0082	AD−0.0037
Impact resistance	0.0096	0.0003	0.2375	0.0806	BD−0.0064

Note: A is forming pressure, B is moisture content, and D is heating temperature.

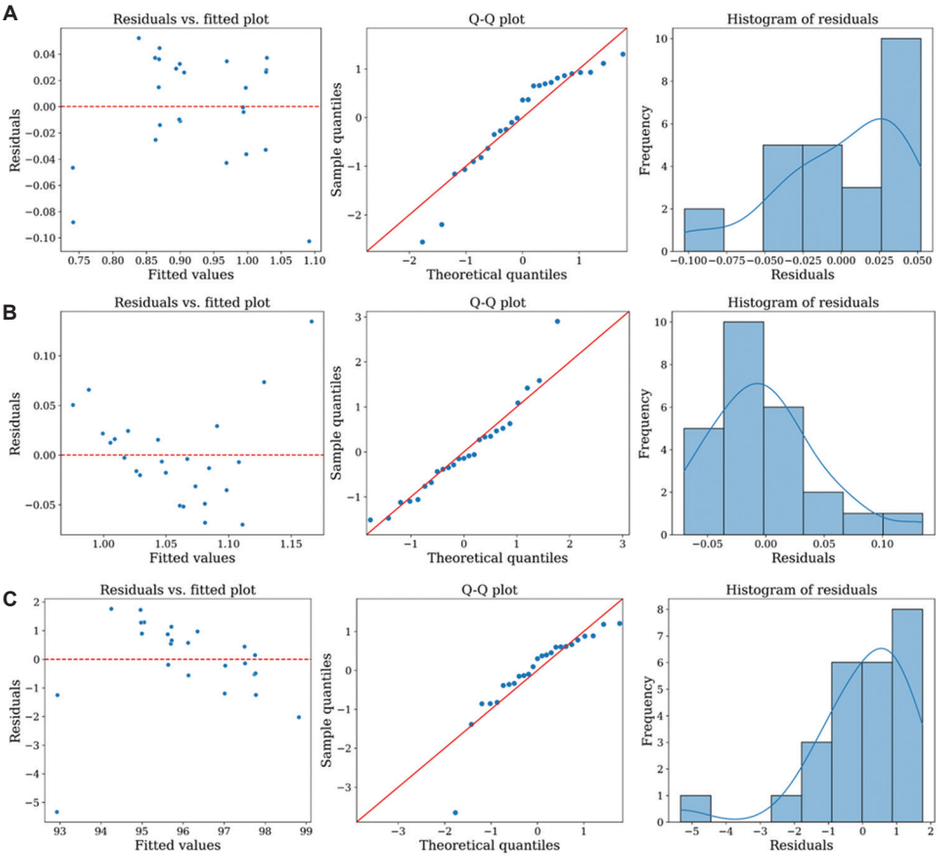


Figure 2. Residual analysis plots. (A) Relaxed density, (B) Relaxation ratio, and (C) Impact resistance

4.2. Analysis of cross-sectional temperature field distribution of densified biofuel

4.2.1. Temperature distribution and results of cross-sectional densified biofuel

Infrared thermography captured cross-sectional temperature profiles of densified biofuel, with subsequent data processing and pixel-level temperature extraction performed using THE SmartView Classic 4.4 software. Equation IV was applied to calculate the temperature MSD for each experimental group's pellet cross-section.

Figure 3 displays experimental groups and heating temperatures on the x-axis, whereas the y-axis presents temperature MSD, moisture content, and binder addition ratio. Bar heights quantitatively measure temperature MSD (Kt).

Figure 3 reveals that experimental group 13 (50 MPa forming pressure, 16% moisture content, 4% binder addition ratio, 170°C) exhibited the maximum temperature MSD of 14.0294. Corresponding infrared thermography in Figure 4A demonstrates pronounced temperature variation within the densified biofuel cross-section (white outline), confirming significant temperature field heterogeneity, which aligns with experimental measurements.

Conversely, group 14 (20 MPa, 10% moisture, 1% binder, 170°C) achieved the minimum MSD (0.3677). Figure 4B displays near-uniform thermal coloration in

the cross-section, indicating homogeneous temperature distribution.

Comparative analysis revealed that non-uniform temperature distributions correlated with surface cracking and rough cross-sections with material fragmentation (Figure 4), whereas uniform distributions produced smooth surfaces and shell-like structural integrity, enhancing transport stability.

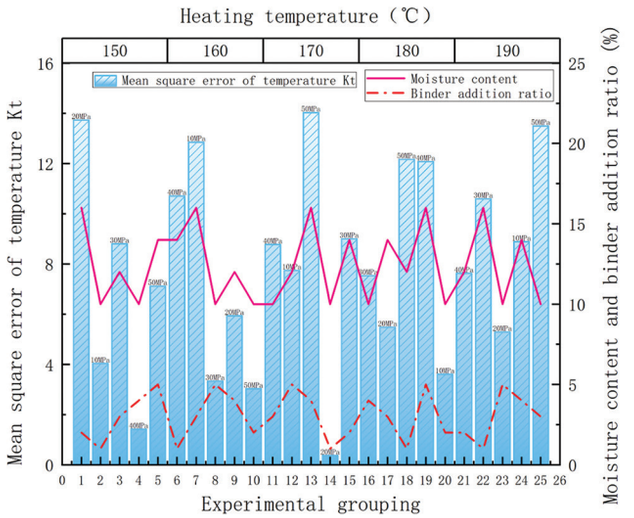


Figure 3. The temperature mean square deviation for each experimental group

Notes: The x-axis (top) represents the heating temperature, the y-axis (right) represents the moisture content and binder addition ratio, the y-axis (left) represents the temperature standard deviation, the bar chart shows the values of the temperature standard deviation, and the forming pressure is indicated directly above the bar chart.

Other researchers have employed different approaches to evaluate temperature field uniformity in their studies. Vanherck *et al.*[34] used the difference between maximum and minimum temperatures as an indicator of temperature uniformity. Bai *et al.*[35] analyzed temperature gradient variations by simulating temperature field distributions at different time points, comparing pavement damage under various temperature field conditions to indirectly assess uniformity impacts. Huang *et al.*[36] defined temperature uniformity as the temperature differences between measurement points inside a drying shed, with computational fluid dynamics simulations revealing higher temperatures in the bottom area compared to the top, whereas water vapor was concentrated in the top and outlet areas.

4.2.2. Effects of experimental factors on temperature field distribution

Using the Design-Expert software, variance analysis was performed with the two-factor interaction model to evaluate the effects of experimental factors (A, B, C, D) on the temperature MSD (Kt). The regression equation relating temperature MSD to the experimental factors is presented in Equation VIII:

$$Kt=8.61+1.61A+3.52B+0.4184C+0.4589D-0.227AB-AC+2.87AD-0.239BC-1.69BD+0.9081CD \quad (VIII)$$

The coefficient of determination for the regression equation, $R^2 = 0.8377$, indicates that the selected factors can explain 83.77% of the variation in the temperature MSD (Kt).

Table 4 displays the analysis of variance results for experimental factors affecting temperature field

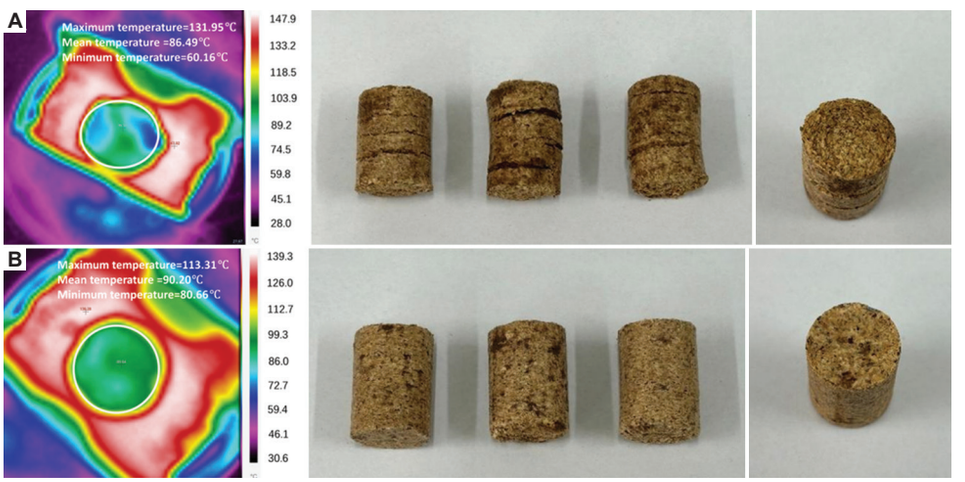


Figure 4. Temperature field distribution and appearance of densified biofuel. (A) The 13th experimental group and (B) The 14th experimental group

Table 4. Variance analysis results of the effects of various experimental factors on temperature field uniformity

Source of variation	Sum of squares	Degrees of freedom	Mean square	*F*-value	*p*-value
Model	315.16	10	31.52	7.23	0.0005**
A (Forming pressure)	25.28	1	25.28	5.80	0.0304*
B (Moisture content)	183.74	1	183.74	42.12	<0.0001**
C (Binder addition ratio)	1.74	1	1.74	0.3990	0.5378
D (Heating temperature)	2.07	1	2.07	0.4749	0.5020
AB	0.2826	1	0.2826	0.0648	0.8028
AC	3.68	1	3.68	0.8430	0.3741
AD	41.77	1	41.77	9.57	0.0079**
BC	0.3075	1	0.3075	0.0705	0.7945
BD	19.33	1	19.33	4.43	0.0538
CD	3.79	1	3.79	0.8697	0.3668
Residual	61.07	14	4.36		
Total	376.23	24			

Note: Statistical significance determined at *$0.01 \leq p < 0.05$ and **$p<0.01$.

uniformity, as computed by the Design-Expert software. The analysis reveals that moisture content (B) and the pressure-temperature interaction (AD) exhibited highly significant effects on temperature MSD ($p<0.01$), while molding pressure (A) showed significant influence ($p<0.05$). *F*-value comparisons established the factor importance ranking as B (moisture content) > A (pressure) > D (temperature) > C (binder addition ratio), with moisture content emerging as the dominant factor. This predominance stems from moisture's capacity to form insulating layers that impair interlayer bonding and cause irregular heat transfer. The moisture content is a critical parameter in biomass densification, significantly influencing both the process and final product quality.[37] It directly impacts key metrics such as density and mechanical strength, with research showing that an optimal moisture range is crucial for superior pellet properties. The relationship is complex; exceeding the optimum can decrease pellet durability,[38] while in some cases, quality increases with moisture up to a certain point.[39] This behavior is partly linked to moisture's effect on interparticle forces, which can impact energy consumption and molding quality.[40] Crucially, moisture content is closely interlinked with processing temperature, and both must be co-optimized to achieve the best results.[41] The presence of moisture significantly improves the thermal conduction efficiency of biomass.[42] Uneven distribution of moisture can lead to spatial differences in the temperature field. The moisture content affects the temperature difference between the center and the outer surface of particles.[43] It reduces the glass transition temperature of lignin through hydrogen bonding, and lignin's glass transition temperature decreases linearly with increasing moisture content.[44] In addition, moisture acts as a natural lubricant, but in excess, it increases viscous resistance, which in turn raises energy consumption and amplifies temperature fluctuations.[45] Therefore, precise moisture control is a foundational strategy for regulating temperature distribution during compaction and enhancing final densified biofuel quality, which corroborates the findings presented in our study. Consequently, the moisture content's impact on temperature MSD should be prioritized in future temperature field uniformity investigations.

Given the highly significant interaction effect between forming pressure (A) and heating temperature (D) on temperature MSD (Kt), their response surface was analyzed while maintaining moisture content (B) and binder addition ratio (C) at central levels (Figure 5).

The response surface exhibited pronounced curvature variations with changing pressure and temperature. Notably, lower forming pressures (10 MPa) combined with elevated temperatures (190°C) significantly reduce K_t, indicating improved temperature field uniformity.

Thus, optimal process conditions for temperature field homogeneity involve: (i) 10 MPa forming pressure, (ii) 190°C heating temperature, and (iii) stable moisture/binder levels. This configuration minimizes K_t while maintaining other quality parameters.

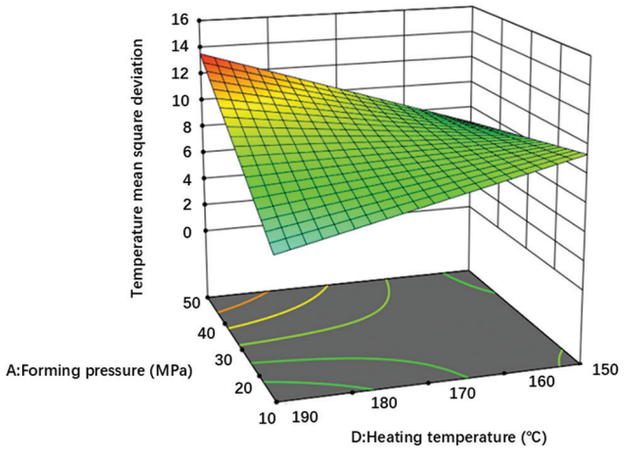


Figure 5. Response surface plot for forming pressure and heating temperature

To verify the reliability of the conclusions drawn from the response surface analysis and to assess the influence of temperature field uniformity on densified biofuel quality, a multiobjective optimization was performed using the Design-Expert 13.0 software on the experimental data from Table 1. The optimal parameter combination was predicted as follows: forming pressure = 10.0003 MPa, moisture content = 10%, binder addition ratio = 3.16532%, and heating temperature = 190℃, which aligns with the response surface plots.

Validation experiments confirmed that under these optimal conditions, the pellets exhibited a relaxed density of 0.964 g/cm^3, a relaxation ratio of 1.076, and an impact resistance of 98.78%. This parameter combination ensures that the pellets achieve maximized relaxed density and impact resistance while minimizing relaxation ratio and specific energy consumption, allowing for low-pressure compaction of biomass feedstock while maintaining high pellet quality.

4.2.3. The effect of temperature field uniformity on densified biofuel quality

To investigate the relationship between temperature field uniformity and biomass densification quality, Spearman correlation analysis was conducted using the Statistical Package for the Social Sciences software (version 2022 to assess associations between temperature MSD and both impact resistance and relaxed density. This nonparametric method was selected due to the nonnormal distribution of MSD data.

The correlation analysis revealed a significant negative correlation ($\rho = -0.633$, $p<0.001$) between temperature MSD and relaxed density, indicating that increased temperature heterogeneity (higher MSD) corresponds to reduced relaxed density. This phenomenon likely resulted from insufficient lignin softening and bonding under non-uniform temperature conditions.

A moderately negative correlation ($\rho = -0.500$, $p=0.011$) exists between MSD and impact resistance, attributable to structural inhomogeneity caused by uneven heat distribution. However, the non-significant relationship with relaxation ratio ($\rho = -0.199$, $p=0.339$) suggests minimal MSD influence, implying dominant effects from other factors.

Temperature field uniformity critically affects densified biofuel quality. Uniform heating (low MSD) promotes homogeneous lignin activation, enhancing interparticle bonding and consequently improving both relaxed density and impact resistance.

5. Conclusion

This study developed an innovative pine sawdust densification methodology based on temperature field optimization, providing an effective solution for forestry waste valorization. The investigation demonstrated that forming pressure, moisture content, and heating temperature critically influence pellet quality. Statistical analysis revealed that forming pressure, moisture content, heating temperature, and their interactions exhibited extremely significant effects ($p<0.01$) on both relaxed density and impact resistance, whereas heating temperature and its interaction with pressure significantly affected the relaxation ratio. The relative importance of factors affecting temperature MSD follows the hierarchy: moisture content (most influential) > forming pressure > heating temperature > binder addition ratio (least influential). Process optimization suggests that reduced moisture content combined with elevated temperature effectively minimizes temperature variation. Importantly, strong negative correlations exist between temperature MSD and both relaxed density and impact resistance, confirming that precise temperature field control substantially improves densified biofuel quality.

Acknowledgments

None.

Funding

This study was funded by the Beijing Forestry University (Award Number: 31500478, Grant Recipient: Zhongjia Chen).

Conflict of interest

The authors declare that they have no known competing financial interests or personal relationships that could have appeared to influence the work reported in this paper.

Author contributions

Conceptualization: Zhongjia Chen, Zhiyuan Ma
Formal analysis: Zhuoying Chen, Zhongsai Li
Funding acquisition: Zhongjia Chen
Investigation: Zhongjia Chen, Zhiyuan Ma, Zhongsai Li
Methodology: Zhuoying Chen, Zhiyuan Ma
Writing – original draft: Zhuoying Chen, Zhongsai Li
Writing – review & editing: Xiangyue Yuan

Availability of data

All data analyzed have been presented in the paper.

References

1. Wang R, Cai WJ, Yu L, *et al.* A high spatial resolution dataset of China's biomass resource potential. *Sci Data*. 2023;10:384. doi: 10.1038/s41597-023-02227-7
2. Sette CR Jr., De Moraes MDA, Coneglian A, Ribeiro RM, Hansted ALS, Yamaji FM. Forest harvest byproducts: Use of waste as energy. *Waste Manage*. 2020;114:196-201. doi: 10.1016/j.wasman.2020.07.001
3. Pradhan P, Mahajani SM, Arora A. Production and utilization of fuel pellets from biomass: A review. *Fuel Process Technol*. 2018;181:215-232. doi: 10.1016/j.fuproc.2018.09.021
4. Jiang L, Liang J, Yuan X, *et al.* Co-pelletization of sewage sludge and biomass: The density and hardness of pellet. *Bioresour Technol*. 2014;166:435-443. doi: 10.1016/j.biortech.2014.05.077
5. Li C, Wang Y, Xie S, *et al.* Synergistic treatment of sewage sludge and food waste digestate residues for efficient energy recovery and biochar preparation by hydrothermal pretreatment, anaerobic digestion, and pyrolysis. *Appl Energy*. 2024;364:123203. doi: 10.1016/j.apenergy.2024.123203
6. Tumuluru JS, Yancey NA, Kane JJ. Pilot-scale grinding and briquetting studies on variable moisture content municipal solid waste bales-impact on physical properties, chemical composition, and calorific value. *Waste Manage*. 2021;125:316-327. doi: 10.1016/j.wasman.2021.02.013
7. García R, Gil MV, Rubiera F, Pevida C. Pelletization of wood and alternative residual biomass blends for producing industrial quality pellets. *Fuel*. 2019;251:739-753. doi: 10.1016/j.fuel.2019.03.141
8. García R, González-Vázquez MP, Pevida C, Rubiera F. Pelletization properties of raw and torrefied pine sawdust: Effect of co-pelletization, temperature, moisture content and glycerol addition. *Fuel*. 2018;215:290-297. doi: 10.1016/j.fuel.2017.11.027
9. Gil MV, Oulego P, Casal MD, Pevida C, Pis JJ, Rubiera F. Mechanical durability and combustion characteristics of pellets from biomass blends. *Bioresour Technol*. 2010;101(22):8859-8867. doi: 10.1016/j.biortech.2010.06.062
10. Chen WS, Chang FC, Shen YH, Tsai MS. The characteristics of organic sludge/sawdust derived fuel. *Bioresour Technol*. 2011;102(9):5406-5410. doi: 10.1016/j.biortech.2010.11.007
11. Wang X, Chen Z, Yu G, Yuan X. Effects of poplar fibres as solid bridge on the physical characteristics of biomass briquette made from sawdust and bamboo powder. *Wood Res*. 2018;63:141-153.
12. Wang T, Li Y, Zhang J, *et al.* Evaluation of the potential of pelletized biomass from different municipal solid wastes for use as solid fuel. *Waste Manage*. 2018;74:260-266. doi: 10.1016/j.wasman.2017.11.043
13. Venter P, Naude N. Evaluation of some optimum moisture and binder conditions for coal fines briquetting. *J South Afr Inst Min Metall*. 2015;115(4):329-333.
14. Ezéchiel K, Joel TK, Abdon A, Roger DD. Accessibility and effects of binder types on the physical and energetic properties of ecological coal. *Heliyon.* 2022;8(11):e11410. doi: 10.1016/j.heliyon.2022.e11410
15. Ghiasi B, Kumar L, Furubayashi T, *et al.* Densified biocoal from woodchips: Is it better to do torrefaction before or after densification? *Appl Energy*. 2014;134:133-142. doi: 10.1016/j.apenergy.2014.07.076
16. Zafari A, Kianmehr MH. Effect of temperature, pressure and moisture content on durability of cattle manure pellet in open-end die method. *J Agric Sci*. 2012;4(5):203-208. doi: 10.5539/jas.v4n5p203
17. Dai X, Theppitak S, Yoshikawa K. Pelletization of carbonized wood using organic binders with biomass gasification residue as additive. *Energy Fuels*. 2018;158(1):509-515. doi: 10.1016/j.egypro.2019.01.144
18. Cao L, Yuan XZ, Li H, *et al.* Complementary effects of torrefaction and co-pelletization: Energy consumption and characteristics of pellets. *Bioresour Technol*. 2015;185:254-262. doi: 10.1016/j.biortech.2015.02.045
19. Macak M, Nozdrovický L, Hussein AO. Effect of preheating and different moisture content of

input materials on durability of pellets made from different phytomass content. *Acta Technol Agric*. 2015;18(1):22-27.
doi: 10.1515/ata-2015-0006

20. Ju X, Zhang K, Chen Z, Zhou J. A method of adding binder by high-pressure spraying to improve the biomass densification. *Polymers*. 2020;12(10):2374.
doi: 10.3390/polym12102374
21. Li C, Chen Z, Wang Q. Effect of temperature on densification pressure and the unit density in production of corn straw pellet with a post-heating method. *Energies*. 2022;15(3):842.
doi: 10.3390/en15030842
22. Zhang K, Song S, Chen Z, Zhou J. Effects of brown sugar water binder added by spraying method as solid bridge on the physical characteristics of biomass pellets. *Polymers*. 2020;12(3):674.
doi: 10.3390/polym12030674
23. Wang YM, Chen ZJ, Yuan XY, Yu GS. Influence of die temperature and moisture content on the densification of bamboo powder using die heating method. *Wood Res*. 2018;63(4):655-668.
24. Obi OF, Pecenka R, Clifford MJ. A review of biomass briquette binders and quality parameters. *Energies*. 2022;15(7):2426.
doi: 10.3390/en15072426
25. Ajimotokan HA, Ibitoye SE, Odusote JK, Adesoye OA, Omoniyi PO. Physico-mechanical properties of composite briquettes from corncob and rice husk. *J Bioresour Bioprod*. 2019;4(3):159-165.
doi: 10.12162/jbb.v4i3.004
26. State Forestry Administration of the People's Republic of China. Bamboo-Based Solid Biofuel (Standard No. LY/T 2552-2015). Beijing: State Forestry Administration of the People's Republic of China; 2015.
27. National Energy Administration of the People's Republic of China. Quality Grading of Biomass Solid Biofuel (Standard No. NB/T 34024-2015). Beijing: National Energy Administration of the People's Republic of China; 2015.
28. Zhao C, Cao A, Wang L, *et al.* Analysis of effect on temperature field of tire curing process by initial temperatures and condensate discharging. *Appl Therm Eng*. 2024;257:124424.
doi: 10.1016/j.applthermaleng.2024.124424
29. Cai Y, Liu G, Zhu X, Tu Q, Hong G. Aerodynamic interference significance analysis of two-dimensional front wing and rear wing airfoils with stagger and gap variations. *J Aerosp Eng*. 2019;32(6):04019098.
doi: 10.1061/(ASCE)AS.1943-5525.0001090
30. Stoffel MA, Nakagawa S, Schielzeth H. RptR: Repeatability estimation and variance decomposition by generalized linear mixed-effects models. *Methods Ecol Evol.* 2017;8:1639-1644.
doi: 10.1111/2041-210X.12797
31. Adesanya SA, Ibrahim JS, Kuhe A, Ndah AA. Assessment of mechanical, physical, and thermal characterization of jujube seed shell briquettes. *Bioresour Technol Rep.* 2024;26:101868.
doi: 10.1016/j.biteb.2024.101868
32. Jia Y, Shi Y. The research progress of biomass energy utilization. *Sci Technol Rev*. 2023;41(16):55-75.
doi: 10.3981/j.issn.1000-7857.2023.16.005
33. Cheng XT, Xu XH, Liang XG. Homogenization of temperature field and temperature gradient field. *Sci China Ser E-Tech Sci*. 2009;52:2937-2942.
doi: 10.1007/s11431-009-0244-8
34. Vanherck T, Jean G, Gonon M, Lobry J, Cambier F. Spark plasma sintering: homogenization of the compact temperature field for non conductive materials. *Int J Appl Ceram Technol*. 2015;12:E1-E12.
doi: 10.1111/ijac.12187
35. Bai Z, Guo D, Li S, Hu Y. Analysis of temperature and humidity field in a new bulk tobacco curing barn based on CFD. *Sensors (Basel)*. 2017;17(2):279.
doi: 10.3390/s17020279
36. Huang Y, Finell M, Larsson S, *et al.* Biofuel pellets made at low moisture content-Influence of water in the binding mechanism of densified biomass. *Biomass Bioenergy*. 2017;98:8-14.
doi: 10.1016/j.biombioe.2017.01.002
37. Matúš M, Križan P, Beniak J, Šooš Ľ. Effects of initial moisture content on the production and quality properties of solid biofuel. *Acta Polytech*. 2015;55:335-341.
doi: 10.14311/AP.2015.55.0335
38. Jiang X, Cheng W, Liu J, *et al.* Effect of moisture content during preparation on the physicochemical properties of pellets made from different biomass materials. *Bio Res*. 2020;15(1):557-573.
doi: 10.15376/biores.15.1.557-573
39. Styks J, Wróbel M, Frączek J, Knapczyk A. Effect of compaction pressure and moisture content on quality parameters of perennial biomass pellets. *Energies*. 2020;13(8):1859.
doi: 10.3390/en13081859
40. Li Z, Sun H, Lei Z, Xu S, Qiao Z, Li B. Correction: Mechanistic study on the fine-scale arch effect of moisture content on the dense moulding of mushroom pomace particles. *Waste Biomass Valorization*. 2025; 16(4):1939.
doi: 10.1007/s12649-024-02786-9
41. Zhang X, Cai Z, Chen L, Zhang D, Zhang Z. Effects of moisture content and temperature on the quality of water hyacinth pellets. *Bio Res*. 2015;11(1): 1407-1416.
doi: 10.15376/biores.11.1.1407-1416
42. Zine O, El-Alaoui A, Taoukil D, Kadri EH, El Abbassi I. Influence of density and water content on

the thermal diffusivity of wood chips. *E3S Web Conf*. 2021;321:02010.
doi: 10.1051/e3sconf/202132102010

43. Liu W, Chen G, Zheng D, Ge M, Liu C. Effects of the broken kernel on heat and moisture transfer in fixed-bed corn drying using particle-resolved CFD model. *Agriculture*. 2023;13(8):1470.
doi: 10.3390/agriculture13081470
44. Li Z, Wang HQ, Gao YH, Yan L, Wang P, De XH. Bonding mechanism of dense forming of salix biomass fuel particles. *Trans Chin Soc Agric Eng*. 2019;35(21):235-241.
doi: 10.11975/j.issn.1002-6819.2019.21.029
45. Zhang J, Guo YM, Yun HX. Effect of raw material moisture content on the forming effect of biomass solid fuel. *J Shanxi Agric Sci*. 2012;40(1): 65-71.
doi: 10.3969/j.issn.1002-2481.2012.01.20

Asian Journal of Water, Environment and Pollution. Vol. 22, No. 6 (2025), pp. 73-88.
doi: 10.36922/AJWEP025120081

ORIGINAL RESEARCH ARTICLE

Machine learning-based discharge coefficient estimation in trapezoidal-arched labyrinth weirs

Mohammad Heidarnejad[1]*, Jamal Feili[2], Mehdi Fuladipanah[3], and Upaka Rathnayake[4]*

[1]Department of Water Science Engineering, Ahv. C., Islamic Azad University, Ahvaz, Iran
[2]Khuzestan Water and Power Organization, Ahvaz, Khuzestan, Iran
[3]Department of Civil Engineering, Ramh. C., Islamic Azad University, Ramhormoz, Iran
[4]Department of Civil Engineering and Construction, Faculty of Engineering and Design, Atlantic Technological University, Sligo, Connacht, Ireland

***Corresponding authors:** Mohammad Heidarnejad (mo.heidar@iau.ac.ir); Upaka Rathnayake (upaka.rathnayake@atu.ie)

Received: March 17, 2025; 1st revised: June 17, 2025; 2nd revised: July 8, 2025; Accepted: July 9, 2025; Published online: August 13, 2025

Abstract: Weirs represent a frequently employed mechanism for regulating water surface elevations and managing flow within canals and hydraulic infrastructures. Among these, labyrinth weirs constitute a distinctive variant capable of accommodating a specific discharge while maintaining a reduced upstream water level compared to conventional linear weirs. The present investigation delved into the evaluation of the effectiveness of multilayer perceptron (MLP) networks, support vector machine (SVM), gene expression programming (GEP), and multivariate adaptive regression splines (MARS), aiming to predict the discharge coefficient (C_d) of a trapezoidal-arched labyrinth weir with an expanded central cycle. A dataset including 108 laboratory observations was utilized. The dimensionless parameters were obtained from the parameters including inside apex width of the middle cycle (w_1), inside apex width of the end cycles (w_2), weir height on the upstream side (B), unsubmerged total upstream head on the weir (H_d), and gravitational acceleration (g). The model was developed with the dimensionless parameters and C_d. Root mean square error (RMSE), determination coefficient (R^2), mean absolute error (MAE), and developed discrepancy ratio (DDR) were used as performance assessment criteria. Based on these metrics, all four models exhibited the latent capacity to predict the C_d value. However, the MLP model demonstrated superior performance among the models during both training (RMSE = 0.024, MAE = 0.020, R^2 = 0.816, and $C_{d[DDRmax]}$ = 8.07) and testing (RMSE = 0.011, MAE = 0.006, R^2 = 0.688, and $C_{d[DDRmax]}$ = 11.32) phases. Sequentially, the subsequent standings were secured by the SVM, GEP, and MARS. MLP outperformed SVM, GEP, and MARS models in predicting C_d, achieving the highest R^2 and lowest RMSE/MAE values.

Keywords: Discharge coefficient; Laboratory observations; Machine learning models; Prediction; Trapezoidal-arched labyrinth weir

1. Introduction

Weirs, both linear and non-linear in configuration, are critical hydraulic structures designed for the regulation of excess flow and the precise management of water levels. These structures form an integral component of hydraulic systems, serving a pivotal role in flow regulation.[1] Engineering applications incorporate

weirs of various geometries, each exhibiting distinct hydraulic characteristics that significantly influence flow behavior.[2,3] Among these, labyrinth weirs represent a notable category widely employed in hydraulic engineering. These weirs are characterized by their intricate platforms, which often adopt geometric configurations such as triangular, rectangular, or trapezoidal shapes. The zigzag design of labyrinth weirs increases the effective crest length relative to linear weirs, thereby enhancing their discharge efficiency. This structural advantage enables them to convey larger volumes of water under lower upstream hydraulic heads. Furthermore, labyrinth weirs are recognized for their cost-effectiveness in terms of construction and operation.

The study of labyrinth weir hydraulics was initially undertaken by Gentilini,[4] who introduced triangular weirs by aligning several oblique weirs in sequence. Modern advancements in labyrinth weir design began with Taylor[5] and were subsequently refined by Hay and Taylor.[6] In 1985, the Bureau of Reclamation in the United States formalized a design methodology to assist engineers in designing and constructing labyrinth weirs for public infrastructure projects.[7] Meanwhile, Kocahan and Taylor[8] highlighted that labyrinth weirs, despite their passive flow control nature, can convey significantly higher discharge rates compared to standard ogee weirs during the initial stages of flood events. In a study, Crookston and Tullis[9] investigated the hydraulic efficiency of conventional and inverted labyrinth weirs in channels, concluding that orientation had no impact on performance. Subsequently, Christensen and Tullis[10] expanded the understanding of flow characteristics over arched labyrinth weirs, while Seamons[11] evaluated the effects of geometric variations on their efficiency and the accuracy of design predictions.

Due to the intricate three-dimensional flow patterns over labyrinth weirs, determining an exact analytical solution for the head-discharge relationship remains challenging. For example, Bijankhan and Kouchakzadeh[12] conducted experimental and theoretical studies on water flow through triangular plan labyrinth weirs under both free and submerged flow conditions. New experimental data were collected for free flow, while the transition threshold between free and submerged regimes was identified experimentally. Using Buckingham π analysis, a head-discharge relationship was developed for submerged flow. A step-by-step calibration method was introduced to derive a unified discharge coefficient (C_d) that applies across free flow, submerged flow, and the transition zone, allowing continuous application of the coefficient under varying flow conditions.

Monjezi *et al*.[13] emphasized the critical role of weirs in dam safety and investigated the C_d of direct and arched weirs in linear and triangular labyrinth forms through laboratory experiments. Arched weirs, due to their curved geometry, increase the effective crest length at a given width, enhancing discharge capacity. Results showed that increasing the ratio of total hydraulic load to weir crest height decreases C_d in all weirs. However, arched shapes improved efficiency by up to 21% in linear weirs and 57% in labyrinth weirs. However, higher hydraulic loads reduced arched weir efficiency due to increased downstream standing wave height.

Furthermore, Seyedian *et al*.[14] investigated the use of machine learning models (MLMs) to predict the C_d of triangular labyrinth weirs, a key parameter in flow control. They developed and evaluated three MLMs: least-square support vector machine (SVM), quantile regression forest, and Gaussian process regression (GPR). Using statistical and visual methods, they found that GPR outperformed the others, achieving a determination coefficient (R^2) of 0.986 and root mean square error (RMSE) of 0.009. Sensitivity analysis revealed the Froude number and weir geometry as the most influential inputs. Notably, GPR not only provided the highest accuracy but also offered reliable prediction intervals, making it the preferred model for C_d prediction.

In the study by Zare *et al*.,[15] they conducted an experimental study on inclined circular labyrinth weirs with inclination angles of 60°, 70°, 80°, and 90° and diameters of 15, 20, 25, and 30 cm under varying flow rates. The flow transitioned from free to submerged as discharge increased, with no air entrainment observed. Results showed that increasing the dimensionless ratio of total hydraulic head to weir height reduced the C_d. The 60° inclined weir achieved the highest C_d, while the vertical (90°) weir had the lowest. Although the 15 cm diameter weir initially exhibited the highest C_d, diameter changes had a minimal overall impact.

Similarly, Nematollahi *et al*.[16] analyzed eight sinusoidal labyrinth weirs with varying heights and effective crest lengths to study C_d and energy loss. Increasing flow rate or upstream depth decreased both metrics, while greater effective length and inlet-to-outlet width ratios increased them. Maximum energy loss occurred at width ratios of 4.60 and 7.67. A 20% increase in weir height led to a 19.8% increase in energy loss. Flow splitters reduced the C_d but increased energy loss. The study also provided equations for C_d and energy loss with high correlation coefficients.

Ahmed and Altalib[17] investigated the effects of cycle number, total arc angle, and semicircular openings on the C_d of arched weirs and arched labyrinth weirs. Reducing the number of cycles increased the C_d by up to 35.94%, with arched weirs performing better than arched labyrinth weirs. Increasing the total arc angle improved the coefficient by up to 32.4%. However, semicircular openings reduced performance, with C_d decreases of 19.54% for arched labyrinth weirs and 12.08% for linear weirs as the opening-to-edge length ratio increased. A predictive equation was developed to predict C_d, showing a strong correlation with experimental data (R = 0.9).

Masoudi *et al*.[18] emphasized the importance of flood discharge from dam reservoirs, typically managed using weirs. Labyrinth weirs, ideal for narrow valleys and large floods, offer high efficiency due to their extended flow paths. This study aimed to enhance the C_d and efficiency of rectangular and trapezoidal labyrinth weirs by replacing uniform, regular labyrinth cycles (congresses) with unequal and irregular ones. Five samples of each weir type were tested in two configurations, differing by the placement of the longest cycle (center vs. sides). Experimental results showed that using unequal and irregular congresses improved the C_d by 40.7% for rectangular weirs and 35.3% for trapezoidal ones.

Similarly, Hadi and Majeed[19] investigated the C_d of side weirs installed in the side wall of a rectangular channel, focusing on trapezoidal labyrinth weirs with side wall angles of 15°, 30°, 45°, 60°, 75°, and a linear side weir at 90°. Using six physical models, they developed hydraulic equations relating discharge and head over the weir. Results showed that the C_d increases with larger side wall angles and is highest at 75°, approaching the value for a straight (90°) weir. Computational fluid dynamic simulations using the k-omega shear stress transport model and volume of fluid scheme confirmed the experimental findings, showing strong agreement.

Non-linear weirs demonstrate a superior overflow capacity relative to linear weirs, attributable to their extended crest length. The C_d plays a critical and notable role in the hydraulic performance of non-linear weirs. The usual discharge equation for a labyrinth weir is given in Equation I.

$$Q=\frac{2}{3}C_d L_c \sqrt{2g} H_T^{1.5} \quad (I)$$

where Q is the overflow rate, Lc is the effective crest length, H_T denotes the total upstream head, and g is the acceleration due to gravity. The C_d values are influenced by hybrid hydraulic-geometry parameters, prompting numerous studies and research endeavors to elucidate this effect. Table 1 summarizes a list of C_d predictors presented by various researchers.

The adoption of recently developed MLMs as a state-of-the-art approach has supplanted the need for costly, limited, and time-intensive experimental tests. MLMs employ training and testing phases to uncover intricate and hidden relationships between dependent and independent variables, thereby facilitating accurate forecasting of target variables.[27] Table 2 presents a comprehensive summary of various studies aiming to predict the C_d in overflows of differing shapes.

As evident from Table 2, accurately determining the C_d for structures such as labyrinth, piano-key, and lateral weirs has long been a focus of research due to its potential to enhance performance efficiency. The use of MLMs has demonstrated superior accuracy compared to traditional regression models and empirical equations. In addition, the exploration and development of new configurations inspired by the geometry of the labyrinth weir is a burgeoning area of study. To address these aspects, this study employs four MLMs–SVM, gene expression programming (GEP), artificial neural network (ANN), and multivariate adaptive regression splines (MARS)–to simulate the C_d of a trapezoidal-arched labyrinth weir (TALW). A review of existing literature reveals a gap in research specifically focused on this topic.

2. Materials and methods

2.1. Data series

The experimental procedures for this research were conducted in the hydraulic laboratory of the Khuzestan Water and Power Authority, Iran. The weir models were installed within an 8 m long, 0.6 m wide, and 0.6 m high test flume with transparent Plexiglas walls, facilitating the observation of water surface profiles and flow conditions. The flume was operated under free-flow conditions. To ensure the accuracy of the results, the flume was designed to be watertight and seamless. The test equipment and components of the flume comprised the flume's groundwater tank, a digital flowmeter with an accuracy of 0.2 L/s, a tranquilizer, a floating electric pump with a maximum flow rate of 140 m^3/h, and a constant-head tank (Figure 1A). The digital magnetic flowmeter was calibrated against a 90° V-notch weir installed at the flume outlet. The weir's

Table 1. Summary of predictive equations for the discharge coefficient of labyrinth weirs

References	Equation	Recommendation
Darvas[20]	$C_d = \frac{Q_{max}}{Wh_{max}^2}$ (II)	Triangular labyrinth weir; $0.2 \le \frac{H_T}{P} \le 0.6$; side wide angle $\ge 0.8\alpha_{max}$
Lux and Hinchliff[21]	$C_d = \frac{Q_{cycle}}{\frac{\frac{w}{P}}{\frac{w}{P}+k} w\sqrt{g}H_T^{1.5}}$ (III)	Labyrinth weir with one cycle; $\frac{w}{P} > 2$; k is the apex shape constant
Melo *et al.*[22]	$C_d = \frac{Q}{k_{,-CW} W\sqrt{2g}H_T^{1.5}}$ (IV)	Circular labyrinth weir; $1 \le k_{\theta\text{-}CW} \le 1.4$
Crookston[23]	$C_d = A(\frac{H_T}{P})^{(B(\frac{H_T}{P})^C)} + D$ (V)	Labyrinth weir with half-round and quarter-round crests; A, B, C, and D are curve-fit coefficients; $6 \le \alpha \le 35$
Emiroglu *et al.*[24]	$C_d = (18.6 - 23.535[\frac{L}{B}]^{0.012} + 6.769[\frac{L}{l}]^{0.112} - 0.502(\frac{W}{y_1})^{4.024} + 0.094\sin_{,} - 0.393Fr_l^{2.155})^{-1.431}$ (VI)	Triangular labyrinth weir with one cycle
Karami *et al.*[25]	$C_d = 0.012(\frac{y_1}{W})^{-2.5} + 0.881r_{,}^{0.248} + 2.97Fr_2^{1.79}$ (VII)	Asymmetric triangular with one cycle
Bonakdari *et al.*[26]	$C_d = 0.466 + 0.388\frac{P}{y} - 0.183\frac{L}{W} - 0.022\frac{L}{y} + 0.31Fr + 0.12\sin\theta$ (VIII)	Triangular labyrinth weir

discharge equation ($Q = 1.417 \cdot H^{2.5}$) was validated, with head measurements accurate to ±0.1 mm. Calibration tests across the experimental flow range (5–50 L/s) confirmed flowmeter deviations within ±0.15 L/s, ensuring high-fidelity discharge data. The bottom of the flume was a fixed-bed type and maintained as horizontally as practically possible.

Water was initially pumped from the groundwater tank into the head tank, from where it flowed through a 0.3 m diameter pipe toward the inlet of the test flume, regulated by a globe valve. Water entered the flume at a low flow rate, gently passing over the weir. By varying the flow rate, the hydraulic conditions at the upstream, over, and downstream of the weir were recorded. Ultimately, water exited the flume into a downstream channel, entered the pumping tank, and was recirculated back into the system. A representation of the geometry dimension is illustrated in Figure 1B. A series of 120 tests was conducted using 12 models of TALW with an expanded middle cycle. Table 3 represents parameters included for the tests.

A schematic representation of the labyrinth weir is provided in Figure 2, detailing its geometric parameters relative to the weir crest. A represents the inside apex width, t_w indicates the wall thickness, α is the sidewall angle, W corresponds to the apron width, w denotes the cycle width, P represents the weir height, and T indicates the pier thickness.

2.2. Dimensional analysis

The values of C_d for TALW can be considered a function dependent on the following parameters:

$$C_d = F(Q, w_1, w_2, B, H_d, g) \quad \text{(IX)}$$

Where Q is the flow rate, w_1 is the inside apex width of the middle cycle, w_2 is the inside apex width of the

Table 2. Summary of machine learning model applications to predict discharge coefficient

References	MLMs included	Weir type	Findings
Mahmoud *et al.*[28]	HI-MLP, ANFIS, SVR, MLP, GA	LW	HI-MLP demonstrates the highest accuracy.
Nourani *et al.*[3]	SVM-PSO, GA, SVM-GA	CCOW	The SVM-GA hybrid model outperforms the others.
Emami *et al.*[29]	Hybrid (LSHADE- XGB), ANFIS, GEP, SAELM, ANN	PCLW	The hybrid model demonstrates higher accuracy.
Majedi-Asl *et al.*[30]	SVM, GEP	PKW, LW	GEP demonstrates higher accuracy.
Mustafa *et al.*[31]	NLR, BPNN, GA, PSO	TSLW	GA-BPNN and PSO-BPNN exhibit notably accurate prediction results.
Wang *et al.*[32]	ANFIS, SVM, M5-tree, LSSVM, LSSVM-BA	CLW	LSSVM-BA demonstrates the highest accuracy during the training and testing phases.
Hu *et al.*[33]	CFD; ANFIS, ANFIS-FA	LW	ANFIS-FA demonstrates significantly higher accuracy.
Mahmoud *et al.*[34]	SAELM	NLW, ILW	SAELM exhibits reasonable accuracy.
Shafiei *et al.*[35]	LSSVM, ELM, BELM, LR	PKW	BELM demonstrates excellent performance.
Norouzi *et al.*[36]	SVM	LW, ALW	The SVM-based model demonstrates higher accuracy.
Olyaie *et al.*[37]	ANN, GP, ELM	TLW	ELM demonstrates superior performance.
Roushangar *et al.*[38]	LGP, MLR, NLR	RSW	Mathematical models demonstrate higher accuracy.
Uyumaz *et al.*[39]	ANFIS, ANN, NLR, MLR	TLSW	ANFIS is more successful in modeling.
Emiroglu and Kisi[40]	ANFIS, NLR	SESW	ANFIS demonstrates higher accuracy.

Abbreviations: ALW: Arched-labyrinth weir; ANFIS: Adaptive neural-fuzzy inference system; ANN: Artificial neural network; BA: Bat algorithm; BELM: Bayesian extreme learning machine; BPNN: Back-propagation neural network; CCOW: Circular-crested oblique weir; CFD: Computational fluid dynamics; CLW: Curved labyrinth weir; ELM: Extreme learning machine; FA: Firefly algorithm; GA: Genetic algorithm; GEP: Gene expression programming; GP: Genetic programming; HI-MLP: Hydraulic-informed multilayer perceptron; ILW: Inverted orientation labyrinth weir; LGP: Linear genetic programming; LM: Levenberg–Marquardt algorithm; LR: Logistic regression; LSHADE: Linear population size reduction history-based adaptive differential evolution; LSSVM: Least-square support vector machine; LW: Labyrinth weir; MLP: Multilayer perceptron; MLR: Multiple linear regression; NLR: Non-linear regression; NLW: Normal orientation labyrinth weir; PCLW: Pseudo-cosine labyrinth weir; PKW: Piano key weir; PSO: Particle swarm optimization; RBFNN: Radial basis function neural network; RSW: Rectangular side weir; SAELM: Self-adaptive extreme learning machine; SESW: Semi-elliptical side weir; SVR: Support vector regression; TLSW: Trapezoidal labyrinth side weir; TSLW: Triangle shape of labyrinth weir; XGB: Extreme gradient boosting algorithm.

end cycle, B is the weir height on the upstream side, H_d is the unsubmerged total upstream head on the weir, and g is the gravitational acceleration. These parameters collectively inform the calculation of C_d and capture the complex interactions between hydraulic and geometric factors that affect the flow behavior of these structures. For conducting dimensional analysis, the parameters P, g, and Q were identified as repeating variables, leading to the derivation of dimensionless parameters as outlined in Equation X.

$$C_d = F\left(\frac{H_d}{B}, \frac{gB^5}{Q^2}, \frac{w_1}{B}, \frac{w_2}{B}\right) \quad (X)$$

The influence of the gravitational acceleration $\frac{gB^5}{Q^2}$, which represents the Froude number, is incorporated through the dimensionless parameter $\frac{H_d}{B}$. Given these conditions, Equation X is simplified to the following Equation XI:

$$C_d = F\left(\frac{w_1}{B}, \frac{H_d}{B}, \frac{w_1}{w_2}\right) \quad \text{(XI)}$$

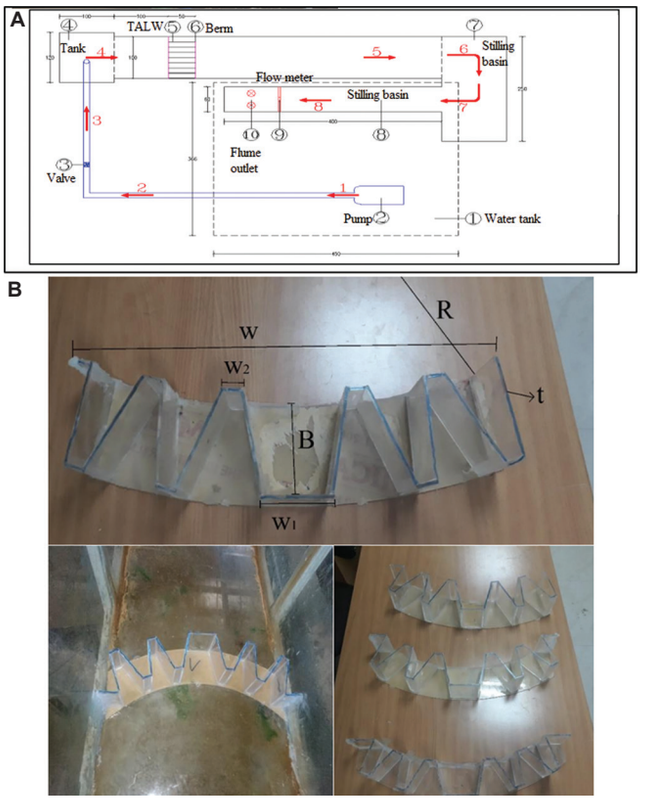


Figure 1. Flume and weirs model of experiments: (A) Plan view of the setting. (B) Geometry parameters of the trapezoidal-arched labyrinth weirs (TALWs)
Notes: B is the weir height on the upstream side; R is the arc radius; t is the crest thickness; W is the width of a cycle; W_1 is the inside apex width of the middle cycle; W_2 is the inside apex width of the end cycle.

2.3. MLMs

2.3.1. SVM

Developed by Cortes and Vapnik,[41] the SVMs are a class of supervised learning methods used for classification and regression tasks in machine learning. They are particularly well-suited for binary classification problems, though extensions to multiclass classifications exist. The core concept behind SVM is the construction of hyperplanes in a high-dimensional space that can be used to separate different classes of data points.[38] Given a training dataset $\{(X_i, y_i)\}_{i=1}^{N}$, where $X_i \in \mathbb{R}^n$ represents the feature vectors and $y_i \in \{-1,1\}$ represents the class labels, the objective of SVM is to find a hyperplane that maximally separates the two classes.[42]

To model a problem using SVM, the first step is to clearly define the problem by determining whether it is a classification, regression, or outlier detection task. Once the task is identified, the next step involves collecting and preprocessing the dataset to ensure that the data are clean, normalized, and suitable for modeling. Based on the nature and structure of the data, an appropriate kernel function is then selected to transform the input space if necessary. After selecting the kernel, the dataset is split into training and testing sets, typically using an 80:20 ratio, to evaluate the model's performance on unseen data. The next step is to set the key hyperparameters of the SVM model. These include the regularization parameter C, which controls the trade-off between achieving a wide margin and minimizing classification errors, and other kernel-specific parameters, such as γ for the radial basis function (RBF) kernel or the degree for polynomial kernels. With the data prepared and parameters set, the model is trained using the training dataset. During training, the SVM algorithm attempts to maximize the margin between classes in classification

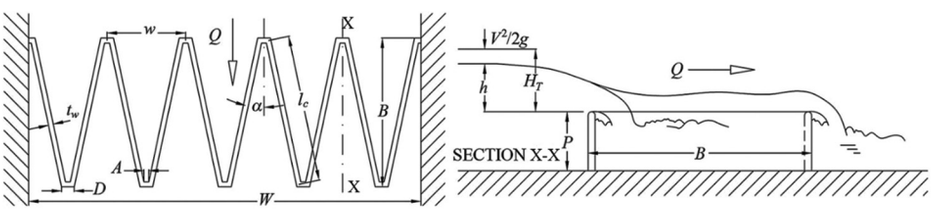


Figure 2. Shape and geometric parameters of the labyrinth weir
Notes: α is the wall angle; A is inside apex width, X-X is cross section of the weir; B is the weir length; D is the apex width; H is the depth head; H_t is the total upstream head; h_t is the velocity head; L_c is the wall length; P is the weir height; Q is the flow discharge; T is the weir height; t is the crest thickness; W is the total width; w is the width of a cycle.

Table 3. Summary of hydraulic and geometric parameters

No.	W (cm)	R (cm)	L (cm)	t (mm)	N	$\frac{w_2}{w_1}$	$\frac{B}{w_1}$	Q (L/s)
1	60	45	66	5	-	-	-	5–50
2			136		5	0.42	1.00	
3			136			0.35	1.00	
4			136			0.30	1.00	
5			152			0.42	1.25	
6			152			0.35	1.25	
7			152			0.30	1.25	
8			170			0.42	1.50	
9			170			0.35	1.50	
10			170			0.30	1.50	

Notes: B is the weir height; L is the weir length; N is the number of cycles; R is the arc radius; t is the crest thickness; W is the width of a cycle; W_1 is the inside apex width of the middle cycle; W_2 is the inside apex width of the end cycle.

tasks or fit a hyperplane within an ε-insensitive region in regression tasks. Following training, model validation is conducted through cross-validation to assess performance and identify opportunities for improvement. Hyperparameters are then fine-tuned using techniques such as grid search or random search. Finally, the model is evaluated on the testing dataset using appropriate evaluation metrics, including accuracy, precision, recall, F1-score for classification tasks, and RMSE and mean absolute error (MAE) for regression tasks. This final evaluation provides insights into the model's generalization capability and overall effectiveness.

2.3.2. GEP

The GEP is an evolutionary algorithm that creates models and solutions by evolving computer programs or expressions. Developed by Ferreira,[43] the GEP is an extension of genetic programming and genetic algorithms. It combines the strengths of both approaches to effectively solve complex problems in various fields, including artificial intelligence, bioinformatics, and engineering.

Chromosomes and expression trees (ETs), functions and terminals, and fitness functions are three fundamental concepts of the GEP. Chromosomes in GEP are linear strings of fixed length composed of genes, which encode the solutions. Each gene consists of a head and a tail. The head contains functions and terminals, while the tail contains only terminals. These linear chromosomes are translated into ETs, which are the functional representation of the chromosome. ETs are hierarchical structures that represent the solution in a form that can be evaluated. On the other hand, functions are mathematical operations (e.g., addition and subtraction) or logical operations, while terminals are variables or constants that serve as the input for the functions. A fitness function evaluates how well a chromosome solves the problem at hand. It compares the output of the ET with the desired output, assigning a fitness score to each chromosome.[44]

To begin modeling with GEP, the first step is to clearly define the problem, whether it involves regression, classification, or symbolic modeling. After identifying the problem type, a suitable dataset is collected and carefully preprocessed to handle missing values and normalize or standardize features if necessary, ensuring the data quality supports accurate modeling. Once the data is ready, the next step is to split it into training and testing subsets – typically allocating 70–80% of the data for training and the remainder for testing, which allows for evaluation of the model's predictive capability. With the data split, the structure of the GEP model is configured by setting parameters such as the number of genes, head size, function set (e.g., mathematical operators like +, –, *, and/), and terminal set (input variables and constants). The evolutionary process then begins, during which a population of random solutions is generated and evolved over several generations using genetic operators, such as mutation, transposition, and recombination. The fitness of each chromosome is evaluated based on fitness functions, such as mean squared error for regression and classification accuracy for classification tasks. Through successive generations, the population evolves to produce increasingly accurate solutions. Once the model training is complete, the optimally evolved expression or model is selected, and its performance is evaluated on the testing dataset using appropriate metrics. Finally, the resulting symbolic expression can be interpreted and, if necessary, simplified for use in practical applications or further analysis.[45]

2.3.3. ANN

The ANN stands as an advanced mathematical approach proficient in mapping intricate systems rooted in datasets. A prevalent category of ANN is the multilayer perceptron (MLP), which is extensively employed in research studies. The effective deployment of an MLP model necessitates the specification of suitable transfer functions and the configuration of an optimal structure,

taking into account computational efficiency. It is plausible to assess diverse transfer functions to identify the most appropriate one. An ANN may encompass one or more hidden layers. After finalizing the MLP structure (including the number of hidden layers and the number of neurons within each hidden layer), the determination of weights and biases ensues, a phase referred to as model training.[46]

The process of the MLP model design entails a sequence of strategic stages:

(i) Evaluation of hidden layer count: The initial phase involves assessing the optimal number of hidden layers in the network architecture
(ii) Determination of neuron quantity in each layer: The second step entails deciding on the suitable number of neurons within each hidden layer
(iii) Specification of transfer functions: The identification of appropriate transfer functions for neuron activations is pursued
(iv) Selection of training algorithm: The selection of an effective training algorithm for network optimization concludes the design process.

To achieve an optimal MLP model configuration, a systematic approach is adopted. Initially, a single hidden layer is proposed, where the neuronal count aligns with the quantity of input features. Subsequently, various transfer functions, such as log-sig, tan-sig, and pure-line, are systematically assessed. Once an appropriate activation function is determined, the augmentation of predictive precision is pursued. This entails the progressive elevation of the count of hidden layers and neurons within these layers, thereby capturing intricacies within the data and refining model performance through an iterative refinement process.[47]

2.3.4. MARSs

The inception of MARS, attributed to Friedman,[48] has permeated various branches of engineering, particularly hydraulic engineering, demonstrating broad utilization. MARS is an adaptable tool, facilitating the establishment of relationships between independent and dependent variables within a targeted system. By leveraging the MARS method, latent patterns within complex datasets are discerned, unveiling hidden insights in intricate designs. The pattern recognition process involves the proposal of a range of coefficients and basis functions, validated through regression operations performed on the relevant dataset. A key strength of the MARS lies in its aptitude for effectively mapping input parameters to desired outputs, constructing uncomplicated yet resilient models, and offering a judicious balance in computational expense.[49]

To simulate and model a problem using the MARS algorithm, the first step is to define the objective of the modeling process, whether it involves predicting a continuous variable (regression) or classifying data. Once the problem is clearly understood, a relevant dataset is collected and preprocessed by handling missing values, removing outliers if necessary, and normalizing or scaling the features to ensure consistent input data. After preparing the dataset, it is typically divided into training and testing sets to allow for subsequent performance evaluation. The MARS model is then initialized by selecting key parameters, such as the maximum number of basis functions, the degree of interactions allowed between variables, and any penalties for model complexity to prevent overfitting.

The training process begins by allowing the model to construct a set of piecewise linear basis functions, which adaptively split the data at optimal points (called knots). MARS adds these functions in a forward stepwise manner to minimize residual error and capture non-linear relationships and interactions between variables. After building a complex model in the forward phase, a backward pruning process is applied to eliminate redundant or less important basis functions, resulting in a simpler and more generalizable model. Once training is complete, the model's performance is evaluated using the testing dataset. Finally, the resulting MARS model yields an interpretable set of rules or functions that describe the underlying patterns in the data, rendering it useful for both predictions and understanding variable relationships.[50]

2.4. Performance assessment criteria of MLMs

Several key metrics were used to assess the effectiveness of the employed algorithms in ML prediction and forecasting models. These metrics encompassed the R^2, the RMSE, the MAE, and the developed discrepancy ratio (DDR), as detailed in Equations XII-XV.[51]

$$R^2 = \frac{\sum_{i=1}^{N}(O_i - \bar{O})(P_i - \bar{P})}{\sqrt{\sum_{i=1}^{N}(O_i - \bar{O})^2}\sqrt{\sqrt{\sum_{i=1}^{N}(P_i - \bar{P})^2}}} \quad \text{(XII)}$$

$$RMSE = \sqrt{\frac{\sum_{i=1}^{N}(O_i - P_i)^2}{N}} \quad \text{(XIII)}$$

$$MAE = \frac{\left|\sum_{i=1}^{N}(O_i - P_i)\right|}{N} \quad \text{(XIV)}$$

$$DDR=\frac{P}{O}-1 \quad \text{(XV)}$$

Where O and P are observed and predicted values, respectively; $\bar{O}$ and $\bar{P}$ are the mean of the observed and the predicted values, respectively; and N is the total dataset number. The first three criteria assess the mean error values associated with the implemented models. To address this deficiency, Noori *et al*.[51] introduced the DDR index. To enhance interpretation and visualization, the Gaussian distribution of DDR values should be depicted as a standard normal distribution. To achieve this, two steps are followed. First, the DDR values (C_d) are standardized, resulting in the calculation of the normalized DDR value ($C_{d[DDR]}$) using a Gaussian function. Second, a plot is created, where $C_{d(DDR)}$ values are plotted against their standardized counterparts (Z_{DDR}). In the Z_{DDR} vs. $C_{d(DDR)}$ graph, a greater alignment of error distribution toward the centerline and larger $C_{d(DDR)}$ values indicate increased accuracy.

2.5. Overall methodology

Machine learning prediction models were developed using the discussed SVM, GEP, ANN, and MARS methods. Of the aggregate data gathered from the experiments, the proportions allocated for the phases of the model's training and testing were 70% and 30%, respectively. The developed models were then tested for their performance as per the metrics given in Equations XII-XV.

3. Results and discussion

Table 4 presents an overview of the statistical performance criteria for the predicted models. For the establishment of the SVM, an evaluation was conducted on both the RBF and the polynomial kernel function. Subsequent testing of these kernel functions revealed that the RBF kernel function outperformed the polynomial function. In the SVM setup, the values of tuning parameters C and γ were determined as 67 and 5.5, respectively. The values of RMSE, MAE, R^2, and $C_{d(DDRmax)}$ during both the training and testing phases were as follows: 0.02679, 0.02318, 0.79808, and 7.50, respectively; and 0.0113, 0.0066, 0.7573, and 10.36, respectively.

Table 5 summarizes the setting parameters of the superior GEP model. The values for RMSE, MAE, R^2, and $C_{d(DDRmax)}$ were observed as follows: 0.03847, 0.03275, 0.74962, and 5.35, respectively, during the training phase and 0.0181, 0.0109, 0.5624, and 6.32, respectively, during the testing phase. The operators involved in the GEP are +, −, ×,/, √, e^x, ln, x^2, x^3, $x^{\frac{1}{3}}$. Figure 3 demonstrates the ET of the GEP output. The corresponding values in Figure 3 are G1C1 = −0.476807, G2C0=2.40567, G2C1=−0.476807, G3C0=−0.395355, G3C1 = −0.665436. It is worth noting that d0, d1, and d2 stand for $\frac{B}{w_1}$, $\frac{H_d}{P}$, and $\frac{w_1}{w_2}$, respectively.

The MLP model in this study has the following performance metric values (RMSE, MAE, R^2, and $C_{d[DDRmax]}$) associated with it: 0.02426, 0.02031, 0.81602, and 8.07, respectively, during the training phase, and 0.0111, 0.0065, 0.6878, and 11.32, respectively, during the testing phase. The last model employed in this investigation is the MARS model, with performance metrics reaching 0.04995, 0.04381, 0.51011, and 4.02, respectively, during the training phase and 0.0245, 0.0149, 0.5593, and 4.64, respectively, during the testing phase. In the process of the MARS model development, an initial set of 21 basis functions was taken into account during the first step. Subsequently, during the second step (pruning step), 18 of these basis functions were removed. Ultimately, the optimal MARS model, consisting of three basis functions, was obtained. The representation of the acquired MARS model is presented in Equation XVI, while the elaborated representation is detailed in Table 6.

Table 4. Summary of the model performance

Model	Training phase				Testing phases			
	RMSE	MAE	R^2	$C_{d\ (DDRmax)}$	RMSE	MAE	R^2	$C_{d\ (DDRmax)}$
SVM	0.02679	0.02318	0.79808	7.50	0.0113	0.0066	0.7573	10.36
GEP	0.03847	0.03275	0.74962	5.35	0.0181	0.0109	0.5624	6.32
MLP	0.02426	0.02031	0.81602	8.07	0.0111	0.0065	0.6878	11.32
MARS	0.04995	0.04381	0.51011	4.02	0.0245	0.0149	0.5593	4.64

Notes: R^2 is the determination coefficient; $C_{d\ (DDRmax)}$ is the maximum normalized developed discrepancy ratio value.
Abbreviations: GEP: Gene expression programming; MAE: Mean absolute error; MARS: Multivariate adaptive regression splines; MLP: Multilayer perceptron; RMSE: Root mean square error; SVM: Support vector machine.

Table 5. Tuning parameters of the gene expression programming model

Parameter	Value/description
Population size	110
Number of genes	3
Gene head length	10
Gene tail length	11
Mutation rate	0.044
Inversion rate	0.1
Gene transposition rate	0.1
One point recombination rate	0.3
Two-point recombination rate	0.3
Gene recombination rate	0.1
Fitness function	Root mean square error

Table 6. Multivariate adaptive regression splines model's basis functions and their corresponding coefficients

Basis function	Coefficient	Equation
$h_1(x)$	0.0025329	$\text{Max}\left(0, 0.00765854 - \frac{H_d}{P}\right)$
$h_2(x)$	−0.0012013	$\text{Max}\left(0, \frac{B}{w_1} - 1\right)$
$h_3(x)$	0.0020736	$\text{Max}\left(0, \frac{w_2}{w_1} - 0.003\right)$

$$C_d = 0.00409658 + \sum_{i=1}^{3} {}^{2}{}_{m} h_m(X) \quad \text{(XVI)}$$

Figure 4 presents a comparative analysis of the performance of the four distinct models, evaluated through the distribution of data points along a line with a 1:1 slope, during both the training and testing phases. Enhanced model performance is indicated by reduced proximity to this reference line. In the testing phase, the output data of the GEP and MARS models exhibit a notable deviation from the ideal line. In contrast, the MLP and the SVM models demonstrate data distribution closer to the reference line, suggesting their superior performance. The MLP model demonstrates a relatively higher efficacy than the SVM model due to its data's closer alignment with the 1:1 reference line. In general, it can be inferred that among the four models under consideration, the MLP model exhibits greater consistency with the actual measured C_d values. In the data distribution plot of the testing phase, the outcomes unequivocally demonstrate the supremacy of the MLP model in comparison to the remaining three models.

Table 7 presents the statistical indices of the residual values for the output of each of the four MLMs employed in this study during both the training and testing phases. As observed, the MLP model exhibits the lowest deviation in both phases, indicating superior performance in terms of consistency and accuracy. On the other hand, the MARS model shows the highest error in estimating C_d among the four models. The mean prediction errors for the MLP model during the training and testing phases are −0.002 and 0.002, respectively – these are the lowest values among all evaluated models. Conversely, the MARS model demonstrates the highest deviation in this metric. The total residual error for the MLP model is −0.14 in the training phase and 0.086 in the testing phase, which are also the smallest among the models, further confirming its accuracy and robustness. Overall, analysis of the residual error values clearly indicates that the MLP model provides higher prediction accuracy for C_d compared to the other models.

A graphical representation of the residual error variations during the training and testing phases for all four MLMs is provided in Figure 5. In this figure, the residual error values for the MLP model are highlighted in red. As can be seen, the MLP model's errors are closest to the horizontal axis, indicating the highest accuracy (i.e., the smallest deviation) among all models.

Figure 6 presents a comparative evaluation of model performance in the training and testing phases, assessed using the DDR index. As elucidated in the index description, elevated values along the vertical axis, coupled with a bell-shaped curve in its vicinity, signify enhanced performance. Based on these criteria, the MLP model exhibits the best performance in the training and testing phases. The values of $C_{d(DDRmax)}$ for the training and testing stages are 8.07 and 11.32, respectively. Subsequently, the SVM, GEP, and MARS models sequentially secure the second to fourth positions in terms of performance ranking.

Predicting C_d of different weirs is important due to various hydraulic and environmental reasons. The C_d governs the flow over the weirs; therefore, it determines the efficiency of flow, which can be handled over the weir. The flood water discharges or diversion over the weir can be efficiently and optimally controlled through accurate prediction of the weir C_d. Labyrinth weirs are capable of increasing discharges without raising the headwater level. Therefore, these are fine hydraulic structures for water control in reservoirs and irrigation systems. In addition, accurate C_d predictions prevent

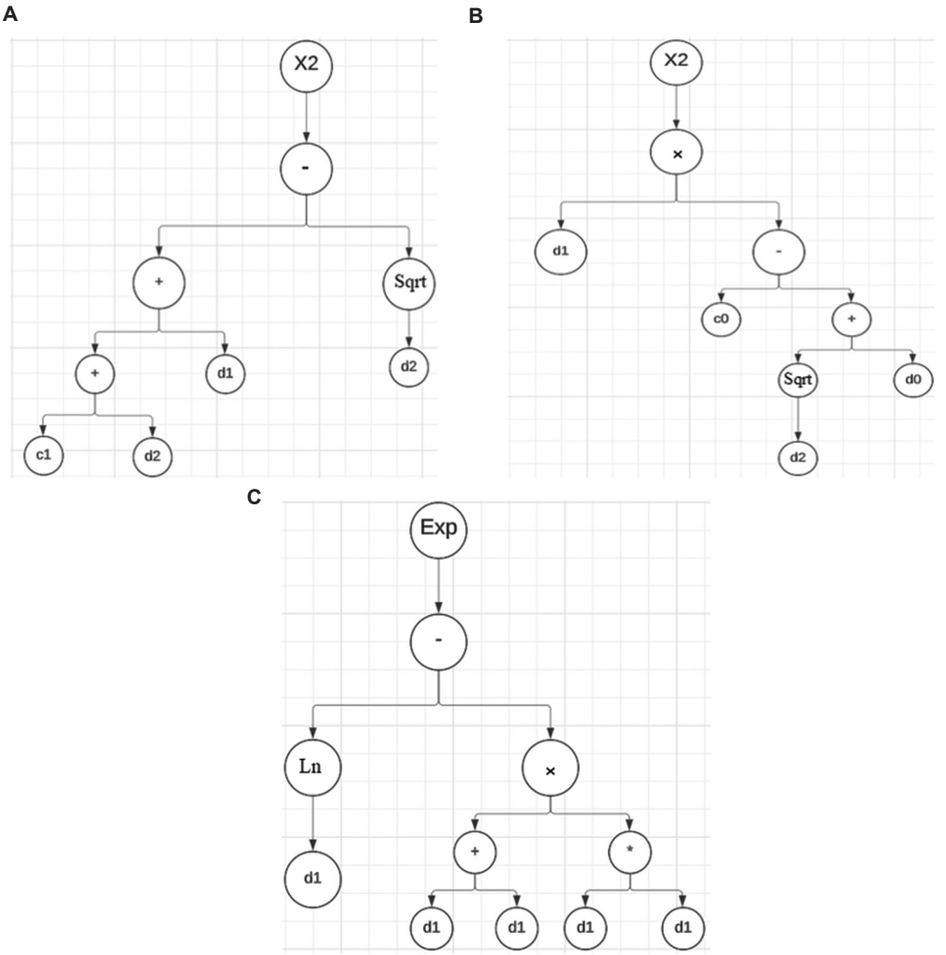


Figure 3. Developed gene expression programming output. (A) Sub-expression tree 1. (B) Sub-expression tree 2. (C) Sub-expression tree 3.

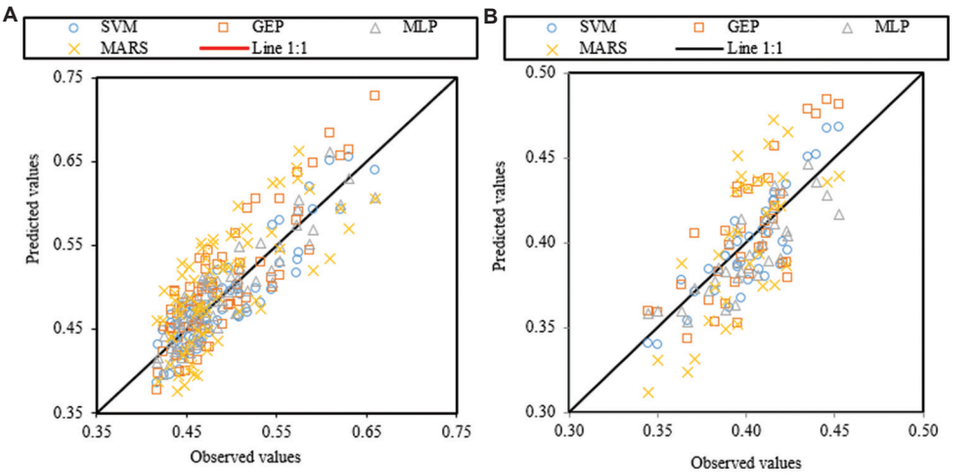


Figure 4. Scatter plots of the observed and predicted values of the C_d across the four models. (A) Training phase. (B) Testing phase.

Abbreviations: GEP: Gene expression programming; MARS: Multivariate adaptive regression splines; MLP: Multilayer perception; SVM: Support vector machine.

Table 7. Residual analysis of the machine learning models' outputs

Model	Training phase				Testing phase			
	Maximum	Minimum	Mean	Sum	Maximum	Minimum	Mean	Sum
SVM	0.0549	−0.041	0.006	0.454	0.0327	−0.022	0.004	0.140
GEP	0.0485	−0.078	−0.012	−0.862	0.0440	−0.043	−0.004	−0.146
MLP	0.0393	−0.052	−0.002	−0.140	0.0235	−0.028	0.002	0.086
MARS	0.0743	−0.090	−0.013	−0.902	0.0431	−0.071	−0.005	−0.191

Abbreviations: GEP: Gene expression programming; MARS: Multivariate adaptive regression splines; MLP: Multilayer perceptron; SVM: Support vector machine.

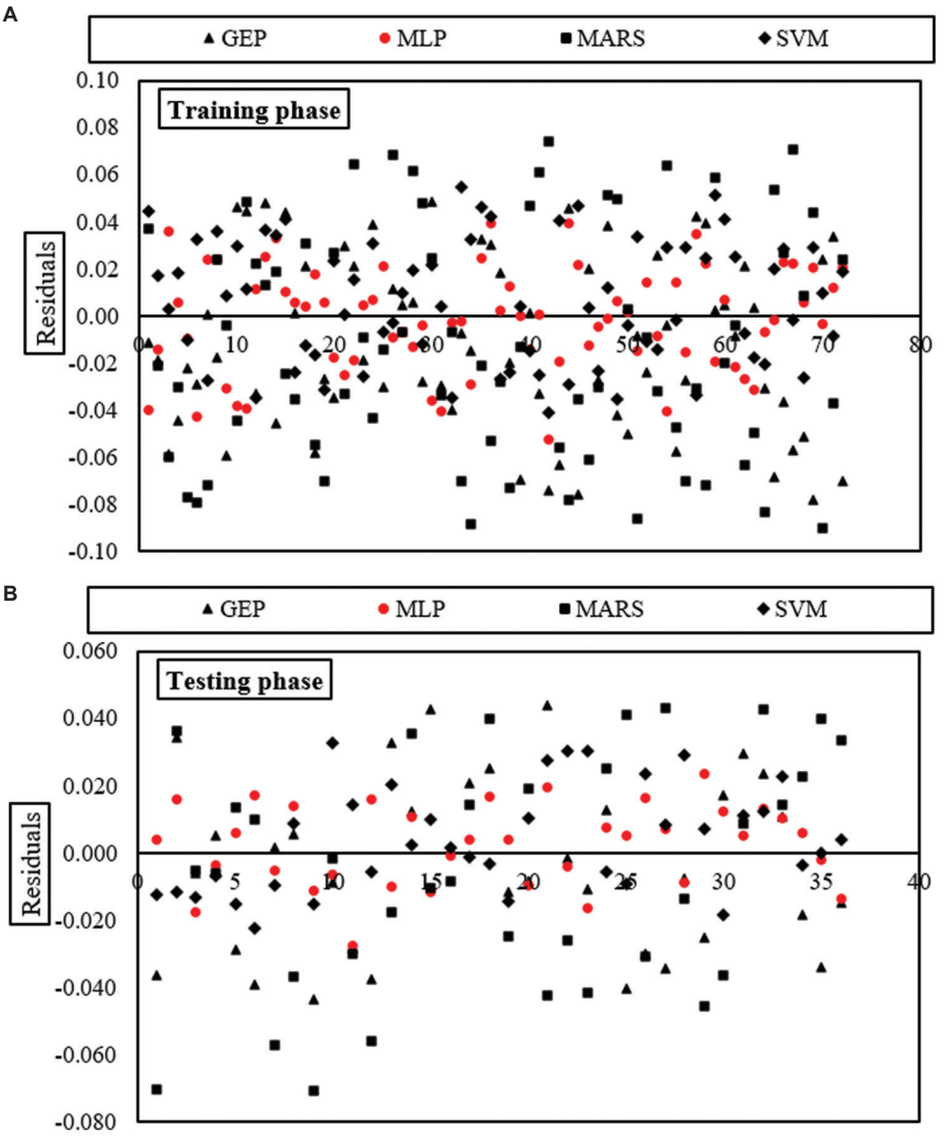


Figure 5. Residual error variation of the machine learning models' outcomes. (A) Training phase. (B) Testing phase.

Abbreviations: GEP: Gene expression programming; MARS: Multivariate adaptive regression splines; MLP: Multilayer perception; SVM: Support vector machine.

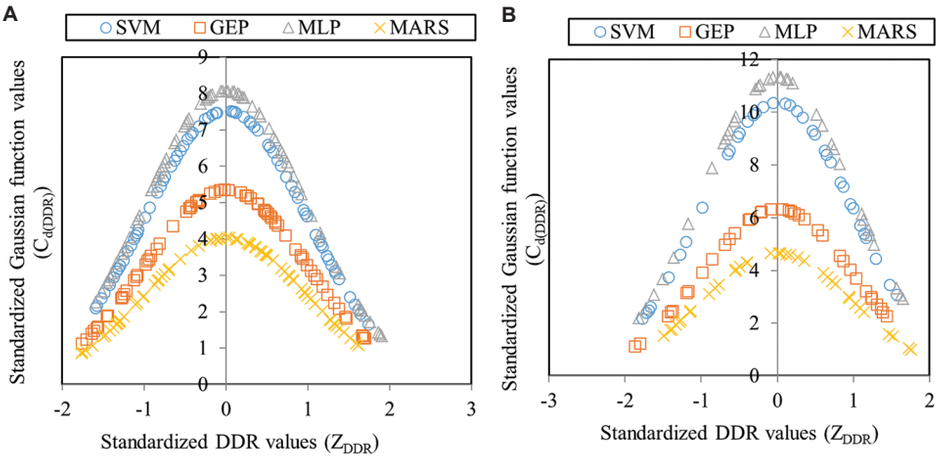


Figure 6. Performance assessment of the machine learning models' outcome using the DDR index. (A) Training phase. (B) Testing phase.

Abbreviations: GEP: Gene expression programming; MARS: Multivariate adaptive regression splines; MLP: Multilayer perception; SVM: Support vector machine.

overdesigns or underdesigns and save construction costs. They also allow proper overtopping from dams and prevent or mitigate dam failures in extreme weather conditions. Climate change has significantly enhanced the chances of extreme weather conditions; therefore, some of the hydraulic structures made for usual weather conditions might not withstand properly. Therefore, having an accurately predicted labyrinth weir in such conditions would be beneficial.

Ecosystem protection is another attribute of the properly designed labyrinth weir. Downstream soil erosion and excessive sediment transportation can be mitigated through the accurate prediction of C_d. These advantages are aligned with the Sustainable Development Goals (SDGs) – SDG6: clean water and sanitation, SDG9: industry, innovation, and infrastructure, SDG 11: sustainable cities and communities, SDG 13: climate action, and SDG 15: life on land. Therefore, the research presented here has a greater practical potential in achieving the SDGs. Furthermore, the impact on developing countries would be significant. Labyrinth weirs are more cost-effective compared to traditional spillways and offer greater benefits to rural communities facing water management challenges.

4. Conclusion

Given the pivotal significance of C_d in the operational efficacy of weirs, alongside the advancing application of data-driven models for predicting this coefficient, the avenue for forthcoming research in the domain of TALW is explored. The present research employed four distinct models – SVM, GEP, MLP, and MARS – to anticipate the C_d of TALW. The assessment of performance evaluation metrics, while affirming the capabilities of the quartet mentioned above, revealed the preeminence of the MLP model in contrast to its three counterparts. This ascendancy was consistently evident across both the training and testing phases. The outcomes underscored that the SVM, GEP, and MARS models secured successive positions as commendable simulators following the MLP model.

While this study provides robust MLMs for predicting C_d in TALW under controlled laboratory conditions, translating these findings to field applications faces inherent limitations. Laboratory models assume optimal structural integrity, whereas field structures are subjected to factors such as concrete erosion, joint displacement, and corrosion over time, which may alter their hydraulic performance. Furthermore, reservoir sedimentation and organic debris accumulation – both absent in lab settings – can reduce effective crest length and amplify local head losses, systematically biasing C_d. Field environments also introduce hydrologic uncertainties, such as stage measurement errors (e.g., gauge drift and thermal effects) and unsteady flow regimens not replicated in steady-state experiments. Critically, neglected maintenance (e.g., spillway cracking and gate misalignment) may induce unexpected flow behavior, as evidenced by real-world failures like the Oroville Dam incident in 2017,[52] where operational stresses exceeded design assumptions. These real-world complexities necessitate field validation of the models and the integration of probabilistic safety margins in

design protocols to account for infrastructure aging and measurement uncertainties.

Acknowledgments

None.

Funding

None.

Conflict of interest

Upaka Rathnayake is an Editorial Board Member of this journal but was not in any way involved in the editorial and peer-review process conducted for this paper, directly or indirectly. Separately, other authors declared that they have no known competing financial interests or personal relationships that could have influenced the work reported in this paper.

Author contributions

Conceptualization: Mohammad Heidarnejad, Jamal Feili
Formal analysis: Mehdi Fuladipanah
Methodology: Upaka Rathnayake, Mohammad Heidarnejad
Writing–original draft: Mehdi Fuladipanah
Writing–review & editing: Upaka Rathnayake, Mohammad Heidarnejad

Availability of data

The data that support the findings of this study are available on request from the corresponding author. The data are not publicly available due to privacy or ethical restrictions.

References

1. Afaridegan E, Amanian N, Parsaie A, Gharehbaghi A. Hydraulic investigation of modified semi-cylindrical weirs. *Flow Meas Instrum.* 2023;93:102405. doi: 10.1016/j.flowmeasinst.2023.102405
2. Bekheet AA, AboulAtta NM, Saad NY, El-Molla DA. Effect of the shape and type of piano key weirs on the flow efficiency. *Ain Shams Eng J.* 2022;13(3):101620. doi: 10.1016/j.asej.2021.10.015
3. Nourani B, Arvanaghi H, Pourhosseini FA, Javidnia M, Abraham J. Enhanced support vector machine with particle swarm optimization and genetic algorithm for estimating discharge coefficients of circular-crested oblique weirs. *Iran J Sci Technol Trans Civil Eng.* 2023;47(5):3185-3198. doi: 10.1007/s40996-023-01110-0
4. Roushangar K, Alami MT, Shiri J, Asl MM. Determining discharge coefficient of labyrinth and arced labyrinth weirs using support vector machine. *Hydrol Res*. 2018;49(3):924-938. doi: 10.2166/nh.2017.214
5. Taylor G. *The Performance of Labyrinth Weirs*. PhD Thesis. Nottingham, UK: University of Nottingham; 1968.
6. Hay N, Taylor G. Performance and design of labyrinth weirs. *J Hydraul Div.* 1970;96(11):2337-2357. doi: 10.1061/JYCEAJ.0002766
7. Lux F. Design and construction of labyrinth spillways. In: *15th Commission Internationale des Grands Barrages*. Ontario: Canadian Dam Association; 1985. p. 249-274.
8. Kocahan H, Taylor G. Rehabilitation of Black Rock Dam (Seepage & Inadequate Spillway). In: *Association of State Dam Safety Officials Conference*. Arlington, VA, USA; 2002.
9. Crookston BM, Tullis B. *Labyrinth Weirs*. *Hydraulic Structures*. Vol. 59. United States: Utah States University; 2010.
10. Christensen NA, Tullis BP. *Arced Labyrinth Weir Flow Characteristics*. United States: Utah States University; 2012.
11. Seamons TR. *Labyrinth Weirs: A Look into Geometric Variation and its Effect on Efficiency and Design Method Predictions*. United States: Utah State University; 2014.
12. Bijankhan M, Kouchakzadeh S. Unified discharge coefficient formula for free and submerged triangular labyrinth weirs. *Flow Meas Instrum.* 2017;57:46-56. doi: 10.1016/j.flowmeasinst.2017.08.007
13. Monjezi R, Heidarnejad M, Masjedi A, Purmohammadi MH, Kamanbedast A. Laboratory investigation of the discharge coefficient of flow in arced labyrinth weirs with triangular plans. *Flow Meas Instrum.* 2018;64:64-70. doi: 10.1016/j.flowmeasinst.2018.10.011
14. Seyedian SM, Haghiabi A, Parsaie A. Reliable prediction of the discharge coefficient of triangular labyrinth weir based on soft computing techniques. *Flow Meas Instrum.* 2023;92:102403. doi: 10.1016/j.flowmeasinst.2023.102403
15. Zare H, Vaghefi M, Mahmoudi A, Behroozi AM. Experimental exploration of flow hydraulics and discharge coefficient for an inclined circular labyrinth weir. *Water Resour Manag.* 2023;37(11):4521-4536. doi: 10.1007/s11269-023-03577-y
16. Nematollahi S, Izadinia E, Khoshfetrat A. Investigation of discharge coefficient and flow energy loss in sinusoidal-labyrinth weirs. *Iran J Sci Technol Trans Civil Eng.* 2025:1-10.

doi: 10.1007/s40996-025-01820-7
17. Ahmed AM, Altalib AN. Determination of discharge coefficient of arced labyrinth weir with semicircular openings. *Iran J Sci Technol Trans Civil Eng.* 2025:1-12. doi: 10.1007/s40996-025-01747-z
18. Masoudi MH, Yari A, Sadeghian J, Norouzi H. Experimental investigation of the discharge coefficient of the rectangular and trapezoidal labyrinth weirs considering variable congress lengths. *Model Earth Syst Environ.* 2024;10(2):2819-2832. doi: 10.1007/s40808-023-01925-w
19. Hadi ZM, Majeed HQ. Experimental and Numerical Study of the Discharge Capacity of a Labyrinth Side Weir in a Straight Channel. *In: AIP Conference Proceedings*. Vol. 3091. Melville, NY: AIP Publishing; 2024.
20. Darvas LA. Discussion of performance and design of labyrinth weirs, by Hay and Taylor. *J Hydraul Eng.* 1971;97:1246-51.
21. Lux F, Hinchliff D. Design and Construction of Labyrinth Spillways. *In: 15th Congress International Commission on Large Dams ICOLD*. Vol. 4. Lausanne, Switzerland: 1985. p. 249-274.
22. Melo JF, Ramos CM, Magalhães AP. Descarregadores Com Soleira em Labirinto de um Ciclo em Canais Convergentes. In: *Determinação da Capacidade de Vazão Proceedings 6th Congresso da Água*. 2002.
23. Crookston BM. *Labyrinth Weirs*. Doctor of Philosophy, Utah State University [PhD Dissertation]; 2010.
24. Emiroglu ME, Kaya N, Agaccioglu H. Discharge capacity of labyrinth side weir located on a straight channel. *J Irrig Drain Eng.* 2009;136(1):37-46. doi: 10.1061/(ASCE)IR.1943-4774.0000112
25. Karami H, Karimi S, Bonakdari H, Shamshirband S. Predicting discharge coefficient of triangular labyrinth weir using extreme learning machine, artificial neural network and genetic programming. *Neural Comput Appl.* 2018;29(11):983-989. doi: 10.1007/s00521-016-2588-x
26. Bonakdari H, Ebtehaj I, Gharabaghi B, Sharifi A, Mosavi A. Prediction of discharge capacity of labyrinth weir with gene expression programming. *In: Proceedings of SAI Intelligent Systems Conference*. Cham: Springer International Publishing; 2020. p. 202-217. doi: 10.1007/978-3-030-55180-3_17
27. Khani M, Shabanlou S. Assessment of discharge coefficient in trapezoidal and rectangular canals through regularized extreme learning machine. *Measurement*. 2021;180:109493. doi: 10.1016/j.measurement.2021.109493
28. Mahmoud A, Hu T, Zeng X, Jing P, Li X, Ribeiro EDC. Hydraulic informed multi-layer perceptron for estimating discharge coefficient of labyrinth weir. *Eng Appl Artif Intell.* 2023;123:106435. doi: 10.1016/j.engappai.2023.106435
29. Emami H, Emami S, Parsa J. A walnut optimization algorithm applied to discharge coefficient prediction on labyrinth weirs. *Soft Comput.* 2022;26:12197-12215. doi: 10.1007/s00500-022-07041-8
30. Majedi-Asl M, Fuladipanah M, Arun V, Tripathi RP. Using data mining methods to improve discharge coefficient prediction in piano key and labyrinth weirs. *Water Supply.* 2022;22(2):1964-1982. doi: 10.2166/ws.2021.304
31. Mustafa M, Mansoor T, Muzzammil M. Support vector machine (SVM) approach to develop the discharge prediction model for triangular labyrinth weir. *Water Supply.* 2022;22:8942-8956. doi: 10.2166/ws.2022.393
32. Wang F, Zheng S, Ren Y, Liu W, Wu C. Application of hybrid neural network in discharge coefficient prediction of triangular labyrinth weir. *Flow Measure Instrument.* 2022;83:102108. doi: 10.1016/j.flowmeasinst.2021.102108
33. Hu Z, Karami H, Rezaei A, *et al*. Using soft computing and machine learning algorithms to predict the discharge coefficient of curved labyrinth overflows. *Eng Appl Comput Fluid Mech.* 2021;15(1):1002-1015. doi: 10.1080/19942060.2021.1934546
34. Mahmoud A, Yuan X, Hajilounezhad T, Yuan Y. Investigation on labyrinth spillway multi-objective optimization with an emphasis on predicting discharge coefficient through different artificial neural networks. *Measurement*. 2021;174:109036. doi: 10.1016/j.measurement.2021.109036
35. Shafiei S, Najarchi M, Shabanlou SA. Novel approach using CFD and neuro-fuzzy-firefly algorithm in predicting labyrinth weir discharge coefficient. *J Braz Soc Mech Sci Eng.* 2020;42:44. doi: 10.1007/s40430-019-2109-9
36. Norouzi P, Rajabi A, Izadbakhsh MA, Shabanlou S, Yosefvand F, Yaghoubi B. A new non-tuned self-adaptive machine-learning approach for simulating the discharge coefficient of labyrinth weirs. *Irrig Drainag.* 2020;69(3):398-416. doi: 10.1002/ird.2423
37. Olyaie E, Banejad H, Heydari M. Estimating discharge coefficient of PK-weir under subcritical conditions based on high-accuracy machine learning approaches. *Iran J Sci Technol Trans Civil Eng.* 2019;43:89-101. doi: 10.1007/s40996-018-0150-z
38. Roushangar K, Alami MT, Shiri J, Asl MM. Determining discharge coefficient of labyrinth and arced labyrinth weirs using support vector machine. *Hydrol Res.* 2018;49(3):924-938. doi: 10.2166/nh.2017.214
39. Uyumaz A, Danandeh Mehr A, Kahya E, Erdem H. Rectangular side weirs discharge coefficient estimation in circular channels using linear genetic programming approach. *J Hydroinform.* 2014;16(6):1318-1330. doi: 10.2166/hydro.2014.112

40. Emiroglu ME, Kisi O. Prediction of discharge coefficient for trapezoidal labyrinth side weir using a neuro-fuzzy approach. *Water Resour Manag.* 2013;27:1473-1488. doi: 10.1007/s11269-012-0249-0
41. Cortes C, Vapnik V. Support-vector networks. *Mach Learn.* 1995;20:273-297. doi: 10.1007/BF00994018
42. Sandamal K, Shashiprabha S, Muttil N, Rathnayake U. Pavement roughness prediction using explainable and supervised machine learning technique for long-term performance. *Sustainability*. 2023;15(12):9617. doi: 10.3390/su15129617
43. Ferreira C. Gene expression programming: A new adaptive algorithm for solving problems. *Complex Syst*. 2001;13:87-129. doi: 10.48550/arXiv.cs/0102027
44. Fuladipanah M, Shahhosseini A, Rathnayake N, *et al*. In-depth simulation of rainfall-runoff relationships using machine learning methods. *Water Pract Technol.* 2024;19(6):2442-2459. doi: 10.2166/wpt.2024.147
45. Perera A, Hazi MD, Upaka R. Comparison of different artificial neural network (ANN) training algorithms to predict the atmospheric temperature in Tabuk, Saudi Arabia. *MAUSAM*. 2021;71(2):233-244. doi: 10.54302/mausam.v71i2.22
46. Agbasi JC, Egbueri JC. Prediction of potentially toxic elements in water resources using MLP-NN, RBF-NN, and ANFIS: A comprehensive review. *Environ Sci Pollut Res Int*. 2024;31:30370-30398. doi: 10.1007/s11356-024-33350-6
47. Lukas P, Melesse AM, Kenea TT. Predicting reservoir sedimentation using multilayer perceptron - artificial neural network model with measured and forecasted hydrometeorological data in gibe-III reservoir, omo-gibe river basin, Ethiopia. *J Environ Manag.* 2024;359:121018. doi: 10.1016/j.jenvman.2024.121018
48. Friedman JH. Multivariate adaptive regression splines. *Ann Statis.* 1991;19:1-67. doi: 10.1214/aos/1176347963
49. Garai S, Paul RK, Yeasin M, Paul AK. CEEMDAN-based hybrid machine learning models for time series forecasting using MARS algorithm and PSO-optimization. *Neural Process Lett.* 2024;56(2):92. doi: 10.1007/s11063-024-11552-w
50. Fuladipanah M, Azamathulla HM, Kisi O, Kouhdaragh M, Mandala V. Quantitative forecasting of bed sediment load in river engineering: An investigation into machine learning methodologies for complex phenomena. *Water Supply*. 2024;24(2):585-600. doi: 10.2166/ws.2024.017
51. Noori R, Khakpour A, Omidvar B, Farokhnia A. Comparison of ANN and principal component analysis-multivariate linear regression models for predicting the river flow based on developed discrepancy ratio statistic. *Expert Syst Appl.* 2010;37(8):5856-5862. doi: 10.1016/j.eswa.2010.02.020
52. Koskinas A, Tegos A, Tsira P, *et al*. Insights into the Oroville dam 2017 spillway incident. *Geosciences*. 2019;9(1):37. doi: 10.3390/geosciences9010037

Asian Journal of Water, Environment and Pollution. Vol. 22, No. 6 (2025), pp. 89-102.
doi: 10.36922/AJWEP025250204

ORIGINAL RESEARCH ARTICLE

Enhanced adsorption desulfurization performance of metal-modified Y zeolites

Jiefei Li[1]*, Xianrong Meng[1], Mingyang Song[1], and Mei Xue[2]*

[1]Department of Chemical Engineering and Technology, School of Petrochemical Engineering, Shenyang University of Technology, Liaoyang, Liaoning, China
[2]Department of Materials Physics and Chemistry, School of Chemistry and Chemical Engineering, Inner Mongolia University, Hohhot, Inner Mongolia, China
***Corresponding authors:** Jiefei Li (lijf@sut.edu.cn);
Mei Xue (setsubai@sina.cn)

Received: June 20, 2025; Revised: July 22, 2025; Accepted: July 25, 2025; Published online: August 18, 2025

Abstract: Y-zeolite is a promising adsorbent for removing organic sulfides from fuel. However, its application is limited by low adsorption capacity for refractory sulfur compounds. In this study, metal-modified Y-zeolite (MY) adsorbents, incorporating Ru^{3+}, Bi^{3+}, Zr^{4+}, and Sb^{3+} ions, were successfully synthesized via a solid-state reaction method. X-ray diffraction analysis confirmed that metal ion incorporation did not alter the crystalline framework of Y-zeolite. Nitrogen adsorption–desorption isotherms revealed that the Ru-modified Y-zeolite (RuY) possessed a notably high specific surface area of 735.23 m^2/g, whereas NH_3-temperature programmed desorption (NH_3-TPD) measurements showed that it also had the highest concentration of acidic sites (2.375 mmol/g). The effects of metal ion type, loading amount, and oxidation state on thiophene removal were systematically investigated via batch adsorption experiments. Sulfur removal efficiency increased in the following order: HY (43%) <BiY-1 (53%) <SbY-1(62%) <ZrY-1 (63%) <RuY-1 (68%). The RuY adsorbent exhibited the best adsorption performance, with Ru^{4+} ions acting as the primary active sites. The adsorption behavior followed the Langmuir isotherm model, indicating a monolayer adsorption process. Sulfur removal efficiency correlated positively with the sulfur–metal (S–M) bond strength in MY adsorbents. Compared to unmodified HY, MY adsorbents also showed improved selectivity for thiophene in the presence of competing toluene. The superior desulfurization performance of RuY is attributed to its smaller ionic radius (62 pm), higher charge (Ru^{4+}), larger specific surface area, and abundance of Lewis acid sites.

Keywords: Adsorption; Metal ion; Y-zeolite; Thiophene; Desulfurization

1. Introduction

Commercial gasoline and diesel typically contain 300–500 parts per million by weight (ppmw) of organic sulfur compounds, contributing to sulfur oxide emissions, acid rain, and particulate matter pollution.[1,2] Removing these compounds is crucial, but conventional hydrodesulphurization (HDS), though effective for sulfides, struggles to eliminate thiophene and its alkylated derivatives.[3] Ultra-low sulfur fuels (<1 ppmw) are vital for fuel cells to prevent catalyst poisoning.[4] Among various desulfurization methods, adsorption has attracted considerable attention for its ability to achieve deep desulfurization under ambient conditions.[5]

Metal ion-modified porous materials employed in the adsorption processes include zeolite, mesoporous materials, activated carbon, silica gel, alumina, mixed metal oxides, and metal organic frameworks (MOF_S).[6-13] Y-zeolite, a prototypical large-pore molecular sieve, has attracted considerable attention in adsorptive

desulfurization owing to its three-dimensional interconnected supercage structure (pore diameter ~1.3 nm) and exceptionally high specific surface area (>700 m^2/g). Its framework is enriched with abundant Brønsted and Lewis acid sites, facilitating acid-base interactions with sulfur-containing molecules and enabling efficient removal of bulky organosulfur compounds such as thiophene, benzothiophene, and dibenzothiophene. Furthermore, Y-zeolite exhibits outstanding thermal stability and highly tunable structural properties, which can be optimized through ion exchange, steam treatment, and chemical modifications.

Nevertheless, pristine Y-zeolite suffers from inherent limitations in practical applications. Its adsorption primarily relies on physical interactions and weak acid-base affinities, which are inadequate for capturing low-polarity, refractory sulfur species. Moreover, competitive adsorption of non-sulfur aromatic hydrocarbons in complex fuel matrices leads to poor selectivity, hindering the achievement of deep desulfurization at ultra-low sulfur levels (<10 ppm). In addition, repeated adsorption-regeneration cycles tend to degrade the framework's acidity and pore architecture, ultimately compromising long-term operational stability.

Incorporating metal ions into adsorbents has been shown to enhance their performance, as the introduced metal species can act as active sites for the adsorption of sulfur-containing compounds. Most studies have focused on reactive adsorption mechanisms, which can be broadly categorized into two types: (i) π-complexation-based adsorbents, such as metal-ion-exchanged Y-type zeolites (denoted as MY-zeolites, where M represents metal ions including copper(I) (Cu^+), silver(I) (Ag^+), nickel(II) (Ni^{2+}), zinc(II) (Zn^{2+}), and palladium(II) (Pd^{2+})); and (ii) adsorbents that rely on direct sulfur–metal (S–M) interactions, where the Y-type zeolite is modified with high-charge metal ions such as cerium(IV) (Ce^{4+}) and lanthanum(III) (La^{3+}).[14,15] Compared to adsorbents based on π-complexation, those utilizing direct S–M interactions generally demonstrate higher selectivity for sulfur compounds, particularly in the presence of competing aromatic hydrocarbons. Recently, new zeolite nanofiber bundle catalysts developed by Tang *et al.* demonstrated sulfur reduction to below 10 ppmw in diesel using the HDS process.[16] This has underscored the importance of adsorption selectivity over sulfur uptake in achieving the ultra-low sulfur fuel standard. A lot of high-selectivity sulfur adsorbents incorporating Ce-modified microporous materials have been reported, such as CeY,[17,18] Ce-modified mesoporous structure Y-zeolite,[19,20] Ce-doped MCM-41 frameworks,[21] aluminized MCM-41 and SBA-15 grafted with Ce^{3+},[22] Ni-Ce/alumina-silica (Al_2O_3-SiO_2),[23] Ce-Fe/activated carbon (AC) composites.[24] A few studies have also reported on the use of ruthenium complexes for the extraction of dibenzothiophene (DBT) from petroleum feedstocks. For instance, the binuclear ruthenium complex, $[CpRu(CO)_2(\mu_2\text{-}\eta^1(S)\text{: }\eta^6\text{-DBT})RuCp^*][PF_6]_2$ was used for desulfurization of DBT, in which one Ru is η^1(S)-coordinated to DBT whereas the other Ru is η^6(S)-coordinated to the same DBT molecule.[25,26] As noted, the strength of the direct S–M σ bond is mainly dependent on the metal ion's charge and ionic radius. Specific metal ions with strong ionic polarities are able to enhance direct S–M interaction and further improve adsorption selectivity for sulfur compounds.

Traditionally, the liquid phase ion-exchange method has been used to prepare the metal ion-modified Y-zeolites,[14,15,27,28] while only a few studies have explored the solid state reaction method.[29,30] In this study, the solid-state reaction method was used to develop high-selectivity S–M interaction adsorbents. A series of metal ions with high charge number and lower ionic radius—namely, ruthenium(III) (Ru^{3+}), bismuth(III) (Bi^{3+}), zirconium(IV) (Zr^{4+}), and antimony (III) (Sb^{3+})—were selected as active sites for the modification of Y-zeolite. The desulfurization performance of these MY-zeolite adsorbents was evaluated using batch adsorption of thiophene (TP) from a model gasoline containing 20 ppmw sulfur. We investigated the effect of various parameters, such as the metal type, metal ion form, chemical state, and loading amount, on the TP removal efficiency.

2. Materials and methods

2.1. Preparation of MY-zeolite (MY-1 and RuY-X series) adsorbents

Metal-ion-modified Y-type zeolite adsorbents were prepared using the solid-state ion exchange method. One gram of ammonium-exchanged Y-zeolite (NH_4Y-zeolite) was thoroughly mixed and ground for 1 h with a stoichiometric amount of ruthenium(III) chloride hydrate ($RuCl_3 \cdot xH_2O$), antimony(III) chloride ($SbCl_3$), zirconyl chloride octahydrate ($ZrOCl_2 \cdot 8H_2O$), or bismuth(III) nitrate pentahydrate ($Bi(NO_3)_3 \cdot 5H_2O$), with an initial molar ratio of metal ion to ammonium ion (M/NH_4^+) equal to 1. The mixtures were subsequently calcined in air at 500°C for 2 h. These resulting adsorbents were denoted as MY-1 and RuY-X, where M represents the metal ion (Ru^{3+}, Sb^{3+}, Zr^{4+}, or Bi^{3+}), and X indicates the initial molar ratio of ruthenium(III)

to ammonium ion. The NH_4Y-zeolite was obtained from Wako, Japan (SiO_2/Al_2O_3 = 7.0), whereas all metal salts—$RuCl_3 \cdot xH_2O$ (37.5% Ru), $ZrOCl_2 \cdot 8H_2O$ (99%), $SbCl_3$ (99%), and $Bi(NO_3)_3 \cdot 5H_2O$ (99%)—were purchased from Sinopharm Group Chemical Reagent (China). The hydrogen-form Y-zeolite (HY sample) was prepared by calcining the NH_4Y-zeolite at 500°C for 2 h in air.

2.2. Adsorption experiment

Adsorption experiments were performed using a batch method. A model gasoline solution was prepared consisting of n-heptane (99 wt%), toluene (1 wt%), and TP (20 ppmw of sulfur). N-heptane (98.5%), TP (99%), and toluene (99%) were purchased from Sinopharm Group Chemical Reagent (China). The model gasoline (10 mL) and the adsorbent (0.1 g) were mixed in a Teflon tube, and the mixture was stirred at 80°C. After adsorption, the sulfur concentration in the liquid phase was analyzed using a gas chromatograph with a flame ionization detector (GC-FID; Agilent 7890, Agilent Technologies Co., LTD., USA) equipped with a capillary column (Thermo TG-WAXMS; USA; 30 m × 0.53 mm × 1 μm).

The adsorption capacity (q_e) and sulfur removal efficiency were calculated using Equations I and II.

$$q_e = \frac{V(C_0 - C_i)}{m} \quad \text{(I)}$$

$$\text{Sulfur removal } (\%) = \frac{(C_0 - C_i)}{C_0} \times 100 \quad \text{(II)}$$

where V (mL) is the volume of model gasoline; C_0 and C_i (mg/L) are the concentrations of sulfur in the model gasoline before and after adsorption, respectively; and m (g) is the mass of adsorbents.

2.3. Adsorbent characterization

The powder X-ray diffraction (XRD) patterns were performed on a PANalytical Empyrean diffractometer (PANalytical B.V., Holland) operated at 40 kV and 40 mA, using copper K-alpha radiation. X-ray photoelectron spectroscopy (XPS) analysis was carried out using a THS-103X spectrometer (Thermo Fisher Scientific, USA) equipped with an aluminum K-alpha X-ray source (photon energy, hv = 1486.6 eV). The nitrogen (N_2) adsorption-desorption isotherms were measured on a 3H-2000PM2 system (Tianjin Xianquan Instrument Co., LTD, China) at –196°C. The adsorbents were degassed at 300°C for 5 h. The Horvath–Kawazoe (HK) method was used to calculate the surface area, based on adsorption data in the relative pressure range from 0.0000165 to 0.1546. The pore width and volume were also calculated using the HK method. Hydrogen temperature-programmed reduction (H_2-TPR) of the adsorbents was measured by a Micromeritics AutoChem 2920 analyzer (Micromeritics Instrument Co., LTD, USA). The adsorbents were swiped at 300°C for 30 min under helium flow (10 mL/min) and then cooled to 40°C before being reacted with H_2. The profile was recorded by increasing the temperature from 100°C to 800°C at a ramp rate of 10°C/min.

Temperature-programmed desorption of ammonia (NH_3-TPD) was used to calculate the intensity and number of acidic sites in the adsorbents. This was conducted using a TP-5080 automatic analyzer (Tianjin Xianquan Instrument Co., LTD, China). About 0.1 g of adsorbent was placed in a U-shaped quartz microreactor. The adsorbent was activated at 550°C for 30 min under helium flow (20 mL/min), cooled to 100°C, then exposed to ammonia. The adsorbents were flushed again in helium for 3 h to remove any physisorbed ammonia. A desorption profile was then recorded by increasing the adsorbent temperature from 100°C to 800°C at a ramp rate of 10°C/min.

The pyridine-Fourier transform infrared (Py-FTIR) was used to analyze the amount and type of acidic sites, with pyridine as the probe molecule. Measurements were conducted using an FTIR spectrometer (Tensor 27, BRUKER Technology Co., LTD, USA). Transmission electron microscopy (TEM) imaging was performed on a FEI Tecnai F20 system (FEI Co., LTD, USA) operated at an accelerating voltage of 200 kV. The size and morphology of the adsorbents were observed by using field emission scanning electron microscopy (FE-SEM) (Hitachi s-4800, Hitachi, Japan).

3. Results and discussion

3.1. Adsorbent characterization

3.1.1 XRD analysis of adsorbents

XRD patterns of the MY-1 adsorbents and NH_4Y-zeolite are shown in Figure 1. Both adsorbents maintained the characteristic framework structure of NH_4Y-zeolite framework, although a reduction in the intensity of some diffraction peaks was observed for the MY-1 samples. This decrease is attributed to partial lattice collapse following calcination treatment. In addition to the typical diffraction peaks of NH_4Y-zeolite, the BiY-1, ZrY-1, and RuY-1 samples exhibited the additional peaks corresponding to the oxide phases of the incorporated metals. Specifically, diffraction peaks for

Bi_2O_3 at the (012) plane (JCPDF No.: 41-1449), ZrO_2 at the (111) plane (JCPDF No.: 37-1484), and RuO_2 at the (101) and (110) planes (JCPDF No.: 43-1027) were observed. Interestingly, SbY-1 did not show detectable diffraction peaks corresponding to Sb oxide. However, energy-dispersive X-ray spectroscopy (EDX) analysis (Figure S1B) confirmed the presence of Sb elements, suggesting a high degree of homogeneity and dispersion of Sb within the Y-zeolite matrix.

These results indicate that, except for SbY-1, the MY-1 adsorbents consist of two distinct phases: a MY-zeolite phase and a bulk metal oxide phase (M_xO_y). In contrast, SbY-1 appears to be a single-phase system with Sb ions uniformly dispersed within the zeolite.

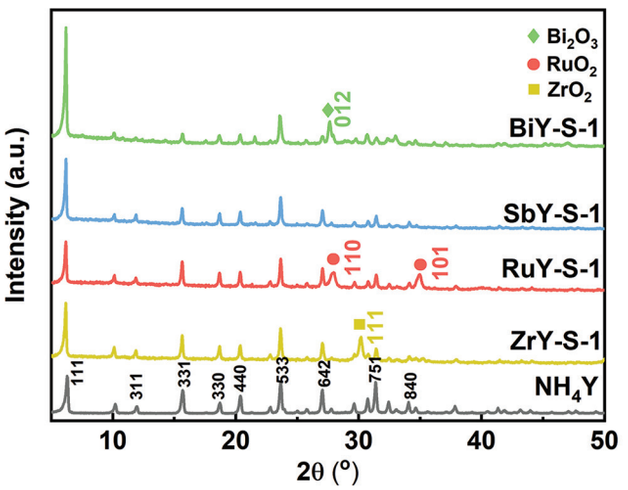


Figure 1. XRD patterns of NH_4Y and MY-1 adsorbents. The characteristic peaks of the metal oxides are marked.

Abbreviations: Bi_2O_3: Bismuth(III) oxide; MY: Metal ion-modified Y-zeolite; NH_4Y: Ammonium-form Y-zeolite; RuO_2: Ruthenium(IV) oxide; SbY: Antimony-modified Y-zeolite; XRD: X-ray diffraction; Y-zeolite: Faujasite-type zeolite; ZrO_2: Zirconium(IV) oxide.

The XRD patterns of the Ru-modified zeolites with varying initial molar ratios of Ru to ammonium ion (Ru/NH_4^+) are shown in Figure S2. All samples exhibited characteristic peaks of Y-zeolite along with the RuO_2 phase. As the Ru/NH_4^+ ratio decreased, the intensity of the RuO_2 diffraction peaks also diminished, indicating reduced loading of bulk RuO_2 with lower initial Ru content.

3.1.2. SEM and TEM images of adsorbents

The SEM (Figure 2) image exhibited that MY-1 adsorbents retained the particle morphology of the original NH_4Y, exhibiting particles with crystal habits smaller than 0.9 μm.

The morphology and elemental distribution of MY-1 were further examined using SEM and EDX. The SEM image exhibited that MY-1 adsorbents retained the particle morphology of the original NH_4Y, exhibiting particles with crystal habits smaller than 0.9 μm. The SEM images of RuY-1 and ZrY-1 showed that Y-zeolite particles were covered by bulk RuO_2 and ZrO_2 nanoparticles, respectively. In contrast, the BiY-1 sample exhibited particle conglutination. The EDX (Figure S1) spectra confirmed the presence of Ru, Sb, Bi, and Zr in their respective MY-1 samples. The metal content of RuY-1, SbY-1, ZrY-1 and BiY-1 was 5.02, 13.85, 10.28 and 16.22 wt%, respectively (Table S1).

Low magnification TEM images of NH_4Y-zeolite and the RuY-X series are shown in Figure 3. The nano-rod-like particles of RuO_2 with a width of 30–40 nm and a length of 30–100 nm can be observed at the surfaces of RuY-1 and RuY-1/2 samples. In contrast, RuO_2 was not observed in RuY-1/4, RuY-1/8, and RuY-1/16 samples, indicating a significant reduction in RuO_2 content with decreasing initial Ru (Ru/NH_4^+ mole ratio from 1 to 1/16). These observations are consistent with the XRD results (Figure S1). The high-resolution TEM image of RuO_2 is shown in the inset of Figure 3B,

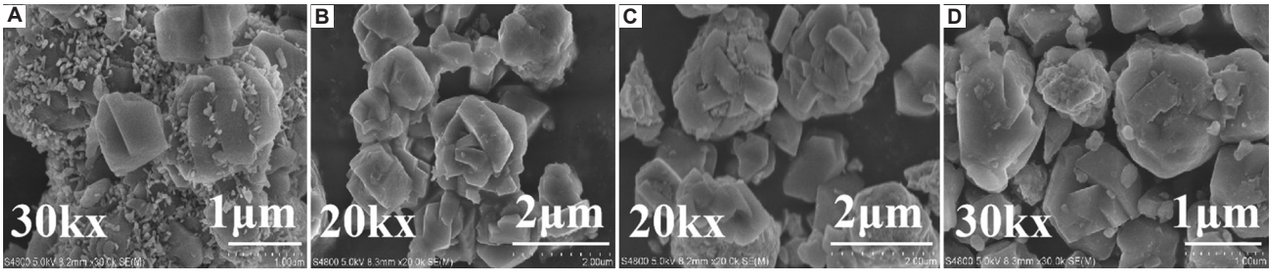


Figure 2. SEM images of adsorbents. (A) RuY-1. (B) SbY-1. (C) BiY-1. (D) ZrY-1.

Abbreviations: BiY: Bismuth-modified Y-zeolite; RuY: Ruthenium-modified Y-zeolite; SbY: Antimony-modified Y-zeolite; SEM: Scanning electron microscopy; ZrY: Zirconium-modified Y-zeolite.

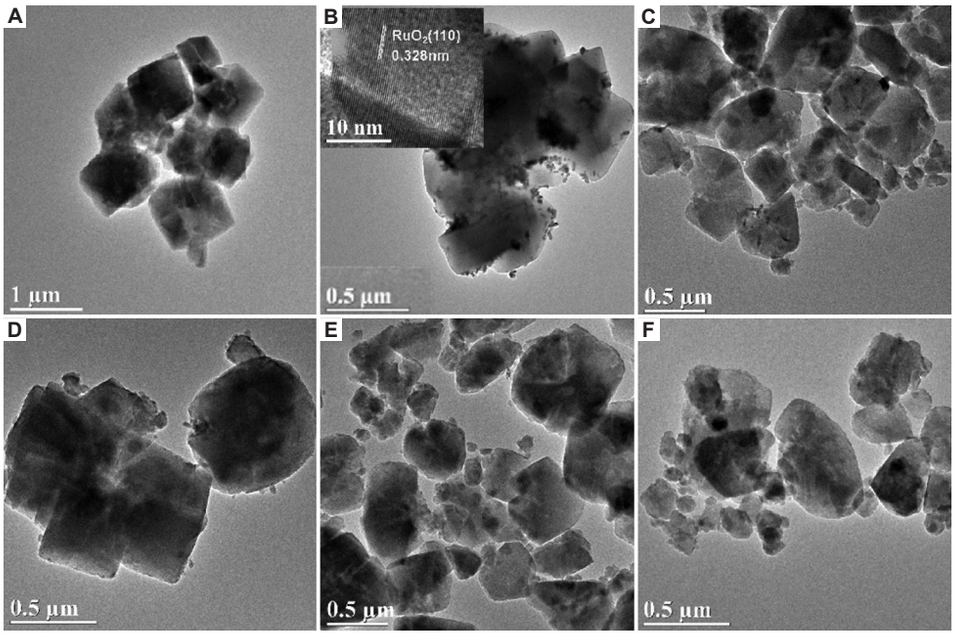


Figure 3. TEM image of adsorbents. (A) NH_4Y. (B) RuY-1. (C) RuY-1/2. (D) RuY-1/4. (E) RuY-1/8. (F) RuY-1/16. Abbreviations: NH4Y: Ammonium-form Y-zeolite; RuY: Ruthenium-modified Y-zeolite; TEM: Transmission electron microscopy.

where a lattice fringe of 0.328 nm corresponds to the (110) plane of single-crystalline RuO_2. Based on combined XRD, SEM, and TEM studies, we propose the following mechanism for MY-1 formation during calcination: a portion of the NH_4^+ ions in NH_4Y-zeolite undergo thermal decomposition to volatilize NH_3, whereas another portion is ion-exchanged with the added metal ions, which diffuse into the Y-zeolite framework to form MY. The residual metal salts that are not incorporated into the framework are converted into bulk metal oxide phases (M_xO_y). Therefore, MY-1 adsorbent is not a simple MY zeolite phase, which consists of MY zeolite and bulk M_xO_y phases.

3.1.3. XPS results of adsorbents

The chemical state of metal species in the MY-1 sample was investigated by XPS study. Figure 4 presents the Ru 3d spectrum of the RuY-1 sample, with $RuCl_3 \cdot xH_2O$ used as the reference for Ru^{3+}. The C 1s peak at 284.8 eV likely originates from carbonaceous contamination.[31,32] Due to the overlap between the C 1s and Ru $3d_{3/2}$, only the Ru $3d_{5/2}$ binding energy region is discussed. In the $RuCl_3 \cdot xH_2O$ sample, the peak at a binding energy of 281.5 eV corresponds to Ru^{3+}. In the RuY-1 sample, the Ru $3d_{5/2}$ peak appears at 281.2 eV, which is assigned to Ru^{4+}. This peak is slightly shifted to a higher binding energy compared to that of bulk RuO_2 (280.7 eV). The Ru^{4+} species in RuY-1 may exist in the form of RuO_x cluster ions, such as $Ru(IV)O_x^{(4-2x)+}$ ($0 < x < 2$). Several studies have reported that Ru cluster ions are more electron-deficient than bulk RuO_2.[33-35]

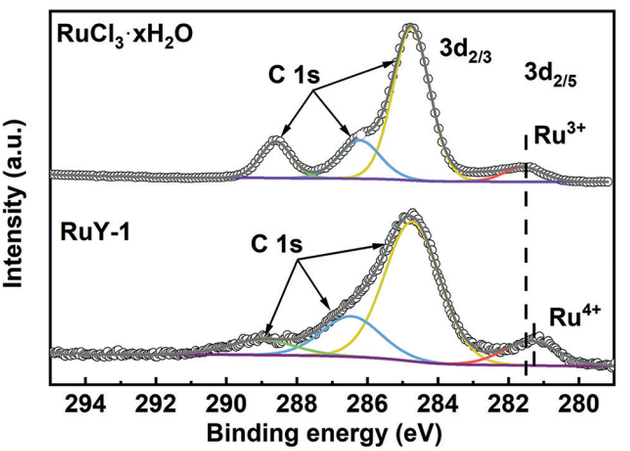


Figure 4. XPS spectra of the RuY-1 adsorbent. Abbreviations: RuY: Ruthenium-modified Y-zeolite; XPS: X-ray photoelectron spectroscopy.

XPS spectra of the SbY-1, ZrY-1, and BiY-1 samples are displayed in Figure S3, with $SbCl_3$, $ZrOCl_2 \cdot 8H_2O$, and $Bi(NO_3)_3 \cdot 5H_2O$ used as references for Sb^{3+}, Zr^{4+} and Bi^{3+}, respectively. Three characteristic peaks are observed in the Sb 3d spectrum of SbY-1: two peaks at 530.7eV ($3d_{5/2}$) and 540.1eV ($3d_{3/2}$) corresponding to Sb^{3+} of $SbCl_3$ and Sb_2O_3, and another peak at

532.1eV corresponding to Sb^{5+} of Sb_2O_5, indicating the coexistence of Sb^{3+} and Sb^{5+} in the SbY-1 sample.[36] The peak area of Sb^{5+} is smaller than that of Sb^{3+}, indicating that the Sb(III)Y in the SbY-1 is the dominant phase.

In the Zr 3d spectrum, peaks at 182.5 eV ($3d_{5/2}$) and 185 eV ($3d_{3/2}$) are attributed to Zr^{4+} for the $ZrOCl_2 \cdot 8H_2O$ and bulk ZrO_2.[37] The peaks at 182.7 eV ($3d_{5/2}$) and 185.2eV($3d_{3/2}$) for the ZrY-1 are shifted slightly by 0.2eV toward higher binding energy, and are attributed to Zr^{4+}. Similar to RuY-1, the Zr^{4+} species may exist as ZrO_x cluster ions in ZrY-1. In the Bi 4f spectrum of BiY-1, the peaks at 159.8 eV ($4f_{7/2}$) and 165.2 eV ($4f_{5/2}$) are attributed to Bi^{3+}, consistent with $Bi(NO_3)_3 \cdot 5H_2O$ and BiOCl references.[38]

These findings indicate oxidation of the metal species occurred in the RuY-1and SbY-1 samples during the calcinations at 500°C, but not in the ZrY-1 and BiY-1 samples. The chemical state of metal species in RuY-1and SbY-1 adsorbents was changed to Ru^{4+} and Sb^{5+}. This suggests that metal species in MY-zeolite do not exist as simple metal ions (M^{n+}), but rather as MOx cluster ions. For example, in RuY, the Ru species likely exist in a cluster form. It is well known that tetravalent metal ions usually exist as polymeric or cluster oxide or hydroxide ions.[34]

To further investigate the distribution of Ru species in Y-zeolite micropores, depth-profile XPS analysis of the RuY-1/2 sample was conducted at different penetration depths (10, 20, and 30 nm). The XPS spectra are shown in Figure S4. The Ru $3d_{5/2}$ peak at 281.2eV at all penetration depths confirms the presence of Ru^{4+} species within the Y-zeolite micropores.

3.1.4. H_2-TPR of adsorbents

H_2-TPR is often used to investigate the metal-support interaction and surface properties such as metal stability, species, and distribution. To gain deep insight into the location of Ru species in the RuY-X samples, the reducibility of RuY-X and NH_4Y-zeolite samples was studied using H_2-TPR (Figure 5). No reduction peak was observed for the NH_4Y-zeolite, indicating that it does not consume hydrogen in this temperature range. RuY-1 showed several reduction peaks, indicating the existence of different kinds of Ru oxide species. The peak at 133°C corresponds to the reduction of supported RuO_2 nanoparticles on the external surface of Y-zeolite, whereas the peak located at 163°C corresponds to the reduction of RuOx clusters in the supercages of the Y-zeolite, where they strongly interact with the framework.[33] The peak centered at 300–550°C is attributed to RuOx clusters located in the small inner channels of Y-zeolite, such as the sodalite unit or hexagonal prism. These clusters exhibit stronger interactions with the framework, making them more resistant to hydrogen reduction. These results suggest that calcination of RuY-1 led to partial migration of Ru species from supercages into the smaller internal channels. Similar reduction patterns were observed in RuY-1/2 and RuY-1/8 samples. However, the RuY-1/8 sample lacked the reduction peak corresponding to RuO_x clusters in the supercages. Literature reports indicate that the reducibility of metal species in zeolites typically follows the order: supercage >sodalite cage >hexagonal prism.[39-41] Based on TEM, XPS, and H_2-TPR results, it can be concluded that Ru species in RuY-X samples are primarily present as RuO_2 nanoparticles on the external surface and as RuO_x clusters dispersed within both supercages and inner channels of the Y-zeolite.

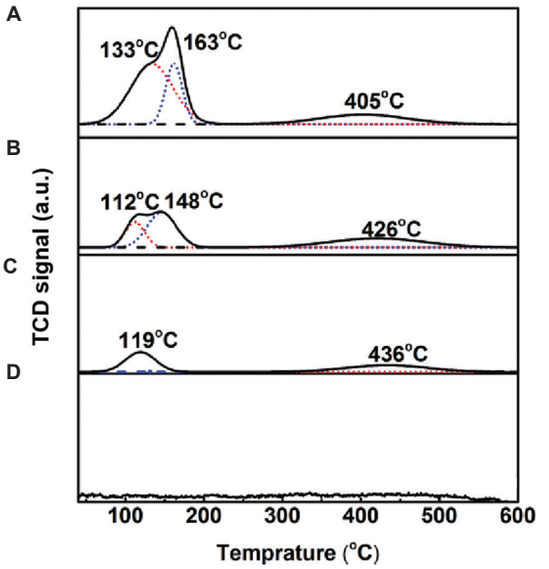


Figure 5. H_2-TPR spectra of adsorbents. (A) NH_4Y. (B) RuY-1/8. (C) RuY-1/2. (D) RuY-1.
Abbreviations: H_2-TPR: Hydrogen temperature-programmed reduction; NH_4Y: Ammonium-form Y-zeolite; RuY: Ruthenium-modified Y-zeolite; TCD: Thermal conductivity detector; TEM: Transmission electron microscopy.

3.1.5. Py-FTIR spectra of adsorbents

To investigate the effects of acidity present in the MY-1 adsorbents on the TP removal performance, the acidity of MY-1 was determined by Py-FTIR analysis (Figure 6). Since pyridine molecules are too large to enter the micropore channel of Y-zeolite, Py-FTIR analysis only detects acidity on the external surface.

Two types of acid sites were identified on the external surface of MY-1: one peak at 1540 cm^{-1} corresponding to the vibration of pyridine molecules bound at Brønsted acid sites and the other peak at 1450 cm^{-1} attributed to the ring C-C stretching vibration of pyridine adsorbed on Lewis acid sites. Another intense band was observed at 1490 cm^{-1}, arising from the combined presence of Lewis acidic and Brønsted acid sites.[42,43] These results indicate that MY-1 adsorbents possess both Lewis acidic and Brønsted acid sites, suggesting that the incorporation of metal ions modifies the acidity of the adsorbent surfaces.

Quantitative data on acid site concentrations are presented in Table 1. The total acidity (T) and strong acidity (S) were calculated by desorption of pyridine at 150°C and 450°C, respectively. The difference between T and S corresponds to the content of weak acid sites (W). The concentrations of Lewis acid and Brønsted acid sites were calculated using Equations III and IV.

$$L\ (mol/g) = 3.73 \times A_L \quad (III)$$

$$B\ (mol/g) = 9.90 \times A_B \quad (IV)$$

where L and B are the concentrations of Lewis acid and Brønsted acid (mol/g), respectively, and A_L and A_B are the absorbance intensity at 1450 cm^{-1} and 1540 cm^{-1}, respectively.[44]

The T of the MY-1 external surface follows the order: SbY-1 >ZrY-1 >BiY-1 >RuY-1. For all samples, the Brønsted acid site concentration (T_B) was greater than that of Lewis acid sites (T_L). SbY-1 exhibited the strongest acidity, consistent with the XRD analysis, which identified SbY as its main crystalline phase. These findings suggest that the acidity of MY-1's external surface is mainly contributed by the metal ions within the MY structure, whereas the M_xO_y contributes minimally. RuY-1 sample exhibited the weakest acidity, with barely visible peaks in the magnified view of Figure S5. Notably, it had the lowest Lewis acidity (S_L = 0.38 × 10^{-4} mol/g), suggesting a limited presence of Ru ions on the external surface of RuY-1.[19,45]

3.1.6. NH_3-TPD of adsorbents

Pyridine-FTIR can only detect the external surface acidity of MY-1 samples. However, the NH_3 molecule is smaller than the pyridine molecule and can easily enter

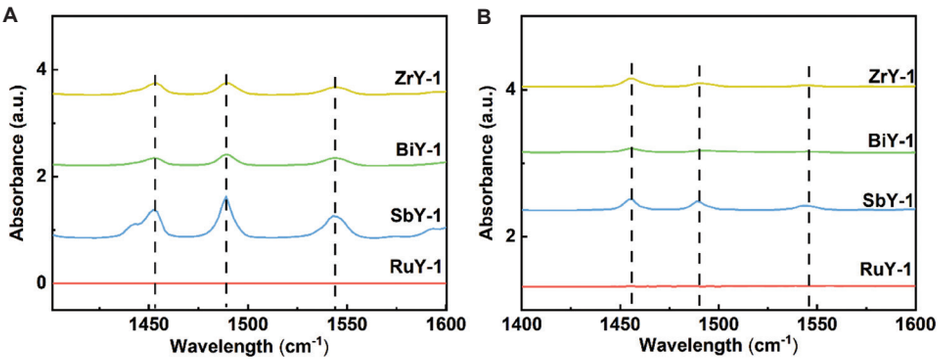


Figure 6. Py-FTIR pattern of MY-1 adsorbents. Spectrum after desorption of pyridine at 150 °C (A) and 450°C (B) are shown.

Abbreviations: BiY: Bismuth-modified Y-zeolite; PY-FTIR: Pyridine-Fourier-transform infrared spectroscopy; RuY: Ruthenium-modified Y-zeolite; SbY: Antimony-modified Y-zeolite; ZrY: Zirconium-modified Y-zeolite.

Table 1. Surface acid content of MY-1 adsorbents

Adsorbents	Concentration (10^{-4} mol/g)						
	T	T_B	T_L	S_B	S_L	W_B	W_L
SbY-1	56.16	38.13	18.03	9.50	4.05	28.63	13.98
ZrY-1	22.4	14.15	8.09	1.06	3.96	13.09	4.13
BiY-1	18.9	13.73	5.17	0.76	1.81	12.97	3.36
RuY-1	1.28	0.82	0.46	0	0.38	0.82	0.08

Abbreviations: MY: Metal ion-modified Y-zeolite; T: Total acid; T_B: Total Brønsted acid; T_L: Total Lewis acid; S_B: Strong Brønsted acid; S_L: Strong Lewis acid; W_B: Weak Brønsted acid; W_L: Weak Lewis acid.

the micropore channels of Y-zeolite. Therefore, the acidity of MY-1 was further investigated using NH_3-TPD analysis. The NH_3-TPD spectra of the MY-1 adsorbents are shown in Figure 7. The total acidic content of MY-1 decreased in the following order: RuY-1 (2.375 mmol/g) >HY (1.821 mmol/g) >SbY-1 (1.344 mmol/g) >ZrY-1 (1.205 mmol/g) >BiY-1 (1.196 mmol/g). The SbY-1, ZrY-1, and BiY-1 samples displayed similar NH_3 desorption peak intensities in the temperature range of 100–500°C. A desorption peak around 190°C corresponds to physisorbed NH_3, whereas the peak near 300°C indicates the presence of weak acidic sites. The peak at approximately 420°C is assigned to strong acidic sites, likely contributed by the metal species incorporated into the MY-1 samples. RuY-1 exhibited a broad and asymmetric NH_3 desorption peak over a wide temperature range (100–800°C), suggesting the presence of multiple types of acid sites associated with Ru cluster ions. Specifically, desorption peaks at 400°C and 640°C were attributed to strong acidic sites. According to previous studies, NH_3-TPD analysis of ZSM-type zeolite shows desorption peaks at 60–100°C (physisorbed NH_3 on the external surface), 150–230°C (weak acidic sites), and 420–500°C (strong acidic sites), with the latter attributed to a mixture of Brønsted and Lewis acid sites.[46]

From these acidity studies, we propose that the concentration of Ru cluster ions on the external surface of RuY-1 zeolite is relatively low. This conclusion is supported by Py-FTIR results, which revealed weak acid intensity and the lowest Lewis acidity for RuY-1. However, the NH_3-TPD results indicate that most of the Ru cluster ions are located within the micropores of Y-zeolite, contributing significantly to strong acidity at high temperatures. These internal Ru cluster ions are expected to play an important role in the desulfurization of TP. Nickel (Ni)-supported mesoporous AlMCM-41 and Ni-modified mesoporous silica have also been reported for the desulfurization of fuel. Ni enhances both Brønsted and Lewis acid site intensity, and such high acidity will play a significant role in fuel desulfurization.[21,47]

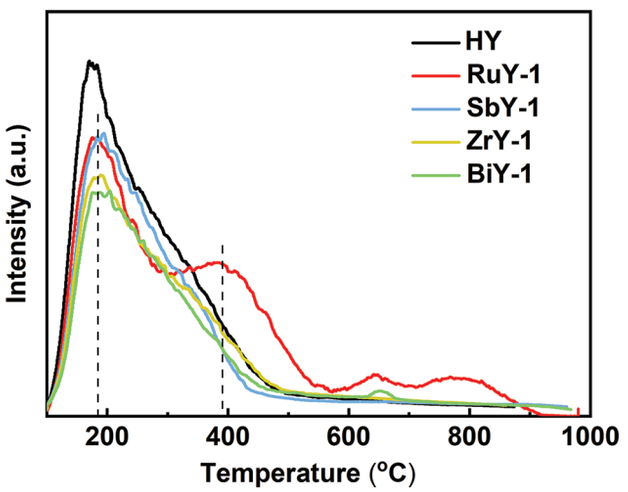


Figure 7. NH_3-TPD profiles of the adsorbents. Abbreviations: BiY: Bismuth-modified Y-zeolite; HY: Proton-form Y-zeolite; NH_3: Ammonia; RuY: Ruthenium-modified Y-zeolite; SbY: Antimony-modified Y-zeolite; TPD: Temperature-programmed desorption; ZrY: Zirconium-modified Y-zeolite.

3.1.7. N_2 adsorption-desorption isotherms of adsorbents

Figure 8 and Table S2 display the N_2 adsorption-desorption isotherms and pore structure parameters of the MY-1 and NH_4Y samples. Adsorption isotherms correspond to Brunauer–Deming–Deming–Teller type I isotherms with a single pore size distribution. Brunauer–Emmett–Teller (BET) surface area decreases in the order: NH_4Y-zeolite >RuY-1 >ZrY-1 >SbY-1 >BiY-1. This decline is likely due to the partial blockage of the microporous channels in Y zeolite and/or the conglutination of zeolite particles. A reduction in BET surface area mass transfer efficiency interrupts interaction between the internal active sites and the adsorbed molecules.[48] BiY-1 showed the smallest external area (28.16 m^2/g), indicating that significant agglomeration of Y-zeolite particles after calcination treatment, which is in agreement with the SEM images (Figure 2C). The internal surface area and total pore volume also decreased in the order: NH_4Y-zeolite >RuY-1 >ZrY-1 >SbY-1 >BiY-1, suggesting that more M^{n+} entered the Y-zeolite micropore.[49]

3.2. Selective adsorption of TP

3.2.1. Effect of metal species on TP adsorption

The TP adsorption from model gasoline (containing toluene) was studied using batch adsorption experiments over various MY-1 and HY. The S removal increases in the following order: HY (16%) <BiY-1 (20%) <ZrY-1 (25%) <SbY-1(27%) <RuY-1 (38%) (Figure 9). MY-1 samples showed higher sulfur removal compared to the HY sample, suggesting that the metal species in the Y-zeolite play an important role in the selective adsorption of TP. Song *et al.*[45] also reported that HY has a large number of Brønsted acid sites, which are harmful to the desulfurization process.

RuY-1 showed the best sulfur removal performance among all samples. Structural characterization using the

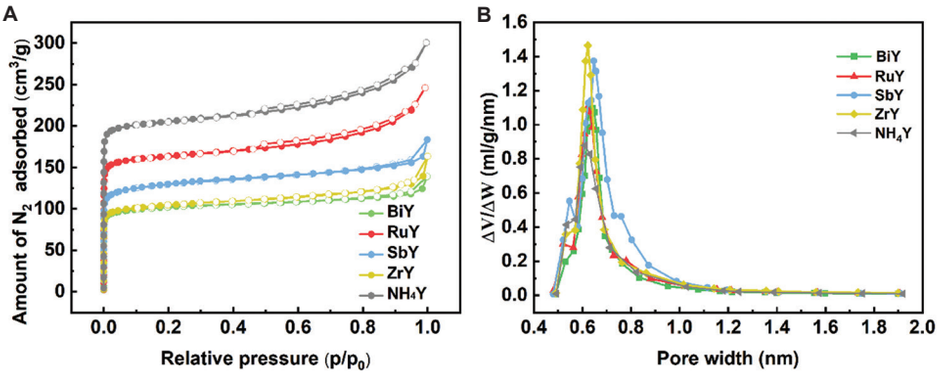


Figure 8. Characteristics of adsorption isotherms of NH_4Y and MY-1 adsorbents. (A) N_2 adsorption-desorption isotherms. (B) Pore size distribution.

Abbreviations: BiY: Bismuth-modified Y-zeolite; MY: Metal ion-modified Y-zeolite; NH4Y: Ammonium-form Y-zeolite; p: Gas pressure at adsorption equilibrium; P_0: Saturation vapor pressure of nitrogen at the experimental temperature; RuY: Ruthenium-modified Y-zeolite; SbY: Antimony-modified Y-zeolite; V: Volume of adsorbed nitrogen under standard temperature and pressure (STP) conditions; W: Weight of the adsorbate (nitrogen); ZrY: Zirconium-modified Y-zeolite.

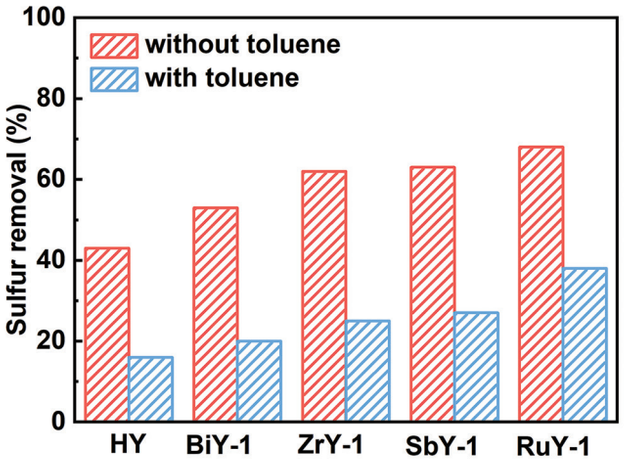


Figure 9. Sulfur removal performance of MY-1 and HY adsorbents from model gasoline with or without toluene. Adsorption conditions: initial sulfur concentration = 20 ppm; model gasoline volume: 10 mL; adsorbent weight = 0.1 g, temperature = 80°C; contact time = 2 h.

Abbreviations: BiY: Bismuth-modified Y-zeolite; HY: Proton-form Y-zeolite; MY: Metal ion-modified Y-zeolite; RuY: Ruthenium-modified Y-zeolite; SbY: Antimony-modified Y-zeolite; ZrY: Zirconium-modified Y-zeolite.

XRD and TEM study indicated that the RuY-1 sample contains both Ru-incorporated Y-zeolite and bulk RuO_2 phases. To clarify the TP adsorptive properties of bulk RuO_2, the simple bulk RuO_2 phase was prepared by calcination of $RuCl_3 \cdot xH_2O$ in air at 500°C. The sample showed a 16% lower sulfur removal, confirming that the M_xO_y phase generally shows poor TP adsorptive properties.[5] Therefore, the MY component of MY-1, rather than the MxOy, plays an important role in TP selectivity. Interestingly, SbY-1 showed high TP selectivity, possibly due to the lower loading or weaker clustering of SbxOy species within the Y-zeolite compared to RuOx. This suggests that sulfur removal efficiency is not only dependent on the M^{n+} type but also on its loading amount.

Commercial gasoline contains TP derivatives, olefins, and aromatic compounds.[18] To investigate the influence of toluene as a competing adsorbate, the TP experiments adsorption was carried out using a model gasoline without toluene (Figure 9). The sulfur removal improved in the following order: HY (43%) <BiY-1 (53%) <SbY-1(62%) <ZrY-1 (63%) <RuY-1 (68%). The desulfurization performance of RuY-1 is comparable to that of other adsorbents reported in Table S3. These results indicate competitive adsorption between toluene and TP, and further confirm the superior selectivity of RuY-1 for sulfur compounds.

3.2.2. Effect of Ru loading of RuY-X for TP adsorption

Since RuY-1 showed high selectivity for TP, a more detailed study was carried out to assess the effect of Ru loading of RuY-X on TP removal (Figure 10). The sulfur removal improved in the following order: RuY-1/2(N_2) (3%) <RuY-1/16 (23%) <RuY-1/8 (28%) <RuY-1/4 (36%) <RuY-1(38%) <RuY-1/2 (44%). RuY-1/2 showed maximum sulfur removal, and this

performance improved with increasing Ru/NH_4^+ molar ratio, suggesting that sulfur removal is strongly dependent on the RuOx clusters present in the RuY-X sample. However, further increases in Ru loading beyond this ratio slightly reduced sulfur removal, likely due to the formation of bulk RuO_2 nanocrystals, which may block the micropores of the Y-zeolite. The RuY-1/2(N_2) sample containing Ru3+ species showed a sulfur removal of only 3%, much lower than that of RuY-1/2 (44%), indicating that Ru^{4+} is more effective for thiophene adsorption.

3.2.3. Effects of adsorbent acidity on TP adsorption

NH_3-TPD analysis showed that the RuY-1 sample exhibits the highest concentration of strong acid sites among the MY-1 series, despite showing the lowest Lewis acidity on the external surface area as observed in the Py-IR study. Meanwhile, the BET study showed that the RuY-1 sample had the largest internal surface area of 665 m^2/g. Based on these findings, it is proposed that the acidity of RuY-1 is predominantly contributed by RuOx clusters located within the internal surface area (micropores) of the Y-zeolite. These RuOx clusters, particularly those containing Ru^{4+}, serve as active sites and significantly enhance thiophene removal.

The distribution of RuOx clusters in the RuY-X series was further studied using H_2-TPR. The results confirmed that the RuOx clusters are highly dispersed within both the supercages and the internal channels of the Y-zeolite. However, only the RuOx clusters located in the supercages contribute significantly to TP selectivity, whereas those migrating into the inner channels show negligible adsorption capability[18]. Furthermore, the H_2-TPR reduction peak area correlates with the amount of RuOx clusters, and RuY-1/2 showed a slightly higher reduction peak area than RuY-1.

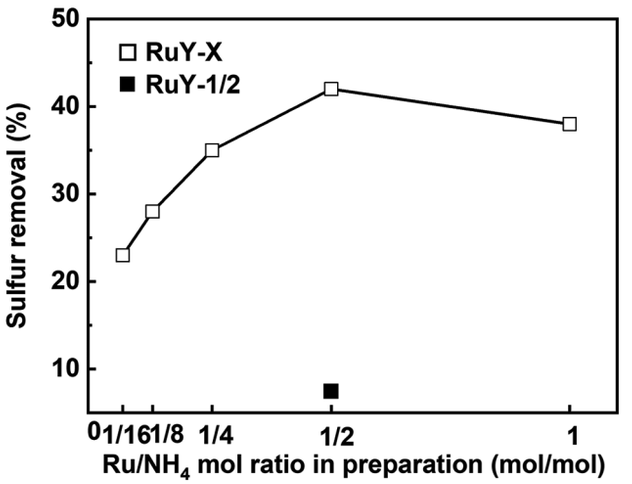


Figure 10. Effect of Ru loading amount in RuY-X on sulfur removal. Adsorption conditions: initial sulfur concentration = 20 ppm; model gasoline volume = 10 mL; adsorbent weight = 0.1 g; temperature = 80°C; contact time = 2 h.

Abbreviations: Ru: Ruthenium; RuY: Ruthenium-modified Y-zeolite.

3.3. Adsorption isotherm

The adsorption isotherms were investigated through batch adsorption experiments. Two models were used to describe the equilibrium data: (1) The Langmuir model explains properties such as physisorption with homogeneous monolayer adsorption, in which all the active sites are equivalent and independent; (2) The Freundlich model is an empirical model that describes adsorption on heterogeneous surfaces and multilayer adsorption. The Langmuir equation and the Freundlich equation are described in Equations V and VI, respectively.[50,51]

$$\frac{C_e}{q_e} = \frac{1}{q_m K_L} + \frac{C_e}{q_m} \quad \text{(V)}$$

$$q_e = K_F C_e^{1/n} \quad \text{(VI)}$$

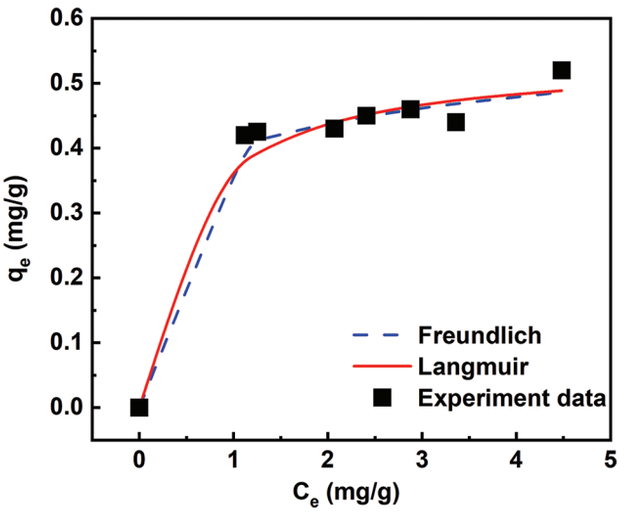


Figure 11. Adsorption isotherm for TP using RuY-1/2 adsorbent. Experimental conditions: Initial TP concentration = 20 ppm; model gasoline volume = 10 mL; adsorbent weight = 0.1 g; temperature = 80°C; contact time = 2 h.

Abbreviations: C_e: Remaining concentration of TP at equilibrium (mg/L), q_e: Amount of TP adsorbed at equilibrium (mg/g); RuY: Ruthenium-modified Y-zeolite; TP: Thiophene.

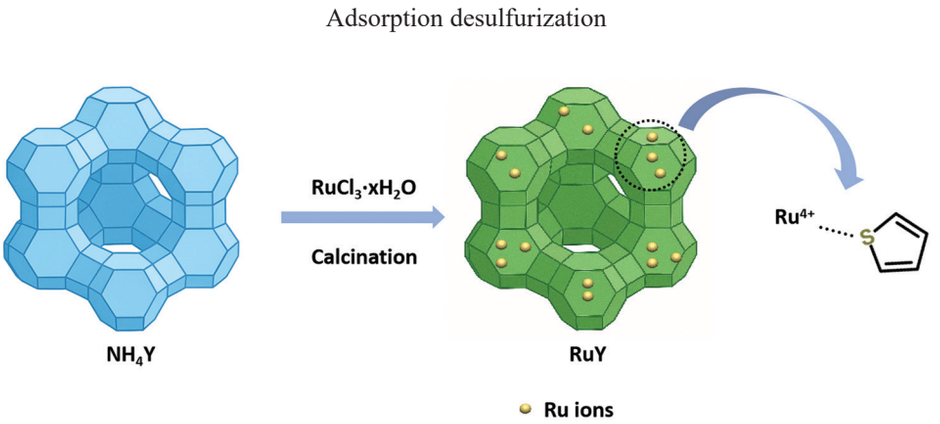


Figure 12. The adsorption mechanism diagram of TP on the RuY adsorbent.
Abbreviations: NH_4Y: Ammonium-form Y-zeolite; Ru: Ruthenium; RuY: Ruthenium-modified Y-zeolite.

Table 2. Langmuir and Freundlich isotherm parameters for TP adsorption on RuY-1/2 adsorbent

Model	K_L	q_m (mg/g)	n	K_F	R^2
Langmuir	1.52	0.488	-	-	0.975
Freundlich	-	-	7.704	0.412	0.687

Abbreviations: K_F: Freundlich constant; K_L: Langmuir constant; n: Freundlich heterogeneity factor; q_m: Maximum adsorption capacity; R^2: Coefficient of determination; TP: Thiophene.

where C_e is the remaining concentration of TP at equilibrium (mg/L), q_e is the amount of TP adsorbed at equilibrium (mg/g), q_m is the theoretical maximum adsorption capacity (mg/g), K_L is the Langmuir isotherm constant (L/mg) reflecting the strength of adsorption, K_F is the Freundlich isotherm constant (L/mg) related to multilayer adsorption capacity, and n is the Freundlich empirical constant related to the intensity of adsorption.

The adsorption isotherm of TP on RuY-1/2 adsorbent at 80°C is shown in Figure 11. The equilibrium parameters of the model are summarized in Table 2. The calculated n is 7.074, and 1/n ranges from 0.1 to 0.5, suggesting that the adsorption process can easily occur. The adsorption data fit the Langmuir model better than the Freundlich model, with a higher correlation coefficient (R^2 = 0.9758) compared to the Freundlich model (R^2 = 0.6873). This indicates that TP adsorption on RuY-1/2 proceeds primarily via monolayer adsorption onto a homogeneous surface.

Based on the direct S–M interaction mechanism for thiophene adsorption, the σ-bond interaction between sulfur and metal cations (e.g., Ce^{4+} in CeY, La^{3+} in LaY) is stronger than the π-complexation interaction (e.g., Cu^+ in CuY, Ag^+ in AgY), offering better selectivity and efficiency for ultra-deep desulfurization.[14,29] The S–M σ bond strength depends on the valence state and ionic radius of the M^{n+} in the MY adsorbents. XPS analysis confirmed the oxidation states of the metal ions in the MY-1 adsorbents as Bi^{3+}, Sb^{3+}, Sb^{5+}, Ru^{4+}, and Zr^{4+}. Their ionic radii are as follows: Bi^{3+}: 103 pm; Zr^{4+}: 72 pm; Ru^{3+}: 68 pm; Ru^{4+}: 62 pm; and Sb^{5+}: 60 pm. Smaller ionic radius and higher charge enhance polarization energy, leading to stronger S–M bond formation. Among the tested adsorbents, RuY-1 showed the highest sulfur removal, confirming that Ru^{4+} forms stronger S–M σ bonds than Zr^{4+} or Bi^{3+}. This suggests that smaller-radius and higher-valent metal ions promote stronger interactions with thiophene molecules, enhancing selective adsorption (Figure 12).

4. Conclusion

Metal ion modified MY-1 zeolite adsorbents exhibit selective adsorption for TP from low-sulfur concentration model gasoline. The solid-state reaction method proves effective for preparing these MY-1 adsorbents. Among them, the RuY-1/2 adsorbent, modified with Ru^{4+} cluster ion, showed the highest sulfur removal efficiency. The selectivity of MY-type adsorbents for TP depends on key properties of the incorporated metal ions: smaller ionic radius, higher charge, and greater concentration of Lewis acid sites.

Acknowledgments

None.

Funding

This study was supported by the Basic Scientific Research Project of the Higher Education Department of Liaoning Province (LJ212410142153), Liaoning Province Science and Technology Plan Joint Plan

(Fund) Project (2023-BSBA-251), and Natural Science Foundation of China (No. 21266014).

Conflict of interest

The authors declare no competing interests.

Author contributions

Conceptualization: Mei Xue
Formal analysis: Mingyang Song
Investigation: Xianrong Meng
Methodology: Xianrong Meng
Writing–original draft: Jiefei Li
Writing–review & editing: Mei Xue

Availability of data

Data are available from the corresponding author upon reasonable request

References

1. Yang RT, Hernández-Maldonado AJ, Yang FH. Desulfurization of transportation fuels with zeolites under ambient conditions. *Sci Rep.* 2003;301:79-81. doi: 10.1126/science.1085313
2. Xiao J, Wang X, Fujii M, Yang Q, Chen Y, Song C. A novel approach for ultra-deep adsorptive desulfurization of diesel fuel over TiO_2-CeO_2/MCM-48 under ambient conditions. *AIChE J.* 2013;59:1441-1445. doi: 10.1002/aic.14045
3. Jeevanandam P, Klabunde KJ, Tetzler SH. Adsorption of thiophenes out of hydrocarbons using metal-impregnated nanocrystalline aluminum oxide. *Microporous Mesoporous Mater.* 2005;79:101-110. doi: 10.1016/j.micromeso.2004.09.005
4. Hernández-Maldonado AJ, Yang RT. Denitrogenation of transportation fuels by zeolites at ambient temperature and pressure. *Angew Chem Int Ed.* 2004;116:1022-1022. doi: 10.1002/ange.200462998
5. Xue M, Wen P, Chitrakar R, Ooi K, Feng Q. Screening of inorganic adsorbents for selective adsorption of thiophene from model gasoline. *Sep Sci Technol.* 2012;47:1926-1936. doi: 10.1080/01496395.2012.663755
6. Xue M, Chitrakar R, Sakane K, *et al*. Selective adsorption of thiophene and 1-benzothiophene on metal-ion-exchanged zeolites in organic medium. *J Colloid Interface Sci.* 2005;285:487-492. doi: 10.1016/j.jcis.2004.12.031
7. Tan P, Qin J, Liu X, Yin X, Sun L. Fabrication of magnetically responsive core-shell adsorbents for thiophene capture: $AgNO_3$-functionalized Fe_3O_4@ mesoporous SiO_2 microspheres. *J Mater Chem A.* 2014;2:4698-4705. doi: 10.1039/c3ta15026b
8. Saleh TA, Sulaiman KO, AL-Hammadi SA, Dafalla H, Danmaliki GI. Adsorptive desulfurization of thiophene, benzothiophene and dibenzothiophene over activated carbon manganese oxide nanocomposite: With column system evaluation. *J Clean Prod.* 2017;154:401-412. doi: 10.1016/j.jclepro.2017.04.008
9. Subhan F, Liu BS. Acidic sites and deep desulfurization performance of nickel supported mesoporous AlMCM-41 sorbents. *Chem Eng J.* 2011;178:69-77. doi: 10.1016/j.cej.2011.10.024
10. Xiao J, Sitamraju S, Chen Y, *et al*. Air-promoted adsorptive desulfurization of diesel fuel over Ti-Ce mixed metal oxides. *AIChE J.* 2015;61:631-639. doi: 10.1002/aic.14617
11. Chang G, Huang M, Su Y, *et al*. Immobilization of Ag(I) into a metal-organic framework with -SO_3H sites for highly selective olefin-paraffin separation at room temperature. *Chem Commun.* 2015;51:2859-2862. doi: 10.1039/C4CC09008B
12. Ahmad K, Nazir MA, Qureshi AK, *et al*. Engineering of zirconium based metal-organic frameworks (Zr-MOFs) as efficient adsorbents. *Mater Sci Eng B.* 2020;262:114766. doi: 10.1016/j.mseb.2020.114766
13. Khan NA, Najam T, Shah SSA, *et al*. Development of Mn-PBA on GO sheets for adsorptive removal of ciprofloxacin from water: Kinetics, isothermal, thermodynamic and mechanistic studies. *Mater Chem Phys.* 2020;245:122737. doi: 10.1016/j.matchemphys.2020.122737
14. Tian F, Wu W, Jiang Z, *et al*. The study of thiophene adsorption onto La(III)-exchanged zeolite NaY by FT-IR spectroscopy. *J Colloid Interface Sci.* 2006;301:395-401. doi: 10.1016/j.jcis.2006.04.042
15. Kim JH, Ma X, Zhou A, Song C. Ultra-deep desulfurization and denitrogenation of diesel fuel by selective adsorption over three different adsorbents: A study on adsorptive selectivity and mechanism. *Catal Today.* 2006;111:74-83. doi: 10.1016/j.cattod.2005.11.012
16. Tang T, Zhang L, Fu W, *et al*. Design and synthesis of metal sulfide catalysts supported on zeolite nanofiber bundles with unprecedented hydrodesulfurization activities. *J Am Chem Soc.* 2013;135:11437-11440. doi: 10.1021/ja406393h
17. Lin L, Zhang Y, Zhang H, Lu F. Adsorption and solvent desorption behavior of ion-exchanged modified Y zeolites for sulfur removal and for fuel cell applications. *J Colloid Interface Sci*. 2011;360:753-759. doi: 10.1016/j.jcis.2011.06.040
18. Shi Y, Yang X, Tian F, Jia C, Chen Y. Effects of toluene on thiophene adsorption over NaY and Ce(IV)Y zeolites.

J Nat Gas Chem. 2012;21:421-425.
doi: 10.1016/S1003-9953(11)60394-9

19. Tian F, Shen Q, Fu Z, Wu Y, Jia C. Enhanced adsorption desulfurization performance over hierarchically structured zeolite Y. *Fuel Process Technol.* 2014;128:176-182.
doi: 10.1016/j.fuproc.2014.05.019
20. Lee KX, Valla JA. Investigation of metal-exchanged mesoporous Y zeolites for the adsorptive desulfurization of liquid fuels. *Appl Catal B.* 2017;201:359-369.
doi: 10.1016/j.apcatb.2016.07.028
21. Kalita P, Gupta NM, Kumar R. Synergistic role of acid sites in the Ce-enhanced activity of mesoporous Ce-Al-MCM-41 catalysts in alkylation reactions: FTIR and TPD-ammonia studies. *J Catal.* 2007;245:338-347.
doi: 10.1016/j.jcat.2006.11.004
22. Meng X, Qiu G, Wang G, Cai Q, Wang Y. Durable and regenerable mesoporous adsorbent for deep desulfurization of model jet fuel. *Fuel Process Technol.* 2013;111:78-85.
doi: 10.1016/j.fuproc.2013.03.009.
23. Shen Y, Li P, Xu X, Liu H. Selective adsorption for removing sulfur: A potential ultra-deep desulfurization approach of jet fuels. *RSC Adv.* 2012;2:1700-1711.
doi: 10.1039/C1RA00831A
24. Danmaliki GI, Saleh TA. Influence of conversion parameters of waste tires to activated carbon on adsorption of dibenzothiophene from model fuels. *J Clean Prod.* 2016;117:50-55.
doi: 10.1016/j.jclepro.2016.01.034
25. Vecchi PA, Ellern A, Angelici RJ. Synthetic, structural, and kinetic studies of $[CpRu(CO)_2(\mu_2\text{-}\ \eta^1(S):\mu^6\text{-}DBT)\ RuCp^*][PF_6]_2$: A dibenzothiophene bridge between two ruthenium fragments. *Organometallics.* 2005;24:3725-3730.
doi: 10.1021/om050312s
26. Stoffregen SA, Vecchi PA, Ellern A, Angelici RJ. A new approach to the stabilization of dibenzothiophene (DBT) coordination to metals: Studies of $(\eta^5\text{-}C_5H_4CH_2Ph)Ru(CO)_2(\eta^1(S)\text{-}DBT)^+$. *Inorg Chim Acta.* 2007;360:1711-1716.
doi: 10.1016/j.ica.2006.11.022
27. Song H, Cui X, Song H, Gao H, Li F. Characteristic and adsorption desulfurization performance of Ag-Ce bimetal ion-exchanged Y zeolite. *Ind Eng Chem Res.* 2014;53:14552-14557.
doi: 10.1021/ie503774e
28. Duan L, Gao X, Meng X, *et al*. Adsorption, co-adsorption, and reactions of sulfur compounds, aromatics, olefins over Ce-exchanged Y zeolite. *J Phys Chem C.* 2012;116:25748-25756.
doi: 10.1021/jp308013m
29. Xue M, Chitrakar R, Sakane K, *et al*. Preparation of cerium-loaded Y-zeolites for removal of organic sulfur compounds from hydrodesulfurizated gasoline and diesel oil. *J Colloid Interface Sci.* 2006;298:535-542.
doi: 10.1016/j.jcis.2006.04.028
30. Xing ZM, Gao YX, Shi LY, Liu XQ, Jiang Y, Sun LB. Fabrication of gold nanoparticles in confined spaces using solid-phase reduction: Significant enhancement of dispersion degree and catalytic activity. *Chem Eng Sci.* 2017;158:216-226.
doi: 10.1016/j.ces.2016.10.044
31. Wang W, Guo S, Lee K, *et al*. Hydrous ruthenium oxide nanoparticles anchored to graphene and carbon nanotube hybrid foam for supercapacitors. *Sci Rep.* 2014;4:4452-4460.
doi: 10.1038/srep04452
32. Hwang JY, El-Kady MF, Wang Y, *et al*. Direct preparation and processing of graphene/RuO_2 nanocomposite electrodes for high-performance capacitive energy storage. *Nano Energy.* 2015;18:57-70.
doi: 10.1016/j.nanoen.2015.06.011
33. Qadir K, Kim SM, Seo H, *et al*. Deactivation of Ru catalysts under catalytic CO oxidation by formation of bulk Ru oxide probed with ambient pressure XPS. *J Phys Chem C.* 2013;117:13108-13113.
doi: 10.1021/jp404548n
34. Lee JD. *A New Concise Inorganic Chemistry*. 3rd ed. Japanese: Van Nostrand Reinhold; 1977. p. 323.
35. Zhang Z, Ding L, Gu J, *et al*. 3D charged grid induces a high performance catalyst: Ruthenium clusters enclosed in X-zeolite for hydrogenation of phenol to cyclohexanone. *Catal Sci Technol.* 2017;7:5953-5963.
doi: 10.1039/C7CY01424G
36. Darwiche A, Bodenes L, Madec L, Monconduit L, Martinez H. Impact of the salts and solvents on the SEI formation in Sb/Na batteries: An XPS analysis. *Electrochim Acta.* 2016;207:284-292.
doi: 10.1016/j.electacta.2016.04.140
37. Thunyaratchatanon C, Luengnaruemitchai A, Chaisuwan T, Chollacoop N, Chen SY, Yoshimura Y. Synthesis and characterization of Zr incorporation into highly ordered mesostructured SBA-15 material and its performance for CO_2 adsorption. *Microporous Mesoporous Mater.* 2017;253:18-28.
doi: 10.1016/j.micromeso.2017.05.012
38. Xu L, Yan P, Li H, *et al*. Metallic Bi self-doping BiOCl composites: Synthesis and enhanced photoelectrochemical performance. *Mater Lett.* 2017;196:225-229.
doi: 10.1016/j.matlet.2017.02.025
39. Zheng HY, Wang JZ, Li Z, Yan LF, Wen JZ. Characterization and assessment of an enhanced CuY catalyst for oxidative carbonylation of methanol prepared by consecutive liquid-phase ion exchange and incipient wetness impregnation. *Fuel Process Technol.* 2016;152:367-374.
doi: 10.1016/j.fuproc.2016.01.023
40. Tang Q, Wang Y, Zhang Q, Wan H. Preparation of metallic cobalt inside NaY zeolite with high catalytic

activity in Fischer-Tropsch synthesis. *Catal Commun.* 2003;4:253-258.
doi: 10.1016/S1566-7367(03)00024-4

41. Cao Y, Zhuang TT, Yang J, Liu HD, Huang W, Zhu H. Promoting zeolite NaY as efficient nitrosamines trap by cobalt oxide modification. *J Phys Chem C.* 2007;111:538-548.
doi: 10.1021/jp066034u
42. Ge X, Shi L, Wang X. Dechlorination of reformate via chemical adsorption reactions by Ce-Y zeolite. *Ind Eng Chem Res.* 2014;53:6351-6357.
doi: 10.1021/ie404071z
43. Ahmed MHM, Muraza O, Jamil AK, Shafei EN, Yamani ZH, Choi K. Steam catalytic cracking of n-dodecane over Ni and Ni/Co bimetallic catalyst supported on hierarchical BEA zeolite. *Energy Fuels.* 2017;31:5482-5490.
doi: 10.1021/acs.energyfuels.7b00413
44. Zeng YJ, Yu HJ, Shi L. Surface acidity and catalytic activity of Y-zeolite catalysts. *J East China Univ Sci Technol Nat Sci Ed*. 2008;34(5):635-640.
45. Wang WY, Pan MX, Qin YC, Wang LT, Song LJ. Effects of surface acidity on the adsorption desulfurization of Cu(I) Y zeolites. *Acta Phys-Chim Sin.* 2011;27(5):1176-1180.
doi: 10.3866/PKU.WHXB20110442
46. Skarlis SA, Berthout D, Nicolle A, Dujardin C, Granger P. Multisite modeling of NH_3 adsorption and desorption over Fe-ZSM5. *J Phys Chem C.* 2012;116:8437-8448.
doi: 10.1021/jp302324q
47. Aslam S, Subhan F, Yan Z, *et al*. Unusual nickel dispersion in confined spaces of mesoporous silica by one-pot strategy for deep desulfurization of sulfur compounds and FCC gasoline. *Chem Eng J.* 2017;321:48-57.
doi: 10.1016/j.cej.2017.03.043
48. Bartholomew CH. Mechanisms of catalyst deactivation. *Appl Catal A Gen.* 2001;212:17-60.
doi: 10.1016/S0926-860X(00)00843-5
49. Song H, Jiang BL, Song HL, Jin ZS, Sun XL. Preparation of AgY zeolite and study on its adsorption equilibrium and kinetics. *Res Chem Intermed.* 2015;41:3837-3854.
doi: 10.1007/s11164-014-1844-z
50. Li J, Gyoten H, Sonoda A, Feng Q, Xue M. Removal of trace arsenic to below drinking water standards using a Mn-Fe binary oxide. *RSC Adv.* 2017;7:1490-1497.
doi: 10.1039/C6RA24862D
51. Xiong J, Yang L, Chao Y, *et al*. Boron nitride mesoporous nanowires with doped oxygen atoms for the remarkable adsorption desulfurization performance from fuels. *ACS Sustain Chem Eng.* 2016;4:4457-4464.
doi: 10.1021/acssuschemeng.6b00914

ACCSCIENCE PUBLISHING

Asian Journal of Water, Environment and Pollution. Vol. 22, No. 6 (2025), pp. 103-119.
doi: 10.36922/AJWEP025180139

ORIGINAL RESEARCH ARTICLE

Impacts of land use and land cover changes on groundwater recharge in the Dire Dawa watershed, Ethiopia

Tariku Takele[1]*, Adula Bayisa[2], and Muralitharan Jothimani[3]

[1]Department of Geology, College of Natural and Computational Sciences, Dilla University, P.O. Box 419, Dilla, Ethiopia
[2]Groundwater resource study and Design, Ministry of Water and Energy, P.O.Box-5744, Addis Ababa, Ethiopia
[3]Department of Geology, College of Natural and Computational Sciences, Arba Minch University, P.O. Box 21, Arba Minch, Ethiopia
***Corresponding author:** Tariku Takele (tariku.takele@du.edu.et)

Received: May 4, 2025; 1st revised: June 13, 2025; 2nd revised: June 22, 2025; Accepted: June 25, 2025; Published online: August 22, 2025

Abstract: Land use and land cover (LULC) change is a growing global concern, particularly in water-scarce regions, where it directly influences hydrological systems and groundwater sustainability. The Dire Dawa watershed in eastern Ethiopia exemplifies this challenge. This study investigates the impacts of LULC changes on groundwater recharge in the Dire Dawa watershed from 2000 to 2022. The LULC changes were analyzed using ERDAS IMAGINE 2015 and geographic information systems, while the effects on groundwater recharge were assessed using the Soil and Water Assessment Tool (SWAT) model. The performance of the SWAT model was evaluated using the sequential uncertainty fitting 2 technique, demonstrating good model performance, with R^2 values of 0.84 (calibration) and 0.79 (validation), Nash-Sutcliffe efficiency values of 0.75 and 0.72, and percent bias values of −0.1 and −11, respectively. The results indicated that, over the 22 years, agricultural land expanded by 52.6%, while built-up areas increased by nearly 79.2%. In contrast, shrublands and forests declined by 23.7% and 62.8%, respectively. These shifts resulted in a 24.5% reduction in groundwater recharge (−48.8 mm/y) and a 19.9% increase in surface runoff (42.8 mm/y). These findings reflect broader regional patterns and emphasize the importance of integrated land and water resource management to support ecological stability and community resilience.

Keywords: Dire Dawa watershed; Land use and land cover change; Groundwater recharge; Soil and water assessment tool; Image processing

1. Introduction

Groundwater is one of the most essential yet often overlooked natural resources that sustain life on Earth. It serves as a critical backbone for ecosystems, agriculture, and the daily needs of billions of people worldwide. In regions where surface water is limited or unpredictable, groundwater becomes the primary, sometimes the only source of water security.[1] This resource is integral to ensuring water security, particularly as urbanization, industrialization, and climate change continue to reshape our environment.[2-5] As the pressures of rapid urbanization, industrial growth, and climate change intensify, safeguarding groundwater is no longer a local challenge; it is a global imperative. Recognizing its value is not just about hydrology or resource management; it

is about securing a sustainable and dignified future for humanity and the planet we share.[6,7]

Land use and land cover (LULC) and climate change, in particular, are disrupting vital processes such as groundwater recharge, surface runoff, and overall watershed hydrology, making it even harder to manage and sustain these resources.[8-10] Furthermore, LULC changes, driven by both urban sprawl and industrial growth, have compounded these challenges, particularly in arid and semi-arid regions where water scarcity is already a pressing concern.[11,12]

Understanding how LULC changes affect groundwater recharge is vital, especially as urban areas expand and natural landscapes transform.[4,13,14] These changes disrupt the natural water balance, impacting ecosystems, agriculture, and the daily lives of communities. Groundwater sustainability, therefore, is not only a scientific challenge but also a pressing human concern.[9] Effective groundwater management is crucial for preserving ecosystem health and maintaining watershed functionality.[15,16] Without it, groundwater depletion could lead to severe consequences, including increased water scarcity and ecological degradation at both local and regional scales.[17,18]

In response to these challenges, the Soil and Water Assessment Tool (SWAT) has emerged as an essential tool in groundwater studies.[14,19,20] When combined with geographical information systems (GIS) and remote sensing data, SWAT provides a robust and integrated framework for evaluating the influence of environmental factors on water balance components across various watershed scales.[21,22] Its ability to simulate spatial and temporal variations makes the SWAT particularly effective in regions facing environmental stressors, such as climate change and rapid urbanization.[4,9,23] This modeling capacity is especially relevant in vulnerable areas, such as the Dire Dawa watershed in eastern Ethiopia, where shifting LULC patterns and climate variability necessitate informed, scenario-based analyses to support sustainable water management.

In Ethiopia, groundwater is a critical resource for irrigation, industrial use, and domestic consumption. However, the country's water resources are under increasing stress due to rapid urbanization, population growth, and climate variability.[3,24,25] Accurate assessments of groundwater recharge potential are essential for guiding sustainable water management practices and ensuring long-term water security.[3,26] The Dire Dawa watershed in Ethiopia's Awash River basin (Figure 1) exemplifies these challenges. As urbanization and industrial activities have grown, local water resources have been depleted for several decades.[27-29] Despite growing concerns over water scarcity, groundwater depletion and the LULC changes in the region have impacted the groundwater potential of the area.

This study aims to investigate the impacts of LULC changes on groundwater recharge in the Dire Dawa watershed in Ethiopia from 2000 to 2022. Unlike previous research that primarily focused on surface runoff and flood hazards[30] or employed broader spatial models, such as WetSpass, to estimate groundwater recharge,[31] a process-based and temporally detailed simulation was utilized in this study using the SWAT. By integrating recent LULC data with hydrological modeling, a more comprehensive understanding of how landscape changes influence groundwater availability is provided, addressing a gap that has not yet been fully explored in the Dire Dawa context.

The analysis of this study's results offers insights into sustainable watershed management. It contributes to Ethiopia's broader climate resilience efforts, including the Green Legacy Initiative, which serves as an essential component of national environmental policies, focusing on reforestation and conservation goals.[32] The efforts made toward reforestation directly contribute to groundwater recharge through their impact on the infiltration of soil water, reduction of surface runoff, and improvement of groundwater recharge dynamics. The sustainability and long-term water security of the local water resources in the region depend on these conservation methods, which aim to mitigate environmental degradation and promote sustainable resource management.[32]

2. Methodology

2.1. Study area

2.1.1. Geographical setting

The Dire Dawa watershed is situated in eastern Ethiopia, within the Awash River basin, south of the Afar Depression. It is located between latitudes 9°26'00" and 9°45'30" N and longitudes 41°41'00"–42°06'30" E, approximately 515 km from Addis Ababa (Figure 1).

The research area is situated within a semi-arid zone, and the match between climate and landform is a crucial factor in determining water resources. Located in the basin of the foothills surrounding the mountains, the catchment is supplied by several rivers, the largest of which cuts through the area's core. The region experiences a bimodal rainfall pattern, with the highest rainfall intensities occurring between July and

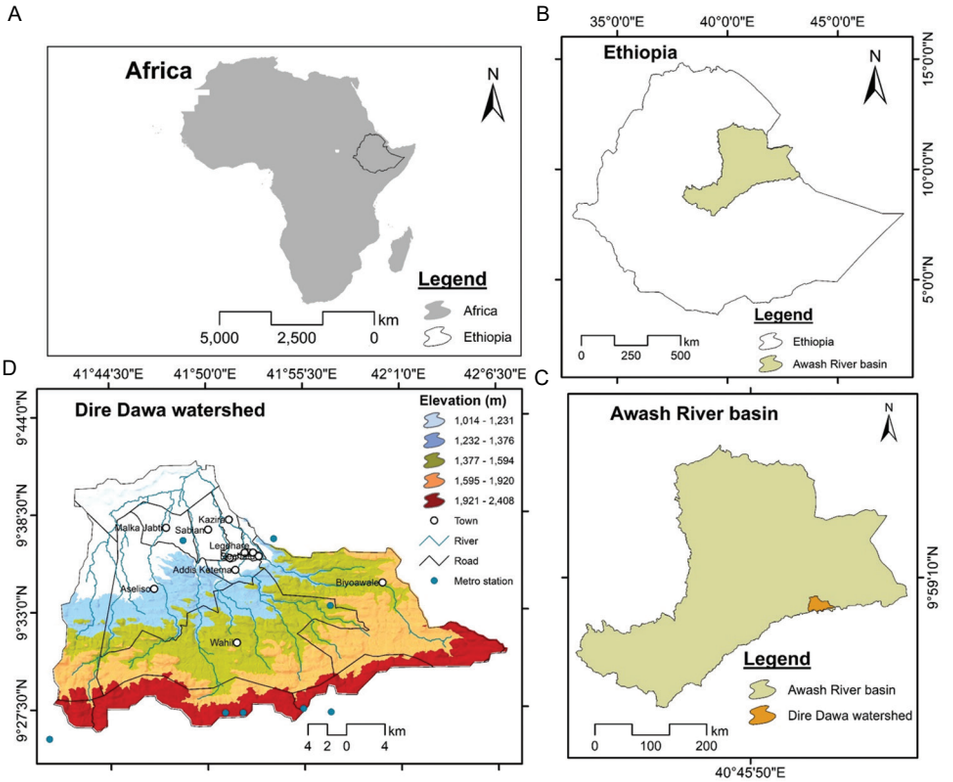


Figure 1. Maps depicting the location of the study area: (A) Ethiopia; (B) Awash river basin; and (C) the study site (Dire Dawa watershed). Maps aquired from https://www.ethiogis-mapserver.org/; https://search.earthdata.nasa.gov/

September, reaching up to 450 mm. The dry season spans from November to February, resulting in strong seasonal differences in water resources. The weather is usually mild (9.8–20.9°C), and the two warmest months are February and March. Under this climate, the cyclic changes in rainfall play a crucial role in shaping the runoff and groundwater recharge patterns. During the rainy season, the land experiences high runoff, resulting in water scarcity. The landscape is characterized by a diverse mix of plateaus, escarpments, and valleys, all of which are shaped by volcanic activity. With elevations ranging from 1,014 m to 2,408 m, the area encompasses steep mountains, flat plains, and fault-induced landforms, including half-grabens and horsts. These landforms directly impact how water moves through the region. The steep slopes and rocky surfaces result in high runoff and limited water retention, particularly during intense rainfall.

2.1.2. Geological and hydrogeological setting

The geology of the Dire Dawa region is characterized by ancient Precambrian basement rocks overlain by Mesozoic sedimentary formations, including the Adigrat sandstone, Hamaneli limestone, and Amba Aradam sandstone. These units, together with the Tertiary volcanic basalts from the Afar volcanic series and the recent Quaternary alluvial deposits, form the main hydrogeological framework. The Precambrian basement rocks are highly weathered and fractured, creating secondary porosity; however, the porous sandstones and limestones serve as the region's primary aquifers. The volcanic basalts contribute to groundwater flow predominantly through fractures and weathered zones. The Quaternary alluvial sediments, particularly in the lower-elevation areas within the Afar Depression, are significant groundwater reservoirs.

The groundwater flow in the area is strongly influenced by major fault systems associated with the East African Rift and the Afar Depression tectonics, creating zones of enhanced permeability and acting as preferential flow pathways. The hydrogeology of the Dire Dawa watershed is shaped by the complex interaction of geological formations, tectonic activity, and the region's varied topography. Groundwater occurs mainly in two primary systems: the rugged escarpment and the adjacent plains. The escarpment features a complex geology composed

of sedimentary, basement, and volcanic rocks, and is deeply fractured by predominantly east-west trending faults, significantly influencing groundwater flow and availability (Figure 2**).**

In contrast, the basin at the foot of the escarpment is dominated by thick alluvial deposits, forming extensive aquifers that serve as crucial water sources for local communities. These alluvial aquifers display variable thicknesses and sediment types, resulting in fluctuating groundwater levels and transmissivity rates. Volcanic rock formations in the elevated areas generally yield limited groundwater, except in localized zones. Meanwhile, the upper sandstone layers exhibit moderate to high groundwater potential, reflecting their variable permeability and porosity.

2.2. Datasets and methods

Figure 3 presents the methodology applied in this study

2.2.1. Datasets

This study employed a modeling approach to assess the impact of land-use changes on groundwater recharge, integrating various datasets (Table 1). Meteorological data were sourced from the Ethiopian Meteorological Institute's river flow data from the Ministry of Water and Energy, and spatial data from remote sensing, GIS, and global positioning systems (GPS). These datasets were used to develop a conceptual framework illustrating how land cover alterations influence groundwater systems. Meteorological data were collected from eight stations within the watershed, supplemented by the data from the

Table 1. Data sources and details

Data type (resolution)	Data source/references
Digital elevation model (12.5 m×12.5 m)	Earthdata Search (https://search.earthdata.nasa.gov/)
Landsat images (30 m×30 m)	USGS (https://earthexplorer.usgs.gov/)
Precipitation and temperature (daily)	Ethiopian Meteorological Institute (https://www.ethiomet.gov.et/)
Geological map (shape file)	Mapserver Ethiopia: https://www.ethiogis-mapserver.org/
Daily discharge (daily)	Ministry of Water and Energy of Ethiopia
Soil data (12.5 m×12.5 m)	FAO (https://www.fao.org/ethiopia/en/)

Abbreviations: FAO: Food and agriculture organization; USGS: United States geological survey.

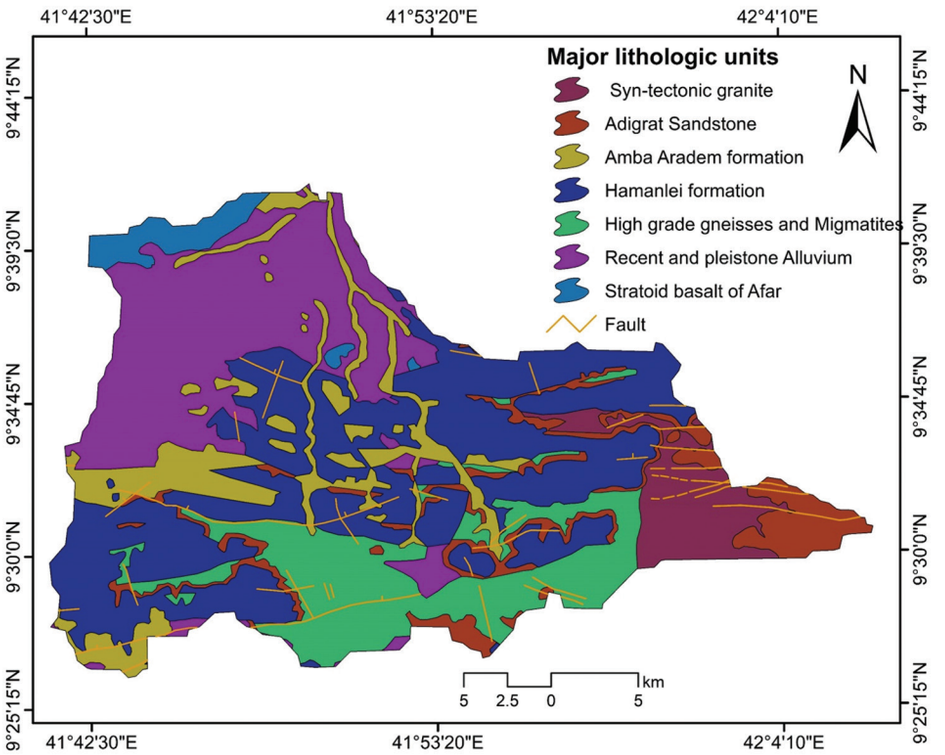


Figure 2. Simplified geological map of the study area. Map aquired from: https://www.ethiogis-mapserver.org/

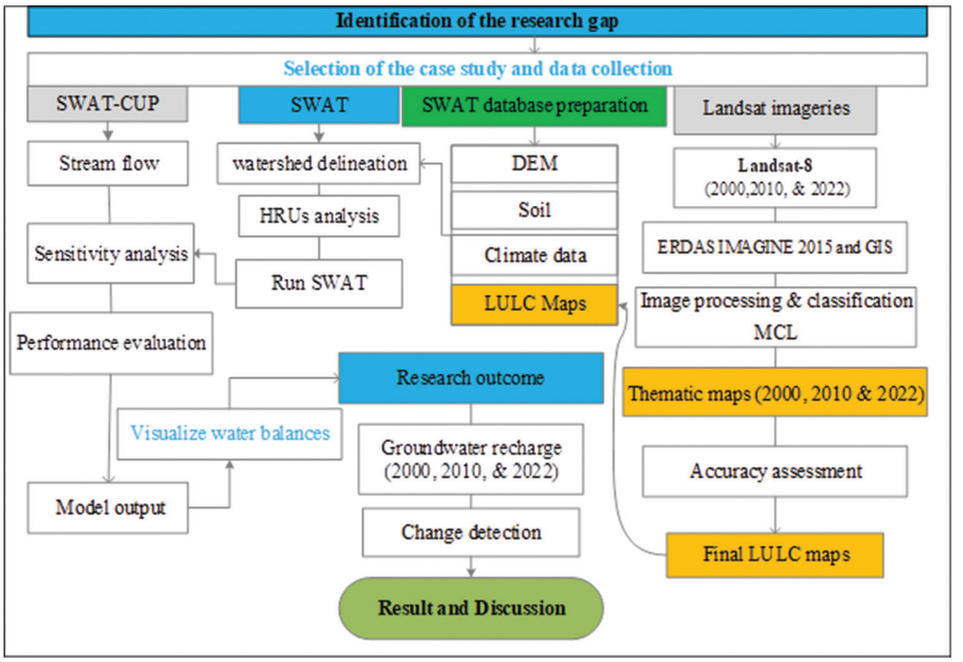


Figure 3. Methodologies in this study

Abbreviations: CUP: Calibration and uncertainty program; DEM: Digital elevation model; GIS: Geographical information system; HRU: Hydrological response units; LULC: Land use and land cover; MLC: Maximum likelihood classification; SWAT: Soil and water assessment tool.

nearest station with a long-term, continuous record. The dataset spans the period from 1979 to 2022 and includes variables such as evapotranspiration, temperature, relative humidity, sunshine hours, and wind speed. Due to the presence of missing or inconsistent data, an averaging method was applied for bias correction. Stations with significant data gaps were excluded from the analysis.

2.2.2. LULC analysis

The LULC detection and change analysis for the target watershed were performed with ERDAS IMAGINE 2015 (Hexagon, Sweden) and ArcGIS 10.8 software (Esri, United States). In this study, satellite images with cloud cover <10% of the imagery were selected to acquire accurate LULC data (Table 2). Landsat 7 was used for the 2000 LULC map, Landsat 5 for the 2010 LULC map, and Landsat 8 for the 2022 LULC map. Image processing and classifications were conducted using algorithms such as contrast enhancement, edge detection, and haze correction to enhance the satellite images based on the ERDAS IMAGINE 2015 software. The maximum likelihood classification method was employed, based on region-specific training information, to delineate LULC within the watershed. This algorithm has been used previously.[33]

2.2.3. Accuracy assessment of LULC map

The accuracy of remote sensing classifications is crucial to ensure that the classifications are consistent with field-grade reference data.[3,34,35] The classification of LULC types was further validated by the researchers' experiences, literature reviews, and Google Earth Pro. This study utilized both qualitative and quantitative methodologies, adhering to established scientific recommendations.[35] One of the most popular tools for achieving this is the confusion matrix, from which important measures such as overall accuracy (OA), producer's accuracy (PA), user accuracy (UA), and the kappa coefficient (κ_c) can be derived. OA is a measure of global classification accuracy, while UA is a measure of the ability of a pixel classified in the presumed category to be similar to the real-world category. PA represents the proportion of a map in which a reference pixel is correctly classified, whereas κ_c represents the proportion of agreement between the classification and reference data after correcting for chance. The κ_c values have the following interpretations: >0.80 indicates high agreement, 0.40–0.80 indicates moderate agreement, and <0.40 indicates poor agreement[35,36] The κ_c was calculated using Equation I:

$$\kappa_c = \frac{\sum_i (N_{ii} - x)}{N^2 - x} \quad \text{(I)}$$

Table 2. Satellite imagery used for watershed analysis

Satellite/sensor	Resolution	Path/row	Acquisition date	Cloud cover (%)
Landsat 7	30 m×30 m	166/053	January 22, 2000	<10
Landsat 5	30 m×30 m	166/053	January 25, 2010	<10
Landsat 8	30 m×30 m	166/053	January 26, 2022	<10

where N is the total number of observations (the sum of all pixels in the confusion matrix), N_{ii} represents the correct classifications (values along the matrix diagonal), and x accounts for the expected agreement due to chance, based on the row and column totals of the matrix. This approach offers a comprehensive classification accuracy assessment, considering both actual data and potential random misclassification. Accuracy was validated using Google Earth imagery and field data, with metrics such as UA, PA, and κ_c. The final reclassification ensured a reliable depiction of land-use changes, supporting informed land management decisions for environmental sustainability.

2.2.4. LULC change detection

This study employed a post-classification image comparison method to analyze LULC changes over 3 time periods: 2000–2010, 2010–2022, and 2000–2022. Satellite images for each reference year were classified independently and compared to assess shifts in land cover. LULC changes over the past two decades were evaluated in three 10-year intervals, starting from 2000. To calculate the relative percentage of change (P), the area of each land cover type at the start and end of each period was compared (Equation II):

$$P(\%) = \frac{\left(A_{Lf} - A_{Li}\right)}{A_{Li}} \times 100 \quad \text{(II)}$$

where A_{Lf} is the area at the final time point (2010 or 2022) and A_{Li} is the area at the initial time point (2000 or 2010). In addition, the rate of change (ΔR) was calculated to assess the speed of land cover transitions (Equation III):

$$\Delta R = \left(\frac{A_{Lf - A_{Li}}}{T} \right) \quad \text{(III)}$$

where T is the number of years in the period. These calculations provide insight into how land use has evolved, offering valuable information on its effects on local resources and ecosystems, and informing sustainable land management strategies.

2.2.5. The SWAT model development and input datasets

The SWAT model has been widely applied for hydrological modeling due to its user-friendly interface and convenient access to datasets for hydrological analysis. Alongside SWAT, the SWAT calibration and uncertainty program (SWAT-CUP) is commonly used to evaluate the performance of the SWAT model.[37] SWAT-CUP helps with calibrating and validating SWAT models, and it integrates several advanced algorithms, such as sequential uncertainty fitting (SUFI-2), generalized likelihood uncertainty estimation, parameter solution, Markov chain Monte Carlo, and particle swarm optimization.[37,38] These algorithms are used for sensitivity analysis, uncertainty analysis, and performance analysis. Various objective functions, including the coefficient of determination (R^2), Nash-Sutcliffe efficiency (NSE), and percent bias (PBIAS), improve the model accuracy and reliability. Among these algorithms, SUFI-2 was chosen in this study as it has been widely used in hydrological modeling and is known for its ability to quantify model uncertainty and optimize calibration effectively.[8,20]

2.2.6. SWAT input datasets

2.2.6.1. Digital elevation model (DEM)

This study obtained a free 12.5 m × 12.5 m spatial resolution DEM from the Earthdata Search database (Table 1). The database is one of the key data sources for various applications, including watershed delineation, slope, and drainage network and pattern calculations, all of which are used to simulate water balance using SWAT modeling. The DEM was pre-processed in ArcGIS 10.8, where null values were filled using the spatial analysis tools in ArcToolbox, and then incorporated into ArcSWAT for watershed delineation and parameterization following SWAT procedures. This approach ensures that the DEM is complete and ready for accurate analysis, effectively defining watershed boundaries and flow patterns. The hydrological features, such as watersheds, stream networks, and slopes, were derived from the region's DEM using the ArcSWAT model.

2.2.6.2. Slope map

The slope map was constructed from DEM-derived elevation data. The study area was discretized into five slope classes, each interpreted as having different levels of steepness. These classes were then further re-classified into percentages, providing a more readily recognizable picture of the five slope classes. They were created using ArcSWAT dunging model parametrizations based on slope percentage gradients of the study area. This was done to provide a more detailed description of the topography of the target region.

2.2.6.3. Soil data

In the Dire Dawa watershed, key soil characteristics, such as texture, bulk density, saturated hydraulic conductivity, and available water content, were re-established and input into the SWAT model for hydrological simulation. These features influence the water flow, infiltration, and runoff processes. Such soil information was manually entered into the file (soil.dat) using ArcSWAT to meet specific modeling needs. In addition, the calibration of soil parameters was at the core of improving the accuracy of water balance and runoff forecasts, considering local land-use management variables. This approach laid the groundwork for assessing recharge and land-use-associated effects at the watershed scale.

2.2.6.4. LULC

Land use has a significant impact on a watershed's hydrology. The LULC is a key variable determining groundwater recharge in a watershed. To validate the scenarios considered by the SWAT model, a realistic land-use map was generated to delineate the hydrological response units (HRUs). All six LULC types were assigned different codes for model feasibility and were associated with a SWAT code to assess the influence of different land covers on groundwater recharge during the study period (2000–2022).

2.2.6.5. Meteorological data

Accurate weather data are essential for the SWAT model; hence, daily precipitation and temperature data (1982–2022) were used in the study. These data were primarily sourced from the local weather stations within and around the watershed. In cases where data gaps existed, linear regression and arithmetic methods were employed to interpolate missing values. To address the uneven distribution of weather stations, local data were supplemented with records from the National Centers for Environmental Prediction's Climate Forecast System Reanalysis. All meteorological data were processed into formats compatible with the SWAT model, ensuring seamless integration and reliable model inputs.

2.2.6.6. Hydrological data (river flow)

To substantiate the SWAT model, data on river discharge from observed gauging stations in the watershed were used. The discharge data from 2000 to 2014, collected from the Ministry of Water and Energy of Ethiopia, were analyzed to calibrate and validate the SWAT model. These data were of particular importance, as they tested and calibrated the model, assessing the fidelity with which the model can reproduce river flow patterns in the watershed. Hydrogeologists have continuously applied this observed data for watershed hydrological modeling. In this study, based on the availability of the data, discharge data spanning from 2000 to 2014 were utilized to calibrate and validate the SWAT model.

2.2.7. The SWAT model setup

The SWAT model was executed at a 12.5 m DEM in the Earthdata Search database to delineate the watershed. With the SWAT model, flexible modeling of hydrological processes can be achieved using the computationally efficient Soil Conservation Service (SCS) Curve Number (CN) procedure[39] for surface runoff calculation. ArcSWAT was downloaded for free (https://swat.tamu.edu/software/arcswat/) based on ArcGIS (version 10.8). In this study, potential evapotranspiration was estimated using the Hargreaves techniques,[40] selected based on the availability of climate data. The calibration and validation of the model were performed using SWAT-CUP and the SUFI-2 algorithm, both of which are also recognized for producing accurate results with minimal iterations.[38] Detailed model equations and units are presented in the SWAT documents.[41] SWAT simulates the water balance components daily (Equation IV):

$$SW_t = SW_0 + \sum_{i=1}^{t}\left(R_{day} - Q_{surf} - E_a - W_{seep} - Q_{gw}\right) \quad \text{(IV)}$$

where SW_t is the final soil water content (mm) at time t, SW_0 is the initial soil water content at a t of 0 (or $i = 0$), R_{day} is the total precipitation for day i (mm), Q_{surf} is the surface runoff for day i (mm), E_a is the evapotranspiration for day i (mm), W_{seep} is the inflow to the vadose zone from the soil profile for day i (mm), and Q_{gw} is the return flow for day i (mm). This equation considers the contributing factors in soil water processes, including precipitation, runoff, evapotranspiration, seepage, and return flow, and is used to model hydrological processes in watershed applications. ArcSWAT partitions the watershed into sub-basins and HRUs according to

soil type, slope, and land cover. The HRUs were superimposed with soil and land cover data to model elementary hydrological processes such as runoff and infiltration. Weather data (air temperature and rainfall) were employed to tune model performance. Soil data from National Agricultural institute were cross-checked with the Food and Agriculture Organization soil map, and slope and elevation maps were produced from the DEM of the region.

2.2.7.1. Watershed delineation and hydrologic response units

Flow accumulation and direction were developed using ArcSWAT with the region's DEM. These steps are crucial for characterizing the watershed. This study divided the watershed into 30 sub-watersheds, facilitating the detailed visualization of hydrological units for the simulation of groundwater recharge employed in the SWAT model. The land use, soil, and slope data were combined to define HRUs using thresholds of 20% for land use, 10% for soil, and 20% for slope-based slope distribution of the region. This unit is one of the advances made by SWAT in simulating water balances for watersheds. These HRUs were employed to simulate hydrological processes (e.g., surface runoff and groundwater recharge) in the SWAT model.

2.2.7.2. Weather data integration

Daily data on precipitation and temperature from eight weather stations were processed for the ArcSWAT model. Meteorological variables (e.g., humidity, wind speed, and solar radiation) for which values were unavailable were estimated using the Weather Generator (WGEN-USER), with default values derived from the United States' climate data. This merging of weather data, combined with watershed and HRU delineations, enabled the simulation of groundwater recharge using the procedures provided in the ArcSWAT model.

2.2.7.3. Sensitivity analysis, model calibration, and model validation

Sensitivity analysis was conducted to understand the contribution of model input to the outputs, to calibrate the model, and to reduce uncertainty.[8,37] This process was crucial to enhancing the model's accuracy. During the process, some essential parameters for adjustment were identified, thereby reducing time and improving the accuracy of predictions.[37,38] The SWAT-CUP with the SUFI-2 methodology identified 13 parameters that significantly affected streamflow simulations (Table 3). These parameters were calibrated to align with local conditions, improving the model reliability.[17,42] Focusing on these critical parameters enhanced the model accuracy, ensuring alignment with observed data and improving its ability to simulate future hydrological responses to changes in land use and climate. Detailed descriptions of the parameters are available in the SWAT user manual for replication or further refinement.[43,44]

In this study, both manual and automated techniques were employed using observed river flow data for SWAT model calibration. The combination of these approaches was chosen to ensure greater accuracy and reliability, as manual techniques allow for expert judgment, while automated methods enhance efficiency and minimize human error.[13] To allow the model to stabilize, the first 2 years (2000 and 2001) were excluded as a warm-up period, following established hydrological modeling practices.[41] Calibration was based on 2002–2007 data, while validation used 2008–2014 data. For manual calibration, parameters were adjusted through trial and error to enhance the model performance.[38,43] In addition, the SUFI-2 method was employed to fine-tune parameters within defined ranges, thereby improving accuracy through a robust statistical approach.[17,45] To evaluate the model performance, metrics such as R^2, NSE, and PBIAS were applied. Calibration was accepted as successful if the mean flow difference was within ±15%, $R^2 > 0.60$, and NSE > 0.50, as previously reported.[8,45] The results showed a strong correlation between the simulated and observed river discharge during validation, confirming the model's reliability for predicting future hydrological changes and responses to land-use changes and climate variations (Figure 4).

2.2.7.4. Model performance metrics

Model validation demonstrated that a site-specific model could be used to predict without error, and the "sufficiency of accuracy" depended on project aims.[46,47] This involved using the model with calibrated parameters and comparing the model outputs to the observed

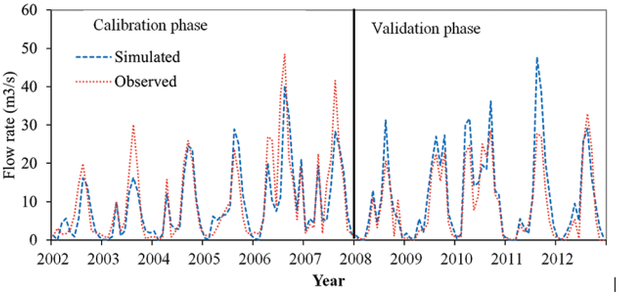


Figure 4. Comparison of measured and simulated river flow during the calibration and validation phases

Table 3. Sensitivity analysis results

Sensitivity rank	Parameters	Description	Parameter range	Fitted value
1	Curve number 2	Soil Conservation Service runoff curve number: Represents runoff potential based on land use, soil type, and cover.	±0.25	0.05
2	GW-DELAY	Groundwater delay: Time delay (in days) for groundwater flow to reach the stream channel, affecting baseflow dynamics.	0–500	59.4
3	CH-K2	Effective hydraulic conductivity in main channels: Influences baseflow and subsurface runoff through stream channels.	0–500	99.43
4	SOL-AWC	Available water capacity of soil layer: The soil's capacity to store water; important for hydrological modeling.	±0.25	0.04
5	CANMAX	Maximum canopy storage: The amount of water the canopy can hold before it is lost to evaporation or throughfall.	0–100	0.48
6	ALPHA-BF	Baseflow alpha factor: Defines the rate of baseflow contribution to streamflow.	0–1	0.03
7	ESCO	Soil evaporation compensation factor: Adjusts soil evaporation based on moisture availability.	0–1	0.97
8	EPCO	Plant uptake compensation factor: Adjusts plant transpiration based on soil moisture availability.	0–1	0.96
9	GW-QMN	Threshold depth of water in the shallow aquifer: Depth at which groundwater starts contributing to baseflow.	0–500	179.75
10	SOL-K	Saturated hydraulic conductivity: The rate at which water can flow through saturated soil, affecting groundwater recharge.	±0.25	0.07
11	CH-N2	Manning's value for main channels: Roughness coefficient for stream channels, influencing flow velocity and runoff.	0.01–0.3	0.14
12	SOL-Z	Depth from soil surface to bottom of layer: Specifies the depth of the soil profile, influencing water retention and plant root penetration.	±0.25	−0.02
13	RCHRG-DP	Deep aquifer percolation fraction: Fraction of water percolating into deep aquifers, influencing groundwater recharge.	0–1	0.24

data.[37,38] The analysis employed two primary measures for evaluating the SWAT model: NSE and R^2. These were the measures of a model's accuracy, reproducibility, and ability to fit observed data. R^2 represents the percentage of variance explained by the model and serves as a measure of goodness of fit, with values ranging from 0 to 1. It is computed as (Equation V):

$$R^2 = \frac{[\sum_i^n (Qobs - Qmo)(Qs - Qms)]^2}{\sum_i^n (Qobs - Qmo)^2 \sum_i^n (Qs - Qms)^2} \quad \text{(V)}$$

where Q_{obs} is the observed flow (m³/s) and Q_{mo} is its mean; Q_s is the simulated flow (m³/s) and Q_{ms} is its mean. An R^2 of 1 indicates a perfect fit, while 0 suggests a poor accuracy. The NSE measures the residual error relative to the variance of the observed data.[38,48] The NSE value ranges from −∞ to 1, with values closer to 1 indicating a better fit between observed and simulated data. An NSE value >0 suggests an acceptable model performance, while values below 0 indicate poor model fit, meaning the simulated data does not closely match the observed flow values.[37] The calibration and validation results demonstrate that the SWAT model effectively simulates monthly river discharge in the region, with high R^2 and NSE values indicating an accurate representation of hydrological dynamics (Table 4). The result aligns with the scholars' recommendations.[38] In addition, the results are consistent with previous studies that demonstrated SWAT's capability to model hydrological processes across various watersheds.[49] The model's performance validated its reliability for predicting the future impacts of land-use changes on water resources, providing a robust tool for sustainable water resource planning and management. Table 4 presents the performance metrics for the SWAT model, including the calibration and validation results.

In Table 4, R^2, NSE, and PBIAS values highlight the model accuracy and reliability during calibration

Table 4. The soil and water assessment tool model performance metrics

Gauging station	Model stage	Objective function		
		R^2	NSE	PBIAS
Germam	Calibration	0.84	0.75	−0.1
	Validation	0.79	0.72	−11

Abbreviations: NSE: Nash-sutcliffe efficiency; PBIAS: Percent bias.

and validation phases. The SWAT model performed well during both the calibration and validation periods. The model closely matched the observed data with an R^2 of 0.84 during calibration and 0.79 in validation. The SWAT model accurately estimated groundwater recharge, with NSE values of 0.75 (calibration) and 0.72 (validation) and minimal bias (PBIAS: −0.1 and −11, respectively). These results confirm its reliability for water resource management in the region.

2.2.8. Groundwater recharge estimation using the SWAT and change detection

In this study, groundwater recharge in the Dire Dawa watershed was assessed using the SWAT model, combined with remote sensing data and environmental variables. To isolate the impact of LULC changes on hydrological processes, change detection was performed using satellite imagery from 2000, 2010, and 2020. The LULC maps were compared using several methods, including image differencing, which highlighted significant land cover changes by subtracting one map from another; post-classified comparison, where each year's LULC map was independently classified and then compared to quantify the changes; and change matrix analysis, which assessed the accuracy of the LULC classifications and the nature of the transitions. These change detection results were integrated into the SWAT model to simulate how varying LULC scenarios influenced groundwater recharge and surface runoff. This approach provides a clear understanding of how LULC changes influence hydrological processes, while accounting for other factors that may affect groundwater recharge and surface runoff.

3. Results

3.1. Accuracy assessment

This research utilized LULC maps from 2000, 2010, and 2022, created using ERDAS IMAGINE 2015 and ArcGIS 10.8 software. Ground truth data were collected using GPS and Google Earth Pro, achieving an accuracy standard of 85% and a kappa coefficient of >0.85. In this study, 50 ground truth data points per land-use class in the watershed were utilized to optimize the accuracy of classification (Table 5). The accuracy assessment result achieved PA and UA values that met the required standard, allowing for further analysis.[35]

3.2. LULC change

This study analyzed the effects of LULC changes on groundwater recharge in the Dire Dawa watershed from 2000 to 2022. Six dominant LULC classes, that is, shrubland, forest, agriculture, settlement, desert, and river sand, were identified for the years 2000, 2010, and 2022 (Figure 5). The results show that agricultural and built-up areas increased while shrubland decreased. In addition, forest land, which covered approximately 85.3 km^2 (12.1%) in 2000, was drastically reduced to 55.7 km^2 (7.9%) by 2010 (Table 6). These alterations are primarily attributed to agricultural expansion and urbanization in this region. Impunity led to changes in the watershed's hydrology, modifying water infiltration, soil erosion, evapotranspiration, and runoff patterns. These results highlight the growing problem of land degradation and underscore the importance of sustainable land management and soil conservation as a safeguard against groundwater depletion and maintaining hydrological equilibrium within the watershed.

Remotely sensed imagery plays a significant role in monitoring LULC conversion, offering high spatial and temporal resolution for area conversion. In this study, a mixed approach involving both supervised and unsupervised image classification was employed, as it is widely used in remote sensing data analysis. This method focuses on the transitions between LULC classes and provides explicit information, facilitating the interpretation of valuable patterns. Areal extent measurements across different temporal periods were used to estimate the magnitude of LULC changes. The results of the LULC change analysis for the years 2000, 2010, and 2022, presented in Figure 5 and Table 6, illustrate the spatial and temporal variability of LULC across the watershed during the study period.

3.3. Hydrological impacts of LULC changes

The impacts of LULC changes on the groundwater recharge and surface runoff in the Dire Dawa watershed from 2000 to 2022 were evaluated using the SWAT model. The water balance components, specifically recharge and runoff, were estimated independently for each study period. Change detection was then conducted

Table 5. Accuracy assessment result of LULC classification

LULC classes	Shrubland	Agriculture	Forest	Built up	Bare land	Riverside sand	Total	Diagonal	UA (%)	PA (%)
Shrubland	10	0	0	0	0	0	10	10	100	77
Agriculture	1	7	0	0	0	0	8	7	88	78
Forest	1	0	7	0	0	0	8	7	88	100
Built up	0	1	0	7	0	0	8	7	88	100
Bare land	0	0	0	0	6	0	6	6	100	86
Riverside sand	1	1	0	0	1	7	10	7	70	100
Total	13	9	7	7	7	7	50	Overall accuracy (88%)		

Abbreviations: LULC: Land use and land cover; PA: Producer's accuracy; UA: User accuracy.

Table 6. Areal extent and relative change in land use and land cover (LULC) types

LULC classes	Areal extent of LULC types						Relative change in LULC types					
	2000		2010		2022		2010−2000		2022−2010		2022−2000	
	km²	%	km²	%	km²	%	km²	%	km²	%	km²	%
Shrubland	352.4	49.9	322.2	45.6	269	38.1	−30.2	−8.6	−53.2	−16.5	−83.4	−23.7
Agricultural land	217.8	30.9	262	37.1	332.5	47.1	44.2	20.3	70.5	26.9	114.7	52.6
Forested land	85.3	12.1	55.7	7.9	31.7	4.5	−29.6	−34.7	−24	−43.1	−53.6	−62.8
Built-up area	22.6	3.2	35.5	5	40.5	5.7	12.9	57.1	5	14.1	17.9	79.2
Bare land	20	2.8	22	3.1	23.4	3.3	2	10	1.4	6.4	3.4	17
Riverside sand	7.7	1.1	8.6	1.2	8.8	1.2	0.9	11.7	0.2	2.3	1.1	14.3

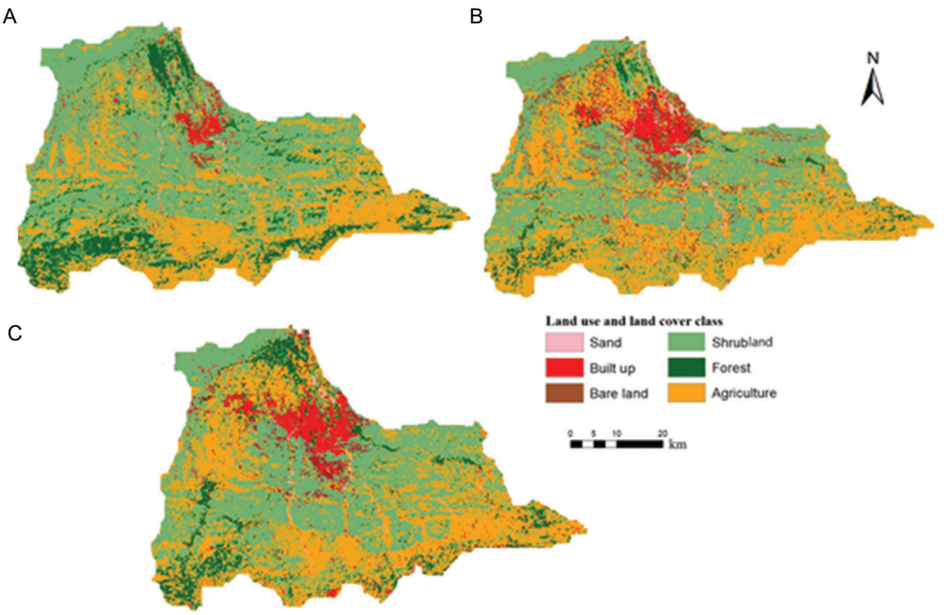


Figure 5. Land use and land cover maps of the study area for (A) 2000, (B) 2010, and (C) 2022

using GIS tools. To identify the impacts of LULC changes on groundwater recharge, all input factors used in the model, except the variable LULC, were kept constant. The analysis indicated that between 2000 and 2010, groundwater recharge decreased by 40.6 mm/y (20.4%), while surface runoff increased by 32.9 mm/y (15.3%). From 2010 to 2020, groundwater recharge continued to decline at a slower rate of 8.2 mm/y (5.2%),

while runoff rose by an additional 9.84 mm/y (4.0%). Over the entire study period, groundwater recharge decreased by 48.8 mm/y (24.5%), and surface runoff increased by 42.8 mm/y (19.9%). Table 7 presents the results of the change analysis.

These findings underscore the increasing pressure on water resources in the Dire Dawa watershed, resulting from urbanization and agricultural expansion. The SWAT model demonstrates how changes in land cover, such as the loss of shrubland and forests, disrupt the natural water cycle, leading to reduced groundwater recharge and increased surface runoff. To mitigate these effects, sustainable land management strategies, including ecosystem restoration and improved urban planning, are crucial for restoring the water balance in the region.

The areal variation of groundwater recharge over the Dire Dawa watershed is significant, with the highest recharge occurring in the eastern and northwestern sub-watersheds. In contrast, the central and northern regions have experienced a rapid decline in recharge (Figure 6). These results underscore the need for continuous, high-resolution monitoring to understand spatial and temporal effects of land-use changes on watershed hydrology. Maintaining a balance between land use and water resources is critical for the long-term sustainability of the watershed. Through adaptive management strategies, the sustainability of groundwater resources can be ensured, and the ecological integrity of the area, as well as the way of life that relies on its water supply, can be maintained.

4. Discussion

Using the SWAT model, this study examined the impacts of LULC changes on groundwater recharge in the Dire Dawa watershed, Ethiopia, from 2000 to 2022. The analysis indicates significant transformations in LULC, where agricultural land expanded by 114.7 km^2 (52.6%), built-up areas increased by 17.8 km^2 (79.2%), shrublands decreased by 83.4 km^2 (23.7%), and the forested regions declined by 53.6 km^2 (62.8%). The hydrological modeling results demonstrate that these LULC changes substantially reduced groundwater recharge by 48.8 mm/y (24.5%) and increased surface runoff by 42.8 mm/y (19.9%). These findings underscore the urgent need for sustainable land and water management strategies in the region. The SWAT model performance was assessed using key statistical metrics: R^2 values of 0.84 and 0.79, NSE values of 0.75 and 0.72, and PBIAS values of −0.1 and −11 during the calibration and validation periods, respectively. Based on established evaluation benchmarks, these results indicate strong model performance, characterized by high R^2 and NSE values and low PBIAS.[47] The model effectively simulates the hydrological processes within the study area and is well-suited for projecting river discharge and assessing future hydrological changes driven by land-use changes and climate variations.

Table 7. Average annual recharge and surface runoff changes due to land use and land cover changes (2022–2000)

Year	Simulated values			
	Groundwater recharge		Surface runoff	
	mm/y	%	mm/y	%
2000	199.4	39.2	215.2	29.8
2010	158.9	31.2	248.1	34.4
2022	150.7	29.6	258.0	35.8
	Changes			
2010−2000	−40.6	−20.4	32.9	15.3
2022−2010	−8.2	−5.2	9.8	4.0
2022−2000	−48.8	−24.5	42.8	19.9

The study by Jin *et al*.,[50] in the Jing River basin in China, demonstrated that LULC changes significantly reduced runoff and altered hydrological cycle processes. These findings align with those of the present study, confirming that urbanization and deforestation contribute to increased surface runoff and reduced groundwater recharge. Similarly, Lindle *et al*.[51] investigated groundwater recharge in the Limpopo province, South Africa, and revealed that ephemeral river flow and LULC changes significantly influence recharge rates. This supports the conclusion that land-use changes disrupt natural recharge mechanisms, highlighting the need for improved water resource management. In another related study, Mechal *et al*.[13] analyzed groundwater recharge in the Ziway Lake watershed of the Ethiopian Rift using the SWAT model and concluded that recharge rates vary significantly due to topographic and climatic influences. This finding is comparable to the present study's results, which show that climate variability and terrain characteristics play pivotal roles in recharge patterns. Collectively, these studies reinforce the importance of integrating climate variability into land-use planning.

The study by Bucha *et al*.[25] in Ethiopia's Lake Chamo sub-basin observed increased surface runoff and decreased infiltration due to land-use changes, aligning with the present study's conclusions. Additional studies support these findings. For example, a study of the

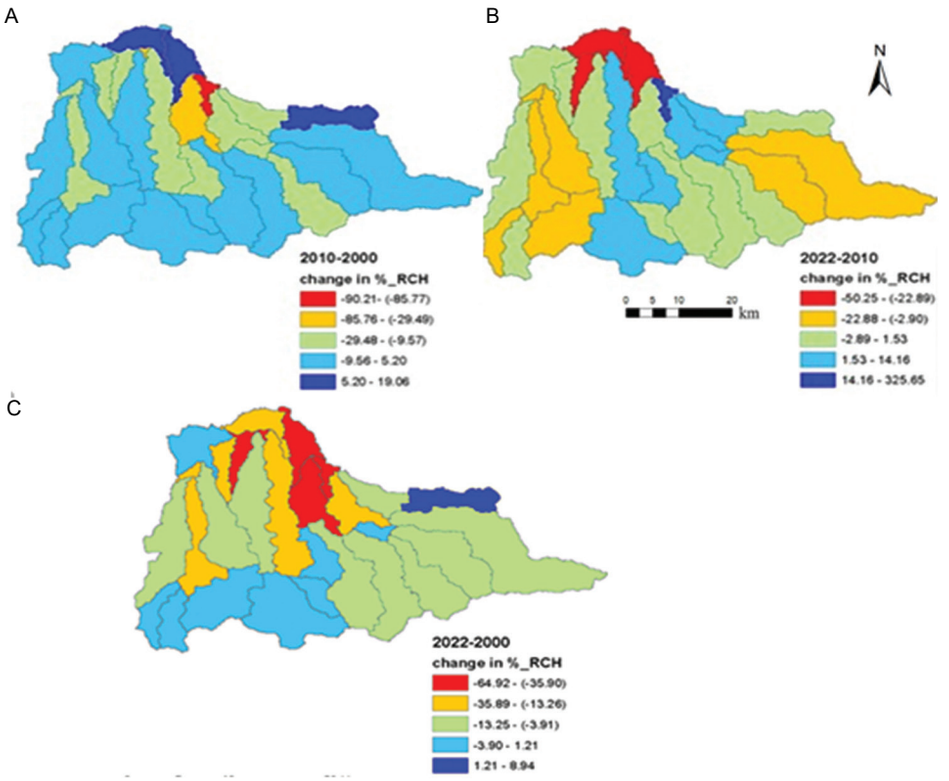


Figure 6. Groundwater recharge (RCH) changes due to land use and land cover: (A) 2010−2000, (B) 2022−2010, and (C) 2022−2000

Kanari River in India used the SWAT model to estimate groundwater recharge and surface runoff, revealing that 46.2% of precipitation contributed to surface runoff.[20] With NSE values of 0.83 and 0.71 for the calibration and validation, respectively, the model demonstrated good performance in hydrological assessment. Likewise, Yifru *et al*.[18] in South Korea integrated SWAT-MODFLOW to analyze spatiotemporal variations in groundwater recharge, demonstrating improved low-streamflow estimations and highlighting the benefits of coupling hydrological models. In the Afram Plains watershed of Ghana, a GIS-based recharge zone mapping approach categorized recharge potential into various zones, emphasizing the importance of spatial analysis in groundwater assessment.[52] The Olifants basin study in Southern Africa reported significant declines in groundwater recharge due to urbanization and agricultural expansion,[14] mirroring the present study's findings on LULC impacts. Meanwhile, the Lower Chenab Canal irrigation study in the Indus Basin projected a 37–40% increase in groundwater recharge under climate change scenarios,[53] contrasting with the declining recharge trends in the Dire Dawa watershed, highlighting the significance of regional climatic variability on groundwater dynamics.

This study utilized the SWAT model, which, despite its widespread application, carries inherent uncertainties related to land-use classifications. The accuracy of LULC change detection was influenced by the classification techniques used; although ERDAS IMAGINE and GIS tools were employed, potential errors in classification could have impacted the results. Future research should integrate climate models to assess the combined impacts of LULC changes and climate change on hydrological processes. Incorporating remote sensing techniques and machine learning approaches could enhance prediction accuracy. Furthermore, policy-oriented studies examining the socio-economic drivers of LULC change and their implications for sustainable water resource management would be valuable.

5. Conclusion

This study examined how LULC changes affect groundwater recharge and surface runoff in the Dire Dawa watershed from 2000 to 2022. Using remote sensing and GIS data, alongside the SWAT hydrological model, the research provides compelling evidence

of how human-driven landscape transformations are impacting the region's water resources. The SWAT model, calibrated and validated using the SUFI-2 method, showed strong performance, with R^2 values of 0.84 and 0.79, NSE values of 0.75 and 0.72, and PBIAS values of −0.1 and −11 for calibration and validation, respectively. Over the past two decades, forests and shrublands in the watershed have steadily declined, replaced by expanding agricultural lands and urban areas. These shifts have altered the watershed's hydrological behavior, reducing its capacity to absorb and store water. SWAT model results indicate a 24.5% decrease in groundwater recharge and a 19.9% increase in surface runoff during the study period. SWAT-CUP simulations further confirmed a 20% reduction in recharge, primarily linked to deforestation, urban growth, and agricultural expansion.

Land-use analysis showed a 79.2% increase in built-up areas and a 52.6% rise in agricultural land, while scrubland and forest areas decreased by 23.7% and 62.8%, respectively. These changes demonstrate the direct and measurable impact of LULC transformation on the watershed's hydrological system. The findings serve as a clear call to action: Without integrated and sustainable land management strategies, the Dire Dawa watershed will continue to face declining water availability and increased runoff risks. Protecting natural land cover, guiding urban expansion, and promoting sustainable agricultural practices are essential steps to preserving this vital ecosystem and its water resources for future generations.

To restore balance in the region's water cycle, this study recommends adopting sustainable land management practices. The findings offer important policy implications for protecting groundwater resources and ultimately achieving water security in a future characterized by expanding anthropogenic stress. Key recommendations include reforestation, improved agricultural methods, and efficient urban planning strategies to mitigate the adverse effects of rapid urbanization and land degradation. The effective management of groundwater recharge, through both conservation and sustainable development practices, will be a key to meeting future water needs and supporting regional resilience to climate change and population growth. This study contributes to the development of effective hydrological management strategies that address the immediate challenges of groundwater depletion in the study area and lay the foundation for sustainable watershed management in Ethiopia. Moreover, the findings offer insights that could be applicable to other regions facing similar environmental pressures, thereby supporting the resilience of both human and ecological systems globally. Future research is encouraged to integrate the MODFLOW groundwater model with the SWAT hydrological model. Such integration could enhance the accuracy of groundwater recharge estimates by more effectively capturing surface water-groundwater interactions, thereby improving model reliability and informing more effective water resource management strategies.

Acknowledgments

The authors would like to acknowledge the National Meteorological Institute and the Ministry of Water and Energy of Ethiopia for providing meteorological and hydrological data, respectively.

Funding

None.

Conflict of interest

The authors declare no conflicts of interest related to this work or with any institution or organization.

Author contributions

Conceptualization: Tariku Takele, Adula Bayisa
Data curation: Tariku Takele, Adula Bayisa
Methodology: Tariku Takele, Adula Bayisa
Supervision: Tariku Takele, Muralitharan Jothimani
Validation: All authors
Visualization: All authors
Writing–original draft: Tariku Takele, Adula Bayisa
Writing–review & editing: All authors

Availability of data

The data used in this study are available from the corresponding author on reasonable request.

References

1. Krueger E, Rao PSC, Borchardt D. Quantifying urban water supply security under global change. *Glob Environ Change.* 2019;56:66-74.
doi: 10.1016/j.gloenvcha.2019.03.00
2. Adger WN, Crépin AS, Folke C, *et al*. Urbanization,

migration, and adaptation to climate change. *One Earth*. 2020;3(4):396-399.
doi: 10.1016/j.oneear.2020.09.016

3. Takele T, Mechal A, Berhe BA. Evaluation of groundwater recharge potential using geospatial analysis in the Ziway Lake Watershed, Ethiopian Rift: A GIS and AHP-based methodological framework. *Environ Sustain Indic*. 2025;26:100692.
doi: 10.1016/j.indic.2025.100692
4. Ogbu KN, Ndulue EL, Ahaneku IE, Ubah IJ. Evaluation of the impact of climate change on streamflow using SWAT model. *ASM Sci J*. 2020;13:1-8.
doi: 10.32802/asmscj.2020.494
5. Das SK, Ahsan A, Khan M.H.R.B., Tariq M.A.U.R., Muttil, N., Ng, A.W.M. Impacts of climate alteration on the hydrology of the Yarra River Catchment, Australia using GCMs and SWAT model. *Water*. 2022;14(3):445.
doi: 10.3390/w14030445
6. Tola TL, Zhang K, Chukalla AD, *et al*. Spatiotemporal lakes surface area changes over 35 years and potential causes in the Central Rift Valley, Ethiopia. *J Hydrol Reg Stud*. 2024;54:101863.
doi: 10.1016/j.ejrh.2024.101863
7. Ware HH, Chang SW, Lee JE, Chung IM. Assessment of hydrological responses to land use and land cover changes in forest-dominated watershed using SWAT model. *Water*. 2024;16(4):528.
doi: 10.3390/w16040528
8. Zhao J, Zhang N, Liu Z, Zhang Q, Shang C. SWAT model applications: From hydrological processes to ecosystem services. *Sci Total Environ*. 2024;931:172605.
doi: 10.1016/j.scitotenv.2024.172605
9. Oo HT, Zin WW, Kyi CCT. Analysis of streamflow response to changing climate conditions using SWAT model. *Civil Eng J*. 2020;6(2):194-209.
doi: 10.28991/cej-2020-03091464
10. Mechal A, Birk S, Dietzel M, *et al*. Groundwater flow dynamics in the complex aquifer system of Gidabo River Basin (Ethiopian Rift): A multi-proxy approach. *Hydrogeol J*. 2016;25(2):519-538.
doi: 10.1007/s10040-016-1489-5
11. Hoogesteger J. Regulating agricultural groundwater use in arid and semi-arid regions of the Global South: Challenges and socio-environmental impacts. *Curr Opin Environ Sci Health*. 2022;27:100341.
doi: 10.1016/j.coesh.2022.100341
12. Hailesilassie W, Tegaye T. Comparative assessment of the water quality deterioration of Ethiopian Rift lakes: The case of Lakes Ziway and Hawassa. *Environ Earth Sci Res J*. 2019;6(4):162-166.
doi: 10.18280/eesrj.060403
13. Mechal A, Takele T, Meten M, Deyassa G, Degu Y. A modeling approach for evaluating the impacts of land use/land cover change for Ziway Lake Watershed hydrology in the Ethiopian Rift. *Model Earth Syst Environ*. 2022;8(4):4793-4813.
doi:10.1007/s40808-022-01472-w
14. Chen P, Ma X, Ma J, *et al*. Discrepancy and estimates of groundwater recharge under different land use types on the Loess Plateau. *J Hydrol Reg Stud*. 2024;53:101793.
doi: 10.1016/j.ejrh.2024.101793
15. Musie M, Sen S, Chaubey I. Hydrologic responses to climate variability and human activities in Lake Ziway Basin, Ethiopia. *Water.* 2020;12(1):164.
doi: 10.3390/w12010164
16. Zhang Z, Si H, Feng B, Wang Y, Lv M, Wagan B. Research of hydrological responses to land-use variability in a semiarid watershed based on SWAT model. *Fresenius Environ Bull*. 2014;23(5):1190-1197.
17. Mosase E, Ahiablame L, Park S, Bailey R. Modelling potential groundwater recharge in the Limpopo River Basin with SWAT-MODFLOW. *Groundw Sustain Dev*. 2019;9:100260.
doi: 10.1016/j.gsd.2019.100260
18. Yifru BA, Chung IM, Kim MG, Chang SW. Assessment of groundwater recharge in agro-urban watersheds using integrated SWAT-MODFLOW model. *Sustainability*. 2020;12(16):6593.
doi: 10.3390/su12166593
19. Takele T, Mechal A, Berhe BA. Assessing groundwater potential in the Ziway Lake Watershed using geographical information system, analytic hierarchy process, and drinking water quality index. *Glob Chall*. 2025;9:2400354.
doi: 10.1002/gch2.202400354
20. Trivedi A, Awasthi MK, Nandeha N, Gautam VK, Mehla MK. Addressing water security challenges through groundwater recharge for revival of Kanari River using AHP and geospatial techniques. *Discover Water.* 2024;4(1):59.
doi: 10.1007/s43832-024-00124-7
21. Arnold JG, Srinivasan R, Muttiah RS, Williams JR. Large area hydrologic modeling and assessment part I: model development. *J Am Water Resour Assoc*. 1998;34(1):73-89.
doi: 10.1111/j.1752-1688.1998.tb05961.x
22. Wagner PD, Bieger K, Arnold JG, Fohrer N. Representation of hydrological processes in a rural lowland catchment in Northern Germany using SWAT and SWAT+. *Hydrol Process*. 2022;36(5):e14589.
doi: 10.1002/hyp.14589
23. Sakulchai EKS, Charoen SY, Kamolsin YP. Assessment of the impact of land use change on runoff in Lam Phachi Basin using satellite data and SWAT model. *Kasetsart Univ J Sci Technol*. 2018;7(3):11-26.
24. Desta H, Lemma B. SWAT based hydrological assessment and characterization of Lake Ziway sub-watersheds, Ethiopia. *J Hydrol Reg Stud*. 2017;13:122-137.
doi: 10.1016/j.ejrh.2017.08.002
25. Bucha NM, Goshime DW, Awas AA, Asnake AB.

Hydrologic responses contemplating to land use land cover change and water balance of Lake Chamo sub-basin of Ethiopia. *Sustain Water Resour Manag.* 2024;10(1):29.
doi: 10.1007/s40899-023-01003-0

26. Kenea U, Adeba D, Regasa M, Nones M. Hydrological responses to land use land cover changes in the Fincha'a Watershed, Ethiopia. *Land.* 2021;10(9):916.
doi: 10.3390/land10090916
27. Beker BA, Kansal ML. Complexities of the urban drinking water systems in Ethiopia and possible interventions for sustainability. *Environ Dev Sustain.* 2023;26(2):4629-4659.
doi: 10.1007/s10668-022-02901-7
28. Gonza DK, Tekleweld FA, Hishe TG, Shumey EE, Birhane BS. Performance analysis of water meters for measuring domestic water consumption, the case of Dire Dawa, Ethiopia. *Int J Energy Water Resources.* 2021;5:405-412.
doi: 10.1007/s42108-021-00130-8
29. Tenaw D, Assfaw A. Households willingness to pay for improved urban water supply in Dire Dawa city administration: The role of socio-economic factors and water supply-related perceptions. *Sustain Water Resour Manag*. 2022;8(1):24.
doi: 10.1007/s40899-022-00625-0
30. Erena SH, Worku H. Dynamics of land use land cover and resulting surface runoff management for environmental flood hazard mitigation: The case of Dire Dawa city, Ethiopia. *J Hydrol Reg Stud*. 2019;22:100598.
doi: 10.1016/j.ejrh.2019.100598
31. Tilahun K, Merkel BJ. Estimation of groundwater recharge using a GIS-based distributed water balance model in Dire Dawa, Ethiopia. *Hydrogeol J*. 2009;17(6):1443-1457.
doi: 10.1007/s10040-009-0455-x
32. Beyene AD, Shumetie A. *Green Legacy Initiative for Sustainable Economic Development in Ethiopia*. Addis Ababa. Ethiopia: Ethiopian Economic Association (EEA); 2023.
33. Desta H, Fetene A. Land-use and land-cover change in Lake Ziway watershed of the Ethiopian Central Rift Valley Region and its environmental impacts. *Land Use Policy*. 2020;96:104682.
doi: 10.1016/j.landusepol.2020.104682
34. Teklay A, Dile YT, Asfaw DH, Bayabil HK, Sisay K. Impacts of climate and land use change on hydrological response in Gumara Watershed, Ethiopia. *Ecohydrol Hydrobiol*. 2020;21(2):315-332.
doi: 10.1016/j.ecohyd.2020.12.001
35. Foody GM, Mathur A. A relative evaluation of multiclass image classification by support vector machines. *IEEE Trans Geosci Remote Sens.* 2004;42(6):1335-1343.
doi: 10.1109/tgrs.2004.827257
36. Ougahi JH, Karim S, Mahmood SA. Application of the SWAT model to assess climate and land use/cover change impacts on water balance components of the Kabul River Basin, Afghanistan. *J Water Clim Change*. 2022;13(11):3977-3999.
doi: 10.2166/wcc.2022.261
37. Abbaspour KC. SWAT calibration and uncertainty programs: A user manual. 2015;103:17-66.
38. Abbaspour KC, Vejdani M, Haghighat S. *MODSIM07 - Land, Water and Environmental Management: Integrated Systems for Sustainability, Proceedings*; 2007.
39. Soil Conservation Service (SCS). *National Engineering Handbook, Section 4: Hydrology*. Department of Agriculture, Washington DC; 1972. p .762.
40. Hargreaves GH, Samani ZA. Estimating potential evapotranspiration. *J Irrig Drain Div*. 1982;108(3):225-230.
doi: 10.1061/jrcea4.0001390
41. Arnold JG, Kiniry JR, Srinivasan R, Williams JR, Haney EB, Neitsch SL. *Soil and Water Assessment Tool: Input/Output Documentation*. Version 2012. TR-439. United States: Texas Water Resources Institute, College Station; 2012. p. 1-650.
42. Fuka DR, Walter MT, MacAlister C, Steenhuis TS, Easton ZM. SWATModel: A multi-operating system, multi-platform SWAT model package in R. *J Am Water Resour Assoc*. 2014;50(5):1349-1353.
doi: 10.1111/jawr.12170
43. Arnold J, Srinivasan R, Neitsch S, *et al*. *Soil and Water Assessment Tool (SWAT) Global Applications*. Bangkok, Thailand: World Association of Soil and Water Conservation; 2009.
44. Neitsch SL, Williams JR, Arnold JG, Kiniry JR. *Soil and Water Assessment Tool Theoretical Documentation*. Version 2009. United States: Texas Water Resources Institute, College Station; 2011.
45. Bailey RT, Park S, Bieger K, Arnold JG, Allen PM. Enhancing SWAT+ simulation of groundwater flow and groundwater-surface water interactions using MODFLOW routines. *Environ Model Softw*. 2020;126:104660.
doi: 10.1016/j.envsoft.2020.104660
46. Pandit A, Hogan S, Mahoney DT, *et al*. Establishing performance criteria for evaluating watershed-scale sediment and nutrient models at fine temporal scales. *Water Res*, 2025;274:123156.
doi: 10.1016/j.watres.2025.123156
47. Moriasi DN, Gitau MW, Daggupati P, Pai N. Hydrologic and water quality models: Performance measures and evaluation criteria. *Trans ASABE.* 2015;58(6):1763-1785.
doi: 10.13031/trans.58.10715
48. Mengistu AG, Van Rensburg LD, Woyessa YE. Techniques for calibration and validation of SWAT model in data scarce arid and semi-arid catchments in South Africa. *J Hydrol Reg Stud*. 2019;25:100621.
doi: 10.1016/j.ejrh.2019.100621

49. Mechal A, Wagner T, Birk S. Recharge variability and sensitivity to climate: The example of Gidabo River Basin, Main Ethiopian Rift. *J Hydrol Reg Stud.* 2015;4:644-660.
doi: 10.1016/j.ejrh.2015.09.001
50. Jin T, Zhang X, Xie J, Liang J, Wang T. Study on hydrological response of runoff to land use change in the Jing River Basin, China. *Environ Sci Pollut Res*. 2023;30(45):101075-101090.
doi: 10.1007/s11356-023-29526-1
51. Lindle J, Villholth KG, Ebrahim GY, Sorensen JPR, Taylor RG, Jensen KH. Groundwater recharge influenced by ephemeral river flow and land use in the semiarid Limpopo Province of South Africa. *Hydrogeol J*. 2023;31(8):2291-2306.
doi: 10.1007/s10040-023-02682-x
52. Dekongmen BW, Anornu GK, Kabo-Bah AT, *et al*. Groundwater recharge estimation and potential recharge mapping in the Afram Plains of Ghana using SWAT and remote sensing techniques. *Groundwater Sustain Dev*. 2022;17:100741.
doi: 10.1016/j.gsd.2022.100741
53. Awan UK, Ismaeel A. A new technique to map groundwater recharge in irrigated areas using a SWAT model under changing climate. *J Hydrol*. 2014;519:1368-1382.
doi: 10.1016/j.jhydrol.2014.08.049

ACCSCIENCE PUBLISHING

Asian Journal of Water, Environment and Pollution. Vol. 22, No. 6 (2025), pp. 120-133.
doi: 10.36922/AJWEP025110078

ORIGINAL RESEARCH ARTICLE

Eco-friendly treatment of laboratory wastewater using plantain pseudo-stem

Hemalatha Kuppusamy[1]* and Ilangeswaran Dhanasamy[2]

[1]Department of Chemistry, Justice Basheer Ahmed Sayeed College for Women, Chennai, Tamil Nadu, India
[2]Department of Chemistry, Rajah Serfoji Government College, Thanjavur, Tamil Nadu, India
***Corresponding author**: Hemalatha Kuppusamy (hemalatha.k@jbascollege.edu.in)

Received: March 16, 2025; 1st revised: June 12, 2025; 2nd revised: July 15, 2025; 3rd revised: August 4, 2025; Accepted: July 25, 2025; Published online: August 28, 2025

Abstract: Chemical waste accumulates in the environment due to the improper disposal of laboratory wastewater. Wastewater generated after inorganic analysis typically contains hardness-causing substances, resulting in elevated oxygen demand. However, conventional wastewater treatment is often prohibitively expensive, especially in resource-limited settings. An eco-friendly method is therefore essential for recycling laboratory wastewater for washing purposes. In this study, laboratory wastewater was treated using a natural adsorbent—raw plantain pseudo-stem (RPPS)—and its powdered form (PPPS). Post-treatment analysis showed significant improvement in the physical and chemical parameters. Water quality indicators, such as pH, total dissolved solids (TDS), turbidity, conductivity, biological oxygen demand, chemical oxygen demand, and concentrations of heavy metals (lead, cadmium, mercury, iron, and copper), were assessed before and after treatment using inductively coupled plasma mass spectrometry. Results showed that both RPPS and PPPS were effective, eco-friendly, and cost-efficient for laboratory wastewater treatment, with PPPS exhibiting superior adsorption performance.

Keywords: Plantain pseudo-stem; Natural adsorbent; Wastewater treatment; Total dissolved solids; Biological oxygen demand; Chemical oxygen demand

1. Introduction

Water is indispensable for all living organisms. With the increasing global population, water demand is rising daily, while groundwater and surface water levels are diminishing due to excessive use.[1,2] Water treatment and reuse are widely recognized as effective solutions to address water supply challenges.[3] As water is continuously used, it becomes contaminated; thus, purification at the end of use is essential and is typically achieved through various treatment methods. It has been found that in developing countries, more than 1.6 billion people use unhygienic water, resulting in widespread incidence of diarrhea and other waterborne diseases.[4,5] Researchers have explored the use of natural materials—including fruits, vegetables, seeds, leaves, roots, and stem peels of plants—for their potential in water purification.[1,3,6-9] Various techniques have been investigated for the removal of heavy metal ions from water, including precipitation, membrane filtration, ion exchange, coagulation and flocculation, magnetic separation, biosorption, and adsorption.[10-20]

Agricultural biomass is a readily available, inexpensive, easy-to-handle, and environmentally benign material, making it a viable option for biosorption and adsorption of heavy metal ions from water.[17,18,21-25]

The banana fruit, an agricultural commodity valued at USD 63.6 billion, has a projected global production of 127.3 million tons.[22,24] India, accounting for 29% of global production, is the largest producer of bananas, followed by China and the Philippines. Notably, 60–80 tons of plantain stems per hectare are produced during fruit harvesting.[26,27] The plantain stem is the heaviest component of the banana plant, while the plantain pseudo-stem is hard, fibrous, and non-edible.[7,13,28]

In India, banana trees are integral to many auspicious rituals, particularly in South India, resulting in the widespread availability of plantain pseudo-stems. Once the fruit ripens and is harvested, the pseudo-stem—no longer functional—is chopped and often converted into waste biomass. While plantain stems are utilized for their therapeutic properties, the pseudo-stem is typically discarded.[29-31] Both the pseudo-stem and the stem play a crucial role in the transport of nutrients from the soil to the fruit. After harvest, the banana plant ceases to be useful, and the pseudo-stems are often burned or disposed of in rivers and lakes.[32,33]

Due to their high cellulose content and hygroscopic properties, banana stems are effective as a porous medium.[34] The stem filter media is capable of significantly lowering chemical oxygen demand (COD), total suspended solids levels, and turbidity during wastewater treatment processes.[35,36] Furthermore, chemical pre-treatments can reduce energy usage by improving the fibrillation of cellulose materials, altering the adsorbent surface, and boosting its capacity for ion adsorption.[22,37-39]

Chemicals used in laboratories are often disposed of as waste. However, improper disposal practices result in the discharge of water with persistence of hardness and other contaminants, leading to high oxygen demand, heavy metal accumulation, and environmental pollution. The high cost of wastewater treatment, especially under resource constraints, poses a significant challenge. This study examines the use of accessible and cost-effective pseudo-stems as a potential adsorbent for the purification of laboratory wastewater.

2. Materials and methods

2.1. Materials

The pseudo-stems were sourced from local vegetable markets in Chennai, India. The raw pseudo-stems were thoroughly cleaned with distilled water to remove dirt and debris, and then chopped into small fragments.

These fragments were oven-dried at 120°C for 4 h, ground using a high-speed grinder, and sieved through a 100-micron mesh to obtain uniform powdered material. For chemical activation, the pseudo-stem powder was treated with 5% acetic acid (Sigma-Aldrich, India) at 60°C for 2 h to enhance its porosity and surface area (Figure 1).

Laboratory wastewater was collected using sterile 5 L polyethene containers (Tarsons, India) placed beneath a laboratory sink during peak usage hours. Composite samples were obtained over a 3-h period to account for variability in discharge. The collected samples were immediately stored at 4°C and analyzed within 24 h.

2.2. Laboratory wastewater treatment with raw plantain pseudo-stem (RPPS)

Chopped RPPS was added at a concentration of 50 g/L to inert glass containers (Borosil, India), each containing 1 L aliquots of the untreated laboratory wastewater samples (S1–S5), Table 1. Each mixture was left undisturbed for 24 h at room temperature (25 ± 2°C). No pH adjustment was performed, and natural pH (5.5–6.8) was retained to reflect real laboratory conditions.

After treatment, the supernatant was decanted and filtered, yielding first-stage filtrate, referred to as F1. This process was repeated using fresh RPPS for up to four treatment cycles, producing sequential filtrates F2 through F4. F2–F3 are considered intermediate-stage treated water, while F4 is the final-stage treated water.

For each stage, the following parameters were measured: pH, TDS, turbidity, conductivity, COD, biological oxygen demand 5 days (BOD_5), and metal concentrations (lead, cadmium, mercury, iron, and copper). Digital pH meters (Systronics,

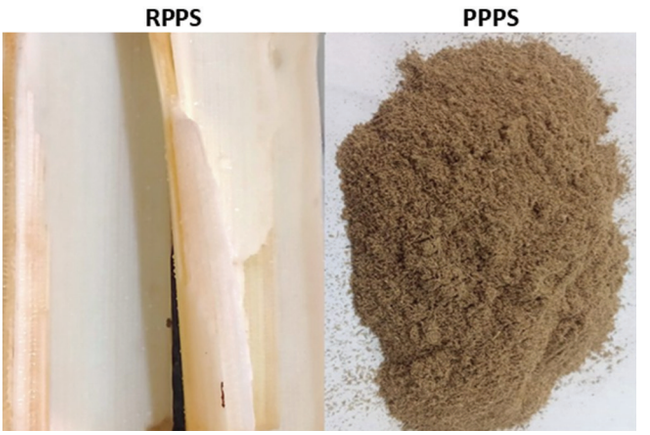


Figure 1. Photos of raw and powdered plantain pseudo-stem (RPPS and PPPS)

Table 1. Characteristics of laboratory wastewater samples

Sample	Metal	pH	TDS (mg/L)	COD (mg/L)	BOD_5 (mg/L)	Conductivity (mS/cm)	Turbidity (NTU)
S1	Lead	6.8	1660	42.6	5.4	2.4	27.0
S2	Cadmium	6.6	1750	56.0	4.8	2.6	22.2
S3	Mercury	5.5	1520	60.8	4.7	2.2	45.0
S4	Iron	5.8	1620	48.5	8.0	2.4	30.8
S5	Copper	6.0	1820	50.6	6.2	2.6	40.8

Abbreviations: BOD_5: Biological oxygen demand (5 days); COD: Chemical oxygen demand; mS/cm: milliSiemens per centimeter; NTU: Nephelometric turbidity unit; TDS: Total dissolved solids.

India), conductivity meters (Systronics, India), and TDS meters (Eutech Instruments, Singapore) were used. Turbidity was measured with a nephelometer (HACH 2100Q, USA; supplied in India). COD and BOD_5 were analyzed according to the standard methods provided by the American Public Health Association (APHA) for the examination of water and wastewater. Metal concentrations were determined using inductively coupled plasma mass spectrometry (Agilent 7900, USA). Fourier transform infrared spectroscopy (FTIR) analysis (PerkinElmer Spectrum Two, USA) was conducted. Scanning electron microscopy (SEM) analysis (Carl Zeiss, India) was conducted. All treatments were conducted in triplicate (n = 3), and the results are reported as mean ± standard deviation.

2.3. Laboratory wastewater treatment with chemically activated powdered plantain pseudo-stem (PPPS)

One gram of PPPS was added to 1 L screw-capped conical flasks (Borosil, India) containing the wastewater samples (S1–S5). The mixture was left for 24 h at room temperature (25 ± 2°C) under natural pH conditions (5.5–6.8). After settling, the mixture was filtered to obtain filtrate-1 (F1). This was then subjected to a second round of treatment with fresh PPPS (1 g), yielding filtrate-2 (F2).

All physicochemical parameters and heavy metal concentrations were analyzed for both raw and treated samples, following the same protocols and instrumentation as in the RPPS treatment.

A blank control (PPPS and distilled water) and a negative control (wastewater without PPPS) were processed alongside experimental samples to confirm treatment-specific effects.

2.4. Derivation of adsorption parameters

The experimental data in Table 2 were used to derive parameters for adsorption isotherm modeling. The amount of lead ions (Pb^{2+}) adsorbed at equilibrium (qe, mg/g) was calculated using the mass balance equation (Equation I):

$$qe = \frac{(Cs - Ce) \times V}{m} \quad \text{(I)}$$

Where Cs is the initial concentration of Pb^{2+} (fixed at 150 mg/L),

Ce is the equilibrium concentration (mg/L),

V is the volume of the solution (L),

and m is the mass of the adsorbent (g).

The derived parameters include: (1) Ce/qe for linearized Langmuir isotherm fitting; (2) ln(Ce) and ln(qe) for Freundlich isotherm fitting; and Ce/(Cs − Ce) and Ce/[(Cs − Ce) × qe] for Brunauer-Emmett-Teller (BET) isotherm analysis.

All logarithmic values are natural logarithms. These transformations enable direct comparison with the respective linear forms of the adsorption models and were applied uniformly across all experimental data.

2.5. Statistical analysis

Statistical analysis was performed using one-way analysis of variance to assess significant differences between treatment groups, with a significance threshold set at p<0.05. All analyses were carried out using ORIGIN 8 Pro software (OriginLab Corporation, USA).

2.6. Recovery of PPPS

Following biosorption, the PPPS underwent a recovery process to evaluate its potential for reuse in multiple adsorption cycles. The spent biosorbent was treated with 0.1 M hydrochloric acid, using a solid-to-liquid ratio of 1 g powder to 30 mL of eluent. The suspension was shaken for 60 min to facilitate desorption of the metal ions, after which it was separated by filtration.[40] The recovered biosorbent was thoroughly washed with distilled water to remove acid residues and then dried in a hot air oven at 120°C for 2 h.

Table 2. Experimental and calculated parameters for adsorption isotherm modeling

Ce (mg/L)	qe (mg/g)	Ce/qe	ln (Ce)	ln (qe)	Cs−Ce	Ce/(Cs−Ce)	Ce/([Cs−Ce]×qe)
10	1.2	8.33	2.30	5.30	140	0.0714	0.0595
20	2.0	10.00	3.00	6.90	130	0.1538	0.0769
40	3.0	13.33	3.69	8.50	110	0.3636	0.1212
60	3.6	16.67	4.10	9.43	90	0.6667	0.1852
80	4.0	20.00	4.38	10.09	70	1.1429	0.2857
100	4.2	23.81	4.61	10.61	50	2.0000	0.4762

Notes: All calculations assume a constant initial concentration of Cs=150 mg/L. Derived parameters were computed for the linearization of Langmuir, Freundlich, and BET isotherm models.
Abbreviations: BET: Brunauer–Emmett–Teller; Ce: Equilibrium concentration; Cs: Initial concentration; qe: Amount adsorbed at equilibrium.

3. Results and discussion

Before assessing the effectiveness of RPPS and PPPS in treating laboratory wastewater, control samples were examined. The blank controls (distilled water with RPPS or PPPS) showed minimal changes across all measured parameters, confirming that the adsorbents alone did not release significant contaminants or interfere with the readings. In the negative controls (untreated wastewater maintained under identical conditions), no notable changes in pH, TDS, turbidity, BOD_5, COD, or metal concentrations were observed after 24 h. These findings indicate that passive settling or environmental factors did not significantly contribute to parameter reductions, confirming that the improvements observed in treated samples were specifically attributable to RPPS and PPPS.

3.1. Physical characteristics of water samples

The untreated wastewater samples exhibited strong turbidity, dark coloration, and unpleasant odor, indicative of high pollutant load. In contrast, water treated with RPPS and PPPS showed noticeable improvement in color, clarity, and odor. These qualitative changes suggest effective removal or reduction of both organic and inorganic contaminants.

3.2. Variation in physicochemical parameters

Significant improvements in physicochemical parameters were observed post-treatment. Figures 2-4 display the comparative data for untreated and treated water across both RPPS and PPPS treatments.

Laboratory analysis showed consistent improvements in water quality after treatment. The pH values stabilized within the optimal range (6.0–7.5), and the acidic samples showed an increase in pH39. Alkaline samples exhibited a slight decrease in pH, indicating the buffering action of the biosorbent (Figures 2A and 3A). Significant reductions were observed in TDS, electrical conductivity (Figures 2B-C and 3B-C), and turbidity (70–90%) (Figures 2D and 3D), indicating efficient deionization and removal of suspended particulates. In addition, both COD and BOD_5 markedly decreased (Figures 2E-F and 3E-F), pointing to substantial removal of organic matter and microbial load.[35] Heavy metal removal exceeded 90% for lead, cadmium, mercury, iron, and copper, with PPPS demonstrating slightly better performance than RPPS (Figure 4).

3.3. FTIR analysis

3.3.1. FTIR analysis of PPPS

FTIR spectrum of PPPS (Figure 5) revealed characteristic peaks associated with cellulose (1026, 1423, and 891 cm^{-1}), lignin (1511 and 1635 cm^{-1}), and hemicellulose esters and acetyl groups (1736 cm^{-1}). Strong hydroxyl group absorption at 3417 cm^{-1}, important for adsorption processes, was also observed, along with peaks at 2920 cm^{-1} and 2850 cm^{-1}, corresponding to aliphatic groups, likely representing waxes or lipophilic substances.

3.3.2. FTIR analysis of Pb^{2+}-adsorbed PPPS

The FTIR analysis of Pb^{2+}-adsorbed PPPS (Figure 6) confirmed that adsorption occurs through complexation with hydroxyl and carboxyl groups, interaction with lignin/aromatic and alcohol sites, and structural modifications reflected by shifts and suppression of key absorption bands (Table 3).

3.4. Batch adsorption study

A batch adsorption experiment was conducted to assess the efficacy of pre-treated plantain pseudo-stem as a biosorbent for removing Pb^{2+} from aqueous solutions. The system was maintained under controlled conditions using a constant volume of 100 mL and a

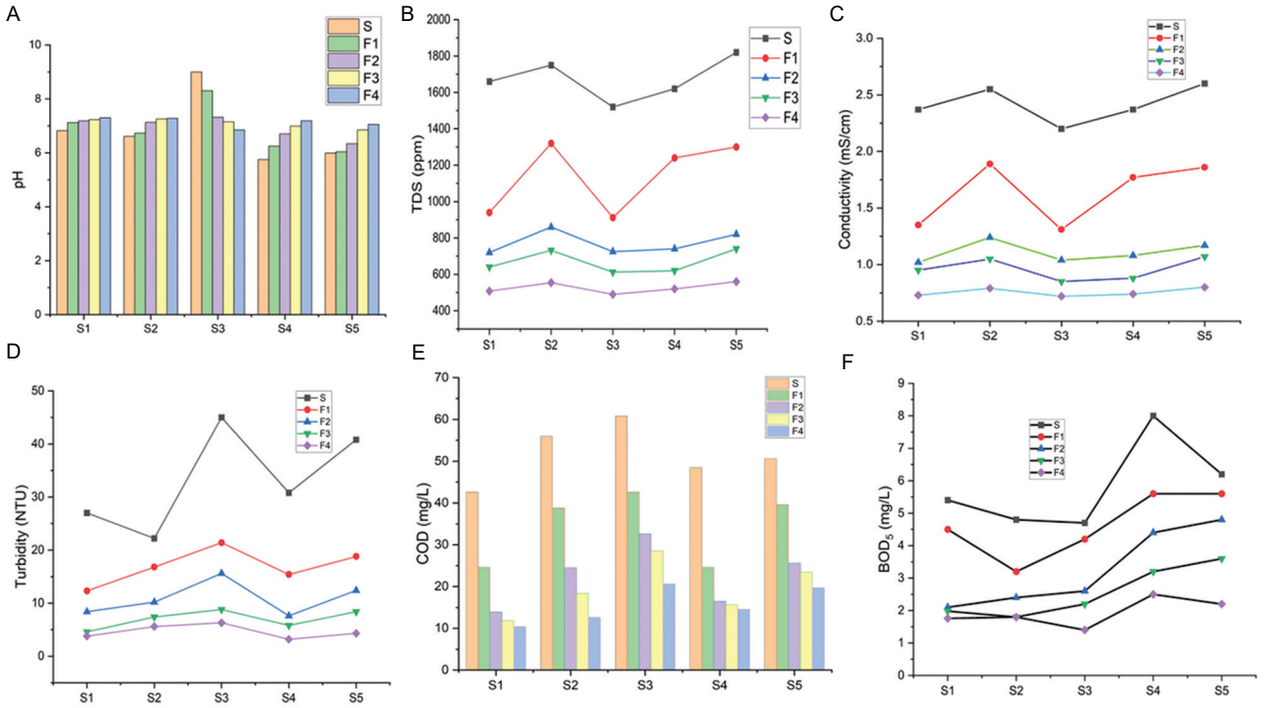


Figure 2. Variation of pH, TDS, electrical conductivity, turbidity, COD, and BOD_5 in the water samples treated with RPPS. Five wastewater samples (S1–S5) were untreated (S) or subjected to multiple rounds of RPPS treatment (F1–F4)

Abbreviations: BOD_5: Biological oxygen demand (5 days); COD: Chemical oxygen demand; mS/cm: millisiemens per centimetre; NTU: Nephelometric turbidity unit; RPPS: Raw plantain pseudo-stem; TDS: Total dissolved solids

Table 3. FTIR analysis of PPPS before and after adsorption of Pb^{2+}

Wavenumber (cm^{-1})	Peak (unadsorbed)	Peak (Pb^{2+} adsorbed)	Functional group	Interpretation
~3417	3417.53	3416.13	O–H stretching	Slight shift of H-bonding affected by Pb^{2+} interaction with hydroxyl groups
~2920	2920.10	2923.82	C–H (aliphatic)	Minor shift, possibly due to structural reordering
~1736	1736.28	Absent	C=O (carbonyl)	Disappearance suggests Pb^{2+} complexation with carboxyl groups in hemicellulose
~1635	1635.45	1636.24	Aromatic C=C/H_2O	Unchanged lignin/aromatic region
~1511	1511.37	Absent	Lignin (C=C)	Disappearance may indicate Pb^{2+} interaction with aromatic rings
~1423	1423.84	1435.50	CH_2 bending	Slight shift due to structural rearrangement
~1247	1247.64	1249.03	C–O–C (ether)	Retained, suggesting minimal effect
~1026	1026.76	1033.26	C–O stretching	Shifted indicates interaction between Pb^{2+} and alcohol/ether groups
~891	891.63	894.20	β-glycosidic bonds	Retained, indicating cellulose backbone stability

Abbreviations: FTIR: Fourier transform infrared spectroscopy; Pb: Lead; PPPS: Powdered plantain pseudo-stem.

fixed adsorbent dosage of 2 g, resulting in a working concentration of 20 g/L. The initial Pb^{2+} concentration was set at 150 mg/L to simulate moderate contamination levels. The pH of the solution was adjusted and maintained within the optimal range of 4.5–5.5, where maximum adsorption is anticipated due to the favorable

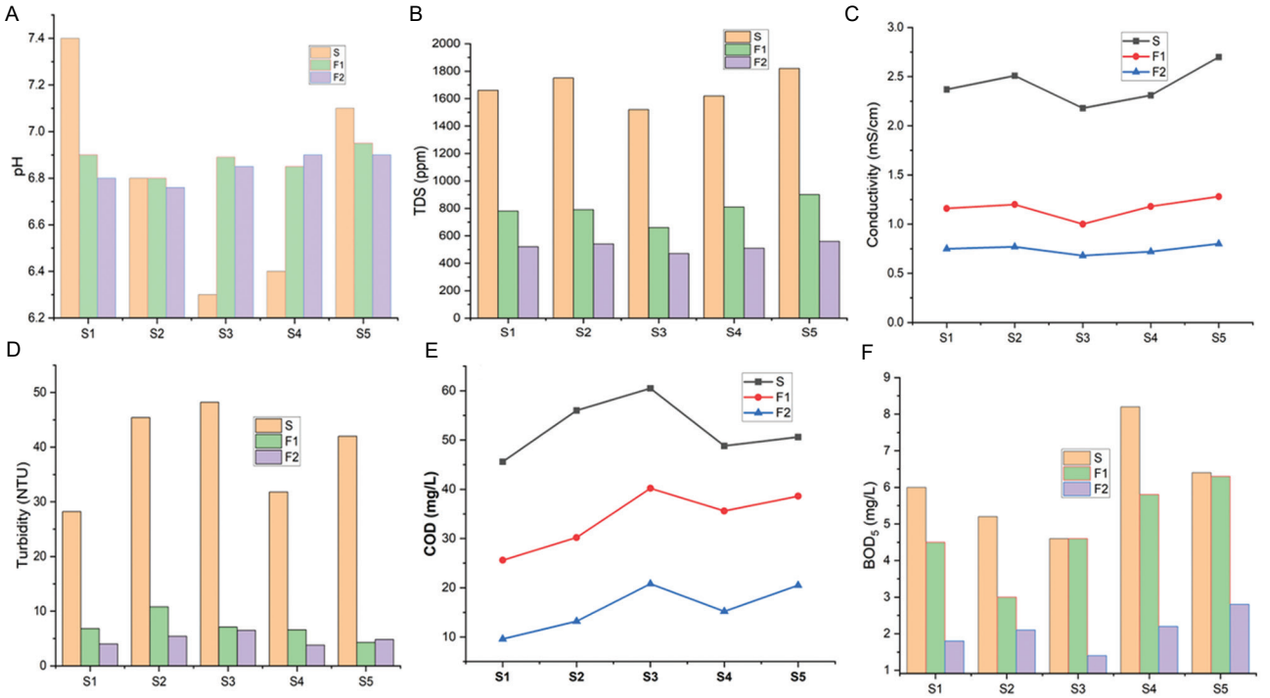


Figure 3. Variation of pH, TDS, electrical conductivity, turbidity, COD, and BOD_5 in the water samples treated with PPPS. Five wastewater samples (S1–S5) were untreated (S) or subjected to multiple rounds of PPPS treatment (F1–F2)

Abbreviations: BOD_5: Biological oxygen demand (5 days); COD: Chemical oxygen demand; mS/cm: millisiemens per centimetre; NTU: Nephelometric turbidity unit; PPPS: Powdered plantain pseudo-stem; TDS: Total dissolved solids

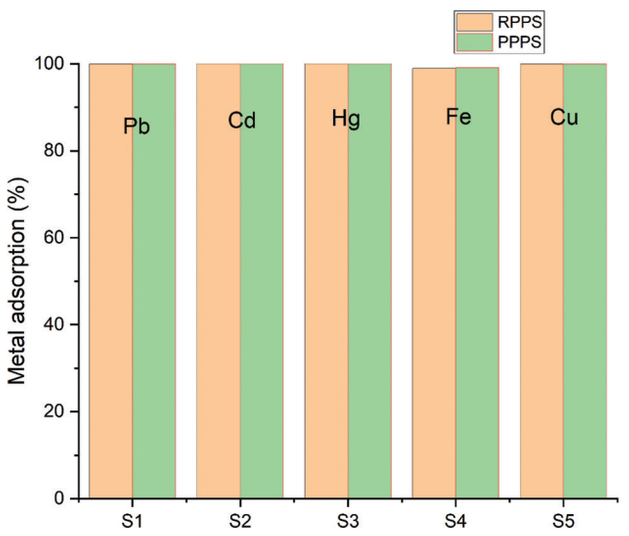


Figure 4. Percentage of metal adsorption in the water samples (S1–S5) treated with RPPS and PPPS Abbreviations: Cd: Cadmium; Cu: Copper; Fe: Iron; Hg: Mercury; Pb: Lead; PPPS: Powdered plantain pseudo-stem; RPPS: Raw plantain pseudo-stem

ionization of active surface functional groups. The temperature during the study was kept constant between 25°C and 30°C to replicate typical ambient conditions. Contact time was varied from 0 to 180 min at 30-min intervals to monitor adsorption kinetics. Samples were collected at each time point and analyzed for residual Pb^{2+} concentrations. This experimental setup facilitated the evaluation of adsorption capacity, equilibrium time, and overall performance of the plantain pseudo-stem adsorbent, providing a foundation for kinetic and isotherm modeling.[41]

3.4.1. Langmuir adsorption isotherm

The adsorption data were analyzed using the Langmuir isotherm model to evaluate the monolayer adsorption capacity and the surface affinity of the adsorbent for Pb^{2+}. The linearized form of the Langmuir equation is shown in Equation II.

$$\frac{1}{qe} = \frac{1}{q_{max}.KL}.\left(\frac{1}{Ce}\right) + \frac{1}{q_{max}} \quad \text{(II)}$$

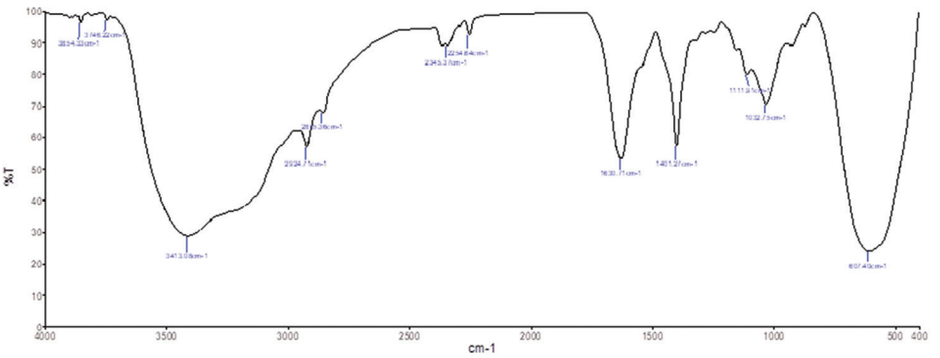


Figure 5. FTIR spectrum of PPPS
Abbreviations: FTIR: Fourier transform infrared spectroscopy; PPPS: Powdered plantain pseudo-stem

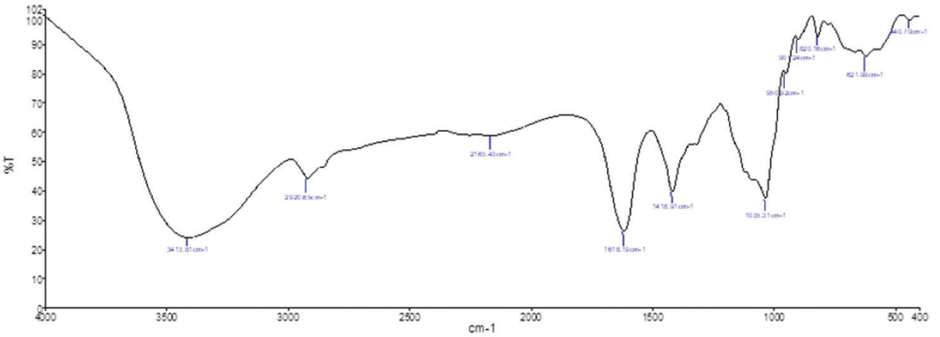


Figure 6. FTIR spectrum of Pb^{2+}-adsorbed PPPS
Abbreviations: FTIR: Fourier transform infrared spectroscopy; Pb: Lead; PPPS: Powdered plantain pseudo-stem

Where, qe = Amount of adsorbate adsorbed at equilibrium (mg/g)

q_{max} = Maximum monolayer adsorption capacity (mg/g)

KL = Langmuir adsorption constant related to the affinity of the binding sites (L/mg)

Ce = Equilibrium concentration of adsorbate in solution (mg/L).

A plot of 1/qe versus 1/Ce (Figure 7) yielded a straight line with an excellent linear fit ($R^2 = 0.99994$). The slope and intercept of the linear regression were 6.62334 and 0.17019, respectively. From these values, the Langmuir constants were calculated as follows: (1) the monolayer adsorption capacity (q_{max} = 1/ intercept) was 5.876 mg/g. (2) The Langmuir constant (KL = Slope/intercept) was 38.93 L/mg. The high q_{max} indicates that the adsorbent possesses a substantial number of active sites capable of binding the target ion. In contrast, the large value of KL reflects a strong affinity between the adsorbate and the surface. The near-unity R^2 value confirms that the adsorption process adheres to the Langmuir model exceptionally well, suggesting that adsorption occurs as a monolayer on a homogeneous surface with uniform energies of adsorption. No significant interactions between

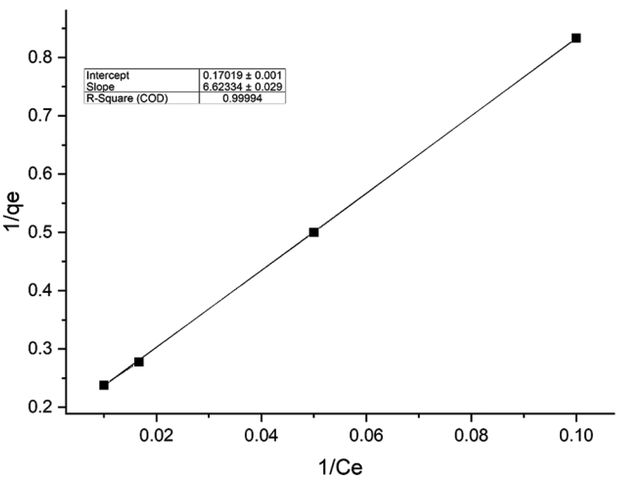


Figure 7. Langmuir isotherm modeling of Pb^{2+} adsorption by PPPS
Abbreviations: Ce: Equilibrium concentration; qe: Amount adsorbed at equilibrium; Pb: Lead; PPPS: Powdered plantain pseudo-stem

adsorbed molecules were observed, further supporting the validity of the Langmuir assumptions.

3.4.2. Freundlich adsorption isotherm

The experimental adsorption data were also evaluated using the Freundlich isotherm, an empirical model describing adsorption on heterogeneous surfaces. The linearized form of the Freundlich equation is given in Equation III.

$$\ln q_e = \ln K_F + \frac{1}{n} \ln Ce \quad \text{(III)}$$

where, qe = Amount of adsorbate adsorbed at equilibrium (mg/g)

KF= Freundlich adsorption constant indicative of adsorption capacity ([mg/g][L/mg]$^{1/n}$)

n = Freundlich intensity parameter related to adsorption favorability (dimensionless)

Ce = Equilibrium concentration of adsorbate in solution (mg/L).

A plot of ln qe versus ln Ce (Figure 8) yielded a perfectly linear relationship (R^2 = 1.000), indicating an excellent fit to the Freundlich model. The slope of the plot was 2.303, corresponding to 1/n, which represents the adsorption intensity. Thus, the Freundlich constant (n = 1/2.303) is 0.434, suggesting a chemically favorable adsorption process, as n <1 typically reflects strong interactions between adsorbate and adsorbent. The pronounced linearity of the Freundlich plot indicates that adsorption likely takes place on a heterogeneous surface with sites of varying energies and supports the presence of multilayer adsorption. In addition, the model's strong fit demonstrates that the adsorbent is effective across a wide range of adsorbate concentrations. Overall, the Freundlich isotherm accurately characterizes the adsorption behavior, and the high slope value indicates strong affinity and a non-uniform energy distribution among adsorption sites.

3.4.3. BET adsorption isotherm

The linearized BET equation is given in Equation IV.

$$\frac{Ce}{(Cs - Ce)qe} = \frac{1}{qm.C} + \frac{C-1}{qm.C}.\left(\frac{Ce}{Cs}\right) \quad \text{(IV)}$$

Where, Ce = Equilibrium concentration of adsorbate in solution (mg/L)

Cs = Initial adsorbate concentration in the solid phase (mg/L)

qe = Amount of adsorbate adsorbed at equilibrium (mg/g)

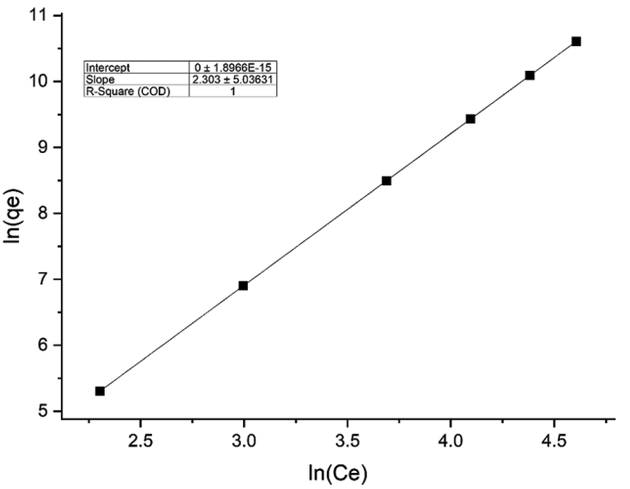


Figure 8. Freundlich isotherm modeling of Pb^{2+} adsorption by PPPS

Abbreviations: Ce: Equilibrium concentration; Cs: Initial concentration; qe: Amount adsorbed at equilibrium; Pb: Lead; PPPS: Powdered plantain pseudo-stem

qm = Maximum monolayer adsorption capacity (mg/g)

C = Dimensionless constant related to adsorption affinity.

A plot of Ce/(Cs−Ce) versus Ce/([Cs−Ce] qe) (Figure 9) yielded a highly linear trend (R^2 = 0.99983), indicating excellent agreement between the experimental data and the BET model. The slope and intercept were obtained as 0.21563 and 0.04268, respectively. Using these values, the BET constants were calculated: (1) Monolayer adsorption capacity (qm = 1/[slope + intercept]) is 3.98 mg/g; and (2) BET constant (C = 1 + [slope/intercept]) is 6.05.

These results indicate that multilayer adsorption plays a significant role and that the adsorbent has a well-defined surface with moderate affinity for Pb^{2+} beyond monolayer coverage. The high C value suggests favorable adsorbate–adsorbent interactions in the first adsorption layer, which is a key feature of BET-type behavior.

Overall, the adsorption data suggest that the monolayer plateau begins near a qe value of 4.2 mg/g, indicating a good fit for the Langmuir isotherm, which assumes monolayer adsorption on a homogeneous surface. However, the non-linear and increasing qe values at higher concentrations suggest a better fit with the Freundlich isotherm, which accounts for heterogeneous surface energies and multilayer adsorption behavior.

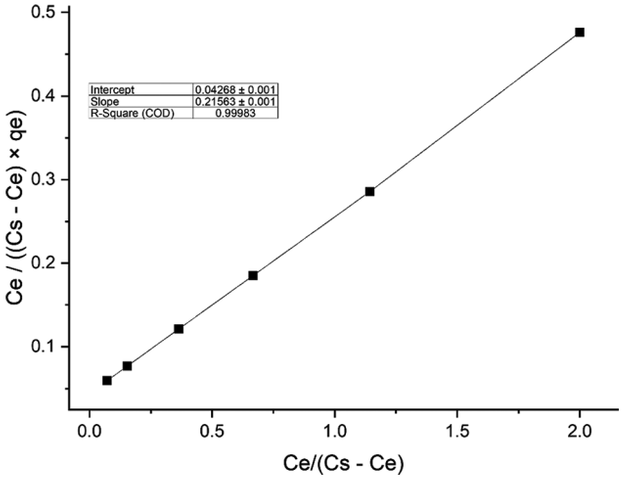


Figure 9. BET isotherm modeling of Pb^{2+} adsorption by PPPS

Abbreviations: BET: Brunauer–Emmett–Teller; Ce: Equilibrium concentration; qe: Amount adsorbed at equilibrium; Pb: Lead; PPPS: Powdered plantain pseudo-stem

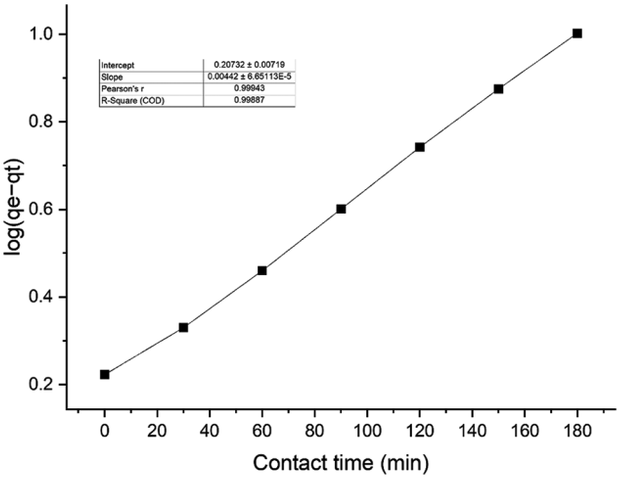


Figure 10. Pseudo-first-order kinetic model for the adsorption of Pb^{2+} by PPPS

Abbreviations: qe: Amount adsorbed at equilibrium; qt: Amount of adsorbate adsorbed at time t; Pb: Lead; PPPS: Powdered plantain pseudo-stem

Moreover, the trend beyond 80 mg/L shows signs of additional adsorption layers forming, which supports the applicability of the BET model for multilayer adsorption at higher concentrations.

3.5. Adsorption kinetics

Kinetic studies are crucial for understanding the adsorption mechanism and rate-controlling steps, which aid in optimizing adsorption processes. Among the commonly used models, the pseudo-first-order model typically describes physisorption, while the pseudo-second-order model is often associated with chemisorption as the rate-limiting step. Comparing model parameters and correlation coefficients helps identify the best-fitting mechanism and provides insights into the adsorbate–adsorbent interaction and system efficiency.

3.5.1. Pseudo-first-order

The adsorption kinetics were evaluated using the pseudo-first-order model. A linear plot of Figure 10 showed excellent correlation ($R^2 = 0.99887$), indicating good agreement with the model. The rate constant (k1) was calculated from the slope ($0.00442 \pm 6.65 \times 10^{-5}$), and the intercept ($0.20732 \pm 0.00719$) corresponds to log(qe). The high Pearson's correlation coefficient ($R = 0.99943$) and the low residual sum of squares (5.57×10^{-4}) confirm that the adsorption follows pseudo-first-order kinetics under the studied conditions.[41]

3.5.2. Pseudo-second-order

The adsorption kinetics were further evaluated using the pseudo-second-order model, which is based on the assumption that the adsorption process may involve chemisorption through electron sharing or exchange between the adsorbent and adsorbate. A linear plot of t/qt versus time (Figure 11) yielded a high correlation coefficient ($R^2 = 0.99023$), indicating that the experimental data fit the model well. The slope and intercept of the plot were 0.2294 ± 0.01019 and 2.42643 ± 1.10253, respectively, from which the equilibrium adsorption capacity and the pseudo-second-order rate constant were determined. The high Pearson's R value (0.9951) and the relatively low residual sum of squares (13.09) further support the applicability of this model.[41] These results suggest that the adsorption process follows pseudo-second-order kinetics, implying that chemisorption is likely the rate-limiting step. Overall, the model provides a good description of the experimental data and indicates a strong interaction between the adsorbate and adsorbent.

3.6. Comparative performance: RPPS versus PPPS

A comparative assessment between RPPS and PPPS treatments revealed that PPPS achieved equal or superior contaminant removal using only two treatment cycles, compared to five cycles required for RPPS. The enhanced efficiency of PPPS is attributed to its greater surface area, fibrous structure, and porous morphology, which collectively increase the number of active adsorption sites.

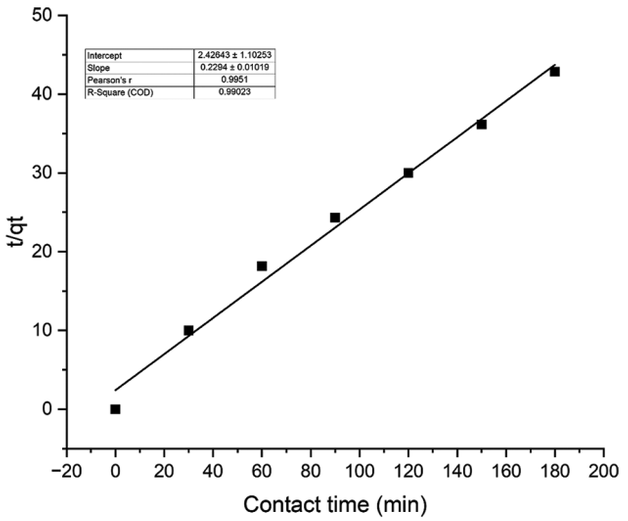


Figure 11. Pseudo-second-order kinetic model for the adsorption of Pb^{2+} by PPPS

Abbreviations: qe: Amount adsorbed at equilibrium; qt: Amount of adsorbate adsorbed at time t; Pb: Lead; PPPS: Powdered plantain pseudo-stem

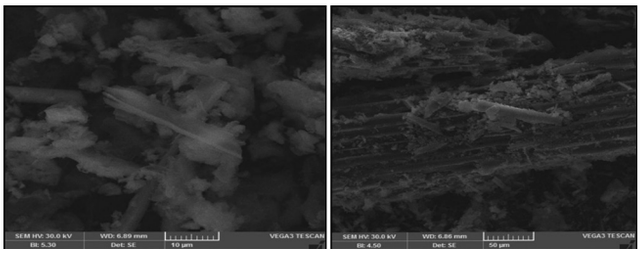


Figure 12. SEM images of PPPS

Abbreviations: SEM: Scanning electron microscopy; PPPS: Powdered plantain pseudo-stem

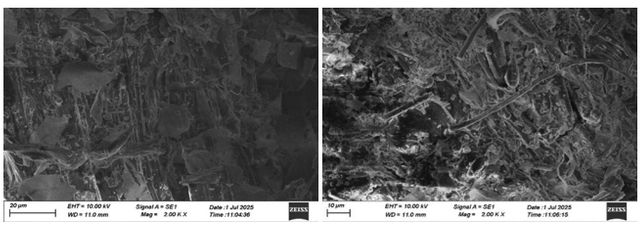


Figure 13. SEM images of the Pb^{2+} adsorbed PPPS

Abbreviations: SEM: Scanning electron microscopy; Pb: Lead; PPPS: Powdered plantain pseudo-stem

3.6.1. Morphological analysis and adsorption potential of PPPS

The SEM analysis (Figure 12) of PPPS reveals a rough, porous surface interspersed with fibrous structures, significantly increasing its active surface area. This structural characteristic is advantageous for adsorption applications, as the increased surface exposure provides a greater number of binding sites for metal ions, thereby improving adsorption capacity.

Furthermore, the observed variation in particle size and shape may contribute to non-uniform binding efficiency across different regions of the material. However, the overall adsorption potential remains high due to the presence of extensive surface structures available for interaction. Notably, the presence of elongated fibrous structures, likely representing lignocellulosic bundles, suggests incomplete delignification, particularly if the material underwent pre-treatment for fiber extraction. Residual lignin and hemicellulose could influence the surface chemistry and metal ion affinity, highlighting the need for further investigation into their role in adsorption efficiency.

3.6.2. SEM analysis of Pb^{2+}-adsorbed PPPS

After exposure to Pb^{2+} ions, the surface undergoes a notable morphological transformation as shown in Figure 13. The previously defined fibrous structure appears distorted and irregular, with amorphous and granular deposits visible on the surface. These particulates are likely lead complexes or precipitates, formed as Pb^{2+} interacts with functional groups on the plant matrix. Increased roughness, pore formation, and fiber fragmentation are also evident, indicating that metal ion binding may have caused localized swelling, collapse, or chemical etching of the biomass surface. These changes suggest the formation of surface complexes between Pb^{2+} ions and oxygen-containing functional groups.

These morphological changes strongly support the hypothesis that Pb^{2+} adsorption on plantain pseudo-stem occurs through a combination of surface complexation and ion-exchange, facilitated by the natural porosity and functional groups in the biomass. The post-adsorption surface damage and particle deposition are clear indications of successful metal uptake. These findings, when combined with FTIR results, suggest that hydroxyl, carbonyl, and ether groups play a significant role in metal binding. This underscores the adsorptive potential of plantain pseudo-stem for heavy metal removal from aqueous systems.

3.6.3. SEM analysis of recovered PPPS

The surface morphology of the recovered plantain pseudo-stem (Figure 14) reveals a noticeably more porous and rough texture, resulting from the degradation of hemicellulose and partial delignification during the treatment process. These structural alterations are

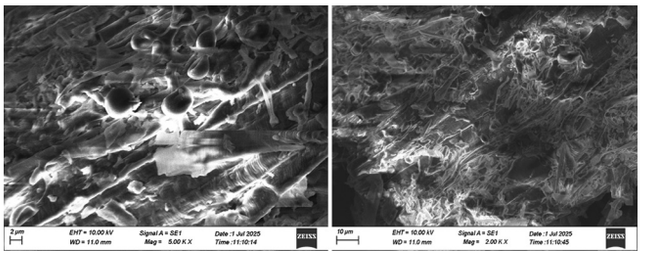


Figure 14. SEM images of the recovered PPPS
Abbreviations: SEM: Scanning electron microscopy; PPPS: Powdered plantain pseudo-stem

accompanied by visible cracks, micro fissures, and loosened fiber bundles, which collectively contribute to an increased surface area—an advantageous feature for subsequent adsorption-based applications. Disruption at the cell wall level is also evident, with signs of rupture and swelling, particularly in samples subjected to microbial or chemical hydrolysis, indicating active biodegradation on the surface. In addition, the presence of granular or crystalline deposits suggests residual salts or precipitates from wastewater exposure. Compared to untreated material, the treated pseudo-stem appears cleaner but more fragmented, with a clearer delineation of fiber bundles due to the separation of the supporting matrix. These changes demonstrate the enhanced suitability of the processed pseudo-stem for further functionalization or use in value-added applications, such as biosorption, composite development, or enzymatic hydrolysis.

3.7. Reusability of PPPS

The regeneration efficiency of PPPS was assessed over three consecutive cycles. The first cycle maintained high removal of Pb^{2+}, while the second and third cycles retained approximately 75% and 50% of the initial adsorption capacity, respectively. The sustained performance in later cycles is attributed to the acid treatment's ability to restore a significant proportion of active sites by desorbing bound Pb^{2+} ions, while preserving the structural integrity of the biomass. A gradual decline in capacity likely results from irreversible binding, structural degradation, or partial loss of functional groups during repeated use.

3.8. Comparative performance of PPPS with other biosorbents

As reported in Section 3.4.1, the monolayer adsorption capacity of PPPS for Pb^{2+} was approximately 5.88 mg/g. When compared with other agricultural biosorbents, such as banana peel (3.6–5.1 mg/g),[42] orange peel (4.8–6.2 mg/g),[43] and sugarcane bagasse (4.5–7.4 mg/g),[44] PPPS demonstrates competitive performance. This highlights its effectiveness and suitability as a low-cost, high-potential biosorbent. Furthermore, unlike many biosorbents that require extensive chemical pre-treatment, PPPS performed well with minimal processing, making it more accessible and environmentally favorable for real-world applications.

3.9. Applicability and environmental impacts

Although the chemical parameters of the treated water did not fully meet the drinking water standards set by Indian regulatory agencies, biosorption with plantain pseudo-stem significantly improved water quality. Parameters, such as pH, TDS, COD, BOD_5, and heavy metal concentrations were notably reduced, making the treated water suitable for non-potable applications, such as laboratory washing and industrial reuse. This has meaningful implications for water conservation in resource-limited settings, where potable water must be preserved for essential uses. The study suggests that while the biosorbent may not yet replace conventional purification technologies for potable water, it offers a promising, cost-effective solution for secondary water treatment.

The study highlights the simplicity and cost-effectiveness of the plantain pseudo-stem in the purification process. A container is sufficient for PPPS and RPPS methods, requiring minimal infrastructure and equipment. Furthermore, plantain pseudo-stems are commonly available waste biomass, making them an attractive choice for utilization as a biosorbent. This makes the purification process environmentally friendly and sustainable, as it utilizes a renewable and abundant resource.

The observed fungal growth on the plantain pseudo-stem after RPPS treatment indicates that it undergoes degradation easily. The demonstrated reusability of PPPS further enhances the sustainability of the purification process by reducing waste generation and resource consumption.

4. Conclusion

The increasing discharge of laboratory wastewater, laden with chemical residues, poses a significant challenge to environmental sustainability. Given the indispensable role of chemicals in scientific research, particularly in the field of chemistry, there is a pressing need for environmentally responsible treatment strategies that do not compromise the integrity of research.

In this study, we experimentally demonstrated a sustainable and efficient approach to laboratory wastewater treatment using plantain pseudo-stem, an abundant agricultural by-product in India, traditionally discarded after ceremonial use. Both raw and powdered samples were evaluated as biosorbents. The findings reveal substantial improvements in water quality, including significant reductions in pH imbalance, turbidity, TDS, electrical conductivity, BOD_5, COD, and heavy metal concentrations. Notably, PPPS exhibited enhanced adsorption capacity with fewer treatment cycles, due to its higher surface area and porous morphology.

Beyond its technical efficacy, this biosorbent offers broader environmental benefits. Treated water, although not potable, meets the quality criteria for secondary applications, such as laboratory washing, thereby reducing freshwater dependency. Furthermore, the spent biosorbent, being biodegradable, can be repurposed as compost, closing the loop within a circular waste management framework.

This work underscores the viability of plantain pseudo-stem as a cost-effective, eco-friendly biosorbent for decentralized wastewater treatment in academic and research laboratories. Its implementation supports not only environmental conservation but also promotes the utilization of agro-waste in practical, scalable applications. Looking forward, the development of filtration units or column-based systems incorporating PPPS could enable continuous flow treatment, further extending its utility in real-world settings. Integrating such bio-based solutions into laboratory infrastructure represents a meaningful advancement in the pursuit of green chemistry and sustainable research practices.

Acknowledgments

The authors are grateful to the Chemistry department, Microbiology department, and Multi-Disciplinary Research and Consultancy Centre (MRCC) of Justice Basheer Ahmed Sayeed College for Women for providing instrument facilities.

Funding

This work was partially supported by the MRCC of Justice Basheer Ahmed Sayeed College for Women, Chennai.

Conflict of interest

The authors declare no competing interests.

Author contributions

Conceptualization: All authors
Investigation: Hemalatha Kuppusamy
Methodology: Hemalatha Kuppusamy
Formal analysis: All authors
Writing – original draft: Hemalatha Kuppusamy
Writing – review & editing: All authors

Availability of data

Data are available from the corresponding author upon reasonable request.

Further disclosure

Part of the findings have been presented in an international conference on "Frontiers of Sustainable Research in Healthcare, Food, Agriculture and Environment Management" (ICSURE-2024), organized by Guru Nanak College, Chennai.

References

1. Demirbas A. Heavy metal adsorption onto agro-based waste materials: A review. *J Hazard Mater*. 2008;157(2-3):220-229.
doi: 10.1016/j.jhazmat.2008.01.024
2. Gaber MM, Samy M, Shokry H. Effective degradation of synthetic micropollutants and real textile wastewater via a visible light-activated persulfate system using novel spinach leaf-derived biochar. *Environ Sci Pollut Res*. 2024;31:25163-25181.
doi: 10.1007/s11356-024-32829-6
3. Pathak PD, Mandavgane SA, Kulkarni BD. Fruit peel waste as a novel low-cost bio adsorbent. *Rev Chem Eng*. 2015;31(4):361-381.
doi: 10.1515/revce-2014-0041
4. Naragundkar NS, Kavya BK, Manoj Kumar KS, Ganga MM, Manoj SK. *Industrial Waste Water Tretment Using Banana Stem Extract* [Easy Chair Preprint]; 2022.
5. Ferronato N, Paoli R, Romagnoli F, Tettamanti G, Bruno D, Torretta V. Environmental impact scenarios of organic fraction municipal solid waste treatment with black soldier fly larvae based on a life cycle assessment. *Environ Sci Pollut Res*. 2024;31(12):17651-17669.
doi: 10.1007/s11356-023-27140-9

6. El-Maghraby A, Taha NA, Mahmoud A, El-Aziz A. Preparation of activated carbon (chemically and physically) from banana pith for heavy metal removal from wastewater. *Sci-Afric J Sci Issues Res Essays*. 2014;2:399-403.
7. Kokate S, Parasuraman K, Prakash H. Adsorptive removal of lead ion from water using banana stem scutcher generated in fiber extraction process. *Results Eng*. 2022;14:100439. doi: 10.1016/j.rineng.2022.100439
8. Suhani N, Saphira M, Mohamed R, *et al*. Removal of COD and ammoniacal Nitrogen by banana trunk fiber with chitosan adsorbent. *Malays J Fundam Appl Sci*. 2020;16:243-247. doi: 10.11113/mjfas.v16n2.1926
9. Fernanda OD, Putri TF, Marfuah S, Aliyatulmuna A, Fajaroh F. Utilization of banana peels extracts in the synthesis of ZnO nanoparticles. *AIP Conf Proc*. 2021;2330:070004. doi: 10.1063/5.0043386
10. Venkatesh AL, Chandralekha D, Bhoomika S, Sreenidhi S, Abhijith GS. Waste water treatment of industrial effluents using banana stem extract. *Int Res J Eng Technol.* 2021;8:357-361.
11. Qasem NAA, Mohammed RH, Lawal DU. Removal of heavy metal ions from wastewater: A comprehensive and critical review. *NPJ Clean Water*. 2021;4(1):36. doi: 10.1038/s41545-021-00127-0
12. Al-Qodah Z, Yahya MA, Al-Shannag M. On the performance of bioadsorption processes for heavy metal ions removal by low-cost agricultural and natural by-products bioadsorbent: A review. *Desalination Water Treat*. 2017;85:339-357. doi: 10.5004/dwt.2017.21256
13. Costa WD, Da Silva Bento AM, De Araújo JAS, *et al*. Removal of copper(II) ions and lead(II) from aqueous solutions using seeds of *Azadirachta indica* A. Juss as bioadsorvent. *Environ Res*. 2020;183:109213. doi: 10.1016/j.envres.2020.109213
14. Burakov AE, Galunin EV, Burakova IV, *et al*. Adsorption of heavy metals on conventional and nanostructured materials for wastewater treatment purposes: A review. *Ecotoxicol Environ Saf*. 2018;148:702-712. doi: 10.1016/j.ecoenv.2017.11.034
15. Awual MR, Hasan MM. Novel conjugate adsorbent for visual detection and removal of toxic lead(II) ions from water. *Microporous Mesoporous Mater*. 2014;196:261-269. doi: 10.1016/j.micromeso.2014.05.021
16. Awual MR. Mesoporous composite material for efficient lead(II) detection and removal from aqueous media. *J Environ Chem Eng*. 2019;7(3):103124. doi: 10.1016/j.jece.2019.103124
17. Tariba Lovaković B. Cadmium, arsenic, and lead: Elements affecting male reproductive health. *Curr Opin Toxicol*. 2020;19:7-14. doi: 10.1016/j.cotox.2019.09.005
18. Shahat A, Hassan HMA, Azzazy HME, El-Sharkawy EA, Abdou HM, Awual MR. Novel hierarchical composite adsorbent for selective lead(II) ions capturing from wastewater samples. *Chem Eng J*. 2018;332:377-386. doi: 10.1016/j.cej.2017.09.040
19. Amin MT, Alazba AA, Amin MN. Absorption behaviours of copper, lead, and arsenic in aqueous solution using date palm fibres and orange peel: Kinetics and thermodynamics. *Pol J Environ Stud*. 2017;26(2):543-557. doi: 10.15244/pjoes/66963
20. Lan Y, Lei X, Zhao C, *et al*. Study on the polypeptide-functionalized magnetic chitosan microspheres that specifically adsorb Hg (II) ions. *Sep Purif Technol*. 2023;323:124386. doi: 10.1016/j.seppur.2023.124386
21. Sousa Neto VO, Oliveira AG, Teixeira RNP, *et al*. Use of coconut bagasse as alternative adsorbent for separation of copper (II) ions from aqueous solutions: Isotherms, kinetics, and thermodynamic studies. *Bioresources*. 2011;6(3):3376-3395. doi: 10.15376/biores.6.3.3376-3395
22. Senthil Kumar P, Ramalingam S, Abhinaya RV, Kirupha SD, Murugesan A, Sivanesan S. Adsorption of metal ions onto the chemically modified agricultural waste. *Clean (Weinh)*. 2012;40(2):188-197. doi: 10.1002/clen.201100118
23. Feng N, Guo X, Liang S, Zhu Y, Liu J. Biosorption of heavy metals from aqueous solutions by chemically modified orange peel. *J Hazard Mater*. 2011;185(1):49-54. doi: 10.1016/j.jhazmat.2010.08.114
24. Giraldo L, Moreno-Piraján JC. Pb2+ adsorption from aqueous solutions on activated carbons obtained from lignocellulosic residues. *Braz J Chem Eng*. 2008;25(1):143-151. doi: 10.1590/S0104-66322008000100015
25. Escudero-Oñate C, Villaescusa I. The thermodynamics of heavy metal sorption onto lignocellulosic biomass. In: *Heavy Metals.* London: IntechOpen; 2018. doi: 10.5772/intechopen.74260
26. Shreya Rajendra U, Rani RA. Wastewater treatment using banana pith powder. *Int J Innov Sci Eng Technol*. 2021;8:622-630.
27. Abdulfatai J, Saka AA, Afolabi AS, Micheal O. Development of adsorbent from banana peel for wastewater treatment. *Appl Mech Mater*. 2013;248:310-315. doi: 10.4028/www.scientific.net/amm.248.310
28. Rizwan S NP, Sheela JS, Prema MK, Gifta CC. Waste water treatment using banana stem extract from textile industries. *Int J Appl Environ Sci*. 2018;13:105-119.
29. Nguyen TT, Thi BTN, Phan PT, *et al*. Synthesis of

microcrystalline cellulose from banana pseudo-stem for adsorption of organics from aqueous solution. *Eng Appl Sci Res*. 2021;48(4):368-378.
doi: 10.14456/easr.2021.39

30. Kusumawardani Y, Subekti S, Astuti W, Soehartono S. Portable wastewater treatment plant using banana stem filter media in small scale motor vehicle washing services. In: *IOP Conf Ser Earth Environ Sci*. 2021;746:012039.
doi: 10.1088/1755-1315/746/1/012039
31. Venkatachalam CD, Govindaraj A, Sengottian M, Ravichandran SR. Recent trends in advanced oxidation processes for tannery effluent treatment - a review. In: *Development in Wastewater Treatment Research and Processes: Advanced Oxidation Processes for Tannery Effluent*. Netherlands: Elsevier; 2024. p. 75-87.
doi: 10.1016/B978-0-323-95656-7.00006-3
32. Alwi H, Idris J, Musa M, Ku Hamid KH. A preliminary study of banana stem juice as a plant-based coagulant for treatment of spent coolant wastewater. *J Chem*. 2013;2013:165057.
doi: 10.1155/2013/165057
33. Subagyo A, Chafidz A. *Banana Pseudo-Stem Fiber: Preparation, Characteristics, and Applications*. 2018.
doi: 10.5772/intechopen.82204
34. Kani KM, Gopika GL. Accessing the suitability of using banana pith juice as a natural coagulant for textile wastewater treatment. *Int J Sci Eng Res*. 2016;7(4):260-264.
35. Kusumawardani Y, Soehartono S, Subekti S. The effectiveness of reducing COD, TSS, and detergent using banana stem filter media in the wastewater treatment of motor vehicles waste treatment. *J Pres Media Komunikasi Pengembangan Teknik Lingkungan*. 2021;18(1):37-44.
doi: 10.14710/presipitasi.v18i1.37-44
36. Mokhtar NM, Priyatharishini M, Kristanti RA. Study on the effectiveness of banana peel coagulant in turbidity reduction of synthetic wastewater. *Int J Eng Technol Sci*. 2019;6(1):82-90.
doi: 10.15282/ijets.v6i1.2109
37. Matsedisho B, Otieno B, Kabuba J, Leswifi T, Ochieng A. Removal of Ni(II) from aqueous solution using chemically modified cellulose nanofibers derived from orange peels. *Int J Environ Sci Technol*. 2024;22:2905-2916.
doi: 10.1007/s13762-024-05819-x
38. Ramu S. *Treatment of Wastewater Using Banana and Lemon Peels as Adsorbents*; 2017. Available from: https://www.researchgate.net/publication/323473059 [Last accessed on 2025 Jun 30].
39. Harshananda TN, Ayisha TM, Priyanka PR, Dildar Mather KN, Vijayakumar R. Removal of colour from textile effluent by adsorption using banana stem and coffee husk: A review. *IOSR J Mech Civil Eng*. 2020;17(4):32-41.
doi: 10.9790/1684-1704013241
40. Pawar S, Bagali S, Uma K, Gowrishankar BS. Column study using modified banana pseudo stem as adsorbent for removal of Pb (II). *Heliyon*. 2023;9(5):e15469.
doi: 10.1016/j.heliyon.2023.e15469
41. Rahman MW, Nipa ST, Rima SZ, *et al*. Pseudo-stem banana fiber as a potential low-cost adsorbent to remove methylene blue from synthetic wastewater. *Appl Water Sci*. 2022;12(10):242.
doi: 10.1007/s13201-022-01769-2
42. Annadurai G, Juang RS, Lee DJ. Adsorption of heavy metals from water using banana and orange peels. *Water Sci Technol*. 2002;47:185-190.
43. Fernandez ME, Nunell GV, Bonelli PR, Cukierman AL. Activated carbon developed from orange peels: Batch and dynamic competitive adsorption of basic dyes. *Ind Crops Prod*. 2014;62:437-445.
doi: 10.1016/j.indcrop.2014.09.015
44. Gupta VK, Ali I. Removal of lead and chromium from wastewater using bagasse fly ash - a sugar industry waste. *J Colloid Interface Sci*. 2004;271(2):321-328.
doi: 10.1016/j.jcis.2003.11.007

Asian Journal of Water, Environment and Pollution. Vol. 22, No. 6 (2025), pp. 134-141.
doi: 10.36922/AJWEP025240198

ORIGINAL RESEARCH ARTICLE

Treatment of antibiotic fermentation effluents using charcoal adsorption

Salah Mohammed Aleid[1]*, Siddig H. Hamad[1], and Sam Al-Dalali[2,3]*

[1]Department of Food and Nutrition Sciences, College of Agriculture and Food Sciences, King Faisal University, Al Ahsa, Eastern Province, Saudi Arabia
[2]School of Food and Health, Guilin Tourism University, Guilin, Guangxi, China
[3]Department of Food Science and Technology, Faculty of Agriculture and Food Science, Ibb University, Ibb, Yemen
***Corresponding authors:** Salah Mohammed Aleid (seid@kfu.edu.sa);
Sam Al-Dalali (salihsam4@gmail.com)

Received: June 15, 2025; Revised: August 3, 2025; Accepted: August 11, 2025; Published online: August 28, 2025

Abstract: Activated carbon (AC) is widely used as an adsorbent in multiple sectors, including the pharmaceutical, chemical, beverage, and food industries. This study investigates the removal of organic materials from antibiotic fermentation effluents using powdered AC at various temperatures. Pristinamycin was synthesized by cultivating *Streptomyces pristinaespiralis* with date syrup as a glucose substitute. The fermentation effluent was treated with activated charcoal to reduce biochemical oxygen demand (BOD) and chemical oxygen demand (COD). Optimal removal was achieved with 30 mg/L of activated charcoal at 25°C. Under these conditions, COD decreased by approximately 52%, and 5-day BOD decreased by approximately 9.1% compared to the untreated effluent. Increasing the AC dose enhanced the efficiency of COD removal. Based on these findings, AC adsorption of antibiotic pristinamycin from wastewater appears to be a viable treatment option.

Keywords: Antibiotic fermentation; Biochemical oxygen demand; Chemical oxygen demand; Adsorption; Charcoal; Pristinamycin

1. Introduction

Wastewater produced by biopharmaceutical facilities contains high concentrations of organic and microbial contaminants, substantially increasing the biochemical oxygen demand (BOD) and chemical oxygen demand (COD) of the effluent. Cations such as potassium (K^+), sodium (Na^+), magnesium (Mg^{2+}), and calcium (Ca^{2+}) ions significantly complicate the treatment process.[1,2] Adsorption is among the most commonly employed techniques for treating antibiotic waste effluents in the industry. Adsorption of lactic or other organic acids from fermentation broth at room temperature has been investigated using several anionic adsorbents, including IRA-92,[3] IRA-67,[4] IRA-425,[5] and IRA-400,[6] as well as non-polar adsorbents such as activated carbon (AC).[4,7]

AC is widely used as an adsorbent in multiple sectors, including the pharmaceutical, chemical, beverage, and food industries.[8,9] Its widespread use is attributed to its cost-effectiveness, simplicity, non-toxicity, and low energy requirements.[8] Adsorption onto AC has demonstrated significant effectiveness in purifying industrial wastewaters and improving effluent quality from biologically treated facilities.[9] The extensive use of AC in water and wastewater treatment is attributed to its vast surface area (approximately 1,100 m^2/g) and

highly porous structure. Its non-polar nature under varied pH conditions also confers a unique affinity for organic acids such as lactic, acetic, and butyric acids.[7,10]

Pradhan *et al*.[11] conducted an experimental study on the separation of lactic acid (<10 g/L) from a model fermentation solution using granular AC. Thermodynamic analysis demonstrated that optimal lactic acid adsorption occurs at a pH below the pKa of lactic acid (3.86) through a physical adsorption mechanism. The optimal conditions for using AC to remove amoxicillin and tetracycline (TC) have also been examined.[12,13] Umrantezcanun *et al*.[12] reported a maximum COD removal of 91.2% at 20°C and pH 5, using 0.15 g of AC and an initial TC concentration of 100 mg/L after a 24-h adsorption period. Ranaweera *et al*.[8] applied AC adsorption with 200 mL of TC solution and 200 mg of AC, achieving a high TC removal efficiency (>95%) from synthetic wastewater. Spit *et al*.[14] investigated the effects of coagulation, ozonation, and granular AC filtration on the removal of small organic pollutants from treated wastewater, with particular focus on pharmaceutical residues. Abbas and Trari[13] identified the optimal conditions for amoxicillin removal as a dose of 0.124 g, a temperature of 45°C, and pH 5.03, using the desirability function.

Mullai and Rajesh[15] examined the post-treatment of antibiotic wastewater using AC as the adsorbent. The findings indicated that the color removal efficiency of the wastewater increased over time, reaching equilibrium after 120 min with 100 mg of AC under shaking conditions. The maximum COD removal efficiency achieved was 43.3% with 100 mg of AC after 120 min. Zhanga *et al*.[16] employed an integrated approach combining powdered AC with ultrafiltration and reverse osmosis to treat waste liquor generated from TC production. The study demonstrated that the performance of ultrafiltration–reverse osmosis was enhanced by incorporating AC into the waste liquor, with an optimal concentration of 8.0 mg/L.

BOD represents the total dissolved oxygen (DO) required by microorganisms to decompose organic material in a water sample. Elevated BOD levels indicate reduced oxygen availability in the analyzed water body.[17] DO in water samples contributes to the degradation of both organic and nitrogenous matter. The BOD curve comprises two distinct components: Carbonaceous BOD and nitrogenous BOD. The initial 5 days' demand primarily reflects carbonaceous BOD, which constitutes approximately 70% of the total BOD. The 5-day BOD (BOD_5) value generally indicates the oxygen demand associated with organic matter decomposition.[18]

In our previous study, the antibiotic pristinamycin was synthesized by cultivating *Streptomyces pristinaespiralis* with date syrup as a glucose substitute. In this study, the effluent from this process was continuously treated with different charcoal concentrations at various temperatures to reduce its BOD and COD.

The present study aims to remove organic materials from the antibiotic fermentation effluent using powdered AC at varying concentrations (10, 20, and 30 mg/L) and temperatures (25, 50, and 75°C), and to determine the optimal concentration and temperature for effective removal.

2. Materials and methods

2.1. Samples

The antibiotic fermentation broth was collected from the fermentative bioreactors as described in our previous study.[19] Samples were obtained from three different batches, with three replicates per batch for further analysis.

2.2. Determination of physicochemical properties

The pH of the sample was measured directly using a pH meter (MP512-03, Hangzhou Tuqi Instrument Co., Ltd, China). Color of the sample was analyzed using a colorimetric equipment (CR-400 Konica Minolta, Japan), and total solids were determined using a gravimetric approach, which involved drying and measuring the residue after a specified volume of material had been evaporated. Sugar content, expressed as glucose, was determined using high-performance liquid chromatography (Agilent 1260, infinity, Germany) based on the method established by Aleid,[20] where different concentrations of glucose were prepared to plot a calibration curve for quantification. Elemental composition was determined using atomic absorption spectroscopy (NOVA 300, USA).

2.3. Treatment of antibiotic fermentation effluents

After fermentation, the antibiotic fermentation broth was treated with three doses of AC (Sigma-Aldrich, United States [USA]) at 10, 20, and 30 mg/L, under three temperatures (25, 50, and 75°C). Nine treatments were analyzed, as presented in Table 1.

2.4. Adsorption treatment

After 144 h of fermentation in a 100-L fermentor, 200 mL of pristinamycin fermentation broth was

Table 1. Three-level experimental design showing nine treatments of activated carbon dose and temperature

Treatments	Values
C_1T_1	10 mg/L, 25°C
C_1T_2	10 mg/L, 50°C
C_1T_3	10 mg/L, 75°C
C_2T_1	20 mg/L, 25°C
C_2T_2	20 mg/L, 50°C
C_2T_3	20 mg/L, 75°C
C_3T_1	30 mg/L, 25°C
C_3T_2	30 mg/L, 50°C
C_3T_3	30 mg/L, 75°C

Abbreviations: C: Carbon; T: Temperature.

added to an Erlenmeyer flask containing the adsorbent material. The pH of the fermentation broth was 6.8. The mixture was heated for 120 min in a shaking water bath at 50 rpm (Gilson, USA). Samples were then collected for further analysis.

2.5. COD measurement

COD measures the amount of oxidizable organic matter in a wastewater sample. In an aqueous sample, organic and oxidizable inorganic substances are oxidized by potassium dichromate in a 50% (v/v) sulfuric acid solution. The excess dichromate is titrated with standard ferrous ammonium sulfate using orthophenanthroline ferrous complex (ferroin) as an indicator.[21] The sample was reacted with acidic potassium dichromate in the presence of a silver catalyst and digested for 2 h at 150°C. Oxidizable organic compounds reduce dichromate ion to chromic ion. COD values are expressed as milligrams of oxygen consumed per liter of sample (mg/L).[22] The COD was calculated according to the standard method (Equation I):[21]

$$COD\left(mg/L\right)=\frac{\left[\left(A-B\right)\times C\times 8000\right]-50D}{Sample\ volume\ \left(mL\right)}\times 1.2 \quad \text{(I)}$$

where A is the volume of ferrous ammonium sulfate for the blank, B is the volume of ferrous ammonium sulfate for the sample, C is the normality of ferrous ammonium sulfate, D is the chloride correction from the calibration curve, and 1.2 is a compensation factor accounting for the extent of chloride oxidation, which differs in systems containing organic and non-organic material.

2.6. BOD measurement

The BOD_5 was measured following the standard method established by the American Public Health Association (5210 B) (http://standardmethods.org).[23] BOD measured in effluent samples over a 5-day incubation period at 25°C is referred to as BOD_5. The procedure involves filling an airtight bottle of the designated size with the sample until it overflows and incubating it at the specified temperature for 5 days. DO is measured at the beginning and end of incubation, with BOD calculated as the difference between initial and final DO levels.

BOD determination is an empirical test using standardized laboratory procedures to assess the relative oxygen demands of wastewater effluents and polluted waters. It is most commonly applied to assess waste loadings to treatment plants and evaluate BOD removal efficiency in these systems.[22] The test quantifies the molecular oxygen consumed during a defined incubation period for the biochemical degradation of organic material (carbonaceous demand) and the oxygen utilized for the oxidation of inorganic substances, including sulfides and ferrous iron. The measurement may also quantify oxygen used to oxidize reduced nitrogen forms (nitrogenous demand), unless an inhibitor prevents their oxidation. Seeding and dilution procedures yield an estimate of BOD at a pH range of 6.5–7.5.[23]

For each test bottle exhibiting a minimum DO depletion of 2.0 mg/L and a residual DO of at least 1.0 mg/L, BOD is calculated based on the following formula (Equation II):[22]

$$BOD\ (mg/L)=\frac{\left(D_1-D_2\right)-\left(S\right)V_s}{P} \quad \text{(II)}$$

where D_1 is the DO of the diluted sample immediately after preparation (mg/L), D_2 is the DO of the diluted sample after 5 days of incubation at 20°C (mg/L), S is the oxygen uptake of the seed (Δ DO/mL seed suspension added per bottle; $S = 0$ if samples are not seeded), V_S is the volume of seed in the respective test bottle (mL), and P is the decimal volumetric fraction of the sample used (1/P = dilution factor).

2.7. Statistical analysis

All results are presented as mean ± standard deviation. Figures were plotted using Origin 2022 (developer, country). Analysis of variance was performed using SAS version 9.1 (developer, country) to statistically compare the effects of different doses of AC combined with varying temperatures.

3. Results and discussion

3.1. Physicochemical properties

The physicochemical properties of the fermentation broth, containing organic materials and cells of *S. pristinaespiralis*, were evaluated (Table 2). The broth was semi-transparent with a creamy-yellow color. The total solids and sugars were 6.5 g/L and 3.84 g/L, respectively, while the concentrations of K^+, Na^+, Mg^{2+}, and Ca^{2+} were 100, 150, 360, and 560 ppm, respectively.

Table 2. Physicochemical properties of the fermentation broth effluent

Parameter	Value
Color	Creamy yellow
pH	6.8±0.11
Total solids (g/L)	6.5±0.20
Sugars (g/L)	3.8±0.15
Calcium ion (ppm)	560±5.46
Sodium ion (ppm)	360±4.89
Potassium ion (ppm)	150±2.33
Magnesium ion (ppm)	100±3.12
Zinc (II) ion (ppm)	3.0±0.25
Copper (II) ion (ppm)	0.1±0.001
Chromium (II) ion (ppm)	0.1±0.001

3.2. Effects of AC dose and temperature on organic materials

Biopharmaceutical wastewater typically exhibits high BOD and COD levels due to the presence of microorganisms and organic compounds. This section discusses the application of different concentrations of AC at varying temperatures to reduce COD and BOD in pristinamycin fermentation broth. The pH of the fermentation broth was 6.8. However, no significant change was observed in the pH of treated effluents following AC treatment (data not shown). Neither increasing the AC dosage nor temperature significantly affected pH values. This may be attributed to the use of relatively low carbon concentrations, with the maximum being 30 mg/L.

3.2.1. Effects of AC dose and temperature on COD

The application of 30 mg/L AC at 25°C to antibiotic fermentation broth reduced COD from approximately 172,000 mg/L to 82,300 mg/L (Figure 1). COD reduction was significantly higher (p<0.05) at 30 mg/L than at 10 mg/L. Treatments with 10 mg/L and 20 mg/L AC did not yield significant reductions in COD relative to the control group at 25°C (p>0.05). However, increasing the treatment temperature to 50°C and 75°C for the 20 mg/L treatment led to significant COD reductions (p<0.05), yielding residual COD values of 100,000 mg/L and 68,100 mg/L, respectively.

No statistically significant difference (p>0.05) was observed between the 30 mg/L and 20 mg/L treatments at 75°C, which achieved maximum COD reductions of 66% and 62%, respectively. The reduced adsorption at elevated temperatures is primarily due to weak interactions between the active sites of the adsorbent and the adsorbate molecules.[11,24] Farhadpour and Bono[25] reported that acid extraction by granular AC and amine groups is exothermic and decreases with increasing temperature due to: (i) decreased adsorption affinity for adsorbate molecules, (ii) a shift in equilibrium toward the liquid phase, and (iii) enhanced desorption in exothermic reactions.

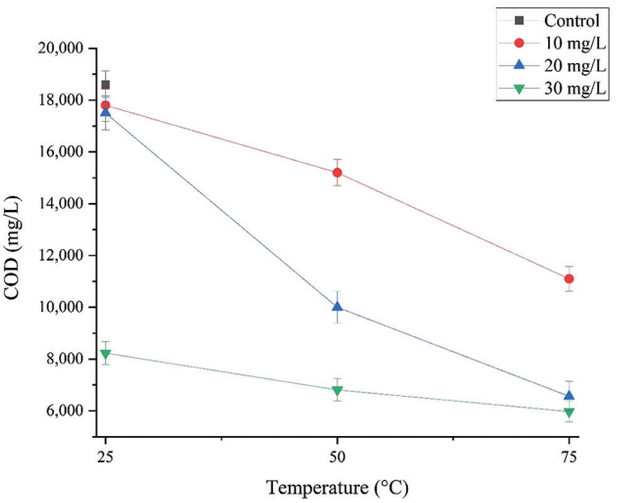


Figure 1. Effect of activated carbon dosage and temperature on COD reduction in the pristinamycin fermentation broth. Dosages of 10, 20, and 30 mg/L were evaluated, with the control receiving no activated carbon treatment.

Abbreviation: COD: Chemical oxygen demand.

Increasing the AC dosage resulted in greater COD removal efficiency (Figure 1). Mullai and Rajesh[15] observed a similar trend, attributing the enhanced efficiency to the abundant active sites present on the charcoal surface, which facilitate the removal of organic substances from fermentation broth.[15] Umrantezcanun *et al.*[12] investigated the effects of adsorbent dose, pH, temperature, initial antibiotic

concentration, and agitation duration on TC removal. TC removal efficiency was temperature-dependent; however, it improved with increasing adsorbent dose, pH, initial antibiotic concentration, and agitation duration. At 20°C, pH 5, with 0.15 g AC and an initial TC concentration of 100 mg/L, the COD concentration decreased from 1,000 mg/L to 88 mg/L after 24 h, indicating a removal efficiency of 91.2%. Based on these findings, AC adsorption of TC from wastewater appears to be a viable treatment option.

3.2.2. Effects of AC dose and temperature on BOD

BOD quantifies the oxygen consumed by bacteria and other microorganisms during the aerobic decomposition of organic matter at a designated temperature.[26] During the 5-day incubation period, the DO in the antibiotic fermentation broth is primarily utilized for the decomposition of organic matter. BOD_5 represents the amount of DO consumed by microorganisms while converting organic matter into carbon dioxide and water. To reduce the BOD_5 of the fermentation broth, samples were treated with AC at concentrations of 10, 20, and 30 mg/L, under temperature conditions of 25°C, 50°C, and 75°C for each treatment. The BOD_5 was subsequently measured for each treatment group and untreated samples. The results are illustrated in Figure 2.

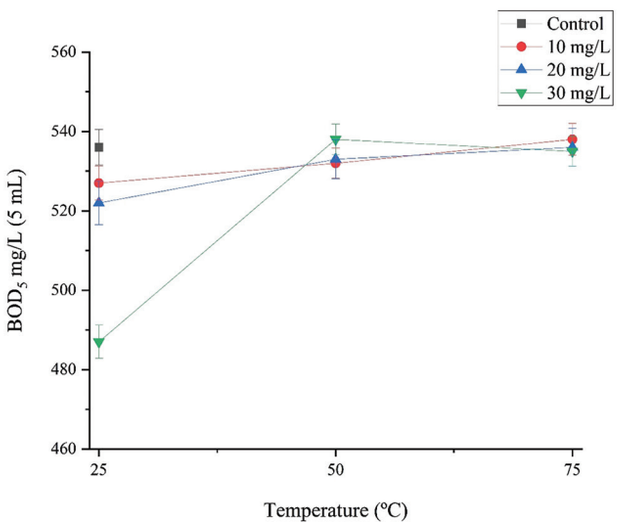


Figure 2. Effect of activated carbon dosage and temperature on BOD_5 reduction in the pristinamycin fermentation broth. Dosages of 10, 20, and 30 mg/L were evaluated, with the control receiving no activated carbon treatment.

Abbreviation: BOD_5: Biochemical oxygen demand over 5 days.

The most significant decrease in BOD_5 occurred when the broth was treated with 30 mg/L of AC at 25°C, where the BOD reduction was significantly higher ($p<0.05$) at 30 mg/L than at 10 mg/L. The treatment reduced the BOD_5 from 536 mg/L in the untreated sample to 487 mg/L in the treated sample (Figure 2). Unlike COD, BOD reduction was temperature-dependent, as the introduction of charcoal at 50°C or 75°C did not significantly decrease ($p>0.05$) the BOD_5 of the fermentation broth. This may be attributed to 25°C being a biologically optimal temperature for BOD testing, reflecting the natural decomposition of organic waste in aquatic ecosystems. Elevated temperatures (e.g., 75°C) facilitate procedures such as thermal hydrolysis or COD testing but compromise BOD analysis by killing the microorganisms essential to the test.

Elevated BOD values indicate increased oxygen depletion in the analyzed pristinamycin fermentation broth. The BOD results indicate the oxygen demand associated with pristinamycin organic waste discharge, supporting the assessment of its impact on the oxygen levels of the receiving water body. Data from BOD tests may be used to establish treatment criteria for the design of pristinamycin wastewater treatment facilities.[22]

Antibiotic fermentation broths produce effluents containing residual antibiotics, organic byproducts, and nutrients, which pose environmental risks by potentially promoting antimicrobial resistance and disrupting aquatic ecosystems. Pristinamycin, a streptogramin antibiotic derived from the fermentation of *S. pristinaespiralis*, results in effluents that contain residual antibiotics, organic acids, and macromolecular byproducts such as proteins and sugars. Effluents containing pristinamycin pose environmental risks due to their persistence and potential to disseminate antimicrobial resistance genes.[27] Adsorption using an adsorbent material provides an effective treatment method by utilizing its extensive surface area and chemical affinity to capture pristinamycin and related organic compounds. The processes involved in binding antibiotics onto AC include hydrophobic interactions, hydrogen bonding, and π–π interactions.[28] The most effective adsorption was observed at a pH range of 6–7, which closely aligns with the isoelectric point of pristinamycin, thereby reducing electrostatic repulsion.[27] In this study, treatment with 30 mg/L of AC at 25°C resulted in a 52% reduction in COD in antibiotic fermentation effluent. Although lower than the findings reported by Umrantezcanun *et al*.,[12] this likely reflects our ultra-low adsorbent dosage (30 mg/L) compared

to their dosage (150 mg/L), as well as the resistant characteristics of antibiotics.

Ranaweera *et al*.[8] reported that AC adsorption was more successful in hospital wastewater, removing 50% of total organic carbon compared to 34% in ordinary wastewater. AC adsorption efficiently eliminated COD from effluent at a dose of 2 g/L, with a clearance rate of 66.2% in hospital wastewater and 65% in ordinary sewage. This is consistent with the findings from previous research, which reported a 55% COD elimination at 3–5 g/L and over 90% at 16 g/L.[29,30] Uniform outcomes across different wastewater types illustrate AC's adaptability in adsorbing a range of organic molecules.

Consistent with earlier research, this study found that AC effectively removed COD and BOD. According to several studies, AC can effectively remove dissolved organic matter (DOM) and can be further optimized by doping or modifying commercial AC. For example, Choi *et al*.[31] discovered that AC adsorbs TC more efficiently than sulfonamides in synthetic wastewater, but DOM interferes in high-DOM conditions. Zhou *et al*.[32] proposed that ferroferric oxide nanoparticles could increase AC's adsorption capacity. In addition, Zhang *et al*.[33] demonstrated that modified AC made from petroleum coke had twice the adsorption capacity of commercial AC, lending credence to this finding. AC adsorption is extensively utilized in sewage treatment processes. The capital expenditure and operational expenditure associated with AC adsorption are significantly influenced by plant capacity, system configurations, and the removal or management of the adsorbent.[34-37] Due to the frequent requirement for adsorbent replacement or regeneration, cost analyses show that AC adsorption incurs substantial operational expenditure but modest capital expenditure.[38,39]

The 52% COD removal achieved at 30 mg/L demonstrates effective treatment performance; however, the economic feasibility of large-scale application is hindered by the costs associated with adsorbents. Hybrid systems integrating biological pretreatment with targeted charcoal application may achieve over 80% removal efficiency at approximately one-tenth the cost. However, charcoal regeneration is feasible only for facilities with a capacity exceeding 50,000 m^3/day.

4. Conclusion

The traditional AC adsorption technique effectively removed pristinamycin, demonstrating high adsorption capacity and rapid kinetics. AC adsorption reduced COD, BOD, and antimicrobial concentrations in fermentation wastewater. Treatment of antibiotic fermentation effluent with 20 mg/L of adsorbent material at 75°C resulted in a maximum COD reduction of 62%. Increasing the adsorbent material dose further enhanced the COD removal efficiency. The most significant decrease in BOD_5 occurred when the broth was treated with 30 mg/L of AC at 25°C, achieving a reduction of about 9.1%. AC effectively removes pristinamycin from fermentation effluents, but process efficiency depends on charcoal modification, pH, and effluent complexity. Further studies are warranted to explore the integration of adsorption with membrane filtration or biodegradation, which could enhance selectivity and cost-effectiveness while mitigating antimicrobial resistance risks in a sustainable manner.

Acknowledgments

None.

Funding

This study was funded by the Date Palm Research Center of Excellence, King Faisal University.

Conflict of interest

The authors declare that they have no known competing financial interests, and this manuscript has not been submitted to any other journal in parallel or published previously.

Author contributions

Conceptualization: Salah Mohammed Aleid
Formal analysis: Salah Mohammed Aleid, Sam Al-Dalali
Investigation: Salah Mohammed Aleid, Siddig H. Hamad
Methodology: Salah Mohammed Aleid, Siddig H. Hamad
Writing–original draft: Salah Mohammed Aleid, Sam Al-Dalali
Writing–review & editing: Sam Al-Dalali

Availability of data

Data are available from the corresponding author upon reasonable request.

References

1. Bódalo-Santoyo A, Gómez-Carrasco JL, Gómez-Gómez E, Máximo-Martín F, Hidalgo-Montesinos AM. Application of reverse osmosis to reduce pollutants present in industrial wastewater. *Desalination*. 2003;155:101-108. doi: 10.1016/S0011-9164(03)00287-x
2. Jarusutthirak C, Amy G, Croué JP. Fouling characteristics of wastewater effluent organic matter isolates on NF and UF membranes. *Desalination*. 2002;145:247-255. doi: 10.1016/S0011-9164(02)00419-8
3. Tong WY, Fu XY, Lee SM, *et al*. Purification of L-(+) lactic acid from fermentation broth with paper sludge as a cellulosic feedstock using weak anion exchanger Amberlite IRA-92. *Biochem Eng J*. 2004;18:89-96. doi: 10.1016/S1369-703X(03)00170-0
4. Yousuf A, Bonk F, Oyanedel JRB, Schmidt JE. Recovery of carboxylic acids produced during dark fermentation of food waste by adsorption on amberlite IRA-67 and activated carbon. *Bioresour Technol*. 2016;217:137-140. doi: 10.1016/j.biortech.2016.02.035
5. Antonio GR, Vaccari G, Dosi E, Trilli A, Rossi M, Matteuzzi D. Enhanced production of L-(+) lactic acid in chemostat by *Lactobacillus casei* DSM 20011 using ion-exchange resins and cross-flow filtration in a fully automated pilot plant controlled via NIR. *Biotechnol Bioeng*. 2000;67:147-156.
6. Cao X, Yun HS, Koo YM. Recovery of L-(+)-lactic acid by anion exchange resin amberlite IRA-400. *Biochem Eng J*. 2002;11:189-196. doi: 10.1016/S1369-703X(02)00024-4
7. Gao MT, Shimamura T, Ishida N, Takahashi H. pH-uncontrolled lactic acid fermentation with activated carbon as an adsorbent. *Enzyme Microb Technol*. 2011;48:526-530. doi: 10.1016/j.enzmictec.2010.07.015
8. Ranaweera R, Wu X, Ng D, *et al*. Comparative study of adsorption, thermally activated peroxymonosulfate and wet air oxidation for tetracycline removal and wastewater treatment. *J Water Process Eng*. 2025;72:107559. doi: 10.1016/j.jwpe.2025.107559
9. Cheremisinoff NP, Cheremisinoff PN. *Carbon Adsorption for Pollution Control [Process and Pollution Control Equipment Series]*; 1993
10. Park KM, Nam HG, Lee KB, Mun S. Adsorption behaviors of sugars and sulfuric acid on activated porous carbon. *J Ind Eng Chem*. 2016;34:21-26.
11. Pradhan N, Rene ER, Lens PNL, *et al*. Adsorption behaviour of lactic acid on granular activated carbon and anionic resins: Thermodynamics, isotherms and kinetic studies. *Energies*. 2017;10:665. doi: 10.3390/en10050665
12. Tezcanun U, Ocal SE, Gul A. Removal of antibiotic wastes by adsorption method. *Int J Adv Sci Eng Technol*. 2018;6(4):40-43.
13. Abbas M, Trari M. Removal of amoxicillin from wastewater onto activated carbon: Optimization of analytical parameters by response surface methodology. *Dose Response*. 2024;22:15593258241271655. doi: 10.1177/15593258241271655
14. Spit T, Van der Hoek JP, De Jong C, Van Halem D, De Kreuk M, Perez BB. Removal of antibiotic resistance from municipal secondary effluents by ozone-activated carbon filtration. *Front Environ Sci*. 2022;10:834577. doi: 10.3389/fenvs.2022.834577
15. Mullai P, Rajesh V. Post treatment of antibiotic wastewater by adsorption on activated carbon. *AIP Conf Proc*. 2018;1927:020002. doi: 10.1063/1.5021190
16. Zhanga J, Lidietta Giornob L, Driolib E. Study of a hybrid process combining PAC^s and membrane operations for antibiotic wastewater treatment. *Desalination*. 2006;194:101-107. doi: 10.1016/j.desal.2005.11.004
17. EPA. *Reduction in Mean Biochemical Oxygen Demand [BOD5] Due to Tree Cover*. EnviroAtlas: Led by the U.S. Environmental Protection Agency; 2014. p. 1-2.
18. Penn MR, Pauer JJ, Mihelcic JR. Biological oxygen demand. In: *Sabjic A, editor. Environment and Ecological Chemistry. Encyclopedia of Life Support System*. Vol. 2. Isle of Man, UK: UNESCO; 2009. p. 278.
19. Aleid SM, Hamad SH, Delaunay S, Fick M, Olmos E. Pristinamycin production using *Streptomyces pristinaespiralis* and date sirup as substrate-process modeling, optimization, and scale-up. *Prep Biochem Biotechnol*. 2022;52:1044-1050. doi: 10.1080/10826068.2021.2024849
20. Aleid SM. Chromatographic separation of fructose from date syrup. *Int J Food Sci Nut*. 2006;57:83-96. doi: 10.1080/09637480600658286
21. EPA. *Chemical Oxygen Demand (Titrimetric, High Level for Saline Waters). Method 410.3*. United States: EPS; 1978.
22. EPA. *Methods for Chemical Analysis of Water and Wastes. Biological Oxygen Demand (5201B) 5-day BOD Test*. EPA/600/4-79/020. Cincinnati, Ohio, USA: EPA Environmental Monitoring Laboratory; 1983.
23. APHA, American Public Health Association. Standard methods for the examination of water and wastewater. In: Greenberg AE, Eaton AD, Clesceri LS, Franson, MAH, editors. *Joint Editorial Board*. 20th ed. Publication Office: American Public Health Association, Washington, USA; 1998.
24. Ye C, Wang X, Wang H, Wang Z. Effects of counter anions on the adsorption properties of 4-methylimidazolium-modified silica materials. *J Taiwan Instit Chem Eng*. 2014;45:2868-2877.
25. Farhadpour FA, Bono A. Sorptive separation of ethanol-water mixtures with a bi-dispersed hydrophobic

molecular sieve, silicalite: Determination of the controlling mass transfer mechanism. *Chem Eng Process*. 1996;35:141-155.
doi: 10.1016/0255-2701(95)04138-9

26. Delzer GC, McKenzie SW. *Five-Day Biochemical Oxygen Demand. USGS TWRI Book 9-A7*. 3rd ed. Reston: USGS; 2003. p. 1-21.
27. Grenni P, Ancona V, Barra CA. Ecological effects of antibiotics on natural ecosystems: A review. *Microchem J.* 2018;136:25-39.
doi: 10.1016/j.microc.2017.02.006
28. Ahmedna M, Marshall WE, Rao RM. Production of granular activated carbons from select agricultural by-products and evaluation of their physical, chemical, and adsorption properties. *Bioresour Technol*. 2000;71(2):113-123.
doi: 10.1016/S0960-8524(99)00070-X
29. Margot J, Kienle C, Magnet A, *et al*. Treatment of micropollutants in municipal wastewater: Ozone or powdered activated carbon? *Sci Total Environ*. 2013;461-462:480-498.
doi: 10.1016/j.scitotenv.2013.05.034
30. Bansode RR, Losso JN, Marshall WE, Rao RM, Portier RJ. Pecan shell-based granular activated carbon for treatment of chemical oxygen demand (COD) in municipal wastewater. *Bioresour Technol*. 2004;94(2):129-135.
doi: 10.1016/j.biortech.2003.12.009
31. Choi KJ, Kim SG, Kim SH. Removal of tetracycline and sulfonamide classes of antibiotic compound by powdered activated carbon. *Environ Technol*. 2008;29(3):333-342.
doi: 10.1080/09593330802102223
32. Zhou J, Ma F, Guo H. Adsorption behavior of tetracycline from aqueous solution on ferroferric oxide nanoparticles assisted powdered activated carbon. *Chem Eng J*. 2020;384:123290.
doi: 10.1016/j.cej.2019.123290
33. Zhang D, Yin J, Zhao J, Zhu H, Wang C. Adsorption and removal of tetracycline from water by petroleum coke-derived highly porous activated carbon. *J Environ Chem Eng*. 2015;3(3):1504-1512.
doi: 10.1016/j.jece.2015.05.014
34. Viegas RMC, Mesquita E, Campinas M, Rosa MJ. Pilot studies and cost analysis of hybrid powdered activated carbon/ceramic microfiltration for controlling pharmaceutical compounds and organic matter in water reclamation. *Water*. 2019;12(1):33.
doi: 10.3390/w12010033
35. Ighalo JO, Omoarukhe FO, Ojukwu VE, Iwuozor KO, Igwegbe CA. Cost of adsorbent preparation and usage in wastewater treatment: A review. *Clean Chem Eng*. 2022;3:100042.
doi: 10.1016/j.clce.2022.100042
36. Garcia L, Leyva-Diaz JC, Diaz E, Ordonez S. A review of the adsorption-biological hybrid processes for the abatement of emerging pollutants: Removal efficiencies, physicochemical analysis, and economic evaluation. *Sci Total Environ*. 2021;780:146554.
doi: 10.1016/j.scitotenv.2021.146554
37. Yasir HA, Zein SH, Holliday MC, Jabbar KJ, Ahmed U, Jalil AA. Comparison of activated carbon and low-cost adsorbents for removal of 2,4-dichlorophenol from wastewater using Aspen adsorption and response surface methodology. *Environ Technol*. 2024;45(15):3029-3047.
doi: 10.1080/09593330.2023.2202829
38. Jaria G, Calisto V, Esteves VI, Otero M. Overview of relevant economic and environmental aspects of waste-based activated carbons aimed at adsorptive water treatments. *J Clean Prod*. 2022;344:130984.
doi: 10.1016/j.jclepro.2022.130984
39. Sulistiyo CD, Cheng KC, Su'andi HJ, *et al*. Removal of hexavalent chromium using durian in the form of rind, cellulose, and activated carbon: Comparison on adsorption performance and economic evaluation. *J Clean Prod*. 2022;380:135010.
doi: 10.1016/j.jclepro.2022.135010

Asian Journal of Water, Environment and Pollution. Vol. 22, No. 6 (2025), pp. 142-169.
doi: 10.36922/AJWEP025120083

ORIGINAL RESEARCH ARTICLE

Assessment of groundwater quality for drinking purposes near the industrial area of Bharatpur, Chitwan, Nepal: Physicochemical, microbiological, and statistical approaches

Shiv Narayan Yadav[1], Asbin K. C.[2], Dhruba Acharya[2], Rabiraj Subedi[2], Saugat Rizal[1], Shishir Tamang[1], and Ajaya Bhattarai[1]*

[1]Department of Chemistry, Faculty/Institute of Science and Technology, Mahendra Morang Adarsh Multiple Campus, Tribhuvan University, Biratnagar, Koshi, Nepal
[2]Department of Science, Faculty/Institute of Science and Technology, Saptagandaki Multiple Campus, Tribhuvan University, Chitwan, Bagmati, Nepal
***Corresponding author:** Ajaya Bhattarai (ajaya.bhattarai@mmamc.tu.edu.np)

Received: March 21, 2025; 1st revised: June 25, 2025; 2nd revised: July 15, 2025; 3rd revised: August 2, 2025; 4th revised: August 6, 2025; Accepted: August 11, 2025; Published online: September 8, 2025

Abstract: Groundwater quality in rapidly urbanizing Bharatpur areas with unregulated industries remains a critical, understudied challenge. This study addresses this knowledge gap by comprehensively assessing the physicochemical and microbiological contamination of drinking water near the Bharatpur industrial area, Nepal, using a statistical approach. Twelve physicochemical and microbiological parameters were analyzed based on the Nepal Drinking Water Quality Standard (NDWQS) and the World Health Organization (WHO) guidelines. Statistical methods (correlation and regression) and an index-based assessment (water quality index [WQI]) were used to interpret contamination patterns. The results showed that the mean values of pH, conductivity, total dissolved solids, hardness, alkalinity, and Cl^- were within the WHO/NDWQS guidelines. However, NO_3^-, PO_4^{3-} (4.3–9.8 mg/L), NH_3 (7–19.5 mg/L), free Carbon dioxide (CO_2), and *Escherichia coli* (0–9 colony-forming unit/100 mL) exceeded the limits, indicating industrial and fecal contamination. The WQI values ranged from 560 to 663, indicating that all groundwater samples were unsuitable for drinking without treatment. Statistical analysis revealed strong positive correlations among key parameters. Conductivity was strongly associated with total dissolved solid, hardness, alkalinity, CO_2, NH_3, Cl^-, PO_4^{3-}, and *E. coli*. Hardness, alkalinity, and CO_2 showed near-perfect intercorrelations, while additional strong associations were observed between Cl^- and *E. coli*, PO_4^{3-} and NO_3^-, and pH and NO_3^-. Further validation was performed using regression analysis with a first-degree linear equation. The findings indicate that groundwater near Bharatpur's industrial zone is critically contaminated, necessitating the urgent need for policy interventions, such as wastewater treatment to safeguard public health.

Keywords: Groundwater quality parameters; Statistical analysis; Correlation coefficient; Regression coefficient; Water quality index; Drinking water contamination; Industrial area

1. Introduction

Water is a fundamental component of life, playing a crucial role in the daily functioning of living organisms and influencing climatic conditions and land formation. Groundwater, which resides beneath the Earth's surface, represents the most abundant source of usable freshwater, constituting approximately 99% of the total volume. In comparison, surface water in lakes, rivers, and wetlands accounts for 0.87%, while atmospheric moisture constitutes 0.16%.[1,2] Around one-third of the world's population depends on groundwater for drinking.[3] This resource is especially essential in dry and semi-arid areas, where surface water and rainfall are limited.[4] Maintaining a safe and sustainable groundwater supply is a key to long-term national progress. Clean water is essential for the survival of living organisms and the proper functioning of communities, ecosystems, and economies.[5] Therefore, it is imperative to regularly assess the quality of untreated groundwater to minimize health risks before consumption.[6] Nevertheless, groundwater quality is increasingly threatened by urbanization, agricultural practices, industrial activities, and climate change. Water contamination primarily results from increased waste discharge associated with population growth and various human activities, raising significant concerns about maintaining a safe water supply.[7,8] Heavy chemical contaminants frequently enter groundwater due to untreated industrial and agricultural discharges in urban areas.[9] The presence of chemical impurities in groundwater can have detrimental impacts on public health.[10] Contamination may occur not only at the source but also through the formation of chemical by-products during groundwater movement.[11] Consequently, water must meet specific physical, chemical, and microbiological standards to be considered potable and safe for consumption.[12]

Contaminants, such as toxic metals, hydrocarbons, trace organic compounds, pesticides, microplastics, and nanoparticles pose significant threats to human health, ecosystems, and sustainable development.[13,14] Many of these groundwater pollutants originate from naturally occurring mineral deposits dissolved in the Earth's crust.[15,16] Groundwater contamination occurs when harmful substances are introduced into the subsurface due to human activities. These contaminants are often colorless and odorless, making their detection and their impacts on human health both challenging and chronic.[17] Remediation of contaminated groundwater is complex and costly due to its subsurface location and long residence times.[18-20] Even after contamination sources are removed, natural purification of groundwater can take hundreds of years.[21] Contaminants are typically categorized into chemical, biological, and radioactive types.[22] Toxic metals and metalloids present significant health risks to both humans and the environment. High levels of these substances can lead to severe poisoning, although some are essential as trace micronutrients.[23] For example, exposure to hexavalent chromium is linked to a higher risk of cancer.[24] Arsenic is classified as a human carcinogen by both the United States Environmental Protection Agency and the International Agency for Research on Cancer.[25,26] Over 200 organic contaminants, many of which are carcinogenic, have been detected in groundwater, and this number continues to rise.[27,28] These organic substances, derived from carbohydrates, proteins, fats, and oils, may degrade slowly or not at all, posing a persistent threat to groundwater quality.[29,30]

Contaminated groundwater can adversely impact human health, environmental quality, and socioeconomic development. Excessive levels of fluoride (F^-), chloride (Cl^-), nitrate (NO_3^-), metals, and organic pollutants are associated with significant health risks.[31] Infants are particularly vulnerable to these contaminants.[15,18,31] In addition, the use of untreated groundwater containing heavy metals and persistent contaminants for irrigation can lead to the accumulation of toxic elements in crops, posing risks to consumers.[32-35] Groundwater contamination also negatively affects soil and forest quality, with high groundwater salinity contributing to soil salinization in arid agricultural regions.[36] Furthermore, contamination-induced water shortages may exacerbate conflicts over water resources and hinder socioeconomic development.[37]

Groundwater quality research worldwide encounters considerable challenges due to the large number of water quality parameters, limited data availability, and the complex nature of groundwater systems. Çiner *et al*.[38] explored the carcinogenic risks associated with arsenic exposure in South-Central Turkey, where levels frequently exceeded guideline limits. Their study utilized multivariate statistical analysis to identify trace elements, revealing that geogenic processes played a substantial role in contamination. Yadav *et al*.[39] assessed groundwater quality in relation to arsenic in the Nawalparasi district, Nepal, using multivariate statistical techniques. The study found that nickel (Ni), cadmium (Cd), lead (Pb), chromium (Cr), and arsenic (As) levels exceeded the World Health Organization (WHO) permissible limits for drinking water, with arsenic concentrations ranging from 60 to 31,000 μg/L during the pre-monsoon and monsoon

periods, respectively. Variations in water quality were primarily associated with water-rock interactions, mineralization, and anthropogenic inputs. Industrial activities and municipal waste have been identified as significant sources of groundwater contamination. Raja *et al*.[40] investigated the impact of industrial activities and municipal dumpsites on metal contamination in Virudhunagar, India. This research is crucial for developing strategies to mitigate industrial impacts on groundwater. In Uttar Pradesh, India, Tiwari and Singh[41] conducted a hydrogeochemical investigation, revealing that groundwater was alkaline and exceeded desirable limits for NO_3^-, F^-, total dissolved solids (TDS), and total hardness (TH). This underscores the importance of considering multiple water quality parameters in assessments. Ali *et al*.[42] assessed groundwater quality in the Achnera block, Agra district, India, using the water quality index (WQI) and principal component analysis (PCA). Analysis of 50 groundwater samples revealed that the water was alkaline, with WQI values ranging from 105 to 185, indicating that most samples were unsuitable for drinking. PCA identified pH, sodium ions, calcium ions (Ca^{2+}), bicarbonate ions (HCO_3^-), and F^- as key factors related to geogenic F^- contamination. Thus, treatment is necessary to render the water potable. Similarly, Mahato *et al.*[43] investigated aquifer contaminants and groundwater quality, observing that all parameters under analysis fell within the WHO's permissible limits for drinking water, except for pH, iron, ammonia (NH_3), and turbidity. F^- and manganese concentrations did not meet the Nepal Drinking Water Quality Standards (NDWQSs).[44]

In the Terai region of Nepal, extensive exploitation of aquifers through tube wells supplies water to approximately 90% of the population. Fractured basement aquifers are predominantly replenished by monsoon precipitation.[45] Over 98% of groundwater withdrawals connected to rivers flowing across the Siwalik Hills are found to be enriched with arsenic,[46,47] potentially due to baseflow contributions. Globally, aquifers face increasing pollution threats from industrial and urban activities. Thus, extensive studies on groundwater quality are necessary to inform practical measures for protecting groundwater resources.[1] Unregulated and mismanaged groundwater exploitation has led to significant health impacts, with an estimated 25,000 deaths occurring daily due to water contamination. Moreover, one-third of urban dwellers in developing nations do not have access to clean drinking water.[48] Addressing these issues through targeted research and periodic water quality parameters is essential for regulating hydrochemical processes and safeguarding groundwater quality.

The groundwater quality in the industrial area of Bharatpur, Chitwan district, is potentially affected by anthropogenic activities, such as industrial discharge, agricultural runoff, and improper waste disposal. Contaminants, such as NO_3^-, heavy metals, and pathogens, may pose health risks to the population. This study introduces a novel assessment of groundwater quality near the industrial area, which has not been previously explored, highlighting a significant research gap in this context. By focusing on the specific impacts of industrial activities on groundwater, this research uncovers critical contamination issues that have not been extensively documented in this region to date. A systematic assessment of groundwater quality is essential to ensure safe drinking water and to inform policy decisions. Despite the heavy reliance on groundwater in Chitwan, comprehensive data on its physicochemical characteristics and quality remain limited. Existing studies of nearby areas, such as Kathmandu and Lalitpur,[49-51] are often localized or focus on specific contaminants, leaving a gap in understanding the overall groundwater quality and its spatial and temporal variations. Therefore, the novelty of this work lies in it being the first detailed analysis of groundwater quality in the Bharatpur industrial zone, where no prior studies have systematically examined contamination risks. Moreover, the integration of statistical analyses (correlation and regression) to identify pollution sources and interrelationships between parameters has not previously been applied in this region. The findings provide critical baseline data for local authorities to enforce industrial waste management regulations.

This study aims to evaluate the groundwater quality near the industrial area of Bharatpur, Chitwan, Nepal, a region facing unregulated industrial discharges, to assess its suitability for drinking and to identify contamination sources by applying statistical tools, such as correlation, regression, and the WQI to interpret contamination patterns. It also aims to determine whether the groundwater parameters comply with the WHO[48] and NDWQS[44] standards. The investigation of increased pollutants, such as NH_3, phosphate (PO_4^{3-}), and *Escherichia coli* represents a pioneering approach to evaluating the extent and sources of groundwater contamination due to industrial processes. The implications of these findings are substantial for both national prosperity and public health. These techniques help identify the major factors affecting groundwater quality and potential contamination sources. The

findings will assist policymakers, environmental agencies, industrial stakeholders, and local authorities in addressing water quality concerns and implementing necessary interventions to protect public health, safeguard groundwater resources, ensure public health, and support sustainable industrial development.

2. Materials and methods

2.1. Study area

The area under investigation (Figure 1) is located in Bharatpur Metropolitan City, Wards No. 8 and 9, Chitwan, Nepal. Bharatpur Metropolitan City spans an area of 433 km^2 within the Terai region and is situated at an elevation of 208 m above sea level. The city lies along the banks of the Narayani River. It is the third most populous city in Nepal and the second largest metropolitan area by land area. The city comprises 29 wards and functions as the commercial and service hub of the district, offering significant facilities for higher education, healthcare, and transportation.

Groundwater samples for this investigation were collected from the Gondrang area of Bharatpur, Wards 8 and 9. This area lies to the south of the East–West Highway, near the Bandevi Barandabhar forest corridor, and is part of the semi-urban region of Bharatpur.

2.2. Site selection

The study area was selected based on its proximity to industrial facilities and human settlements, focusing on a 4-km stretch encompassing both densely populated areas with significant anthropogenic activities and relatively less populated zones. Sewage discharge from factory drainage sites is shown in Figure 2. Groundwater samples were collected in the 1st week of February 2024. Physicochemical parameters were analyzed at the Saptagandaki Multiple Campus (SMC) laboratory, Tribhuvan University, Nepal, and microbiological parameters were tested at the Water Quality Testing Laboratory of Bharatpur Metropolitan City.

Sampling was conducted at three distinct locations (Table 1), chosen based on their association with industrial activities and identified using a portable Global Positioning System. The selected sites were: Iron factory (IF; Site 1), Royal Paint factory (RPF; Site 2), and Coca-Cola factory (CF; Site 3). Each site was divided into four sampling zones—East, West, North, and South—relative to the industrial facilities. Samples were labeled as follows: Site 1 – Samples A, B, C, and D; Site 2 – Samples E, F, G, and H; and Site 3 – Samples I, J, K, and L.

2.3. Sampling and analytical methods

2.3.1. Sample collection

Assessing water quality involves a range of complex processes, making it challenging to design a standardized procedure that meets specific evaluation objectives.[52] For this investigation, groundwater samples were collected from handpumps located near three industrial facilities. A total of 12 samples were randomly obtained from residential households situated within 50 m of the industries.



Figure 1. Satellite image of the study area (Google Earth)

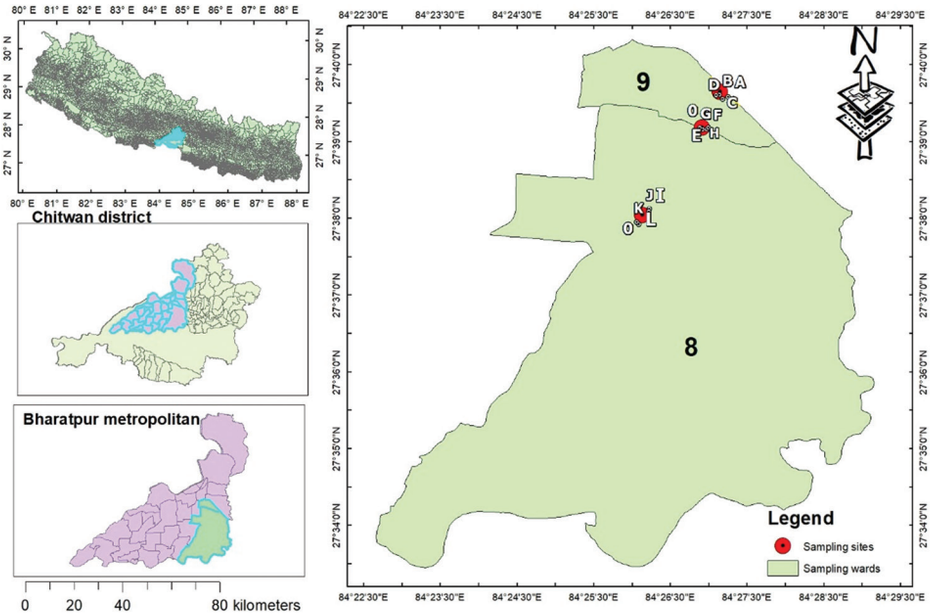


Figure 2. Sewage outflow from the factories (drainage sites)

Table 1. Global Positioning System locations of sampling points and site descriptions

Sites	Latitude	Longitude	Elevation (m)	Site description	Population pressure	Human influence
Iron factory	27°37’55.7”	084°26’05.6”	182	Near buffer zone	Less populated	Minimal human activities
Royal Paint factory	27°39’09.7”	084°26’55.5”	121	Near buffer zone	Moderately populated	Limited human activities
Coca-Cola factory	27°39’36.9”	084°27’08.9”	196	North of East–West Highway	Densely populated	High human activities

The water samples were collected in February 2024, before the onset of the monsoon season. On-site measurements included temperature, pH, dissolved oxygen, conductivity, and other basic parameters. Samples for additional analyses were collected in clean, sterile plastic bottles, transferred, and stored under refrigeration. Before collection, bottles were first rinsed with distilled water. Groundwater was then collected directly into these bottles from the sampling sites. The bottles were properly labeled and sealed with both inner and outer cover caps to prevent contamination and air ingress. The samples were subsequently transported to the SMC laboratory and stored in a refrigerator until analysis was carried out using standardized procedures and calibrated instruments. To preserve the samples for chemical analysis, they were stored at 4°C in pre-cleaned plastic bottles with nitric acid (pH <2) to prevent metal adsorption, following American Public Health Association (APHA) guidelines. Microbial analysis was conducted within 24 h, and chemical parameters were analyzed within 7 days. Instruments, such as pH meters and spectrophotometers were calibrated daily. In addition, 10% of the samples were tested in duplicates to ensure precision, maintaining a relative standard deviation of <5%. Rigorous quality assurance/quality control measures were implemented throughout the study. The collection, preservation, and analysis of groundwater samples followed the standard procedures established by the APHA.[7,53-56]

The selection of parameters was based on their relative importance in evaluating groundwater pollution potential.[43] The following criteria guided the selection of groundwater quality parameters:

2.3.1.1. The WzHO/NDWQS regulatory criteria, along with health relevance

As the study focuses on the drinking water quality, parameters were selected based on their direct or

indirect impact on human health. These were guided by the WHO[57] and NDWQS.[44]

2.3.1.2. Previous publications

Selection was also informed by previous studies carried out in similar regions of Nepal and neighboring areas,[17,43,49-51,58-63] which identified key indicators influencing groundwater quality in rural areas and peri-urban settings.

2.3.1.3. Prevalence and local context

Parameters were chosen based on the geographical and anthropogenic context of Bharatpur and surrounding regions, including Terai and Kathmandu.[39,50,51,61,64,65] For instance, hardness is common in groundwater across the Terai, so it was included. Parameters, such as NO_3^- and sulfate, were added due to potential agricultural contamination (from livestock and fertilizers). Microbiological indicators, such as *E. coli* were considered due to poor sanitation and wastewater management in rural areas.[43]

2.3.1.4. Analytical feasibility

Parameters were selected based on the availability of reliable testing techniques and tools, ensuring precise and reproducible outcomes.

By using this systematic approach, the parameters chosen for this study enable a comprehensive assessment of groundwater quality, considering both environmental and public health concerns specific to the industrial region of Bharatpur, Chitwan.

Table 2 presents the specifics of the chosen parameters used for the assessment of groundwater quality, along with their corresponding WHO guideline range.

2.3.2. Analysis of physicochemical parameters

The physicochemical properties of groundwater provide critical information about its quality, suitability for drinking, and potential sources of contamination. The following parameters were analyzed using standard methods:

2.3.2.1. Temperature

Groundwater temperature is a critical parameter that influences various physical, chemical, and biological processes.[73] It was measured using a mercury thermometer, which was immersed in a beaker containing the water sample. The readings were recorded in a field notebook. To ensure measurement accuracy, the thermometer was calibrated against a standard thermometer of known precision.

2.3.2.2. pH

The pH of the water was determined using a digital pH meter. Before use, the meter was calibrated with standard buffer solutions at pH 4 and pH 7. The glass electrode was thoroughly rinsed with distilled water before and after each measurement, and the pH readings were recorded accordingly.

2.3.2.3. Electrical conductivity

Electrical conductivity was measured using a conductivity meter calibrated with a 0.01N potassium

Table 2. Details of selected parameters for groundwater quality analysis with the WHO guideline ranges

No.	Parameters	Unit	WHO guideline range	References
1.	Conductivity	µS/cm	1,000	59,60
2.	Turbidity	NTU	5	54,68
3.	pH	-	6.5–8.5	66,67
4.	Nitrate (NO_3^-)	mg/L	50	60,69
5.	Total hardness ($CaCO_3$)	mg/L	500	66
6.	Phosphate (PO_4^{3-})	mg/L	0.1–1.0	64
7.	Free CO_2	mg/L	No prescribed limits	64,71
8.	*Escherichia coli*	CFU/100	0	49,66
9.	Chloride (Cl^-)	mg/L	250	69
10.	Total alkalinity ($CaCO_3$)	mg/L	500	70
11.	Ammonia	mg/L	1.5	49,64
12.	Total dissolved solids	mg/L	1,000	54,72

Abbreviations: $CaCO_3$: Calcium carbonate; CFU: Colony-forming unit; CO_2: Carbon dioxide; NTU: Nephelometric turbidity unit; WHO: World Health Organization.

chloride standard solution. The electrode was cleaned and rinsed with distilled water before and after immersion in the sample. Conductivity readings were taken once the values stabilized.

2.3.2.4. Total alkalinity

Total alkalinity, indicative of the presence of salts from strong bases and weak acids, was determined through titration. A 100 mL water sample was placed in a conical flask, and two drops of phenolphthalein indicator were added. If a pink color appeared, it indicated the presence of carbonates, which were titrated with 0.02 N sulfuric acid (H_2SO_4) until the color disappeared. Then, two drops of methyl orange indicator were added, and titration continued until the color changed from yellow to red, indicating the presence of HCO_3^-. Alkalinity was calculated using the following formulas from Trivedi and Goel.[52,64,71]

$$PA as CaCO_3\left(mg/L\right)=\frac{A\times Normality\ of\ H_2SO_4\times 1000\times 50}{Volume\ of\ sample} \quad \text{(I)}$$

$$TA as CaCO_3\left(mg/L\right)=\frac{B\times Normality\ of\ H_2SO_4\times 1000\times 50}{Volume\ of\ sample} \quad \text{(II)}$$

where A = volume of H_2SO_4 used with phenolphthalein only;
B = total volume of H_2SO_4 used with phenolphthalein and methyl orange;
PA = phenolphthalein alkalinity; and
TA = total alkalinity.

2.3.2.5. TH

TH was measured using direct complexation titration with ethylene diamine tetraacetic acid (EDTA), which has a high affinity for Ca^{2+} and magnesium (Mg^{2+}) ions. The endpoint of the titration was marked by a color change from wine red to blue using Eriochrome Black T indicator, indicating that all Ca^{2+} and Mg^{2+} had reacted with EDTA.[64,71]

$$Total\ hardness\ as\ CaCO_3\left(mg/\mathrm{L}\right)=\frac{Volume\ of\ EDT\ A used}{Volume\ of\ sample}\times 1000 \quad \text{(III)}$$

2.3.2.6. Total dissolved solids

Total dissolved solids were quantified gravimetrically by evaporating a known volume of the water sample and weighing the remaining solid residue. The weight of the empty basin (W_1) and the final weight after evaporation (W_2) were used to calculate the TDS concentration:[64,71]

$$Amount\ of\ dissolved\ solids\ \left(ppm\right)=\frac{(W_2-W_1)}{100}\times 10^6 \quad \text{(IV)}$$

2.3.2.7. Free carbon dioxide

Free carbon dioxide (CO_2) was estimated by adding 5–10 drops of phenolphthalein to a 100 mL water sample. If the solution did not turn pink, indicating the presence of free CO_2, the sample was titrated with 0.05N sodium hydroxide (NaOH) until a persistent pink color was achieved. The concentration of free CO_2 was calculated using the following formula:[64,71]

$$Free\ CO\ \left(mg\quad L\right)\quad \frac{Volume\ of\ NaOH\ used\times Normality\ of\ \mathrm{NaOH}\times 44\times 1000}{Volume\ of\ sample} \quad \text{(V)}$$

2.3.2.8. Chloride

Chloride concentration was assessed using the argentometric method. A 50 mL sample was mixed with 3–4 drops of potassium chromate indicator and titrated with a standard silver nitrate solution until the yellow color changed to red, indicating the formation of silver chromate. The same procedure was followed for a blank sample using distilled water.[64,71]

2.3.2.9. Nitrate

Nitrate concentration was measured using a colorimetric method. A 10 mL water sample was mixed with 2 mL NaOH, followed by the addition of 10 mL H_2SO_4 and 0.5 mL brucine solution. The mixture was heated in a water bath for 20 min, and then cooled. Absorbance was measured at 410 nm using a spectrophotometer (Spectronic 21; Milton Roy, USA. A standard calibration curve was prepared to quantify NO_3^- concentration.[74]

2.3.2.10. Phosphate

Phosphate concentration was determined using the ammonium molybdate–stannous chloride method. A 50 mL water sample was mixed with 2 mL of ammonium molybdate and five drops of stannous chloride. After 10–15 min, the resulting blue color was measured at 690 nm using a spectrophotometer (Spectronic 21; Milton Roy Company, USA). Distilled water with the same reagents was used as a blank.[52]

2.3.2.11. Ammonia

Ammonia concentration was determined using a colorimetric method. A 20 mL sample was mixed with 2 mL phenol-nitroprusside solution and 2 mL reagent B, and then diluted to 25 mL with distilled water. The mixture was kept in a dark place at 25°C for 1 h before measuring absorbance at 635 nm using a spectrophotometer. A calibration curve was used to determine the NH_3 concentration.

2.3.2.12. E. coli

E. coli was detected using the membrane filtration method. A 100 mL water sample was filtered through Whatman filter paper using a suction pump. The filter paper was then placed in a sterilized petri dish containing M-lauryl sulfate broth to promote bacterial growth. The dish was incubated at 44°C for 24 h, and colonies were enumerated through direct visualization using standardized identification techniques.[64,71]

2.3.3. WQI

The WQI was calculated based on drinking water quality standards using the weighted arithmetic method refined by Brown *et al*.[74] and Shrestha *et al*. and Tirkey *et al*.[49,75] The weighted arithmetic WQI is expressed as:

$$WQI = \sum_{i=1}^{n} W_i Q_i \,/\, \sum_{i=1}^{n} W_i \quad \text{(VI)}$$

where n = number of variables or parameters,
W_i = unit weight for the i-th parameter,
Q_i = quality rating (sub-index) of the i-th water quality parameter.

The unit weight (Wi) for each water quality parameter is inversely proportional to its recommended standard value.

$$W_i = K/S_n \quad \text{(VII)}$$

where, W_i = unit weight for the i-th parameter,
S_n = standard permissible value for the i-th parameter,
K = proportional constant.

The value of K is taken as "1" here and calculated using the following equation:[49,75]

$$K = 1/\sum(1/S_n) \quad \text{(VIII)}$$

The quality rating or sub-index (Qi) is determined by Shrestha *et al*., Brown *et al*. and Tirkey *et al*.:[49,74,75]

$$Q_i = 100\,[(V_0 - V_i)/(S_n - V_i)] \quad \text{(IX)}$$

where V_o = observed value of the i-th parameter at a given sampling site,
V_i = ideal value of the i-th parameter in pure water,
S_n = standard permissible value of the i-th parameter.

For drinking water, the ideal values (Vi) are considered zero for all parameters except pH and dissolved oxygen.[56] The ideal pH value is 7.0 (for pure water), with a permissible upper limit of 8.5 (for polluted water). For dissolved oxygen, the ideal value is 14.6 mg/L, and the permissible minimum is 5 mg/L. Therefore, the quality rating for pH is calculated as:[49,74-76]

$$Q_{pH} = 100[(V_{pH} - 7.0)/(8.5 - 7.0)] \quad \text{(X)}$$

where, V_{pH} = observed pH value.

If $Q_i = 0$, it indicates the complete absence of contaminants. A value of $0 < Q_i < 100$ suggests that contaminants are within acceptable limits, while $Q_i > 100$ indicates that contaminants exceed the standard thresholds.

2.3.4. Data analysis

The collected data were analyzed using MS Excel 2010. Statistical analysis included the calculation of mean, median, and standard deviation. The concentrations of the measured parameters were expressed in mg/L, equivalent to ppm.

3. Results and discussion

3.1. Result of physicochemical parameters

The detailed results of the physicochemical and biological parameters, along with their variations across different sampling sites, are presented in this section.

3.1.1. Temperature

The analysis revealed that groundwater temperatures across the sampled sites ranged from 21°C to 23°C, with an average temperature of 22.0°C. Figure 3 illustrates the temperature variations across the study sites. The highest average temperature was observed near the IF at 22.3°C, while the lowest was recorded near the CF at 21.8°C.

Although not specifically regulated by the WHO or NDWQS, temperature affects various water quality parameters, including gas solubility and biological activity. Groundwater tends to be more thermally stable compared to surface water due to insulation by surrounding soil and rock layers. Temperature variations in groundwater are typically minimal but can influence chemical reactions and microbial processes.[77,78] For instance, higher temperatures may accelerate chemical reactions and microbial growth, potentially increasing levels of contaminants.[79] In this context, the observed temperature range appears stable and is unlikely to significantly affect water quality.

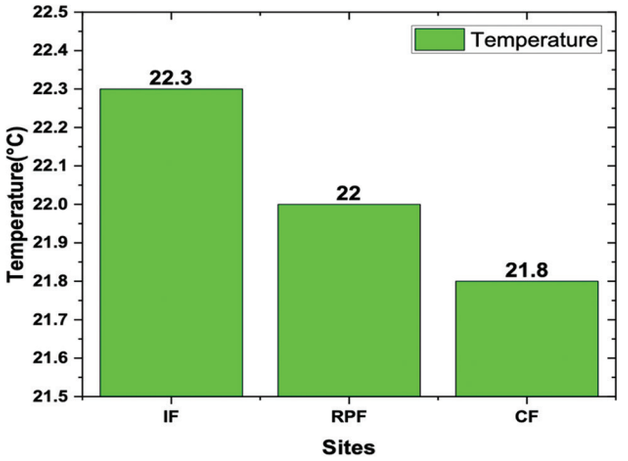


Figure 3. Variation of water temperature in the groundwater of Bharatpur
Abbreviations: CF: Coca-Cola factory; IF: Iron factory; RPF: Royal Paint factory.

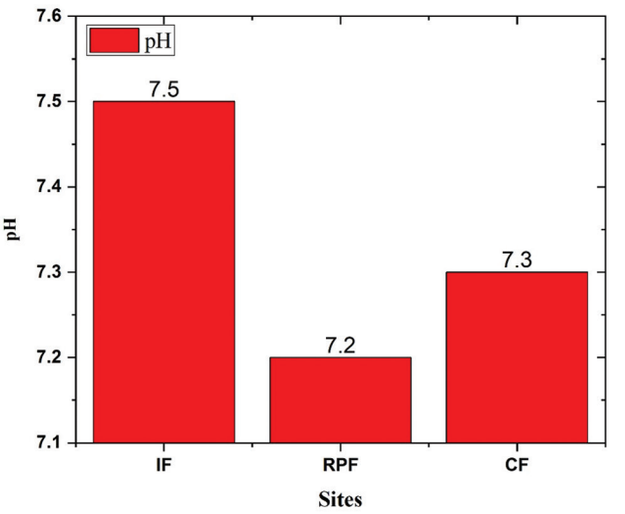


Figure 4. Variation of pH in the groundwater of Bharatpur
Abbreviations: CF: Coca-Cola factory; IF: Iron factory; RPF: Royal Paint factory.

3.1.2. pH

The pH, which reflects hydrogen ion concentration, indicates the acidity or alkalinity of water. Pure water has a neutral pH, serving as a baseline for pH measurements. In this study, average pH values were 7.5 near the IF, 7.2 near the RPF, and 7.3 near the CF. Figure 4 shows that pH was slightly higher around the IF and lower near the RPF. Overall, pH ranged from 7.0 (Sample G) to 7.9 (Sample B), indicating mildly basic conditions.

These values fall within the WHO and NDWQS recommended range of 6.5–8.5. A near-neutral pH is generally optimal for drinking water as it reduces corrosion and scaling in plumbing, ensures chemical stability,[57,80] and minimizes the solubility of toxic metals.[78] pH is influenced by the equilibrium among CO_2, HCO_3^-, and carbonate ions (CO_3^{2-}) and may be altered by industrial effluents, domestic sewage discharge, and atmospheric deposition of acidic compounds.

The observed values suggest that the groundwater is chemically balanced and suitable for consumption. pH is a critical parameter in assessing water quality, as it affects the solubility and toxicity of contaminants.[57] Recent research highlights that maintaining pH within the recommended range is essential for ensuring safe water. For instance, Prest *et al*.[77] emphasize how pH variations can impact the effectiveness of water treatment processes and the stability of disinfectants.

3.1.3. Electrical conductivity

Electrical conductivity refers to the ability of an aqueous solution to conduct electricity[81-84] and is influenced by the concentration, mobility, and valence of dissolved ions, as well as temperature. Electrolytes dissociate into positive and negative ions in solution, contributing to conductivity.

The study found average electrical conductivity values of 280 µS/cm at the IF, 490 µS/cm at the RPF, and 601 µS/cm at the CF (Figure 5). Electrical conductivity ranged from a minimum of 203 µS/cm (Sample B) to a maximum of 994 µS/cm (Sample K) at the IF and CF, respectively. The overall mean EC for all sites was 456.5 µS/cm, with a median of 420 µS/cm —well below the WHO and NDWQS limit of 1500 µS/cm. Conductivity is a key indicator of the ionic content in water, reflecting concentrations of dissolved salts and minerals, which can affect taste and treatment efficiency.[83,84] The observed electrical conductivity levels are acceptable and indicate that the groundwater is not excessively mineralized.

Although high conductivity can suggest increased salinity or pollution, the measured values fall within typical groundwater ranges. Recent studies[5,54,80,85] have confirmed that groundwater with moderate conductivity is generally safe for consumption, though higher values may influence taste and require treatment.

3.1.4. Total alkalinity

The analysis of water samples revealed that the average alkalinity values were 62 mg/L at the IF, 104 mg/L at the RPF, and 137 mg/L at the CF, as illustrated in Figure 6.

The alkalinity across the groundwater samples ranged from a maximum of 215 mg/L (Sample K at CF)

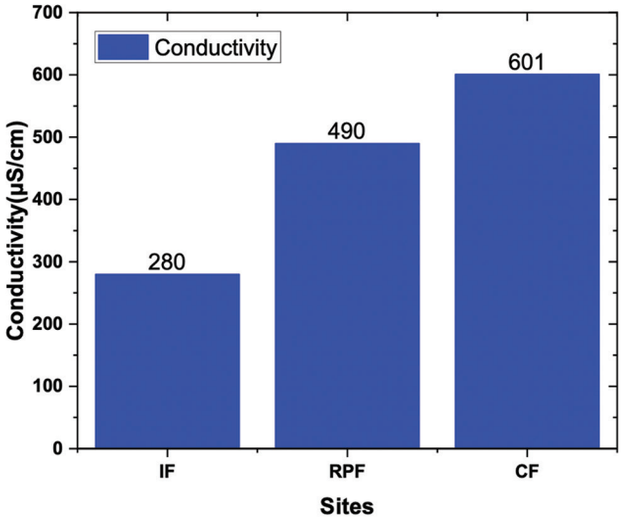


Figure 5. Variation of electrical conductivity in the groundwater of Bharatpur
Abbreviations: CF: Coca-Cola factory; IF: Iron factory; RPF: Royal Paint factory.

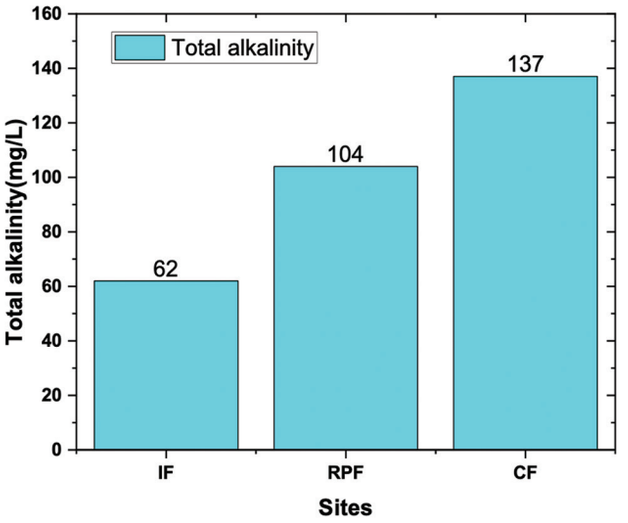


Figure 6. Variation of total alkalinity in the groundwater of Bharatpur
Abbreviations: CF: Coca-Cola factory; IF: Iron factory; RPF: Royal Paint factory.

to a minimum of 53 mg/L (Sample Cat IF). Naturally, less polluted water tends to be more alkaline than acidic. Alkalinity is a reliable indicator of the presence of dissolved inorganic carbon, such as HCO_3^- and CO_3^{2-}. Although not specifically regulated by the WHO or NDWQS, alkalinity is important for buffering capacity and pH stability. Higher alkalinity levels help maintain a stable pH and mitigate acidification.[80,86] Previous investigations[11,87-89] have shown that adequate alkalinity prevents corrosive water conditions and supports the effectiveness of water treatment processes.[90] The observed values indicate a sufficient buffering capacity in the groundwater, supporting its stability and suitability for drinking.

3.1.5. TH

The average TH measured at the IF, RPF, and CF was 137 mg/L, 221 mg/L, and 276 mg/L, respectively, as shown in Figure 7. The TH ranged between 99 mg/L and 405 mg/L, with the highest value recorded at 405 mg/L in Sample K near the CF and the lowest hardness at 99 mg/L in Sample C near the IF.

Water hardness traditionally refers to how well water reacts with soap, with hard water requiring a large amount of soap to form a lather. Hardness is primarily caused by divalent cations, including Ca^{2+}, Mg^{2+}, and other alkaline earth metals, such as iron, manganese, and strontium. These values are below the WHO and NDWQS guideline of <500 mg/L. TH, mainly due to Ca^{2+} and Mg^{2+} ions, can affect water's suitability for various uses.[50,60,90,91] Recent research highlights that while hard water generally does not pose a health risk, it can impact household appliances and plumbing. Previous studies[66,69,92,93] found that water hardness above 300 mg/L can lead to scaling in boilers, making it unsuitable for industrial usage and reducing efficiency in water heaters and other appliances. The observed hardness levels indicate moderate hardness, which is typical for many groundwater sources.

3.1.6. Total dissolved solids

The average TDS in groundwater samples collected from the IF, RPF, and CF were 225 mg/L, 125 mg/L, and 175 mg/L, respectively, as depicted in Figure 8. Samples from the IF exhibited the highest average TDS levels. Overall, TDS values ranged from 0 to 400 mg/L across all samples.

Substances that pass through filter paper but remain as residue when water evaporates include dissolved minerals and salts, as well as organic compounds, such as humic substances and tannins. All measured TDS values are within the WHO and NDWQS limit of <1000 mg/L. TDS is a measure of all dissolved substances in water and affects both water quality and taste.[57,66,80] The observed levels are acceptable for drinking water and suggest that the groundwater is relatively low in dissolved solids, which is desirable for maintaining water quality and taste.

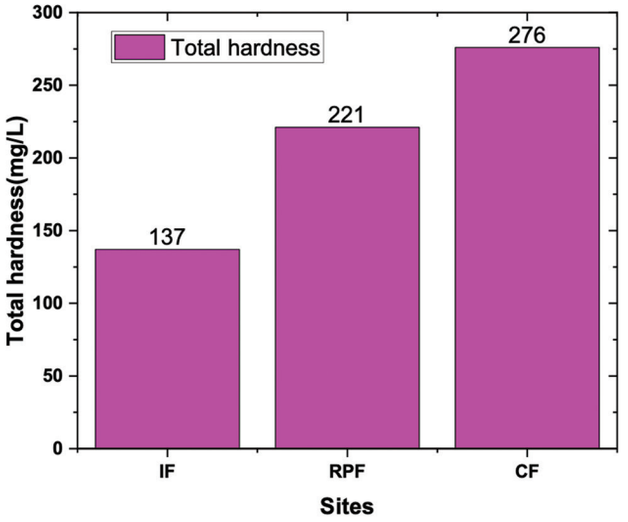


Figure 7. Variation of total hardness in the groundwater of Bharatpur
Abbreviations: CF: Coca-Cola factory; IF: Iron factory; RPF: Royal Paint factory.

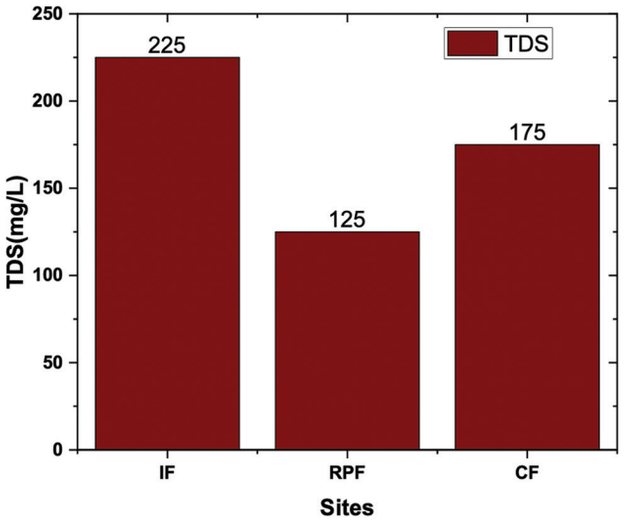


Figure 8. Variation of TDS in the groundwater of Bharatpur
Abbreviations: CF: Coca-Cola factory; IF: Iron factory; RPF: Royal Paint factory; TDS: Total dissolved solids.

According to recent research, lower TDS levels generally correlate with better water quality and palatability. Previous studies[43,94,95] found that water with TDS levels below 500 mg/L is typically considered acceptable for drinking and irrigation purposes. The observed TDS levels suggest that the groundwater is low in dissolved solids and should be suitable for drinking.

3.1.7. Free carbon dioxide

The average concentrations of free CO_2 in groundwater samples were 36 mg/L at IF, 49 mg/L at RPF, and 63 mg/L at CF, as illustrated in Figure 9. CF showed the highest average free CO_2 levels, followed by RPF, while IF had the lowest. The concentration of free CO_2 ranged from a minimum of 28.6 mg/L at IF to a maximum of 89.1 mg/L at CF, with Sample B from IF having the highest concentration and Sample K from CF the lowest.

The primary sources of free CO_2 in water bodies are respiration and decomposition by aquatic organisms. CO_2 reacts with water to partially form calcium bicarbonate; in the absence of HCO_3^-, it can convert into CO_3^{2-}, releasing additional CO_2. High levels of free CO_2 can contribute to the formation of carbonic acid, affecting the pH and corrosiveness of water. Although the WHO and NDWQS do not specify limits for CO_2, its concentration is crucial for understanding water chemistry. Regular monitoring is essential to assess its impact on water chemistry and infrastructure. Recent studies by Khadka and Khanal[71] and Budhathoki[64] highlight that elevated free CO_2 levels can indicate high natural acidity or anthropogenic influences, such as contamination from organic waste. The observed CO_2 levels suggest a moderate presence, which is not likely to cause immediate concern but warrants ongoing monitoring.[64,71]

3.1.8. Chloride

Chloride concentrations were highest around CF at 68 mg/L, lowest around IF at 50 mg/L, and moderate around RPF at 61 mg/L, as shown in Figure 10. Cl^- levels ranged from a minimum of 22.7 mg/L in Sample B to a maximum of 142.2 mg/L in Sample K. The WHO and NDWQS guideline for Cl^- in drinking water is <250 mg/L, indicating that the observed levels are well within safe limits.

Elevated Cl^- levels can render water unpleasant and unsuitable for drinking or watering livestock. Cl^-, a common anion in wastewater, serves as a useful indicator of pollution sources. High Cl^- concentrations can also damage metal pipes and structures and adversely affect agricultural plants. High Cl^- levels can affect taste and contribute to corrosion.[57] They may also indicate pollution sources, such as road salts or industrial discharges. The observed levels are acceptable for drinking water and do not suggest significant contamination.

Previous studies[61,67,96,97] show that while Cl^- is not typically harmful at these concentrations, elevated

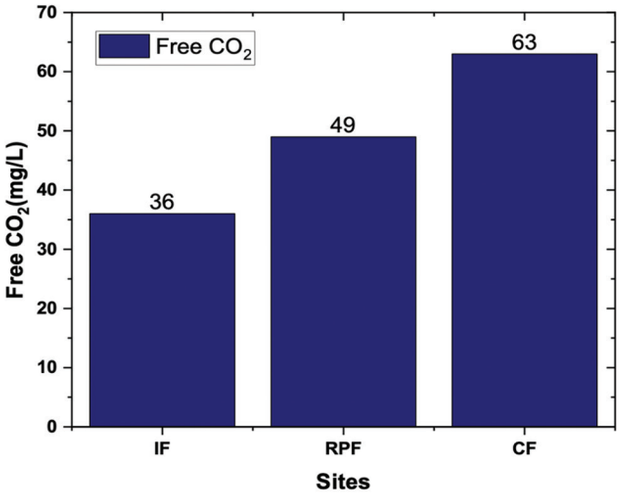


Figure 9. Variation of free CO_2 in the groundwater of Bharatpur
Abbreviations: CF: Coca-Cola factory; IF: Iron factory; RPF: Royal Paint factory; CO_2: Carbon dioxide.

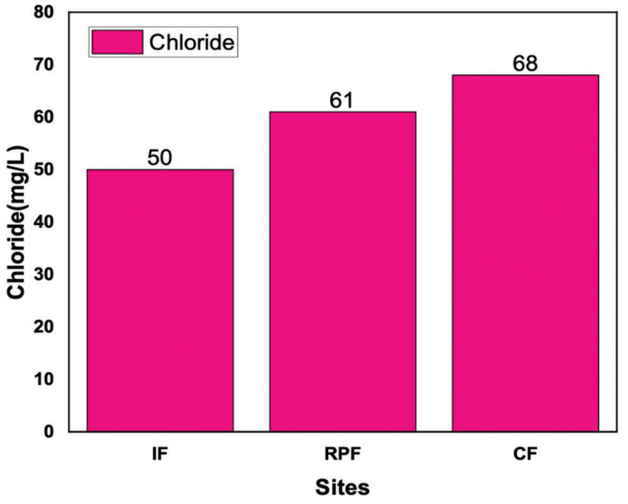


Figure 10. Variation of chloride in the groundwater of Bharatpur
Abbreviations: CF: Coca-Cola factory; IF: Iron factory; RPF: Royal Paint factory.

levels could indicate pollution or saltwater intrusion, especially in coastal areas. The observed Cl^- levels are typical for many groundwater sources and suggest no significant immediate concerns.[6,42,98]

3.1.9. Nitrate

The average NO_3^- concentrations in groundwater samples collected from IF, RPF, and CF were 32 mg/L, 39 mg/L, and 42 mg/L, respectively, as illustrated in Figure 11. CF exhibited the highest average

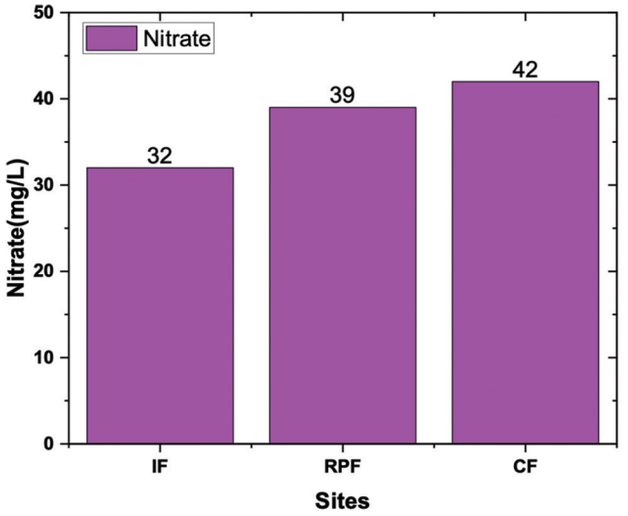


Figure 11. Variation of nitrate in the groundwater of Bharatpur
Abbreviations: CF: Coca-Cola factory; IF: Iron factory; RPF: Royal Paint factory.

NO_3^- concentration. The NO_3^- levels ranged from a minimum of 23.3 mg/L in Sample A to a maximum of 45.8 mg/L in Sample K. These NO_3^- levels are below the WHO and NDWQS guideline of 50 mg/L, indicating that NO_3^- concentrations are generally within safe limits for drinking water. However, the levels are relatively high compared to those in other groundwater sources, which can be a concern as they may contribute to eutrophication and impact water quality. The variability suggests the influence of agricultural runoff or other NO_3^- sources.

Nitrate contamination in groundwater is often linked to agricultural activities, particularly the use of synthetic fertilizers and manure.[64,71,99] Natural sources of NO_3^- include igneous rocks, domestic sewage, land drainage, and the growth and decay of plants. The typical natural concentration of NO_3^- is 0.1 ppm, but this level can increase due to sewage, industrial effluents, and NO_3^- fertilizers. High NO_3^- levels can lead to conditions, such as methemoglobinemia (blue baby syndrome) in infants, where the ability of blood to carry oxygen is reduced.[1,60,96,99,100]

Previous studies[54,89,93,96,99,101,102] have shown that elevated NO_3^- levels are prevalent in areas with intensive agriculture and can pose long-term risks to water quality and human health. The NO_3^- levels observed in this study suggest that while they are within the recommended limits, ongoing monitoring and management practices are crucial to prevent potential increases in contamination.

3.1.10. Phosphate

The average PO_4^{3-} concentration was highest around RPF, at 7.8 mg/L, and lowest around CF at 6.2 mg/L. The concentration of PO_4^{3-} at IF was found to be 6.4 mg/L, as shown in Figure 12. Overall, PO_4^{3-} concentrations varied between 4.3 mg/L (minimum) in Sample E and 9.8 mg/L (maximum) in Samples F and K.

Although there are no specific WHO or NDWQS guidelines for PO_4^{3-}, these levels are generally acceptable for groundwater. High PO_4^{3-} concentrations can contribute to the eutrophication of water bodies and promote algal blooms if the water is used in surface water bodies or for irrigation. The observed levels are within a typical range and do not pose immediate health risks.[2,60,93]

Recent research[2,69,87,103,104] highlights that while moderate levels of PO_4^{3-} are generally not a health risk, high concentrations can lead to environmental concerns and impact water quality. In natural water and wastewater, phosphorus is present as orthophosphates, polyphosphates, and organically bound PO_4^{3-}. Orthophosphates, often used as fertilizers on agricultural land, can enter water bodies through runoff and percolation. The PO_4^{3-} levels observed in this study are within a typical range for groundwater, but should be monitored to prevent potential environmental impacts.[2,60,93]

3.1.11. Ammonia

The NH_3 concentrations in groundwater samples were highest around the CF at 11.7 mg/L, moderate around IF at 8.1 mg/L, and lowest around RPF at 8.0 mg/L, as depicted in Figure 13. The NH_3 concentrations ranged from a minimum of 7.0 mg/L in Sample I to a maximum of 19.5 mg/L in Sample L, both from the same site. The average NH_3 concentration was 9.3 mg/L, with a median value of 8.1 mg/L. Both WHO and NDWQS recommend a maximum of 1.5 mg/L for NH_3, indicating that the observed levels are significantly higher. Elevated NH_3 levels can be indicative of pollution from agricultural runoff or wastewater discharge and pose health risks, including toxicity to aquatic life and potential impacts on water taste and odor. Immediate remediation and monitoring are recommended to address potential sources of contamination.[49,105]

Recent studies[49,43,64,103,105] confirm that high NH_3 concentrations are often linked to agricultural and industrial sources, highlighting the need for targeted pollution control measures. The high levels observed in this study suggest that immediate action may be needed to address potential contamination sources and ensure water safety. One possible reason for the higher NH_3 concentrations may be the presence of industries and agricultural areas.

3.1.12. Microbiological parameter

The enumeration of *E. coli* colonies in the water samples, determined using the membrane filtration method and direct visualization, ranged from 0 to 9 colonies/100 mL sample. The average colony count was 4.3 per sample at the CF, 2.5 per sample at the IF, and 1.4 per sample at the RPF, as illustrated in Figure 14. The overall mean colony count across all samples was 2.8.

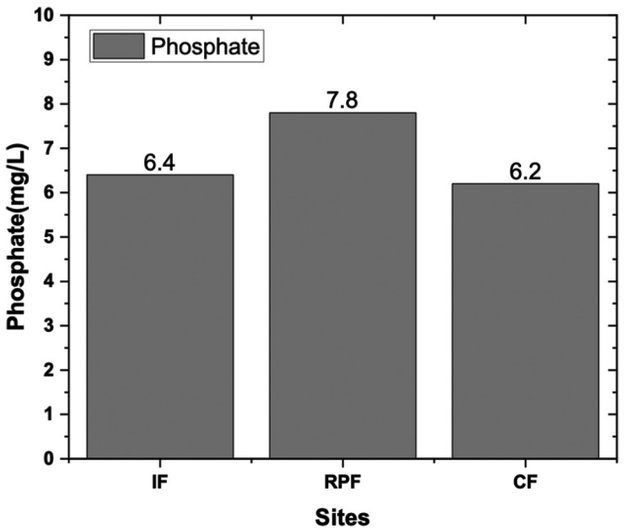


Figure 12. Variation of phosphate in the groundwater of Bharatpur

Abbreviations: CF: Coca-Cola factory; IF: Iron factory; RPF: Royal Paint factory.

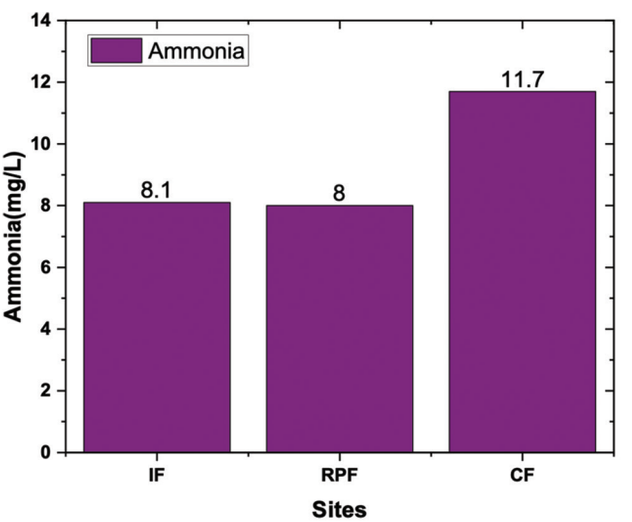


Figure 13. Variation of ammonia in the groundwater of Bharatpur

Abbreviations: CF: Coca-Cola factory; IF: Iron factory; RPF: Royal paint factory.

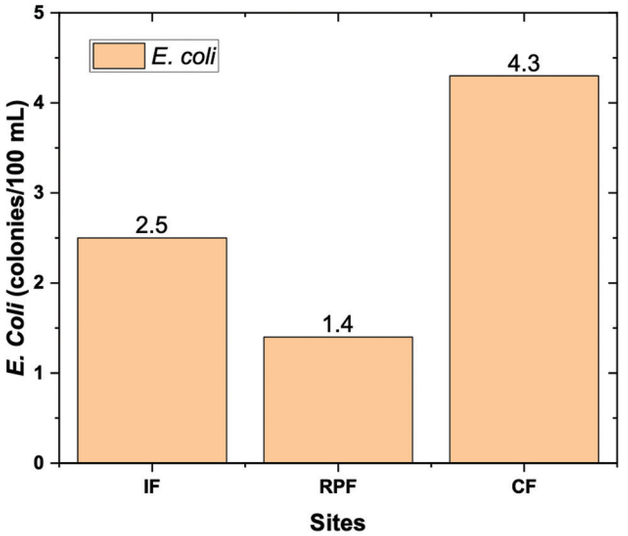


Figure 14. Variation of *Escherichia coli* in the groundwater of Bharatpur
Abbreviations: CF: Coca-Cola factory; IF: Iron factory; RPF: Royal paint factory.

Out of 12 samples, one-third—that is, Samples A, C, E, and G—from sites IF and RPF contained zero colonies per 100 mL of sample water. However, all other samples—B, D, F, H, I, J, K, and L—contained 1, 9, 1, 6, 3, 7, 2, and 5 colonies per 100 mL of water, respectively. All four samples from site CF exceeded the permissible limit of drinking water quality (Figure 15).

E. coli is a key indicator of fecal contamination and the presence of pathogenic microorganisms in water. Both WHO[48] and NDWQS[44] set a standard of 0 colonies/100 mL for drinking water, indicating that the presence of *E. coli* at any detectable level is a concern.

The presence of *E. coli* in groundwater suggests potential contamination from animal waste, inadequate sewage treatment, or other sources of fecal pollution.[106] Even low levels of *E. coli* indicate a risk of exposure to harmful pathogens, which can cause gastrointestinal illnesses and other health problems. Recent studies[49,89,106,107] emphasize the importance of maintaining zero *E. coli* levels in drinking water to ensure safety. They also highlight that even low levels of *E. coli* can pose health risks, particularly in areas with poor sanitation infrastructure. From this study, the presence of *E. coli* might be due to animal waste, leakage from septic tanks, or improper sewage treatment from industrial areas.[106] Therefore, despite the relatively low mean concentration observed, it is crucial to address the sources of contamination and implement effective water treatment and sanitation practices.

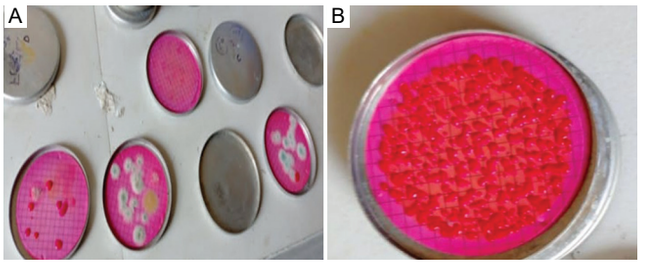


Figure 15. Result of microbiological analysis for samples from the Coca-Cola factory. (A) *E. Coli.* colony formation in agar (B) Total Coliform in sample water.

3.2. WQI

The results of the WQI, as referenced in the literature,[60,74,108,109] are presented in Table 3.

The calculated WQI values ranged from 560 to 663. Analysis of these WQI values indicates that none of the sampling sites fall into the categories of excellent, good, poor, or even very poor quality. Instead, all samples from the sites were classified as 100% unsuitable for drinking. This finding suggests that the groundwater in the Gondrang area, located near industrial activities in Chitwan, Nepal, does not meet the WHO standards for potable water.

The WQI values[110-112] calculated in this study range from 560 to 663 (Tables S1, S2, and S3), indicating that all samples from the selected sites are deemed unsuitable for drinking. Detailed physicochemical and microbiological parameters of water samples from different sites are given in Table S4. This finding contrasts with the results reported by Ram *et al*.,[76] who observed WQI values between 4.75 and 115.93. Their study suggested that groundwater in their area was generally safe for consumption, except for a few sites in the Charkhari and Jaitpur blocks. Das *et al.* and Das and Choudhary[59,60] reported WQI values ranging from 84.54 to 403.14, noting that elevated WQI values were attributed to higher levels of turbidity, free CO_2, and arsenic. That study emphasized the need for groundwater treatment and protection against contamination.

Comparatively, the WQI values obtained in this study are substantially higher than those reported by both Ram *et al*.[76] and Das *et al*. and Das and Choudhary.[59,60] The WQI values from Das *et al*. are closer to our obtained values, whereas those reported by Ram *et al*. are much lower. The elevated WQI values observed in the present study are primarily due to higher concentrations of NH_3, PO_4^{3-}, and free CO_2.

3.3. Statistical analysis

All 12 samples from three sites, values were analyzed using descriptive statistics. Maximum, minimum, mean, median, standard deviation, and range were calculated from the observed values. The standard deviation indicates the spread of values from the mean, while the median represents the middle value. The calculated standard deviation and range are presented in Table 4.

3.3.1. Comparison of parameters with water quality standards

The observed values of all parameters were compared with NDWQS, WHO, and Irrigation Water Quality Standards. From this comparison (Table 5), the average pH, conductivity, TDS, TH, total alkalinity, and Cl^- concentrations were found below the specified limits of both NDWQS and WHO. The concentration of NO_3^- was found below the NDWQS value but above the recommended standard of the WHO. Parameters, such as free CO_2, NH_3, and PO_4^{3-} exceeded the standard value of the WHO guidelines.

3.3.2. Discussion of physicochemical parameters

Water is a vital resource for all living organisms, and its management influences environmental, economic, and social aspects. This study examined the physical, chemical, and microbiological characteristics of groundwater to assess its quality. The results (Tables S1-S4) highlight differences in groundwater quality at three distinct sites within the study area based on the evaluated physicochemical parameters.

3.3.3. Statistical analysis of water quality parameters

Using Statistical Package for the Social Sciences (SPSS) software, the correlation coefficient values (r) were determined for each set of water quality measurements. The following formula was used to calculate the correlation coefficient (r) between two variables, X and Y:[66]

$$r = \frac{\sum XY - \frac{\sum X \sum Y}{n}}{\sqrt{[\sum X^2 - \frac{(\sum X^2)}{n}][\sum Y^2 - \frac{(\sum Y^2}{n}]}} \quad \text{(XI)}$$

Table 3. Comparison of WQI standard values with observed values[60,74,108,109]

Category of water	WQI range	Percentage of samples	Sample sites	Class
Very good water	0–25	0	-	A
Good water	26–50	0	-	B
Poor water	51–75	0	-	C
Very poor water	76–100	0	-	D
Unsuitable for drinking	>100	100	IF, RPF, CF	E

Abbreviations: CF: Coca-Cola factory; IF: Iron factory; RPF: Royal Paint factory; WQI: Water quality index.

Table 4. Maximum, minimum, mean, median, standard deviation, and range of measured parameters

Parameters	Minimum	Maximum	Mean	Median	SD	Range
Temperature (°C)	21	23	22.0	22	0.7	21–23
pH	7.0	7.9	7.3	7.3	0.3	7.0–7.9
Conductivity (µs/cm)	203	994	456.5	420	222	203–994
TDS (mg/L)	0	400	175	200	154.5	0–400
Total hardness (mg/L)	99	405	211.2	208	82.3	99–405
Total alkalinity (mg/L)	53	215	101.2	98	44.7	53–215
Free CO_2 (mg/L)	28.6	89.1	49.5	45.1	17.3	28.6–89.1
Chloride (mg/L)	22.7	142.2	60	48.4	38.1	22.7–142.2
Phosphate (mg/L)	4.25	9.8	6.8	6.8	1.8	4.3–9.8
Ammonia (mg/L)	7.0	19.5	9.3	8.1	3.4	7.0–19.5
Nitrate (mg/L)	23.3	45.8	37.8	40	7.8	23.3–45.8
Escherichia coli (colonies/100 mL)	0	9	2.8	1.5	3.2	0–9

Abbreviations: CO_2: Carbon dioxide; TDS: Total dissolved solids.

Table 5. Comparison of observed parameters with water quality standards

Parameters	IF	RPF	CF	NDWQS	WHO
Temperature (°C)	22.3	22.0	21.8	-	-
pH	7.5	7.2	7.3	6.5–8.5	6.5–8.5
Conductivity (μs/cm)	280	490	601	1500	1500
TDS (mg/L)	225	125	175	1000	1000
Total hardness (mg/L)	137	221	276	500	300
Total alkalinity (mg/L)	62	104	137	-	-
Free CO_2 (mg/L)	36	49	63	-	-
Chloride (mg/L)	50	61	68	250	250
Phosphate (mg/L)	6.4	7.8	6.2	-	-
Ammonia (mg/L)	8.1	8.0	11.7	1.5	1.5
Nitrate (mg/L)	32	39	42	50	10
Escherichia coli (colonies/100 mL)	2.5	1.4	4.3	0	0

Abbreviations: CF: Coca-cola factory; CO_2: Carbon dioxide; IF: Iron factory; NDWQS: Nepal Drinking Water Quality Standard; RPF: Royal Paint Factory; TDS: Total dissolved solids; WHO: World Health Organization.

A strong association between two variables, *X* and *Y*, is indicated if their correlation coefficient (*r*) is relatively large. The linear equation of the form y = Ax + B becomes valid under such conditions.[66]

Traditional graphs used to display groundwater quality data may not adequately illustrate the true relationships between variables, especially when multiple parameters are involved. Given that each parameter falls into a distinct quality class, analyzing them individually becomes complex when additional parameters are introduced into the evaluation. This makes interpreting the results challenging. Accurately analyzing the type and extent of water pollution thus becomes difficult and complicated.[113] Correlation analysis is a widely used and effective statistical method for studying water quality, as it reveals which properties influence water chemistry. It demonstrates the relationships between the variables. Two variables are said to be positively correlated if an increase in one causes an increase in the other, and negatively correlated if an increase in one results in a decrease in the other. The correlation coefficient (*r*) ranges from +1 to −1.[92] According to Das *et al*. and Das and Das,[92,114] correlation is considered weak if its magnitude lies in the range 0.0 ± 0.5, moderate if it lies between ±0.5 and ±0.8, and very strong if it lies between ±0.8 and ±1.0.[66,114] Equation XI was used to calculate the correlation coefficient. The interaction mode of the parameters was further examined using regression analysis. Linear regression can be applied to determine the relationships between parameters.[92]

To identify the most significant groundwater quality parameters and their relationships with other relevant factors, a correlation matrix analysis was conducted. To describe the type and strength of relationships among highly correlated characteristics, the concentrations of dependent parameters were plotted against independent variables. SPSS was used to perform regression analysis between parameters with strong correlations (Figures 16 and S1-S10). Table 6 presents the Pearson correlation (P. correlation) coefficient values for 12 parameters.

3.3.4. Correlation results

The groundwater datasets are complex and contain various variables. This complexity highlights the importance of developing sustainable water management plans and solutions. Correlation and regression analyses simplify these datasets by emphasizing the most important factors, making the data more accessible to scientists, decision-makers, and the general public.[96] As such, regression and correlation are essential methods for analyzing groundwater quality, helping to identify patterns, predict trends, and demonstrate relationships among various WQIs. Another advantage of correlation analysis is that it measures the strength and direction of the linear relationship between two parameters. For instance, if conductivity and NO_3^- levels are positively correlated, this could indicate that NO_3^- contamination is associated with higher salinity. Regression analysis builds upon correlation by also offering a predictive equation. This allows for the simulation of how

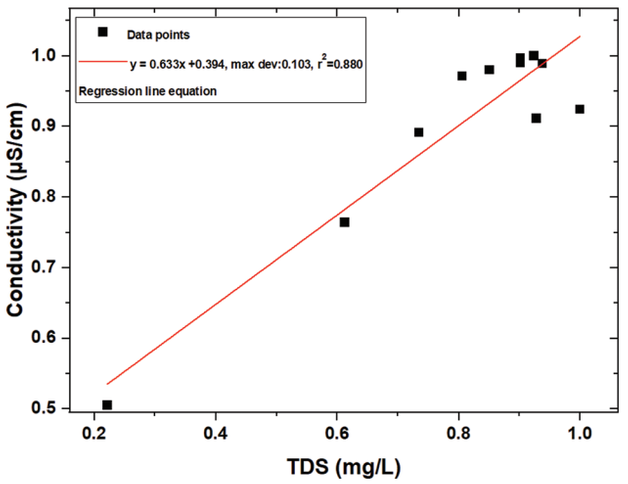


Figure 16. Regression plot of conductivity versus TDS
Abbreviation: Max dev: Maximum deviation; TDS: Total dissolved solids.

one water quality variable (e.g., TDS) responds to changes in another (e.g., Cl^- concentration).[43,54,85,115-121] Perfect positive and negative linear relationships are indicated by correlation coefficient values close to +1 and −1, respectively, while a value of 0 denotes no linear relationship. Strong correlations are typically represented by *P. correlation* values near +1 or −1, as shown in Table 6. The statistical significance of a correlation is determined by its significance (Sig. [2-tailed]) value—a value <0.05 indicates significance at the 5% level, while a value <0.01 denotes significance at the 1% level. Asterisks indicate statistically significant correlations (*at the 0.05 level; **at the 0.01 level).

Regression and correlation analysis not only allow the interpretation of groundwater quality data but also help relate observed patterns to hydrogeological processes. These methods are valuable for describing the groundwater system and providing insights into its behavior. The simple correlation coefficient (r) quantifies the degree of linearity between any two water quality measures.[54,85,115-120] Table 6 presents the significance levels (2-tailed) and correlation matrix for several key water quality parameters.

The following important findings are derived from the statistical analysis (Table 6). Conductivity was strongly positively correlated with TDS (r = 0.924, p=0.025), significant at the 0.05 level. This high correlation is expected, as TDS comprises charged ions that contribute to electrical conductivity. In addition, conductivity was significantly positively correlated at the 0.01 level with TH (r = 0.990, p=0.001), indicating that increased dissolved minerals (ions) contribute to both parameters. The correlation between conductivity and total alkalinity was also strong (r = 0.997, p=0.000), likely due to the presence of CO_3^{2-} and HCO_3^-, which contribute to both alkalinity and conductivity. A strong positive correlation was observed between conductivity and free CO_2 (r = 0.980, p=0.003), signifying that CO_2 dissolution increases ion concentration, thus enhancing conductivity through the formation of carbonic acid or HCO_3^-. Moreover, Cl^- showed a strong positive correlation with conductivity (r = 0.989, p=0.001), consistent with the fact that Cl^- is highly conductive in water. Similarly, a significant correlation existed between conductivity and NH3 (r = 0.971, p=0.006), showing that NH_3 increases conductivity by forming ammonium ions (NH_4^+) in water. A positive correlation between conductivity and PO_4^{3-} (r = 0.891, p=0.042) indicates that PO_4^{3-} also contributes to conductivity. In addition, conductivity was positively correlated with *E. coli* (r = 0.911, p=0.032), implying that *E. coli* presence may be associated with increased organic and inorganic dissolved substances, thus influencing conductivity.

TH showed an almost perfect positive correlation, significant at the 0.01 level, with alkalinity (r = 0.995, p=0.000), indicating that both parameters are influenced by dissolved minerals, such as calcium, magnesium, and carbonates, which explains their strong relationship. Furthermore, a very strong positive correlation was observed between TH and free CO_2, significant at the 0.01 level (r = 0.994, p=0.001), suggesting that CO_2 dissolution in water affects hardness, possibly through precipitation or dissolution of carbonate compounds. In addition, TH showed a strong correlation with NH_3 (r = 0.969, p=0.007). The presence of NH_3 correlates with hardness, likely due to NH_3 forming complex compounds with dissolved minerals. In addition, total alkalinity showed a very strong positive correlation, significant at the 0.01 level, with free CO_2 (r = 0.990, p=0.001), indicating that alkalinity and free CO_2 are chemically linked through the carbonate buffer system. Total alkalinity also showed a strong correlation with NH_3 (r = 0.981, p=0.003), suggesting a possible interaction between NH_3 and alkalinity parameters, likely due to NH_3's effect on pH and carbonate equilibrium. Moreover, Cl^- and *E. coli* demonstrated a strong positive correlation, significant at the 0.01 level (r = 0.961, p=0.009), indicating a potentially concerning relationship. High Cl^- levels may signal contamination sources (e.g., sewage or industrial waste) that also contribute to *E. Coli* presence. *E. coli* is a fecal

Table 6. Statistical table of correlations between various water quality parameters

Parameters	pH	Conductivity	TDS	Total hardness	Total alkalinity	Free CO_2	Cl^-	PO_4^{3-}	NH_3	NO_3^-	*Escherichia coli*
pH											
P. correlation	1.00	-	-	-	-	-	-	-	-	-	-
Sig. (2-tailed)	-	-	-	-	-	-	-	-	-	-	-
Conductivity (µS/cm)											
P. correlation	0.505	1.00	-	-	-	-	-	-	-	-	-
Sig. (2-tailed)	0.385	-	-	-	-	-	-	-	-	-	-
TDS (mg/L)											
P. correlation	0.222	0.924*	1.00	-	-	-	-	-	-	-	-
Sig. (2-tailed)	0.719	0.025	-	-	-	-	-	-	-	-	-
Total hardness (mg/L)											
P. correlation	0.601	0.990**	0.902*	1.00	-	-	-	-	-	-	-
Sig. (2-tailed)	0.284	0.001	0.036	-	-	-	-	-	-	-	-
Total alkalinity (mg/L)											
P. correlation	0.562	0.997**	0.902*	0.995**	1.00	-	-	-	-	-	-
Sig. (2-tailed)	0.324	0.000	0.036	0.000	-	-	-	-	-	-	-
Free CO_2 (mg/L)											
P. correlation	0.665	0.980**	0.851	0.994**	0.990**	1.00	-	-	-	-	-
Sig. (2-tailed)	0.221	0.003	0.068	0.001	0.001	-	-	-	-	-	-
Cl− (mg/L)											
P. correlation	0.385	0.989**	0.938*	0.960**	0.977**	0.944*	1.00	-	-	-	-
Sig. (2-tailed)	0.522	0.001	0.018	0.010	0.004	0.016	-	-	-	-	-
PO_4^{3-} (mg/L)											
P. correlation	0.823	0.891*	0.735	0.943*	0.917*	0.959**	0.817	1.00	-	-	-
Sig. (2-tailed)	0.087	0.042	0.157	0.016	0.028	0.010	0.091	-	-	-	-
NH_3 (mg/L)											
P. correlation	0.641	0.971**	0.806	0.969**	0.981**	0.985**	0.945*	0.917*	1.00	-	-
Sig. (2-tailed)	0.244	0.006	0.099	0.007	0.003	0.002	0.015	0.028	-	-	-
NO_3^- (mg/L)											
P. correlation	0.886*	0.764	0.613	0.846	0.799	0.864	0.665	0.970**	0.796	1.00	-
Sig. (2-tailed)	0.045	0.133	0.272	0.071	0.105	0.059	0.221	0.006	0.107	-	-
Escherichia coli (colonies/100 mL)											
P. correlation	0.117	0.911*	0.928*	0.847	0.880*	0.816	0.961**	0.627	0.829	0.440	1.00
Sig. (2-tailed)	0.851	0.032	0.023	0.070	0.049	0.092	0.009	0.257	0.082	0.459	-

Notes: *Significant correlation at the 0.05 level (2-tailed). **Significant correlation at the 0.01 level (2-tailed). High values (>0.5) are indicated in bold.

Abbreviations: Cl^-: Chloride; CO_2: Carbon dioxide; NH_3: Ammonia; NO_3^-: Nitrate; PO_4^{3-}: Phosphate; P. correlation: Pearson correlation; Sig.: Significance; TDS: Total dissolved solids.

doi: 10.36922/AJWEP025120083

indicator, and its correlation with Cl^- suggests sewage leakage or wastewater infiltration into groundwater.[87,89] Therefore, while Cl^- is not a direct contaminant, its association with *E. coli* implies co-contamination from organic waste. PO_4^{3-} and NO_3^- showed a very strong positive correlation, significant at the 0.01 level (r = 0.970), indicating that both nutrients often originate from similar sources (e.g., agricultural runoff or wastewater). Furthermore, pH and NO_3^- displayed a moderate positive correlation, significant at the 0.05 level (r = 0.886, p=0.045), implying that higher NO_3^- levels may be associated with higher pH, possibly due to the presence of alkaline substances or their effect on the buffering capacity of water. Free CO_2 demonstrated a strong correlation with NH_3 (r = 0.985, p=0.002), suggesting that NH_3 levels may be influenced by CO_2 levels, likely through pH shifts affecting the NH_4^+/NH_3 equilibrium. Free CO_2 also showed a strong positive correlation with Cl^- (r = 0.944, p=0.016), possibly indicating a shared source, such as industrial pollution or waste discharge. A strong correlation was also found between Cl^- and NH_3 (r = 0.945, p=0.015), suggesting a link between Cl^- and NH_3 levels, potentially from human or animal waste or fertilizer application. Similarly, TDS and *E. Coli* showed a strong positive correlation (r = 0.928, p=0.023), indicating that high levels of dissolved solids are associated with microbial contamination, likely due to the presence of organic matter. Meanwhile, TH and E. *coli* demonstrated a moderate correlation (r = 0.847, p=0.070), suggesting a potential link between water hardness and bacterial presence. Some parameters exhibited low correlation (r < 0.5), indicating minimal or no relationship—for example, pH and E. *coli* (r = 0.117, p=0.851), suggesting no direct link between pH and microbial contamination. Similarly, pH and PO_4^{3-} (r = 0.823, p=0.087) demonstrated a moderate but not statistically significant correlation. Similarly, NO_3^- and *E. Coli* showed a weak correlation (r = 0.440, p=0.459), suggesting that NO_3^- levels alone do not significantly influence the presence of *E. coli*.

Conductivity was highly correlated with nearly all other parameters, especially TH, total alkalinity, free CO_2, and Cl^-, indicating that dissolved minerals significantly influence water chemistry. This suggests that conductivity is a good indicator of overall water quality, as it reflects the concentration of dissolved ions. TH and total alkalinity are almost perfectly correlated, reinforcing the idea that they are influenced by similar factors (e.g., dissolved CO_3^{2-} and HCO_3^-). *E. coli* showed strong positive correlations with Cl^- and conductivity, indicating contamination likely linked to human, animal, or industrial waste, as both are associated with sewage inputs. Importantly, no strongly negative correlations were observed in the dataset. The findings align with previously reported statistical evaluations of groundwater quality in the literature.[2,54,66,85,88,89,96,115,117-119,121,122]

There was a strong and favorable correlation between F^- and sulfate, as reported by Dobaradaran *et al.*[123] However, a negative correlation between NO_3^- and pH and sulfate was observed. Memon *et al*.[66] also computed correlation coefficients among various parameters, showing less significant correlations between them. A linear regression equation was developed to predict the concentration of elements influencing water quality. There was a very strong positive correlation, ranging between 1% and 5%, across many parameters. The results for sulfate (0.994), Cl^- (0.988), and TH (0.969) were deemed significant using the conventional significance criterion (0.05). However, there were no appreciable changes in overall water quality.[66] Mumtaz *et al.*[54] collected groundwater samples to determine the WQI and measured the levels of water quality parameters that exceeded standard limits. As these districts do not meet APHA standards, they are considered unfit for human consumption according to the WQI scale. However, neither arsenic nor total suspended solids were detected in any of the samples.[54] To assess the present state of groundwater quality, Ashfaq and Ahmad[70] also evaluated groundwater characteristics in Agra city, including pH, Cl^-, turbidity, TDS, TH, and alkalinity. As a result, the correlation and regression analyses by identifying the most influential variables and measuring the strength and direction of their linear relationships helped simplify and better interpret the complexity of groundwater quality variations. The statistical study revealed a substantial positive association between conductivity and TDS, alkalinity, hardness, free CO_2, NH_3, and PO_4^{3-}. There was a modest correlation between TH and PO_4^{3-}, and a strong positive correlation between TH and total alkalinity, CO_2, and NH_3. Regression analysis using a first-degree linear equation further validated the correlations among the aforementioned water quality metrics.

In 2024, Das *et al.*[113] carried out more sophisticated research by examining and monitoring groundwater pollution in coastal areas using state-of-the-art technologies, including PCA and factor analysis (FA), multiple linear regression (MLR), and the ground-WQI (GWQI). By using these advanced methods over conventional approaches, complicated analytical tasks

were further simplified.[113] Eight groundwater quality parameters were evaluated in this study. PCA/FA identified three principal components that explained nearly 81% of the total variation. Based on GWQI results, approximately 13% of the samples were categorized as "awful" to "extremely poor," while 87% were classified as "good." A model incorporating turbidity, iron, electrical conductivity, manganese, TH, and Cl^- as independent variables was proposed as a more realistic predictor of GWQI, based on the MLR analysis. Furthermore, our MLR model demonstrated that turbidity, with the highest beta coefficient (0.820), was the most substantial contributor to groundwater quality in the affected area.

3.3.5. Regression analysis

A simple linear regression analysis was conducted using SPSS software, with temperature as the dependent variable and the other components as independent variables. Among all the parameters considered, the effects of total alkalinity, conductivity, TDS, PO_4^{3-}, and TH were found to be significant at the standard significance level (0.05). However, these parameters failed to sufficiently explain fluctuations in the dependent variable, as evidenced by the adjusted r^2 values, which were observed to be moderate to very low in many cases. The correlations between these parameter pairs are graphically displayed in the regression charts below (Figure 16). The r^2 value provides information on the goodness of fit, with values closer to 1 denoting a better fit, while the slope indicates the direction and strength of the relationship.

3.3.5.1. Conductivity versus total dissolved solids

The regression line equation: y = 0.633x + 0.394 (maximum deviation = 0.103, r^2 = 0.880) was obtained by plotting conductivity against TDS, as shown in Figure 16. The regression analysis revealed a strong, statistically significant, positive linear relationship, as indicated by the high r^2 value (0.880). This equation suggests that for every unit increase in TDS, conductivity increases by 0.633 units. This relationship is consistent with the expected behavior, as TDS represents the total concentration of dissolved ions in water, and conductivity measures the water's ability to conduct electricity,[82-85] which is directly influenced by the presence of those ions. The small maximum deviation (0.103) further confirms the robustness of the regression model in predicting conductivity based on TDS.

3.3.5.2. Conductivity versus TH

The regression line equation for the conductivity versus TH regression plot in Figure S1 is y = 0.762x + 0.226 (maximum deviation = 0.107, r^2 = 0.925). This high r^2 value indicates an extremely strong positive linear association. Thus, it can be concluded that there is a strong correlation between conductivity and TH. The equation suggests that for every unit increase in TH, conductivity increases by 0.762 units. This relationship is consistent with the expected behavior, as higher TH, typically due to dissolved ions, such as Ca^{2+} and Mg^{2+}, leads to increased conductivity. The small maximum deviation (0.107) further confirms the robustness of the regression model in predicting conductivity based on TH.

3.3.5.3. TH versus total dissolved solids

The regression line equation for the TH versus TDS plot in Figure S2 is y = 0.447x + 0.555 (maximum deviation = 0.320, r^2 = 0.700). This value indicates a strong and statistically significant positive linear relationship. The equation implies that for every unit increase in TH, TDS increases by 0.447 units. This relationship is expected, as TH, primarily caused by dissolved Ca^{2+} and Mg^{2+}, contributes to the overall TDS in water. The maximum deviation of 0.320 indicates that while the regression model provides a reasonable fit to the data, other factors may also influence TDS.

3.3.5.4. TH versus free carbon dioxide

The regression line equation y = 1.09x − 0.0849 (maximum deviation = 0.0931, r^2 = 0.942) was obtained by plotting TH against free CO_2, as shown in Figure S3. The regression analysis revealed a strong positive linear relationship, as indicated by the high coefficient of determination (r^2 = 0.942). This equation suggests that for every unit increase in free CO_2, TH increases by 1.09 units. This relationship is consistent with the expected behavior, as free CO_2 in water can react with carbonate minerals (e.g., calcium carbonate) to form HCO_3^-, which contributes to TH. The small maximum deviation (0.0931) further confirms the robustness of the regression model in predicting TH based on free CO_2.

3.3.5.5. TH versus ammonia

The regression line equation y = 0.995x + 0.0231 (maximum deviation = 0.115, r^2 = 0.905) was obtained by plotting TH against NH_3, as depicted in Figure S4. The regression analysis revealed a strong positive linear relationship, indicated by the high r^2 value (0.905). This equation suggests that for every unit increase in NH_3, TH increases by 0.995 units. This relationship may

be attributed to the interaction of NH_3 with minerals in the water (such as calcium and magnesium) or its influence on the solubility of carbonate minerals, which contribute to TH. The small maximum deviation (0.115) further confirms the robustness of the regression model.

3.3.5.6. TH versus total alkalinity

The regression line equation y = 1.10x − 0.0963 (maximum deviation = 0.0440, r^2 = 0.974) was obtained by plotting TH against total alkalinity, as shown in Figure S5. The high r^2 value (0.974) indicates a very strong positive relationship. Moreover, this r^2 value is higher than for TH versus NH_3 (0.905), free CO_2 (0.942), conductivity (0.925), and TDS (0.700), suggesting that total alkalinity is the strongest predictor of TH among the variables analyzed. This difference may be due to the direct relationship between total alkalinity and the carbonate minerals that contribute to TH.

3.3.5.7. Total alkalinity versus chloride

The regression line equation y = 0.664x + 0.331 (maximum deviation = 0.196, r^2 = 0.902) was obtained by plotting total alkalinity against Cl^-, as shown in Figure S6. The r^2 value of 0.902 indicates a strong positive linear relationship. This equation implies that for every unit increase in Cl^- concentration, total alkalinity increases by 0.664 units. This relationship may be attributed to the coexistence of Cl^- ions with other ions (such as sodium, Ca^{2+}, or Mg^{2+}) that contribute to alkalinity, or it may reflect indirect geochemical processes linking Cl^- and alkalinity. The relatively small maximum deviation (0.196) further supports the reliability of the regression model in predicting total alkalinity based on Cl^- concentration.

3.3.5.8. Total alkalinity versus ammonia

The regression line equation y = 1.11x − 0.0804 (maximum deviation = 0.0909, r^2 = 0.899) was obtained by plotting total alkalinity against NH_3, as shown in Figure S7. The regression analysis revealed a strong positive linear relationship, as indicated by the high coefficient of determination (r^2 = 0.899). This equation suggests that for every unit increase in NH_3 concentration, total alkalinity increases by 1.11 units. This relationship may be attributed to the reaction of NH_3 with water to form NH_4^+, which can influence the buffering capacity of water and contribute to alkalinity. In addition, NH_3 may coexist with other ions (such as CO_3^{2-} or HCO_3^-) that directly contribute to alkalinity. The small maximum deviation (0.0909) further confirms the robustness of the regression model in predicting total alkalinity based on NH_3 concentration.

3.3.5.9. Conductivity versus total alkalinity

The regression line equation y = 0.876x + 0.119 (maximum deviation = 0.0370, r^2 = 0.983) was obtained by plotting conductivity against total alkalinity, as depicted in Figure S8. The regression analysis revealed a very strong positive linear relationship, as indicated by the high coefficient of determination (r^2 = 0.983). This equation suggests that for every unit increase in total alkalinity, conductivity increases by 0.876 units. This relationship is consistent with the expected behavior, as total alkalinity is primarily influenced by CO_3^{2-} and HCO_3^-, which are conductive and contribute to the overall ion concentration in water. The very small maximum deviation (0.0370) further confirms the robustness of the regression model.

The r^2 value for total alkalinity versus conductivity (0.983) is higher than those for total alkalinity versus Cl^- (0.902), NH_3 (0.899), and TH (0.974). This suggests that total alkalinity is the strongest predictor of conductivity among the variables analyzed.

3.3.5.10. Free carbon dioxide versus ammonia

The regression line equation y = 0.906x + 0.103 (maximum deviation = 0.0898, r^2 = 0.951) was obtained by plotting free CO_2 against NH_3, as depicted in Figure S9. The regression analysis revealed a very strong positive linear relationship, as indicated by the high value of r^2 (0.951). This equation suggests that for every unit increase in NH_3 concentration, free CO_2 increases by 0.906 units. This relationship may be attributed to the reaction of NH_3 with water to form NH_4^+ and hydroxide ions, which can influence the equilibrium of CO_2 in water and shift it toward the formation of more free CO_2. The small maximum deviation (0.0898) further supports the robustness of the regression model.

3.3.5.11. Escherichia coli versus total dissolved solids

The regression line equation y = 1.18xm − 0.187 (maximum deviation = 0.280, r^2 = 0.953) was obtained by plotting *E. coli* against TDS, as shown in Figure S10. The regression analysis revealed a very strong positive linear relationship, indicated by the high r^2 value. This equation suggests that for every unit increase in TDS, *E. coli* concentration increases by 1.18 units. This relationship may be attributed to the fact that higher TDS levels often indicate the presence of organic matter, nutrients, or other dissolved substances that support the growth and survival of *E. coli* and other

bacteria. The relatively small maximum deviation (0.280) further confirms the robustness of the regression model in predicting *E. coli* concentration based on TDS.

4. Limitations

Groundwater samples for this investigation were collected only from the Gondrang area of Bharatpur Metropolitan City, specifically Wards no. 8 and 9 of Chitwan. Only a limited number of parameters were analyzed, namely, pH, temperature, electrical conductivity, free chlorine, alkalinity, hardness, PO_4^{3-}, NO_3^-, Cl^- ions, TDS, and NH_3. In addition, the study was confined to the pre-monsoon season.

5. Recommendations

Based on the findings of this study, the following recommendations are proposed to improve groundwater quality and mitigate associated health risks:

(i) To address groundwater quality issues near industrial areas, it is crucial to implement strict regulations on industrial discharges and to establish routine groundwater monitoring and assessment programs.

(ii) To ensure that water quality remains within safe limits, regular monitoring of residential areas adjacent to industrial sites should be implemented, focusing on parameters, such as TDS, hardness, NO_3^-, and *E. coli*.

(iii) To ensure safe drinking water quality for local communities, it is essential to promote groundwater treatment methods, such as activated carbon filtration, membrane-based techniques, such as reverse osmosis for removing particulate matter and contaminants, and disinfection techniques, such as chlorination, ultraviolet treatment, or ozonation. Additional methods, including coagulation-flocculation or chemical precipitation, should also be considered where appropriate.

(iv) To identify potential sources of contamination and their impacts on human health and the environment, detailed investigations (including multi-seasonal data) should be conducted. These investigations can involve comprehensive assessments of additional water quality parameters, particularly heavy metals (e.g., Pb, Cd, As), and larger sample sizes. Such studies will support the development of more precise and targeted water management strategies.

6. Conclusion

Findings from the present investigation revealed that all tested parameters, except NO_3^-, PO_4^{3-}, NH_3, free CO_2, and *E. coli*, complied with NDWQS and WHO standards. The WQI values ranged from 560 to 663, indicating that the groundwater is unsuitable for drinking purposes. This poor rating is primarily attributed to elevated concentrations of NH_3, free CO_2, and PO_4^{3-}, suggesting significant groundwater contamination. Elevated levels of TDS and hardness reflect substantial mineral content, likely resulting from nearby industrial activities, such as iron processing. Increased Cl^- and PO_4^{3-} levels further suggest contributions from industrial processes and discharges, which may have harmful effects on human health. The presence of *E. coli* in the samples indicates microbial contamination, potentially arising from inadequate waste disposal or sanitation practices associated with industrial activities in the studied area, contributing to various waterborne diseases. Elevated concentrations of pollutants were detected, including NH_3 (7–19.5 mg/L), PO_4^{3-} (4.3–9.8 mg/L), and free CO_2. In addition, increased NO_3^- levels and the presence of *E. coli* (0–9 colony-forming unit/100 mL) indicated potential health risks.

Descriptive statistics, such as mean, standard deviation, and minimum and maximum values were calculated. In addition, correlation and regression simplified the complexities of variance by highlighting the most significant variables, making data interpretation easier, and quantifying the degree and direction of linear relationships between variables. The statistical analysis indicates the following key findings: Conductivity is strongly positively correlated with TDS (r = 0.924, p=0.025), TH (r = 0.990, p=0.001), total alkalinity (r = 0.997, p=0.000), free CO_2 (r = 0.980, p=0.003), NH_3 (r = 0.971, p=0.006), Cl^- (r = 0.989, p=0.001), PO_4^{3-} (r = 0.891, p=0.042), and *E. coli* (r = 0.911, p=0.032), signifying that higher conductivity is associated with higher values of these parameters. TH showed an almost perfect positive correlation with total alkalinity (r = 0.995, p=0.000), free CO_2 (r = 0.994, p=0.001), and NH_3 (r = 0.969, p=0.007). Total alkalinity also demonstrated a very strong positive correlation with free CO_2 (r = 0.990, p=0.001) and NH_3 (r = 0.981, p=0.003). Moreover, Cl^- and *E. coli* (r = 0.961, p=0.009) were strongly positively correlated. pH and NO_3^- exhibit a moderate positive correlation (r = 0.886, p=0.045). Free CO_2 was strongly correlated with NH_3 (r = 0.985, p=0.002), suggesting that NH_3 is influenced by CO_2 levels, likely through pH shifts affecting NH_4^+/NH_3

equilibrium. Free CO_2 also showed a strong positive correlation with Cl^- (r = 0.944, p=0.016), which may indicate a common source, such as industrial pollution or waste discharge. A strong correlation between Cl^- and NH_3 (r = 0.945, p=0.015) suggests a shared source, potentially from human/animal waste or fertilizers. Similarly, the strong positive correlation between PO_4^{3-} and NO_3^- (r = 0.970, p=0.006) suggests a common origin, such as agricultural runoff or wastewater contamination. Regression analysis using a first-degree linear equation further supported the correlations between many of the aforementioned water quality metrics. These findings provide useful insights for decision-makers in developing mitigation plans to monitor water quality in the studied areas and reduce the health risks associated with contaminated groundwater.

Overall, the findings highlight an urgent need for improved water treatment, continuous monitoring, and stringent pollution control measures to address the adverse effects of industrial activities on groundwater quality and public health.

Acknowledgments

The authors acknowledge the Department of Science, Faculty/Institute of Science and Technology, Saptagandaki Multiple Campus, Tribhuvan University, Chitwan, Nepal, for providing essential chemical support for the experiments. We also extend our thanks to the Department of Chemistry, Faculty/Institute of Science and Technology, Mahendra Morang Adarsh Multiple Campus, Biratnagar, Tribhuvan University, Nepal, for the provision of internet access, which was vital for data analysis.

Funding

None.

Conflict of interest

The authors declare that they have no competing interests.

Author contributions

Conceptualization: Shiv Narayan Yadav, Ajaya Bhattarai
Formal analysis: Dhruba Acharya
Investigation: Shiv Narayan Yadav and Asbin K.C.
Methodology: Asbin K.C., Saugat Rizal
Project administration: Saugat Rizal
Resources: Shishir Tamang
Software: Shishir Tamang
Validation: Rabiraj Subedi
Visualization: Rabiraj Subedi
Writing – original draft: Shiv Narayan Yadav
Writing – review & editing: Ajaya Bhattarai

Availability of data

Data are available from the corresponding author upon reasonable request.

References

1. Oluseyi T, Olayinka K, Adeleke I. Assessment of ground water pollution in the residential areas of Ewekoro and Shagamu due to cement production. *Afr J Environ Sci Technol.* 2011;5:786-794.
2. Boateng TK, Opoku F, Acquaah SO, Akoto O. Groundwater quality assessment using statistical approach and water quality index in Ejisu-Juaben municipality, Ghana. *Environ Earth Sci.* 2016;75:489. doi: 10.1007/s12665-015-5105-0
3. Milanović P, Stevanović Z. Fifty years of history of the karst commission of the international association of hydrogeologists. *Hydrogeol J.* 2021;29:7-19. doi: 10.1007/s10040-020-02261-4
4. Li P, Tian R, Xue C, Wu J. Progress, opportunities, and key fields for groundwater quality research under the impacts of human activities in China with a special focus on Western China. *Environ Sci Pollut Res.* 2017;24:13224-13234. doi: 10.1007/s11356-017-8753-7
5. Kassegne AB, Leta S. Assessment of physicochemical and bacteriological water quality of drinking water in Ankober District, Amhara Region, Ethiopia. *Cogent Environ Sci.* 2020;6:1791461. doi: 10.1080/23311843.2020.1791461
6. Sitaram DU. Study of the physio-chemical parameters for testing water: A review. *World J Adv Res Rev.* 2022;14:570-575. doi: 10.30574/wjarr.2022.14.3.0600
7. Reza R, Singh G. Physico-chemical analysis of ground water in Angul-Talcher region of Orissa, India. *J Am Sci*. 2009;5:53-58.
8. Harter T. *Groundwater Quality and Groundwater Pollution*. California: University of California, Agriculture and Natural Resources; 2003. doi: 10.3733/ucanr.8084
9. Qureshi SS, Channa A, Memon SA, *et al*. Assessment of physicochemical characteristics in groundwater quality parameters. *Environ Technol Innov.* 2021;24:101877. doi: 10.1016/j.eti.2021.101877

10. Daud MK, Nafees M, Ali S, *et al*. Drinking water quality status and contamination in Pakistan. *Biomed Res Int.* 2017;2017:7908183. doi: 10.1155/2017/7908183
11. Haile Reda A. Physico-chemical analysis of drinking water quality of Arbaminch Town. *J Environ Anal Toxicol.* 2016;6:2. doi: 10.4172/2161-0525.1000356
12. Ottong DJ, Ekanem JO. Physicochemical and heavy metals analysis of Udo Awankwo River in Ikot Ekpene, South-South, Nigeria. *World J Adv Res Rev.* 2021;10:392-398. doi: 10.30574/wjarr.2021.10.3.0282
13. Li P. To make the water safer. *Expo Health*. 2020;12:337-342. doi: 10.1007/s12403-020-00370-9
14. Li P, Wu J. Sustainable living with risks: Meeting the challenges. *Hum Ecol Risk Assess.* 2019;25:1-10. doi: 10.1080/10807039.2019.1584030
15. Subba Rao N, Ravindra B, Wu J. Geochemical and health risk evaluation of fluoride rich groundwater in Sattenapalle Region, Guntur District, Andhra Pradesh, India. *Hum Ecol Risk Assess.* 2020;26:2316-2348. doi: 10.1080/10807039.2020.1741338
16. He X, Li P, Wu J, Wei M, Ren X, Wang D. Poor groundwater quality and high potential health risks in the Datong Basin, Northern China: Research from Published Data. *Environ Geochem Health*. 2021;43:791-812. doi: 10.1007/s10653-020-00520-7
17. Chakraborti D, Rahman MM, Mukherjee A, *et al*. Groundwater arsenic contamination in Bangladesh-21 years of research. *J Trace Elem Med Biol*. 2015;31:237-248. doi: 10.1016/j.jtemb.2015.01.003
18. He X, Li P, Ji Y, Wang Y, Su Z, Elumalai V. Groundwater arsenic and fluoride and associated arsenicosis and fluorosis in China: Occurrence, distribution and management. *Expo Health.* 2020;12:355-368. doi: 10.1007/s12403-020-00347-8
19. Wang D, Wu J, Wang Y, Ji Y. Finding high-quality groundwater resources to reduce the hydatidosis incidence in the Shiqu County of Sichuan Province, China: Analysis, assessment, and management. *Expo Health*. 2020;12:307-322. doi: 10.1007/s12403-019-00314-y
20. Su Z, Wu J, He X, Elumalai V. Temporal changes of groundwater quality within the groundwater depression cone and prediction of confined groundwater salinity using grey Markov model in Yinchuan Area of Northwest China. *Expo Health*. 2020;12:447-468. doi: 10.1007/s12403-020-00355-8
21. Tatti F, Petrangeli Papini M, Torretta V, Mancini G, Boni MR, Viotti P. Experimental and numerical evaluation of groundwater circulation wells as a remediation technology for persistent, low permeability contaminant source zones. *J Contam Hydrol.* 2019;222:89-100. doi: 10.1016/j.jconhyd.2019.03.001
22. Elumalai V, Nethononda VG, Manivannan V, Rajmohan N, Li P, Elango L. Groundwater quality assessment and application of multivariate statistical analysis in Luvuvhu Catchment, Limpopo, South Africa. *J Afr Earth Sci*. 2020;171:103967. doi: 10.1016/j.jafrearsci.2020.103967
23. Hashim MA, Mukhopadhyay S, Sahu JN, Sengupta B. Remediation technologies for heavy metal contaminated groundwater. *J Environ Manage.* 2011;92:2355-2388. doi: 10.1016/j.jenvman.2011.06.009
24. He X, Li P. Surface water pollution in the middle Chinese loess plateau with special focus on hexavalent chromium (Cr6+): Occurrence, sources and health risks. *Expo Health.* 2020;12:385-401. doi: 10.1007/s12403-020-00344-x
25. Abbas G, Murtaza B, Bibi I, *et al*. Arsenic uptake, toxicity, detoxification, and speciation in plants: Physiological, biochemical, and molecular aspects. *Int J Environ Res Public Health*. 2018;15:29. doi: 10.3390/ijerph15010059
26. Rebelo FM, Caldas ED. Arsenic, lead, mercury and cadmium: Toxicity, levels in breast milk and the risks for breastfed infants. *Environ Res.* 2016;151:671-688. doi: 10.1016/j.envres.2016.08.027
27. Lesser LE, Mora A, Moreau C, *et al*. Survey of 218 organic contaminants in groundwater derived from the world's largest untreated wastewater irrigation system: Mezquital valley, Mexico. *Chemosphere*. 2018;198:510-521. doi: 10.1016/j.chemosphere.2018.01.154
28. Sorensen JPR, Lapworth DJ, Nkhuwa DCW, *et al*. Emerging contaminants in urban groundwater sources in Africa. *Water Res*. 2015;72:51-63. doi: 10.1016/j.watres.2014.08.002
29. Lapworth DJ, Baran N, Stuart ME, Manamsa K, Talbot J. Persistent and emerging micro-organic contaminants in chalk groundwater of England and France. *Environ Pollut.* 2015;203:214-225. doi: 10.1016/j.envpol.2015.02.030
30. Schulze S, Zahn D, Montes R, *et al*. Occurrence of emerging persistent and mobile organic contaminants in European water samples. *Water Res.* 2019;153:80-90. doi: 10.1016/j.watres.2019.01.008
31. Wu J, Zhang Y, Zhou H. Groundwater chemistry and groundwater quality index incorporating health risk weighting in Dingbian County, Ordos Basin of Northwest China. *Chem Erde*. 2020;80:125607. doi: 10.1016/j.chemer.2020.125607
32. Jenifer MA, Jha MK. Comprehensive risk assessment of groundwater contamination in a weathered hard-rock aquifer system of India. *J Clean Prod*. 2018;201:853-868. doi: 10.1016/j.jclepro.2018.08.005

33. Jha MK, Shekhar A, Jenifer MA. Assessing groundwater quality for drinking water supply using hybrid fuzzy-GIS-based water quality index. *Water Res.* 2020;179:115867. doi: 10.1016/j.watres.2020.115867
34. Yuan Y, Xiang M, Liu C, Theng BKG. Chronic impact of an accidental wastewater spill from a smelter, China: A study of health risk of heavy metal (Loid)s via vegetable intake. *Ecotoxicol Environ Saf.* 2019;182:109401. doi: 10.1016/j.ecoenv.2019.109401
35. Njuguna SM, Makokha VA, Yan X, Gituru RW, Wang Q, Wang J. Health risk assessment by consumption of vegetables irrigated with reclaimed waste water: A case study in Thika (Kenya). *J Environ Manage*. 2019;231:576-581. doi: 10.1016/j.jenvman.2018.10.088
36. Wu J, Li P, Qian H, Fang Y. Assessment of soil salinization based on a low-cost method and its influencing factors in a semi-arid agricultural area, Northwest China. *Environ Earth Sci*. 2014;71:3465-3475. doi: 10.1007/s12665-013-2736-x
37. Schillinger J, Özerol G, Güven-Griemert Ş, Heldeweg M. Water in war: Understanding the impacts of armed conflict on water resources and their management. *Wiley Interdiscipl Rev Water* 2020;7:e1480. doi: 10.1002/wat2.1480
38. Çiner F, Sunkari ED, Şenbaş BA. Geochemical and multivariate statistical evaluation of trace elements in groundwater of Niğde Municipality, South-Central Turkey: Implications for arsenic contamination and human health risks assessment. *Arch Environ Contam Toxicol*. 2021;80:164-182. doi: 10.1007/s00244-020-00759-2
39. Yadav IC, Devi NL, Mohan D, Shihua Q, Singh S. Assessment of groundwater quality with special reference to arsenic in Nawalparasi District, Nepal using multivariate statistical techniques. *Environ Earth Sci.* 2014;72:259-273. doi: 10.1007/s12665-013-2952-4
40. Raja V, Lakshmi RV, Sekar CP, Chidambaram S, Neelakantan MA. Health risk assessment of heavy metals in groundwater of industrial Township Virudhunagar, Tamil Nadu, India. *Arch Environ Contam Toxicol*. 2021;80:144-163. doi: 10.1007/s00244-020-00795-y
41. Tiwari AK, Singh AK. Hydrogeochemical investigation and groundwater quality assessment of Pratapgarh District, Uttar Pradesh. *J Geol Soc India*. 2014;83:329-343. doi: 10.1007/s12594-014-0045-y
42. Ali S, Verma S, Agarwal MB, *et al*. Groundwater quality assessment using water quality index and principal component analysis in the Achnera Block, Agra District, Uttar Pradesh, Northern India. *Sci Rep.* 2024;14:5381. doi: 10.1038/s41598-024-56056-8
43. Mahato S, Mahato A, Karna PK, Balmiki N. Investigating aquifer contamination and groundwater quality in Eastern Terai Region of Nepal. *BMC Res Notes*. 2018;11:321. doi: 10.1186/s13104-018-3445-z
44. National Drinking Quality Standards and Directives (NDWQS). Implementation directives for national drinking water quality standards. Government of Nepal, Ministry of Physical Planning and Works, Kathmandu. *Tribhuvan Univ J Microbiol.* 2023;5:83-88.
45. Andermann C, Longuevergne L, Bonnet S, Crave A, Davy P, Gloaguen R. Impact of transient groundwater storage on the discharge of Himalayan rivers. *Nat Geosci*. 2012;5:127-132. doi: 10.1038/ngeo1356
46. Mukherjee A, Fryar AE, Shea BMO. Major Occurrences of Elevated Arsenic. Vol. 6. United States: John Wiley & Sons, Ltd. Inc.; 2008. p. 1-47. doi: 10.1002/9780470741122.ch6
47. Diwakar J, Johnston SG, Burton ED, Shrestha S. Das arsenic mobilization in an alluvial aquifer of the Terai Region, Nepal. *J Hydrol Reg Stud*. 2015;4:59-79. doi: 10.1016/j.ejrh.2014.10.001
48. WHO. *Guidelines for Drinking-Water Quality: Fourth Edition Incorporating the First and Second Addenda.* Geneva: World Health Organization; 2022.
49. Shrestha S, Bista S, Byanjankar N, Shrestha S, Joshi DR, Prasai Joshi T. Groundwater quality evaluation for drinking purpose using water quality index in Kathmandu Valley, Nepal. *Water Sci*. 2023;37:239-250. doi: 10.1080/23570008.2023.2237278
50. Ghimire M, Regmi T, Kayastha SP, Bhuiyan C. Groundwater quality and community health risk in Lalitpur Metropolitan City, Nepal-a geospatial analysis. *Geocarto Int.* 2023;38:2168069. doi: 10.1080/10106049.2023.2168069
51. Sarkar B, Mitchell E, Frisbie S, Grigg L, Adhikari S, Maskey Byanju R. Drinking water quality and public health in the Kathmandu Valley, Nepal: Coliform bacteria, chemical contaminants, and health status of consumers. *J Environ Public Health*. 2022;2022:3895859. doi: 10.1155/2022/3895859
52. Trivedy RK, Goel PK. Chemical and biological methods for water pollution studies, Karad (India): Environmental publications. *J Raman Spectrosc*. 1986;6:10. doi: 10.1128/jcm.34.12.2914-2920.1996
53. Wagner B. Resolution submitted to APHA protecting children from overexposure to lead in candy and protecting children by lowering the blood lead "level of concern" standard. *J Nevada*. 2005;1:8-13.
54. Mumtaz M, Jahanzaib SH, Khan S, Ismail S, Hussain W, Khan FA. Implementation of water quality index for measuring groundwater quality. *Migr Lett.* 2024;21:273-287. doi: 10.59670/ml.v21is11.10691
55. Hasan AA, Al-Obaidi I, Abed ZM. Using lime to remove chromium from tannery factory industrial wastewater in

Baghdad. *J Eng Sustain Dev.* 2025;29:120-126.
doi: 10.31272/jeasd.1220

56. Xu Z. *Dissolved Oxygen Dynamics and Modeling - a Case Study in a Subtropical Shallow Lake*. Vol. 22. Netherlands: Elsevier Sci. Ltd.; 2014. p. 114.
57. Sayato Y. WHO guidelines for drinking-water quality. *Eisei Kagaku*. 2022;35:307-312.
doi: 10.1248/jhs1956.35.307
58. Khatri N, Tyagi S, Rawtani D, Tharmavaram M, Kamboj RD. Analysis and assessment of ground water quality in Satlasana Taluka, Mehsana District, Gujarat, India through Application of Water Quality Indices. *Groundw Sustain Dev.* 2020;10:100321.
doi: 10.1016/j.gsd.2019.100321
59. Das BD, Mishra RK, Choudhary SK. Groundwater quality in Biratnagr of Morang District, Nepal. *Int J Res GRANTHAALAYAH*. 2021;9:368-377.
doi: 10.29121/granthaalayah.v9.i5.2021.3961
60. Das BD, Choudhary SK. Application of water quality index (WQI) for groundwater quality assessment of Biratnagar, Nepal. *Our Nat.* 2021;19:54-61.
doi: 10.3126/on.v19i1.41260
61. Pant BR. Ground water quality in the Kathmandu valley of Nepal. *Environ Monit Assess.* 2011;178:477-485.
doi: 10.1007/s10661-010-1706-y
62. Oinam JD, Ramanathan AL, Singh G. Geochemical and statistical evaluation of groundwater in Imphal and Thoubal District of Manipur, India. *J Asian Earth Sci.* 2012;48:136-149.
doi: 10.1016/j.jseaes.2011.11.017
63. Verma A, Pandey G. Study of some physico-chemical parameters of groundwater in Gorakhpur District. *Int J Eng Res Technol*. 2013;2:2967-2973.
64. Budhathoki R. *Analysis of the Physico-Chemical and Bacteriological Parameters of Bottled Water Available in Kathmandu Valley a Case Study on the Partial Fulfillment of the Requirements for M. Sc., First Year, Environment Science, T. U.; M.Sc. Thesis, Central Department of Microbiology*, TU; 2010. p. 1-36.
65. Paudyal R, Kang S, Sharma CM, Tripathee L, Sillanpaä M. Variations of the physicochemical parameters and metal levels and their risk assessment in urbanized Bagmati River, Kathmandu, Nepal. *J Chem*. 2016;2016:6025905.
doi: 10.1155/2016/6025905
66. Memon YI, Qureshi SS, Kandhar IA, *et al*. Statistical analysis and physicochemical characteristics of groundwater quality parameters: A case study. *Int J Environ Anal Chem.* 2023;103:2270-2291.
doi: 10.1080/03067319.2021.1890064
67. Laghari AN, Siyal ZA, Bangwar DK, Soomro MA, Walasai G, Shaikh FA. Groundwater quality analysis for human consumption. *Technol Appl Sci Res.* 2018;8:2616-2620.
68. Walter N. A review of the principles of turbidity measurement. *Prog Phys Geography Br J Haematol*. 2009;8:2616-2622.
doi: 10.1177/0309133317726540
69. García-Ávila F, Zhindón-Arévalo C, Valdiviezo-Gonzales L, Cadme-Galabay M, Gutiérrez-Ortega H, del Pino LF. A comparative study of water quality using two quality indices and a risk index in a drinking water distribution network. *Environ Technol Rev.* 2022;11:49-61.
doi: 10.1080/21622515.2021.2013955
70. Ashfaq A, Ahmad F. Study on assessment of underground water quality. *Int J Curr Microbiol Appl Sci*. 2014;3:612-616.
71. Khadka D, Khanal G. Assessment of physicochemical parameters of drinking water in the schools of Bagnashkali, Palpa, Nepal. *Tribhuvan J.* 2023;2:1-10.
doi: 10.3126/tribj.v2i1.60215
72. Wang BB. Research on drinking water purification technologies for household use by reducing total dissolved solids (TDS). *PLoS One*. 2021;16:e0257865.
doi: 10.1371/journal.pone.0257865
73. Wood WW. *Guidelines for Collection and Field Analysis of Groundwater Samples for Selected Unstable Constituents. Techniques of Water-resources Investigations of the United States Geological Survey*. Vol. 1. Reston, VA: U.S. Geological Survey; 1981. p. D2-11.
74. Brown RM, McClelland NI, Deininger RA, O'Connor MF. A water quality index - crashing the psychological barrier. *Indic Environ Qual.* 1972;6:173-182.
doi: 10.1007/978-1-4684-2856-8_15
75. Tirkey P, Bhattacharya T, Chakraborty S. Water quality indices- important tools for water quality assessment. *Int J Adv Chem*. 2013;1:15-28.
76. Ram A, Tiwari SK, Pandey HK, Chaurasia AK, Singh S, Singh YV. Groundwater quality assessment using water quality index (WQI) under GIS framework. *Appl Water Sci.* 2021;11:46.
doi: 10.1007/s13201-021-01376-7
77. Prest EI, Hammes F, van Loosdrecht MCM, Vrouwenvelder JS. Biological stability of drinking water: Controlling factors, methods, and challenges. *Front Microbiol.* 2016;7:1-24.
doi: 10.3389/fmicb.2016.00045
78. Riffat R, Husnain T. *Fundamentals of Wastewater Treatment and Engineering*. 2nd ed. London: Taylor & Francis; 2022.
79. Li P, Karunanidhi D, Subramani T, Srinivasamoorthy K. Sources and consequences of groundwater contamination. *Arch Environ Contam Toxicol.* 2021;80:1-10.
doi: 10.1007/s00244-020-00805-z
80. Mohammadi AA, Morovati M, Najafi Saleh H, *et al*. Groundwater quality evaluation for drinking and industrial purposes. A case study in Northeastern Iran. *Int J Environ Anal Chem.* 2022;102:6094-6104.
doi: 10.1080/03067319.2020.1807533

81. Narayan S, Rai S, Behera M, Ranjan A. Dynamic assembly and stabilization of surfactant-dye-polyelectrolyte complexes: An overview. *J Mol Liq.* 2025;421:126897. doi: 10.1016/j.molliq.2025.126897
82. Yadav SN, Rai S, Sinha B, Bhattarai A. Influence of polyelectrolyte (NaCMC) on surfactant (DTAB) in the absence and presence of methyl orange dye in ethanol - water mixed solvent at three different temperatures. *ChemistrySelect*. 2024;9:202404772. doi: 10.1002/slct.202404772
83. Narayan S, Rai S, Bhattarai A, Sinha B. Impact of sodium polystyrene sulfonate on micellization behaviour of Cetyltrimethylammonium bromide in the presence of methyl red in ethanol - water mixture: A conductometric investigation. *J Mol Liq.* 2024;399:124387. doi: 10.1016/j.molliq.2024.124387
84. Narayan S, Rai S, Shah P, Roy N, Bhattarai A. Spectrophotometric and conductometric studies on the interaction of surfactant with polyelectrolyte in the presence of dye in aqueous medium spectrophotometric and conductometric studies on the interaction of surfactant with polyelectrolyte in the presence. *J Mol Liq.* 2022;355:118949. doi: 10.1016/j.molliq.2022.118949
85. Dohare D, Deshpande S, Kotiya A. Analysis of ground water quality parameters: A review. *Res J Eng Sci*. 2014;3:2278-9472.
86. Devi S, Premkumar R. Physicochemical analysis of groundwater samples near industrial Area, Cuddalore District, Tamil Nadu, India. *Int J ChemTech Res.* 2012;4:29-34.
87. Mengstie YA, Desta WM, Alemayehu E. Assessment of drinking water quality in urban water supply systems: The case of Hawassa City, Ethiopia. *Int J Anal Chem.* 2023;2023:8880601. doi: 10.1155/2023/8880601
88. Susaiappan S, Somanathan A, Sulthan MT, Masilamani IP. Groundwater quality variation and regression analysis a case study around municipal dumpsite in India. *Rev Chim.* 2021;72:133-145. doi: 10.37358/rc.21.1.8410
89. Kothari V, Vij S, Sharma SK, Gupta N. Correlation of various water quality parameters and water quality index of districts of Uttarakhand. *Environ Sustain Indic.* 2021;9:100093. doi: 10.1016/j.indic.2020.100093
90. Porsan ZP, Zarei A, Alimohammadi M. Evaluation of corrosion and scaling potential of drinking groundwater in Gonbad-e Kavus. *Desalin Water Treat.* 2020;195:19-25. doi: 10.5004/dwt.2020.25895
91. Al-Khashman OA, Jaradat AQ. Assessment of groundwater quality and its suitability for drinking and agricultural uses in arid environment. *Stoch Environ Res Risk Assess.* 2014;28:743-753. doi: 10.1007/s00477-013-0787-x
92. Das CR, Das S, Panda S. Groundwater quality monitoring by correlation, regression and hierarchical clustering analyses using WQI and PAST tools. *Groundw Sustain Dev.* 2022;16:100708. doi: 10.1016/j.gsd.2021.100708
93. Alemu CM, Aycheh YF, Angualie GS, Engidayehu SS. Modeling on comprehensive evaluation of groundwater quality status using geographic information system (GIS) and water quality index (WQI): A case study of Bahir Dar City, Amhara, Ethiopia. *Water Pract Technol.* 2024;19:1084-1098. doi: 10.2166/wpt.2024.076
94. Abolli S, Nasab MA, Yaghmaeian K, Alimohammadi M. Determination the effects of physico-chemical parameters on groundwater status by water quality index (WQI). *Desalin Water Treat.* 2022;269:84-92. doi: 10.5004/dwt.2022.28755
95. Ji Y, Wu J, Wang Y, Elumalai V, Subramani T. Seasonal variation of drinking water quality and human health risk assessment in Hancheng City of Guanzhong Plain, China. *Expo Health.* 2020;12:469-485. doi: 10.1007/s12403-020-00357-6
96. Khan MK, Ayoub W, Saied S, *et al*. Statistical and geospatial assessment of groundwater quality in the megacity of Karachi. *J Water Resour Prot.* 2019;11:311-332. doi: 10.4236/jwarp.2019.113018
97. Abbasnejad B, Abbasnejad A, Derakhshani R. Groundwater evaluation of Northern Jazmourian (South Iran) for drinking, agriculture, and associated health risks of nitrate and fluoride contamination. *Hum Ecol Risk Assess.* 2023;29:36-57. doi: 10.1080/10807039.2022.2140028
98. Mohan U, Singh R. Water quality assessment and physicochemical parameters of groundwater in District Hapur, Uttar Pradesh, India. *Environ Conserv J.* 2013;14:143-149.
99. Picetti R, Deeney M, Pastorino S, *et al*. Nitrate and nitrite contamination in drinking water and cancer risk: A systematic review with meta-analysis. *Environ Res.* 2022;210:112988. doi: 10.1016/j.envres.2022.112988
100. Dahiya S, Singh B, Gaur S, Garg VK, Kushwaha HS. Analysis of groundwater quality using fuzzy synthetic evaluation. *J Hazard Mater.* 2007;147:938-946. doi: 10.1016/j.jhazmat.2007.01.119
101. Ding F, Chen L, Sun C, Zhang W, Yue H, Na S. An upgraded groundwater quality evaluation based on hasse diagram technique & game theory. *Ecol Indic.* 2022;140:109024. doi: 10.1016/j.ecolind.2022.109024
102. Subba Rao N. Groundwater quality from a part of Prakasam District, Andhra Pradesh, India. *Appl Water Sci.* 2018;8:1-18. doi: 10.1007/s13201-018-0665-2

103. Thakur JK, Diwakar J, Singh SK. Hydrogeochemical evaluation of groundwater of Bhaktapur Municipality, Nepal. *Environ Earth Sci.* 2015;74:4973-4988. doi: 10.1007/s12665-015-4514-4
104. Hanipha M, Hussain Z. Study of groundwater quality at Dindigul Town, Tamilnadu, India. *Int Res J Environ Sci.* 2019;2:68-73.
105. Pei-Yue L, Hui Q, Jian-Hua W. Groundwater quality assessment based on improved water quality index in Pengyang County, Ningxia, Northwest China. *E-J Chem.* 2010;7:209-216. doi: 10.1155/2010/451304
106. Olaolu TD. Pollution indicators and pathogenic microorganisms in wastewater treatment: Implication on receiving water bodies. *Int J Environ Prot Policy*. 2014;2:205. doi: 10.11648/j.ijepp.20140206.12
107. Yu F, Okamto S, Nakasone K, *et al*. Molecular cloning and functional characterization of α-humulene synthase, a possible key enzyme of Zerumbone biosynthesis in shampoo ginger (Zingiber Zerumbet Smith). *Planta*. 2008;227:1291-1299. doi: 10.1007/s00425-008-0700-x
108. Kar S. Determination of water quality index (WQI) during mass bathing in different Ghats of river ganga in Howrah and North 24 Parganas District, West Bengal, India. *Int J Res Appl Sci Eng Technol.* 2017;887:1097-1104. doi: 10.22214/ijraset.2017.9159
109. Das Kangabam R, Bhoominathan SD, Kanagaraj S, Govindaraju M. Development of a water quality index (WQI) for the Loktak Lake in India. *Appl Water Sci.* 2017;7:2907-2918. doi: 10.1007/s13201-017-0579-4
110. Lumb A, Sharma TC, Bibeault JF. A review of genesis and evolution of water quality index (WQI) and some future directions. *Water Qual Expo Health*. 2011;3:11-24. doi: 10.1007/s12403-011-0040-0
111. Şener Ş, Şener E, Davraz A. Evaluation of water quality using water quality index (WQI) method and GIS in Aksu River (SW-Turkey). *Sci Total Environ*. 2017;584-585:131-144. doi: 10.1016/j.scitotenv.2017.01.102
112. Bora M, Goswami DC. Water quality assessment in terms of water quality index (WQI): Case study of the Kolong River, Assam, India. *Appl Water Sci.* 2017;7:3125-3135. doi: 10.1007/s13201-016-0451-y
113. Das CR, Das S, Panda S. MLR index-based principal component analysis to investigate and monitor probable sources of groundwater pollution and quality in coastal areas: A case study in East India. *Environ Monit Assess.* 2023;195:1158. doi: 10.1007/s10661-023-11804-7
114. Das CR, Das S. Assessment of surface water quality for drinking by combining three water quality indices with their usefulness: Case of Damodar River in India. *Water Air Soil Pollut.* 2023;234:327. doi: 10.1007/s11270-023-06342-4
115. Olasehinde P, Amadi A, Dan-Hassan M, Jimoh M. Statistical assessment of groundwater quality in Ogbomosho, Southwest Nigeria. *Am J Min Metall.* 2015;3:21-28. doi: 10.12691/ajmm-3-1-4
116. Jena V, Sinha D. Physicochemical analysis of ground water of selected areas of Raipur City. *Indian J Sci Res*. 2017;13:61-65.
117. Gulgundi MS, Shetty A. Groundwater quality assessment of Urban Bengaluru using multivariate statistical techniques. *Appl Water Sci.* 2018;8:43. doi: 10.1007/s13201-018-0684-z
118. Singh EJK, Gupta A, Singh NR. Groundwater quality in Imphal West District, Manipur, India, with multivariate statistical analysis of data. *Environ Sci Pollut Res.* 2013;20:2421-2434. doi: 10.1007/s11356-012-1127-2
119. Trabelsi R, Zouari K. Coupled geochemical modeling and multivariate statistical analysis approach for the assessment of groundwater quality in irrigated areas: A study from North Eastern of Tunisia. *Groundw Sustain Dev.* 2019;8:413-427. doi: 10.1016/j.gsd.2019.01.006
120. Singh CK, Shashtri S, Mukherjee S. Integrating multivariate statistical analysis with GIS for geochemical assessment of groundwater quality in Shiwaliks of Punjab, India. *Environ Earth Sci*. 2011;62:1387-1405. doi: 10.1007/s12665-010-0625-0
121. Kim JH, Kim RH, Lee J, Cheong TJ, Yum BW, Chang HW. Multivariate statistical analysis to identify the major factors governing groundwater quality in the coastal area of Kimje, South Korea. *Hydrol Process*. 2005;19:1261-1276. doi: 10.1002/hyp.5565
122. Molekoa MD, Avtar R, Kumar P, Minh HVT, Kurniawan TA. Hydrogeochemical assessment of groundwater quality of Mokopane Area, Limpopo, South Africa using statistical approach. *Water (Switzerland)*. 2019;11:1891. doi: 10.3390/w11091891
123. Dobaradaran S, Mahvi AH, Dehdashti S, Dobaradaran S, Shoara R. Correlation of fluoride with some inorganic constituents in groundwater of Dashtestan, Iran. *Fluoride*. 2009;42:50-53.

Asian Journal of Water, Environment and Pollution. Vol. 22, No. 6 (2025), pp. 170-179.
doi: 10.36922/AJWEP025140101

ORIGINAL RESEARCH ARTICLE

A greenhouse pot experiment assessing the zinc-accumulating behavior of *Lupinus uncinatus* Schldl

Muhammad Ehsan[1,2]*, Vicente Espinosa Hernández[1], Dilawar Hassan[3], Ayesha Sani[3], Francisco Marcelo Lara Viveros[4], Jorge Luis Becerra López[5], Eduardo Baltierra Trejo[6], Rehana Gulzar[7], Nisbat Ali[8], and Shahid Bashir[9]

[1]Department of Soil Science, Postgraduate College of Agricultural Sciences, Montecillos, State of Mexico, Mexico
[2]Centro de Bachillerato Tecnológico Agropecuario No. 162 (Agricultural and Livestock Technology College No. 162), Francisco I. Madero, Tlaxcala, Mexico
[3]Department of Nanotechnology, School of Sciences and Engineering, Tecnológico de Monterrey, Atizapán de Zaragoza, State of Mexico, Mexico
[4]Department of Biosciences and Agrotechnology, Centro de Investigación en Química Aplicada (Center for Research in Applied Chemistry), Saltillo, Coahuila, Mexico
[5]Climate Change and Natural Resources Conservation Laboratory, Ecological Studies Centre, Faculty of Biological Sciences, Universidad Juárez del Estado de Durango, Gomez Palacio, Durango, Mexico
[6]Researchers for Mexico Program, Consejo Nacional de Humanidades, Ciencias y Tecnologías (CONAHCyT – National Council of Humanities, Sciences and Technologies), Mexico City, Mexico
[7]Department of English, Faculty of Languages and Literature, International Islamic University, Islamabad, Pakistan
[8]Department of Management Science, Faculty of Management Sciences, National University of Modern Languages, Islamabad, Pakistan
[9]Department of Marketing, Business School, Tecnológico de Monterrey, Atizapán de Zaragoza, State of Mexico, Mexico
***Corresponding author:** Muhammad Ehsan (Muhammadehsan2000@yahoo.com)

Received: April 3, 2025; Revised: July 6, 2025; Accepted: July 16, 2025; Published online: September 9, 2025

Abstract: A greenhouse pot experiment was conducted to evaluate the zinc (Zn) accumulation potential of *Lupinus uncinatus* Schldl. The effects of varying Zn concentrations on plant dry matter yield, metal tolerance, and Zn accumulation and distribution in roots, stems, and leaves were investigated. Zn was applied as $ZnCl_2$ at rates of, 200, 400, and 600 mg/kg. One-way analysis of variance followed by Tukey's multiple comparison test ($p<0.05$) revealed significant effects of Zn on root dry weight, Zn uptake in roots, stems, and leaves, and the shoot-to-root Zn ratio. Root dry weight was significantly reduced, with the highest Zn treatment (600 mg/kg) causing a 57% reduction compared to control plants. However, no significant differences were observed in overall plant dry matter yield. Metal tolerance declined with increasing Zn stress. Zn accumulation in leaves reached 9,632 mg/kg and 14,771 mg/kg at soil Zn application rates of 400 mg/kg and 600 mg/kg, respectively. The shoot-to-root Zn ratio exceeded one, and more than 64% of the total Zn absorbed by *L. uncinatus* was translocated to the shoots at 600 mg/kg. These results position *L. uncinatus* as a promising species for Zn phytoremediation, encouraging future studies under field conditions and with other toxic metals.

Keywords: Metal uptake; Zinc toxicity**;** Phytoremediation; Tolerance index; Lupin plants; Soil contamination

1. Introduction

Modern advancements in agriculture, industry, and urban development have led to significant growth, but they have also resulted in serious environmental issues, particularly the accumulation of heavy metals and toxic substances in soil.[1-4] Large regions worldwide are impacted by anthropogenic deposition of heavy metals.[5] In recent years, concerns have grown regarding the health and ecological impacts of heavy metals in soil and their subsequent absorption by plants, prompting the scientific community to explore effective mitigation strategies.[6] Human activities such as mining, smelting, waste disposal, manufacturing, battery disposal, and agricultural practices, including the use of inorganic fertilizers and pesticides, are recognized as major sources of environmental pollution.[7] Soil contamination directly affects the health of living organisms because toxic substances can readily enter the food chain.[8] As a result, the widespread distribution of toxic elements in soil, water, and air poses serious and unpredictable risks to human health.[9]

At low concentrations, however, heavy metals are crucial for biological functions. They serve as cofactors for many enzymes, including proteinases, dehydrogenases, and peptidases. Zinc (Zn), for example, is essential for the synthesis of carbohydrates, proteins, phosphates, auxins, RNA, and ribosomes,[10] and it plays a vital role in the metabolic processes of both plants and animals. Nevertheless, Zn can accumulate to toxic levels in the environment, adversely affecting plants as well as soil-dwelling organisms.[11] Although Zn is an integral part of Earth's biogeochemical cycles and is required by plants in trace amounts, human activities such as excessive agrochemical use, industrial and municipal waste disposal, and mining have led to elevated Zn concentrations in soils, which may become detrimental to plants[12,13] and frequently reach toxic levels for soil microbes.[14] Phytoextraction, the process of removing heavy metals from soil using plants, is increasingly regarded as an eco-friendly and cost-effective approach to the remediation of soils contaminated with potentially toxic substances.[15-18] More broadly, phytoremediation, the use of plants to restore polluted soils, is considered an innovative and promising strategy for soil decontamination, offering several advantages over traditional methods, such as being *in situ*, cost-effective, and environmentally friendly.[19,20] Recent studies have demonstrated that certain plant species, due to their unique traits, possess the capability to absorb and metabolize xenobiotics contaminating the environment.[21]

Plants selected for the uptake of toxic elements from soil should be contamination-specific, meaning they must be capable of tolerating the specific pollutants present, thrive under local soil and climatic conditions, accumulate metals in harvestable tissues, and possess root systems that spatially align with the geographical distribution of contaminants. *Lupinus* species exhibit ecophysiological traits that enable them to solubilize and absorb toxic elements from soil due to their extensive and deep root systems. These plants also demonstrate adaptability to environmental stress factors, such as excess nitrates, low root temperatures, detopping,[22,23] lime excess,[24] and salinity,[25] that would otherwise inhibit normal plant growth.[26]

Reay and Waugh[27] have reported the uptake of manganese (Mn) and aluminum (Al) by *Lupinus* shoots and roots, while other studies have shown the absorption of cadmium (Cd) and mercury (Hg).[28,29] *Lupinus albus* L. has shown the ability to detoxify water by absorbing Cd, plumbum (Pb), and chromium (Cr),[30] with Cd retention attributed to thiol groups in cell walls.[31] These findings highlight the considerable potential of this genus for remediating contaminated soils.[32] Furthermore, *Lupinus luteus* L. (yellow lupine) has been demonstrated to grow without toxicity when exposed to benzo(a)pyrene. Endophytes associated with this species not only enhanced plant growth and tolerance to benzo(a)pyrene but also improved resistance to other organic pollutants such as diesel and polychlorinated biphenyls. These endophytes were also capable of metabolizing some of the organic pollutants.[33]

Unlike hyperaccumulator plants such as *Thalspi caerulescense*, *Lupinus* species act as metal excluders, restricting the movement of metals from roots to shoots across a broad range of soil metal concentrations. This exclusion mechanism may involve alterations in membrane permeability, changes in the metal-binding capacity of cell walls, or the exudation of chelating substances from roots, as has been proposed for *L. albus*.[34]

In a recent study by Saladin *et al*.,[35] *L. albus*. exposed for 3 weeks in a greenhouse to soils from former French mines (Pontgibaud and Vaulry) contaminated with metal(loid)s, including high concentrations of arsenic (As) and Pb (772–1,064 mg/kg and 121–12,340 mg/kg, respectively), showed less growth inhibition than two other species (common vetch and buckwheat). This resilience was attributed to lower metal(loid) concentrations in the roots and aerial tissues of lupins, suggesting that *L. albus* may be the most suitable species for phytostabilization among the crops

tested. However, much of the existing research on this genera has been conducted in non-soil media, such as hydroponic systems, with limited information available on its performance in contaminated soils. Therefore, it was important to evaluate the response of *Lupinus uncinatus*—an understudied species within the same genus as *L. albus*—to varying soil Zn treatments.

2. Materials and methods

A greenhouse pot experiment was conducted to evaluate the phytoremediation potential of *L. uncinatus*. Soil was collected from the top 25 cm layer of an agricultural field at San Pablo Ixayoc, State of Mexico, Mexico, and analyzed for Zn concentration along with other physical and chemical properties (Table 1). Seeds of *L. uncinatus* were also collected from the same site.

Plastic pots (15 cm diameter) were filled with 5 kg of soil. Seeds were sown directly in the pots and germinated within 5–7 days. One week after germination, seedlings were thinned to three plants per pot. After 4 weeks of growth, plants were treated with $ZnCl_2$ at concentrations of 200, 400, and 600 mg/kg, applied in 15 mL of deionized water.

The pots were arranged in a randomized design under normal greenhouse conditions. Average daytime and nighttime temperatures ranged between 25–29°C and 8–11°C, respectively. Pots were re-randomized 3 times during the experiment. Four replicates were established per treatment (200, 400, and 600 mg/kg) and for the control (no Zn added only having background soil Zn concentration of 65 mg/kg). Pots were irrigated with distilled water every 2–3 days to maintain 70% of field capacity. Plant growth was assessed by measuring dry weight accumulation under each Zn treatment, while Zn content and distribution in roots, stems, and leaves were determined at harvest, which marked the end of the experiment.

Table 1. Selected physical and chemical characteristics of pot soil

Parameter	Value
pH	6.29
Electrical conductivity	0.16 dS/m
Organic matter	1.19%
Soil texture	Sand (34%); silt (32%); clay (34%)
Bulk density	1.13 Mg/m^3
Total zinc content	65 mg/kg

Two weeks after Zn application, plants were harvested and separated into roots, stems, and leaves. Plant tissues were thoroughly washed with tap water, followed by repeated rinsing with deionized water. Samples were then oven-dried at 70°C for 72 h to record dry weight, ground to a fine powder, and subsampled (0.1 g) for digestion with nitric perchloric acid. Zn concentrations (mg/kg) in plant organs were quantified using an atomic absorption spectrophotometer (Model 3110, Perkin-Elmer, USA).

Data were analyzed using one-way analysis of variance, and Tukey's test was applied for multiple comparisons of means at a significance level of $p<0.05$. Homogeneity of variance was verified using Levene's test ($p>0.05$). All statistical analyses were performed using SAS software (version 9.1; SAS Institute, United States).[36]

Metal tolerance was calculated using Equation I:

$$X = \frac{A}{B} \times 100 \quad \text{(I)}$$

Where A = mean dry weight of plants grown under Zn treatments, and B = mean dry weight of control plants (no Zn treatment).

Accordingly, a tolerance index of 50% indicates that plants produced 50% of the optimum biomass relative to the control, which is considered the minimum acceptable biomass under toxic soil conditions.[37]

3. Results and discussion

3.1. Plant growth and dry matter yield

The dry matter yield of *L. uncinatus* plants after 2 weeks of exposure to varying Zn supply levels is presented in Table 2. The roots, being in direct contact with the heavy metal and serving as primary sites of toxic action, showed a significant decrease in dry matter

Table 2. Dry matter yield of *Lupinus uncinatus* after 2 weeks of exposure to different zinc supply levels

Zinc supply levels (mg/kg)	Dry matter yield (g/pot)		
	Shoot	Root	Plant
Control	1.90±0.18^{b}	0.56±0.04^{a}	2.46±0.17^{b}
200	3.29±0.27^{a}	0.31±0.02^{b}	3.60±0.26^{a}
400	2.99±0.21^{a}	0.30±0.03^{bc}	3.29±0.21^{a}
600	3.36±0.31^{a}	0.32±0.02^{c}	3.68±0.30^{c}

Note: Values in the same column followed by different letters differ significantly ($p<0.05$) according to Tukey's test ($n=4$).

with increasing Zn supply levels, as expected. At the 600 mg/kg treatment, root dry matter was reduced by 57% compared to control plants.

The negative effects of toxic elements on root growth are well documented. For example, Luo *et al*.[38] reported that elevated Zn levels inhibited the growth of *Jatropha* seedlings by disrupting normal cellular metabolism and inducing visible injuries and physiological disorders. Moreover, root growth was identified as the first visible site of damage under excessive Zn, due to reduced cell division.[39] Additionally, cell walls have been reported to rupture under physical stress when their elasticity is significantly reduced by Pb and Cd exposure.[40] Significant decreases in plant biomass production have also been reported in *Lupinus ballianus*[41] and *Lupinus termis* when grown either in 100% mine waste substrates containing 3,780 mg/kg Zn or in soil-filled pots supplemented with 100 mg/L Zn solutions, respectively.[42]

Shoot dry matter yield per pot ranged from 1.90 g to 3.36 g. A significant increase in shoot dry matter was observed compared to the control, and total plant biomass followed the same trend. Similar increases in plant biomass in response to heavy metal treatments have been reported by other researchers for Mn and copper,[43] as well as Cd.[44,45]

3.2. Metal tolerance

In this study, we employed the index of tolerance (IT) to evaluate the ability of *L. uncinatus* to withstand Zn treatments after 2 weeks of growth in contaminated soil. Figure 1 illustrates the tolerance of *Lupinus* plants under Zn exposure. An IT of 50% represents 50% of optimum plant growth and is considered the minimum acceptable biomass for plants grown in the presence of toxic soil elements.[37]

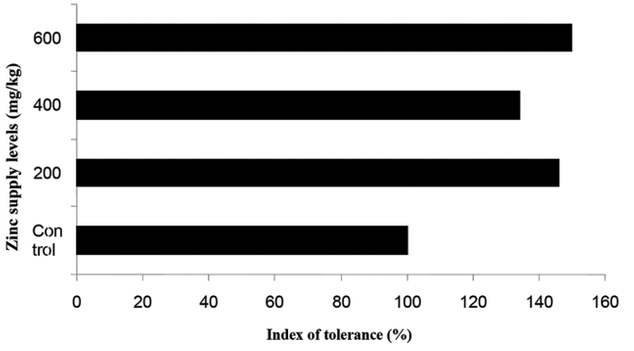


Figure 1. Index of tolerance exhibited by *Lupinus uncinatus* exposed to different zinc supply levels for 2 weeks (*n* = 4)

Zinc treatments appeared to have a stimulatory effect on plant dry matter yield, as IT values for Zn supply levels of 200, 400, and 600 mg/kg were 146%, 134% and 150% respectively. Two fundamental mechanisms have been reported for plant tolerance to toxic elements: Metal exclusion and metal detoxification.[46] In the exclusion pathway, plants restrict metal absorption into the roots, thereby preventing translocation and accumulation in aerial tissues.[47] By contrast, hyperaccumulator species actively take up toxic elements and tolerate them through internal detoxification mechanisms. Several hyperaccumulator species have been identified for Zn. To cope with excess Zn in the cytoplasm, plants may employ one or more of the following pathways: (i) Reduced accumulation across the plasma membrane, (ii) sequestration in subcellular organelles, (iii) precipitation as insoluble salts, (iv) binding of Zn to low-molecular-weight organic compounds, and (v) removal through the plasma membrane into the apoplast.[48]

The IT values obtained in this study were compared with those reported in other investigations (Table 3). The results indicate that *Lupinus* species (both *L. uncinatus* in the present study and *L. albus*[32]) exhibited a high capacity for Zn accumulation and efficient translocation to aerial tissues, particularly the stem, and consequently demonstrated higher tolerance indices compared to other hyperaccumulator plants. However, these comparisons should be interpreted cautiously, as the experimental conditions differed among studies in terms of exposure duration, soil pH, texture, and growth medium.

Further research is required to directly compare the effectiveness of different plant genera in phytoextraction of heavy metals. To date, only a few species have been reported in the literature as potential soil Zn hyperaccumulators, notably those belonging to the genera *Thlaspi* and *Brassica* spp.; however, confirmation under standard growth conditions remains necessary.

The high metal IT values observed in this study indicate that *L. uncinatus* has considerable potential for application in Zn phytoremediation. However, biochemical mechanisms conferring metal tolerance and uptake are both species-specific and metal-specific. A deeper understanding of the physiological and biochemical characteristics of *Lupinus* species that enable them to tolerate excessive concentrations of metals is essential to fully harness their phytoremediation potential.

3.3. Plant accumulation and transport of zinc

An unresolved issue in phytoremediation, apart from tolerance, is the uptake and internal distribution

Table 3. Comparison of different phytoremediation strategies

Plant	Zinc Concentration in medium (mg/kg)	Zinc concentration in plant (mg/kg)	Medium, time of exposure	Tolerance index (%)	References
Lupinus uncinatus	600	10,000 (root); 18,000 (shoot)	Soil in pot, 14 days	149	The present study
Lupinus albus	500	5,200 (root); 1,638 (shoot)	Soil in pots, 84 days	38	32
Brassica juncea	6.5 mg/L	10,000 (root); 1,500 (shoot)	Hydroponics, 12 days	122	49
Thlaspi caerulescens	210	1,200 (root); 8,700 (shoot)	Soil in pots (industrial contamination), 100 days	–	50
Hordeum vulgare (barley, non-tolerant)	100	1 (root); 4.5 (plant)	Soil in pots, 48 days	41	51

of metals within plants, particularly their transport from roots to aerial tissues. Despite the relative short exposure period of 2 weeks, considerably elevated Zn concentrations were detected in the roots, stems, and leaves of *L. uncinatus*.

As shown in Figure 2, Zn concentrations in all plant parts increased proportionally with rising Zn supply levels, indicating the substantial accumulation potential of this species under the experimental conditions. These findings are consistent with previous reports for *L. albus* by Ximénez-Embún *et al*.[37] and Pastor *et al*.[32] In *L. uncinatus*, Zn concentrations in stems ranged from 3,720 mg Zn/kg to 14,771 mg Zn/kg, while leaves contained 3,090–4,062 mg Zn/kg. Roots accumulated between 5,818 and 10,568 mg Zn/kg. For comparison, *Noccaea caerulescens* (formerly known as *Thlaspi caerulescens*) can accumulate up to 40,000 mg Zn/kg in shoot dry biomass without toxic symptoms,[52,53] whereas the normal Zn concentration in most plants is 30–100 mg/kg dry mass.[54]

These results demonstrate that *L. uncinatus* is capable of substantial Zn uptake under slightly acidic conditions (as tested in the present study). Given that neutral soils are among the preferred environments of this species,[55] it is reasonable to infer that similar uptake potential may also occur under neutral conditions.

They also align with observations by Pastor *et al*.,[32] who reported Zn uptake of 3,605 mg Zn/kg in *L. albus* grown in acidic soil contaminated with 300 mg Zn/kg. Furthermore, lupins have been reported to accumulate other heavy metals. For instance, *L. albus* accumulated 4,900, 2,300, 400, and 200 mg/kg of Cd, Hg, Pb, and Cr, respectively, when grown in contaminated sand.[37] In related experiments using soil and nutrient solution, Zn and Cd accumulation in different plant parts of *L. uncinatus* was also observed.[56,57] Similarly, Vázquez *et al*.[58] reported that the growth of *L. albus* grown in perlite containing

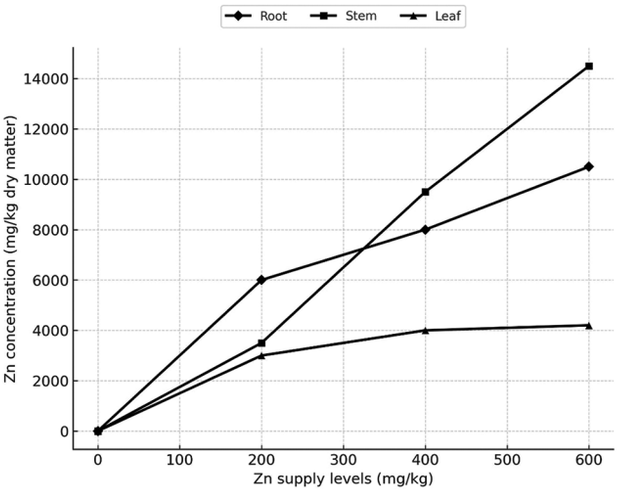


Figure 2. Zinc (Zn) uptake by roots and its accumulation and transport to aerial tissues (stems and leaves) of *Lupinus uncinatus* exposed to different Zn supply levels for 2 weeks

Notes: Vertical bars represent ± SE (n=4). Zn 000 corresponds to the control (65 mg/kg soil Zn without additional Zn application); Zn 200, Zn 400, and Zn 600 represent Zn supply levels of 200, 400, and 600 mg/kg, respectively.

10–100 μM As showed enhanced tolerance to arsenate, supporting its potential application in phytoremediation or revegetation of As-contaminated sites.

Additional studies further confirm the capacity of lupins to thrive under metal stress. For example, *L. albus* grown in vermiculite with elevated Zn concentrations at pH 6.7 for 3 weeks achieved Zn concentrations of 1,400 mg/kg of Zn in shoots and 4,100 mg/kg in roots.[32] Among Andean high-elevation plants, *L. ballianus* exhibited the highest Cd accumulation in roots, with 287.3 mg/kg dry matter when grown in a substrate consisting entirely of mine waste.[41]

Martínez-Alcalá *et al.*[59] reported that Zn concentrations were slightly higher in shoots (46 ± 10 μg/g) than in roots (34 ± 1 μg/g of *L. albus* cultivated for 74 days in calcareous pot soil containing high levels of Zn and Pb (2,058 and 2,947 μg/g, respectively). Similar shoot concentrations (40–70 μg/g) were reported in *L. albus* without apparent detrimental effects.[60] In contrast, other studies have demonstrated that Zn absorbed by this species can accumulate predominantly in roots, particularly when soil amendments are applied to stabilize metals in the soil.[31,61] Taken together with the findings of the present study, *Lupinus* species hold considerable potential for phytoremediation of metal-contaminated soils.

A notable feature of Zn accumulation in *L. uncinatus* is the relatively high concentrations detected in stems and leaves compared with roots, as reflected by shoot-to-root ratios approaching 1.78 at the 600 mg/kg treatment (Table 4). Ratios >1 indicate efficient translocation of Zn from roots to shoots, with Zn mobility increasing with high Zn additions to the soil.

Lupin plants have also demonstrated strong root-to-shoot transport capacity in the case of Hg hyperaccumulation,[37] suggesting the presence of an underlying cellular mechanism for heavy metal transport. In addition to efficient uptake, it is possible that lupin roots may also enhance the bioavailability of heavy metals in the rhizosphere, thereby enlarging the pool of Zn available for uptake.[50] In general, Zn-efficient genotypes (e.g., oilseed rape) tend to contain lower Zn concentrations in roots and higher concentrations in young leaves, indicating a superior capacity for Zn translocation and utilization.[62]

The mechanisms governing Zinc uptake and translocation in lupins, as well as the effect of soil factors on these processes, remain poorly characterized due to the limited literature available. Nonetheless, the observed accumulation and distribution patterns highlight the potential value of *Lupinus* species as phytoremediators in slight acidic or neutral soils.

Table 4. Shoot-to-root Zn concentration ratios in *Lupinus uncinatus* grown in Zn-contaminated soil (*n*=4)

Zn supply levels (mg/kg)	Shoot: Root Zn ratio
Control	1.06±0.10
200	1.17±0.14
400	1.63±0.22
600	1.78±0.19

Abbreviation: Zn: Zinc.

3.4. Metal distribution within *L. uncinatus* at various zinc concentrations

The distribution of Zn in leaves, stems, and roots varied across treatments. Zn concentration in the shoots (stems and leaves) increased, while root concentrations decreased, with increasing Zn supply levels from 200 to 600 mg Zn/kg (Figure 3).

At 200 mg Zn/kg, 54% of total Zn uptake was allocated to the shoots (stems + leaves) and 46% to the roots. By contrast, at 600 mg Zn/kg, shoot allocation increased to 64% while root allocation decreased to 36%. These results indicate that:

(i) At higher Zn concentrations, shoots tend to accumulate a greater proportion of the absorbed metal, as previously reported;[36]

(ii) The shift in Zn partitioning with increasing contamination may represent an adaptive response mechanism to mitigate the imposed metal stress.

The presented data indicate that L. uncinatus possesses a considerable capacity for Zn accumulation, reflected in high metal IT values, shoot-to-root ratios above 1, and increased dry biomass under Zn stress. Although root growth showed a significant reduction in dry weight after 2 weeks of exposure, overall plant biomass exhibited a stimulatory effect relative to the control.

The mobility of Zn within plants is generally considered intermediate, falling between highly mobile elements such as potassium and phosphorus and relatively immobile elements such as calcium.[54] Nevertheless, Zn has been found to be readily transported in the phloem of some species (e.g., wheat).[63-65] Furthermore, Zn

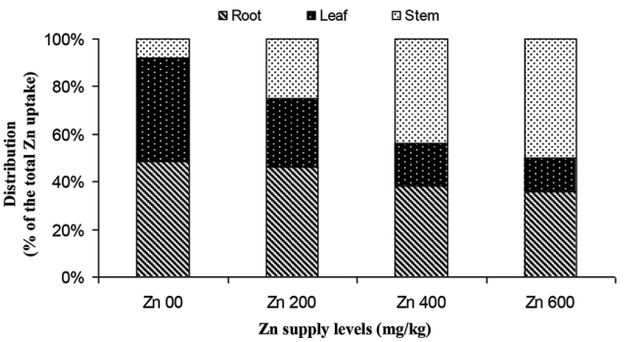


Figure 3. Zinc (Zn) distribution in different plant parts of *Lupinus uncinatus* grown at different Zn supply levels for 2 weeks (*n* = 4)

Notes: Zn 00 corresponds to the control (65 mg/kg soil Zn without additional Zn application; Zn 200, Zn 400, and Zn 600 represent Zn supply levels at 200, 400, and 600 mg/kg, respectively.

redistribution has been reported to depend on plant age and the Zn concentration in source organs.[66]

4. Conclusion

The response of *L. uncinatus* to elevated soil Zn concentrations—evaluated in terms of plant survival, toxicity symptoms, and vegetative growth (increased dry matter)—demonstrated the ability of this species to withstand adverse conditions. The high Zn concentrations detected in different plant organs, coupled with efficient translocation to shoots and elevated IT values, confirm the considerable potential of *Lupinus* species for the phytoremediation of Zn-contaminated soils.

Future research should be conducted under open-field conditions to verify the accumulation potential of this species, not only for Zn but also for other toxic metals. The present experiment was designed to provide preliminary insights into the response of *Lupinus* plants to high Zn concentrations and their pattern of metal accumulation, forming a foundation for broader applications in phytoremediation.

Acknowledgments

The authors extend their thanks to the various departments of Colegio de Postgraduados, Montecillo, Mexico, for their generous support in carrying out this research project. The scholarly guidance and valuable suggestions of Professors Jesús Pérez Moreno, Enrique Ojeda Trejo, David Jaen Contreras, and Alejandrina Ruiz Bello are gratefully acknowledged.

Funding

The principal author, Muhammad Ehsan, expresses his gratitude to the Governments of Pakistan and Mexico for awarding the doctoral scholarship, without which this research would not have been possible.

Conflict of interest

Muhammad Ehsan is an Editorial Board Member of this journal but was not involved in any way in the editorial and peer-review process conducted for this paper, either directly or indirectly. Separately, the other authors declare that they have no known competing financial interests or personal relationships that could have influenced the work reported in this paper.

Author contributions

Conceptualization: Muhammad Ehsan, Vicente Espinosa Hernández
Investigation: Muhammad Ehsan
Methodology: Muhammad Ehsan
Writing–original draft: Muhammad Ehsan
*Writing–review & editing***:** Vicente Espinosa Hernández, Dilawar Hassan, Ayesha Sani, Francisco Marcelo Lara Viveros, Jorge Luis Becerra López, Eduardo Baltierra Trejo, Rehana Gulzar, Nisbat Ali, Shahid Bashir

Availability of data

Data are available from the corresponding author upon reasonable request.

References

1. Bhattacharya P, Mukherjee AB, Jacks G, Nordqvist S. Metal contamination at a wood preservation site: Characterisation and experimental studies on remediation. *Sci Total Environ*. 2002;290(1-3):165-180. doi: 10.1016/s0048-9697(01)01073-7
2. McGrath S. Long-term studies of metal transfers following application of sewage sludge. In: *Pollutants Transport and Fate in Ecosystems.* Oxford: Blackwell; 1987. p. 310-317.
3. Mulligan CN, Yong RN, Gibbs BF. Remediation technologies for metal-contaminated soils and groundwater: An evaluation. *Eng Geol*. 2001;60(1-4):193-207. doi: 10.1016/S0013-7952(00)00101-0
4. Weissenhorn I, Leyval C, Berthelin J. Bioavailability of heavy metals and abundance of arbuscular mycorrhiza in a soil polluted by atmospheric deposition from a smelter. *Biol Fertil Soils*. 1995;19(1):22-28. doi: 10.1007/BF00336342
5. Klang-Westin E, Eriksson J. Potential of *Salix* as phytoextractor for Cd on moderately contaminated soils. *Plant Soil*. 2003;249(1):127-137. doi: 10.1023/A:1022585404481
6. Cieśliński G, Van Ree KC, Szmigielska AM, Krishnamurti GS, Huang PM. Low-molecular-weight organic acids in rhizosphere soils of durum wheat and their effect on cadmium bioaccumulation. *Plant Soil*. 1998;203(1):109-117. doi: 10.1023/A:1004325817420
7. Cui Y, Wang Q, Dong Y, Li H, Christie P. Enhanced uptake of soil Pb and Zn by Indian mustard and winter wheat following combined soil application of elemental sulphur and EDTA. *Plant Soil*. 2004;261(1-2):181-188.

doi: 10.1023/B: PLSO.0000035551.22918.01
8. Morton-Bermea O, Hernández-Álvare E, Gaso I, Segovia N. Heavy metal concentrations in surface soils from Mexico City. *Bull Environ Contam Toxicol*. 2002;68(3):383-388. doi: 10.1007/s001280265
9. Nriagu JO, Pacyna JM. Quantitative assessment of worldwide contamination of air, water and soils by trace metals. *Nature*. 1988;333(6169):134-139. doi: 10.1038/333134a0
10. Ahmad E, Zaidi A, Khan MS, Oves M. Heavy metal toxicity to symbiotic nitrogen-fixing microorganism and host legumes. In: *Toxicity of Heavy Metals to Legumes and Bioremediation*. U.S.A: Springer; 2012. p. 29-44.
11. Lock K, Janssen CR. Ecotoxicity of zinc in spiked artificial soils versus contaminated field soils. *Environ Sci Technol*. 2001;35(21):4295-4300. doi: 10.1021/es0100219
12. Kabata-Pendias A. *Trace Elements in Soils and Plants*. Boca Ratón, Florida: CRC Press; 2010.
13. Kiesken L. Zinc *Heavy Metals in Soils*. London: Blackie Academic and Professional; 1995. p. 284-305.
14. Chaney RL. Plant uptake of inorganic waste constituents. In: *Land Treatment of Hazardous Wastes*. New Jersey: Noyes Data Corp; 1983. 50-76.
15. Chaney RL. Improving metal hyperaccumulator wild plants to develop commercial phytoextraction systems: Approaches and progress. In: *Phytoremediation of Contaminated Soil and Water*. Boca Raton, Florida: Lewis, CRC Press; 1999. p. 129-158.
16. McGrath S, Dunham S, Correll R. Potential for phytoextraction of zinc and cadmium from soils using hyperaccumulator plants. In: *Phyoremediation of Contaminated Soil and Water*. New York: Lewis; 2000. p. 129-158.
17. Salt DE, Smith RD, Raski I. Phytoremediation. *Annu Rev Plant Physiol Plant Mol Biol*. 1998;49(1):643-668. doi: 10.1146/annurev.arplant.49.1.643
18. Zhao FJ, Lombi E, McGrath SP. Assessing the potential for zinc and cadmium phytoremediation with the hyperaccumulator *Thlaspi caerulescens*. *Plant Soil*. 2003;249(1):37-43. doi: 10.1023/A:1022530217289
19. Long X, Yang X, Ni W. Advance and perspectives in technologies for remediation of heavy metal polluted soils. *Ying Yong Sheng Tai Xue Bao*. 2002;13:757-762.
20. Oubohssaine M, Dahmani I. Phytoremediation: Harnessing plant power and innovative technologies for effective soil remediation. *Plant Stress*. 2024;14:100578. doi: 10.1016/j.stress.2024.100578
21. Mocek-Płóciniak A, Mencel J, Zakrzewski W, Roszkowski S. Phytoremediation as an effective remedy for removing trace elements from ecosystems. *Plants (Basel)*. 2023;12(8):1653. doi: 10.3390/plants12081653
22. De Lorenzo C, Iannetta PP, Fernandez-Pascual M, *et al*. Oxygen diffusion in lupin nodules: II. Mechanisms of diffusion barrier operation. *J Exp Bot*. 1993;44(9):1469-1474. doi: 10.1093/jxb/44.9.1469
23. Iannetta PP, De Lorenzo C, James EK, *et al*. Oxygen diffusion in lupin nodules: I. Visualization of diffusion barrier operation. *J Exp Bot*. 1993;44(9):1461-1467.
24. Tang C, Robson AD. *Lupinus* species differ in their requirements for iron. *Plant Soil*. 1993;157(1):11-18. doi: 10.1007/BF02390222
25. Fernández-Pascual M, De Lorenzo C, De Felipe M, *et al*. Possible reasons for relative salt stress tolerance in nodules of white lupin cv. Multolupa. *J Exp Bot*. 1996;47(11):1709-1716. doi: 10.1093/jxb/47.11.1709
26. Hopmans JW, Qureshi AS, Kisekka I, *et al*. Critical knowledge gaps and research priorities in global soil salinity. *Adv Agron*. 2021;169:1-191. doi: 10.1016/bs.agron.2021.03.001
27. Reay PF, Waugh C. Mineral-element composition of *Lupinus albus* and *Lupinus* angustifolius in relation to manganese accumulation. *Plant Soil*. 1981;60(3):435-444. doi: 10.1007/BF02149639
28. Carpena R, Peñalosa J, Esteban E, *et al*. Effects of As and Cd on Lupinus albus L. potential use in phytoremediation. In: *Phytoremediation of trace elements in contaminated soils and waters* (*with special emphasis on Zn, Cd, Pb and As*). Cost Action 837 WG2 Workshop 2001. p. 55-57.
29. Vera R, Millán R, Schmid T, Tallos A, Recreo F. Behaviour of mercury in the soil-plant system. Application to phytoremediation studies. In: *Sustainable use and Management of Soils in Arid and Semi Arid Regions*. Vol. 2. Cartegena, Spain: Quaderna; 2002. p. 482-483.
30. Ximénez-Embún P, Madrid-Albarrán Y, Cámara C, Cuadrado C, Burbano C, Múzquiz M. Evaluation of *Lupinus* species to accumulate heavy metals from waste waters. *Int J Phytoremediation*. 2001;3(4):369-379. doi: 10.1080/15226510108500065
31. Zornoza P, Vázquez S, Esteban E, Fernández-Pascual M, Carpena R. Cadmium-stress in nodulated white lupin: Strategies to avoid toxicity. Plant Physiol Biochem. 2002;40(12):1003-1009. doi: 10.1016/S0981-9428(02)01464-X
32. Pastor J, Hernández AJ, Prieto N, Fernández-Pascual M. Accumulating behaviour of *Lupinus albus* L. Growing in a normal and a decalcified calcic luvisol polluted with Zn. *J Plant Physiol*. 2003;160(12):1457-1466. doi: 10.1078/0176-1617-01007
33. Gutiérrez-Ginés MJ, Hernández AJ, Pérez-Leblic MI, Pastor J, Vangronsveld J. Phytoremediation of soils co-contaminated by organic compounds and heavy metals: Bioassays with *Lupinus* luteus L. And associated endophytic bacteria. *J Environ Manage*.

2014;143:197-207.
doi: 10.1016/j.jenvman.2014.04.028
34. Martínez-Alcala I, Hernández E, Esteban E, Walker DJ, Bernal MP. Responses of *Noccaea caerulescens* and *Lupinus albus* in trace elements-contaminated soils. Plant Physiol Biochem. 2013;66:47-55.
doi: 10.1016/j.plaphy.2013.01.017
35. Saladin G, Soubrand M, Joussein E, Benjelloun I. Efficiency of metal(loid) phytostabilization by white lupin (*Lupinus albus* L.), common vetch (Vicia sativa L.), and buckwheat (*Fagopyrum esculentum* Moench). *Environ Sci Pollut Res*. 2024:31(43):55822-55835.
doi: 10.1007/s11356-024-34911-5
36. SAS Institute. *SAS Institute SAS Version 9.1*. Cary, NC: SAS Institute; 2000.
37. Ximénez-Embún P, Rodríguez-Sanz B, Madrid-Albarrán Y, Cámara C. Uptake of heavy metals by lupin plants in artificially contaminated sand: Preliminary results. *Int J Environ Anal Chem*. 2002;82(11-12):805-813.
doi: 10.1080/0306731021000102275
38. Luo ZB, He XJ, Chen L, Tang L, Gao S, Chen F. Effects of Zinc on growth and antioxidant responses in *Jatropha curcas* seedlings. *Int J Agric Biol*. 2010;12:119-124.
39. Prasad KV Saradhi PP, Sharmila P. Concerted action of antioxidant enzymes and curtailed growth under zinc toxicity in *Brassica juncea*. *Environ Exp Bot*. 1999;42(1):1-10.
doi: 10.1016/S0098-8472(99)00013-1
40. Barcelo J, Poschenrieder CH, Andreu I, Gunse B. Cadmium-induced decrease of water stress resistance in bush bean plants (*Phaseolus vulgaris* L. cv. Contender) I. Effects of Cd on water potential, relative water content, and cell wall elasticity. *J Plant Physiol*. 1986;125(1-2):17-25.
doi: 10.1016/S0176-1617(86)80239-5
41. Jara-Peña E, Gómez J, Montoya H, Chanco M, Mariano M, Cano N. Phytoremediation capacity of five high andean species from soils contaminated with heavy metals. *Rev Peru Biol*. 2014;21(2):145-154.
42. Ahmed AHM, Latif HH. Phytoremediation of soil contaminated with zinc and lead by using *Zea mays* L. *Bangladesh J Bot*. 2015;44(2):293-298.
doi: 10.3329/bjb.v44i2.38519
43. Kidd PS Díez J, Martínez C. Tolerance and bioaccumulation of heavy metals in five populations of *Cistus ladanifer* L. Subsp. *Ladanifer*. *Plant Soil*. 2004;258(1):189-205.
doi: 10.1023/B: PLSO.0000016550.49264.f3
44. Vassilev A, Lidon FC, Ramalho JC, Matos MDC, Bareiro MG. Shoot cadmium accumulation and photosynthetic performance of barley plants exposed to high cadmium treatments. *J Plant Nutr*. 2004;27(5):775-795.
doi: 10.1081/PLN-120030613
45. Yang XE, Long XX, Ye HB, He ZL, Calvert DV, Stoffella PJ. Cadmium tolerance and hyperaccumulation in a new Zn-hyperaccumulating plant species (*Sedum alfredii* Hance). *Plant Soil*. 2004;259(1-2):181-189.
doi: 10.1023/B: PLSO.0000020956.24027.f2
46. Baker AJ. Accumulators and excluders strategies in response of plants to heavy metals. *J Plant Nutr*. 1981;3(1-4):643-654.
doi: 10.1080/01904168109362867
47. De Vos CH, Schat, De Waal MA, Vooijs R, Ernst WH. Increased resistance to copper-induced damage of the root cell plasmalemma in copper tolerant *Silene cucubalus*. *Physiol Plant*. 1991;82(4):523-528.
doi: 10.1111/j.1399-3054.1991.tb02942.x
48. Brune A, Urbach W, Dietz KJ. Compartmentation and transport of zinc in barley primary leaves as basic mechanisms involved in zinc tolerance. *Plant Cell Environ*. 1994;17(2):153-162.
doi: 10.1111/j.1365-3040.1994.tb00278.x
49. Ebbs SD, Kochian LV. Phytoextraction of zinc by oat (*Avena sativa*), barley (*Hordeum vulgare*), and Indian mustard (*Brassica juncea*). *Environ Sci Technol*. 1998;32(6):802-806.
doi: 10.1021/es970698p
50. Knight B, Zhao FJ, McGrath SP, Shen ZG. Zinc and cadmium uptake by the hyperaccumulator *Thlaspi caerulescens* in contaminated soils and its effects on the concentration and chemical speciation of metals in soil solution. *Plant Soil*. 1997;197(1):71-78.
doi: 10.1023/A:1004255323909
51. Luo Y, Rimmer DL. Zinc-copper interaction affecting plant growth on a metal-contaminated soil. *Environ Pollut*. 1995;88(1):79-83.
doi: 10.1016/0269-7491(95)91050-u
52. Saison C, Schwartz C, Morel JL. Hyperaccumulation of metals by *Thlaspi caerulescens* as affected by root development and Cd-Zn/Ca-Mg interactions. *Int J Phytorem*. 2004;6:49-61.
doi: 10.1080/16226510490439981
53. Shen ZG, Zhao FJ, McGrath SP. Uptake and transport of zinc in the hyperaccumulator *Thlaspi caerulescens* and the non-hyperaccumulator *Thlaspi ochroleucum*. *Plant Cell Environ*. 1997;20:898-906.
doi: 10.1046/j.1365-3040.1997.d01-134.x
54. Marschner H. *Mineral Nutrition of Higher Plants*. 2nd ed. San Diego: Elsevier Science; 1995.
55. Lopez-Bellido L, Fuente M. Lupin crop as an alternative source of protein. *Adv Agron*. 1986;40:239-295.
doi: 10.1016/S0065-2113(08)60284-9
56. Ehsan M, Santamaría-Delgado K, Alderete-Chavez A, De La Cruz-Landero N, Jaén-Contreras D, Molumeli PA. Phytostabilization of cadmium contaminated soils by *Lupinus* uncinatus Schldl. *Spanish J Agric Res*. 2009;7(2):390-397.
doi: 10.5424/sjar/2009072-430

57. Ehsan M, Viveros FL, Hernandez V, *et al*. Zinc and cadmium accumulation by *Lupinus* uncinatus Schldl. grown in nutrient solution. *Int J Environ Sci Technol*. 2015;12(1):307-316. doi: 10.1007/s13762-013-0456-0
58. Vázquez S, Esteban E, Carpena RO. Evolution of arsenate toxicity in nodulated white lupine in a long-term culture. *J Agric Food Chem*. 2008;56(18):8580-8587. doi: 10.1021/jf801673c
59. Martínez-Alcalá I, Clemente R, Bernal MP. Metal availability and chemical properties in the rhizosphere of *Lupinus albus* L. Growing in a high-metal calcareous soil. *Water Air Soil Pollut*. 2009;201(1-4):283-293. doi: 10.1007/s11270-008-9944-0
60. Kerley SJ. Changes in root morphology of white lupin (*Lupinus albus* L.) and its adaptation to soils with heterogeneous alkaline/acid profiles. *Plant Soil*. 2000;218(1-2):197-205. doi: 10.1023/A:1014967720952
61. Castaldi P, Santona L, Melis P. Heavy metal immobilization by chemical amendments in a polluted soil and influence on white lupin growth. *Chemosphere*. 2005;60(3):365-371. doi: 10.1016/j.chemosphere.2004.11.098
62. Adriano DC. *Zinc Trace Elements in Terrestrial Environments*. New York: Springer; 2001. p. 219-261.
63. Haslett B, Reid R, Rengel Z. Zinc mobility in wheat: Uptake and distribution of zinc applied to leaves or roots. *Ann Bot*. 2001;87(3):379-386. doi: 10.1006/anbo.2000.1349
64. Herren T, Feller U. Transfer of zinc from xylem to phloem in the peduncle of wheat. *J Plant Nutr*. 1994;17(9):1587-1598. doi: 10.1080/01904169409364831
65. Pearson JN, Rengel Z, Jenner CF, Graham RD. Transport of zinc and manganese to developing wheat grains. *Physiol Plant*. 1995;95(3):449-455. doi: 10.1111/j.1399-3054.1995.tb00862.x
66. Herren T, Feller U. Effect of locally increased zinc contents on zinc transport from the flag leaf lamina to the maturing grains of wheat. *J Plant Nutr*. 1996;19(2):379-387. doi: 10.1080/01904169609365128

Asian Journal of Water, Environment and Pollution. Vol. 22, No. 6 (2025), pp. 180-197.
doi: 10.36922/AJWEP025310242

ORIGINAL RESEARCH ARTICLE

Energy-efficient light-emitting diode retrofit and advanced control in municipal street lighting: A case study from Bulgaria

Plamen Tsankov[1,2]*, Milko Yovchev[1,2], and Hristo Ibrishimov[1,2]

[1]Department of Electric Power Distribution and Equipment, Faculty of Electrical Engineering and Electronics, Technical University of Gabrovo, Gabrovo, Bulgaria

[2]Laboratory Eco-friendly, Energy-saving, and Electromagnetically Compatible LED and Renewable Energy Components and Technologies, Center of Competence "Intelligent Mechatronics, Eco- and Energy-Saving Systems and Technologies," Gabrovo, Bulgaria

***Corresponding author:** Plamen Tsankov (plamen@tugab.bg)

Received: August 1, 2025; 1st revised: August 15, 2025; 2nd revised: August 18, 2025; Accepted: August 19, 2025; Published online: September 11, 2025

Abstract: Modernizing street lighting through light-emitting diode (LED) retrofits and advanced controls is recognized as an effective strategy for reducing energy use and costs. While numerous studies confirm these benefits in Western Europe, little is known about their performance in Eastern European municipalities. This study addresses this knowledge gap by presenting a case study of municipal street lighting in Bulgaria. It presents the methodology, implementation, and evaluation of an energy-efficient modernization project for municipal street lighting systems in the Bulgarian cities of Pavlikeni and Byala Cherkva. He project involved a complete transition from outdated lighting technologies (e.g., high-pressure sodium, compact fluorescent, and mercury vapor lamps) to high-efficiency LED luminaires, integrated with an intelligent control and monitoring system. An energy audit, conducted in accordance with national regulations and European standards (EN 13201), revealed that over 90% of luminaires had exceeded their operational lifespan and no longer complied with photometric and technical requirements. Lighting design classifications were applied in accordance with EN 13201:2016 to ensure compliance with the standard's requirements for luminance, uniformity, and glare control. An optimization problem was defined and solved using specialized software to determine the lowest luminaire power, minimum pole height, and smallest bracket tilt angle, with fixed pole spacing, while maintaining regulatory compliance. Using DIALux evo, multi-scenario photometric simulations and optimizations were performed, resulting in 47 optimized lighting models tailored to specific street segments. The upgraded system incorporates adaptive dimming features, enabling nighttime power reduction through pre-programmed driver settings. A centralized cloud-based management system was implemented for remote monitoring and control, enhancing reliability and reducing maintenance. Post-implementation analysis demonstrated 79.5% energy savings (549,082 kWh/year), along with carbon dioxide emission reductions of 1,349 t/year and a financial payback period of 6.2 years. This case study highlights the technical, economic, and ecological viability of large-scale LED retrofit projects with smart controls, offering a replicable model for municipalities across Central and Eastern Europe seeking improved energy efficiency and reduced environmental impact.

Keywords: Light-emitting diode street lighting; Street lighting audit; Street lighting modeling and optimization; Energy efficiency; Smart lighting control; Carbon dioxide emission reduction; Public lighting retrofit

1. Introduction

The judicious utilization of electrical energy in road lighting is regarded as a pivotal element for urban sustainability. Public street lighting typically contributes around 1–1.5% of a country's electricity consumption and can account for up to 30–50% of municipal energy expenditures, depending on the specific local circumstances.[1]

Conventional lighting technologies, such as high-pressure sodium (HPS) and mercury vapor lamps, present several drawbacks. These include low luminous efficacy (approximately 80–100 lm/W), limited operational life (approximately 12,000–24,000 h), and high maintenance demands.[2] Conversely, light-emitting diodes (LEDs) typically achieve luminous efficacies of at least 150 lm/W, provide service lifetimes of at least 50,000 h, and significantly reduce maintenance costs.[3,4]

In accordance with European standards, such as EN 13201, objective metrics—including power per length (PL [W/m]) and power per illuminated area (PA [W/m^2])—are employed to evaluate the performance of lighting systems.[5] Retrofit initiatives frequently yield energy savings of 50–70%, while intelligent control strategies, such as adaptive dimming, increase total savings to over 80%.[6]

A longitudinal monitoring study in Turin by Valetti *et al*.[3] documented a 51% annual energy reduction following LED retrofits, with photometric degradation being lower than predicted by standard models. Aghemo *et al*.[4] reported complementary findings across urban lighting installations. The carbon footprint of LED street lighting systems has been quantitatively assessed, with estimated reductions ranging from 0.4 to 0.7 kg CO_2/luminaire/year, depending on operational conditions and energy mix sources.[7] These findings highlight the substantial potential of LED-based lighting solutions to contribute significantly to climate mitigation.

Adaptive smart-city lighting projects—such as those integrating the Internet of Things and agent-based control—have demonstrated up to 35% additional energy savings over fixed-schedule designs. Smart dimming strategies linked to predictive traffic flows and environmental conditions further enhance performance.[8]

Large-scale municipal dimming experiments, such as the one conducted in Tucson involving approximately 20,000 luminaires, yielded approximately a 5% reduction in zenith sky brightness, corresponding to an overall street lighting contribution of around 14% to urban skyglow.[9] The adoption of warmer white or amber LEDs within spectral design frameworks has been demonstrated to simultaneously reduce ecological impacts while maintaining efficiency.[10]

Real-world case studies, including the retrofit of approximately 3,768 luminaires in Kraków, achieved notable reductions in energy consumption and carbon emissions, while also delivering improved economic performance through savings on emissions allowances.[11] Similar initiatives in European towns demonstrate consistent compliance with technical standards, safety, and environmental outcomes.[12]

The findings, when considered collectively, demonstrate that the implementation of LED-based public lighting, in conjunction with adaptive control strategies, has the potential to significantly contribute to the European Union's 55% greenhouse gas reduction target by 2030. This integration of lighting and control systems is expected to yield several key benefits, including enhanced operational cost-efficiency, improved road safety, and a reduction in environmental degradation.

The evolution of technologies in street lighting modernization in Bulgaria over the past three decades can be divided into two main periods[13]:

(i) Transition from mercury to HPS and compact fluorescent lamps (CFLs) (1995–2010).
(ii) Transition from HPS lamps and CFL to LEDs (2010–2015).

The approximate number of lamps of different types installed in outdoor luminaires in Bulgaria in 2010–2011 is shown in Table 1.[14]

The lamps used for outdoor lighting in Bulgarian municipalities at the end of the transition from mercury to sodium and CFL technologies (2010–2011) were as follows[15]:

(i) HPS lamps of 50W, 70W, 100W, 150W, 250W, and 400W.
(ii) CFLs of 11W, 13W, 36W, and 55W.
(iii) Metal halide lamps of 35W, 70W, 100W, 150W, and 250W.

Table 1. Distribution of luminaires by lamp type in Bulgaria (2010–2011)

Lamp type	Number	Share (%)
Sodium high pressure	450,000	53.0
Mercury vapor	136,000	16.0
Compact fluorescent	222,000	26.2
Metal halide	36,000	4.3
Light-emitting diode	4,500	0.5
Total	848,500	100

(iv) Mercury lamps of 80W, 125W, 250W, and 400W.
(v) LED modules of 20–150W.

This period marked the appearance of the first demonstration projects for outdoor LED lighting.

After 2010, the rapid increase in efficiency and reduction in the cost of LED technology coincided with the completion of the 15–20-year service life of the luminaries from the previous transition to sodium lamps. This convergence accelerated the widespread adoption of LED lights in outdoor lighting and initiated the transition from HPS and CFLs to LED light sources. The process was gradual, but all new street lighting systems were implemented with LED luminaires. The expansion of LED use in recent years has been highly dynamic across different Bulgarian cities, making it difficult to establish precise general data.

2. Methodology

This study presents the development, results, and the associated energy and environmental benefits of a project aimed at the energy-efficient modernization of street lighting systems in the Bulgarian municipality of Pavlikeni.

The research methodology consisted of the following stages:

(i) Conducting an energy audit of the existing street lighting systems.
(ii) Optimizing street lighting design through computational modeling using specialized software.
(iii) Implementing a modern street lighting management and control system.
(iv) Assessing energy efficiency, financial savings, and environmental benefits of the proposed modernization.

2.1. Energy audit of the existing street lighting systems

Conducting an energy audit of the existing street lighting systems is an important initial stage, as confirmed by several authoritative studies.[16-20]

The energy audit of the street lighting systems in the municipality of Pavlikeni was carried out in accordance with the applicable Bulgarian legislation, specifically Ordinance No. E-RD-04-05/04.10.2016 issued by the Ministry of Energy, which regulates the structure, content, and methodology for energy audits of industrial systems.[21] The audit also aligns with the principles and procedures outlined in EN 16247-2:2014,[22] which establishes the European standard for energy audits of buildings and technical systems, including outdoor lighting.[23] In compliance with these standards, the audit included an inventory of all lighting fixtures, measurements of installed and consumed power, nighttime observations of lighting quality, and verification of the system's conformity with applicable lighting design criteria.

The audit results revealed that over 90% of the existing luminaires equipped with HPS lamps had reached the end of their technical and operational life cycle. Common problems identified during the survey were mechanical failure of fixings, missing or damaged diffusers (Figure 1A-D), and a lack of moisture protection for the starting and control gear (Figure 1D). In some cases, LED and CFL lamps were installed in luminaires originally designed for HPS lamps (Figure 1C-F), leading to reduced luminance and illuminance levels on the roadway.

Steel street and park poles predominate in the central urban areas of the settlements, while reinforced concrete poles are mostly found in the outlying districts and villages. A significant proportion of luminaire cantilevers exhibit large tilt angles, ranging from 30° to 60°, which are inappropriate for the roadway widths, ranging from 4 to 9 m. These angles reduce the effective roadway coverage and illuminance while increasing glare and causing an unnecessarily large portion of the luminaire's light output to be directed onto the opposite sidewalks and building facades. In some cases, the luminaire bracket was misaligned, either rotated incorrectly around the horn axis or oriented in the opposite direction from the roadway.

Based on a detailed survey of the condition of the street and park lighting fixtures, the pole network, power lines, and the locations of the transformer substations and street lighting cassettes, a digital graphical model of the existing street lighting system in Pavlikeni was developed. This model integrates the survey data across separate map sheets, on which the collected information was plotted. Different types of luminaires, poles, power lines, and the positions of the control points and cabinets are indicated using appropriate graphic symbols. Figure 2 presents a section of one such map sheet from the digital graphical model, which was developed using AutoCAD (Autodesk Inc., USA). The graphic model is accompanied by detailed information about the existing lighting systems on all streets: The distances between the poles; the type and height of the poles; the length and angle of the bracket for mounting the luminaires; the type of luminaire and the technology; and the power of the light sources.

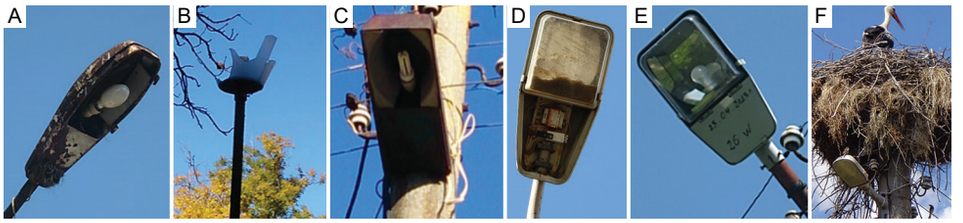


Figure 1. (A-F) Condition of depreciated street and park luminaires

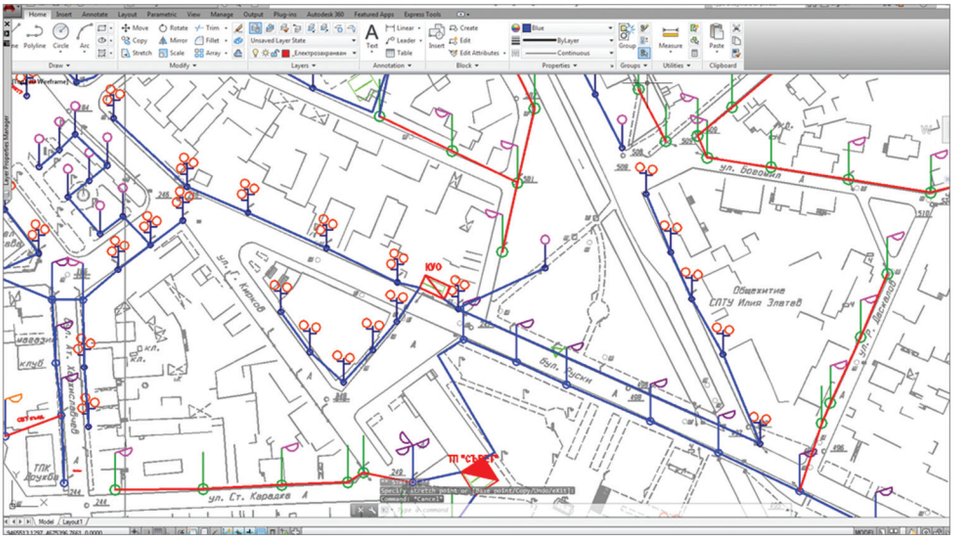


Figure 2. Section of a map sheet showing the plotted locations of the street lighting system in Pavlikeni

Figure 3 presents the distribution by type and power rating of the existing street and park luminaires in Pavlikeni. Street lighting accounts for 83.8% of the installed luminaires, while park lighting represents 16.2%. In the town of Pavlikeni, however, park luminaires constitute 48.3% of the total, whereas their share in the other settlements is negligible.

The predominant type of light source is HPS, representing 50.4% of all luminaires, followed by CFLs, which account for 36.5%. Street luminaires equipped with high-pressure mercury vapor lamps are outdated models, exceeding 25 years of service, and are significantly depreciated. In many cases, the lamps are missing, and only about 5% of the high-pressure mercury vapor luminaires remain operational.

In total, the street lighting system in Pavlikeni comprises 4,663 street luminaires and 901 park luminaires, resulting in a combined total of 5,564. In addition, there are 5,942 poles without luminaires—5,880 are reinforced concrete, 46 are steel, and 16 are wooden.

The total electrical power of the existing street and park lighting in all settlements in Pavlikeni is 280,153 W. Figure 4 illustrates the distribution of electrical power across the 20 settlements, while Figure 5 depicts the monthly electrical energy consumption for street and park lighting over the course of 1 year.

The municipality has a permanent population of 22,059, and the specific electricity consumption is calculated at 56 kWh/capita/year.

Based on the detailed survey analysis, the following energy-saving measures are proposed: Replacement of the existing street and park luminaires with new energy-efficient LED luminaires of lower installed power, implementation of an intelligent system for lighting control system, and optimization of the switching schedule.

2.2. Street lighting design optimization through computational modeling

2.2.1. Lighting classification and standardization

Based on a detailed audit of the geometric parameters of the street lighting installations in the individual settlements within the municipality of Pavlikeni, it was established that significant variability exists only in the two towns—Pavlikeni and Byala Cherkva—while the remaining settlements are small, relatively uniform villages. This finding justifies the need for detailed classification, standardization, and optimization

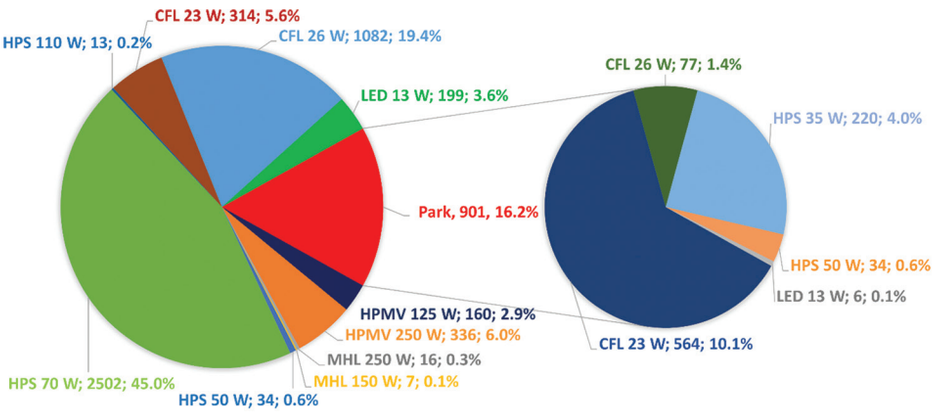


Figure 3. Distribution of the existing street and park luminaires by type and power rating (lamp type, number, and percentage share)

Abbreviations: CFL: Compact fluorescent lamp; HPMV: High-pressure mercury vapor; HPS: High-pressure sodium; LED: Light-emitting diode; MHL: Metal-halide lamp.

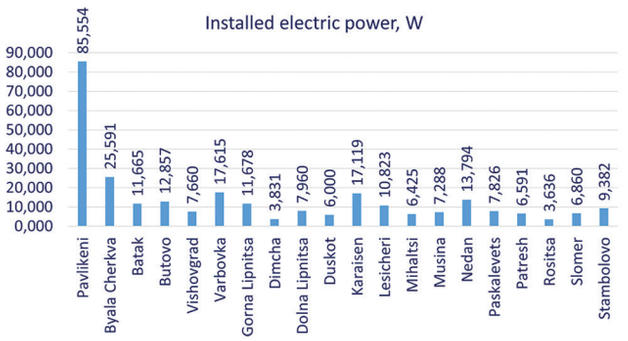


Figure 4. Installed electric power in existing street and park lighting systems in the settlements of the Pavlikeni municipality

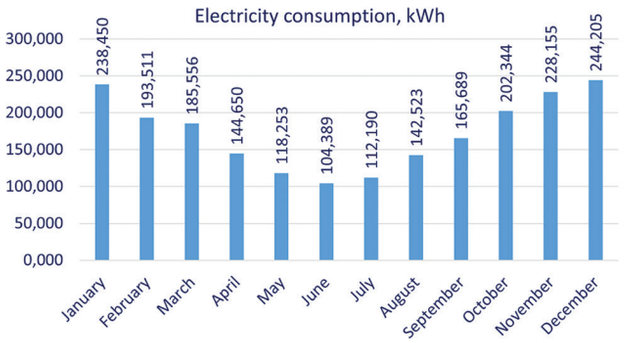


Figure 5. Monthly electricity consumption over 1 year for street and park lighting in the Pavlikeni municipality

calculations to be conducted specifically for these two urban areas within the municipality.

Before conducting lighting design calculations, the urban street network must be classified in accordance with current European standards. The standardization of the proposed street lighting designs in Pavlikeni and Byala Cherkva was carried out in accordance with the European street lighting standard BDS EN 13201:2016.[24] According to this standard, traffic on the streets in both towns primarily involves motorized vehicles, along with pedestrians and slow-moving vehicles, particularly on certain street types.

The lighting classification of the streets is defined as follows:

(i) M4: Regional arterial roads.
(ii) M5: Collector streets.
(iii) M6: Service (local residential) streets.
(iv) P6: Pedestrian streets, streets used by slow-moving vehicles, or short street segments unsuitable for luminance-based classification.

The lighting classification of the street network in Pavlikeni in accordance with BDS EN 13201:2016 is illustrated in Figure 6.

Table 2 presents the standard values for the quantitative and qualitative indicators of street lighting according to BDS EN 13201:2016. For classes M4, M5, and M6, the quantitative photometric parameter is the average road surface luminance (L_{avg}), while the qualitative parameters include overall uniformity (U_o), longitudinal uniformity (U_l), threshold increment (f_{TI}) as an indicator of glare, and the average horizontal illuminance of the surrounding area (R_{EI}).[24]

For streets and areas classified under lighting class P6, the standardized parameters are based on the average maintained illuminance (E_{avg}) and the minimum maintained illuminance (E_{min}), as shown in Table 3.[24]



Figure 6. Lighting classification of the street network in the town of Pavlikeni in accordance with EN 13201

Table 2. Standard lighting performance indicators for lighting classes M4, M5, and M6

Lighting class	Road surface luminance			Threshold increment	Surround ratio
	L_{avg}, cd/m^2	U_o	U_l	f_{TI}, %	R_{EI}
M4	≥0.75	≥0.40	≥0.60	≤15	≥0.30
M5	≥0.50	≥0.35	≥0.40	≤15	≥0.30
M6	≥0.30	≥0.35	≥0.40	≤20	≥0.30

Notes: f_{TI}: Glare index; L_{avg}: Average luminance; R_{EI}: Surround ratio; U_l: Longitudinal uniformity; U_o: Overall Uniformity.

Table 3. Standard lighting performance indicators for lighting class P6

Lighting class	Horizontal illuminance	
	E_{avg}, lx	E_{min}, lx
P6	≥2.00	≥0.40

Notes: E_{avg}: Average horizontal illuminance; E_{min}: Minimum horizontal illuminance.

2.2.2. Optimization of street lighting design

The energy efficiency of LED technology in lighting fixtures has steadily improved in recent years, reaching high yet variable performance levels. A wide range of luminaires with differing luminous flux outputs and light distribution characteristics is currently available on the market. In this study, two types of LED luminaires with luminous efficacy exceeding 120 lm/W and distinct light distribution characteristics were proposed, as required by the contract with the municipal street lighting maintenance company, as illustrated in Figures 7 and 8. The technical characteristics of the LED street luminaires, including the range of possible settings for electric power, luminous flux, and luminous efficacy, are presented in Table 4. These characteristics are utilized in the lighting calculations for Pavlikeni and Byala Cherkva.

According to the technical specifications prepared by the municipality of Pavlikeni, and to minimize investment costs in the modernization of street lighting, it was specified that the new LED lights should be installed only on existing poles. This requirement was supported by the findings of the comprehensive energy audit, which confirmed the satisfactory condition of the electrical supply network utilized for street lighting. The cost of implementing the project would be more than 10 times higher if the

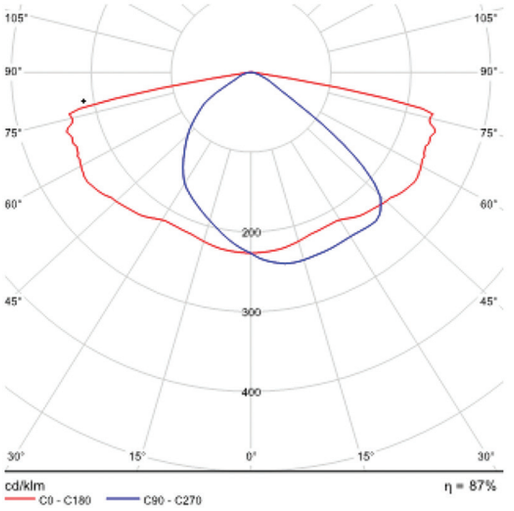


Figure 7. Light distribution of a street light-emitting diode luminaire, type 1

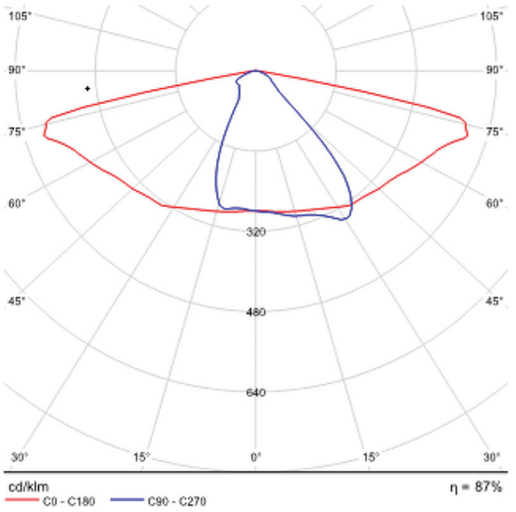


Figure 8. Light distribution of a street light-emitting diode luminaire, type 2

old poles were removed and replaced with new ones, together with a new electrical network. A further rationale for maintaining the existing poles is that a significant proportion of the reinforced concrete poles are owned by the electricity distribution company and are also used to provide electricity to domestic and small business consumers.

For standard optimization tasks involving completely new lighting systems, and in accordance with the two energy performance indicators introduced in EN 13201—power density (D_P [W/m^2]), and annual energy consumption per unit area (D_E [kWh/m^2/year])—the optimal solution from a technical and economic perspective was sought through a combination of the largest pole spacing, the smallest pole height, and the shortest bracket length and lowest slope angle, while ensuring compliance with the requirements of the given lighting class.

For the project in Pavlikeni and Byala Cherkva, where the spacing between poles (luminaire) is fixed, a non-standard optimization problem must be defined to determine the lowest luminaire power, combined with the lowest pole height and smallest bracket tilt angle that together satisfy the requirements of the designated lighting class.

The formulation of the optimization problem, where the pole spacing is fixed and the luminaire power, mounting height, and tilt angle are optimized to meet the requirements of a given M-class according to EN 13201, is as follows:

2.2.2.1. Given (parameters)

The listed parameters represent the key inputs for optimizing road lighting design: Road geometry defines the layout of the street lighting system, the EN 13201 lighting class specifies performance requirements (luminance, uniformity, glare, edge illumination), and the road surface R-table, together with luminaire photometry, provide the data required for accurate lighting calculations.

(i) Road geometry: Pole spacing, carriageway width, number of lanes, curbs, and medians.
(ii) Lighting class under EN 13201: M_k, with the required limits specified in Table 2—L_{req}, $U_{o,req}$, $U_{l,req}$, TI_{max}, and EIR_{req}.
(iii) Road surface type and R-table.
(iv) Luminaire photometry (Illuminating Engineering Society-format light distribution file).

2.2.2.2. Decision variables

The decision variables are calculated based on the following equation (Equation I):

$$x = (P, H, \theta) \quad \text{(I)}$$

where:

(i) P denotes the luminaire electrical power (equivalently, luminous flux/dimming level).
(ii) H signifies the mounting height.
(iii) θ represents the luminaire tilt angle.
(iv) Domain constraints are

$$P \in [P_{\min}, P_{\max}], \quad H \in [H_{\min}, H_{\max}], \quad \theta \in [\theta_{\min}, \theta_{\max}]$$

2.2.2.3. Objective function

To minimize installed power (or, equivalently, energy use per unit road length), the following equation is employed (Equation II):

$$\min_x f(x) = P \quad \text{(II)}$$

2.2.2.4. Constraints (EN 13201 class M_k)

Based on the photometric simulation, the design must meet the quantitative and qualitative criteria of street lighting according to EN 13201 for the relevant class Mk, including average luminance, overall and longitudinal uniformity, glare limitation (TI, accounting for veiling luminance Lv), edge illuminance ratio, and the geometric limits of the lighting system layout.

(i) Average road luminance: $L_{ave}(x) \geq L_{\text{req}}$ (III)

(ii) Overall uniformity: $U_o(x) = \dfrac{L_{\min}(x)}{L_{ave}(x)} \geq U_{o,\text{req}}$ (IV)

(iii) Longitudinal uniformity:

$$U_l(x) = \frac{L_{\text{min,along line}}(x)}{L_{\text{max,along line}}(x)} \geq U_{l,\text{req}} \quad \text{(V)}$$

(iv) Glare (threshold increment [*TI*]):

$$TI(x) = 65\,\frac{L_v(x)}{L_{ad}(x)^{0.8}} \leq TI_{\max} \quad \text{(VI)}$$

where L_v is veiling luminance from glare sources and $L_{ad} \approx L_{ave}$ for typical road viewing conditions.

(v) Edge illuminance ratio (if required):

$$EIR(x) = \frac{\overline{E}_{\text{outside edge lane}}(x)}{\overline{E}_{\text{inside edge lane}}(x)} \geq EIR_{\text{req}} \quad \text{(VII)}$$

(vi) Geometric limits:

$$H_{\min} \leq H \leq H_{\max}, \quad \theta_{\min} \leq \theta \leq \theta_{\max}, \quad S = \text{const} \quad \text{(VIII)}$$

2.2.2.5. Solving approach

Such lighting optimization tasks can be solved using specialized software tools, such as DIALux evo (DIAL GmbH, Germany). This software enables the solution of a constrained non-linear optimization problem, because the relationship between the decision variables (e.g., luminaire power, mounting height, tilt) and the objectives/constraints (e.g., L_{ave}, U_o, U_l, *TI*, and *EIR*) is non-linear. This problem can be classified as black-box optimization, as no analytical formulas are available for the objectives/constraints (e.g., L_{ave}, U_o)—they are obtained from the simulation software. In the simulation-based solution, the variables are restricted to discrete steps (e.g., height in 0.2 m increments, tilt in 1° increments), thereby forming a mixed-integer non-linear programming problem.

The constrained search approach includes the following steps:

(i) Use a global optimizer over (*P, H, θ*).
(ii) For each candidate:
(a) Set *P* via luminous flux.
(b) Set *H* and *θ*.
(c) Run the simulation → extract L_{ave}, U_o, U_l, *TI*, and *EIR*.
(d) Select the best feasible point with the lowest *P*.

Practical bounds and starting points used in the DIALux evo simulation are:

(i) *H*: 4–12 m (road dependent), step 0.2 m.
(ii) *θ*: 0–20° (per luminaire specification), step 1–2°.
(iii) *P*: From the minimum dimming level to nominal power (driver-specific steps from Table 4).

The process of modeling and optimization in DIALux evo for street lighting on a given street was carried out in the following sequence:

(i) Fix geometry, R-table, and pole spacing *S*.
(ii) Choose luminaire optics (fixed photometric file).
(iii) Run a coarse grid over (*H,θ*); for each pair, determine the minimum *P* that meets $L_{ave} \geq L_{req}$.
(iv) From the candidate solutions, check uniformities and *TI*; remove non-compliant cases.
(v) Fine-tune around the best points (local search) to obtain (*P, H, θ*) that satisfy all EN 13201 criteria.

In this study, and following the above-described methodology using DIALux evo (Figure 9), a multi-variant lighting modeling and optimization process was conducted for all streets with diverse geometrical characteristics in Pavlikeni and Byala Cherkva, involving the optimization of the power rating, mounting height, and tilt angle of the street LED luminaires.

For park lighting, the project included an LED luminaire with a rated power of 14.4 W, a luminous flux of 1,730 lm, and a luminous efficacy of 120.1 lm/W, with its light distribution shown in Figure 10. This luminaire is intended to replace the existing park fixtures mounted on 4.5-m-high poles in pedestrian zones in Pavlikeni, classified under lighting class P6.

A maintenance factor of *MF* = 0.81 was used in the lighting calculations, reflecting luminous flux depreciation to 90% of the initial value over the luminaire's lifetime (L90F10). If a luminaire with greater luminous flux depreciation is supplied, its electrical power must be proportionally increased. Conversely, for luminaires equipped with drivers that maintain constant luminous output over time (constant light output [CLO]), the required power may be reduced accordingly.

The LED street luminaires were mounted on existing poles made of tubular steel and reinforced concrete. The project included the replacement of existing park luminaires with new street-type LED luminaires on

Table 4. Main technical characteristics of light-emitting diode street luminaires used in optimized lighting calculations

Dimming level steps of the luminaire electric power									
Electric power (W)	10.8	16.6	20.5	22.0	25.0	28.5	34.5	41.0	50.0
Luminous flux (lm)	1,401	2,167	2,601	3,061	3,503	3,941	4,681	6,130	7,282
Luminous efficacy (lm/W)	129.7	130.6	126.9	139.1	140.1	138.3	135.7	149.5	145.6

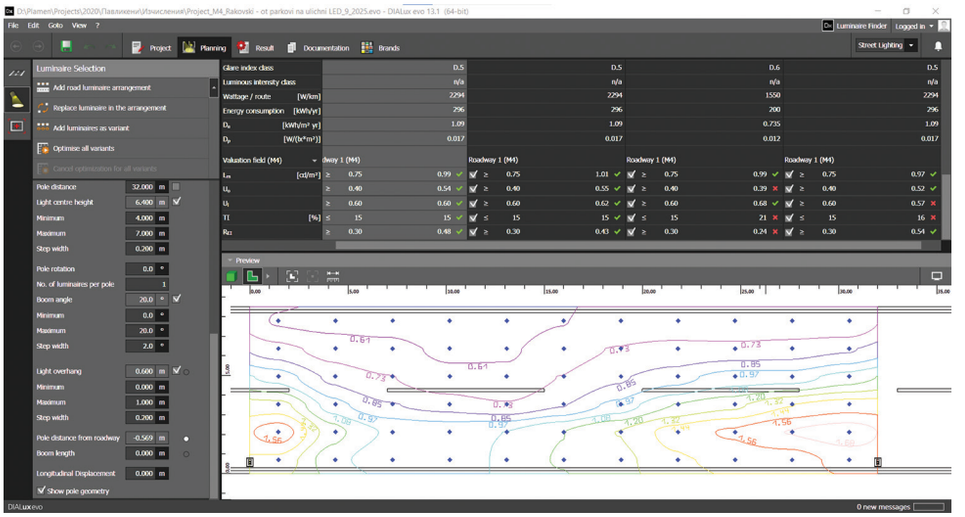


Figure 9. Multi-variant street lighting modeling and optimization in DIALux evo

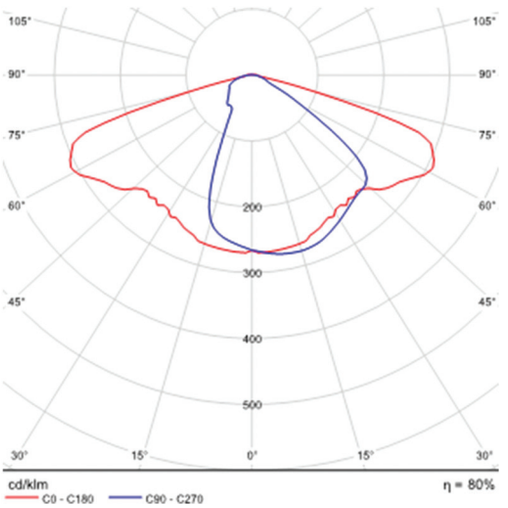


Figure 10. Light distribution of a park light-emitting diode luminaire

traffic streets of lighting classes M4, M5, and M6 in Pavlikeni.

Given that attempts to meet the regulatory requirements of the current European Union standard for traffic roads of lighting classes M4, M5, and M6 using park-type luminaires result in excessive glare beyond acceptable limits, this study proposed a technical solution involving the extension of the existing park poles and the installation of street-type LED luminaires (Figure 11). A maximum mounting height of 6.4 m was proposed when replacing park luminaires with new street LED luminaires on existing poles fitted with two- or three-arm brackets. A maximum mounting height of 5 m is proposed for poles without brackets. The pole extension details have been designed and specified in the Geometric Configuration columns of the tables presenting the results from the simulation calculations (Table 5).

Table 5 presents the achieved lighting performance indicators for a sample street of class M4 in Pavlikeni. The project includes detailed lighting calculations performed by specialized software[25,26]—DIALux evo—for all class M4 and M5 streets in Pavlikeni, M5-class streets in Byala Cherkva, as well as for the remaining M6- and P6-class streets based on generalized geometric configurations. The lighting calculations also incorporate two energy performance indicators introduced in BDS EN 13201—D_P and D_E. Table 5 is shown as an example, presenting the results from simulation calculations for all 32 streets and street groups with various geometric configurations and lighting classes.

Across multi-scenario optimization of lighting calculations using DIALux evo[27-29] for all streets in the two towns, the optimal luminaire types and rated power levels were determined for each individual street



Figure 11. Photographs illustrating the technical solution involving the extension of existing park poles and the installation of street-type light-emitting diode luminaires

segment. By updating the luminaire specifications and their respective power ratings in the graphical model developed during the energy audit, the accurate quantitative and energy performance parameters of the modernized lighting system were established.

A summary of the luminaire types, rated power, and quantities implemented in the modernized street lighting systems is provided in Table 6.

2.3. Implementation of a modern street lighting management and control system

Modern street lighting control systems use wireless[30] communication technologies based on global system for mobile communications (GSM)/general packet radio service (GPRS), Internet of Things,[31] and other smart systems for digital and cloud-based management.[32-34]

The control system was modernized by replacing the old power supply boxes (Figure 12) with new control and monitoring cabinets (CMCs) (Figure 13). These cabinets are equipped with the necessary protective, switching, and metering devices, as well as a GSM/GPRS controller-modem for communication with a centralized monitoring and control station running dedicated application software.

Communication between the CMCs and the centralized monitoring and control center is facilitated through the GSM network of a mobile operator, as illustrated in Figure 14.

The new street lighting control system must provide, at a minimum, the following functionalities:

(i) Remote switching of street lighting on and off from a central control (dispatcher) center.
(ii) Real-time (online) information on electricity consumption.
(iii) Alarm notifications in case of unauthorized connection to the street lighting network or unauthorized access to the lighting cabinet.
(iv) Information on non-functioning street luminaires, indicating the affected circuit branch and the number of defective units.
(v) Backup battery for autonomous emergency operation during prolonged power outages.
(vi) Archived data on the operational status of the street lighting system.

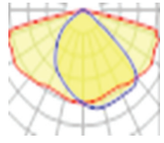
The system should also support the integration of additional functionalities, if needed, either through updates to the existing software modules, the addition of new ones, or by integrating new technical components. This would enable effective energy management for the street lighting system and facilitate planning and optimization of maintenance operations.

The project proposes dimming of the power and luminous flux of the LED luminaires, allowing for energy reduction through pre-programmed or remotely controlled LED drivers. This applies to streets of higher lighting classes, where luminaires can be dimmed to a certain percentage of their nominal power during nighttime periods with reduced traffic intensity. During these hours, the lighting class of the street is considered to temporarily shift to a lower class with less stringent requirements.

In the present project, dimming was implemented via pre-programmed drivers, reducing the luminaires' power output on streets of lighting classes M4 and M5 to 60% of their nominal power during the time period from 11 p.m. to 5 a.m.

The interface of the cloud-based control and monitoring software for the street lighting system in Pavlikeni is presented in Figure 15, and the power dimming process visualization module is shown in Figure 16.

Table 5. Achieved lighting performance indicators for a sample street of class M4 in the town of Pavlikeni

Street: "St. St. Cyril and Methodius" Town: Pavlikeni				**Geometric configuration**	**Standard lighting parameters for class M4 (BDS EN 13201:2016)**					**Energy performance indicators (BDS EN 13201:2016)**	
Lighting class: M4											
LED street luminaire parameters used in the lighting calculations					$L_m \geq 0.75$ cd/m^2	$U_o \geq 0.40$	$U_l \geq 0.60$	$f_{TI} \leq 15\%$	$R_{EI} \geq 0.30$		
Electric power (P), W	Luminous flux (Φ), lm	Efficacy (κ), lm/W	Light distribution type	• Roadway width: 8 m • Number of traffic lanes: 2 • Reflective road surface type: R3 • Pole spacing: 30 m • Luminaire arrangement: one-sided • Mounting height: 6.2 m • Tilt angle: 15° • Overhang: 0.5 m • Section length: 1,020 m	Achieved lighting performance indicators (with maintenance factor=0.81)						
					Average luminance (L_{ave}), cd/m^2	Overall uniformity (U_o)	Longitudinal uniformity (U_l)	Threshold increment (glare index; f_{TI}), %	Surround ratio (R_{EI})	D_p, W/(lx.m^2)	D_E, kWh/m^2.г
50	7,282	145.6	 Type 1		0.83	0.51	0.60	15	0.57	0.016	0.833

Abbreviation: LED: Light-emitting diode.

doi: 10.36922/AJWEP025310242

Table 6. Type, rated power, and number of luminaires in the modernized street lighting systems

Town	Flood-lights	Road type luminaires										Park type luminaires		Total number of street and park luminaires	Total installed electrical power, W
	LED power, W	LED power, W									Total number	CFL	LED		
	120	10.8	16.6	20.5	22	25	28.5	34.5	41	50		23	14.4		
Pavlikeni	16	78	807	113	36	61	77	59	50	28	1,325	-	52	1,377	29,221
Byala Cherkva	-	-	369	-	-	-	85	-	-	-	454	43	-	497	9,537
Total	16	78	1,176	113	36	61	162	59	50	28	1,779	43	52	1,874	38,758

Abbreviation: LED: Light-emitting diode.



Figure 12. Existing power supply box for street lighting with outdated protective and switching equipment

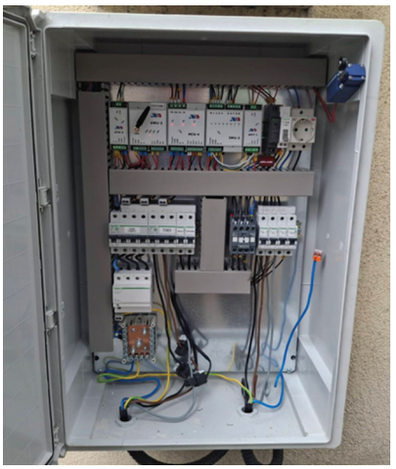


Figure 13. Modern control cabinet for street lighting with integrated global system for mobile communications/general packet radio service communication and monitoring

3. Evaluation of energy efficiency, financial savings, and environmental benefits of the proposed modernization

The calculations were prepared in connection with the main objective of the current investment working project—an application submitted by Pavlikeni municipality under the program "Renewable Energy, Energy Efficiency, Energy Security" of the European Economic Area Financial Mechanism 2014–2021, Procedure No. BGENERGY-2.001, titled "Rehabilitation and Modernization of Municipal Infrastructure—Systems for Outdoor Artificial Lighting in Municipalities." The calculated energy and economic indicators were comparable to those used in energy efficiency projects by leading researchers.[35-37]

In Bulgaria, the mandatory state regulation Ordinance No. E-RD-04-3 of May 4, 2016, titled "On eligible measures for the implementation of energy savings in final consumption, methods for demonstrating the energy savings achieved, requirements for assessment methodologies, and means of confirmation,"[23] is in force, according to which specialized methodologies, approved by the Bulgarian Sustainable Energy Development Agency, must be employed.

3.1. Energy and carbon dioxide savings calculations

The methodology for energy and CO_2 savings calculations, according to the national regulatory document[38], includes the sequential calculation of final energy savings at an end-user site (*FEStot*) (Equation IX), primary energy savings at an end-user site (*PEStot*) (Equation X), and CO_2 emission reductions (Equation XI).

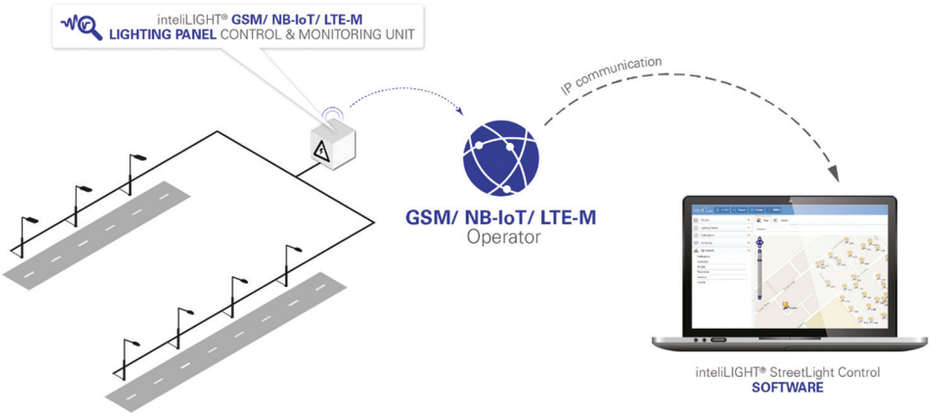


Figure 14. System architecture of centralized street lighting control via global system for mobile communications (GSM)/general packet radio service communication
Abbreviations: IoT: Internet of Things; LTE-M: Long-term evolution machine type communication.

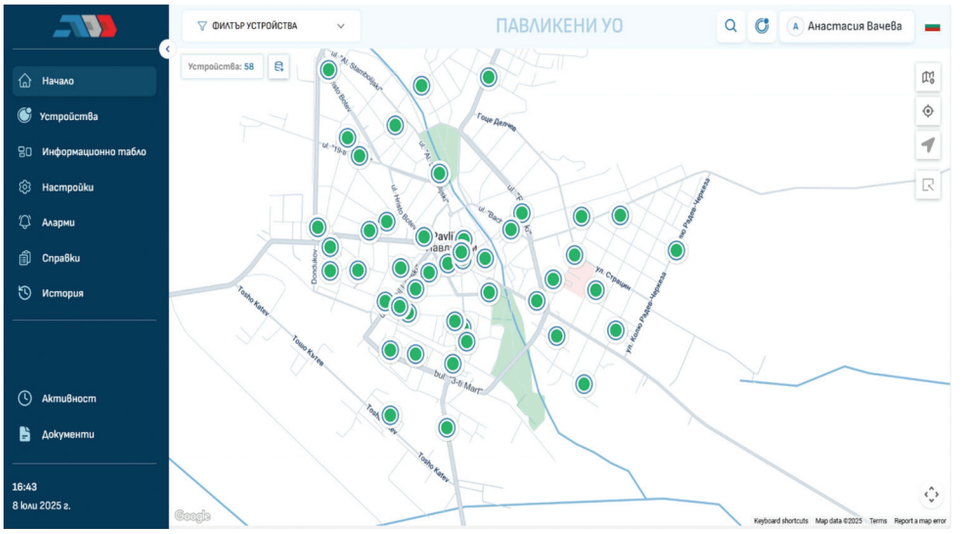


Figure 15. Interface of the cloud-based street lighting control and monitoring system in Pavlikeni

3.1.1. Energy savings at an end-user site

$$FEStot = \frac{(N_{ref,old}P_{old}\ k_{pra,old} - N_{ref,new}P_{new}k_{pra,new})T_{year}}{1000},[MWh/year] \quad \text{(IX)}$$

where:

(i) *FEStot*: Energy savings at an end-user site (MWh/year).

(ii) N_{ref_old}, N_{ref_new}: Number of replaced luminaires in the existing installation and number of new luminaires replacing them, which meet the current normative lighting requirements.

(iii) P_{old}, P_{new}: Nominal power (kW) of the replaced luminaire and of the new luminaire, respectively, both satisfying the updated normative lighting requirements. The power of the new luminaire should reflect the actual operational values of its maintenance (operational) elements.

(iv) $k_{pra,\ old}$, $k_{pra,\ new}$: Coefficients accounting for losses in the control gear of the existing and replacement luminaires, respectively, including potential losses from CLO-type control devices.

(v) T_{year}: Annual operating time (utilization) of the lighting system (hours/year).

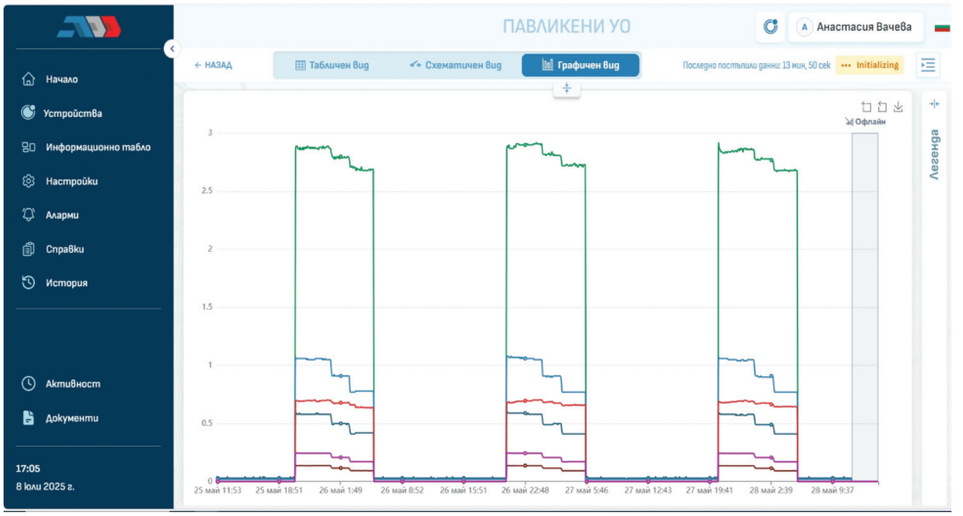


Figure 16. Visualization module for the luminaire power dimming process

3.1.2. Primary energy savings at an end-user site

$$PEStot = FEStot\ e_p, [MWh / year] \quad (X)$$

where:
(i) *PEStot*: Primary energy savings at an end-user site (MWh/year).
(ii) *FEStot*: Total final energy savings (MWh/year).
(iii) e_p: Primary energy factor from Table 7.

3.1.3. Carbon dioxide emission reductions

$$CO_2 = \frac{FEStot\ f_i}{1000}, [t\ CO_2 / year] \quad (XI)$$

where:
(i) CO_2: CO_2 emission reduction (t CO_2/year).
(ii) *FEStot*: Total final energy savings (kWh/year).
(iii) f_i: Ecological equivalent coefficient of energy (fuel) (g CO_2/kWh) from Table 7.

4. Energy, economic, and environmental impact assessment of the street lighting modernization project

Based on the energy efficiency measures and technical solutions proposed in the project—including the implementation of new LED lighting, optimized control and operational modes of the street lighting system, and the bill of quantities and costs—as well as the findings of the *Energy Efficiency Audit Report* for the outdoor artificial lighting systems in Pavlikeni and Byala Cherkva, calculations were performed to determine the achieved energy and economic performance indicators of the project. These indicators are summarized in Table 8. The approach is consistent with similar large-scale modernization initiatives aimed at reducing energy consumption and improving lighting infrastructure.[39-41]

For the "Renewable Energy, Energy Efficiency, Energy Security" Program, Table 9 presents the

Table 7. Reference values of the conversion factor, considering losses from extraction, production, and transmission of energy (including fuels), and reference values of the coefficient of ecological equivalent of energy

Type of energy resource/energy	Conversion factor from FES to PES, considering energy losses	Ecological equivalent coefficient
	e_p	f_i, gCO_2/kWh
Industrial gas oil, diesel	1.10	267
Fuel oil	1.10	279
Natural gas	1.10	202
Propane-butane	1.10	227
Black coal	1.20	341
Lignite/brown coal	1.20	364
Anthracite coal	1.20	354
Coal briquettes	1.25	351
Firewood, pellets	1.05	43
Heat from district heating	1.30	290
Electrical energy	3.00	819

Abbreviations: FES: Final energy saving; PES: Primary energy saving.

Table 8. Results of energy and economic calculations for the current investment project

Parameter	Unit	Town		Total
		Pavlikeni	Byala Cherkva	
Energy consumption before the project	kWh/year	C532,355	158,138	690,493
Energy consumption after the project	kWh/year	105,385	36,025	141,411
Investment (new luminaires)	BGN	354,452	113,257	467,709
Investment (control system, cabinets)	BGN	76,500	16,500	93,000
Investment (PV-powered luminaires)	BGN	7,200	-	7,200
Installation works	BGN	64,249	14,581	78,830
Total investment (+5% unforeseen costs)	BGN	528,282	151,733	680,015
Energy savings	kWh/year	426,970	122,113	549,082
Energy savings percentage	%	80.2	77.2	79.5
Average electricity price	BGN/kWh	0.1991	0.1991	0.1991
Cost savings	BGN/year	85,027	24,318	109,344
Payback period	years	6.21	6.24	6.22
CO_2 emissions saved	tCO_2/year	1,049	300	1,349
Investment efficiency	BGN/tCO_2	503.57	505.72	504.05

Abbreviations: CO_2: Carbon dioxide; PV: Photovoltaic.

Table 9. "Renewable Energy, Energy Efficiency, Energy Security" program indicators

Indicator	Unit	Pavlikeni	Byala Cherkva	Total
Estimated annual CO_2 reduction	tCO_2/year	1,049	300	1,349
Estimated annual energy savings	MWh/year	427	122	549
Estimated annual cost savings	EUR/year	43,474	12,433	55,907
People benefiting (men)	persons	4,569	820	5,389
People benefiting (women)	persons	4,893	849	5,742
Total beneficiaries	persons	9,462	1,669	11,131

Abbreviations: CO_2: Carbon dioxide; EUR: Euro.

indicators illustrating the contribution of the project to improved energy efficiency in buildings, industry, and municipalities.

The analysis of the results presented in Table 9 demonstrates that, through detailed project design and optimization of the energy-saving measures proposed in the *Energy Efficiency Audit Report*, the project implemented technical solutions that significantly improve the values of the technical, economic, and program-specific indicators defined by the "Renewable Energy, Energy Efficiency, Energy Security" program under the European Economic Area Financial Mechanism 2014–2021, Procedure No. BGENERGY-2.001, titled "Rehabilitation and Modernization of Municipal Infrastructure—Systems for Outdoor Artificial Lighting in Municipalities."

5. Conclusion

The LED retrofit project implemented in the municipalities of Pavlikeni and Byala Cherkva highlights the transformative potential of high-efficiency lighting technologies combined with intelligent control and management systems. Achieving over 79% energy savings, substantial CO_2 emission reductions, and a favorable economic payback period, the initiative exemplifies a holistic approach to sustainable public infrastructure. This study offers a replicable blueprint for municipalities across Central and Eastern Europe and holds relevance for urban planners and energy efficiency stakeholders worldwide seeking scalable solutions that align with contemporary environmental standards.

Acknowledgments

This research was funded by the European Regional Development Fund under the Operational Program "Scientific Research, Innovation, and Digitization for Smart Transformation 2021–2027," Project CoC "Smart Mechatronics, Eco- and Energy Saving Systems and Technologies" (BG16RFPR002-1.014-0005).

Funding

The design and implementation of the energy-efficient LED retrofit and advanced control project in the towns of Pavlikeni and Byala Cherkva are funded by the Municipality of Pavlikeni through the European Union's National Recovery and Sustainability Plan for the Republic of Bulgaria.

Conflict of interest

The authors declare they have no competing interests.

Author contributions

Conceptualization: Plamen Tsankov
Formal analysis: Plamen Tsankov, Milko Yovchev
Investigation: All authors
Methodology: Plamen Tsankov
Writing – original draft: All authors
Writing – review & editing: Plamen Tsankov

Availability of data

Data are available from the corresponding author upon reasonable request.

References

1. Pardo-Bosch F, Blanco A, Sesé E, Ezcurra F, Pujadas P. Sustainable strategy for the implementation of energy efficient smart public lighting in urban areas: Case study in San Sebastian. *Sustain Cities Soc*. 2022;76:103454. doi: 10.1016/j.scs.2021.103454
2. Kostic A, Kremic M, Djokic L, Kostic M. Light-emitting diodes in street and roadway lighting-a case study involving mesopic effects. *Light Res Tech*. 2013;45(2):217-231. doi: 10.1177/1477153512440771
3. Valetti L, Piccablotto G, Taraglio R, Pellegrino A. Long-term monitoring campaign of LED street lighting systems: Focus on photometric performances, maintenance and energy savings. *Sustainability*. 2023;15(24):16910. doi: 10.3390/su152416910
4. Aghemo C, Pellegrino A, Fisanotti D, *et al*. Environmental and energy performance of public lighting installations: Results of a measurement campaign. In: *Proceedings of EEEIC/I&CPS Europe*. 2018. p. 1-6. doi: 10.1109/eeeic.2018.8494348
5. Belloni E, Buratti C, Lunghi L, Martirano L. A new street lighting control algorithm based on forecasted traffic data for electricity consumption reduction. *Light Res Technol*. 2023;56(5):481-501. doi: 10.1177/14771535231194536
6. Petritoli E, Leccese F, Pizzuti S, Pieroni F. Smart lighting as basic building block of smart city: An energy performance comparative case study. *Measurement*. 2019;136:466-477. doi: 10.1016/j.measurement.2018.12.095
7. Muthu SS, editor. Energy footprint and sustainability. In: *Case Studies*. Cham: Springer; 2024. doi: 10.1007/978-3-031-63057-6
8. Escolar S, Carretero J, Marinescu MC, Chessa S. Estimating energy savings in smart street lighting by using an adaptive control system. *Int J Distrib Sens Netw*. 2014;10:971587. doi: 10.1155/2014/971587
9. Barentine JC, Kundracik F, Kocifaj M, *et al*. Recovering the city street lighting fraction from skyglow measurements in a large-scale municipal dimming experiment. *J Quant Spectrosc Radiat Transfer*. 2020;253:107120. doi: 10.1016/j.jqsrt.2020.107120
10. Barentine JC, Walker CE, Kocifaj M, *et al*. Skyglow changes over Tucson, Arizona, resulting from a municipal LED street lighting conversion. *J Quant Spectrosc Radiat Transfer*. 2018;212:10-23. doi: 10.1016/j.jqsrt.2018.02.038
11. Sędziwy A, Basiura A, Wojnicki I. Roadway lighting retrofit: Environmental and economic impact of greenhouse gases footprint reduction. *Sustainability*. 2018;10(11):3925. doi: 10.3390/su10113925
12. Tähkämö L, Halonen L. Life cycle assessment of road lighting luminaires - comparison of lightemitting diode and highpressure sodium technologies. *J Clean Prod*. 2015;93:234-242. doi: 10.1016/j.jclepro.2015.01.025
13. Tsankov PT. Solar energy and lighting in Bulgaria. In: Pavlovic T, editor. *The Sun and Photovoltaic Technologies. Green Energy and Technology*. Cham: Springer; 2020. p. 323-382. doi: 10.1007/978-3-030-22403-5_6
14. Platikanov S, Tsankov P. *Design and Modernization of Road Lighting in Bulgarian Cities, Seventh International Forum Lux junior, Ilmenau, Germany*; 2005.
15. *Energy Saving Outdoor Lighting (ESOLi)*. Available from: https://bserc.eu/en/energy-efficiency-and-energy-services/energy-saving-outdoor-lighting-esoli [Last

accessed on 2025 Aug 24].
16. Karakosta C, Vryzidis I. Cost-effective energy retrofit pathways for buildings: A case study in greece. *Energies*. 2025;18(15):4014.
doi: 10.3390/en18154014
17. Pasolini G, Toppan P, Toppan A, *et al*. Comprehensive assessment of context-adaptive street lighting: Technical aspects, economic insights, and measurements from large-scale, long-term implementations. *Sensors (Basel)*. 2024;24(18):5942.
doi: 10.3390/s24185942
18. Kostic M, Djokic L. Recommendations for energy efficient and visually acceptable street lighting. *Energy*. 2009;34(10):1565-1572.
doi: 10.1016/j.energy.2009.06.056
19. Sikora R, Markiewicz P, Korzeniewska E. Evaluation of maintenance and modernization of road lighting systems using energy performance indicators. *Energies*. 2025;18(16):4328.
doi: 10.3390/en18164328
20. *Methodology for Detailed Energy Audit of Public Lighting System*. Available from: https://managenergy.ec.europa.eu/document/download/1d44cd56-bdb0-44f1-b09c-3e15ff2d52b1_en?filename=DL_3_1a_Standardised-Methodology_arranged-1%20%281%29.pdf&prefLang=sl [Last accessed on 2025 Aug 24].
21. Ministry of Energy, Republic of Bulgaria. *Ordinance No. E-RD-04-05/04.10.2016 for Determining the Energy Consumption Indicators, the Energy Performance of Enterprises, Industrial Systems and Outdoor Artificial Lighting Systems, as Well as for Determining the Conditions and Procedures for Carrying Out an Energy Efficiency Audit and Preparing an Energy Savings Assessment*. Sofia: State Gazette; 2016. Available from: https://dv.parliament.bg/DVWeb/showMaterialDV.jsp?idMat=108084 [Last accessed on 2025 Aug 24].
22. European Committee for Standardization (CEN). EN 16247:2022. *Energy Audits*. Brussels: CEN; 2022. Available from: https://bds-bg.org/en/project/show/bds: proj:109839 [Last accessed on 2025 Aug 24].
23. Ministry of Energy, Republic of Bulgaria. *Ordinance N○ E-RD-04-3 Of 4.05.2016 on Eligible Measures for the Implementation of Energy Savings in Final Consumption, Ways of Demonstrating the Energy Savings Achieved, the Requirements for their Assessment Methodologies and Ways of Confirmation*. Sofia: State Gazette; 2016. Available from: https://www.seea.government.bg/documents/naredba_erd043_ot_4052016t.pdf [Last accessed on 2025 Aug 24].
24. European Committee for Standardization (CEN). *EN 13201-2:2016 Road Lighting - Part 2: Performance Requirement*. Brussels: CEN; 2016. Available from: https://bds-bg.org/en/project/show/bds: proj:90712 [Last accessed on 2025 Aug 24].
25. Wojnicki I, Komnata K, Kotulski L. Comparative study of road lighting efficiency in the context of CEN/TR 13201 2004 and 2014 lighting standards and dynamic control. *Energies*. 2019;12(8):1524.
doi: 10.3390/en12081524
26. Valencia Pavón NG, Aguila Téllez A, García Torres M, Rojas Urbano J, Krishnan N. Optimal selection of distribution, power, and type of luminaires for street lighting designs using multi-criteria decision model. *Energies*. 2024;17(9):2194.
doi: 10.3390/en17092194
27. Wicaksono HIS, Abdullah AG, Hakim DL. Optimizing public street lighting and redesign of public road lighting based on DIALux and fuzzy logic. *IOP Conf Ser Mater Sci Eng*. 2021;1098:042013.
doi: 10.1088/1757-899X/1098/4/042013
28. Jamaludin MH, Ismail WZ, Husini EM, Bahror NA. Study of LED retrofit lamps in HSPV luminaires based on photometric method for road lighting. *Pertanika J Sci Technol*. 2024;32(3):1187-1201.
doi: 10.47836/pjst.32.3.1
29. Zima K, Ciepłucha W. Efficiency analysis of roadway lighting replacement in a selected polish municipality. *Appl Sci*. 2023;13(5):3257.
doi: 10.3390/app13053257
30. Park S, Kang B, Choi M, Jeon S, Park S. A micro-distributed ESS-based smart LED streetlight system for intelligent demand management of the micro grid. *Sustain Cities Soc*. 2018;39:801-813.
doi: 10.1016/j.scs.2017.10.023
31. Xiaoling Z, Jianping Z. Design of intelligent light control system based on NB-IoT. In: *Proceedings of MLCSS*. 2022. p. 346-349.
doi: 10.1109/mlcss57186.2022.00069
32. Selvalakshmi CB, Raja Alagurishi N, Aravind T. Iot based adaptive street lighting system for rural area. In: *Proceedings of ICDECS*. 2024. p. 1-4.
doi: 10.1109/ICDECS59733.2023.10502780
33. Ożadowicz A, Grela J. Energy saving in the street lighting control system-a new approach based on the EN-15232 standard. *Energy Effic*. 2017;10:563-576.
doi: 10.1007/s12053-016-9476-1
34. Kumari MG, Aarthi M, Elakkia J, Jayasutha V. Design and implementation of smart street light management system. *J Next Gener Technol*. 2024;4(2):1-8.
35. Szafranko E. Assessment of the economic efficiency of energy-saving projects, methodology based on simple and compound methods. *Energy Sci Eng*. 2022;10:423-438.
doi: 10.1002/ese3.1032
36. Chen TA. Technical and economic evaluation of energy-saving measures. In: *Energy Saving and Carbon Reduction*. Berlin: Springer; 2022. p. 465-496.
doi: 10.1007/978-981-19-5295-1_11
37. Polyvianchuk A, Malyarenko V, Kapustenko P, Polyvianchuk N, Petruk H, Arsenyeva O. Estimation of energy, economic and environmental efficiency for

renovation of building heating system. *Clean Technol Envir*. 2025.
doi: 10.1007/s10098-025-03150-8

38. Ministry of Energy, Republic of Bulgaria. *Methodology for Assessing Energy Savings when Implementing Energy Saving Measures in Artificial Lighting Systems in Industrial Systems, Approved by Ordinance No. E-rd-16-96/15.02.2022*. Available from: https://www.seea.government.bg/documents/Metodika_9.rar [Last accessed on 2025 Aug 24].
39. European Commission. *Support for Energy-Efficient Street Lighting Systems - Pavlikeni Municipality*; 2023. Available from: https://commission.europa.eu/projects/support-energy-efficient-street-lighting-systems-pavlikeni-municipality_en [Last accessed on 2025 Aug 24].
40. Borba.BG. *Energy-Efficient Lighting Worth Nearly Bgn 1 Million in Pavlikeni and Byala Cherkva*; 2024. Available from: https://www.borbabg.com/2024/01/22/energospestyavashho-osvetlenie-za-blizo-1-mln-lv-pravyat-v-pavlikeni-i-byala-cherkva [Last accessed on 2025 Aug 24].
41. Diamant.BG. *Energy Efficiency for Outdoor Artificial Lighting Systems*; 2025. Available from: https://diamant.bg/en/za-sistemi-za-vanshno-izkustveno-osvetlenie [Last accessed on 2025 Aug 24].

Asian Journal of Water, Environment and Pollution. Vol. 22, No. 6 (2025), pp. 198-209.
doi: 10.36922/AJWEP025320249

ORIGINAL RESEARCH ARTICLE

Stage-wise performance evaluation of the Kalobe waste stabilization ponds in Mbeya, Tanzania: Efficiency in organic load and nutrient removal

Eline Gerson[1,2], Gislar E. Kifanyi[1], Omary R. Shegwando[1,2], and Fredrick Ojija[3]*

[1]Department of Civil Engineering, College of Engineering and Technology, Mbeya University of Science and Technology, Mbeya, Tanzania
[2]Department of Technical, Mbeya Water Supply and Sanitation Authority, Mbeya, Tanzania
[3]Department of Earth Sciences, College of Science and Technical Education, Mbeya University of Science and Technology, Mbeya, Tanzania
***Corresponding author:** Fredrick Ojija (fredrick.ojija@must.ac.tz)

Received: August 9, 2025; Revised: August 29, 2025; Accepted: September 3, 2025; Published online: October 3, 2025

Abstract: Globally, waste stabilization ponds (WSPs) in warm climates have demonstrated high treatment efficiencies for organic matter and suspended solids. This study evaluates the stage-wise performance and overall treatment efficiency of the Kalobe WSPs in Mbeya city, Tanzania, which treat approximately 15,000–18,000 m^3/day of mixed domestic and industrial wastewater, compared with a design capacity of 28,800 m^3/day. The system comprises anaerobic, facultative, and maturation ponds operating in parallel. Field sampling and laboratory analysis were conducted to determine pollutant concentrations across each treatment stage, focusing on key parameters including biochemical oxygen demand (BOD), 5-day, chemical oxygen demand (COD), total suspended solids (TSSs), ammonia, nitrite, and total dissolved solids (TDS). Results revealed that while the WSP system demonstrated high removal efficiencies for organic and solid pollutants, achieving reductions of 58.1% for BOD, 87.3% for COD, and 87.2% for TSS, its performance in nutrient and dissolved solids removal remained limited. Ammonia was moderately reduced (80.5%), whereas nitrite and TDS exhibited low removal efficiencies of 17.4% and 13.7%, respectively. The final effluent BOD (39 mg/L) and COD (78 mg/L) exceeded Tanzania's national discharge standards, indicating partial non-compliance. The study also found that flow variations, particularly from industrial contributors such as Pepsi and Tanzania Breweries Limited, introduced intermittent hydraulic shocks, which may impair treatment consistency. The findings highlight the need for system upgrades, enhanced industrial pre-treatment enforcement, and the integration of post-treatment units to improve nutrient polishing. Overall, while Kalobe WSPs remain a cost-effective solution, strategic interventions are necessary to ensure sustained regulatory compliance and environmental protection.

Keywords: Waste stabilization ponds; Treatment efficiency; Organic load reduction; Nutrient removal; Anaerobic ponds; Facultative ponds; Maturation ponds

1. Introduction

Effective wastewater treatment is essential for safeguarding public health and environmental quality, particularly in urban centers of low- and middle-income countries where infrastructure expansion often lags behind population growth.[1-3] Urban wastewater management in Sub-Saharan Africa is often constrained by limited financial resources, poor planning, and outdated infrastructure, leading to frequent treatment failures and environmental contamination.[4] Waste stabilization ponds (WSPs) have gained prominence as an affordable, low-maintenance solution for municipal wastewater treatment in such contexts due to their reliance on natural treatment mechanisms, minimal operational requirements, and resilience to hydraulic and organic load fluctuations.[5,6] Their design and application follow well-established principles suited to tropical climates, making them ideal for many Sub-Saharan African countries.[7,8]

WSPs are widely adopted in developing regions because of their simple operation and ability to handle variable influent loads without the need for complex mechanical equipment.[6] In Tanzania, many urban areas rely on WSPs as the primary treatment technology. Mbeya city, located in the southern highlands of Tanzania, is served by the Kalobe WSPs, which treat a mixture of domestic and industrial wastewater. The system was designed to accommodate 28,800 m^3/day of wastewater; however, actual inflows vary between 15,000 and 18,000 m^3/day depending on rainfall and industrial activity. Major contributors to the influent load include large beverage industries such as Tanzania Breweries Limited (TBL), Coca-Cola Kwanza, and Pepsi, which are required to pre-treat their wastewater before discharging it into the municipal system.[9] However, evidence suggests that these pre-treatment processes are inconsistently effective, resulting in high influent organic and nutrient loads that compromise the WSP's performance.[10,11]

The Kalobe WSP system comprises a series of anaerobic, facultative, and maturation ponds arranged sequentially. These primary units are complemented by a preliminary screening chamber, grit channel, sludge drying beds, and a natural wetland that serves as a polishing component. Anaerobic ponds facilitate sedimentation and biological degradation under anoxic conditions, while facultative ponds support both aerobic and anaerobic processes. Maturation ponds provide final polishing, primarily targeting pathogen and nutrient reduction before discharge. While the system is theoretically capable of achieving significant reductions in biochemical oxygen demand (BOD), chemical oxygen demand (COD), and total suspended solids (TSSs), its performance in terms of nutrient removal and final effluent quality has raised concerns in recent years.[7,12]

Globally, WSPs in warm climates have demonstrated high treatment efficiencies for organic matter (BOD, COD) and suspended solids. However, challenges persist in nutrient and pathogen removal.[6,7,13] In Sub-Saharan cities, treated effluent from WSPs is sometimes reused for irrigation and aquaculture, necessitating stricter effluent standards to protect public health.[14] Ammonia removal in WSPs is often temperature-dependent, and without adequate aeration or nitrification steps, most ammonia persists in the final effluent.[15] Regular sludge removal and continuous influent monitoring are essential to sustain WSP performance and prevent pond overloading.[7] At Kalobe WSPs, elevated levels of BOD, total dissolved solids (TDS), and nutrients in the final effluent indicate that process inefficiencies and intermittent shock loads from industrial discharges may be limiting the system's ability to meet Tanzania's effluent discharge standards.[16]

This study aims to assess the stage-wise performance of the Kalobe WSPs using field data collected at the inlet and outlet points of the anaerobic, facultative, and maturation ponds. Six key parameters, which are BOD, COD, TSS, ammonia (NH_3–N), nitrite (NO_2^-–N), and TDS, were analyzed to determine individual and cumulative removal efficiencies. The study further examines how flow variability, influent composition, and industrial contributions affect treatment outcomes. Findings from this evaluation are expected to inform future infrastructure upgrades, industrial compliance enforcement, and integration of tertiary treatment options to improve the overall system efficiency.

2. Materials and methods

2.1. Description of the study area

The Kalobe WSPs are located at 8°55'S, 33°28'E (UTM Zone 36S; Easting 9,014,865.14 m; Northing 544,767.03 m) in Mbeya city, situated in the southern highlands of Tanzania. This study was conducted during the dry season (April 2025); therefore, the results should be interpreted as baseline dry-season conditions rather than a full annual performance assessment. The facility receives wastewater from both municipal sources and major beverage industries, including TBL, Pepsi, and Coca-Cola Kwanza. The system comprises two anaerobic ponds, four facultative ponds, and one maturation pond,

which operate in parallel to allow flexible hydraulic distribution and enhance treatment performance under variable loading conditions. This configuration enables the ponds to accommodate fluctuating industrial flows by distributing influent across multiple units rather than operating strictly in series.

Figure 1 presents the location of the study area. Photographs of the anaerobic, facultative, and maturation ponds are provided in Figure 2 to enhance visualization of the treatment process. In addition, Figure 3 illustrates the layout of the Kalobe WSP system.

The treatment process comprises three unit operations arranged as parallel trains, with serial flow within each train: Two units of anaerobic ponds (for primary sedimentation and anaerobic digestion under oxygendeficient conditions), four units of facultative ponds (for combined aerobic–anaerobic treatment, further organic degradation, suspended solids removal, and algal–bacterial oxygen transfer), and one unit of maturation pond (for final polishing and pathogen reduction before discharge). In addition, a screening chamber, a grit channel, sludge drying beds, and a natural wetland serve as preliminary and tertiary treatment components. This layout supports flexible influent distribution across ponds while maintaining stage-wise treatment within each train. Figure 3 shows the schematic layout of WSP.

2.2. Methods

2.2.1. Sampling strategy

To evaluate the stage-wise and overall performance of the Kalobe WSP system, a structured sampling strategy was developed to assess influent and effluent quality across each treatment stage. Composite grab samples were collected from four critical points within the system: The inlet point, located just upstream of the anaerobic ponds, representing untreated domestic and industrial influent; the anaerobic pond outlet, reflecting conditions after primary sedimentation and anaerobic digestion; the facultative pond outlet, situated downstream of the aerobic–anaerobic hybrid treatment zones; and the maturation pond outlet, representing the final effluent before environmental discharge.

Sampling followed the guidelines outlined by the American Public Health Association (APHA) for wastewater quality monitoring.[17] A total of 12 composite samples per point were collected over 4 weeks (May–June), covering Monday, Wednesday, and Friday each week, to account for weekly fluctuations and peak industrial discharges, a practice supported by previous WSP studies.[6,16] This 4-week monitoring period corresponds to the dry season baseline; while it provides robust insights under relatively stable hydraulic conditions, it does not capture wet-season variability. This limitation is therefore explicitly acknowledged

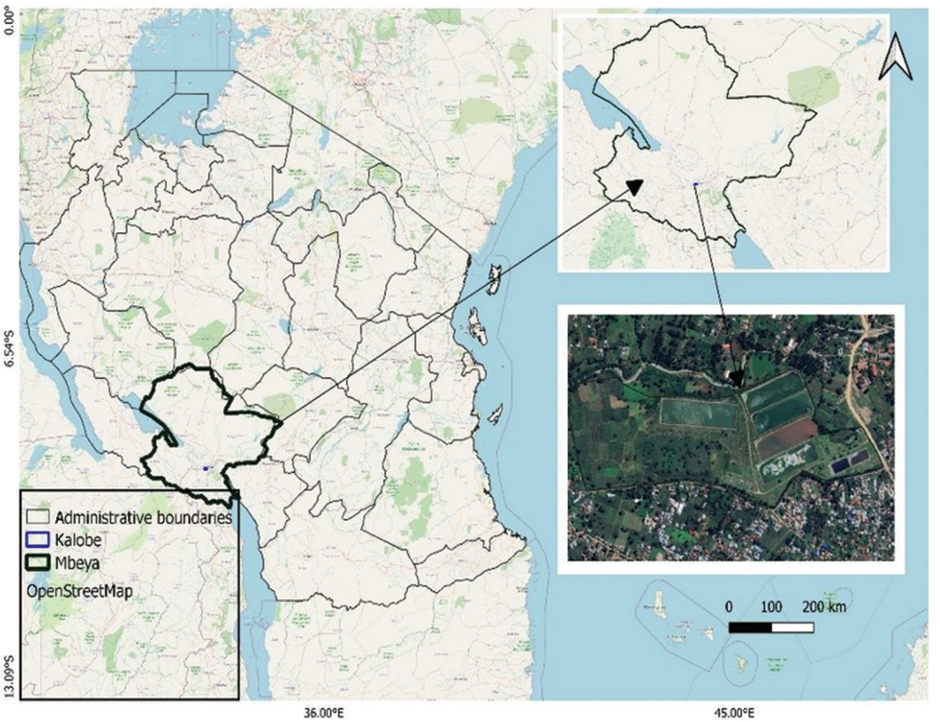


Figure 1. Location of Mbeya municipal waste stabilization ponds

in the study's conclusions. Samples were collected in sterilized high-density polyethylene bottles, stored in portable coolers at 4°C, and transported within 2 h to the Mbeya Water Quality Laboratory for analysis. Field parameters such as temperature, odor, color, and the presence of scum were also documented onsite using standardized visual indicators.[5] This strategy ensured representative and reliable data for calculating removal efficiencies and understanding temporal and spatial pollutant dynamics within the WSP system.

2.2.2. Parameters measured

The performance of the Kalobe WSP system was assessed using six key physicochemical parameters, selected based on their regulatory importance and relevance to both domestic and industrial wastewater monitoring. These parameters provide insight into organic load, solids content, and nutrient removal efficiency across the pond system.



Figure 2. Kalobe waste stabilization ponds. (A) Anaerobic ponds; (B) Facultative ponds; (c) Maturation pond.

The parameters measured included BOD, 5-day (BOD_5), which indicates the concentration of biodegradable organic matter and serves as a key measure of wastewater strength and treatment efficiency; COD, representing the total quantity of both biodegradable and non-biodegradable organic compounds; TSS, reflecting particulate matter that can settle or be filtered, and therefore indicating sedimentation performance; NH_3–N, a primary form of nitrogen relevant for assessing nitrification potential and nutrient removal; NO_2^-–N, an intermediate compound in the nitrogen cycle, whose presence can signal incomplete nitrification; and TDS, which indicate the ionic content of wastewater and may reflect industrial salt contributions or mineral solubilization.

The selection of these parameters was based on standard wastewater treatment performance indicators outlined by APHA.[17] and in accordance with Tanzanian environmental regulations.[18] Furthermore, these parameters are widely used in evaluating the efficiency of WSPs in tropical environments.[6,16] All parameters were analyzed at each of the four designated sampling points—raw influent, anaerobic pond outlet, facultative pond outlet, and final maturation pond outlet. This approach enabled the calculation of both stage-wise and overall removal efficiencies.

2.2.3. Instrumentation and laboratory methods

The physicochemical parameters (Table 1) were analyzed using standard procedures outlined in the Standard Methods for the Examination of Water and Wastewater.[17] Analyses were conducted at the Mbeya Zonal Water Quality Laboratory under controlled conditions, immediately after sample delivery, to ensure accuracy and prevent sample deterioration.

All equipment was calibrated before use using certified standards, and measurements were conducted in triplicate to ensure reproducibility. Quality assurance and control protocols were followed, including the use

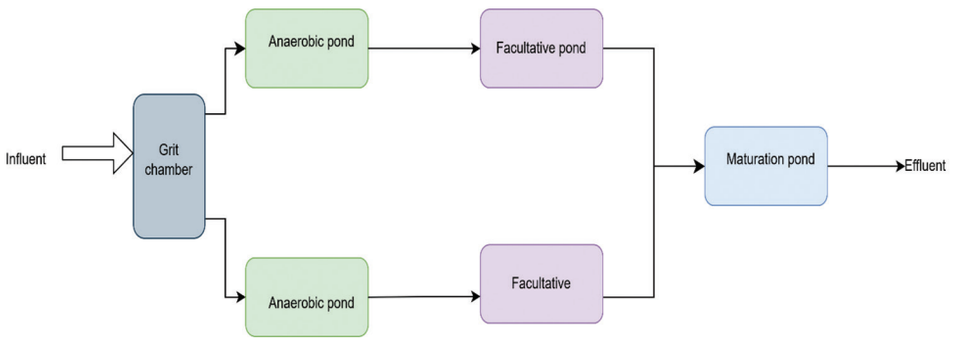


Figure 3. Schematic layout of Kalobe waste stabilization ponds.

Table 1. Analytical instruments and methods used for the analysis of wastewater quality parameters

Parameter	Analytical method	Standard method reference	Instrument used	Detection wavelength/output
BOD_5 (mg/L)	5-day incubation, dilution method	5210 B (APHA, 2017)[17]	BOD incubator+DO meter (HANNA HI9147)	DO depletion (mg/L)
COD (mg/L)	Closed reflux, colorimetric	5220 D (APHA, 2017)[17]	COD reactor (Lovibond®)+ spectrophotometer	600 nm
TSS (mg/L)	Gravimetric (drying at 105°C)	2540 D (APHA, 2017)[17]	Glass fiber filters+ Analytical balance	Mass difference (mg)
Ammonia (mg/L)	Nesslerization	4500-NH_3 C (APHA, 2017)[17]	UV-vis spectrophotometer (Hach DR 6000)	425 nm
Nitrite (mg/L)	Diazotization	4500-NO_2 B (APHA, 2017)[17]	UV-vis spectrophotometer (Hach DR 6000)	543 nm
TDS (mg/L)	Conductivity measurement	2540 C (APHA, 2017)[17]	TDS meter (Hanna HI 2300)	µS/cm converted to mg/L

Abbreviations: APHA: American Public Health Association; BOD_5: Biochemical oxygen demand, 5-day; COD: Chemical oxygen demand; DO: Dissolved oxygen; TDS: Total dissolved solids; TSS: Total suspended solids; UV-vis: Ultraviolet–visible light.

of blanks, duplicates, and spiked samples to detect contamination or analytical drift. These procedures ensured that all data collected were scientifically valid and comparable to those from other peer-reviewed studies of WSP systems in similar climatic and operational settings.[7,5]

2.3. Flow measurement and load calculations

2.3.1. Flow estimation

The Kalobe WSP system is designed to treat 28,800 m^3/day, but actual influent volumes range from 15,000 to 18,000 m^3/day, as recorded at the main inlet chamber using V-notch weirs and visual log sheets maintained by plant operators. Flow fluctuations are primarily attributed to variable domestic discharge patterns and irregular industrial loading from TBL, Coca-Cola Kwanza, and Pepsi. To estimate the average daily flow during the sampling period, recorded values over four representative weeks were averaged to obtain a typical daily influent flow of 16,500 m^3/day, aligning with seasonal operational averages reported in previous internal documents. To account for reporting variability, an uncertainty margin of ±5% was applied. These flows include contributions from the three major beverage industries (Pepsi, TBL, Coca-Cola Kwanza), which together discharged ~1,224 m^3/day during the monitoring period.

2.3.2. Pollution load calculations

Pollution load for each parameter was calculated to quantify the total mass of pollutants entering and exiting each treatment stage. This enables performance evaluation in terms of mass balance and efficiency. Pollutant loadings were calculated using the following equation.[18]

$$\text{Load}\left(\frac{\text{kg}}{\text{day}}\right)=\frac{\text{C}\times\text{Q}}{1{,}000} \quad \text{(I)}$$

Where:

- C = Concentration of the pollutant (mg/L)
- Q = Flow rate (m^3/day)
- 1,000 = Conversion factor (mg to kg)

Pollution load calculations were conducted for the six key parameters—BOD_5, COD, TSS, ammonia, nitrite, and TDS—at four defined sampling points: The inlet to the anaerobic ponds, the anaerobic pond outlet, the facultative pond outlet, and the maturation pond outlet, which represents the final discharge.

This approach allows determination of absolute removal (kg/day) at each stage and comparison against influent loads, which is more insightful than percentage removal alone, particularly under fluctuating flow regimes.[18]

2.3.3. Importance of load evaluation

Mass load evaluation is crucial in assessing real-world pond capacity, estimating sludge accumulation rates, and determining potential overload situations. Moreover, it supports long-term monitoring and decision-making related to system upgrades, desludging needs, and regulatory compliance.[18]

2.4. WSP treatment efficiency evaluation

The evaluation of treatment performance at Kalobe WSPs was conducted by analyzing the removal efficiencies of six selected parameters (BOD, COD, TSS, ammonia, nitrite, and TDS) across the three major units: Anaerobic, facultative, and maturation ponds.

2.4.1. Efficiency calculation method

The treatment efficiency for each parameter at each stage was calculated using the conventional removal efficiency formula:

$$\text{Removal efficiency}\,(\%) = \left(\frac{\text{cin-cout}}{\text{cin}}\right) \times 100 \qquad \text{(II)}$$

Where:

- Cin = Influent concentration to the unit
- Cout = Effluent concentration from the unit

This calculation was applied at two levels: (i) Stage-wise performance, covering the sequential treatment units from anaerobic to facultative to maturation ponds, and (ii) overall system performance, measured from the inlet to the final effluent. The results were expressed both as percentage removals and as mass load reductions (kg/day), using flow-weighted calculations, as described in Section 2.5.

2.4.2. Evaluation criteria

Performance was assessed against three benchmarks. First, compliance was evaluated relative to the Tanzania National Environmental Standards (URT, 2007), which specify maximum final effluent limits of BOD ≤ 30 mg/L, COD ≤ 60 mg/L, TSS ≤ 100 mg/L, NH_3–N ≤ 10 mg/L, NO_2–N ≤ 1 mg/L, and TDS ≤ 2,000 mg/L.[19] Second, results were compared to typical tropical WSP performance ranges reported in the literature, where BOD removal is generally 70–90%, COD removal 60–80%, and TSS removal 60–90%, while nutrient removals (ammonia and nitrite) tend to vary with temperature, algal activity, and hydraulic retention time (HRT).[7,20] Finally, the evaluation highlighted strengths and limitations of the Kalobe system, with particular emphasis on nutrient removal, which is often reduced in conventional WSPs that lack polishing units such as constructed wetlands or sand filtration.[18]

2.4.3. Data validation

All efficiency values were computed using the verified dataset from field measurements and laboratory analysis. Tabular summaries and graphical comparisons are presented in the results section to visually support the stage-wise trends.

2.4.4. Pollutant load contribution

Pollutant load (kg/day) for each parameter was computed using the standard mass loading equation (Equation I).

The contribution (%) of each industry to total pollutant loading was then derived by comparing each load to the total system load for BOD_5, COD, TSS, ammonia, nitrite, and TDS.

This analysis enabled the identification of industries that are primary contributors to organic, solids, and nutrient loading, helping to pinpoint the most significant sources of stress on the WSP system.

2.4.5. Application and relevance

The findings from the contribution analysis are essential for informing industrial pre-treatment compliance strategies, supporting load-based billing and regulatory mechanisms, and prioritizing pollution control interventions.

Results are presented in Section 3, alongside performance efficiency trends and compliance status.

2.5. Compliance assessment

Compliance assessment was conducted to determine whether the final effluent discharged from the Kalobe WSPs meets the 2018 Tanzanian National Effluent Discharge Standards and other international guidelines, such as the 2006 World Health Organization (WHO) recommendations for safe discharge and reuse.[19,14]

2.5.1. Standards used for compliance check

For the Tanzanian National Standards, allowable limits for key parameters include: BOD_5 ≤ 30 mg/L, COD ≤ 60 mg/L, TSS ≤ 100 mg/L, NH_3–N ≤ 10 mg/L, NO_2–N ≤ 1 mg/L, and TDS ≤ 2,000 mg/L. For WHO guidelines, parameter limits vary depending on the intended reuse (e.g., unrestricted irrigation, restricted irrigation, or discharge into surface waters).[19]

2.5.2. Approach to compliance evaluation

Compliance evaluation was performed by comparing measured effluent concentrations from the final maturation pond with the specified standards. The percentage of compliance for each parameter was determined using the following formula:

$$\text{Compliance}\,(\%) = \left(1\frac{\text{Exceedence}}{\text{Standard}}\right) \times 100 \qquad \text{(III)}$$

Where:

- Exceedance = Max (0, Effluent Concentration − Standard)

Parameters exceeding the allowable limits were flagged for further analysis, and their potential causes were investigated. These included high industrial loads, reduced HRT, or operational challenges such as sediment buildup or algal overgrowth.[5,6]

2.6. Graphical presentation

To better communicate trends and stage-wise pollutant reductions, various chart types were developed using Microsoft Excel and Python-based plotting libraries (Table 2).

These visual tools were selected to highlight treatment efficiency, assess regulatory compliance, and provide decision-makers with easily interpretable insights into system performance.

3. Results

This section presents the validated findings from field sampling and laboratory analysis of the Kalobe WSPs in Mbeya city, Tanzania. The results are structured by treatment stage (anaerobic, facultative, and maturation) and address the core study objectives: assessing influent quality, evaluating removal efficiencies, and determining final effluent compliance with national standards.

3.1. Influent wastewater characteristics

The raw wastewater quality entering the Kalobe WSPs is summarized in Table 3. Mean influent concentrations exceeded Tanzanian discharge standards for all measured parameters, confirming the high-strength nature of the wastewater. Mean influent concentrations exceeded Tanzanian discharge standards for all measured parameters. Day-to-day variability in influent BOD and COD during the sampling campaign was statistically significant (one-way analysis of variance, $p<0.05$). These findings demonstrate the considerable organic and nutrient loads imposed on the system at the inlet.

3.1.1. Anaerobic ponds

Samples collected at the outlet of the anaerobic ponds were analyzed to assess first-stage removal performance. The results indicate substantial reductions in COD and TSS, with moderate removal of BOD and ammonia (Table 4, Figure 4). Reductions in nitrite and TDS remained negligible.

Table 2. Chart types used for graphical presentation

Chart type	Application
Vertical bar charts	For comparing influent and effluent concentrations stage-wise
Stacked bar charts	For showing cumulative removal per parameter across stages
Radar (spider) charts	For visualizing multi-parameter performance per treatment unit
Line charts	For observing seasonal/temporal variation in pollutant concentrations
Traffic-light table	To quickly indicate compliance versus non-compliance per parameter

Table 3. Influent wastewater quality characteristics entering the Kalobe waste stabilization ponds

Parameter	Influent concentration (mg/L)
Biochemical oxygen demand, 5-day	93.0
Chemical oxygen demand	612.0
Total suspended solids	320.0
Ammonia (NH_3)	15.4
Nitrite (NO_2)	0.46
Total dissolved solids	1,034.0

Table 4. Performance of anaerobic ponds: Influent and effluent quality parameters

Parameter	Influent (mg/L)	Anaerobic outlet (mg/L)	% removal efficiency
BOD_5	93.0	60.60	34.84
COD	612.0	284.32	53.53
TSS	320.0	128.78	59.13
Ammonia (NH_3)	15.4	9.68	37.14
Nitrite (NO_2)	0.46	0.42	8.70
TDS	1,034.0	963.00	6.87

Abbreviations: BOD_5: Biochemical oxygen demand, 5-day; COD: Chemical oxygen demand; TDS: Total dissolved solids; TSS: Total suspended solids.

3.1.2. Facultative ponds

Following anaerobic treatment, the wastewater enters the facultative ponds for further treatment. The results show marked reductions in COD, TSS, and ammonia, while nitrite and TDS removal remained limited (Table 5 and Figure 5).

3.1.3. Maturation ponds

The final stage of treatment occurs in the maturation ponds. Effluent samples collected from the outlet of

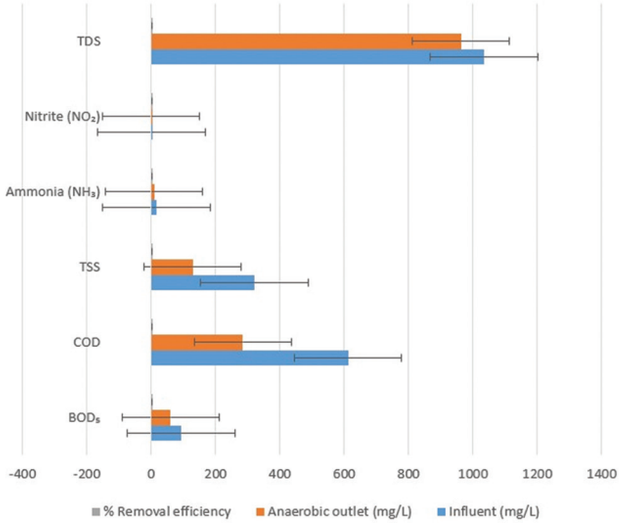


Figure 4. Anaerobic pond: Influent versus outlet concentrations

Abbreviations: BOD_5: Biochemical oxygen demand, 5-day; COD: Chemical oxygen demand; TDS: Total dissolved solids; TSS: Total suspended solids.

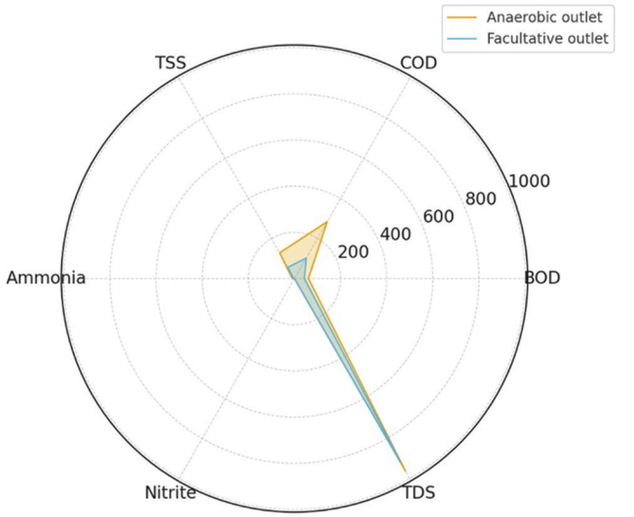


Figure 5. Facultative pond – parameter reduction

Abbreviations: COD: Chemical oxygen demand; TDS: Total dissolved solids; TSS: Total suspended solids.

this unit showed additional polishing of BOD, COD, TSS, and ammonia (Table 6 and Figure 6). Nitrite remained unchanged, while TDS removal continued to be negligible.

3.2. Overall treatment efficiency

The cumulative treatment efficiency of the Kalobe WSP system, from the anaerobic pond inlet to the maturation pond outlet, was calculated for each parameter. The system performed strongly in terms of COD, TSS, and ammonia removal, while BOD reductions were moderate (Table 7 and Figure 7). Nitrite and TDS removal remained poor.

Table 5. Performance of facultative ponds: Effluent characteristics and removal efficiency

Parameter	Anaerobic outlet (mg/L)	Facultative outlet (mg/L)	% removal efficiency (this stage)
BOD_5	60.60	43.05	28.97
COD	284.32	102.27	64.02
TSS	128.78	56.67	55.99
Ammonia (NH_3)	9.68	4.91	49.28
Nitrite (NO_2)	0.42	0.38	9.52
TDS	963.00	920.40	4.42

Abbreviations: BOD_5: Biochemical oxygen demand, 5-day; COD: Chemical oxygen demand; TDS: Total dissolved solids; TSS: Total suspended solids.

Table 6. Performance of maturation ponds: Final effluent characteristics and removal efficiency

Parameter	Facultative outlet (mg/L)	Maturation outlet (mg/L)	% removal efficiency (this stage)
BOD_5	43.05	39.00	9.41
COD	102.27	78.00	23.71
TSS	56.67	41.00	27.61
Ammonia (NH_3)	4.91	3.00	38.90
Nitrite (NO_2)	0.38	0.38	0.00
TDS	920.40	892.00	3.09

Abbreviations: BOD_5: Biochemical oxygen demand, 5-day; COD: Chemical oxygen demand; TDS: Total dissolved solids; TSS: Total suspended solids.

3.3. Seasonal and flow variation effects

Analysis of daily industrial discharge flow data for April 2025 revealed significant fluctuations in the volumes received by Kalobe WSPs (Table 8). Peak inflows toward the end of the period coincided with temporary declines in the performance of anaerobic and facultative stages. During the highest recorded daily inflows, BOD and TSS removals were approximately 10% lower than period averages, indicating that hydraulic shocks can depress treatment efficiency.

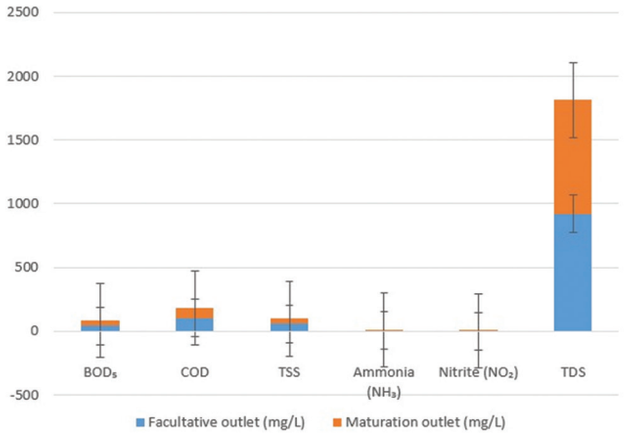


Figure 6. Maturation pond – stage-wise concentration and reduction

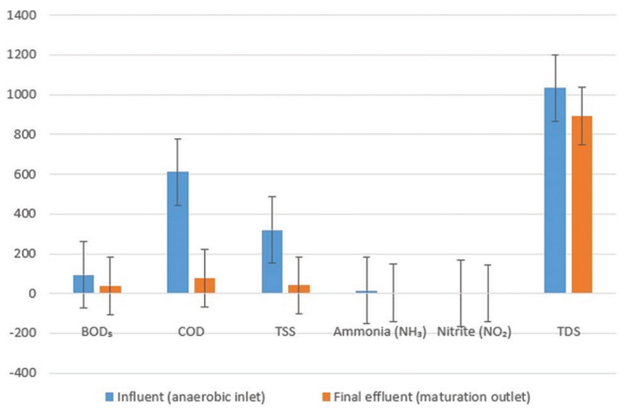


Figure 7. Overall treatment performance: Influent versus final effluent

These variations highlight that Pepsi was the largest contributor in terms of volume. Peak discharges from TBL and Pepsi were observed midweek, with certain days (e.g., April 30: TBL – 700 m^3; Pepsi – 812 m^3) showing substantial hydraulic load spikes.

Such fluctuations may lead to intermittent overloading of the treatment system, particularly affecting sedimentation and biological processes in the anaerobic and facultative stages.[21] This pattern of unregulated peak flows suggests the need to: (i) Install pre-discharge flow equalization tanks at industrial sites, (ii) coordinate discharge scheduling with the utility, and (iii) strengthen flow monitoring and regulation policies to minimize system shock-loading.

4. Discussion

The performance of the Kalobe WSPs demonstrates both the potential and the constraints of pond-based treatment under mixed municipal and industrial loading conditions. Organic matter removal was strong, with COD and TSS reduced to levels typical of well-functioning tropical WSPs, confirming that anaerobic and facultative processes remain effective in high-temperature environments.[22] These results align with findings from similar systems in Ghana, Ethiopia, and Kenya, where COD reductions of 80–90% and TSS reductions of 70–90% have been reported.[13,23]

In contrast, BOD removal was modest and did not consistently achieve Tanzanian discharge standards. This partial non-compliance can be attributed to intermittent hydraulic shock loads originating from industries, particularly during peak discharge days.[21] Comparable challenges have been noted in Ethiopia, where breweries and beverage industries periodically overwhelm pond systems, depressing performance.[13,23] The link observed in this study between peak flows and efficiency declines highlights the need for flow equalization at the industrial source.

Nutrient and salt removal were especially weak. Nitrite removal was negligible, reflecting incomplete nitrification–denitrification pathways, often inhibited by fluctuating organic loads, short retention times, and

Table 7. Cumulative removal efficiencies across the Kalobe waste stabilization pond treatment stages

Parameter	Influent (anaerobic inlet)	Final effluent (maturation outlet)	Overall removal efficiency (%)
BOD_5	93.00	39.00	58.06
COD	612.00	78.00	87.25
TSS	320.00	41.00	87.19
Ammonia (NH_3)	15.40	3.00	80.52
Nitrite (NO_2)	0.46	0.38	17.39
TDS	1,034.00	892.00	13.74

Abbreviations: BOD_5: Biochemical oxygen demand, 5-day; COD: Chemical oxygen demand; TDS: Total dissolved solids; TSS: Total suspended solids.

Table 8. Daily industrial discharge flow data for April 2025

Industry	Total flow (m^3)	Daily average (m^3/d)
Pepsi	20,108	670.3
Tanzania Breweries Limited	12,307	410.2
Coca-Cola Kwanza	4,298	143.3

limited oxygen transfer in facultative zones. Ammonia removal was moderate but fell short of benchmarks reported for tropical WSPs (60–80%), suggesting that algal–bacterial interactions were constrained by organic overload.[24] TDS reduction was minimal, consistent with evidence that conventional ponds are not designed for salt removal, which requires specific polishing processes such as wetlands or ion-exchange media.[8,25]

Ecologically, the persistence of ammonia, nitrite, and TDS in the effluent presents risks for aquatic life in receiving waters. Ammonia concentrations above 3 mg/L are toxic to sensitive fish species, while elevated nitrite interferes with oxygen transport in aquatic organisms. Dissolved solids above 1000 mg/L alter ionic balances and reduce freshwater biodiversity. The observed effluent levels at Kalobe WSPs, therefore, raise concerns about downstream ecological stress.

This study makes a novel contribution by documenting the performance of a Tanzanian WSP receiving combined domestic and industrial wastewater. Unlike most regional studies that evaluate purely municipal systems, this case illustrates the compounded challenges of mixed loading, where brewery and beverage effluents exacerbate nutrient persistence and destabilize biological processes. These findings emphasize that, while WSPs remain a viable low-cost technology in resource-constrained settings, they require complementary interventions—including industrial pre-treatment, flow regulation, and post-treatment polishing—to ensure regulatory compliance and environmental protection.

5. Limitations of the study

This study was limited in several respects that should be acknowledged. First, sampling was conducted during the dry season only; therefore, seasonal variability, particularly the influence of wet-season inflows and dilution, was not captured. Second, while composite grab sampling was applied, daily and diurnal variations in industrial discharges may not have been fully represented. Third, the analysis focused on conventional water quality indicators (BOD_5, COD, TSS, ammonia, nitrite, and TDS) but did not extend to heavy metals or emerging contaminants, which are often present in industrial effluents and may affect long-term pond performance and ecological safety. Finally, the study relied on reported flow data from industries for load calculations, which may contain uncertainties due to irregular monitoring practices.

Despite these limitations, the findings provide valuable baseline information on the functioning of Kalobe WSPs and highlight critical areas for intervention. Future research should incorporate multi-seasonal monitoring, automated flow measurement, and expanded parameter analysis to provide a more comprehensive assessment of treatment dynamics.

6. Conclusion and recommendations

The Kalobe WSPs demonstrated that, even under high-strength mixed municipal and industrial wastewater conditions, stabilization ponds can achieve meaningful reductions in organic matter and suspended solids. Nevertheless, the system did not consistently meet Tanzanian effluent discharge standards, particularly for BOD, nitrite, and TDS.

This study provides novel evidence from Tanzania, where little quantitative data exists on WSPs receiving industrial inputs. By documenting system performance under mixed loadings, the study highlights the persistence of nutrients and dissolved solids, pollutants that are not adequately treated by conventional pond configurations. These findings are important for regulators and utilities in Tanzania and across the region, as they demonstrate both the strengths of WSPs in tropical climates and the critical gaps in nutrient and salt removal.

Policy interventions are therefore needed to address these gaps. Industrial flow regulation and equalization, stricter enforcement of pre-treatment requirements, and the introduction of cost-effective polishing steps (such as constructed wetlands or sand filtration) would improve system reliability. If integrated into existing management strategies, these measures would strengthen the capacity of WSPs to meet national standards and safeguard downstream ecosystems.

Acknowledgments

The authors gratefully acknowledge the technical and logistical support provided by Mbeya Urban Water Supply and Sanitation Authority (Mbeya UWSA) and the participating beverage industries. Special thanks are extended to the staff of Mbeya Zonal Laboratory for their assistance during sampling and analysis. The authors also wish to thank their colleagues and friends who contributed during the design and writing of this article by offering insightful and practical suggestions. Their help in reviewing the manuscript and providing constructive critique greatly improved the quality of the work.

Funding

None.

Conflict of interest

The authors declare no conflicts of interest.

Author contributions

Conceptualization: Eline Gerson
Formal analysis: All authors
Methodology: All authors
Supervision: Gislar E. Kifanyi, Omary R. Shegwando, Fredrick Ojija
Writing–original draft: Eline Gerson
Writing–review & editing: All authors

Availability of data

Data are available from the corresponding author upon reasonable request.

References

1. Lima PDM, Lopes TADS, Queiroz LM, McConville, JR. Resource-oriented sanitation: Identifying appropriate technologies and environmental gains by coupling Santiago software and life cycle assessment in a Brazilian case study. *Sci Total Environ*. 2022;837:155777. doi: 10.1016/j.scitotenv.2022.155777
2. Manga M, Kolsky P, Rosenboom JW, *et al*. Public health performance of sanitation technologies in Tamil Nadu, India: Initial perspectives based on *E. coli* release. *Int J Hyg Environ Health*. 2022;243:1-15. doi: 10.1016/j.ijheh.2022.113987
3. Mupinga RT, Mercer E, Rayavellore Suryakumar A, Pocock J, Septien S. Insight into the stickiness of faecal sludge from dry sanitation technologies: A path toward sustainable and efficient FSM via thermal processes. *Results Eng*. 2025;26:105453. doi: 10.1016/j.rineng.2025.105453
4. Auma B, Musinguzi M, Ojuka, *et al*. Prevalence of diarrhea and water sanitation and hygiene (WASH) associated factors among children under five years in Lira City Northern Uganda: Community-based study. *PLoS One*. 2024;19:e0305054. doi: 10.1371/journal.pone.0305054
5. Mara DD, Mara D. *Domestic Wastewater Treatment in Developing Countries*. 23rd ed. London: Earthscan; 2004.
6. Mara D, Pearson H. *Design Manual for Waste Stabilization Ponds in Mediterranean Countries*. Dubai: Lagoon Technology International; 1998.
7. Gopolang OP, Letshwenyo MW. Performance Evaluation of Waste Stabilisation Ponds. *J Water Resour Prot*. 2018;10:1129-1147. doi: 10.4236/jwarp.2018.1011067
8. Achag B, Mouhanni H, Bendou A. Performance of municipal waste stabilization ponds in the Saharan desert (Morocco). *J Water Clim Change*. 2023;14:1741-1761. doi: 10.2166/wcc.2023.339
9. Cuff G, Turcios AE, Mohammad-Pajooh E, *et al*. High-rate anaerobic treatment of wastewater from soft drink industry: Methods, performance and experiences. *J Environ Manage*. 2018;220:8-15. doi: 10.1016/j.jenvman.2018.05.015
10. Massoud MA, Tarhini A, Nasr JA. Decentralized approaches to wastewater treatment and management: Applicability in developing countries. *J Environ Manage*. 2009;90:652-659. doi: 10.1016/j.jenvman.2008.07.001
11. Shaheen MNF, Elmahdy EM, Rizk NM, *et al*. Evaluation of physical, chemical, and microbiological characteristics of waste stabilization ponds, Giza, Egypt. *Environ Sci Eur*. 2024;36:170. doi: 10.1186/s12302-024-00965-y
12. Kaseva ME, Mwegoha WJS, Kihampa C, *et al*. Performance of a waste stabilization pond system treating domestic and hospital wastewater and its implications to the aquatic environment-a case study in Dar es Salaam, Tanzania. *J Build LAND Dev*. 2018;15(1-2):1-15.
13. Mkude I, Saria J. Assessment of waste stabilization ponds (WSP) efficiency on wastewater treatment for agriculture reuse and other activities a case of Dodoma municipality, Tanzania. *Ethiop J Environ Stud Manag*. 2014;7(3):298-304. doi: 10.4314/ejesm.v7i3.9
14. Jiménez B. Irrigation in developing countries using wastewater. *Int Rev Environ Strategies*. 2006;6(2):229-250.
15. García J, Mujeriego R, Hernández-Mariné M. High rate algal pond operating strategies for urban wastewater nitrogen removal. *J Appl Phycol*. 2000;12:331-339. doi: 10.1023/a:1008146421368
16. Kilingo F, Bernard Z, Hong-Bin C. The analysis of Wastewater treatment system efficiencies in Kenya: A review paper. *Int J Sci Res Publ*. 2021;11:204-215. doi: 10.29322/ijsrp.11.05.2021.p11322
17. APHA. *Standard Methods for the Examination of Water and Wastewater*. 20th ed. Washington DC: American Public Health Association; 1999.
18. Olukanni DO, Ducoste JJ. Optimization of waste stabilization pond design for developing nations using computational fluid dynamics. *Ecol Eng*. 2011;37:1878-1888. doi: 10.1016/j.ecoleng.2011.06.003
19. Kum S, Rowles L. Wastewater reclamation and recycling. *Envir Sci.* 2023:1-37.

doi: 10.1093/acrefore/9780199389414.013.612
20. Nkinda R, Ojija F, Bacaro G, Malunguja G. Land-use/land-cover change in the Ngerengere River Catchment, Tanzania: Insights from 2004 to 2034. *Asian J Water Environ Pollut*. 2025:1-17.
doi: 10.36922/ajwep025180137
21. Sinn J, Lackner S. Enhancement of overloaded waste stabilization ponds using different pretreatment technologies: A comparative study from Namibia. *J Water Reuse Desalination*. 2020;10:500-512.
doi: 10.2166/wrd.2020.021
22. Roebuck P, Kennedy K, Delatolla R. Ultrasonic pretreatment for anaerobic digestion of suspended and attached growth sludges. *Water Qual Res J*. 2019;54(4):265-277.
doi: 10.2166/wqrj.2019.039
23. Kabeto SK, Tolera ST, Woldemichael ED. Evaluation of treatment efficiency of waste stabilization pond and its effluent toxicity in Hawassa University, Southern Ethiopia. *East Afr J Health Biomed Sci*. 2000;4(1):47-60.
24. Johnson M, Camargo Valero MA, Mara DD. Maturation ponds, rock filters and reedbeds in the UK: Statistical analysis of winter performance. *Water Sci Technol* 2007;55:135-142.
doi: 10.2166/wst.2007.364
25. Xu S, Li Z, Yu S, *et al*. Microalgal-bacteria biofilm in wastewater treatment: Advantages, principles, and establishment. *Water*. 2024;16:2561.
doi: 10.3390/w16182561

Asian Journal of Water, Environment and Pollution. Vol. 22, No. 6 (2025), pp. 210-220.
doi: 10.36922/AJWEP025260210

ORIGINAL RESEARCH ARTICLE

Assessment of the surface urban heat island in Ho Chi Minh City using remote sensing and geographic information systems

Lam Van Hao[1,2]*

[1]Department of Oceanology, Meteorology and Hydrology, Faculty of Physics and Engineering Physics, University of Science, Ho Chi Minh, Vietnam
[2]Viet Nam National University-Ho Chi Minh City, Ho Chi Minh, Vietnam
***Corresponding author:** Lam Van Hao (lvhao@hcmus.edu.vn)

Received: June 26, 2025; Revised: July 10, 2025; Accepted: July 15, 2025; Published online: October 3, 2025

Abstract: The rapid urbanization of Ho Chi Minh City (HCMC) has led to an increasingly intense urban heat island (UHI) phenomenon, significantly impacting its environment and inhabitants. This study investigates the spatiotemporal dynamics of the surface UHI (SUHI) in HCMC by utilizing a 36-year time series of Landsat satellite imagery (1988, 1995, 2002, 2010, 2017, and 2024), processed within a geographic information system framework. Land surface temperature (LST) was derived to map and quantify UHI patterns. The results reveal a substantial and progressive intensification of the SUHI effect, with the citywide mean LST increasing from 25.4°C in 1988 to 28.7°C in 2024. Spatially, the SUHI has expanded from the urban core into peripheral suburban zones, particularly toward the east and northwest. A strong and consistent negative correlation ($R^2 > 0.7$) was observed between LST and the normalized difference vegetation index, underscoring the critical role of green spaces in mitigating urban heat. These findings provide crucial, data-driven insights for urban planners and policymakers, highlighting the urgent need for sustainable development strategies—such as enhancing green infrastructure and adopting cool materials—to combat the adverse effects of urban warming in this rapidly expanding tropical metropolis.

Keywords: Geographic information system; Land surface temperature; Landsat; Remote sensing; Urban heat island

1. Introduction

Urbanization is a defining global trend of the 21st century, characterized by the migration of populations to urban centers and the consequent expansion of urban land cover.[1] While this process often drives economic growth, it concurrently induces significant environmental modifications, one of the most prominent being the urban heat island (UHI) effect.[2,3] The UHI phenomenon describes the tendency for urban areas to experience higher atmospheric and surface temperatures than their surrounding rural and undeveloped counterparts.[4]

This thermal disparity is primarily attributed to alterations in the urban surface energy balance. The replacement of natural landscapes with impervious surfaces (e.g., concrete, asphalt) results in lower albedo (reflectivity) and higher thermal admittance, causing more solar energy to be absorbed and stored.[5] This is compounded by reduced evapotranspirational cooling due to diminished vegetation cover, complex urban geometry that traps solar radiation, and anthropogenic heat emissions from buildings, transportation, and industrial activities.[6,7] When referring specifically to surface temperature anomalies observed by remote sensors, the phenomenon is termed surface urban heat island (SUHI).

Conventionally, UHI studies relied on *in situ* air temperature measurements from fixed weather stations.[8] While valuable, this approach often suffers from sparse station networks, limiting its ability to capture the fine-scale spatial heterogeneity of urban thermal environments.[9] Remote sensing technology offers a powerful alternative, providing synoptic, spatially continuous data over large urban expanses with frequent revisit capabilities.[10] Satellite-derived land surface temperature (LST) is a key parameter for SUHI studies, enabling the detailed mapping and monitoring of thermal patterns.[9] The Landsat series of satellites, with its long-term archive and moderate-resolution thermal infrared bands, has been used extensively for LST retrieval and SUHI analysis globally.[11,12] Concurrently, the normalized difference vegetation index (NDVI), another standard satellite-derived product, is used to quantify vegetation density and assess its cooling effect.[13]

Numerous studies have investigated the SUHI phenomenon across diverse urban settings. For instance, research in Bangkok, Thailand, using Landsat 8 imagery, revealed that LST in urban areas was typically 4°C higher than in vegetated suburban areas.[14] Similar investigations in other Asian megacities, such as Shenzhen, China, and New Delhi, India, have also reported significant SUHI effects, with urban LST exceeding that of vegetated areas by 3–4°C and correlating strongly with land use changes and impervious surface expansion.[15,16] These studies underscore the commonality of the SUHI phenomenon while also highlighting the city-specific nature of its intensity and drivers, which are influenced by local geography, climate, and urban form. Ho Chi Minh City (HCMC), Vietnam's largest urban agglomeration and primary economic engine, has undergone exceptionally rapid urbanization over recent decades.[17] With a population exceeding 10 million, this growth has involved a significant transformation of agricultural land into built-up areas, accompanied by extensive infrastructure development.[18] Such land use/land cover (LULC) changes have inevitably impacted the local climate, contributing to the emergence and intensification of the SUHI phenomenon in HCMC.[19,20] Previous research has provided a valuable foundation for understanding this issue. However, a continuous, multi-decadal assessment incorporating the most recent data is needed to fully understand long-term trends and inform effective mitigation strategies.

The novelty and primary contribution of this study lie in its unprecedented temporal scale. By employing a consistent methodology across a 36-year time series from 1988 to 2024, this research provides the most comprehensive long-term assessment of SUHI dynamics in HCMC to date. This multi-decadal approach allows us not only to confirm the existence of SUHI but also to meticulously quantify its evolution, expansion, and changing intensity over time, an insight unattainable from shorter-term studies. This deep historical perspective is critical for developing far-sighted urban planning policies and effective climate change adaptation strategies.

This study aims to contribute to this understanding by: (i) Assessing the spatiotemporal evolution of the SUHI phenomenon in HCMC using a 36-year time series of Landsat imagery (1988–2024); (ii) quantifying LST changes across the urban-rural gradient to analyze the expansion and intensification of the heat island; and (iii) investigating the correlation between LST and NDVI to quantitatively evaluate the role of vegetation in modulating surface temperatures. The findings are expected to provide a comprehensive, updated perspective on SUHI dynamics in HCMC, offering crucial, data-driven insights for urban planners and policymakers to develop effective strategies for sustainable urban development and climate change adaptation.

2. Materials and methods

2.1. Study area

HCMC, located in the southeastern region of Vietnam, is the nation's largest city and a primary economic, cultural, and educational hub. Characterized by substantial growth and urban expansion, the city covers a total area of approximately 2,095 km^2 (Figure 1). HCMC's topography is generally flat, with about 60% of its area lying below an average elevation of 1.0 m. The city experiences a tropical monsoon climate with distinct wet (May–November) and dry (December–April) seasons. The population has grown to over 9 million residents, with an average density of 4,481 people/km^2, and approximately 80% residing in urbanized areas.[18] The rapid and often unplanned urban sprawl has led to significant alterations in land use, contributing to environmental challenges, including the SUHI effect.

2.2. Data collection and pre-processing

This study utilized multi-temporal Landsat satellite imagery from Landsat 5 Thematic Mapper (TM), Landsat 7 Enhanced TM Plus (ETM+), and Landsat 8 Operational Land Imager/Thermal Infrared Sensor.

Cloud-free or minimally clouded scenes covering HCMC for the years 1988, 1995, 2002, 2010, 2017, and 2024 were acquired from the United States Geological Survey Earth Explorer portal.[21] Detailed information on the acquired imagery is presented in Table 1.

Standard pre-processing steps, including radiometric calibration, were performed. For the Landsat 7 ETM+ image acquired after the scan line corrector failure in May 2003, a gap-filling technique using local histogram matching was applied to correct data gaps. Vector data

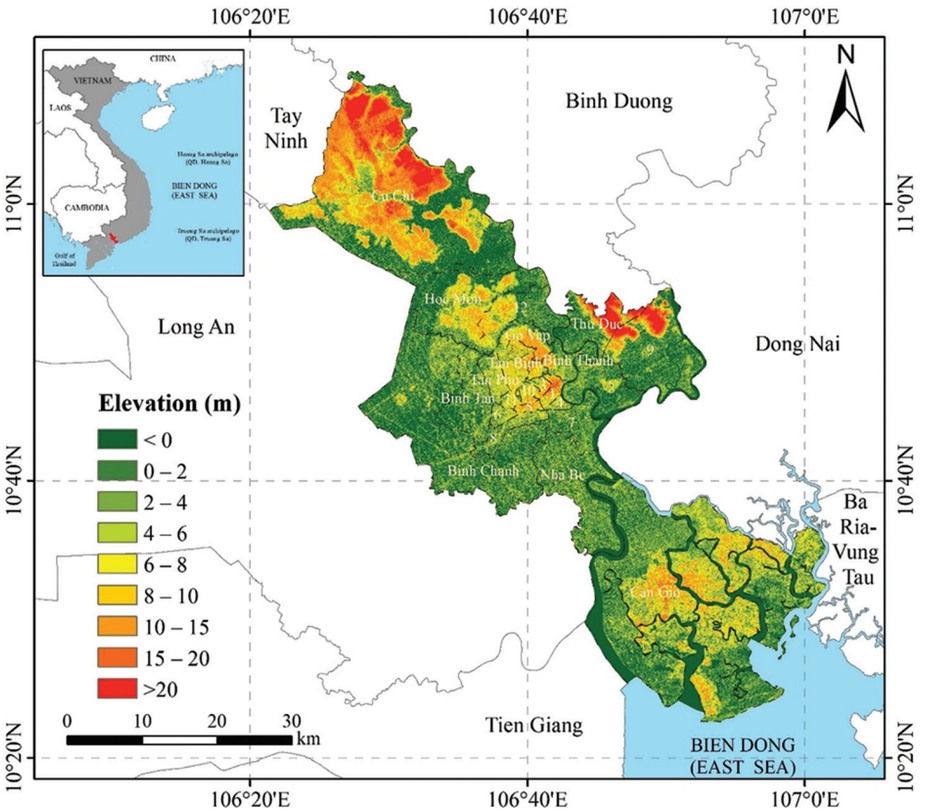


Figure 1. Elevation map of the study area in Ho Chi Minh City

Table 1. Satellite image data used in the study

Sensor	Path/row	Date of acquisition	Cloud coverage (%)	Spatial resolution (m)
Landsat 5 TM	125/053	January 14, 1988	11.00	30
Landsat 5 TM	125/052	January 14, 1988	0.00	30
Landsat 5 TM	125/053	February 02, 1995	5.00	30
Landsat 5 TM	125/052	February 02, 1995	0.00	30
Landsat 7 ETM+	125/053	February 13, 2002	18.00	30
Landsat 7 ETM+	125/052	February 13, 2002	5.00	30
Landsat 5 TM	125/053	February 11, 2010	43.00	30
Landsat 5 TM	125/052	February 11, 2010	1.00	30
Landsat 8 OLI/TIRS	125/053	February 14, 2017	14.75	30
Landsat 8 OLI/TIRS	125/052	February 14, 2017	0.52	30
Landsat 8 OLI/TIRS	125/053	February 18, 2024	22.92	30
Landsat 8 OLI/TIRS	125/052	February 18, 2024	0.06	30

Abbreviations: ETM+: Enhanced thematic mapper plus; OLI: Operational land imager; TIRS: Thermal infrared sensor; TM: Thematic mapper.

defining the administrative boundaries of HCMC were obtained from local government sources and used to delineate the study area.

2.3. Data processing and analysis

All image processing was conducted using established remote sensing algorithms listed below. The overall research workflow is illustrated in Figure 2.

(i) Radiance and reflectance: Digital numbers from level 1 products were converted to at-sensor spectral radiance (L^{λ}) and then to top-of-atmosphere planetary reflectance (ρ^{λ}), using the scaling factors and formulas provided in the image metadata and the Landsat Data Users Handbooks.[22,23] For Landsat 5/7/8, this included a correction for the solar elevation angle.

(ii) NDVI: NDVI was calculated using the reflectance of the red and near-infrared (NIR) bands, as per Equation I:

$$NDVI = \frac{\rho_{Nir} - \rho_{Red}}{\rho_{Nir} + \rho_{Red}} \quad (I)$$

(iii) Land surface emissivity (ε): Land surface emissivity was estimated based on the NDVI-threshold method described by Sobrino *et al*.[9] which assigns emissivity values according to NDVI to differentiate between soil, vegetation, and mixed pixels.

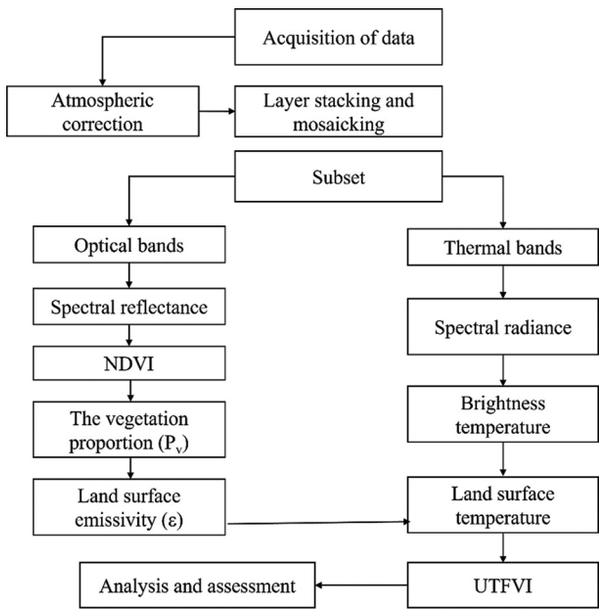


Figure 2. Flowchart of the research methodology, illustrating the process from data acquisition to surface urban heat island analysis

Abbreviations: NDVI: Normalized difference vegetation index; UTFVI: Urban thermal field variance index.

$$\varepsilon = \begin{cases} 0.979 - 0.035_{Red} & NDVI < NDVI_{Min} \\ 0.986 + 0.004P_V & NDVI_{Min} \le NDVI \le NDVI_{Max} \\ 0.99 & NDVI > NDVI_{Max} \end{cases} \quad (II)$$

where P_v is determined from the following formula[13]:

$$P_V = \left[\frac{NDVI - NDVI_{Min}}{NDVI_{Max} - NDVI_{Min}} \right]^2 \quad (III)$$

with $NDVI_{Max} = 0.5$, $NDVI_{Min} = 0.2$.

(iv) LST: First, at-sensor brightness temperature (T_B) was derived from the thermal band's spectral radiance using Planck's law inversion with metadata-provided constants. LST was then calculated in Celsius by correcting T_B for land surface emissivity using the following equation[24,25]:

$$LST\,(C) = \frac{T_B}{1 + \left(T_B / \alpha \right) \ln(\varepsilon)} - 273.15 \quad (IV)$$

where λ is the wavelength of the emitted radiance, and $\alpha = hc/k$ (1.438×10^{-2} mK).

(v) Urban thermal field variance index (UTFVI): The UTFVI is used to assess the SUHI effect based on LST and is divided into six levels of ecological evaluation (Table 2). It is calculated using Equation V[26-28]:

$$UTFVI = \frac{LST - LST_m}{LST_m} \quad (V)$$

where LST is the land surface temperature of each pixel, and LST_m is the mean land surface temperature of the study area.

2.4. SUHI assessment and accuracy

To comprehensively evaluate the characteristics and reliability of the SUHI patterns derived in this study, the following analytical steps were undertaken.

(i) SUHI classification and analysis: The generated LST maps were classified into distinct thermal zones to facilitate analysis. Thresholds were defined based on the overall temperature distribution for each year to represent relative thermal conditions: Low (<26°C), moderate (26–30°C), high (30–34°C), and very high (>34°C). The spatiotemporal trends, intensity, and expansion of the SUHI were assessed through qualitative map comparison, calculation of citywide mean LST, and analysis of mean LST across concentric buffer zones (5, 10, 15, and 30 km radii) from the city center.

(ii) Accuracy assessment: While a full quantitative accuracy assessment using a confusion matrix was

not performed due to the lack of contemporaneous, high-resolution ground-truth temperature data for all historical years, the reliability of the results is supported by several factors. The LST retrieval methods are standardized and widely validated in the scientific literature. Furthermore, the strong and physically consistent correlation observed between LST and NDVI provides confidence in the generated thermal patterns.

(iii) Correlation analysis: The relationship between LST and NDVI was quantified using Pearson's correlation coefficient (R) and the coefficient of determination (R^2) for pixels with positive NDVI values.

3. Results

3.1. Spatiotemporal distribution of the SUHI

The spatial distribution of LST across HCMC from 1988 to 2024 consistently reveals pronounced SUHI characteristics (Figures 3-5). Higher LST values are predominantly concentrated in industrial zones and densely built-up urban districts, where impervious surfaces dominate. Conversely, lower LST values are observed in areas with extensive green cover, such as the agricultural lands of Hoc Mon and Cu Chi, and the Can Gio mangrove forest.

In 1988 (Figure 3A), the highest LST values (30–32°C) were largely confined to the core urban districts. By 1995 (Figure 3B), high LST zones (>30°C) became more widespread, expanding into surrounding areas. This trend of intensification and spatial expansion continued through 2002 and 2010 (Figure 4), as well as 2017 and 2024 (Figure 5), with the highest temperature zones progressively encroaching on formerly cooler suburban areas. The general trend indicates an increasing proportion of the city area experiencing higher LST values, while areas with low LST are diminishing.

Table 2. Threshold values of UTFVI and corresponding ecological evaluation categories

UTFVI	LST-LST$_m$ (°C)	SUHI phenomenon	Ecological evaluation index
<0	<0	None	Excellent
0≤UTFVI<0.005	0≤LST–LSTm<1.5	Weak	Good
0.005≤UTFVI<0.010	1.5≤LST–LSTm<3.0	Middle	Normal
0.010≤UTFVI<0.015	3.0≤LST–LSTm<4.5	Strong	Bad
0.015≤ UTFVI<0.020	4.5≤LST–LSTm<6.0	Stronger	Worse
UTFVI≥0.020	LST–LSTm≥6.0	Strongest	Worst

Abbreviations: LST: Land surface temperature of each pixel; LST$_m$: Mean land surface temperature; SUHI: Surface urban heat island; UTFVI: Urban thermal field variance index.

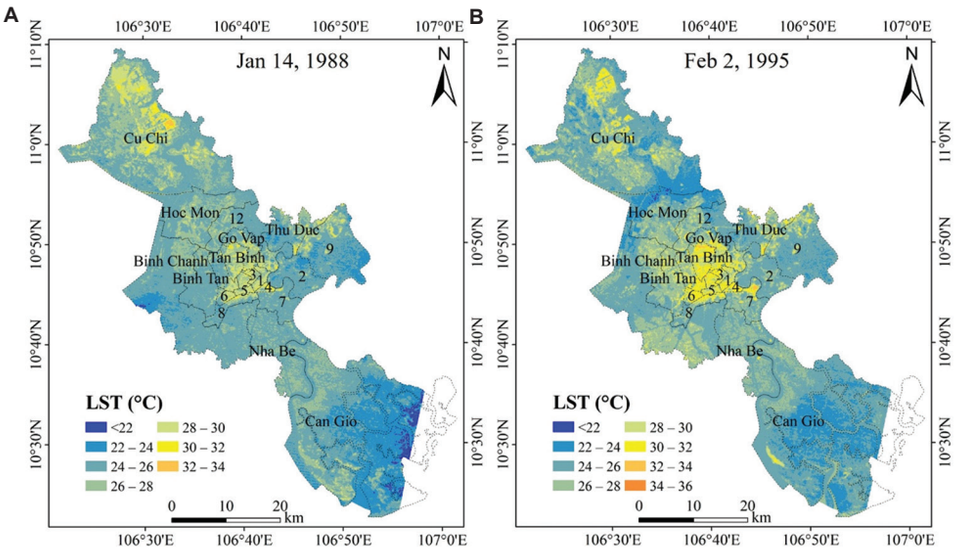


Figure 3. Spatiotemporal distribution of land surface temperature (LST) in Ho Chi Minh City in (A) 1988 and (B) 1995

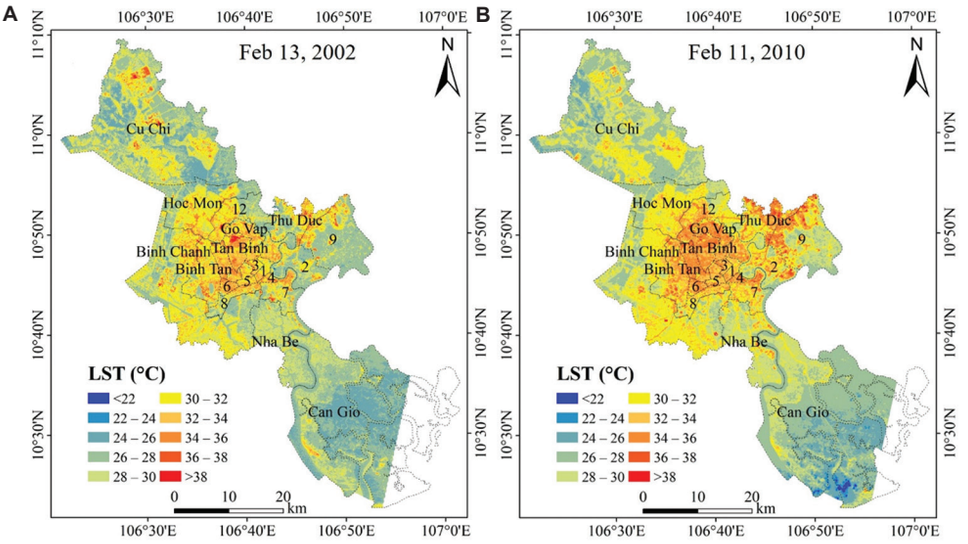


Figure 4. Spatiotemporal distribution of land surface temperature (LST) in Ho Chi Minh City in (A) 2002 and (B) 2010

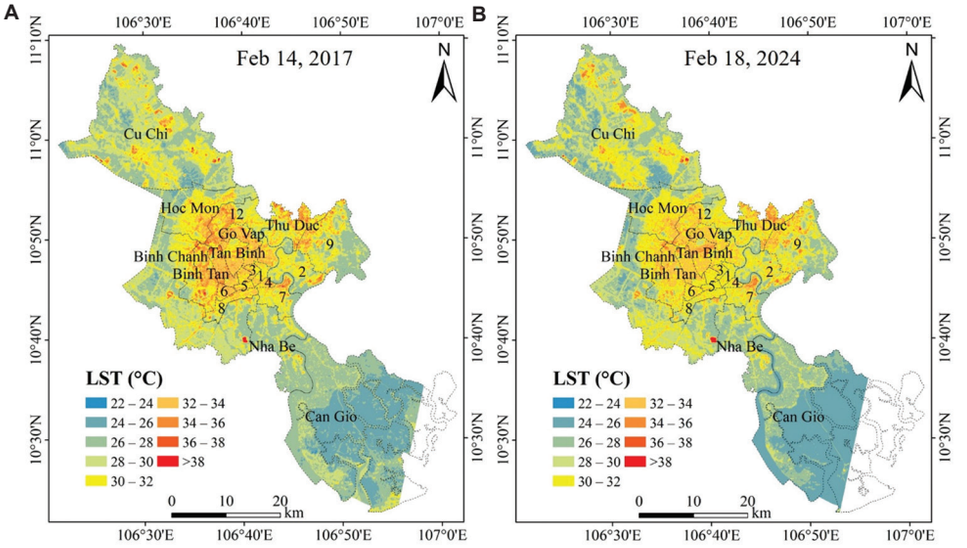


Figure 5. Spatiotemporal distribution of land surface temperature (LST) in Ho Chi Minh City in (A) 2017 and (B) 2024

3.2. Temporal trends and expansion of the UHI

The analysis of mean LST for the entire study area reveals a clear warming trend over the 36-year period (Figure 6). The mean LST for HCMC was 25.4°C in 1988, 25.2°C in 1995, 28.3°C in 2002, 29.4°C in 2010, 28.3°C in 2017 (a slight dip, potentially due to specific meteorological conditions), and 28.7°C in 2024.

To further quantify SUHI expansion, mean LST was analyzed across different distances from the city center (Table 3). The results consistently show that as the distance from the center increases, the mean LST decreases, which is characteristic of a classic UHI profile. The data also reveal a general increasing trend in mean LST at all distances over the 36-year period, with the most significant warming observed in the outer suburban zones. This indicates that the warming is not confined to the urban core but is a broader phenomenon affecting the entire metropolitan region.

3.3. Correlation between LST and NDVI

The relationship between LST and NDVI was investigated to assess the influence of vegetation on

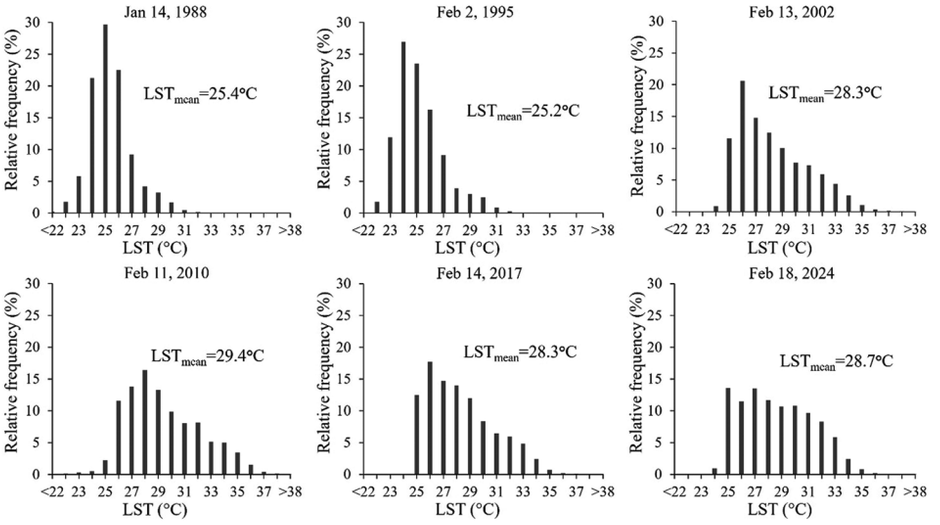


Figure 6. Temporal distribution of land surface temperature (LST) in Ho Chi Minh City from 1988 to 2024

Table 3. Mean land surface temperature (°C) in Ho Chi Minh City at varying distances from the city center (1988–2024), including percentage change

Radius (km)	1988 (°C)	Change (%)	1995 (°C)	Change (%)	2002 (°C)	Change (%)	2010 (°C)	Change (%)	2017 (°C)	Change (%)	2024 (°C)	Change (%)
5	27.4	0	28.9	0	32.5	0	34	0	31.6	0	32.1	0
10	26.1	−4.7	26.9	−6.9	30.9	−4.9	32.7	−3.8	30.8	−2.5	31.4	−2.2
15	25.6	−6.6	26.0	−10.0	29.9	−8.0	31.7	−6.8	29.6	−6.3	30.4	−5.3
30	25.4	−7.3	25.6	−11.4	29	−10.8	30.6	−10.0	28.6	−9.5	29.6	−7.8

surface temperatures. A consistent and strong negative correlation was observed for all analyzed years (Figure 7). The coefficient of determination (R^2) for this relationship was >0.7 in all years, signifying a robust inverse relationship. This indicates that areas with higher vegetation density (higher NDVI) consistently exhibit lower surface temperatures, while areas with sparse or no vegetation (lower NDVI) have higher LST. Detailed regression statistics are presented in Table 4.

Table 4. Regression statistics for the relationship between land surface temperature and normalized difference vegetation index

Year	*R*	R^2	Adjusted R^2	Standard error	*p*-value
1988	0.836	0.699	0.694	0.923	<0.05
1995	0.878	0.771	0.768	1.055	<0.05
2002	0.901	0.811	0.809	1.412	<0.05
2010	0.901	0.812	0.810	1.300	<0.05
2017	0.906	0.821	0.819	1.161	<0.05
2024	0.904	0.816	0.815	1.101	<0.05

4. Discussion

4.1. Spatiotemporal SUHI dynamics in HCMC

The results of this study clearly demonstrate the presence, intensification, and spatial expansion of the SUHI phenomenon in HCMC from 1988 to 2024. The observed patterns—higher LST in densely built-up urban cores and lower LST in vegetated suburban areas—are consistent with established SUHI characteristics reported in numerous cities worldwide.[29] The multi-temporal analysis revealed a substantial rise in mean LST across HCMC, from 25.4°C in 1988 to 28.7°C in 2024. This warming trend, coupled with the outward expansion of the heat island (as shown in Table 3 and Figures 3-5), is a direct consequence of rapid urbanization, the conversion of natural and agricultural land to impervious surfaces, and increased anthropogenic activities.[20]

4.2. Critical role of vegetation in SUHI mitigation

A key finding of this study is the strong and consistent negative correlation ($R^2 > 0.7$) between LST and NDVI.

This empirically validates the crucial role of vegetation in mitigating urban heat through evapotranspirational cooling and shading effects.[24,30] This finding has significant implications for urban planning in HCMC (Table 2). As the city continues to grow, the preservation and strategic integration of green infrastructure—such as parks, green roofs, urban forests, and vegetated corridors—becomes paramount for thermal regulation and for improving urban comfort and resilience.[31]

4.3. SUHI versus canopy layer UHI (CLUHI)

It is important to distinguish between the SUHI, measured by satellite-derived LST, and the CLUHI, measured by *in situ* air temperature at weather stations. SUHI reflects the temperature of surfaces (e.g., roads, rooftops), whereas CLUHI reflects the temperature of the air that people experience. SUHI typically exhibits a much greater thermal amplitude than CLUHI, with peak intensity during the daytime when urban surfaces strongly absorb solar radiation.[2] In contrast, CLUHI is often most intense at night, as urban areas release stored heat more slowly than rural surroundings (Table 5). Our study focuses on SUHI, which provides a spatially comprehensive view of how different land use types affect the surface energy balance, which is the fundamental driver of the entire UHI phenomenon.

4.4. Implications for urban planning and public health

The intensification of the SUHI in HCMC has several potential adverse consequences. These include increased energy demand for cooling, which can strain energy infrastructure and exacerbate greenhouse gas emissions[32]; a heightened risk of heat-related health problems for urban residents, such as heat stress and heat stroke[33]; and negative impacts on local ecosystems and air quality.[24] The expansion of the SUHI into suburban areas suggests that these previously less-affected regions

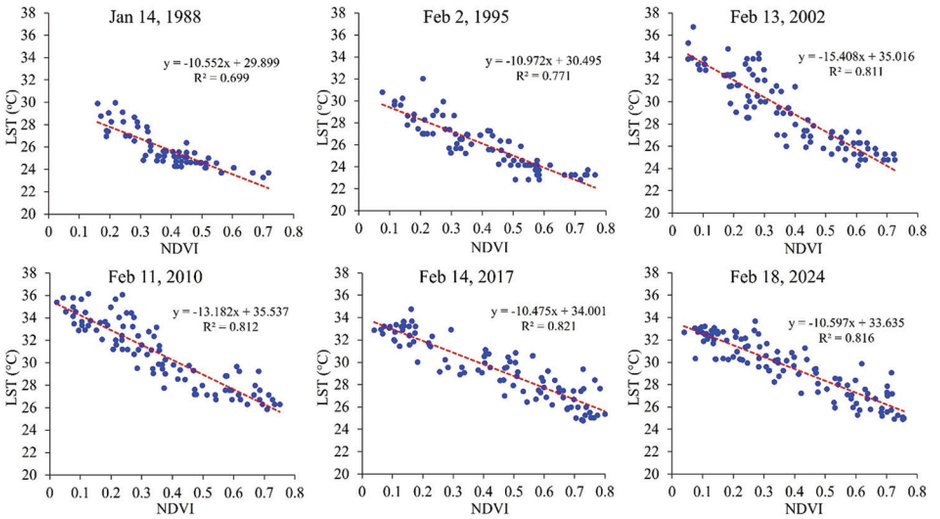


Figure 7. Scatter plots showing the correlation between LST and NDVI for selected years from 1988 to 2024
Abbreviations: LST: Land surface temperature; NDVI: Normalized difference vegetation index.

Table 5. Statistics of the surface UHI phenomenon based on the urban thermal field variance index

UHI phenomenon	Ecological evaluation index	1988		1995		2002		2010		2017		2024	
		ha	%	ha	%	ha	%	ha	%	ha	%	ha	%
None	Excellent	109,964	56.9	117,098	60.6	107,132	55.4	109,334	56.6	108,945	56.4	76,211	39.4
Weak	Good	54,126	28.0	43,019	22.3	27,323	14.1	29,722	15.4	33,972	17.6	30,695	15.9
Middle	Normal	18,213	9.4	18,111	9.4	20,177	10.4	23,129	12.0	20,665	10.7	29,579	15.3
Strong	Bad	7,965	4.1	10,028	5.2	15,698	8.1	15,332	7.9	17,043	8.8	25,088	13.0
Stronger	Worse	2,530	1.3	4,207	2.2	11,614	6.0	11,964	6.2	10,005	5.2	16,431	8.5
Strongest	Worst	436	0.2	1,076	0.6	4,133	2.1	4,146	2.1	2,543	1.3	4,977	2.6

Abbreviation: UHI: Urban heat island.

are becoming more vulnerable to heat stress, potentially impacting agricultural productivity and the well-being of suburban populations. Mitigation strategies are therefore imperative, including the promotion of "cool materials" (high-albedo roofs and pavements), enhancement of the urban tree canopy, and the design of shaded public spaces (Table 5).[34]

4.5. Limitations and future research

While this study provides valuable insights, certain limitations should be acknowledged. The use of Landsat imagery, while offering a good balance of spatial and temporal resolution, is susceptible to cloud cover, which can limit data availability in tropical regions. The LST retrieval algorithms, though widely accepted, involve certain assumptions that may introduce uncertainties. Furthermore, the spatial resolution of the thermal bands, though resampled to 30 m, is natively coarser and may not capture micro-scale thermal variations within complex urban structures. Critically, this study did not perform a detailed quantitative LULC change analysis, but rather illustrated such changes visually.

Future research could build upon these findings by: (i) Integrating higher-resolution thermal imagery (e.g., Advanced Spaceborne Thermal Emission and Reflection Radiometer, ECOsystem Spaceborne Thermal Radiometer Experiment on Space Station) to examine micro-scale SUHI variations; (ii) conducting a quantitative LULC change analysis to model its relationship with LST increases; (iii) incorporating 3D urban morphology data to develop more sophisticated models; and (iv) assessing the socio-economic impacts of SUHI on public health and energy consumption.

5. Conclusion

This study comprehensively assessed the spatiotemporal dynamics of the SUHI in HCMC over a 36-year period (1988–2024). The findings confirm that HCMC experiences a significant and intensifying SUHI effect, characterized by markedly higher LSTs in urbanized areas compared to surrounding rural regions. Our research demonstrated a substantial increase in the city's overall mean LST, from 25.4°C in 1988 to 28.7°C in 2024, with the thermal impacts of urbanization expanding from the urban core into previously cooler suburban areas. Furthermore, a strong and consistent negative correlation between LST and NDVI underscores the critical cooling role of vegetation.

The implications of these findings are significant for urban planning and environmental management. The documented intensification and expansion of the SUHI necessitate proactive measures to mitigate its adverse effects on human health, energy consumption, and urban livability. Strategies must prioritize the preservation and enhancement of green infrastructure, the adoption of cool construction materials, and the implementation of sustainable urban design principles to foster a more resilient and comfortable urban environment in HCMC.

Acknowledgments

The author expresses gratitude to the University of Science, Viet Nam National University- HCMC, for their support.

Funding

This research was funded by the University of Science, Viet Nam National University-HCMC, under grant number T2024-21.

Conflict of interest

The author declares no competing interests.

Author contributions

This is a single-authored article.

Availability of data

Data can be obtained from the corresponding author upon reasonable request.

References

1. United Nations, Department of Economic and Social Affairs, Population Division. *World Urbanization Prospects: The 2018 Revision*. New York: United Nations; 2019.
2. Voogt JA, Oke TR. Thermal remote sensing of Urban climates. *Remote Sens Environ*. 2003;86(3):370-384. doi: 10.1016/S0034-4257(03)00079-8
3. Zhou W, Huang G, Cadenasso ML. Does spatial configuration matter? Understanding the effects of land cover pattern on land surface temperature in Urban landscapes. *Landsc Urban Plann*. 2011;102(1):54-63. doi: 10.1016/j.landurbplan.2011.03.009
4. Arnfield AJ. Two decades of Urban climate research: A review of turbulence, exchanges of energy and water, and the urban heat island. *Int J Climatol*. 2003;23(1):1-26. doi: 10.1002/joc.859

5. Akbari H, Pomerantz M, Taha H. Cool surfaces and shade trees to reduce energy use and improve air quality in Urban areas. *Sol Energy*. 2001;70(3):295-310. doi: 10.1016/S0038-092X(00)00089-X
6. Santamouris M. Cooling the cities-a review of reflective and green roof mitigation technologies to fight heat island and improve comfort in urban environments. *Sol Energy*. 2014;103:682-703. doi: 10.1016/j.solener.2012.07.003
7. Stewart ID, Oke TR. Local climate zones for Urban temperature studies. *Bull Am Meteorol Soc*. 2012;93(12):1879-1900. doi: 10.1175/BAMS-D-11-00019.1
8. Oke TR. City size and the Urban heat Island. *Atmos Environ*. 1973;7(8):769-779. doi: 10.1016/0004-6981(73)90140-6
9. Sobrino JA, Jiménez-Muñoz JC, Paolini L. Land surface temperature retrieval from LANDSAT TM 5. *Remote Sens Environ*. 2004;90:434-440. doi: 10.1016/j.rse.2004.02.003
10. Weng Q. Thermal infrared remote sensing for Urban climate and environmental studies: Methods, applications, and trends. *ISPRS J Photogramm Remote Sens*. 2009;64(4):335-344. doi: 10.1016/j.isprsjprs.2009.03.007
11. Chakraborty T, Lee X. A simplified Urban-extent algorithm to characterize surface Urban heat islands on a global scale and examine vegetation control on their spatiotemporal variability. *Int J Appl Earth Obs Geoinf*. 2019;74:269-280. doi: 10.1016/j.jag.2018.09.015
12. Zhou D, Xiao J, Bonafoni S, *et al*. Satellite remote sensing of surface urban heat islands: Progress, challenges, and perspectives. *Remote Sens*. 2019;11(1):48. doi: 10.3390/rs11010048
13. Carlson TN, Ripley DA. On the relation between NDVI, fractional vegetation cover, and leaf area index. *Remote Sens Environ*. 1997;62(3):241-252. doi: 10.1016/S0034-4257(97)00104-1
14. Keeratikasikorn C, Bonafoni S. Urban heat island analysis over the land use zoning plan of Bangkok by means of Landsat 8 imagery. *Remote Sens*. 2018;10(3):440. doi: 10.3390/rs10030440
15. Mallick J, Rahman A, Singh CK. Modelling urban heat islands in heterogeneous land surface and its correlation with impervious surface area by using night-time ASTER satellite data in highly urbanizing city, Delhi-India. *Adv Space Res*. 2013;52(4):639-655. doi: 10.1016/j.asr.2013.04.025
16. Wang W, Liu K, Tang R, Wang S. Remote sensing image-based analysis of the Urban heat island effect in Shenzhen, China. *Phys Chem Earth A B C*. 2019;110:168-175. doi: 10.1016/j.pce.2019.01.002
17. Katzschner A, Schwartze F, Thanh B, Schmid M. Introduction to Ho Chi Minh City. In: Katzschner A, Waibel M, Schwede D, Katzschner L, Schmid M, Storch H, editors. *Sustainable Ho Chi Minh City: Climate Policies for Emerging Mega Cities*. Berlin: Springer International Publishing; 2016. p. 5-17.
18. General Statistics Office. *Statistical Yearbook of Viet Nam 2022*. Wiley: Statistical Publishing House; 2022.
19. Anh NH, Trang NTD, Nguyen NTT, Trong TV, Son TV. Application of remote sensing of Ho Chi Minh city's surface temperature in period 2016-2020. *J Hydro Meteorol*. 2021;729:29-39. doi: 10.36335/VNJHM.2021(729).41-51
20. Li X, Zhou Y, Asrar GR, Imhoff M, Li X. The surface urban heat island response to Urban expansion: A panel analysis for the conterminous United States. *Sci Total Environ*. 2017;605-606:426-435. doi: 10.1016/j.scitotenv.2017.06.229
21. U.S. Geological Survey. *EarthExplorer*. Available from: https://earthexplorer.usgs.gov [Last accessed on 2024 Jun 05].
22. Chander G, Markham BL, Helder DL. Summary of current radiometric calibration coefficients for Landsat MSS, TM, ETM+, and EO-1 ALI sensors. *Remote Sens Environ*. 2009;113(5):893-903. doi: 10.1016/j.rse.2009.01.007
23. Ihlen V. *Landsat 8 Data Users Handbook*. USA: Department of the Interior U.S. Geological Survey; 2019.
24. Fallmann J, Forkel R, Emeis S. Secondary effects of Urban heat island mitigation measures on air quality. *Atmos Environ*. 2016;125:199-211. doi: 10.1016/j.atmosenv.2015.10.094
25. Rouse JW, Haas RH, Schell JA, Deering DW. *Monitoring Vegetation Systems in the Great Plains with ERTS. NASA. Goddard Space Flight Center 3d ERTS-1 Symposium*. Vol. 1. United States: NASA; 1974. p. 309-317.
26. Naim MNH, Kafy AA. Assessment of Urban thermal field variance index and defining the relationship between land cover and surface temperature in Chattogram city: A remote sensing and statistical approach. *Environ Challen*. 2021;4:100107. doi: 10.1016/j.envc.2021.100107
27. García DH, Díaz JA. Modeling the surface Urban heat island (SUHI) to study of its relationship with variations in the thermal field and with the indices of land use in the metropolitan area of Granada (Spain). *Sustain Cities Soc*. 2022;87:104166. doi: 10.1016/j.scs.2022.104166
28. Zhang Y, Yu T, Gu XF, *et al*. Land surface temperature retrieval from CBERS-02 IRMSS thermal infrared data and its applications in quantitative analysis of Urban heat island effect. *J Remote Sens*. 2006;10(5):789-797. doi: 10.11834/jrs.200605117
29. Peng S, Piao S, Ciais P, *et al*. Surface Urban heat island across 419 global big cities. *Environ Sci Technol*. 2012;46(2):696-703. doi: 10.1021/es2030438
30. Takebayashi H, Moriyama M. Surface heat budget on

green roof and high reflection roof for mitigation of Urban heat island. *Build Environ*. 2007;42(8):2971-2979. doi: 10.1016/j.buildenv.2006.06.017

31. Bowler DE, Buyung-Ali L, Knight TM, Pullin AS. Urban greening to cool towns and cities: A systematic review of the empirical evidence. *Landsc Urban Plann*. 2010;97(3):147-155. doi: 10.1016/j.landurbplan.2010.05.006
32. Santamouris M. Regulating the damaged thermostat of the cities: The increasing story of the Urban heat island. *Energy Build*. 2015;91(2):1-4. doi: 10.1016/j.enbuild.2015.01.027
33. Tan J, Zheng Y, Tang X, *et al*. The Urban heat island and its impact on heat waves and human health in Shanghai. *Int J Biometeorol*. 2010;54(1):75-84. doi: 10.1007/s00484-009-0256-x
34. Akbari H, Kolokotsa D. Three decades of Urban heat islands and mitigation technologies research. *Energy Build*. 2016;133:834-842. doi: 10.1016/j.enbuild.2016.09.067

Asian Journal of Water, Environment and Pollution. Vol. 22, No. 6 (2025), pp. 221-242.
doi: 10.36922/AJWEP025350269

ORIGINAL RESEARCH ARTICLE

Spatiotemporal dynamics of fractional vegetation cover and its relationship with climatic factors in the Yarkand River Basin

Guoqiang Qin[1,2]*, Kai Yuan[1,2], Guoliang Ding[3], Qiang Guo[1,2], and Runbo Wang[1,2]

[1]Department of Hydraulic Engineering Management, College of Hydraulic and Civil Engineering, Xinjiang Agricultural University, Urumqi, Xinjiang, China
[2]Xinjiang Key Laboratory of Water Engineering Safety and Disaster Mitigation, College of Hydraulic and Civil Engineering, Xinjiang Agricultural University, Urumqi, Xinjiang, China
[3]Department of Environmental Protection Engineering, XPCC Surveying and Designing Institute Group Co., Ltd., Urumqi, Xinjiang, China
***Corresponding author:** Guoqiang Qin (qinguoqiang1988@163.com)

Received: August 25, 2025; 1st revised: September 16, 2025; 2nd revised: September 23, 2025; Accepted: September 28, 2025; Published online: October 24, 2025

Abstract: The Yarkand River Basin, an ecologically fragile zone in arid northwest China, is critical for regional ecological management due to its sensitivity to environmental changes. This study examines the spatiotemporal dynamics of fractional vegetation cover (FVC) from 2000 to 2023 and its correlation with climatic factors, using the moderate resolution imaging spectroradiometer (MODIS) normalized difference vegetation index data and climate observations (temperature and precipitation). FVC was estimated using the pixel dichotomy method, with Sen+Mann–Kendall trend analyses, and Pearson correlation was applied to assess temporal trends and climate-vegetation relationships. MODIS land use data were reclassified to evaluate FVC variations across forestland, grassland, farmland, bare land, and other ecological types. Results revealed significant spatiotemporal heterogeneity in FVC. Spatially, Yecheng County exhibited higher FVC than Bachu County, driven by favorable topography. Temporally, FVC showed a significant upward trend post-2000, particularly in grasslands and croplands, stabilizing between 2010 and 2023. Climate analysis indicated divergent responses: farmland and forest FVC were negatively correlated with temperature (ranging from 8°C to over 9°C). In contrast, grassland and forest FVC were positively associated with precipitation (increasing by ~14 mm). A 1–2-month lag effect was observed in precipitation's impact on FVC. The Hurst index suggested a sustained FVC growth in most regions. These findings highlight the role of climate change in driving FVC dynamics, providing a scientific basis for ecological conservation and sustainable water resource management in arid regions.

Keywords: Yarkand River Basin; Fractional vegetation cover; Land use types; Climatic factors; Ecological management

1. Introduction

Fractional vegetation cover (FVC), a standardized ecological indicator, serves as a critical measure for quantifying the extent of surface vegetation, playing an indispensable role in ecosystem material cycles, energy balance, and regional climate regulation.[1] As a key parameter reflecting vegetation growth status, FVC not only visually delineates spatial distribution patterns of vegetation but also provides essential data for assessing ecosystem service functions, such as carbon sequestration and soil conservation. Against the backdrop of global climate change, climatic factors, such as temperature and precipitation, exert a significant influence on FVC, with arid and semi-arid regions displaying heightened sensitivity to these variations.[2,3] The fragile ecosystems in these areas amplify the ecological consequences, where even subtle FVC fluctuations can trigger cascading effects on processes, such as carbon cycling and surface albedo, ultimately influencing regional and global climate systems. This underscores the urgency of monitoring and understanding FVC dynamics to support sustainable environmental management.

Remote sensing technology has emerged as a cornerstone for studying FVC, leveraging its high spatiotemporal resolution and extensive coverage to monitor vegetation dynamics effectively.[4] Core indicators, such as the normalized difference vegetation index (NDVI) and its derivative, FVC, derived from datasets including the moderate resolution imaging spectroradiometer (MODIS) and Landsat, have yielded significant insights across various river basins.[5] Common methodologies include the coefficient of variation (CV) to assess temporal stability, Sen+Mann–Kendall trend analysis for detecting long-term trends, and Pearson correlation analysis to explore climatic relationships. These approaches, widely validated in arid region studies, provide a robust framework for analyzing FVC spatiotemporal patterns. Building on this foundation, this study employs CV, Sen+Mann–Kendall trend analysis, and Pearson correlation to investigate FVC dynamics in the Yarkand River Basin, thereby enhancing the precision and scope of FVC research.

The Yarkand River Basin, located in the northern Tarim Basin of Xinjiang, China, is a core arid region characterized by a fragile ecological environment. Changes in its FVC significantly impact regional balance in ecology and are intricately linked to several key factors, such as water resources. The water resources not only supply the necessary moisture for vegetation growth but also influence the soil environment that sustains such growth, indirectly affecting vegetation.[6] Other key factors include land use and human activities.[7] As an integral part of the Tarim River Basin, the vegetation dynamics of the Yarkand River Basin are shaped by complex terrain—encompassing alpine glaciers, oasis agricultural zones, and desert ecosystems—and diverse vegetation types, including grasslands, shrubs, croplands, and sparse vegetation.[8] Since 2000, global warming has driven temperature increases and altered precipitation patterns, profoundly affecting vegetation growth and distribution.[9] Previous studies have highlighted that FVC in arid areas typically correlates positively with precipitation, while rising temperatures may inhibit growth through enhanced evapotranspiration.[10,11] Human interventions, such as agricultural irrigation, urbanization, and ecological restoration projects, further influence these dynamics.[12,13] However, existing research, often limited to shorter time scales or single vegetation types, lacks a comprehensive analysis of long-term FVC spatiotemporal variations, county-level differences, and the response mechanisms of diverse vegetation types from 2000 to 2023.[14,15] This gap highlights the need for an in-depth investigation into these aspects.

This study, based on remote sensing data from 2000 to 2023, employs CV, Sen+Mann–Kendall trend analysis, and Pearson correlation to systematically explore the spatiotemporal variation characteristics of FVC in the Yarkand River Basin and its relationship with temperature and precipitation. This study utilizes the latest MODIS NDVI data (MOD13Q1 V6) spanning the extended period from 2000 to 2023 to capture long-term FVC trends and analyzes FVC spatial heterogeneity at the county and land use type scales. The significance of this work lies in: (i) enhancing the understanding of vegetation dynamics and climate response mechanisms in the Yarkand River Basin, offering a reference for regional ecosystem research; (ii) providing a scientific foundation for ecological protection and climate adaptation management in arid regions; and (iii) supporting data-driven water resource management and sustainable development initiatives.

2. Materials and methods

2.1. Overview of the study area

The Yarkand River Basin (36°02'–41°22' north, 75°14'–81°47' east), as shown in Figure 1, is located in the northern part of the Tarim Basin in Xinjiang, China, with a total area of approximately 110,000 km^2, accounting for about 10.7% of the area of the Tarim

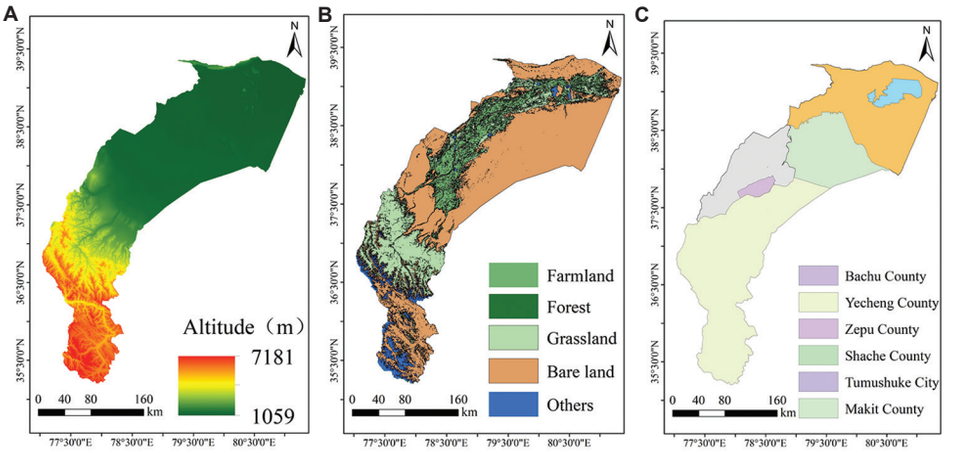


Figure 1. Schematic representation of the Yarkand River Basin. (A) Elevation. (B) Land use types. (C) Administrative division.

Basin.[16] The terrain of this basin is complex, extending from northwest to southeast, covering the alpine glaciers of the Pamir Plateau, the oasis agricultural areas, and the desert area on the edge of the Taklimakan Desert. More than 60% of the area is mountainous and plateau, with an altitude generally above 1,500 m, and the highest peak reaching above 7,000 m.[17] The Yarkand River Basin has a typical continental arid climate. Winters are cold and dry, and summers are short and hot. The average annual temperature ranges from 5 to 12°C. The annual precipitation varies from 300 mm in high mountain areas to <50 mm in lowland oases, showing significant spatial heterogeneity.[18] This climatic condition supports diverse land use types, including bare land, grassland, shrub, farmland, and sparse vegetation. Bare land and sparse vegetation are mainly distributed in arid desert areas, grasslands and shrubs are concentrated in high mountains and the edges of oases, and farmlands are primarily distributed in the irrigated oasis areas along the Yarkand River.[19] These geomorphic and climatic characteristics make the Yarkand River Basin a vital area for studying the relationship between FVC and climate change.[20]

2.2. Remote sensing data sources and processing

2.2.1. Land use type data

In this study, MODIS MCD12Q1 products (2000–2023) were adopted, and land use types in the Yarkand River Basin were extracted and reclassified using the Google Earth Engine (GEE) platform. Based on the 17-category classification system of the International Geosphere-Biosphere Project, the original data were integrated into five categories: forest land, grassland, bare land, farmland, and others, to reflect the ecological functions of the various vegetation types.[21] By leveraging the computing power of the GEE platform, annual land use data from 2000 to 2023 were generated, and GeoTIFF format images were exported using the mode synthesis method, providing high-resolution data support for analyzing the relationship between FVC and climate.[22] This classification and synthesis method provided a reliable data basis for investigating the correlation between vegetation dynamics and climatic factors in the Yarkand River Basin.

2.2.2. NDVI data

This study utilized the MODIS (MOD13Q1) NDVI dataset from the National Aeronautics and Space Administration Earth Observing System/MODIS, with a spatial resolution of 250 m and a time range of 2000–2023. To ensure data accuracy, the image was first processed by cloud, shadow, and water mask processing, and only the NDVI band was retained. Subsequently, the maximum value synthesis method was employed to generate the annual maximum NDVI image, which reflects the optimal state of vegetation growth in the Yarkand River Basin. Through a 5% and 95% quantile analysis, the high and low value ranges of regional NDVI were extracted to characterize the spatiotemporal dynamics of FVC. Similar to the study conducted by Kaur *et al.*,[23] we utilized NDVI thresholding to classify vegetation into several categories, such as sparse, moderate, and dense, adjusting thresholds based on regional vegetation health. The processed NDVI data provide high-resolution support for analyzing the relationship between FVC and temperature and precipitation. In response to concerns about potential errors from relying solely on remote sensing data without

ground validation, we conducted field measurements at selected sites (e.g., Yecheng, Shache, and Zepu counties) using a handheld NDVI device (GreenSeeker RT200, Trimble Inc., United States of America), which showed good agreement between remote sensing data and ground-measured NDVI values, with a correlation coefficient (R^2) exceeding 0.85. This validation enhances the reliability of the MODIS NDVI dataset for ecological analysis in the study area.

2.2.3. Meteorological data

In this study, the China Meteorological Administration (CMA) daily dataset was utilized to obtain temperature and precipitation data for the Yarkand River Basin from 2000 to 2023. Data were collected from approximately 2,400 meteorological stations across China using the Vaisala HMP155A (Vaisala Oyj, Finland) temperature and humidity sensor for temperature measurements, and the Tipping Bucket Rain Gauge RG13-H (Vaisala Oyj, Finland) for precipitation measurements, with a spatial resolution of 1 km. To align with the 250 m resolution of the MODIS NDVI data used for FVC analysis, the CMA data were resampled using ArcGIS software (ArcGIS 10.8, ESRI, United States of America). By overlaying land use type maps (forest land, grassland, bare land, farmland, and others), we generated annual average temperatures and total precipitation for each land type. In addition, by integrating the administrative boundaries of counties and cities, we extracted annual average temperatures and precipitation for each administrative unit to assess the spatial heterogeneity of the regional climate. The annual temperature and precipitation data for the entire region were calculated as average values to reveal the overall trend of climate change. A public access link for the CMA dataset is available at http://data.cma.cn.

2.3. Research methodology

2.3.1. Pixel dichotomy

In this study, the FVC of the Yarkand River Basin for 2000–2023 was estimated using the pixel dichotomy method, which decomposes the image spectra into vegetative and non-vegetative components to calculate the FVC (Equation I).

$$FVC = \frac{NDVI - NDVI_{min}}{NDVI_{max} - NDVI_{min}} \quad \text{(I)}$$

Where NDVI is the image element NDVI value, $NDVI_{max}$ and $NDVI_{min}$ are the 95% and 5% confidence values of the regional NDVI gray scale distribution, reflecting pure vegetation and bare soil characteristics, respectively.[24] Combined with the dynamic adjustment thresholds for land use types (woodland, grassland, bare land, farmland, etc.), the FVC was categorized into five levels: low coverage ($0 \leq FVC < 0.2$), medium-low coverage ($0.2 \leq FVC < 0.4$), medium coverage ($0.4 \leq FVC < 0.6$), medium-high coverage ($0.6 \leq FVC < 0.8$), and high coverage ($0.8 \leq FVC \leq 1$).[25]

2.3.2. CV

In this study, the CV was used to quantify the interannual fluctuations of FVC in the Yarkand River Basin from 2000 to 2023, assessing vegetation stability (Equation II).

$$CV_{FVC} = \frac{\sigma_{FVC}}{\overline{FVC}} \quad \text{(II)}$$

Where σ_{FVC} is the standard deviation, and $\overline{FVC}$ is the mean FVC over the 24 years. A smaller CV_{FVC} indicates lower fluctuation. Combining land use types (forest land, grassland, bare land, farmland, etc.) and county/city classifications, spatial differences in FVC fluctuation were analyzed. FVC fluctuation was categorized into five levels: low fluctuation change ($CV_{FVC} \leq 0.1$), lower fluctuation change ($0.1 < CV_{FVC} \leq 0.15$), medium fluctuation change ($0.15 < CV_{FVC} \leq 0.2$), higher fluctuation change ($0.2 < CV_{FVC} \leq 0.3$), and high fluctuation change ($CV_{FVC} > 0.3$).[26,27]

2.3.3. Sen+Mann–Kendall trend analysis

This study employed the Sen+Mann–Kendall trend analysis to assess the spatiotemporal trends in FVC in the Yarkand River Basin from 2000 to 2023. The Mann-Kendall test determined the presence of a significant trend by comparing the order relationships between data points, without relying on the specific distribution of the data, making it suitable for vegetation studies in arid regions. The Theil-Sen slope quantified the magnitude of change, and spatial heterogeneity was analyzed by combining land use types (forest land, grassland, bare land, farmland, etc.) and county/city classifications. The Mann-Kendall test was used to assess significance. Trends were categorized into five levels: highly significant increase ($S > 0$, $p<0.01$), significant increase ($S > 0$, $0.01 \leq p<0.05$), no significant change ($p \geq 0.05$), significant decrease ($S < 0$, $0.01 \leq p<0.05$), and highly significant decrease ($S < 0$, $p<0.01$).[28,29]

2.3.4. Pearson correlation analysis

This study employed Pearson correlation coefficient analysis using the Matrix Laboratory (MATLAB, MathWorks, Inc., United States of America) platform to

investigate the pixel-by-pixel correlation between FVC and climatic factors (temperature and precipitation) in the Yarkand River Basin from 2000 to 2023. The formula of the correlation coefficient was shown in Equation III.

$$r = \frac{\sum_{i=1}^{n}(x_i - \bar{x})(y_i - \bar{y})}{\sqrt{\sum_{i=1}^{n}(x_i - \bar{x})^2 \sum_{i=1}^{n}(y_i - \bar{y})^2}} \quad \text{(III)}$$

where r is the correlation coefficient of x (FVC) and y (temperature or precipitation), and $\bar{x}$ and $\bar{y}$ are the mean values of variables x and y. Based on the calculated results combined with the significant p-value, the correlation was categorized into five classes: highly significant positive correlation ($r \geq 0.5$, $p<0.01$), significant positive correlation ($0.25 \leq r < 0.5$, $p<0.05$), non-significant correlation ($|r| < 0.25$, $p \geq 0.05$), and significant negative correlation ($-0.5 < r \leq -0.25$, $p<0.05$), and highly significant negative correlation ($r \leq -0.5$, $p<0.01$).[30,31]

2.3.5. Persistence analysis

The Hurst exponent, which can be used to predict future trends based on vegetation health index (VHI) time series, is typically calculated using the rescaled range (R/S) analysis method. It characterizes the long-term memory of the VHI time series, ranging from 0 to 1. The Hurst exponent is estimated through several computational relationships (Equations IV to VIII).

$$\frac{R_\tau}{S_\tau} = (c\tau)^H \quad \text{(IV)}$$

$$R_\tau = max_{1 \leq t \leq \tau} X_{t,\tau} - min_{1 \leq t \leq \tau} X_{t,\tau} \quad \text{(V)}$$

$$S_\tau = \left[\frac{1}{\tau}\sum_{t=1}^{\tau}\left(FVC_t - \overline{FVC}_\tau\right)^2\right]^{\frac{1}{2}} (\tau = 1,2,\cdots,n) \quad \text{(VI)}$$

$$X_{t,\tau} = \sum_{t=1}^{t}\left(FVC_t - \overline{FVC}_\tau\right)(1 \leq t \leq \tau) \quad \text{(VII)}$$

$$\overline{FVC}_\tau = \frac{1}{\tau}\sum_{t=1}^{\tau} FVC_t (\tau = 1,2,\cdots,n) \quad \text{(VIII)}$$

where H represents the Hurst exponent, t is the time variable, τ is the time lag, and c is a constant. Values of H within the ranges of $0 < H < 0.5$, $H = 0.5$, and $0.5 < H < 1$ indicate that the VHI time series exhibits anti-persistence (i.e., future trends are opposite to past behavior), random walk behavior (i.e., future changes are uncorrelated with the past), and persistence (i.e., future trends align with past behavior), respectively. Furthermore, as the value of H approaches 1, the persistence strength of the VHI series increases; conversely, as it approaches 0, the anti-persistence intensity strengthens.

3. Results

3.1. Characteristics of the spatial distribution of FVC

The Yarkand River Basin flows from north to south and passes through six counties and cities: Bachu County, Tumushuke City, Makit County, Shache County, Zepu County, and Yecheng County. The FVC in the basin shows noticeable spatial differences, as shown in Figure 2. Overall, it presents a long and narrow vegetation belt running from northeast to southwest, as well as a vegetation belt spanning from northwest to southeast, respectively. The high and medium-high FVC is mainly distributed in the central part of Bachu County, the middle area between the north and south of Tumushuke City, the long and narrow western area of Makit County, the eastern part of Shache County, the vast northern and central regions of Zepu County, the northwestern area connecting Yecheng County and Zepu County, and the mountainous region in the central part.

FVC and its interannual fluctuation were analyzed across county-level administrative units of the Yarkand River Basin (Tables 1 and 2). The results show that the proportion of low coverage in Bachu and Makit is the highest (close to 80%), and the high fluctuation changes are significant (55.9% in Bachu and 72.63% in Makit), indicating that the FVCs in these two counties are poor and have low stability. The proportions of medium-high and high coverage in Zepu and Tumushuke were the highest (61.01% in total for Zepu and 40.51% in total for Tumushuke), among which the high fluctuation change in Zepu was the lowest (25.41%), indicating that its FVC was good and relatively stable. Within the entire area, the proportion of low coverage reached 65.75%, and the proportion of high fluctuation variation was 55.95%, indicating that the overall FVC level in the study area was relatively low and exhibited significant interannual variation.

From 2000 to 2023, the FVC coverage and volatility in the Yarkand River Basin varied significantly among different land use types (Tables 3 and 4). The high coverage of agricultural land accounted for 51.75%, and the medium-high coverage of forest amounted to 60.81%, indicating that irrigation and natural conditions promote the growth of vegetation. Low coverage in bare land accounted for 95.58% and high fluctuation accounted for 74.51%, indicating high environmental

Table 1. Multi-year average fractional vegetation cover share percentage and acreage in different counties and cities

Degree of coverage	Administrative units in the Yarkand River Basin (%; km²)						
	Bachu County	Makit County	Shache County	Tumushuke City	Yecheng County	Zepu County	Entire area
Low coverage	79.80%; 14,683.20	79.95%; 8,714.55	54.82%; 4,910.23	20.04%; 386.17	59.34%; 16,971.24	20.25%; 200.07	65.75%; 45,875.09
Low to medium coverage	8.83%; 1,624.72	5.43%; 591.87	14.91%; 1,335.49	25.61%; 493.50	26.43%; 7,558.98	10.51%; 103.84	16.78%; 11,707.74
Medium coverage	3.20%; 588.80	2.93%; 319.37	7.17%; 642.22	13.85%; 266.89	7.09%; 2,027.74	8.24%; 81.41	5.62%; 3,921.19
Medium to high coverage	3.33%; 612.72	4.86%; 529.74	10.91%; 977.21	20.02%; 385.79	4.24%; 1,212.64	27.21%; 268.83	5.71%; 3,983.98
High coverage	4.83%; 888.72	6.83%; 744.47	12.19%; 1,091.86	20.49%; 394.84	2.89%; 826.54	33.80%; 333.94	6.14%; 4,284.00

Table 2. Share percentage and acreage of fractional vegetation cover coefficient of fluctuation in different counties and cities

Degree of fluctuation	Administrative units in the Yarkand River Basin (%; km²)						
	Bachu County	Makit County	Shache County	Tumushuke City	Yecheng County	Zepu County	Entire area
Low fluctuation change	3.38%; 621.92	3.49%; 380.41	5.39%; 482.78	6.50%; 125.26	3.33%; 952.38	15.66%; 154.72	3.90%; 2,721.11
Lower fluctuation change	9.16%; 1,685.44	5.95%; 648.55	14.85%; 1,330.12	17.98%; 346.47	12.64%; 3,615.04	37.09%; 366.45	11.46%; 7,995.87
Medium fluctuation change	12.32%; 2,266.88	5.91%; 644.19	13.53%; 1,211.88	20.64%; 397.73	13.86%; 3,963.96	14.57%; 143.95	12.36%; 8,623.82
Higher fluctuation change	19.23%; 3,538.32	12.02%; 1,310.18	19.36%; 1,734.08	23.11%; 445.33	15.03%; 4,298.58	7.27%; 71.83	16.33%; 11,393.77
High fluctuation change	55.90%; 10,285.60	72.63%; 7,916.67	46.88%; 4,199.04	31.76%; 612.02	55.12%; 15,764.32	25.41%; 251.05	55.95%; 39,037.43

Table 3. Multi-year average fractional vegetation cover share percentage and acreage in different land use types

Degree of coverage	Administrative units in the Yarkand River Basin (%; km²)					
	Farmland	Forests	Grassland	Bare land	Others	Entire area
Low coverage	0.85%; 64.07	2.06%; 0.83	26.56%; 4,146.97	95.58%; 40,918.22	14.35%; 469.02	65.75%; 45,874.50
Low to medium coverage	5.32%; 403.03	6.48%; 2.62	42.50%; 6,635.99	4.12%; 1,764.40	85.13%; 2,781.72	16.78%; 11,706.89
Medium coverage	9.72%; 736.80	23.45%; 9.49	19.37%; 3,024.00	0.23%; 96.46	0.31%; 10.03	5.62%; 3,923.86
Medium to high coverage	32.37%; 2,454.50	60.81%; 24.60	9.22%; 1,439.56	0.06%; 26.01	0.13%; 4.20	5.71%; 3,984.98
High coverage	51.75%; 3,923.54	7.19%; 2.91	2.36%; 367.74	0.01%; 4.15	0.08%; 2.63	6.14%; 4,281.77

sensitivity. Grassland has 42.50% of low cover and 34.90% of high fluctuation, which may be affected by precipitation changes. The proportion of low coverage in the whole area is 65.75%, and the proportion of high

Table 4. Share percentage and acreage of fractional vegetation cover coefficient of fluctuation in different land use types

Degree of fluctuation	Administrative units in the Yarkand River Basin (%; km²)					
	Farmland	Forests	Grassland	Bare land	Others	Entire area
Low fluctuation change	23.02; 1,741.53	22.18; 11.82	2.71; 423.27	0.73; 312.08	7.49; 243.17	3.90; 2,719.20
Lower fluctuation change	33.55; 2,538.08	46.16; 24.60	13.70; 2,138.89	4.50; 1,919.62	39.25; 1,274.88	11.46; 7,994.74
Medium fluctuation change	16.81; 1,271.58	21.24; 11.32	19.57; 3,055.42	6.90; 2,945.40	39.03; 1,267.78	12.36; 8,624.87
Higher fluctuation change	13.10; 991.01	7.98; 4.25	29.12; 4,547.28	13.36; 5,704.27	0.63; 20.63	16.33; 11,394.23
High fluctuation change	13.52; 1,022.82	2.44; 1.30	34.90; 5,449.99	74.51; 31,799.37	13.60; 441.65	55.95; 39,038.96

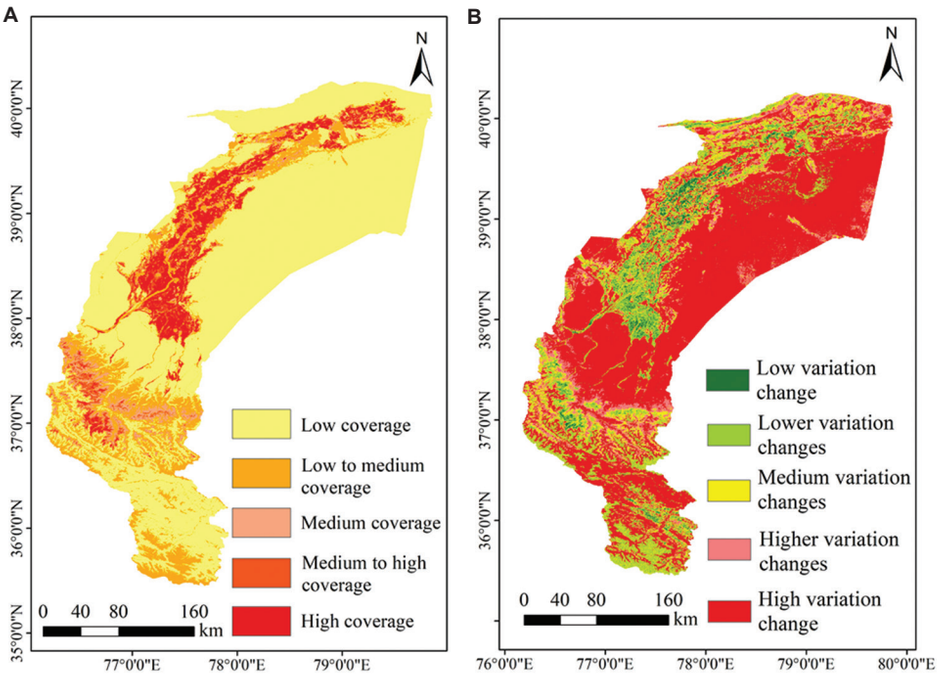


Figure 2. Multi-year data of fractional vegetation cover in the Yarkand River Basin from 2000 to 2023. (A) Mean. (B) Fluctuation.

fluctuation is 55.95%, reflecting the vulnerability of vegetation in arid regions. The lower fluctuation of the forest accounted for 46.16%, with the best stability, which may be related to the adaptation of forest trees. Bare land cover was low and fluctuating, with high difficulty in ecological restoration. The study reveals the role of land use types in regulating the distribution and stability of FVC, providing a basis for environmental management. In the future, it will be necessary to optimize the bare land restoration strategy in combination with land use dynamics to enhance the regional ecological stability.

3.2. Interannual trends of FVC

Between 2000 and 2023, FVC in the Yarkand River Basin exhibited significant spatial and temporal changes (Figure 3). The FVC of the whole area increased from 0.16 to 0.22 and stabilized at 0.21–0.23 after 2010, indicating an overall improvement of FVC. Based on the results of linear regression analysis, the spatial and temporal evolution of FVC in the study area showed significant regional differentiation. Tumushuke showed the strongest growth trend (slope = 0.009, R^2 = 0.819), with its FVC increasing continuously from 0.39 in 2000

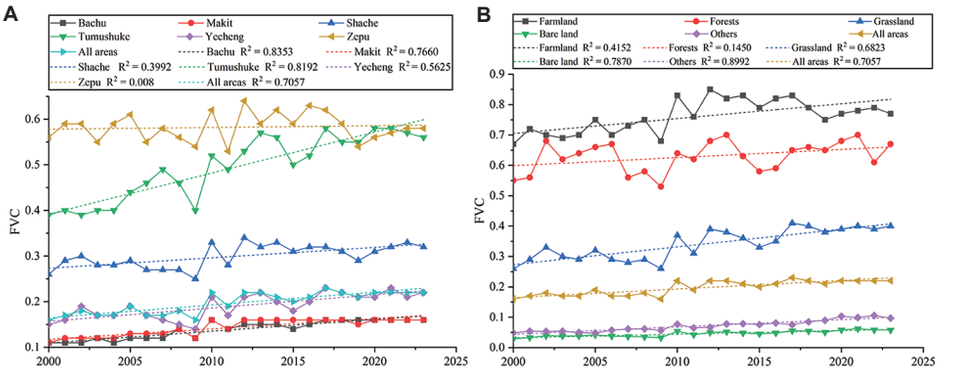


Figure 3. Evolution of FVC in different categories of the Yarkand River Basin. (A) Evolution of FVC in other administrative regions. (B) Evolution of FVC in various land use types.
Abbreviation: FVC: Fractional vegetation cover.

to 0.56 in 2023. Bachu (slope = 0.0026, $R^2 = 0.835$) and Makit (slope = 0.0023, $R^2 = 0.766$) exhibited relatively slow growth but a high goodness-of-fit to the model. It is noteworthy that the Zepu region ($R^2 = 0.008$) lacks statistical significance in its trend due to the high FVC levels (0.56–0.64) over a long period.

On the whole-area scale, FVC showed a stable upward trend (slope = 0.0028, $R^2 = 0.706$), which was consistent with the pattern of change in most counties and cities. However, the model fits of Shache ($R^2 = 0.399$) and Yecheng ($R^2 = 0.563$) were relatively low, suggesting that several factors, such as agricultural expansion or occasional natural disasters, may have interfered with the long-term change pattern of FVC in these regions.

Under different land use type classifications, farmland FVC increased from 0.67 to 0.77, peaking at 0.83 in 2010, reflecting the irrigation management effect; forest FVC increased steadily from 0.55 to 0.70, showing natural adaptation; grassland FVC increased from 0.26 to 0.40, stabilizing after 2017, benefiting from improved water resources; and bare land FVC increased from 0.03 to 0.06, with slow growth and limited ecological restoration; other types FVC increased from 0.05 to 0.10, with a rapid increase after 2020, probably related to land use adjustment. The period from 2000 to 2010 was one of rapid growth, and from 2010 to 2023, the growth leveled off, suggesting that management measures were effective in the early years. The differences in land use types reflect the combined drive of artificial interventions and natural conditions, and the slow growth of bare land requires attention to ecological vulnerability.

From 2000 to 2023, the FVC trend (Sen+Mann–Kendall analysis) in the Yarkand River Basin showed significant regional differentiation (Figure 4). The degree of FVC change in the counties and cities of the Yarkand River Basin is shown in Table 5, with a highly significant increase ($p<0.01$) accounting for 72.55% of the total area, a significant increase of 15.94%, and a decrease of only 8.32%, indicating an overall improvement in FVC. Makit County had the highest percentage of highly significant increase (77.93%) and decrease of only 5.67%, indicating the most significant improvement in FVC. Yecheng County had a highly significant increase of 73.83% and a decrease of 4.67%, indicating significant vegetation recovery. Tumushuke City and Bachu County had an increase of 82.13% and 89.86%, respectively (decrease of 9.60% and 8.24%), with improvement dominating. Shache County experienced a highly significant increase of 71.51% but a decrease of 19.41%, reflecting the coexistence of degradation and improvement, which may be influenced by human interference. Zephyr County experienced a highly significant increase of 47.35% and a highly significant decrease of 40.94%, indicating a balanced trend with both positive and negative outcomes.

The trend of FVC change in the Yarkand River Basin showed significant differences among different land use types, as shown in Table 6. Grassland and bare land accounted for 80.22% and 78.40% of the highly significant increase, indicating that the natural vegetation recovery was evident. Forest accounted for 58.80% of the highly significant increase, and the increase was superior, which may be due to the benefit of ecological protection. Farmland accounted for 51.86% of the highly significant increase; however, the highly significant decrease of 34.28% indicated that management effectiveness and degradation coexist. Other types of significant increase accounted for 85.93%, the decrease v was extremely low, and

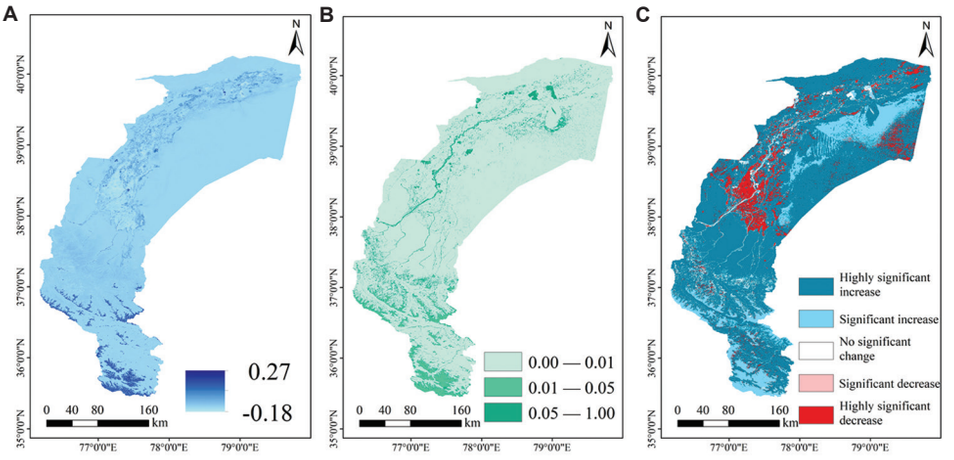


Figure 4. Spatial distribution of annual trends of fractional vegetation cover in the Yarkand River Basin from 2000 to 2023. (A) Slope of change. (B) *p*-value. (C) Zone of significant change.

Table 5. The extent of change in share percentage and acreage of fractional vegetation cover in different counties and cities

Degree of coverage	Administrative units in the Yarkand River Basin (%; km²)						
	Bachu County	Makit County	Shache County	Tumushuke City	Yecheng County	Zepu County	Entire area
Highly significant increase	69.44; 12,763.69	77.93; 8,507.49	71.51; 6,374.62	70.79; 1,353.02	73.83; 21,114.62	47.35; 476.47	72.55; 50,620.16
Significant increase	20.42; 3,753.18	14.57; 1,590.98	4.70; 418.89	11.34; 216.70	17.77; 5,081.43	5.11; 51.40	15.94; 11,120.30
No significant change	1.91; 351.46	1.82; 199.14	4.38; 390.67	8.28; 158.24	3.73; 1,066.94	6.17; 62.06	3.20; 2,229.99
Significant decrease negative increase	0.07; 12.73	0.09; 10.31	0.20; 17.55	0.49; 9.38	0.07; 20.09	0.44; 4.39	0.11; 74.47
Highly significant decrease	8.17; 1,501.06	5.58; 609.59	19.21; 1,712.87	9.11; 174.07	4.60; 1,314.15	40.94; 411.94	8.21; 5,727.08

Table 6. The extent of change in share percentage and acreage of fractional vegetation cover in different land use types

Degree of coverage	Administrative units in the Yarkand River Basin (%; km²)					
	Farmland	Forests	Grassland	Bare land	Others	Entire area
Highly significant increase	51.86; 3,968.19	58.80; 31.34	80.22; 12,321.99	78.40; 33,508.53	7.23; 236.95	72.55; 50,620.16
Significant increase	9.67; 739.63	8.89; 4.74	5.94; 912.07	15.40; 6,582.78	85.93; 2,816.53	15.94; 11,120.30
No significant change	3.78; 289.19	11.20; 5.97	7.63; 1,172.34	1.35; 577.66	5.89; 192.96	3.20; 2,229.99
Significant decrease	0.42; 31.86	0.69; 0.37	0.24; 36.57	0.02; 7.09	0.01; 0.35	0.11; 74.47
Highly significant decrease	34.28; 2,623.45	20.42; 10.88	5.97; 917.11	4.83; 2,065.22	0.95; 31.04	8.21; 5,727.08

the growth was stable. The growth trend of the entire area was consistent with the development of the oasis and water resource management initiatives after 2000. However, the high proportion of decline of farmland

suggested the risk of localized degradation. Differences in land use types reflected the combined drive of artificial intervention and natural conditions, with bare land and grassland showing significant growth, and farmland requiring optimized management.

3.3. Sustainability analysis of FVC

The Hurst index was employed to analyze the long-term memory and persistence of the FVC time series, with results shown in Figure 5. At the regional scale, the annual mean FVC exhibited strong positive persistence, with a Hurst coefficient of 0.81. To validate this finding, the climacogram method was additionally applied, yielding a similar value of 0.896. The close agreement between the R/S and climacogram methods confirmed the robustness of the persistence detected at the regional level. In contrast, the mean Hurst coefficient across the entire raster grid was 0.44, indicating anti-persistence at the local scale, where FVC changes were more likely to reverse existing trends. This spatial divergence reflects the region's complex heterogeneity: oases, supported by irrigated agriculture, typically show higher FVC and local persistence ($H > 0.5$); deserts, constrained by scarce precipitation and significant interannual variability, exhibit very low FVC and anti-persistence ($H < 0.5$); and mountainous areas, shaped by complex topography and limited water availability, display unstable FVC dynamics with generally lower Hurst values. Areas with persistently low FVC or data gaps may further reduce the mean coefficient, contributing to the overall anti-persistent trend at the local scale.

In contrast, the Hurst coefficient of 0.81 (>0.5) for the annual mean FVC indicated strong positive persistence, with FVC changes tending to maintain existing trends (e.g., continuous increase). By spatially averaging FVC across the study area, the differences among oases, deserts, and mountains were smoothed out, highlighting the overall regional trend. In recent years, the Yarkand River Basin has benefited from the expansion of oasis agriculture, afforestation policies, and ecological restoration measures (e.g., windbreak and sand-fixation forest construction), leading to a likely sustained increase in regional mean FVC, particularly in oasis areas supported by irrigation, which enhances FVC stability. The influence of deserts and mountains was diminished after spatial averaging, resulting in a smoother time series for the annual mean FVC, reflecting long-term ecological stability at the regional scale.

From a spatial distribution perspective, the FVC in the plain areas of the Yarkand River Basin generally exhibited positive and strong positive persistence. In contrast, in mountainous regions, it predominantly showed anti-persistence and strong anti-persistence. This is primarily because plain areas, as key regions for irrigated agriculture, benefit from effective water resource management and optimized irrigation

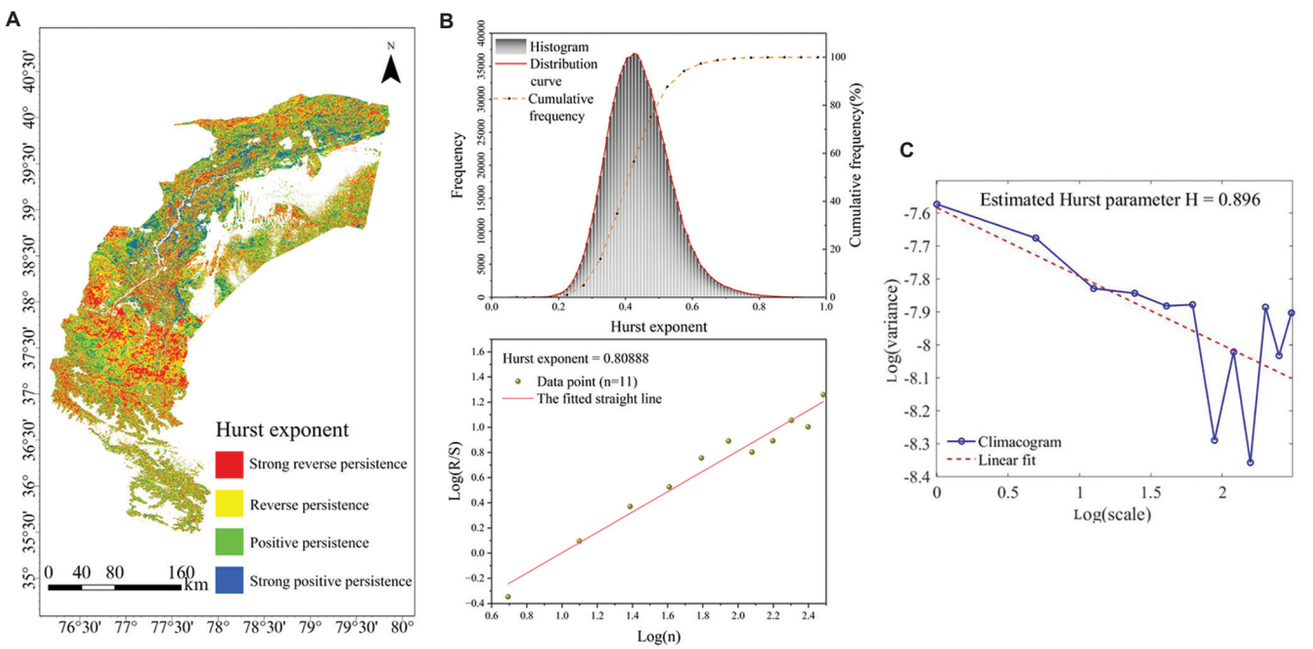


Figure 5. Annual fractional vegetation cover change trends in the Yarkand River Basin from 2000 to 2023. (A) Distribution. (B) Characteristics of sustainability. (C) Climacogram.

techniques, providing favorable conditions for vegetation growth. In addition, farmland protection policies and land reclamation measures create a conducive environment for the development of vegetation. However, in mountainous areas, complex terrain combined with harsh climatic conditions and surface exposure due to snowmelt restricts vegetation growth potential.

The Hurst coefficients in the Yarkand River Basin reflect the impact of spatial heterogeneity on vegetation dynamics. The positive persistence in oasis areas was offset by the anti-persistence in desert and mountainous areas, resulting in a lower mean Hurst coefficient across the entire grid. Desert areas, affected by extreme aridity and wind erosion, experienced significant fluctuations in FVC with easily reversible trends, while mountainous areas, constrained by terrain and climate, exhibited unstable changes in FVC. These local-scale anti-persistent trends, combined with the positive persistence in oasis areas, shaped the spatial distribution of the Hurst coefficient across the region. The regional-scale positive persistence (H = 0.81) highlighted the stabilizing contribution of oasis agriculture and ecological protection measures to overall FVC.

The mean Hurst coefficient for the entire grid (H = 0.44) underscored the spatial heterogeneity and ecological vulnerability of FVC at the local scale in the Yarkand River Basin. The positive persistence in oasis areas indicated that irrigated agriculture and ecological restoration measures (e.g., afforestation) support long-term FVC stability, while the anti-persistence in desert areas reflected constraints from aridity and wind erosion, and mountainous areas were limited by terrain and precipitation, making FVC susceptible to short-term disturbances (e.g., drought, floods). The Hurst coefficient of 0.81 for the annual mean FVC suggested long-term stability of FVC at the regional scale, likely driven by the dominant role of oasis areas and regional ecological policies, such as afforestation, oasis expansion, and optimized water resource management. Climatic factors (e.g., precipitation fluctuation, temperature rise) and human activities (e.g., agricultural reclamation, overgrazing) further exacerbate spatial heterogeneity, shaping the distinct FVC dynamics across different geomorphic units.

3.4. Analysis of drivers of FVC

3.4.1. Spatial distribution and interannual fluctuation of climate factors

The multi-year average temperature data in counties and cities in the Yarkand River Basin showed obvious spatial differentiation patterns (Figure 6). The spatial

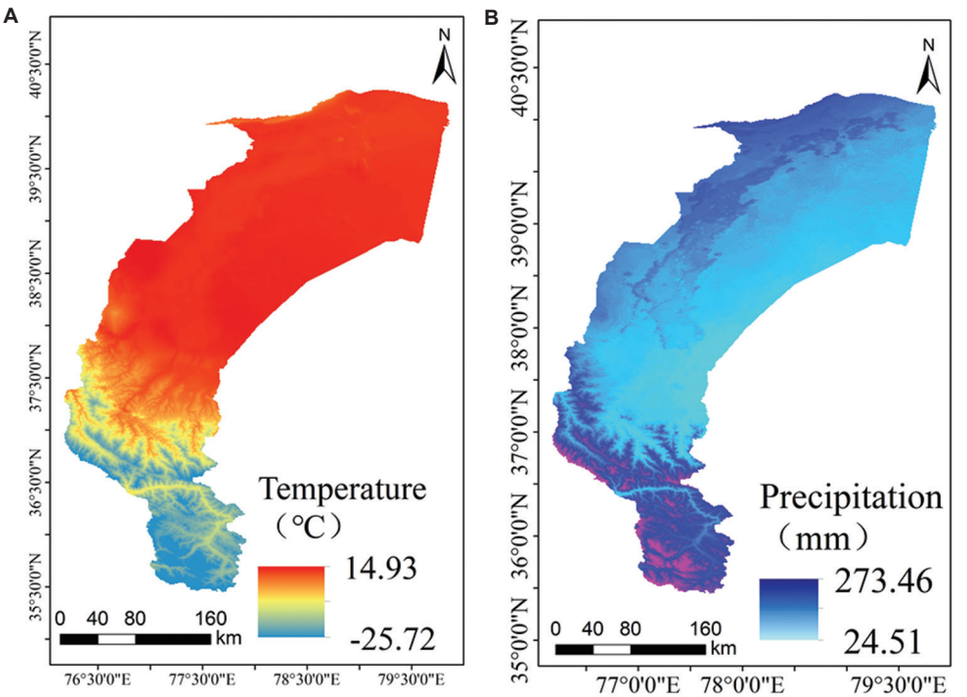


Figure 6. Spatial distribution of the average status of climate factors in the Yarkand River Basin from 2000 to 2023. (A) Spatial distribution of multi-annual mean temperature. (B) Spatial distribution of multi-year precipitation.

interannual variations of climate factors in counties and cities are shown in Figure 7, with higher and least varied temperatures in Bachu County (7.4–14°C), Tumushuke City (11.6–13.3°C), Makit County (13–14.2°C), and Zepu County (13.3–14.4°C). The regional differences in the multi-year mean temperatures in Shache County (−4.8–14.9°C) and Yecheng County (−25.7–14.5°C) were evident, which may be related to the fact that some regions of higher terrain in the northern part of the county were prone to accumulating cold air during winter.[32] Overall, the temperature distribution in the region showed three characteristics: first, the temperature in the plain oasis area generally maintained between 11 and 14°C; second, the temperature fluctuated greatly in the northern region close to the Tianshan Mountains; and third, the temperature varied exceptionally with altitude in the southern Kunlun Mountains. This distribution pattern reflected both the general geographic context and the profound influence of local topography on temperature.[33] Follow-up studies can be conducted to further clarify the specific role of topographic factors in temperature distribution by combining the elevation locations of specific weather stations.

The multi-year average precipitation of the counties and cities in the Yarkand River Basin showed noticeable spatial differences and local peculiarities. Overall, the region was extremely arid, with annual precipitation generally lower than 90 mm, below the national average, except for high values in Yecheng County. In terms of distribution trends, Bachu County and Tumushuke City in the north (34.1–85.3 mm and 40.4–65.7 mm) were slightly higher than Makit County in the south (31.8–61 mm), but Yecheng County (24.5–273.5 mm), due to the proximity of the Kunlun Mountains terrain uplift effect, showed a high value of precipitation rarely seen in the southern Xinjiang, which was probably affected by strong convection in the mountainous areas or the residual water vapor of the Indian Ocean monsoon.[34] The significant difference in precipitation between Shache County (33.9–89.7 mm) and the neighboring Zephyr County (35.9–47.9 mm) may be related to microtopography and oasis effects.[35] Overall, precipitation in the region mainly relied on weak water vapor from the westerly wind belt, while basin topography exacerbated drought. Notably, only Yecheng County formed a unique precipitation pattern due to changes in the elevation gradient.

The trend of temperature and precipitation changes under different land use types in the Yarkand River Basin is shown in Figure 8. Farmland and bare land exhibited the largest increase (1.07°C and 1.03°C, respectively), while other types had the smallest decrease (0.74°C), reflecting regional temperature rise differences. Precipitation increased from 35.01 mm to 49.03 mm, with peaks of 68.52 mm and 80.00 mm in 2003 and 2005, and a significant increase in other types (19.03 mm), indicating improved water resources.[36] Farmland and forest temperature increases were correlated with steady FVC increases. Similarly, an increase in grassland precipitation was consistent with the rise in FVC, while the increase in bare land temperature may suppress FVC. High precipitation but fluctuating FVC in other land types suggested low utilization efficiency (Figures 3, 7, and 8). The trends indicated that warming temperatures and increased precipitation together drove improvements in vegetation, with land use types modulating the intensity of the response.

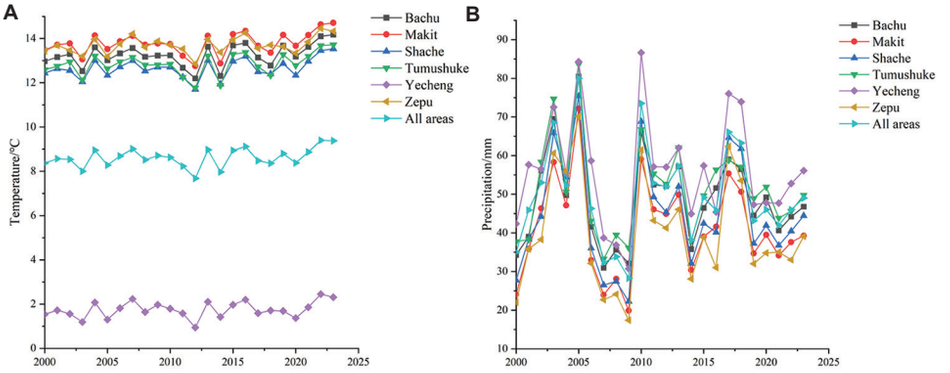


Figure 7. Interannual variation of climatic factors in counties and cities of the Yarkand River Basin. (A) Interannual variation in temperature factors by county and city. (B) Interannual variation in precipitation factors by county and city area.

3.4.2. Correlation analysis between FVC and climate factors

Based on *p*-value significance tests, the correlation between FVC and climate factors in the Yarkand River Basin from 2000 to 2023 is shown in Figures 9 and 10. The correlations for each county are shown in Tables 7 and 8. The positive correlation (extremely significant and significant) between FVC and temperature was the highest in Yecheng County (27.89%), possibly due to the extended vegetation growth cycle caused by rising temperatures, especially in spring, which improves coverage.[37] Zepu County had a negative correlation of 39.44%, while Shache County correlated of 30.30%. High temperatures can exacerbate water evaporation and hinder vegetation growth, particularly during drought years.[38] The proportion of non-significant correlations in Tumushuke City was 50.24%, while Bachu County and Makit County showed balanced positive and negative correlations (27.71% vs. 25.84% and 25.20% vs. 23.79%, respectively), indicating that the impact of temperature on FVC varies by location.[39] Across the entire region, 26.64% showed a positive correlation and 24.52% showed a negative correlation, reflecting the complex effects of temperature.[40]

FVC showed a significant positive correlation with precipitation in Shache County and Yecheng County (62.12% and 60.33%, respectively), with a regional average of 51.77%, indicating that increased precipitation significantly promotes FVC, particularly in water-sensitive areas, possibly due to precipitation that optimized soil moisture.[37] In Tumushuke City, the proportion of negative correlations was 19.52%, and the proportion of non-significant correlations was 64.75%, possibly due to excessive precipitation causing soil erosion or vegetation adapting to drought, with precipitation changes disrupting ecological balance.

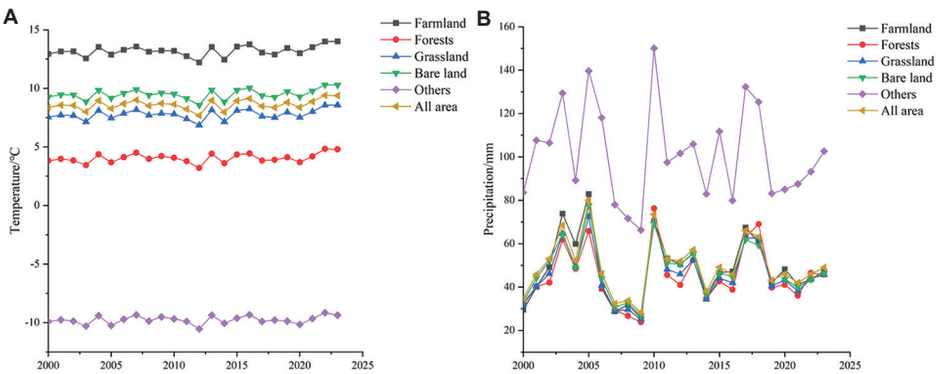


Figure 8. Interannual variation of climatic factors by land use types in the Yarkand River Basin. (A) Interannual fluctuation of temperature factors under different land use types. (B) Interannual fluctuation in precipitation factors for different land use types.

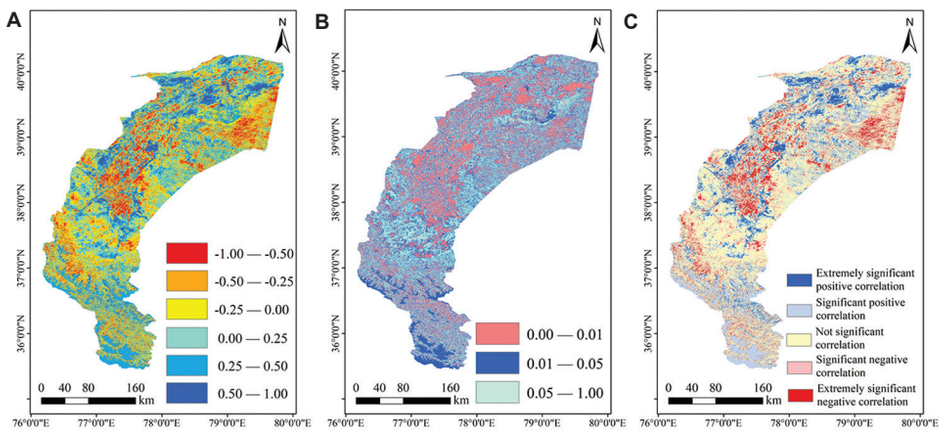


Figure 9. Correlation analysis between fractional vegetation cover changes and annual average temperature in the Yarkand River Basin from 2000 to 2023. (A) Correlation between fractional vegetation cover and annual average temperature. (B) *p*-value. (C) Significant change area.

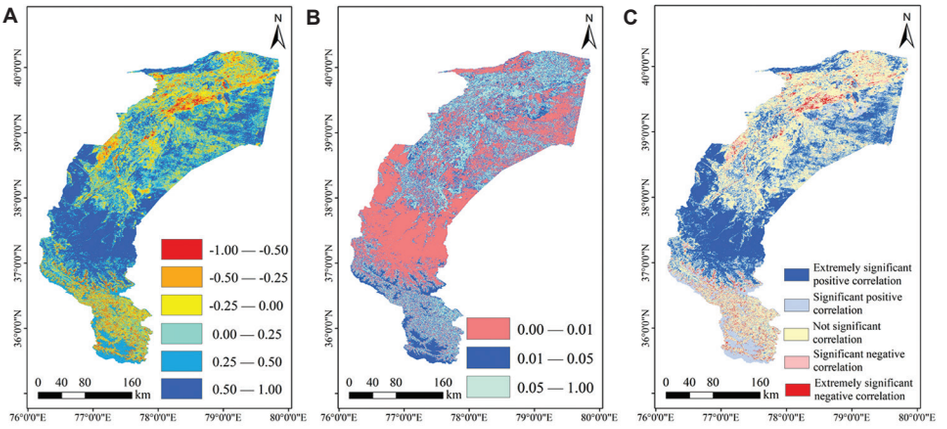


Figure 10. Correlation analysis between fractional vegetation cover changes and annual precipitation averages in the Yarkand River Basin from 2000 to 2023. (A) Correlation between fractional vegetation cover and annual precipitation. (B) *p*-value. (C) Significant change area.

Table 7. Acreage and share percentage of various correlations between fractional vegetation cover and temperature in different counties and cities

Relevance	Administrative units in the Yarkand River Basin (%; km²)						
	Bachu County	Makit County	Shache County	Tumushuke City	Yecheng County	Zepu County	Entire area
Extremely significant positive correlation	15.32; 2,815.38	13.21; 1,442.12	12.50; 1,114.18	16.52; 315.71	8.93; 2,553.06	15.84; 159.50	12.05; 8,405.63
Significant positive correlation	12.39; 2,277.55	11.99; 1,308.92	9.52; 848.50	11.98; 228.86	18.96; 5,422.75	9.00; 90.63	14.59; 10,177.10
Non-significant correlation	45.85; 8,427.78	51.02; 5,570.20	47.69; 4,250.97	50.24; 960.09	50.65; 14,483.76	35.72; 359.59	48.85; 34,080.60
Significant negative correlation	17.52; 3,220.52	14.33; 1,565.03	18.56; 1,654.38	11.49; 219.61	15.23; 4,354.06	23.16; 233.11	16.13; 11,253.34
Extremely significant negative correlation	8.92; 1,638.96	9.46; 1,032.40	11.74; 1,046.56	9.77; 186.70	6.24; 1,783.43	16.28; 163.91	8.39; 5,855.34

Table 8. Acreage and share percentage of various correlations between fractional vegetation cover and precipitation in different counties and cities

Relevance	Administrative units in the Yarkand River Basin (%; km²)						
	Bachu County	Makit County	Shache County	Tumushuke City	Yecheng County	Zepu County	Entire area
Extremely significant positive correlation	26.91; 4,948.81	24.38; 2,661.64	49.69; 4,429.74	7.90; 150.99	41.01; 11,728.25	23.27; 234.23	34.77; 24,261.34
Significant positive correlation	17.57; 3,230.48	17.11; 1,867.84	12.43; 1,108.05	7.84; 149.81	19.32; 5,523.78	18.11; 182.32	17.00; 11,861.97
Non-significant correlation	42.98; 7,902.44	51.66; 5,640.25	30.26; 2,698.09	64.75; 1,237.78	28.69; 8,205.97	52.65; 530.04	37.91; 26,449.53
Significant negative correlation	10.12; 1,861.33	5.54; 605.15	6.37; 567.68	15.77; 301.39	8.07; 2,307.02	4.93; 49.60	8.02; 5,598.30
Extremely significant negative correlation	2.41; 443.88	1.32; 144.10	1.25; 111.50	3.75; 71.68	2.91; 832.34	1.04; 10.49	2.29; 1,600.86

Zepu County had a non-significant correlation of 52.65%, with weak precipitation effects, possibly due to vegetation already adapting to the current precipitation pattern.[39] In Bachu County and Makit County, the proportion of positive correlations was 44.48% and 41.49%, respectively, while the proportion of negative correlations was low (12.53% and 6.86%, respectively), indicating that precipitation moderately promotes vegetation.[37]

Correlation analysis between FVC and climate factors in the Yarkand River Basin from 2000 to 2023 showed high proportions of positive correlations between FVC and precipitation in Shache County and Yecheng County (62.12% and 60.33%, respectively), with Yecheng County exhibiting the strongest positive correlation with temperature (27.89%). In Zepu County and Tumushuke City, negative correlations and insignificant correlations dominated, reflecting regional differentiation. From 2000 to 2023, the correlations between FVC and temperature and precipitation under different land-use types in the Yarkand River Basin are presented in Tables 9 and 10. The correlation between FVC and temperature shows that farmland and forest have a high proportion of extremely significant negative correlations (21.97% and 20.45%, respectively), possibly due to high temperatures inhibiting vegetation growth.[39] Grasslands and bare land showed non-significant correlations exceeding 50% (50.91% and 49.58%, respectively), indicating a strong level of adaptability. Other land use types exhibited significant positive correlations at 71.26%, reflecting the warming-enhancing effect. Across the entire study area, there was a highly significant negative correlation of 8.39% and a significant positive correlation of 14.59%. In the correlation between FVC and precipitation, grasslands and forests showed a high proportion of highly

Table 9. Acreage and share percentage of various correlations between fractional vegetation cover and temperature in different land use types

Relevance	Administrative units in the Yarkand River Basin (%; km²)					
	Farmland	Forests	Grassland	Bare land	Others	Entire area
Extremely significant positive correlation	5.99; 458.36	3.84; 1.58	11.94; 1,864.92	13.61; 5,828.13	7.33; 244.19	12.05; 8,405.63
Significant positive correlation	9.03; 691.32	7.01; 2.89	11.23; 1,753.75	13.48; 5,771.08	71.26; 2,374.42	14.59; 10,177.10
Non-significant correlation	41.61; 3,184.27	40.89; 16.84	50.91; 7,950.35	49.58; 21,228.53	14.24; 474.57	48.85; 34,080.60
Significant negative correlation	21.40; 1,637.63	27.81; 11.45	18.22; 2,844.68	16.58; 7,096.71	3.69; 123.07	16.13; 11,253.34
Extremely significant negative correlation	21.97; 1,681.33	20.45; 8.42	7.70; 1,202.06	6.75; 2,888.92	3.48; 115.96	8.39; 5,855.34

Table 10. Acreage and share percentage of various correlations between fractional vegetation cover and precipitation in different land use types

Relevance	Administrative units in the Yarkand River Basin (%; km²)					
	Farmland	Forests	Grassland	Bare land	Others	Entire area
Extremely significant positive correlation	23.54; 1,783.11	46.75; 19.07	47.91; 7,328.56	34.73; 14,808.27	5.19; 169.69	34.77; 24,261.34
Significant positive correlation	18.87; 1,429.16	21.29; 8.68	9.66; 1,477.72	15.24; 6,498.38	71.78; 2,346.08	17.00; 11,861.97
Non-significant correlation	51.19; 3,876.49	30.29; 12.35	30.75; 4,704.05	39.41; 16,805.70	12.59; 411.48	37.91; 26,449.53
Significant negative correlation	5.61; 424.73	1.57; 0.64	9.08; 1,389.17	8.29; 3,534.86	6.39; 209.00	8.02; 5,598.30
Extremely significant negative correlation	0.79; 59.72	0.10; 0.04	2.59; 396.77	2.33; 991.66	4.05; 132.37	2.29; 1,600.86

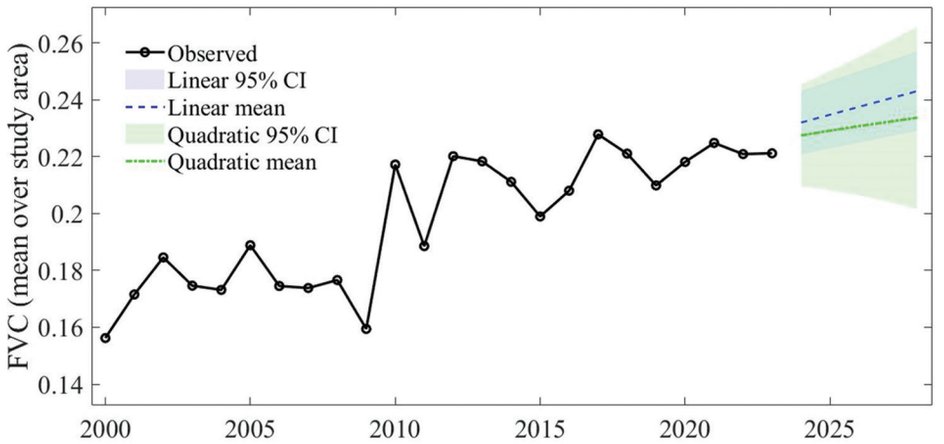


Figure 11. Annual FVC (2000–2023) and 5-year forecasts (2024–2028)
Abbreviations: CI: Confidence interval; FVC: Fractional vegetation cover.

significant positive correlations (47.91% and 46.75%), indicating that precipitation drives vegetation recovery. For farmland, there was a highly significant positive correlation of 23.54% and a significant negative correlation of 5.61%, reflecting a complex response. In terms of bare land, there was a positive correlation of 34.73% and a negative correlation of 10.62%, indicating significant fluctuations. Other land types showed a significant positive correlation of 71.78%, suggesting significant gains. The overall region showed a highly significant positive correlation of 12.05% and a negative correlation of 2.89%. The study reveals the differential effects of climate factors on FVC, with grasslands and forests benefiting from precipitation, farmland requiring optimized management, and bare land exhibiting low stability.

3.5. Short-term regression-based forecast of FVC dynamics

Based on the annual FVC series from 2000 to 2023, both linear and quadratic regression models were applied to forecast the short-term dynamics of FVC for 2024–2028, as shown in Figure 11. The linear regression model indicated a gradual increase in FVC from approximately 0.232 in 2024 to 0.243 in 2028. The quadratic model produced slightly lower estimates, from about 0.227 in 2024 to 0.234 in 2028, suggesting a modest deceleration in the rate of increase. In both cases, the 95% confidence intervals remained narrow, indicating relatively robust short-term forecasts. Overall, the results suggest that FVC in the study area will remain relatively stable with a slight upward trend over the next 5 years.

In particular, the forecasts for the first 2 years highlight the stability of the short-term dynamics. In 2024, the linear regression model predicts an FVC of approximately 0.232 (95% confidence interval [CI]: 0.221–0.243), while the quadratic model yielded a similar value of 0.227 (95% CI: 0.210–0.245). In 2025, both models projected a slight increase, with values of 0.235 (linear) and 0.229 (quadratic), again within narrow confidence intervals. These results suggest that the study area will experience only modest changes in vegetation cover at the beginning of the forecast period, reinforcing the conclusion of overall stability and a gradual upward trend.

4. Discussion

This study analyzed changes in FVC in the Yarkand River Basin based on the MODIS NDVI data from 2000 to 2023, revealing significant spatiotemporal heterogeneity. Before 2000, the average FVC value was 0.16–0.17, with significant fluctuations, reflecting the impacts of arid climate and early human activities. After 2000, due to oasis development and water resource management, FVC increased significantly, stabilizing at 0.21–0.23 after 2010, with approximately 70% of the area showing significant growth ($p < 0.05$, Sen+Mann–Kendall test). The FVC in Tumushuke City increased from 0.39 to 0.58, and the proportion of growth in Makit County reached 75%, indicating significant ecological restoration achievements. However, a local decline of approximately 8% occurred in 2022–2023, potentially related to the abnormal high temperature of 14.01°C, highlighting the regional vulnerability. The Hurst index analysis of the study area's time series reveals its long-term memory and trend persistence. This additional analysis using the climacogram method[41] addressed

the methodological concerns, confirming that the persistence estimated by the R/S approach is reliable and that both methods provide consistent evidence of strong long-term memory in regional FVC dynamics. Results show that the Hurst coefficient for the annual mean FVC is 0.81 (>0.5), indicating strong positive persistence at the regional scale, where FVC changes tend to maintain existing trends (e.g., continuous increase). In contrast, the mean Hurst coefficient for the entire raster grid is 0.44 (<0.5), suggesting anti-persistence at the local scale. This discrepancy arises from the spatial heterogeneity among oases, deserts, and mountainous areas within the region. Despite the overall positive persistence trend, local-scale complexities reduce the mean Hurst coefficient across the entire grid.

The similarity between the Hurst parameters of FVC (0.81–0.90) and those reported for climatic processes, such as temperature and precipitation (e.g., Dimitriadis *et al*.,[42] H ≈ 0.83), suggests a potential linkage between vegetation dynamics and the long-term memory of climate drivers. This resemblance suggests that vegetation cover does not evolve in isolation but may exhibit similar persistence properties to climatic variability at the macroscale. Such findings highlight the coupled and enduring interactions between vegetation and climate in arid ecosystems. Future research could therefore extend Hurst analysis to temperature and precipitation processes in the Yarkand River Basin, providing a more comprehensive understanding of the co-evolution and feedback mechanisms between climate and vegetation.

In terms of climate drivers, the temperature increased from 8.4°C to 9.4°C (an increase of approximately 1°C), promoting an increase in farmland FVC from 0.67 to 0.77 (high coverage of roughly 50%), possibly due to the extended growing season caused by the temperature increase. The FVC of bare land increased from 0.03 to 0.06, indicating a slight upward trend, particularly in Zepu and Bachu counties (low coverage of approximately 80% and high volatility of about 70%), possibly due to accelerated soil moisture evaporation caused by rising temperatures. Precipitation increased from 35 mm to 49 mm, with a peak of approximately 80 mm in 2005, significantly driving grassland FVC from 0.26 to 0.40 (increase of roughly 80%), particularly in Bachu and Tumushuke counties, consistent with improved soil moisture due to increased precipitation. The decrease of approximately 30% in farmland may be related to salinization caused by over-irrigation, contrasting with the increase of approximately 45% in grasslands, reflecting the differing responses of different land-use types.

County-level heterogeneity further supports these trends. FVC in Yecheng County was positively correlated with temperature by approximately 25%, while in Shache County, it was positively correlated with precipitation by approximately 60%, indicating that southern counties and cities benefit from improved water and heat conditions. In Zepu County, FVC was negatively correlated with temperature by approximately 40%, possibly due to high temperatures exacerbating drought stress. The differing responses of forested areas (with medium to high coverage of roughly 60% and fluctuation of approximately 2%) and bare land validate this mechanism.

The results of this study are highly consistent with recent research by Piao *et al.*,[3] which reported that climate change and human activities drive global vegetation greening. This is consistent with the growth trend of FVC in this study, emphasizing the roles of precipitation and oasis management. Wei *et al.*[43] analyzed the impact of climate fluctuation on vegetation growth, consistent with the increase in FVC in farmland. Cao *et al.*[44] found that drought exacerbates agricultural stress, aligning with the decline trend in farmland. Wang *et al.*[45] used MODIS data to analyze land surface temperature and vegetation dynamics, supporting the high-temperature stress mechanism in Zepu County. Qi *et al.*[46] investigated precipitation patterns and vegetation recovery, supporting the mechanism of FVC increase in grasslands. Urban *et al.*[47] explored the interactive effects of climate and land use, supporting the overall driving mechanism. Gao *et al.*[48] emphasize the short-term response of arid zone vegetation to climate fluctuation, consistent with the local decline observed in 2022–2023.

The findings of this study on FVC dynamics in the Yarkand River Basin have been corroborated by related research conducted in other arid and semi-arid regions, thereby reinforcing the robustness and applicability of our conclusions. For example, in the Taihangshan–Yanshan region, Yan *et al.*[49] documented a gradual upward trend in FVC (0.02/10 years) from 2000 to 2021, characterized by spatial heterogeneity primarily influenced by evapotranspiration and surface temperature. This aligns with our findings of significant positive correlations with precipitation ($r > 0.6$) and negative correlations with temperature ($r < -0.5$) in grasslands and farmlands, underscoring the pronounced climatic influence on vegetation dynamics. Similarly, Qiao *et al.*[50] identified a fluctuating upward FVC trend (0.26%/year) from 2000 to 2023 in the Qilian Mountains, exhibiting nonlinear responses to

temperature (a biphasic hump-shaped pattern with a threshold at 0°C) and precipitation (diminishing marginal effects with thresholds at 300 mm and 450 mm). These patterns align with our observed 1–2-month precipitation lag and topographic constraints, resulting in local anti-persistence (Hurst index of 0.44) in desert and mountainous areas. In the Yellow River Basin of Henan Province, Shi *et al.*[51] reported a substantial FVC enhancement (67.7%) from 1990 to 2020, with elevation as the dominant driver (q = 0.3) and strong coupling with precipitation, consistent with our results on elevation-induced spatial heterogeneity and climate-topography interactions. Liu *et al.*[52] observed FVC increases across 90.64% of the Jinghe River Basin area from 1998 to 2019, with significant correlations to the precipitation concentration index (18.47%), supporting our identification of precipitation's notable role in vegetation recovery. Furthermore, Tian *et al.*[53] in the Yangtze River Delta described post-2016 FVC fluctuations (initial decline followed by growth), predominantly driven by climate variables with spatial modulation by elevation and slope, which validates our post-2000 increase, post-2010 stabilization, and regional persistence based on the Hurst index (0.81). These congruences affirm that in arid regions, FVC improvements are primarily climate-mediated, with topographic factors exacerbating spatial variations and thresholds governing nonlinear responses.

The short-term forecasting results based on regression models indicate that FVC in the study area will remain relatively stable, with a slight upward trend, during 2024–2028, resulting in an overall increase of approximately 0.01 over the next 5 years. A closer look at the beginning of the forecast period reveals that in 2024, the linear and quadratic models predict FVC values of 0.232 and 0.227, respectively, which increase slightly in 2025 to 0.235 and 0.229, respectively. These narrow and consistent confidence intervals highlight the robustness of the forecasts, suggesting that no abrupt changes in vegetation are expected in the near term. Such stability aligns with the relatively steady patterns observed over the past two decades. It should be emphasized that these forecasts are derived from a univariate annual time series model and thus primarily represent an extrapolation of historical trends rather than a mechanistic explanation of vegetation dynamics. Consequently, the results are best interpreted as short-term, forward-looking references. Future studies could expand on this work by incorporating additional environmental or ecological drivers, such as climate variability or land-use changes, or by adopting more spatially explicit modeling approaches, to capture potential heterogeneity and provide more targeted insights for ecological management and policy-making.

This study relies on MODIS NDVI (250 m resolution) and 1 km climate data, which may overlook micro-scale fluctuations. Future research should integrate Landsat imagery and field measurements to better assess the impacts of high-temperature anomalies and combine socioeconomic data to explore policy implications. Moreover, clustering approaches based on vegetation types or climatic zones could be applied to identify regions with similar FVC dynamics,[54,55] estimate the relative contributions of climatic and anthropogenic drivers, and improve forecasting accuracy through regression or hybrid models. Such methods have been successfully applied in other scientific domains, demonstrating their potential to deepen the analysis of influencing factors in ecological studies.

Shache and Bachu counties need to protect their water resources to sustain grassland recovery, while Zepu and Tumushuke counties should promote the cultivation of drought-tolerant species. Yecheng and Shache counties should optimize irrigation management, and Zepu and Bachu counties should implement afforestation on bare land. Climate adaptation strategies, such as oasis expansion, are critical, and future monitoring should focus on temperature thresholds and precipitation fluctuation.

In view of the potential uncertainties associated with the application of large-scale remote sensing data, future research will strengthen the deployment of ground-based sampling sites and integrate them with multidimensional remote sensing information to establish a more refined data calibration framework. Moreover, the potential errors of the methods used in this study should be acknowledged. For example, the accuracy of the pixel dichotomy approach depends on the selection of NDVI thresholds, which may lead to underestimation or overestimation of FVC in heterogeneous landscapes. In contrast, Hurst analysis assumes time-series stationarity and may be sensitive to noise and short-term fluctuations, potentially biasing persistence estimates. Similarly, the Sen+Mann–Kendall tests, though widely applied, have been critically assessed by Serinaldi *et al*.,[56] who highlighted their mathematical inconsistencies and limitations under certain conditions, such as sample size and serial correlation. Future research may consider improved procedures, such as the Hamed[57] correction, to better account for long-term persistence. These limitations should be taken into account when interpreting the results. Simultaneously, machine learning methods can

be employed to optimize feature extraction and model fitting of remote sensing data, thereby enabling it to more closely approximate ground-based observations across spatial and temporal scales.

This study primarily examined the spatiotemporal variation characteristics of FVC and its correlation with climatic factors in the Yarkand River Basin from 2000 to 2023. Future research should further integrate anthropogenic indicators, such as population density, industrial development, and socioeconomic activities, to better capture the human footprint on FVC. In addition, time series decomposition methods could be applied to separate seasonal components from long-term trends, which would help reveal intra-annual fluctuations in vegetation dynamics and provide a more refined understanding of temporal variation patterns.

5. Conclusion

In summary, this study integrated MODIS NDVI data and climate observations from 2000 to 2023, utilizing pixel dichotomy modeling, Sen+Mann–Kendall trend analysis, and Pearson correlation to examine the spatiotemporal dynamics and climatic drivers of FVC in the Yarkand River Basin. The key findings are as follows:

(i) Significant spatial heterogeneity: FVC exhibited pronounced spatial variability across the Yarkand River Basin, with agricultural land and forests showing high coverage (51.75% and 60.81% medium-high to high coverage, respectively) compared to bare land's low coverage (95.58%). Yecheng County exhibited higher FVC (33.80% high coverage) compared to Bachu County (79.80% low coverage), primarily due to its favorable topography and irrigation practices. These county-level and land-use-specific patterns provided critical insights into spatially targeted ecological restoration in arid environments.

(ii) Temporal trends and stabilization: FVC increased significantly from 0.16 to 0.22 since 2000, stabilizing at 0.21–0.23 post-2010, with grasslands and croplands showing substantial growth (grassland FVC: 0.26 to 0.40; farmland FVC: 0.67 to 0.77). Bare land FVC remained low (0.03 to 0.06), indicating limited ecological recovery. This trend, supported by oasis expansion and water management, highlighted the efficacy of human interventions in enhancing FVC.

(iii) Persistence dynamics: The Hurst index analysis of the long-term time series revealed strong positive persistence (Hurst coefficient = 0.81), driven by oasis agriculture and ecological restoration, ensuring sustained FVC stability across the region. This positive persistence underscored the long-term effectiveness of environmental management in maintaining FVC, particularly in oasis areas, while highlighting the need for continued conservation efforts to address vulnerabilities in desert and mountainous zones.

(iv) Climatic influences: Temperature negatively impacted crop land and forest FVC (highly significant negative correlation: 21.97% for farmland, 20.45% for forests), especially in Zepu County (39.44% negative correlation), due to enhanced evapotranspiration. Precipitation positively drove grassland and forest FVC (highly significant positive correlation: 47.91% for grasslands, 46.75% for forests), with a 1–2-month lag effect notably in Shache and Yecheng Counties (positive correlation: ~60%). The regional temperature rise (from 8.4°C to 9.4°C) and precipitation increase (from 35 mm to 49 mm) aligned with FVC improvements, emphasizing the climate's critical role.

(v) Practical implications and scientific contributions: These findings provided actionable insights for ecological conservation and sustainable water resource management in arid regions. The high FVC stability in oasis areas (e.g., Tumushuke City, slope = 0.009, R^2 = 0.819) supported scaling irrigation and afforestation policies, while bare land's high volatility (74.51%) called for drought-tolerant species and windbreak plantations.

For climate adaptation, Shache and Yecheng Counties should optimize water allocation, while Bachu and Makit Counties require enhanced afforestation. The study's long-term (2000–2023) multi-scale analysis and novel findings, such as the precipitation lag effect and strong regional persistence, advanced the understanding of vegetation-climate interactions, offering a replicable framework for arid ecosystem research globally (e.g., supporting Sustainable Development Goal 13: Climate Action).

Acknowledgments

None.

Funding

This work was supported by the Sub-project of the Major Science and Technology Special Project of

Xinjiang Uygur Autonomous Region, China (Grant Number 2023A02012-1-3), titled "Research on the System for Optimal Allocation of Water Resources at the Watershed Scale."

Conflict of interest

The authors declare that they have no conflicts of interest. The funders had no role in the design of the study; in the collection, analysis, or interpretation of data; in the writing of the manuscript; or in the decision to publish the results.

Author contributions

Conceptualization: Guoqiang Qin, Kai Yuan, Guoliang Ding
Formal analysis: Guoqiang Qin, Kai Yuan
Investigation: Guoqiang Qin, Kai Yuan, Qiang Guo, Runbo Wang
Methodology: Guoqiang Qin, Kai Yuan
Writing–original draft: Guoqiang Qin, Kai Yuan
Writing–review & editing: Guoqiang Qin, Guoliang Ding

Availability of data

This study utilized datasets that are publicly available from the following sources:

(i) Meteorological data were obtained from the National Meteorological Information Center - China Meteorological Data Service Center (http://data.cma.cn).
(ii) Geospatial and environmental data were acquired from the National Earth System Science Data Center (http://www.geodata.cn).
(iii) Remote sensing data products were sourced from NASA Earth Data (https://earthdata.nasa.gov).
(iv) Data processing and analysis were conducted using the GEE platform (https://earthengine.google.com).

All data supporting the findings of this study are available from the aforementioned public repositories.

References

1. Tucker CJ, Pinzon JE, Brown ME, *et al*. An extended AVHRR 8-km NDVI dataset compatible with MODIS and SPOT vegetation NDVI data. *Int J Remote Sens*. 2005;26(20):4485-4498. doi: 10.1080/01431160500168686
2. Fensholt R, Langanke T, Rasmussen K, *et al*. Greenness in semi-arid areas across the globe 1981–2007 - an Earth Observing Satellite based analysis of trends and drivers. *Remote Sens Environ*. 2012;121:144-158. doi: 10.1016/j.rse.2012.01.017
3. Piao S, Wang X, Park T, *et al*. Characteristics, drivers and feedbacks of global greening. *Nat Rev Earth Environ*. 2019;1(1):14-27. doi: 10.1038/s43017-019-0001-x
4. Xu M, Wu H, Kang S, Chen X, Wang Y. Climate change decreased the effect of meltwater on cotton production in the Yarkant river basin of arid northwest China. *Irrig Sci*. 2024;42(1):99-114. doi: 10.1007/s00271-023-00862-x
5. Zhan C, Liang C, Zhao L, *et al.* Vegetation dynamics and its response to climate change in the yellow river Basin, China. *Front Environ Sci*. 2022;10:892747. doi: 10.3389/fenvs.2022.892747
6. Komissarov A, Komissarov M, Safin K, Ishbulatov M, Kovshov Y. Long-term irrigation effect on soil and vegetation cover of floodplain estuaries in the Southern Urals. *Asian J Water Environ Pollut*. 2020;17(1):83-90. doi: 10.3233/AJW200009
7. Chen Y, Li Z, Fan Y, Wang H, Deng H. Progress and prospects of climate change impacts on hydrology in the arid region of northwest China. *Environ Res*. 2015;139:11-19. doi: 10.1016/j.envres.2014.12.029
8. Li Z, Chen Y, Li W, Deng H, Fang G. Potential impacts of climate change on vegetation dynamics in Central Asia. *JGR Atmos*. 2015;120(24):12345-12356. doi: 10.1002/2015JD023618
9. Lioubimtseva E, Cole R, Adams JM, Kapustin G. Impacts of climate and land-cover changes in arid lands of Central Asia. *J Arid Environ*. 2005;62(2):285-308. doi: 10.1016/j.jaridenv.2004.11.005
10. Xiao J, Jin Z, Wang J. Assessment of the hydrogeochemistry and groundwater quality of the Tarim river basin in an extreme arid region, NW China. *Environ Manag*. 2014;53(1):135-146. doi: 10.1007/s00267-013-0198-2
11. Deng H, Chen Y, Wang H, Zhang S. Climate change with elevation and its potential impact on water resources in the Tianshan Mountains, Central Asia. *Global Planet Change*. 2015;135:28-37. doi: 10.1016/j.gloplacha.2015.09.015
12. Chen Z, Chen Y, Li B. Quantifying the effects of climate variability and human activities on runoff for Kaidu River Basin in arid region of northwest China. *Theor Appl Climatol*. 2013;111(3-4):537-545. doi: 10.1007/s00704-012-0680-4
13. Zhang Q, Gu X, Singh VP, Shi P, Sun P. More frequent flooding? Changes in flood frequency in the Pearl River basin, China, since 1951 and over the past 1000 years. *Hydrol Earth Syst Sci*. 2018;22(5):2637-2653. doi: 10.5194/hess-22-2637-2018
14. Amuti T, Luo G. Analysis of land cover change and its

driving forces in a desert oasis landscape of Xinjiang, northwest China. *Solid Earth*. 2014;5(2):1071-1085. doi: 10.5194/se-5-1071-2014
15. Zhao Y, Cao B, Sha L, *et al*. Land use and cover change and influencing factor analysis in the Shiyang River Basin, China. *J Arid Land*. 2024;16(2):246-265. doi: 10.1007/s40333-024-0071-6
16. Xu J, Chen Y, Li W, Nie Q, Hong Y, Yang Y. The nonlinear hydro-climatic process in the Yarkand River, northwestern China. *Stoch Environ Res Risk Assess*. 2013;27(2):389-399. doi: 10.1007/s00477-012-0606-9
17. Bhambri R, Bolch T, Chaujar RK, Kulshreshtha SC. Glacier changes in the Garhwal Himalaya, India, from 1968 to 2006 based on remote sensing. *J Glaciol*. 2011;57(203):543-556. doi: 10.3189/002214311796905604
18. Fu A, Li W, Wang Y, Bai Y. Basic and target eco-environment water requirements of a dry inland river under typical flow frequencies in China. *PeerJ*. 2020;8:e8285. doi: 10.7717/peerj.8285
19. Hou Y, Chen Y, Ding J, Li Z, Li Y, Sun F. Ecological impacts of land use change in the arid Tarim river Basin of China. *Remote Sens*. 2022;14(8):1894. doi: 10.3390/rs14081894
20. Yi Y, Liu S, Zhu Y, Wu K, Xie F, Saifullah M. Spatiotemporal heterogeneity of snow cover in the central and western Karakoram Mountains based on a refined MODIS product during 2002–2018. *Atmos Res*. 2021;250:105402. doi: 10.1016/j.atmosres.2020.105402
21. Sulla-Menashe D, Friedl MA. *User Guide to Collection 6 MODIS Land Cover (MCD12Q1 and MCD12C1) Product.* Available from: https://lpdaac.usgs.gov/documents/101/MCD12_User_Guide_V6.pdf [Last accessed on 2025 Apr 13]. doi: 10.5067/MODIS/MCD12Q1.006
22. Gorelick N, Hancher M, Dixon M, Ilyushchenko S, Thau D, Moore R. Google earth engine: Planetary-scale geospatial analysis for everyone. *Remote Sens Environ*. 2017;202:18-27. doi: 10.1016/j.rse.2017.06.031
23. Kaur A, Ghosh S, Das SK. Satellite image-based land use/land cover dynamics and forest cover change analysis (1996-2016) in Odisha, India. *Asian J Water Environ Pollut*. 2019;16(1):25-39. doi: 10.3233/AJW190004
24. Li F, Chen W, Zeng Y, Zhao Q, Wu B. Improving estimates of grassland fractional vegetation cover based on a pixel dichotomy model: A case study in inner Mongolia, China. *Remote Sens*. 2014;6(6):4705-4722. doi: 10.3390/rs6064705
25. Jiapaer G, Chen X, Bao A. A comparison of methods for estimating fractional vegetation cover in arid regions. *Agric Forest Meteorol*. 2011;151(12):1698-1710. doi: 10.1016/j.agrformet.2011.07.004
26. Shi S, Yu J, Wang F, Wang P, Zhang Y, Jin K. Quantitative contributions of climate change and human activities to vegetation changes over multiple time scales on the Loess Plateau. *Sci Total Environ*. 2021;755:142419. doi: 10.1016/j.scitotenv.2020.142419
27. Li X, Liu Y, Wang L. Change in fractional vegetation cover and its prediction during the growing season based on machine learning in southwest China. *Remote Sens*. 2024;16(19):3623. doi: 10.3390/rs16193623
28. Fu B, Yang W, Yao H, *et al*. Evaluation of spatio-temporal variations of FVC and its relationship with climate change using GEE and Landsat images in Ganjiang River Basin. *Geocarto Int*. 2022;37(26):13658-13688. doi: 10.1080/10106049.2022.2082551
29. Zeng B, Wen B, Zhang X, *et al*. Analysis on spatiotemporal variation in soil drought and its influencing factors in Hebei province from 2001 to 2020. *Agriculture*. 2025;15(10):1109. doi: 10.3390/agriculture15101109
30. Yang R, Li X, Mao D, Wang Z, Tian Y, Dong Y. Examining fractional vegetation cover dynamics in response to climate from 1982 to 2015 in the Amur River Basin for SDG 13. *Sustainability*. 2020;12(14):5866. doi: 10.3390/su12145866
31. Mao L, Pei X, He C, *et al*. Spatiotemporal changes in vegetation cover and soil moisture in the lower reaches of the Heihe river under climate change. *Forests*. 2024;15(11):1921. doi: 10.3390/f15111921
32. Huang J, Li Y, Fu C, *et al*. Dryland climate change: Recent progress and challenges. *Rev Geophys*. 2017;55(3):719-778. doi: 10.1002/2016RG000550
33. Yao T, Bolch T, Chen D, *et al*. The imbalance of the Asian water tower. *Nat Rev Earth Environ*. 2022;3(10):618-632. doi: 10.1038/s43017-022-00299-4
34. Immerzeel WW, Lutz AF, Andrade M, *et al*. Importance and vulnerability of the world's water towers. *Nature*. 2020;577(7790):364-369. doi: 10.1038/s41586-019-1822-y
35. Duveiller G, Hooker J, Cescatti A. The mark of vegetation change on Earth's surface energy balance. *Nat Commun*. 2018;9(1):679. doi: 10.1038/s41467-017-02810-8
36. Zhu Z, Piao S, Myneni RB, *et al*. Greening of the Earth and its drivers. *Nat Clim Change*. 2016;6(8):791-795. doi: 10.1038/nclimate3004
37. Zhou Q, Chen W, Wang H, Wang D. Spatiotemporal evolution and driving factors analysis of fractional vegetation coverage in the arid region of northwest China. *Sci Total Environ*. 2024;954:176271. doi: 10.1016/j.scitotenv.2024.176271

38. Zhang K, Kimball JS, Nemani RR, Running SW. A continuous satellite-derived global record of land surface evapotranspiration from 1983 to 2006. *Water Resour Res*. 2010;46(9):2009WR008800.
doi: 10.1029/2009WR008800
39. Deng Y, Wang X, Wang K, *et al*. Responses of vegetation greenness and carbon cycle to extreme droughts in China. *Agric Forest Meteorol*. 2021;298-299:108307.
doi: 10.1016/j.agrformet.2020.108307
40. Vicente-Serrano SM, Gouveia C, Camarero JJ, *et al.* Response of vegetation to drought time-scales across global land biomes. *Proc Natl Acad Sci USA*. 2013;110(1):52-57.
doi: 10.1073/pnas.1207068110
41. Dimitriadis P, Koutsoyiannis D. Climacogram versus autocovariance and power spectrum in stochastic modelling for Markovian and Hurst–Kolmogorov processes. *Stoch Environ Res Risk Assess*. 2015;29(6):1649-1669.
doi: 10.1007/s00477-015-1023-7
42. Dimitriadis P, Koutsoyiannis D, Iliopoulou T, Papanicolaou P. A Global-scale investigation of stochastic similarities in marginal distribution and dependence structure of key hydrological-cycle processes. *Hydrology*. 2021;8(2):59.
doi: 10.3390/hydrology8020059
43. Wei S, Li X, Wang K, Wang T, Piao S. Two decades of persistent greening in China despite 2023 climate extremes. *Sci China Earth Sci*. 2025;68(4):1064-1073.
doi: 10.1007/s11430-024-1530-7
44. Cao S, Zhang L, He Y, *et al*. Effects and contributions of meteorological drought on agricultural drought under different climatic zones and vegetation types in Northwest China. *Sci Total Environ*. 2022;821:153270.
doi: 10.1016/j.scitotenv.2022.153270
45. Wang H, Guan H, Liu B, Chen X. Impacts of climate extremes on vegetation dynamics in a transect along the Hu Line of China. *Ecol Indic*. 2023;155:111043.
doi: 10.1016/j.ecolind.2023.111043
46. Qi X, Jia J, Liu H, Lin Z. Relative importance of climate change and human activities for vegetation changes on China's silk road economic belt over multiple timescales. *CATENA*. 2019;180:224-237.
doi: 10.1016/j.catena.2019.04.027
47. Urban MC, Alberti M, De Meester L, *et al*. Interactions between climate change and urbanization will shape the future of biodiversity. *Nat Clim Chang*. 2024;14(5):436-447.
doi: 10.1038/s41558-024-01996-2
48. Gao X, Wen R, Lo K, Li J, Yan A. Heterogeneity and non-linearity of ecosystem responses to climate change in the Qilian Mountains National Park, China. *J Arid Land*. 2023;15(5):508-522.
doi: 10.1007/s40333-023-0101-9
49. Yan F, Guo X, Zhang Y, *et al*. Analysis of the multiple drivers of vegetation cover evolution in the Taihangshan-Yanshan region. *Sci Rep.* 2024;14(1):15306.
doi: 10.1038/s41598-024-66053-6
50. Qiao B, Cao X, Yang H, *et al*. Nonlinear threshold effects of environmental drivers on vegetation cover in mountain ecosystems: From constraint mechanisms to adaptive management. *Ecol Indic*. 2025;173:113328.
doi: 10.1016/j.ecolind.2025.113328
51. Shi S, Wang X, Hu Z, *et al*. Geographic detector-based quantitative assessment enhances attribution analysis of climate and topography factors to vegetation variation for spatial heterogeneity and coupling. *Glob Ecol Conserv*. 2023;42:e02398.
doi: 10.1016/j.gecco.2023.e02398
52. Liu Y, Huang T, Qiu Z, Guan Z, Ma X. Effects of precipitation changes on fractional vegetation cover in the Jinghe River basin from 1998 to 2019. *Ecol Inform*. 2024;80:102505.
doi: 10.1016/j.ecoinf.2024.102505
53. Tian X, Tao Z, Xie Y, Shao W, Zhang S. Spatiotemporal evolution and driving mechanism of fractional vegetation coverage in the Yangtze river delta. *IEEE J Sel Top Appl Earth Observ Remote Sens*. 2024;17:10979-10997.
doi: 10.1109/JSTARS.2024.3407727
54. Marincowitz S, Pham NQ, Wingfield BD, Roets F, Wingfield MJ. Microfungi associated with dying *Euphorbia mauritanica* in South Africa and their relative pathogenicity. *Fungal Syst Evol.* 2023;12(1):59-72.
doi: 10.3114/fuse.2023.12.04
55. Litvinenko V. *Advances in Raw Material Industries for Sustainable Development Goals*. 1st ed. Boca Raton: CRC Press; 2020.
doi: 10.1201/9781003164395
56. Serinaldi F, Chebana F, Kilsby CG. Dissecting innovative trend analysis. *Stoch Environ Res Risk Assess*. 2020;34(5):733-754.
doi: 10.1007/s00477-020-01797-x
57. Hamed KH. Trend detection in hydrologic data: The Mann-Kendall trend test under the scaling hypothesis. *J Hydrol*. 2008;349(3-4):350-363.
doi: 10.1016/j.jhydrol.2007.11.009

ACCSCIENCE PUBLISHING

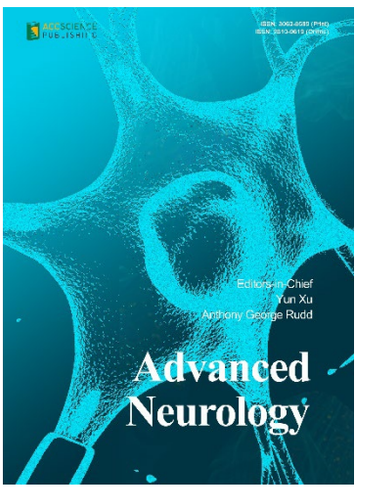
OUR JOURNALS



Organoid Research (OR) is an international, peer-reviewed journal dedicated to advancing the field of organoid science by publishing high-quality research articles, reviews, and perspectives. The journal focuses on studies that provide significant conceptual, experimental, and translational advances in the development and application of organoid technologies.

OR welcomes submissions spanning diverse areas of organoid science, including but not limited to stem cell biology, tissue engineering, regenerative medicine, disease modeling, and drug discovery. The journal encourages papers that explore bioengineered organoids, organoid-based systems biology, and the integration of organoids with clinical research. Special emphasis is placed on contributions that advance novel approaches to organoid development, including the use of cutting-edge bioengineering techniques, materiobiology, and integrative technologies such as artificial intelligence, high-throughput screening, and precision medicine. Additionally, the journal values research that delves into ethical considerations and challenges related to the clinical translation of organoid systems.

Advanced Neurology is a peer-reviewed and open-access journal that aims to publish and disseminate novel research in the breadth of neurology and neuroscience. The journal aims to advance our understanding in the nervous system and provide a platform to neuroscientists and physicians to showcase their findings in original fundamental and clinical research as well as to present new ideas that highlight the changes in the neurological clinical practice.



Advanced Neurology covers subject areas, including but not limited to the following:

- Neurological disorders
- Neurodegenerative disease
- Cerebrovascular disease
- Epilepsy and movement disorders
- Neuroimmune disease
- Neurological infections
- Muscle disease
- Molecular and cellular neuroscience
- Systems neuroscience
- Cognitive neuroscience
- Computational modeling of nervous system

Start a new journal

Write to us via email if you are interested to start a new journal with AccScience Publishing. Please attach your CV, professional profile page and a brief pitch proposal in your email. We shall inform you of our decision whether we are interested to collaborate in starting a new journal.

Contact: info@accscience.com

https://accscience.com/journal/AJWEP



Contact
www.accscience.com
9 Raffles Place, Republic Plaza 1 #06-00 Singapore 048619
Email: editorial@accscience.com
Phone: +65 8182 1586